Vessel Based Imaging Techniques

Diagnosis, Treatment, and Prevention

Chun Yuan
Thomas S. Hatsukami
Mahmud Mossa-Basha
Editors

Springer

Vessel Based Imaging Techniques

Chun Yuan • Thomas S. Hatsukami
Mahmud Mossa-Basha
Editors

Vessel Based Imaging Techniques

Diagnosis, Treatment, and Prevention

Springer

Editors
Chun Yuan
University of Washington
Seattle, WA
USA

Thomas S. Hatsukami
University of Washington
Seattle, WA
USA

Mahmud Mossa-Basha
University of Washington
Seattle, WA
USA

ISBN 978-3-030-25248-9 ISBN 978-3-030-25249-6 (eBook)
https://doi.org/10.1007/978-3-030-25249-6

This Springer imprint is published by the registered company Springer Nature Switzerland AG
The registered company address is: Gewerbestrasse 11, 6330 Cham, Switzerland

Chun Yuan would like to dedicate this book to many Faculty, Fellows, and Staff who have contributed to the work of the Vascular Imaging Lab at the University of Washington.

Tom Hatsukami would like to also dedicate this book to Drs. D. Eugene Strandness and Alexander Clowes for their mentorship and encouragement, and to the many individuals who volunteered to participate in our clinical research studies.

Mahmud Mossa-Basha would like to dedicate this book to the many mentors, collaborators and educators who have helped him throughout his career at Henry Ford Hospital, Johns Hopkins University and University of Washington, as well as his very supportive wife and family.

Contents

Contributors

Muhannad Aboud Abbasi, MD Department of Radiology, Northwestern Memorial Hospital, Chicago, IL, USA

Niranjan Balu, PhD University of Washington, Department of Radiology, Seattle, WA, USA

Liisa L. Bergmann, MD Cardiovascular Imaging Section, Department of Radiology, University of Wisconsin School of Medicine and Public Health, Madison, WI, USA

Waleed Brinijiki, MD Department of Radiology, Mayo Clinic, Rochester, MN, USA

James Carr, MD Department of Radiology, Northwestern Memorial Hospital, Chicago, IL, USA

Eugene M. Cilento, PhD Department of Pathology, University of Washington, School of Medicine, Seattle, WA, USA

Mat J. A. P. Daemen, MD, PhD Department of Pathology, Amsterdam Cardiovascular Sciences (ACS), Amsterdam UMC, University of Amsterdam, Amsterdam, The Netherlands

J. Kevin DeMarco, MD Department of Radiology, Walter Reed National Military Medical Center, Bethesda, MD, USA

Department of Radiology, Uniformed Services University of the Health Sciences, Bethesda, MD, USA

Damini Dey, PhD Biomedical Imaging Research Institute, Cedars-Sinai Medical Center, Los Angeles, CA, USA

Department of Medicine, University of California, Los Angeles, Los Angeles, CA, USA

Aloke V. Finn, MD CVPath Institute Inc., Gaithersburg, MD, USA

Christopher J. François, MD Cardiovascular Imaging Section, Department of Radiology, University of Wisconsin School of Medicine and Public Health, Madison, WI, USA

Zhongbao Gao, MD, PhD Department of Healthcare, Second Medical Center, Chinese PLA General Hospital, Beijing, China

Thomas S. Hatsukami, MD Department of Surgery, University of Washington, Seattle, WA, USA

John Huston III, MD Department of Radiology, Mayo Clinic, Rochester, MN, USA

Matthijs F. Jansen, MD Department of Medical Biochemistry, Amsterdam Cardiovascular Sciences (ACS), Amsterdam UMC, University of Amsterdam, Amsterdam, The Netherlands

Department of Cardiology, Amsterdam UMC, VU Medical Center, Amsterdam, The Netherlands

Hiroyuki Jinnouchi, MD CVPath Institute Inc., Gaithersburg, MD, USA

William Kerwin, PhD University of Washington Vascular Imaging Laboratory, Department of Radiology, Seattle, WA, USA

Frank D. Kolodgie, PhD CVPath Institute Inc., Gaithersburg, MD, USA

Christopher M. Kramer, MD Division of Cardiovascular Medicine and Department of Radiology and Medical Imaging, University of Virginia Health System, Charlottesville, VA, USA

Debiao Li, PhD Biomedical Imaging Research Institute, Cedars-Sinai Medical Center, Los Angeles, CA, USA

Department of Medicine, University of California, Los Angeles, Los Angeles, CA, USA

Department of Bioengineering, University of California, Los Angeles, Los Angeles, CA, USA

João Augusto Costa Lima, MD Johns Hopkins Hospital, Baltimore, MD, USA

Radiology and Epidemiology at the Johns Hopkins School of Medicine, Baltimore, MD, USA

Adrián I. Löffler, MD Division of Cardiovascular Medicine, University of Virginia Health System, Charlottesville, VA, USA

Esther Lutgens, MD, PhD Department of Medical Biochemistry, Amsterdam Cardiovascular Sciences (ACS), Amsterdam UMC, University of Amsterdam, Amsterdam, The Netherlands

Institute for Cardiovascular Prevention (IPEK), Ludwig Maximilians University, Munich, Germany

Michael Markl, PhD Department of Radiology, Northwestern University, Feinberg School of Medicine, Chicago, IL, USA

Department of Biomedical Engineering, McCormick School of Engineering, Northwestern University, Evanston, IL, USA

Mateus Diniz Marques, MD Federal University of Santa Maria, Santa Maria, Brazil

Mary M. McDermott, MD Northwestern University Feinberg School of Medicine, Chicago, IL, USA

Zach Miller, MFA University of Washington Vascular Imaging Laboratory, Department of Radiology, Seattle, WA, USA

Mahmud Mossa-Basha, MD University of Washington, Seattle, WA, USA

Pim van Ooij, PhD Department of Radiology & Nuclear Medicine, Amsterdam University Medical Centers, location AMC, Amsterdam, The Netherlands

Ashitha Pathrose, MD Department of Radiology, Northwestern Memorial Hospital, Chicago, IL, USA

Krishnan Ravindran, MD Department of Radiology, Mayo Clinic, Rochester, MN, USA

Maria Romero, MD CVPath Institute Inc., Gaithersburg, MD, USA

David Saloner, PhD Department of Radiology and Biomedical Imaging, University of California San Francisco, San Francisco, CA, USA

Ali Mostafa Serhal, MD Department of Radiology, Northwestern Memorial Hospital, Chicago, IL, USA

Tessandra Stewart, PhD Department of Pathology, University of Washington, School of Medicine, Seattle, WA, USA

Jie Sun, MD Department of Radiology, University of Washington, Seattle, WA, USA

Renu Virmani, MD CVPath Institute Inc., Gaithersburg, MD, USA

Justin E. Vranic, MD University of Washington, Department of Radiology, Seattle, WA, USA

Bruce Alan Wasserman, MD Division of Neuroradiology, The Russell H. Morgan Department of Radiology and Radiological Sciences, Johns Hopkins University, Baltimore, MD, USA

Yibin Xie, PhD Biomedical Imaging Research Institute, Cedars-Sinai Medical Center, Los Angeles, CA, USA

Noushin Yahyavi-Firouz-Abadi, MD Division of Neuroradiology, The Russell H. Morgan Department of Radiology and Radiological Sciences, Johns Hopkins University, Baltimore, MD, USA

Chun Yuan, PhD University of Washington, Seattle, WA, USA

Jing Zhang, MD, PhD Department of Pathology, University of Washington, School of Medicine, Seattle, WA, USA

Zechen Zhou, PhD Philips Research North America, Cambridge, MA, USA

Introduction

In an article by Skinner et al., with Dr. Russell Ross and James Nelson as the senior authors in the first issue of Nature Medicine, 1995, the authors claimed that magnetic resonance imaging (MRI) was able to non-invasively identify features of the atherosclerotic plaque and their progression in a rabbit model [1]. They further claimed that the advancement in imaging had significant implications for determining risks and benefits associated with various therapeutic approaches. The article was accompanied by comments from Dr. Peter Libby [2], titled "Lesion versus Lumen," that highlighted the information gap between luminal imaging (angiography and Doppler ultrasound) and vessel wall imaging, an area where imaging would play an ever more important role.

These two articles marked the beginning of a new era in vessel wall imaging, and another advancement followed within a year, in an article by Wildy et al. [3], with Dr. D. Eugene Strandness as the senior author. This article linked signals coming from human carotid MRI of atherosclerotic plaques (taking advantage of improved signal-to-noise via a novel MRI coil design by Dr. Cecil Hayes) to a pioneering histology validation process developed by Strandness and colleagues. With a solid footing based on histopathology, this in vivo imaging and ex vivo histology comparison helped propel vessel wall imaging to a much higher level of scientific rigor and acknowledgment of its importance.

The first intracranial vessel wall MRI paper was published by Aoki et al. [4] in 1995, and focused on enhancement of intracranial internal carotid and vertebral arteries and their significant correlation with patient age. The topic was not heavily visited in the literature until Kuker et al. [5] published a case series on the appearance of vasculitis on intracranial vessel wall MRI. The technique however, remained obscure, with only a few institutions worldwide performing the exams. With the publication of utilization of 3D techniques [6] that afforded shorter scans with better visualization of disease due to improved resolution and less need for radiologist scan involvement, the technique began to gain increased attention. With increased research, the value of intracranial vessel wall MRI in its application to all intracranial vascular diseases became apparent.

More than 20 years later, many more advancements have been, and continue to be made, in the field of vessel wall imaging. These advancements have led to a greater understanding of the role imaging can play in studying vessel wall pathology. Dr. Alexander Clowes and colleagues recognized early that advanced vascular imaging techniques provide a non-invasive window to visualize processes involved in the pathogenesis of high-risk atherosclerosis [7]. More recently, increasing evidence highlight the important role of vessel wall imaging for directing clinical diagnosis and treatment. Vessel wall imaging continues to advance in numerous vascular beds, but has now established itself as an important imaging technique for risk stratification and disease differentiation in various vasculopathies. Now, we present this book as a summary of the current state-of-the-art. The intended readers are medical professionals, especially those dealing with vascular disease diagnosis, treatment, pathology, and prevention, and for clinical and basic scientific researchers in imaging, vascular biology, and related fields.

This book is divided into seven sections based on the divisions of vascular systems. Each section generally has a pathological review of the vascular system that sets the stage for introduction of current imaging approaches, followed by a detailed description of vessel wall imaging.

A later section addresses general imaging techniques, analysis tools available for vessel wall imaging as well as new trends in technical developments. New advancements in AI, imaging technology, and clinical advancements continue to make this an exciting field.

Seattle, WA, USA

Thomas S. Hatsukami
Mahmud Mossa-Basha
Chun Yuan

References

1. Skinner MP, Yuan C, Mitsumori L, Hayes CE, Raines EW, Nelson JA, Ross R. Serial magnetic resonance imaging of experimental atherosclerosis detects lesion fine structure, progression and complications in vivo. Nature Medicine. 1995;1(1):69–73.
2. Libby P. Lesion versus lumen. Nat Med. 1995;1(1):17–8. PubMed PMID: 7584941.
3. Wildy KS, Yuan C, Tsuruda JS, Ferguson MS, Wen N, Subramaniam DS, Strandness DE. Atherosclerosis of the carotid artery: evaluation by magnetic resonance angiography. J Magn Reson Imaging. 1996;6(5):726–32. PubMed PMID: 8890010.
4. Aoki S, Shirouzu I, Sasaki Y, Okubo T, Hayashi N, Machida T, et al. Enhancement of the intracranial arterial wall at MR imaging: relationship to cerebral atherosclerosis. Radiology. 1995;194(2):477-81. Epub 1995/02/01. doi: 10.1148/radiology.194.2.7824729. PubMed PMID: 7824729.
5. Kuker W, Gaertner S, Nagele T, Dopfer C, Schoning M, Fiehler J, et al. Vessel wall contrast enhancement: a diagnostic sign of cerebral vasculitis. Cerebrovascular diseases (Basel, Switzerland). 2008;26(1):23–9. Epub 2008/05/31. doi: 10.1159/000135649. PubMed PMID: 18511868; PubMed Central PMCID: PMC2813800.

6. Qiao Y, Steinman DA, Qin Q, Etesami M, Schar M, Astor BC, et al. Intracranial arterial wall imaging using three-dimensional high isotropic resolution black blood MRI at 3.0 Tesla. J Magn Reson Imaging. 2011;34(1):22–30. Epub 2011/06/24. doi: 10.1002/jmri.22592. PubMed PMID: 21698704.
7. Chu B, Yuan C, Takaya N, Shewchuk JR, Clowes AW, Hatsukami TS. Images in cardiovascular medicine. Serial high-spatial-resolution, multisequence magnetic resonance imaging studies identify fibrous cap rupture and penetrating ulcer into carotid atherosclerotic plaque. Circulation. 2006;113:e660–661

Part I
Intracranial Arteries

Chapter 1
Vascular Dysfunction and Neurodegenerative Disease

Zhongbao Gao, Eugene M. Cilento, Tessandra Stewart, and Jing Zhang

The brain is an essential organ for a diverse array of functions within the human body. It is also a complex organ, consisting of nearly 100 billion neurons, the cells responsible for basic and complex neurological processing. To maintain proper neuronal functionality, the brain requires a constant provision of oxygen and nutrients as its own energy stores are scarce [1]. The brain is considered the most metabolically active organ in the human body, consuming about 20% of the body's oxygen and other nutrients supplied by the vascular system, although comprising only 2% of the total body weight. Therefore, the brain must rely on uninterrupted external delivery of oxygen and nutrients within the blood of the vascular system to meet its intense metabolic demands.

Neurodegenerative diseases, e.g., Alzheimer's disease (AD), Parkinson's disease (PD), and amyotrophic lateral sclerosis (ALS), are incurable and debilitating conditions that result from the progressive degeneration and/or death of neurons in the brain and spinal cord. Neurodegeneration results from a combination of genetic factors, viruses, alcoholism, toxins, and repetitive brain injuries, which cumulatively drive changes in brain function, microenvironment, and, ultimately, diminished neuronal survival. Recent evidence also suggests that cerebrovascular dysfunction contributes to dementia and AD [2], PD [3], as well as ALS [4].

The relationship between cerebrovascular dysfunction and neurodegenerative diseases is complex, as they share many of the same risk factors, and their overlap increases with age. Both cerebrovascular and neurodegenerative diseases increase significantly after 60 years of age in almost all populations worldwide [5]. Age is

Z. Gao
Department of Healthcare, Second Medical Center, Chinese PLA General Hospital, Beijing, China

E. M. Cilento · T. Stewart · J. Zhang (✉)
Department of Pathology, University of Washington, School of Medicine, Seattle, WA, USA
e-mail: cilento@uw.edu; stewarth@uw.edu; zhangj@uw.edu

C. Yuan et al. (eds.), *Vessel Based Imaging Techniques*,
https://doi.org/10.1007/978-3-030-25249-6_1

the strongest risk factor for brain degeneration, regardless of whether the mechanism is vascular, neurodegenerative, or a combination. Brains of demented subjects often exhibit more than one type of pathology. For example, in addition to the classical amyloid and tau pathology, vascular lesions are frequently found to coexist with pathological changes related to AD in elderly subjects [6]. Remarkably, the length of brain capillaries is reduced in aging and neurodegenerative disorders [7]. These vascular reductions can diminish transport of energy substrates and nutrients across the blood-brain barrier (BBB) and reduce the clearance of potential neurotoxins from the brain. Impairments of other brain vessel functions including autoregulation, neurovascular uncoupling, BBB leakage, and decreased cerebrospinal fluid are responsible for variable degrees of neurodegeneration in the aging population.

Normal Neurovascular Structure and Function of the Brain

The integrity of the vascular system is accomplished through a vast vascular network of arteries, arterioles, capillaries, and veins to assure the continuous supply of oxygen and nutrients, as well as provide a route for washout of metabolic waste products. Indeed, it has been estimated that nearly every neuron in the human brain has its own capillary [8, 9]. The normal neuronal-vascular relationship is critical for normal brain functioning.

Blood-Brain Barrier

The BBB is a highly specialized structure of the neurovascular system composed of a microvascular endothelium, as well as proximal astrocytes, basement membrane, and pericytes. It maintains separation between the components of the circulating blood and those of the central nervous system (CNS) and controls homeostatic balance between these systems. Under physiologic conditions, the BBB ensures constant supply of nutrients (oxygen, glucose, and other substances) for brain cells and guides the inflammatory cells to respond to the changes of the local environment. To meet the energetic demands of the brain, glial cells work with neurons to regulate the function and dilation of blood vessels in response to metabolic requirements. The concerted efforts of all of these cell types together are conceptualized as the neurovascular unit (NVU), which couples brain activity to vascular supply, allowing the import of metabolic materials, as well as providing for the export of waste, via the BBB.

Anatomically and functionally, endothelial cells (ECs) situate at the interface between the blood and the brain. Cerebral ECs are not fenestrated but are interconnected by tight junctions forming a continuous BBB [10]. It has become apparent that ECs require contacts with various CNS cell types to establish BBB characteristics [11]. They compose the vessel walls and generate a physical barrier imperme-

able to most large or charged molecules through abundant tight junctions. From this position, they perform essential biological functions, including barrier, transport of micronutrients and macronutrients, receptor-mediated signaling, leukocyte trafficking, and osmoregulation. They express a wide variety of transporters and receptors, engaging in transporter- and vesicle-based transfer of molecules between the brain and the blood. Specialized receptors on the membrane of ECs initiate intracellular signaling cascades in response to agonists that activate specific receptors or changes in shear stress at the cell surface produced by changes in the rate of blood flow. The best described transporter is the glucose transporter isoform 1 that becomes highly expressed upon BBB formation. Gap junctions permit cross talk between adjacent ECs allowing the transmission of intracellular responses. Once initiated, these cascades trigger the release of potent vasodilator substances such as nitric oxide (NO) and prostacyclin and vasoconstrictors, such as endothelin and endothelium-derived constrictor factor [12, 13].

Astrocytes are the most numerous cell type in the CNS, and their specialized end-feet cover nearly the entire surface of CNS microvessels. Astrocytes are star-shaped cells with many processes emanating from the cell body and surround most portions of the microvessels and capillaries and as part of the NVU interact with ECs through the end-feet of their processes [14, 15]. Astrocytes in the brain perform an array of homeostatic functions. Their processes encircle the synapses, where they control the extracellular pH, ion balance, and neurotransmitter concentrations necessary for optimal neuronal function. These activities make them ideally suited for sensing the demands of the associated neurons, which they translate to the other cells of the BBB via their end-feet. Thus, they act as a link between synaptic activity and the cerebrovascular cells by translating information between neurons and cerebral microvessels. Astrocytes and ECs also influence each other's structure and function. For example, interaction of astrocytes with ECs can greatly enhance EC tight junctions and reduce gap junctional area, resulting in decreased permeability of the EC layer. Therefore, astrocyte-microvascular EC interactions are essential for a functional NVU [15]. Moreover, during intense activity, astrocytes signal the energy demands of neurons to the vascular cells mediating cerebral blood flow (CBF) which then can signal an increased demand in blood flow [16]. Astrocytes have also been shown to regulate CBF responses by influencing contractile properties of small penetrating intracerebral arteries [17].

Pericytes are mural cells covering the abluminal surface of microvessels. Pericytes are flat, undifferentiated, tissue cells with contractile potential that develop around capillary walls, contributing to stability of microvessels and covering a major part of the abluminal endothelial surface. In the neurovascular unit, pericytes are embedded in a thin layer of basement membrane, which separates them from ECs and end-feet of astrocytes. While most of the pericyte bodies and processes do not attach to ECs because of the basement membrane, interdigitations of pericyte and EC membranes can directly connect in the area lacking basement membrane, forming "peg-and-socket" connections [18, 19]. Together with the ensheathment of brain capillaries by astrocytic end-feet, the close contact of ECs with pericytes via the peg-and-socket junctions within a common basal lamina is crucial for establishing and maintaining

the BBB [20]. The CNS vasculature has significantly higher pericyte coverage compared with peripheral vessels, and pericytes have an important role in regulating capillary diameter, CBF, and extracellular matrix protein secretion. Perivascular pericytes release a large number of growth factors and angiogenic molecules, which regulate microvascular permeability, remodeling, and angiogenesis.

Microglia are the resident macrophages of the brain and play critical roles in innate and adaptive immune responses of the CNS. Once thought to be relatively quiescent in their "resting" state, their ramified processes actually constantly survey the brain parenchyma. Upon stimulation, activated microglia engage in a variety of pro- as well as anti-inflammatory morphologies including phagocytic phenotypes. The pro-inflammatory activated state of microglia typically affects the permeability of the BBB, increasing its permeability via production of reactive oxygen species and inflammatory cytokines such as TNF-α.

Basement membranes in the NVU also significantly contribute to BBB integrity through several mechanisms. The predominant constituents of the cerebrovascular basement membranes include collagen IV, laminin, perlecan, nidogen, and fibronectin, which are extracellular matrix proteins produced by each cell type in the NVU [21, 22]. There are two types of basement membranes in the NVU: (1) an endothelial basement membrane composed of extracellular matrix produced by ECs and pericytes and (2) a parenchymal basement membrane formed by those from astrocytes [23, 24]. Basement membranes function as a physical barrier surrounding the abluminal surface of endothelial cells and anchor the cells in place at the BBB. In addition, they also contribute to BBB regulation, where the extracellular matrix mediates diverse signaling in endothelial cells and pericytes [24].

Neurovascular Unit and Neurovascular Coupling

In brain capillaries, ECs form the tube structure with barrier integrity, in which the abluminal surface is covered by basement membranes composed of extracellular matrix. The endothelial tubes are surrounded by pericytes, astrocyte end-feet, and neurons, comprising the NVU. The cells of the NVU work in concert to maintain homeostasis of the cerebral microenvironment, regulate CBF, control exchange between the BBB and blood, contribute to immune surveillance in the brain, and provide support to brain cells. While physical barrier structures in ECs predominantly control BBB integrity, molecular barrier systems through endothelial transporters can mediate the influx and efflux of specific molecules at the BBB [25–27].

Cerebrovascular health is essential to maintain adequate brain perfusion and preserve normal brain function. This is accomplished through coupling alterations in local CBF (e.g., by increasing vascular dilation in response to elevated metabolic demand) to neuronal activity, a process termed neurovascular coupling. The brain's structural and functional integrity relies on an uninterrupted and well-regulated blood supply, and consequently brain dysfunction and ultimately death often involve interruption of CBF [28]. Mechanisms that ensure adequate neuronal blood supply

and CBF are essential to meet the brain's metabolic demand and support its overall health [16]. Adjustments of CBF must be highly regulated to maintain proper cellular homeostasis and function [29]. This is accomplished through neurovascular coupling orchestrated by an intercellular signaling network [30]. The NVU is functionally integrated to regulate CBF responses to neuronal stimulation which ensures a rapid increase in CBF and oxygen delivery to activated brain regions [1, 31].

Vascular Dysfunction and Neurodegeneration

Aging-related structural and functional disturbances in circulation of the brain contribute to brain degeneration. Aging significantly impairs neurovascular coupling responses. Impairment of the NVU and pathological changes of BBB function is present in a variety of neurodegenerative diseases. Age-related deficits in neurovascular coupling responses are also associated with impaired cognitive function and gait abnormalities [32, 33]. Although the detailed mechanisms of various neurodegenerative diseases remain veiled, it is clear that aging is a vital risk factor in neurodegeneration. It has been speculated that age-related impairments in the NVU, together with alterations in genes and environmental factors, initiate and maintain a self-perpetuating cycle of neurodegeneration.

Cerebrovascular autoregulation is a mechanism that ensures relatively constant CBF and avoids fluctuations of cerebral perfusion resulting from arterial pressure [34]. In elderly patients, inadequate blood flow augmentation often leads to mismatches between supply and demand of oxygen and metabolic substrates and results in dysfunction during neuronal activation [35]. Microvascular degeneration diminishes CBF, resulting in shortages of oxygen supply, energy substrates, and nutrients to the brain. Additionally, microvascular defects compromise clearance of neurotoxic molecules from the brain, resulting in accumulation of pathological deposits in brains cells and interstitial fluid. Reductions in resting CBF or transportation of key brain proteins/metabolites (see below for more discussion) or altered responses to brain activation may occur in different CNS regions in AD, PD, and other CNS disorders.

Oxidative stress plays a critical role in age-related neurovascular uncoupling and participates in the development of various diseases such as arthritis, cancer, and cardiovascular and neurodegenerative diseases. With age, genetic, and environmental risk factors, the redox system becomes imbalanced, and levels of reactive oxygen (ROS) and nitrogen (RNS) species are increased. Mitochondria are one of the main sources of intracellular ROS as they produce 1–5% ROS in normal physiological conditions [36]. Given the high metabolic rates and energy demands, mitochondrial functionality is vital for supporting healthy brain functions such as synapse assembly, generation of action potentials, and synaptic transmission. Therefore, for proper homeostasis, aged or dysfunctional mitochondria must be removed, and adequately functioning mitochondria must be properly recruited and distributed to meet altered metabolic requirements [37].

Oxidative stress and endothelial dysfunction have a critical impact on age-related cerebrovascular impairment and neurovascular uncoupling [38]. Endothelial membrane transporters based on the tight junctions between cerebral endothelial cells manage the trafficking of signaling molecules between the blood and the brain, including macromolecules, ions, amino acids, peptides, and neurotransmitters. Thus, transportation and clearance of toxic components involved with pathogenesis of neurodegenerative diseases are influenced by the integrity of this process [39].

Cerebrovascular Dysfunction in AD

AD is a neurodegenerative disorder often associated with neurovascular dysfunction, cognitive decline, and accumulation in brain of amyloid beta (Aβ) peptide and tau-related lesions in neurons. With age, increasing prevalence of coincident AD and cerebrovascular disease (CVD) has been well-recognized. CVD and vascular risk factors are associated with AD and contribute to neuropathological changes such as selective brain atrophy and accumulation of Aβ in AD [40]. Intracerebral Aβ is removed from the brain through vascular mechanisms involving the lipoprotein receptor protein 1 (LRP1) and P-glycoprotein [41, 42]. A study of the association of vascular pathology and cerebrovascular disease with neuropathologically confirmed neurodegenerative disease revealed that AD has a significantly higher prevalence of cerebrovascular disease and vascular pathology than other related neurodegenerative diseases [43]. Furthermore, AD is more likely to occur in patients presenting cerebral infarctions, as around 70% of patients diagnosed with AD have evidence of coexistent cerebrovascular disease.

Cerebrovascular abnormalities are a common phenomenon in AD. Multiple epidemiological studies have shown a remarkable overlap among risk factors for cerebrovascular disorder and sporadic, late-onset AD. AD is associated with marked alterations in cerebrovascular structure and function of the NVU in both large intracranial vessels and microvessels [44]. Microvascular pathophysiological alterations have a causal role both in the development of AD and related cognitive decline. BBB transport systems are significantly altered in AD patients compared to controls [45]. Amyloid β (Aβ) is a major contributor to BBB dysfunction in AD, and Aβ deposits in the vasculature enhance BBB permeability in the AD brain. Cerebral amyloid angiopathy (CAA), which is characterized by deposition of amyloid fibrils in the walls of small- to medium-sized blood vessels, promotes the degeneration of smooth muscle cells and pericytes, leading to compromised BBB or simply breakdown of BBB [26]. Reduced CBF occurs early in the development of AD, most significantly in areas where tau pathology is associated with AD. These perfusion deficits develop in pre-symptomatic stages before brain atrophy [46, 47]. CBF reductions correlate with dementia, cortical atrophy, and vascular disease in the white matter. AD patients exhibit significant impairment of neurovascular coupling responses. In AD or in CAA, accumulation of Aβ leads to the damage of the vessel wall, increasing the chance of lobar hemorrhages [44]. As neuronal activity continu-

ously determines neurovascular and neurometabolic coupling [48], functional deterioration of the neurons is a pathophysiological characteristic in brain aging and several age-related neuropathological conditions like AD (see below for PD) [1, 49].

Vascular dysfunction also plays a central role in the development of AD. Typical amyloid plaques and neurofibrillary tangles (NFTs) may result from hypoperfusion due to inadequate blood supply. Ischemic conditions may trigger Aβ accumulation and facilitate amyloidogenic cleavage leading to increased levels of toxic Aβ. Indeed, dramatically and consistently increasing accumulation of Aβ has been observed after cerebral ischemia [50]. In vitro, Aβ has been demonstrated to be toxic to both cerebral and peripheral endothelium [51, 52]. The toxic effects of Aβ on cerebral blood vessels may also induce cerebral hypoperfusion and increase vulnerability to ischemic damage. Since amyloid plaques appear to promote ischemia and vice versa, it is plausible that there is a synergistic relationship between the amyloidogenic and vascular features of AD pathology. Cerebral hypoperfusion is an early feature of AD, which occurs several years before the onset of clinical symptoms. The perfusion of precuneus is firstly affected, followed by cingulate gyrus and the lateral part of the parietal lobe, about 10 years before the development of dementia, and then the frontal and temporal lobes.

A strong relationship between age-associated CVD and AD exists; however, it is complicated by the high level of risk factors and overlap that increases with age. As such, the boundary between physiological and pathological aging is not categorical. For example, midlife hypertension and AD are strongly correlated, especially in those not undergoing treatment with antihypertensive drugs [53]. Furthermore, increased blood pressure (BP) in midlife not only leads to pathological changes in blood vessels but also brain atrophy and an increase in senile Aβ plaques and NFTs in the neocortex and hippocampus [54]. Moreover, long-lasting increases in BP may worsen the risk of AD by inducing small vessel disease (SVD), structural white matter alterations, and cerebral hypoperfusion through impairment of normal vascular regulation or atherosclerosis.

Cerebrovascular Dysfunction in PD

PD is the second most common neurodegenerative disorder in the elderly population. It is clinically characterized by parkinsonism (resting tremor, bradykinesia, rigidity, and postural instability), and histopathological changes include progressive loss of neurons in multiple regions, specifically the substantia nigra pars compacta, accompanied by the presence of aggregated deposits known as Lewy bodies and Lewy neurites. The relationship between CVD, vascular risk factors, and PD is variable in clinical, radiological, and pathological studies. Furthermore, large-scale cohort studies have demonstrated that PD is associated with higher risk of CVD [55, 56]. Cerebrovascular pathologies and vascular risk factors are associated with an increased prevalence of PD and cognitive impairment in the elderly [57, 58]. In a

clinicopathological study, prevalence of concomitant PD and cerebrovascular disease, mainly SVD, was 26–40% [59, 60]. A meta-analysis demonstrated that PD is associated with CVD, and patients with PD were at a higher risk of CVD later in their life [61].

The loss of dopaminergic neurons is a hallmark of PD. Dopaminergic neurons are equipped with abundant mitochondria and are therefore easily exposed to high levels of ROS [62]. Mitochondrial DNA is easily damaged by ROS, which results in mitochondrial malfunction. In aged cells, mitophagy is disturbed [63]. Meanwhile, low energy support results in reduced mitochondrial repair [64]. All of these changes can contribute to dopaminergic neuronal loss. In physiological conditions, dopaminergic neurons are well equipped to deal with oxidative stress. Superoxide dismutase (SOD) and glutathione peroxidase (GPX) nonspecifically decompose ROS/NOS. However, when these protective mechanisms are compromised during aging, excess ROS will be produced. The subsequent oxidative stress will then facilitate the aggregation of α-synuclein, eventually leading to formation of Lewy bodies [65].

Neuronal degeneration and bioenergetic derailment in PD are accompanied by cerebrovascular dysfunction and alteration in cerebral metabolism. Decreases in CBF values are observed in basal ganglia, hippocampus, prefrontal cortex, and parietal white matter in PD patients when compared to healthy subjects [66]. In PD patients, CBF reductions in parietal regions correlated with cognitive dysfunction, suggesting a link between cognitive deficits and perfusion [67]. Impaired autoregulation of brain perfusion, independent of dopaminergic treatment, has been demonstrated in PD patients subjected to a drop in BP compared with controls [68].

In addition to neuronal injury, glial cells play a pivotal part in PD development. Dopaminergic neurons are equipped with unmyelinated axons, and thus astrocytes make the most intimate contact with them [69]. Intact astrocytes provide protection and support to dopaminergic neurons through production of antioxidants such as glutathione and by removing toxic molecules including glutamate and α-synuclein [70]. Meanwhile, astrocytic neurotrophic factors protect neurons from damage [71]. However, chronic inflammation in the aged CNS changes the phenotype of astrocytes that become more pro-inflammatory. The senile astrocytes fail to provide protection and support; instead, they produce cytokines, chemokines, and ROS, which harm the integrity of the NVU [69].

Cerebrovascular Dysfunction in ALS

ALS is characterized by progressive loss of motor neurons in the anterior horn of the spinal cord and brain, resulting in progressive weakness, muscle atrophy, and respiratory failure. Although the pathogenesis of ALS remains largely unknown, neuropathologic features and gene mutations associated with ALS have shed important light on the etiology of the disease. Mutations in superoxide dismutase-1 (SOD1) are the most common form of inherited ALS, accounting for almost 25% of

familial cases. Mutations in SOD1 and overproduction of ROS/RNS and dramatic gliosis characterized by abnormalities of astrocytes, widespread astrocytosis, and activated microglial cells are evident in ALS [72].

Impairments of the BBB, blood-spinal cord barrier, or blood-cerebrospinal fluid barrier (BCSFB), aggravating motor neuron damage, are also possible pathogenic mechanism in ALS. These barriers control the exchanges of various substances between the blood and brain/spinal cord and maintain proper homeostasis of the CNS. The first evidence of altered BCSFB affected permeability in ALS was provided in 1980s, with the finding of abnormally high levels of IgG, albumin, and complement component C3a in the CSF of ALS patients [73, 74]. At the same time, IgG deposits and C3 and C4 were found in the spinal cord and motor cortex of patients with ALS, suggesting BBB/BSCB disruption [75]. Compelling evidence of changes in all NVU components, including the BBB/BSCB, in both patients and animal models identifies ALS as a neurovascular disease. Qualitative analyses of spinal cord tissue from ALS patients evidenced markedly decreased perivascular tight junction and basement membrane, as well as astrocyte end-feet dissociated from the endothelium. These results confirmed lost endothelial integrity as one characteristic of BSCB disruption that might contribute to disease progression [76]. It has been suggested that entry of harmful blood-borne substances into areas of motor neuron degeneration may have implications for the pathogenesis of ALS [77]. Circulating ECs are considered markers for endothelial damage [78] and are unexpectedly reduced in peripheral blood of ALS patients with moderate or severe disease [79], providing further support for vascular damage in ALS.

Oxidative stress also plays a crucial role in ALS [80]. Oxidative stress is a major component of the BBB impairment. In physiological conditions, ROS are generated largely from mitochondrial activity in neural cells. Specific endogenous antioxidants such as superoxide dismutase and glutathione peroxidase are able to scavenge ROS. In pathological conditions, however, injury leads to excitotoxicity, activation of inflammatory pathways, mitochondrial dysfunctions, leukocyte recruitment, and microglia activation, all of which increase levels of free radicals [81].

Vasculoprotective Approaches

Nutritional factors are essential to neuroprotection. Development or progression of cognitive impairment and dementia can be slowed by consumption of certain foods and vitamin supplements [82]. Regular consumption of fish is related to lower risk of AD [56] and slower rate of cognitive decline [83]. Fish offers protection by countering inflammation and enhancing vascular tone and countering atherosclerosis. The B vitamins, especially folate, B6, and B12 are implicated as likely to sustain or improve cognitive function in older age [84]. Chronic accumulation of reactive oxygen species in older brains may exhaust antioxidant capacity and trigger neurodegenerative processes as characterized in AD. Dietary supplementation with fruit or vegetable extracts high in antioxidants helps to decrease the enhanced vulnerability

to oxidative stress and improve neuronal communication via increases in neuronal signaling and animal behavior [85].

Changes in lifestyle factors will decrease the risk of developing dementia in later life [86]. Regular exercise can reduce rate of age-related cognitive decline and decreased risk of incident dementia or AD [87]. Increased physical activity in midlife has been found to be associated with less neocortical atrophy in the elderly [88]. Vasculoprotective factors such as nutritional factors, lifestyle factors, and physical activity will not only reduce the risk of onset of degenerative diseases but also slow down the progression of these disorders.

Conclusions and Future Directions

An emerging role of brain vasculature in aging and the pathogenesis of human neurodegenerative diseases, particularly AD, has led to increasingly recognized importance of healthy blood vessels for normal brain functioning. AD can be viewed as a model for other neurodegenerative diseases, e.g., PD and ALS highlighted in this chapter, that are beginning to reveal notable vascular contributions to disease pathophysiology. However, the exact role of the vascular dysfunction in neurodegenerative diseases and whether the vascular modulation is a viable therapeutic target for neurodegenerative diseases remains to be investigated further. It is expected that the molecular definitions of human brain vasculature, BBB, and perhaps NVU will generate an atlas of blood vessels in the human brain during health and disease. Neuroimaging holds the potential to further examine the regional vascular pathophysiology in the living human brain. The advances in imaging and molecular investigation may establish early vascular biomarkers in the living human brain, hopefully revealing untapped novel targets of disease-modifying therapeutics for multiple neurodegenerative disorders. Future studies may also reveal why regional changes in the brain vasculature will lead to disease-specific neurological phenotypes in different neurodegenerative diseases and inform about gene networks and upstream regulators driving the link between cerebrovascular dysfunction and neurodegeneration.

References

1. Iadecola C. The neurovascular unit coming of age: a journey through neurovascular coupling in health and disease. Neuron. 2017;96(1):17–42.
2. Snyder HM, Corriveau RA, Craft S, et al. Vascular contributions to cognitive impairment and dementia including Alzheimer's disease. Alzheimers Dement. 2015;11(6):710–7.
3. Korczyn AD. Vascular parkinsonism--characteristics, pathogenesis and treatment. Nat Rev Neurol. 2015;11(6):319–26.
4. Winkler EA, Sengillo JD, Sullivan JS, Henkel JS, Appel SH, Zlokovic BV. Blood-spinal cord barrier breakdown and pericyte reductions in amyotrophic lateral sclerosis. Acta Neuropathol. 2013;125(1):111–20.

5. Kalaria RN, Maestre GE, Arizaga R, et al. Alzheimer's disease and vascular dementia in developing countries: prevalence, management, and risk factors. Lancet Neurol. 2008;7(9):812–26.
6. Neuropathology Group of the Medical Research Council Cognitive Function and Ageing Study (MRC CFAS). Pathological correlates of late-onset dementia in a multicentre, community-based population in England and Wales. Lancet. 2001;357(9251):169–75.
7. Bailey TL, Rivara CB, Rocher AB, Hof PR. The nature and effects of cortical microvascular pathology in aging and Alzheimer's disease. Neurol Res. 2004;26(5):573–8.
8. Begley DJ, Brightman MW. Structural and functional aspects of the blood-brain barrier. Prog Drug Res Fortschritte der Arzneimittelforschung Progres des recherches pharmaceutiques. 2003;61:39–78.
9. Zlokovic BV. Neurovascular mechanisms of Alzheimer's neurodegeneration. Trends Neurosci. 2005;28(4):202–8.
10. Abbott NJ, Patabendige AA, Dolman DE, Yusof SR, Begley DJ. Structure and function of the blood-brain barrier. Neurobiol Dis. 2010;37(1):13–25.
11. Daneman R, Engelhardt B. Brain barriers in health and disease. Neurobiol Dis. 2017;107:1–3.
12. Golding EM, Marrelli SP, You J, Bryan RM Jr. Endothelium-derived hyperpolarizing factor in the brain: a new regulator of cerebral blood flow? Stroke. 2002;33(3):661–3.
13. Wolburg H, Noell S, Mack A, Wolburg-Buchholz K, Fallier-Becker P. Brain endothelial cells and the glio-vascular complex. Cell Tissue Res. 2009;335(1):75–96.
14. Oberheim NA, Takano T, Han X, et al. Uniquely hominid features of adult human astrocytes. J Neurosci. 2009;29(10):3276–87.
15. Abbott NJ, Ronnback L, Hansson E. Astrocyte-endothelial interactions at the blood-brain barrier. Nat Rev Neurosci. 2006;7(1):41–53.
16. Iadecola C, Nedergaard M. Glial regulation of the cerebral microvasculature. Nat Neurosci. 2007;10(11):1369–76.
17. Kuchibhotla KV, Lattarulo CR, Hyman BT, Bacskai BJ. Synchronous hyperactivity and intercellular calcium waves in astrocytes in Alzheimer mice. Science. 2009;323(5918):1211–5.
18. Bonkowski D, Katyshev V, Balabanov RD, Borisov A, Dore-Duffy P. The CNS microvascular pericyte: pericyte-astrocyte crosstalk in the regulation of tissue survival. Fluids Barriers CNS. 2011;8(1):8.
19. Winkler EA, Bell RD, Zlokovic BV. Central nervous system pericytes in health and disease. Nat Neurosci. 2011;14(11):1398–405.
20. Cheslow L, Alvarez JI. Glial-endothelial crosstalk regulates blood-brain barrier function. Curr Opin Pharmacol. 2016;26:39–46.
21. Yousif LF, Di Russo J, Sorokin L. Laminin isoforms in endothelial and perivascular basement membranes. Cell Adhes Migr. 2013;7(1):101–10.
22. Morris AW, Carare RO, Schreiber S, Hawkes CA. The cerebrovascular basement membrane: role in the clearance of beta-amyloid and cerebral amyloid angiopathy. Front Aging Neurosci. 2014;6:251.
23. Owens T, Bechmann I, Engelhardt B. Perivascular spaces and the two steps to neuroinflammation. J Neuropathol Exp Neurol. 2008;67(12):1113–21.
24. Baeten KM, Akassoglou K. Extracellular matrix and matrix receptors in blood-brain barrier formation and stroke. Dev Neurobiol. 2011;71(11):1018–39.
25. Daneman R, Prat A. The blood-brain barrier. Cold Spring Harb Perspect Biol. 2015;7(1):a020412.
26. Erickson MA, Banks WA. Blood-brain barrier dysfunction as a cause and consequence of Alzheimer's disease. J Cereb Blood Flow Metab. 2013;33(10):1500–13.
27. Zenaro E, Piacentino G, Constantin G. The blood-brain barrier in Alzheimer's disease. Neurobiol Dis. 2017;107:41–56.
28. Moskowitz MA, Lo EH, Iadecola C. The science of stroke: mechanisms in search of treatments. Neuron. 2010;67(2):181–98.
29. Enager P, Piilgaard H, Offenhauser N, et al. Pathway-specific variations in neurovascular and neurometabolic coupling in rat primary somatosensory cortex. J Cereb Blood Flow Metab. 2009;29(5):976–86.

30. Wells JA, Christie IN, Hosford PS, et al. A critical role for purinergic signalling in the mechanisms underlying generation of BOLD fMRI responses. J Neurosci. 2015;35(13):5284–92.
31. Zacchigna S, Lambrechts D, Carmeliet P. Neurovascular signalling defects in neurodegeneration. Nat Rev Neurosci. 2008;9(3):169–81.
32. Sorond FA, Hurwitz S, Salat DH, Greve DN, Fisher ND. Neurovascular coupling, cerebral white matter integrity, and response to cocoa in older people. Neurology. 2013;81(10):904–9.
33. Sorond FA, Kiely DK, Galica A, et al. Neurovascular coupling is impaired in slow walkers: the MOBILIZE Boston study. Ann Neurol. 2011;70(2):213–20.
34. van Beek AH, Claassen JA, Rikkert MG, Jansen RW. Cerebral autoregulation: an overview of current concepts and methodology with special focus on the elderly. J Cereb Blood Flow Metab. 2008;28(6):1071–85.
35. Jessen SB, Mathiesen C, Lind BL, Lauritzen M. Interneuron deficit associates attenuated network synchronization to mismatch of energy supply and demand in aging mouse brains. Cereb Cortex. 2017;27(1):646–59.
36. Wei YH, Lu CY, Wei CY, Ma YS, Lee HC. Oxidative stress in human aging and mitochondrial disease-consequences of defective mitochondrial respiration and impaired antioxidant enzyme system. Chin J Physiol. 2001;44(1):1–11.
37. Sheng ZH. Mitochondrial trafficking and anchoring in neurons: new insight and implications. J Cell Biol. 2014;204(7):1087–98.
38. Toth P, Tarantini S, Tucsek Z, et al. Resveratrol treatment rescues neurovascular coupling in aged mice: role of improved cerebromicrovascular endothelial function and downregulation of NADPH oxidase. Am J Physiol Heart Circ Physiol. 2014;306(3):H299–308.
39. Deane R, Du Yan S, Submamaryan RK, et al. RAGE mediates amyloid-beta peptide transport across the blood-brain barrier and accumulation in brain. Nat Med. 2003;9(7):907–13.
40. Kalaria RN, Akinyemi R, Ihara M. Does vascular pathology contribute to Alzheimer changes? J Neurol Sci. 2012;322(1–2):141–7.
41. Bell RD, Deane R, Chow N, et al. SRF and myocardin regulate LRP-mediated amyloid-beta clearance in brain vascular cells. Nat Cell Biol. 2009;11(2):143–53.
42. Cirrito JR, Deane R, Fagan AM, et al. P-glycoprotein deficiency at the blood-brain barrier increases amyloid-beta deposition in an Alzheimer disease mouse model. J Clin Invest. 2005;115(11):3285–90.
43. Toledo JB, Arnold SE, Raible K, et al. Contribution of cerebrovascular disease in autopsy confirmed neurodegenerative disease cases in the National Alzheimer's coordinating Centre. Brain. 2013;136(Pt 9):2697–706.
44. Weller RO, Boche D, Nicoll JA. Microvasculature changes and cerebral amyloid angiopathy in Alzheimer's disease and their potential impact on therapy. Acta Neuropathol. 2009;118(1):87–102.
45. Montagne A, Zhao Z, Zlokovic BV. Alzheimer's disease: a matter of blood-brain barrier dysfunction? J Exp Med. 2017;214(11):3151–69.
46. Hirao K, Ohnishi T, Hirata Y, et al. The prediction of rapid conversion to Alzheimer's disease in mild cognitive impairment using regional cerebral blood flow SPECT. NeuroImage. 2005;28(4):1014–21.
47. Johnson NA, Jahng GH, Weiner MW, et al. Pattern of cerebral hypoperfusion in Alzheimer disease and mild cognitive impairment measured with arterial spin-labeling MR imaging: initial experience. Radiology. 2005;234(3):851–9.
48. Ledo A, Lourenco CF, Laranjinha J, Brett CM, Gerhardt GA, Barbosa RM. Ceramic-based multisite platinum microelectrode arrays: morphological characteristics and electrochemical performance for extracellular oxygen measurements in brain tissue. Anal Chem. 2017;89(3):1674–83.
49. Lourenco CF, Ledo A, Barbosa RM, Laranjinha J. Neurovascular uncoupling in the triple transgenic model of Alzheimer's disease: impaired cerebral blood flow response to neuronal-derived nitric oxide signaling. Exp Neurol. 2017;291:36–43.
50. Li L, Zhang X, Yang D, Luo G, Chen S, Le W. Hypoxia increases Abeta generation by altering beta- and gamma-cleavage of APP. Neurobiol Aging. 2009;30(7):1091–8.

51. Thomas T, Thomas G, McLendon C, Sutton T, Mullan M. beta-Amyloid-mediated vasoactivity and vascular endothelial damage. Nature. 1996;380(6570):168–71.
52. Sutton ET, Hellermann GR, Thomas T. beta-amyloid-induced endothelial necrosis and inhibition of nitric oxide production. Exp Cell Res. 1997;230(2):368–76.
53. Launer LJ, Andersen K, Dewey ME, et al. Rates and risk factors for dementia and Alzheimer's disease: results from EURODEM pooled analyses. EURODEM Incidence Research Group and Work Groups. European Studies of Dementia. Neurology. 1999;52(1):78–84.
54. Petrovitch H, White LR, Izmirilian G, et al. Midlife blood pressure and neuritic plaques, neurofibrillary tangles, and brain weight at death: the HAAS. Honolulu-Asia aging Study. Neurobiol Aging. 2000;21(1):57–62.
55. Becker C, Jick SS, Meier CR. Risk of stroke in patients with idiopathic Parkinson disease. Parkinsonism Relat Disord. 2010;16(1):31–5.
56. Huang TL, Zandi PP, Tucker KL, et al. Benefits of fatty fish on dementia risk are stronger for those without APOE epsilon4. Neurology. 2005;65(9):1409–14.
57. de Laat KF, van Norden AG, Gons RA, et al. Cerebral white matter lesions and lacunar infarcts contribute to the presence of mild parkinsonian signs. Stroke. 2012;43(10):2574–9.
58. Hatate J, Miwa K, Matsumoto M, et al. Association between cerebral small vessel diseases and mild parkinsonian signs in the elderly with vascular risk factors. Parkinsonism Relat Disord. 2016;26:29–34.
59. Schwartz RS, Halliday GM, Cordato DJ, Kril JJ. Small-vessel disease in patients with Parkinson's disease: a clinicopathological study. Mov Disord. 2012;27(12):1506–12.
60. Jellinger KA. Prevalence of cerebrovascular lesions in Parkinson's disease. A postmortem study. Acta Neuropathol. 2003;105(5):415–9.
61. Hong CT, Hu HH, Chan L, Bai CH. Prevalent cerebrovascular and cardiovascular disease in people with Parkinson's disease: a meta-analysis. Clin Epidemiol. 2018;10:1147–54.
62. Liang CL, Wang TT, Luby-Phelps K, German DC. Mitochondria mass is low in mouse substantia nigra dopamine neurons: implications for Parkinson's disease. Exp Neurol. 2007;203(2):370–80.
63. Palikaras K, Tavernarakis N. Mitophagy in neurodegeneration and aging. Front Genet. 2012;3:297.
64. Gredilla R, Bohr VA, Stevnsner T. Mitochondrial DNA repair and association with aging--an update. Exp Gerontol. 2010;45(7–8):478–88.
65. Takahashi M, Ko LW, Kulathingal J, Jiang P, Sevlever D, Yen SH. Oxidative stress-induced phosphorylation, degradation and aggregation of alpha-synuclein are linked to upregulated CK2 and cathepsin D. Eur J Neurosci. 2007;26(4):863–74.
66. Wei X, Yan R, Chen Z, et al. Combined diffusion tensor imaging and arterial spin labeling as markers of early Parkinson's disease. Sci Rep. 2016;6:33762.
67. Al-Bachari S, Parkes LM, Vidyasagar R, et al. Arterial spin labelling reveals prolonged arterial arrival time in idiopathic Parkinson's disease. Neuroimage Clin. 2014;6:1–8.
68. Vokatch N, Grotzsch H, Mermillod B, Burkhard PR, Sztajzel R. Is cerebral autoregulation impaired in Parkinson's disease? A transcranial Doppler study. J Neurol Sci. 2007;254(1–2):49–53.
69. Rodriguez M, Morales I, Rodriguez-Sabate C, et al. The degeneration and replacement of dopamine cells in Parkinson's disease: the role of aging. Front Neuroanat. 2014;8:80.
70. Rappold PM, Tieu K. Astrocytes and therapeutics for Parkinson's disease. Neurotherapeutics. 2010;7(4):413–23.
71. Drinkut A, Tereshchenko Y, Schulz JB, Bahr M, Kugler S. Efficient gene therapy for Parkinson's disease using astrocytes as hosts for localized neurotrophic factor delivery. Mol Ther. 2012;20(3):534–43.
72. Baltazar MT, Dinis-Oliveira RJ, de Lourdes BM, Tsatsakis AM, Duarte JA, Carvalho F. Pesticides exposure as etiological factors of Parkinson's disease and other neurodegenerative diseases--a mechanistic approach. Toxicol Lett. 2014;230(2):85–103.
73. Leonardi A, Abbruzzese G, Arata L, Cocito L, Vische M. Cerebrospinal fluid (CSF) findings in amyotrophic lateral sclerosis. J Neurol. 1984;231(2):75–8.

74. Annunziata P, Volpi N. High levels of C3c in the cerebrospinal fluid from amyotrophic lateral sclerosis patients. Acta Neurol Scand. 1985;72(1):61–4.
75. Donnenfeld H, Kascsak RJ, Bartfeld H. Deposits of IgG and C3 in the spinal cord and motor cortex of ALS patients. J Neuroimmunol. 1984;6(1):51–7.
76. Miyazaki K, Ohta Y, Nagai M, et al. Disruption of neurovascular unit prior to motor neuron degeneration in amyotrophic lateral sclerosis. J Neurosci Res. 2011;89(5):718–28.
77. Garbuzova-Davis S, Saporta S, Sanberg PR. Implications of blood-brain barrier disruption in ALS. Amyotroph Lateral Scler. 2008;9(6):375–6.
78. Blann AD, Woywodt A, Bertolini F, et al. Circulating endothelial cells. Biomarker of vascular disease. Thromb Haemost. 2005;93(2):228–35.
79. Garbuzova-Davis S, Woods RL 3rd, Louis MK, et al. Reduction of circulating endothelial cells in peripheral blood of ALS patients. PLoS One. 2010;5(5):e10614.
80. Robberecht W. Oxidative stress in amyotrophic lateral sclerosis. J Neurol. 2000;247(Suppl 1):I1–6.
81. Pun PB, Lu J, Moochhala S. Involvement of ROS in BBB dysfunction. Free Radic Res. 2009;43(4):348–64.
82. Morris MC, Evans DA, Bienias JL, Tangney CC, Wilson RS. Vitamin E and cognitive decline in older persons. Arch Neurol. 2002;59(7):1125–32.
83. Morris MC, Evans DA, Tangney CC, Bienias JL, Wilson RS. Fish consumption and cognitive decline with age in a large community study. Arch Neurol. 2005;62(12):1849–53.
84. Kidd PM. Alzheimer's disease, amnestic mild cognitive impairment, and age-associated memory impairment: current understanding and progress toward integrative prevention. Altern Med Rev. 2008;13(2):85–115.
85. Joseph JA, Shukitt-Hale B, Willis LM. Grape juice, berries, and walnuts affect brain aging and behavior. J Nutr. 2009;139(9):1813S–7S.
86. Rovio S, Spulber G, Nieminen LJ, et al. The effect of midlife physical activity on structural brain changes in the elderly. Neurobiol Aging. 2010;31(11):1927–36.
87. Podewils LJ, Guallar E, Kuller LH, et al. Physical activity, APOE genotype, and dementia risk: findings from the Cardiovascular Health Cognition Study. Am J Epidemiol. 2005;161(7):639–51.
88. Scarmeas N, Luchsinger JA, Schupf N, et al. Physical activity, diet, and risk of Alzheimer disease. JAMA. 2009;302(6):627–37.

Chapter 2
Current Imaging Approaches and Challenges in the Assessment of the Intracranial Vasculature

Justin E. Vranic and Mahmud Mossa-Basha

Luminal Imaging Basics

Luminal imaging is a vascular imaging technique that evaluates the caliber of the intracranial vasculature. In some instances, these techniques can also provide information regarding the hemodynamics through vessels of interest. Conclusions regarding underlying vessel pathophysiology are ultimately drawn from the observed luminal irregularity and alterations in flow. Catheter digital subtraction angiography (DSA) is typically performed in a dedicated biplane neuroangiography suite. Before diagnostic images can be taken, intra-arterial access must be first acquired and a vessel(s) of interest must be selectively catheterized. Images are then acquired with high temporal resolution as a bolus of contrast flows through the vasculature of interest. CTA is a noninvasive luminal imaging modality that requires intravenous administration of iodinated contrast prior to image acquisition. Modern CT scanners rely on a multi-detector array for photon detection and image acquisition. Multiplanar reformats are subsequently derived from source data with high spatial resolution [1]. MRA techniques allow for the assessment of the vessel caliber and, in some instances, flow characteristics through intracranial vasculature. MRA acquisitions can be performed with or without intravenous contrast. Contrast-enhanced (CE) MRA relies upon the T1 shortening effects of paramagnetic contrast

J. E. Vranic
University of Washington, Department of Radiology, Seattle, WA, USA
e-mail: justedv@uw.edu

M. Mossa-Basha (✉)
University of Washington, Seattle, WA, USA
e-mail: mmossab@uw.edu

C. Yuan et al. (eds.), *Vessel Based Imaging Techniques*,
https://doi.org/10.1007/978-3-030-25249-6_2

media for luminal visualization [2]. Non-CE-MRA relies upon the intrinsic signal characteristics of flowing blood for luminal visualization. Noncontrast techniques specific to neurovascular imaging include time-of-flight (TOF), phase-contrast (PC), and arterial spin labeling (ASL) MRA.

Technical Aspects of Luminal Imaging

Conventional CTA

Conventional CTA requires the intravenous administration of iodinated contrast prior to image acquisition. A total bolus volume of 45–120 mL of contrast infused at a rate of 3–6 mL/s is generally sufficient for diagnostic quality image acquisition [3–5]. Contrast bolus monitoring techniques are commonly utilized to ensure that image acquisition is performed while the intracranial arteries are sufficiently opacified with contrast. Modern multi-detector CT (MDCT) scanners commonly possess an array of 64- or more detector panels, allowing for the acquisition of submillimeter thick image slices [1]. From this submillimeter thick source data, multiplanar reformats, maximum intensity projections, and 3D volume renderings can all be reconstructed with the goal of aiding in vascular lesion detection and characterization (Fig. 2.1a, b). Despite the improvements made in spatial resolution, conventional CTA continues to have inferior spatial and temporal resolution when compared to catheter DSA [6].

Catheter Digital Subtraction Angiography (DSA)

Catheter DSA (Fig. 2.2) image acquisition requires intra-arterial infusion of contrast into catheter-selected arteries. Contrast volumes ranging from 8 to 20 mL are frequently injected at flow rates ranging from 2 to 6 mL/s per diagnostic run, depending on the size of the intracranial vessel [3]. A range of frame rates for image acquisition can be used depending on the cerebrovascular pathology in question. Commonly, a frame rate of 3–6 frames per second provides adequate temporal resolution for the identification and assessment of rapid arteriovenous shunting. In some instances, frame rates as high as 60 frames per second or more can be acquired, providing superb temporal resolution. However, this comes at the cost of significantly increased radiation exposure to the patient. Modern biplane angiography units allow the operator to use highly customizable imaging projections to optimize visualization of the vessel or vascular lesion in question. The use of three-dimension rotational angiography (3DRA) allows for three-dimensional image acquisition of a specific vessel or vascular lesion. This cerebral angiography technique allows for thorough assessment of the vessel in question and is vital to accurate intervention planning.

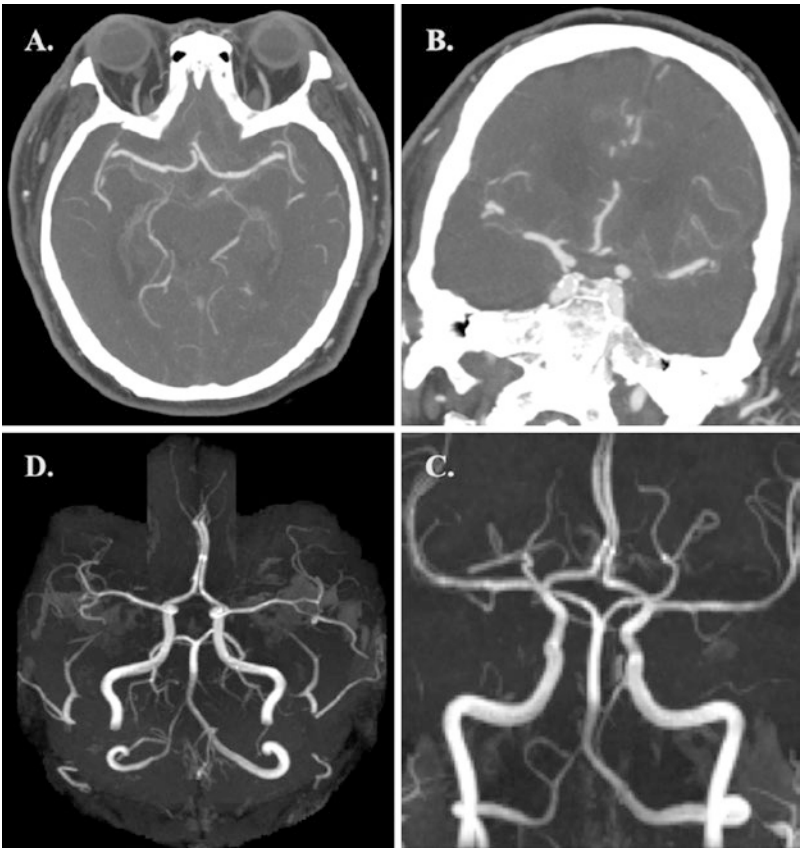

Fig. 2.1 (**a**, **b**) Axial and coronal CTA MIP images demonstrating normal intracranial vasculature. (**c**, **d**) Coronal and axial 3D-TOF-MRA MIP images demonstrating normal intracranial vasculature

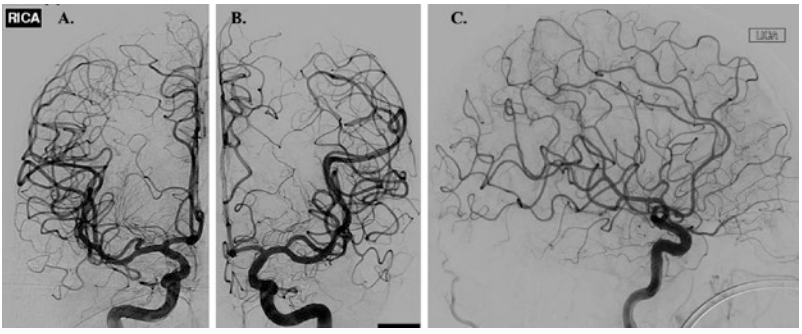

Fig. 2.2 (**a**, **b**) Frontal DSA images of the right and left ICA, respectively, illustrating normal intracranial vasculature. (**c**) Lateral DSA image of the left ICA again demonstrating normal intracranial vasculature

Dual-Energy CTA (DE-CTA)

Dual-energy CT (DE-CT) takes advantage of differences in x-ray attenuation by target materials. These differences in attenuation are dependent upon the energy of the incident photons [7]. The attenuation of materials with a high atomic number is greater with lower energy incident photons than with higher energy incident photons [7]. Similarly, the attenuation of blood vessels is more conspicuous when a low tube voltage is used [7, 8]. When an object of unknown composition is imaged with two distinct energy spectra, materials within the object can be differentiated by comparing the change in differential x-ray attenuation to the x-ray attenuation of known reference materials [7].

There are three DE-CT systems currently available. These include dual-source dual-energy CT (DSDE CT), single-source dual-energy CT (SSDE CT) with fast kilovolt-peak switching, and single-source dual-layer detector CT systems [9, 10]. DSDE CT uses two x-ray tubes that operate at different voltages (80 kVp and 140 kVp) positioned at 90° from each other [10]. In this system, spectral filtration can be independently optimized for each tube-detector pair, thus improving image quality. Due to differences in tube positioning relative to the target, acquisition of the two different datasets occurs at slightly different times, limiting the temporal registration of the DSDE CT images. Because both tubes are simultaneously energized, scattered radiation from one tube may be detected by the detector panel of the other tube (and vice versa), leading to degradation in spectral separation. Implementation of an appropriate scatter-correction algorithm can help correct for this phenomenon [10].

SSDE CT with fast kilovolt-peak switching relies on fast switching between 80 and 140 kVp performed every 250 microseconds during a single projection for spectral separation. This results in the acquisition of 1000 high-energy and 1000 low-energy projections during a single 360° gantry rotation at a full field of view of 50 cm. Unlike DSDE CT, SSDE CT with fast kilovolt-peak switching produces well-preserved spectral separation, and temporal misregistration of the spectral datasets rarely occurs. SSDE CT with a dual-layer energy detector relies on spectral separation at the level of the detector. A layered detector separates low-energy photons collected by the innermost detector layer from high-energy photons collected by the outermost detector layer from a single x-ray source [10].

Acquisition of low-energy monochromatic images with DE-CT allows for improved vessel contrast on CTA. These low-energy monochromatic images prove particularly helpful in delineating small, peripheral vessels [10]. Although the use of a low tube voltage with a traditional single-energy CT scan can produce similar effects, this comes at the cost of increased image noise which is not encountered with DE-CT. Additionally, acquisition of low-energy monochromatic images allows for the use of reduced iodinated contrast volumes while still preserving image quality [10]. This may prove helpful when imaging patients with underlying renal insufficiency in whom there is a clinical desire to minimize iodinated contrast exposure.

DE-CTA allows for the correction of beam-hardening artifact. Beam hardening arises when low-energy photons within a polychromatic x-ray beam are preferentially absorbed as they pass through a target [10]. This can result in streak on the reconstructed imaging and is frequently appreciated near the skull base and within the posterior cranial fossa. DE-CT corrects beam-hardening errors in the iodine- and water-based projection data, resulting in a reduction in beam-hardening artifacts and improved image quality [10].

Metallic implants produce significant streak artifact when imaged on a single-energy CT scanner. Monochromatic images obtained at higher energies with DE-CTA have increased penetration which reduces blooming and metallic streak artifacts [9, 10]. Image data collected at lower energies can then be used to correct for the decreased vessel contrast that occurs at these higher incident photon energies. The reconstructed image will display reduced metallic streak artifact with preserved vascular contrast. This technique proves particularly useful in evaluating vessel lumen patency following intraluminal stent placement. DE-CTA also allows for the subtraction of metallic artifacts, such as intracranial coil masses, from the reconstructed CTA images. This is accomplished through the subtraction of monochromatic images between the two energy levels obtained from the same datasets. In doing so, complete removal of objects with CT attenuation values that reach an upper threshold at both energy levels is achieved. Delineation of the parent vessel remains well-preserved on the subtracted monochromatic images [10]. This same technique can be applied to arterial wall calcifications and adjacent osseous structures, allowing for improved vessel lumen visualization [10–13].

Unlike conventional CTA, DE-CTA allows for reconstruction of virtual noncontrast images (VNC) from DE-CTA source data. Material subtraction images allow for the measurement of CT attenuation values on monochromatic images at 70 keV, which is equal to images acquired on a single-energy CT scanner at 120 kVp. VNC images allow for a reduction in overall radiation exposure, as separate scans acquired before and after contrast administration are no longer necessary [10].

4D-CTA/Timing-Invariant CTA (TI-CTA)

Four-dimensional CTA (4D-CTA), also referred to as timing-invariant CTA (TI-CTA), combines the noninvasive nature of conventional CTA with the dynamic imaging capabilities of catheter DSA [14]. 4D-CTA provides information regarding both the magnitude and directionality of flow through vessels of interest. It also details the angioarchitecture of the vasculature in question [14].

Like catheter DSA, a contrast bolus is delivered intravascularly and then imaged in real-time as it flows through the vasculature of interest. There are three distinct image acquisition techniques for performing 4D-CTA. These include volume mode, toggling-table mode, and shuttle mode scanning. The width of the CT detector ultimately determines which acquisition mode can be used to ensure adequate brain coverage [15].

Volume mode acquisitions are the most versatile, allowing for complete or partial coverage of the intracranial circulation. CTA data can be acquired either continuously throughout a pre-specified time period or discontinuously at either preset fixed or variable time intervals. During discontinuous volume mode acquisitions, the time intervals typically range from 1 to 4 seconds [15]. The datasets obtained at each of these time intervals are then overlaid to produce the final dynamic images [14]. True 4D datasets from continuous volume mode acquisitions can then be retrospectively reconstructed at any time interval. In general, the temporal resolution for this technique is on the order of 0.275–0.5 seconds [15]. Continuous scanning is only possible with volume mode acquisitions. Patients with high-flow vascular malformations benefit from the high temporal resolution of continuous acquisitions. When assessing collateral flow following arterial occlusion, a lower temporal resolution may be used, making the other acquisition techniques viable alternatives [15, 16].

4D-CTA images can be reconstructed from CT perfusion (CTP) datasets. In CTP, multiple CT datasets are acquired at different time intervals following the injection of intravenous contrast. Because 4D-CTA images can be reconstructed from CTP datasets, CTA imaging performed in addition to CTP imaging is not necessary, saving both time and radiation exposure [17]. By reconstructing 4D-CTA from CTP data, it is possible to evaluate both the angioarchitecture of the vasculature in question and the associated cerebral perfusion. The combination of these imaging techniques allows for the comprehensive assessment of the cerebral collateral vessels and the parenchymal perfusion that they supply [17–22].

Maximum intensity projections (MIPs) constructed from the 4D-CTA datasets provide an accurate overview of the vasculature of interest. Bone subtraction post-processing techniques can be used to generate DSA-like images that can be viewed as a temporal sequence that shows the arterial inflow and venous washout of contrast. By filtering the data in the temporal domain, spatial resolution remains intact, while noise is reduced, allowing for TI-CTA reconstructions of the vascular tree [15].

Time-of-Flight MRA (TOF-MRA)

TOF-MRA relies on suppression of background signal by slice-selective gradient echo excitation pulses [2, 24, 33]. In the selected slice or volume, static tissue experiences a rapid series of radiofrequency pulses that cause the tissue to lose most of its T1 signal. Inflowing blood, however, has not experienced these radiofrequency pulses and enters the slice or volume fully magnetized demonstrating a stronger T1 signal relative to the saturated background [24]. Saturation radiofrequency pulses are applied downstream of the slice or slab to suppress inflowing venous spins. Arterial contrast depends upon a combination of the T1 signal of both the arterial blood and background tissue, the radiofrequency pulse spacing and flip angle of the gradient echo sequence, and the velocity of the inflowing blood [33]. TOF-MRA

can be acquired in 2D or 3D formats, with 3D TOF-MRA being more suitable for imaging the intracranial arteries [2] (Fig. 2.1c, d). Three-dimensional acquisitions allow for isotropic voxels with submillimeter slice resolution [33]. Three-dimensional TOF-MRA is associated with longer image acquisition times, however, as well as increased susceptibility to flow dephasing artifacts resulting in loss of flow-related signal [2].

Multiple overlapping thin slab acquisition (MOTSA) is a hybrid of 2D TOF-MRA and single-slab 3D TOF-MRA that produces isotropic voxels with high spatial resolution and allows for larger anatomic areas of coverage [2, 34]. Overlapping subvolumes are sequentially acquired, before then being fused with other subvolumes to create a complete 3D volume [2].

First-pass Contrast-Enhanced MRA (CE-MRA)

First-pass CE-MRA images are commonly acquired using a T1W 3D gradient echo sequence [23, 24]. Artery visualization relies on the T1 shortening effects of intravenously delivered paramagnetic contrast agents, which makes the arteries of interest appear bright on imaging [2]. Suppression of background signal is achieved by the application of a 3D radiofrequency spoiled gradient sequence [2, 24].

First-pass CE-MRA depends upon appropriate contrast bolus concentration and timing to optimize vessel visualization. The volume of contrast required is dependent upon the magnetic field strength used, with lower concentrations and smaller volumes of contrast required when imaging is performed at higher magnetic field strengths. The contrast injection rate determines the arrival time of contrast at the vascular bed of interest. A fast injection ensures a tight bolus of contrast arriving over a short period; however, if the rate of infusion is too rapid, infusion-related artifacts can result. Optimal arterial visualization can generally be achieved using a double dose of contrast (0.2 mmol/kg) infused over a slower rate (2 mL/s) [2].

Standard extracellular contrast media are commonly used for first-pass CE-MRA and provide strong and selective enhancement of the vessels of interest [25, 26]. During the steady state, however, rapid contrast-agent extravasation occurs, resulting in decreases in the vessel contrast-to-noise ratio (CNR) and increased background signal within the surrounding soft tissues [25]. Consequently, these agents have a relative short distribution phase half-life of approximately 100 seconds [18], limiting the time available for image acquisition. Agents such as Gd-DTPA (Magnevist) and Gd-BOPTA (MultiHance) fall into this category.

Unlike standard extracellular contrast media, blood pool agents (BPA) demonstrate a prolonged intravascular distribution, allowing for strong and prolonged intravascular enhancement [25]. BPA provide an increased time frame for image acquisition (up to 60 minutes) and make steady-state MRA with high spatial resolution possible [27, 28]. BPA demonstrate significantly higher signal intensity in prestenotic and post-stenotic vessel segments [27], and MRA performed with BPA has

demonstrated superior image quality of the intracranial vasculature compared to standard extracellular contrast agents [18].

These agents can be divided into three broad categories which include ultrasmall supraparamagnetic iron oxide (USPIO) particles, paramagnetic gadolinium-based macromolecules, and gadolinium-based small molecules with strong reversible protein binding. Of these three classes, USPIO particles and gadolinium-based small molecules with strong reversible protein binding prove to be the most clinically promising. USPIO particles demonstrate strong T1 and T2 shortening effects and are retained within the intravascular space for prolonged periods of time. On T1W imaging, these particles appear bright. Sequences with short echo times are necessary to minimize confounding susceptibility artifacts [25]. Examples of USPIO particles include ferumoxtran-10 (Combidex, Sinerem, Guerbet, France), ferumoxytol (Advanced Magnetics, USA), and SHU-555C (Supravist) (Bremerich 2007). These agents have not yet received FDA approval for clinical use. Although paramagnetic gadolinium-based small molecule agents, such as gadofosveset trisodium (Vasovist/Ablavar), have received FDA approval for use in humans, they are no longer made commercially available by their manufacturers.

First-pass CE-MRA requires the appropriate timing between contrast bolus infusion and image acquisition. The scan time delay between contrast agent infusion and the start of imaging acquisition can be approximated using the following formula [2]:

$$\text{Scan Time Delay} = \text{Contrast Travel Time} + \left(\text{Injection Time} / 2\right) - \left(\text{Scan Time} / 2\right)$$

This formula does not take into account reduced cardiac output, high-grade arterial stenoses, or abnormal shunt vascularity [2]. A contrast test bolus of 1–2 mL that is injected at the same rate as the actual injection can be used to determine the contrast travel time [2]. From this, the appropriate scan delay can be deduced. Automated bolus detection represents an alternative method for coordinating contrast bolus delivery and image acquisition [23]. This technique involves monitoring a vessel of interest for the arrival of contrast. Once an adequate contrast volume is within the vessel, image acquisition is initiated [2].

Optimization of image acquisition parameters is essential to acquiring high-quality angiographic images. Repetition time (TR) should be kept as short as possible (<4 ms) without increasing the bandwidth [2, 24]. By decreasing TR, it is possible to perform multiphase imaging or increase image spatial resolution. As TR is shortened, however, the signal-to-noise ratio (SNR) subsequently decreases. This can be compensated for by increasing the rate of contrast infusion [2, 24]. Like TR, echo time (TE) should also be kept as short as possible (<2 ms). A shortened TE decreases proton dephasing which in turn reduces the loss of intravascular signal [2]. This can also decrease SNR by widening the readout bandwidth. TR, TE, and SNR are each affected by changes in the readout bandwidth, with a high readout bandwidth allowing for shorter TR and TE at the expense of SNR. A readout bandwidth of 32–64 kHz is generally sufficient for CE-MRA. The flip angle typically ranges from 20 to 60° in the case of CE-MRA with most image acquisitions utilizing a flip

angle between 30 and 45° [2]. Low flip angles are better suited for low contrast doses, slow injection rates, and very low TR, whereas high flip angles are better for high contrast doses and imaging with higher TR.

Increasing the magnetic field strength increases SNR which can be used to increase spatial resolution, decrease image acquisition time, or reduce contrast dose [2, 24]. A 3T field strength causes a T1 prolongation of tissue. Subsequently nonvascular tissues with longer T1 relaxivities are more readily suppressed with 3T scanners [24]. Increased magnetic field strength also increases the specific absorption rate (SAR) and generates higher field inhomogeneities when compared to 1.5T. Increased SAR limits the maximum flip angle that can be used, thereby limiting the increase in SNR. Despite these technical limitations, the net gain in signal remains higher at 3T when compared to 1.5T [2].

Time-Resolved Contrast-Enhanced MRA (TR-CE-MRA)

TR-CE-MRA represents a unique form of CE-MRA that provides important temporal information in addition to structural information about angioarchitecture. TR-CE-MRA acquires image sets sequentially at multiple time points during the passage of contrast through vessels of interest [30]. TR-CE-MRA provides high temporal resolution while maintaining sufficient SNR and spatial resolution, allowing for the evaluation of hemodynamic flow and distinction between arterial and venous structures [2]. Precise bolus timing is not necessary with TR-CE-MRA as multiple vascular phases are obtained [2]. Three-dimensional volume acquisitions are possible, providing greater anatomic coverage and higher spatial resolution and SNR [2]. TR-CE-MRA image acquisition techniques include keyhole imaging; contrast-enhanced time-robust angiography (CENTRA); time-resolved imaging of contrast kinetics (TRICKS; GE Healthcare, Chicago, IL); time-resolved echo-shared angiographic technique (TREAT); time-resolved imaging with stochastic trajectories (TWIST; Siemens Healthineers, Erlangen, Germany) (Fig. 2.3); four-dimensional (4D) time-resolved angiography using keyhole (4D-TRAK); vastly undersampled isotropic projection (VIPR); and highly constrained back-projection reconstruction (HYPR) [2, 31].

Keyhole imaging generates a series of images by combining rapidly acquired temporal samples of the central k-space region before performing a single sampling of the outer regions of k-space at the end of the scan [2, 31]. Although this technique provides some sense of the flow dynamics through vessels of interest, high spatial frequency venous signals appear even in the early arterial frames due to late high spatial frequency sampling [31]. CENTRA imaging relies on randomly segmented k-space ordering in which a central sphere of k-space is randomly sampled during the full arterial window. Acquisition of data can extend beyond the time of passage of the contrast bolus through the arteries so that high spatial resolution of a large field of view is achieved [2].

TRICKS imaging samples the center of k-space more frequently than the periphery, and time frames are formed by temporal interpolation [2, 31]. K-space is sub-

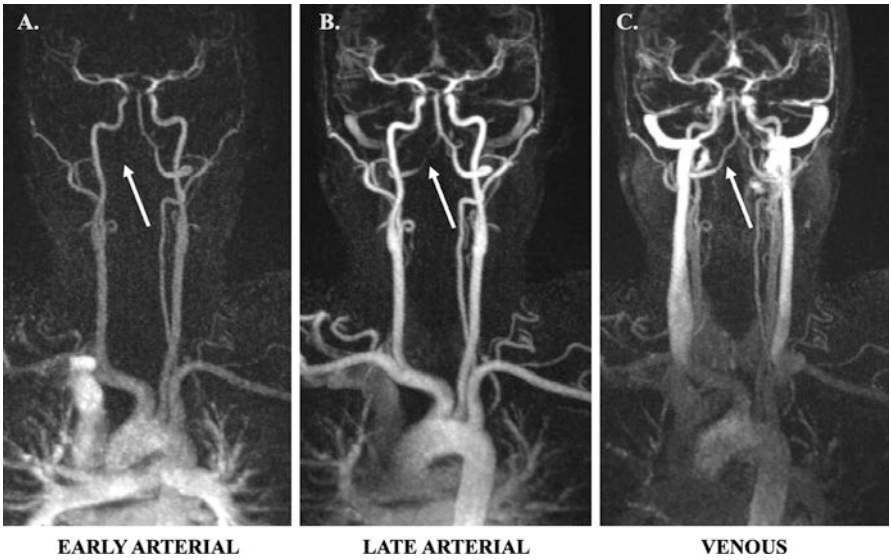

Fig. 2.3 (**a**) Coronal TR-TWIST-MRA acquired during the early arterial phase shows opacification of the pulmonary vasculature, aorta, and the major aortic branch vessels. Although the carotid arteries and left vertebral artery are well visualized, the right vertebral artery is not opacified (arrow). (**b**) A late arterial phase image shows delayed partial opacification of the right vertebral artery (arrow). (**c**) Venous phase image shows increased delayed opacification of the right vertebral artery (arrow). This patient was found to have a right vertebral artery dissection with impaired flow through the vessel. Non-time-resolved MRA techniques could have led to an erroneous diagnosis of vertebral artery occlusion

divided into fixed portions, and a part of the peripheral k-space is updated for every keyhole dynamic. Additionally, a rectangular keyhole is used to acquire full lengths of k-space lines [24]. The TRICKS technique then attempts to estimate missing k-space data by linear interpolation of values from shared data across time frames [30]. TRICKS increases the frame rate of a 3D multiphase examination by a factor of 3–4 [2]. This technique offers a significant improvement over the keyhole method because of the ongoing updating of high spatial frequency information. This technique and subsequent derivate methods are the most prevalent commercially available methods for TR-CE-MRA. Although frames may be updated every few seconds, the data used to form each frame covers a substantial time interval of 10 seconds or more due to the temporal interpolation that is required [31].

Multiple variations of the TRICKS technique exist, each with its own unique name. The main differences between these techniques are the size of the central k-space portion that is sampled and how it is combined with k-space periphery data [24]. Like TRICKS, the TREAT technique uses a rectangular keyhole to acquire full lengths of k-space lines with alternating lines of k-space being sampled with each iteration [32]. The TWIST technique alternates between sampling central and peripheral k-space using a spiral, pseudostochastic trajectory. This trajectory is based on the radial distance from the center of k-space and partially updates the k-space periphery

[24, 32]. 4D-TRAK combines the CENTRA technique with sensitivity encoding (SENSE), partial Fourier, and keyhole techniques [2]. A central keyhole ellipsoid of k-space is acquired at each successive dynamic time point, and the periphery of k-space is acquired at the last dynamic time point. The k-space periphery acquired at the end of the scan is then used to reconstruct all of the previous dynamics where only the central keyhole was acquired, ultimately optimizing the speed with which contrast enhancement is captured [24]. 4D-TRAK allows for more than 60-times accelerated MRA with high spatial resolution [2, 24]. Temporal resolutions of 1.6–3 seconds can be achieved within the intracranial vasculature [2]. The temporal performance of dynamic high-resolution 3D TR-CE-MRA is faster than what can be achieved by conventional first-pass CE- or non-CE-MRA techniques [2].

Phase-Contrast MRA (PC-MRA)

PC-MRA generates image contrast by exploiting inherent differences in transverse magnetization that occurs between stationary and moving tissues, resulting in phase shifts [2]. PC-MRA uses a flow-encoding gradient along multiple planes to visualize flow [2, 24]. Gradients are turned on in one direction at a time for a pre-specified time interval before then being switched in orientation for the same amount of time. The first gradient dephases spins, while the second gradient rephases spins that are stationary. After application of this bipolar gradient, stationary spins associated with background tissue will have a zero phase shift, whereas spins associated with the flowing intravascular blood pool will accumulate a net phase shift that can then be visualized [24, 33]. This phase shift is proportional to the flow velocities within the imaged vessels [2] with higher flow velocities accumulating more phase shift. Velocity-induced phase shift can subsequently be quantified [2, 35].

PC-MRA requires preselection of a velocity-encoding factor (Venc) based on whether faster moving arterial blood or slower moving venous blood will be imaged [2]. Appropriate Venc selection is critical to image quality. If the Venc is too low, velocity aliasing occurs, whereas if the Venc is too high, vascular CNR will be too low due to decreased sensitivity to slow flow near the edge of the vessel lumen [2, 24, 33]. A reference image is acquired in addition to the velocity-encoded scan. The reference image can then be subtracted from the flow-sensitive images to remove phase errors unrelated to flow. Because phase shift is proportional to flow velocity, an image can be generated where pixel intensity directly relates to flow velocity [24].

Arterial Spin Labeling MRA (ASL-MRA)

ASL-MRA labels flowing spins within the blood pool for image generation. ASL-MRA requires that two image sets are acquired and later subtracted for final image generation. These two image sets differ only in the magnetization of inflowing

arterial spins. Pseudocontinuous labeling techniques can also be utilized. In this variant, a stream of radiofrequency energy is applied to a thin (~1 cm thick) labeling plane through which intravascular arterial spins flow before traveling downstream into the vasculature of interest. Pseudocontinuous ASL (pCASL) improves the SNR of vessels near the labeling plane. ASL-MRA allows for high arterial contrast and complete elimination of background signal. The use of extended, multiphase readouts can provide time-resolved ASL data as illustrated by triggered angiography noncontrast-enhanced (TRANCE) MRA (Philips Healthcare; Best, Netherlands) [33].

Clinical Considerations for Luminal Imaging

Catheter DSA

Catheter DSA has superior spatial and temporal resolution when compared to noninvasive, cross-sectional luminal imaging modalities, making it well-suited for the detection of small cerebrovascular lesions, such as blister aneurysms of the supraclinoid ICA, small AVMs, and small dural arteriovenous fistula (dAVF). DSA has been shown to better characterize geometric features of aneurysms, including the width and conformation of the aneurysm neck, when compared to CTA and MRA [36]. Traditionally, DSA has been used to assess changes in the intracranial vasculature following open surgery, endovascular intervention, or radiation therapy. Because intra-arterial access is required to perform DSA, examinations can be easily converted into therapeutic endovascular procedures, such as endovascular aneurysm coiling or parent artery reconstruction, should the need arise.

Catheter angiography is an invasive procedure with associated iatrogenic risks. The most serious of these complications is catheter-associated embolic phenomena capable of producing transient or permanent focal neurological deficits. The risk of transient focal neurological deficits following cerebral angiography is estimated to be 0.9%, whereas the risk of permanent neurological deficit is lower, estimated to be 0.5% [6, 37–40]. Arterial wall dissection is also possible. Puncture site complications include perivascular hematoma, arterial pseudoaneurysm formation, arteriovenous fistula formation, and vessel occlusion. The risk of clinically significant perivascular hematoma requiring either surgical evacuation or blood transfusion is approximately 0.2%. The risk of arterial injury or arterial occlusion requiring surgical thrombectomy or thrombolysis is approximately 0.2% [41].

Catheter angiography exposes both patients and operators to radiation. The dose of radiation that one receives increases with increasing frame rate of image acquisition. An individual's cancer risk is proportional to increases in radiation exposure [6, 42, 43]. Unlike noninvasive luminal imaging, catheter angiography requires the coordination and participation of multiple other clinical providers, including dedicated neurointerventionalists and their associated support staff. This makes catheter angiography a time- and resource-intensive endeavor relative to CTA and MRA.

2D DSA projections can limit detection of subtle vascular lesions due to vessel overlap. In these instances, dedicated 3D rotational angiography (3DRA) acquisitions are helpful in further evaluating a region of interest. Despite catheter angiography's superb spatial and temporal resolution, it does not allow for direct visualization of soft tissues, including the vessel wall. Clinically relevant information regarding vessel wall characteristics such as abnormal wall thickening, atherosclerotic plaque burden and composition, vessel wall inflammation, and the presence of intramural hematoma or intraplaque hemorrhage remain largely unknown when catheter angiography is used to assess the intracranial vasculature. In the case of ICAD, catheter DSA can significantly underestimate plaque burden as plaque remodeling often occurs in an outward fashion early in the disease process without appreciable luminal stenosis.

Conventional CTA

The combination of high spatial resolution, short image acquisition time, and the noninvasive nature of conventional CTA makes it an ideal screening examination, particularly in critically ill individuals or in the emergency department setting where efficient patient triage and throughput is essential to overall departmental function. As such, a patient's clinical stability is less of a concern when it comes to CTA image acquisition. Critically ill patients are often able to complete both noncontrast head CT and CTA image acquisitions without issue.

Compared to DSA, there is little short-term risk to patients in performing CTA. Like DSA, iodinated contrast is utilized in CTA imaging protocols. While rare, allergic reactions occur in approximately 0.2–0.7% of patients exposed to intravenous low-osmolar iodinated contrast media. The majority of these reactions are nonlife-threatening [44]. Like contrast-induced allergic reactions, contrast-induced nephropathy is also considered a rare clinical entity that is most likely to occur in patients with poor baseline renal function, though this topic is controversial [45–48] and some question the existence of post-contrast acute kidney injury. Nonetheless, caution should still be exercised in patients with ordered CTA exams who have severely compromised renal function but continue to produce urine [45, 48–50].

CTA is of limited utility in the evaluation of intracranial vascular lesions following open surgical clipping, coil embolization, or endovascular flow diversion. This is due to significant metallic streak artifact generated by these implanted materials. CT imaging in general has difficulty evaluating the posterior cranial fossa and skull base secondary to beam-hardening artifact and photon starvation caused by the dense surrounding bone.

CTA has difficulty detecting small (<3 mm) aneurysms, including blister aneurysms, small bifurcation aneurysms, perforator artery aneurysms, dissecting aneurysms, and peripheral mycotic and myxomatous aneurysms [38]. CTA, with the exception of time-resolved or multiphase CTA, only provides a single time point of

imaging. This limits its ability to thoroughly evaluate vascular lesions that demonstrate shunting phenomena such as intracranial AVMs and dAVFs. Additionally, CTA provides limited information about pathological processes affecting the intracranial arterial walls. While findings such as eccentric narrowing of the vessel lumen may suggest ICAD, these findings are not accurate for vasculopathy differentiation.

DE-CTA

Relative to conventional CTA, DE-CTA can be used to improve vessel contrast, particularly as it relates to small and peripheral blood vessels. This proves particularly useful in the evaluation of the intracranial vasculature. The distinct high- and low-energy spectra generated by DE-CTA can be used to reduce beam-hardening artifact at the skull base and within the posterior cranial fossa. These spectra can also be used to minimize metallic streak artifact from objects such as aneurysm clips, endovascular coil masses, or endovascular flow diverters. DE-CTA can be used to reliably assess vessel patency following endovascular stent placement as well as to evaluate for residual aneurysm sacs following microsurgical clipping. This imaging modality is highly sensitive to parent vessel compromise and residual aneurysm sac formation following the placement of multiple aneurysm clips [9]. DE-CTA can produce VNC images from DE-CTA datasets which are helpful in assessing for intracranial hemorrhage and differentiating hemorrhage from iodinated contrast [10], potentially allowing for better prediction of hematoma expansion. Unlike conventional CTA where patients must be scanned before and after contrast delivery, DE-CTA requires only one scan from which VNC images can be reconstructed. This ultimately reduces patient radiation exposure.

Despite its many advantages, DE-CTA has several pertinent shortcomings. First, DE-CTA exposes patients to ionizing radiation. However, the total radiation dose for DE-CTA is estimated to be equivalent to or reduced relative to standard CTA imaging [7, 10, 12]. Although VNC images can be generated from DE-CTA datasets, they have more noise than conventionally acquired noncontrast head CT images. This image noise, however, does not appear to adversely affect radiologists' abilities to identify acute intracranial hemorrhage [22].

4D-CTA/TI-CTA

The clinical value of 4D-CTA comes from its ability to provide both vascular structural information and the associated flow characteristics, making it useful for the evaluation of flow patterns in acute stroke, Moyamoya disease, AVMs, dAVFs, and large intracranial aneurysms. Additionally, 4D-CTA can provide information regarding the relationship between intracranial tumors and pertinent arterial vascular supplies and venous drainage pathways that may be useful to surgical planning [14].

4D-CTA possesses several unique clinical advantages relative to other luminal imaging techniques. Good correlation exists between 4D-CTA and DSA for the detection and grading of intracranial high-flow vascular malformations [15, 16]. Retrograde cortical venous flow can be visualized with 4D-CTA [15]. 4D-CTA can more accurately grade collateral vascularity in the setting of acute ischemic stroke than conventional CTA [15, 20, 22].

4D-CTA uses ionizing radiation for image acquisition and therefore exposes patients to nontrivial amounts of radiation. Because multiple image acquisitions are performed, the cumulative radiation dose for 4D-CTA is significantly higher than conventional CTA [15]. Despite this fact, the cumulative radiation dose of 4D-CTA is likely still lower than that of catheter DSA [16]. 4D-CTA generates thousands of images as part of a single study. As such, significant computing power is necessary for fast and efficient image post-processing [15].

First-pass CE-MRA

First-pass CE-MRA is a useful imaging modality for the follow-up evaluation of coiled intracranial aneurysms [2]. Compared to noncontrast 3D TOF-MRA, first-pass CE-MRA is more sensitive to the presence of aneurysm neck remnants [51] and can more accurately classify these remnants [2]. The detection of aneurysm neck remnants with 3D TOF-MRA can be improved, however, by scanning with intravenous contrast [51]. Unlike non-CE-MRA techniques, first-pass CE-MRA is relatively insensitive to artifacts generated by turbulent flow and saturation effects [28].

Unlike other MRA techniques, first-pass CE-MRA requires accurate timing of contrast bolus arrival to ensure that the maximum volume of contrast is within the target vessel lumen at the time of scan initiation [2]. The accuracy of first-pass CE-MRA in detecting vascular lesions such as brain aneurysms is limited by the enhancement of adjacent venous structures if timing is delayed [2]. An obvious example of this is the presence of a cavernous segment ICA aneurysm that is surrounded by the cavernous sinus. After aneurysm coiling, the aneurysm wall may demonstrate thin peripheral enhancement which is postulated to represent some combination of peripherally distributed intra-aneurysmal thrombus, vasa vasorum within the adventitial layer of the aneurysm wall, and/or ingrowth of vascularized tissue about the coil mass due to inflammation or healing. Regardless of the underlying etiology, these findings may be confused with a residual aneurysm sac on all types of CE-MRA [51].

TR-CE-MRA

TR-CE-MRA provides a combination of structural and hemodynamic information about the intracranial vasculature. It provides for evaluation of the complex flow patterns of intracranial AVMs and dAVFs [2]. This technique facilitates the

visualization of arterial feeders, the nidus, and draining veins in AVMs [2, 52–54] and allows for the evaluation of dAVFs due to its sensitivity for the detection of early venous drainage [2].

TR-CE-MRA readily depicts vascular lesions with arteriovenous shunting [24, 30]. It can determine the directionality of flow through vascular structures and has excellent suppression of background tissue signal [24]. Unlike other luminal imaging modalities, TR-CE-MRA is relatively insensitive to the shape and timing of the contrast bolus [29]. The start of image acquisition coincides with the start of intravenous contrast injection, and no timing bolus is required [30].

TR-CE-MRA commonly exhibits a trade-off between spatial and temporal resolution, with greater temporal resolution coming at the expense of spatial resolution. Additional loss of SNR can result from the incorporation of acceleration techniques, such as parallel imaging. Blurring of vessel walls commonly occurs when aggressive undersampling is applied [32]. In consideration of the vascular disease being evaluated, balancing the spatial and temporal resolution and imaging acceleration for optimal disease evaluation is paramount.

TOF-MRA

TOF-MRA is routinely used to image the cervical and intracranial arteries. It provides a useful screening tool for asymptomatic patients at higher risk for cerebral aneurysm [33]. 3D TOF-MRA has proven particularly useful in imaging the intracranial vasculature due to its higher spatial resolution, whereas 2D TOF-MRA is typically reserved for evaluation of the cervical vasculature [55].

The scan time for TOF-MRA is longer than first-pass CE-MRA [56]. Signal loss of in-plane flow due to saturation effects can occur, giving the appearance of pseudostenosis or pseudo-occlusion. Signal loss occurs in vessels with complex or turbulent flow, as can be seen in areas of moderate- or high-grade vascular stenosis, large intracranial aneurysms, or arteriovenous malformations, secondary to intravoxel dephasing [55]. In the setting of arterial stenosis, dephasing artifacts can overexaggerate the degree of stenosis or even present a stenosis as an occluded artery [2].

PC-MRA

PC-MRA is an excellent imaging technique for the visualization of the intracranial veins, allowing for accurate detection of dural venous sinus thrombosis [2]. PC-MRA also offers excellent background signal suppression, improving visualization of the intracranial vasculature [33, 55].

The use of multiple flow-encoding gradients lengthens the scan time for PC-MRA relative to other non-CE-MRA techniques [2]. As with TOF-MRA, PC-MRA experiences signal loss in vessels with turbulent flow because of intravoxel dephasing.

This imaging artifact can lead to an overestimation of luminal stenosis [55]. PC-MRA is susceptible to patient motion because of mask subtraction that occurs as part of image generation [55]. PC-MRA image quality is largely dependent upon appropriate Venc parameters. Finally, PC-MRA image post-processing is complex, making it a time- and resource-intensive endeavor [56].

ASL-MRA

ASL-MRA is an imaging technique that provides complete suppression of background tissues, allowing for high-quality angiographic image generation with high CNR [33]. ASL-MRA is well-suited for imaging vascular regions with rapid flow such as the extracranial or intracranial carotid arteries [56].

ASL-MRA is associated with long image acquisition times, requiring two image acquisitions so that the signal from background tissues can be subtracted out of the final image set [33, 55, 56]. Because image subtraction is performed, ASL-MRA is sensitive to patient motion causing misregistration artifact [33, 56]. Like other non-CE-MRA techniques, in cases of slow flow, ASL provides decreased vascular coverage due to a combination of signal losses and the delayed arrival of spin-labeled protons [33]. This is particularly important in the setting of high-grade stenosis causing severe reduction in downstream flow velocities or in patients with poor cardiac output.

Luminal Imaging Characterization of Cerebrovascular Pathology

Intracranial Aneurysms

Intracranial aneurysms are pathological vessel wall outpouchings which can be located anywhere within the intracranial circulation but are commonly encountered at vessel bifurcation points. DSA better characterizes geometric and morphologic features of aneurysms, flow characteristics of aneurysms, as well as the lesion's relationship to the arterial vasculature and small branch origins when compared to CTA and MRA [36]. DSA has a higher sensitivity and specificity for the detection of small supraclinoid blister aneurysms which prove difficult to identify with either CTA or MRA. Additionally, DSA outperforms CTA in the detection of small dissecting aneurysms, perforator artery aneurysms, and small peripheral infectious or myxomatous aneurysms [38].

DSA allows for accurate aneurysm assessment following treatment with microsurgical clipping, endovascular coiling, or flow diversion. After such interventions, DSA accurately identifies residual aneurysm necks and incompletely thrombosed

aneurysm sacs [57] as well as identifies in-stent stenosis following flow diverter placement [57]. While the use of flow-diverting stents has posed many technical challenges to both conventional CTA and MRA evaluation, DSA has not encountered the same issues. Unlike these other luminal imaging modalities, DSA can accurately and reproducibly quantify the degree of in-stent stenosis following flow-diverter placement [58–60].

Information regarding aneurysm size, dome morphology, direction of dome projection, and location in the intracranial circulation can all be attained from CTA with a high degree of accuracy [61]. With conventional CTA, the sensitivity and specificity for aneurysm detection are more than 80% [62]. Unfortunately, CTA assessment of treated aneurysms proves significantly more difficult. Assessment of the aneurysm neck proves particularly difficult. The use of metallic streak artifact reduction techniques paired with iterative and noise-reduction filters is emerging as a promising CTA imaging technique for the evaluation of treated intracranial aneurysms [63].

Like CTA, MRA can also accurately characterize intracranial aneurysms (Fig. 2.4). 3D TOF-MRA demonstrates a sensitivity and specificity for the detection of intracranial aneurysms ≥3 mm that exceeds 80% [64]. First-pass CE-MRA using a 3D T1W gradient echo sequence with short TE and 3D TOF-MRA with contrast are accurate follow-up imaging modalities for the detection and surveillance of aneurysm recanalization after endovascular treatment [58]. These techniques can be used to reliably monitor intracranial aneurysms that have undergone stent-assisted coiling. In these patients, the presence of a stent in the parent artery at the aneurysm neck does not diminish the accuracy of CE-MRA in the detection of aneurysm remnants [58]. It is important to apply MRA with the shortest possible TE in order to limit metallic susceptibility artifact and prevent obscuration of a potential residual aneurysm lumen [51].

Intracranial Arteriovenous Malformations

Intracranial AVMs are abnormal clusters of blood vessels characterized by feeding arteries coalescing into a central nidus which drains directly into veins, bypassing intervening capillary beds (Fig. 2.5). While rare, these lesions are of high clinical significance given their propensity to bleed. In cases of intracranial AVMs, there is a 2–4% risk of spontaneous hemorrhage per year. Following sentinel bleeding episodes, these lesions have a rebleeding risk as high as 30% within the first year, depending on their location and venous drainage patterns [65]. Accurate identification of the AVM nidus, the abnormal feeding arteries, and the venous drainage pathways is critically important to appropriate management decisions and therapy planning [65–67]. DSA allows for accurate characterization of the angioarchitecture as well as characterization of associated perinidal and intranidal aneurysms which, when present, contribute to rupture risk and may affect lesion management [66].

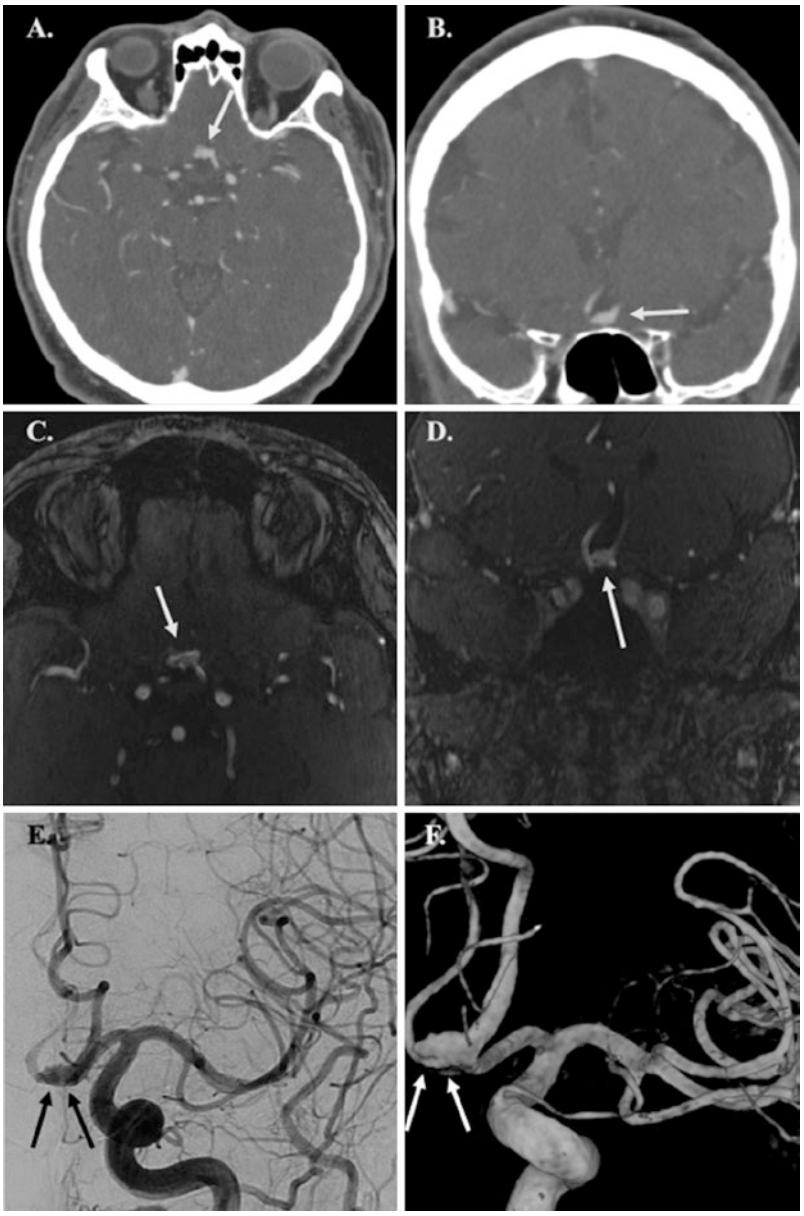

Fig. 2.4 (**a**, **b**) Axial and coronal CTA MIP images demonstrating a saccular aneurysm of the anterior communicating artery (arrows). (**c**, **d**) Axial and coronal 3D-TOF-MRA images again demonstrating a saccular aneurysm of the anterior communicating artery (arrows). (**e**) Frontal DSA projection again demonstrating the anterior communicating artery aneurysm (arrows) visualized on CTA and MRA. (**d**) 3D rotational angiographic image provides better visualization of the aneurysm (arrows). On this image, a focal bleb arising from the right side of the aneurysm sac and a small perforator vessel arising directly from the aneurysm dome are more conspicuous than on 2D DSA alone

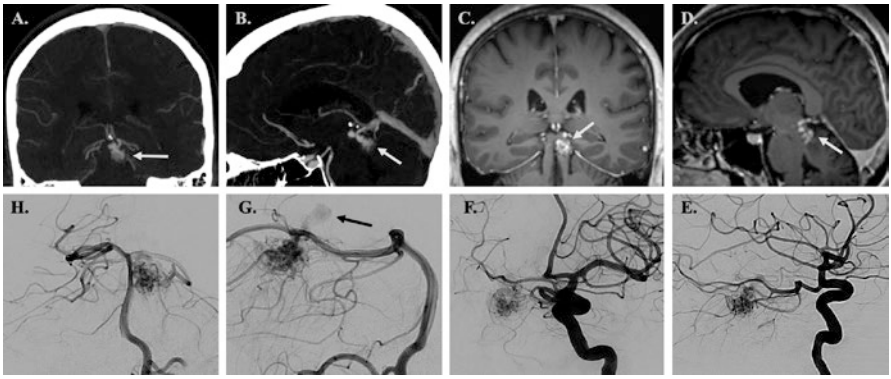

Fig. 2.5 (**a**, **b**) Coronal and sagittal CTA MIP images depicting a small AVM (arrows) within the left midbrain. (**c**, **d**) Coronal and sagittal MPRAGE images again showcasing this small AVM (arrows). (**e**, **f**) Lateral and oblique DSA images show a large left fetal posterior communicating artery supplying blood from the anterior circulation to the AVM nidus. (**g**, **h**) Lateral and transfacial DSA images of a left vertebral artery injection demonstrate a small AVM nidus in the left midbrain that is supplied by left PCA branches. Early faint opacification of a dilated venous varix representing early venous drainage is appreciated (black arrow in image **g**)

The overall sensitivity and specificity of CTA for the detection of underlying vascular anomalies following spontaneous intraparenchymal hemorrhage range from 83.6% to 100% and 77.2% to 100% [68, 69], respectively. When evaluating for only ruptured and unruptured intracranial AVMs, the sensitivity of CTA has been reported to be as high as 90% [70]. This sensitivity increases to more than 95% in cases of unruptured AVM detection. Conversely, the presence of intracranial hemorrhage decreases the sensitivity of CTA to approximately 87% [70]. The sensitivity of CTA for detecting AVMs is also dependent upon lesion size. Small AVMs prove more difficult to detect and evaluate than larger ones. Published reports suggest that the sensitivity of CTA decreases to approximately 60–84% when dealing with AVMs less than 3 cm in diameter [70]. CTA also allows for the identification and characterization of flow-related circle of Willis and perinidal and intranidal aneurysms [65]. Modern CTA has been shown to detect more than 85% of AVM-associated aneurysms [70].

Improvements in the temporal resolution of current TR-CE-MRA techniques have allowed for improved AVM characterization. Current TR-CE-MRA techniques can delineate arterial inflow and identify the AVM nidus [71] as well as increase diagnostic confidence [72]. Despite these improvements, accurate depiction of venous drainage remains difficult. Additionally, MRA generally performs poorly in the identification of flow-related perinidal and intranidal aneurysms [70]. DSA is typically required to both accurately characterize lesional venous drainage and confidently exclude perinidal/intranidal aneurysms following AVM detection with MRA or CTA.

Dural Arteriovenous Fistulas

Dural arteriovenous fistulae (dAVFs) are pathological anastomoses between meningeal arteries and dural sinuses or cortical veins (Fig. 2.6). They are distinguished from pial AVMs by their arterial supply and lack of a parenchymal nidus. The risk of adverse neurological events depends on the degree of dural sinus involvement and the presence of cortical vein reflux, with cortical vein reflux representing a known risk factor for hemorrhage. The pathophysiology underlying the development of these lesions is not well known; however, in a small subset of these lesions, head trauma, infection, tumor, dural sinus thrombosis, or prior craniotomy are favored to represent contributing factors for their formation [73].

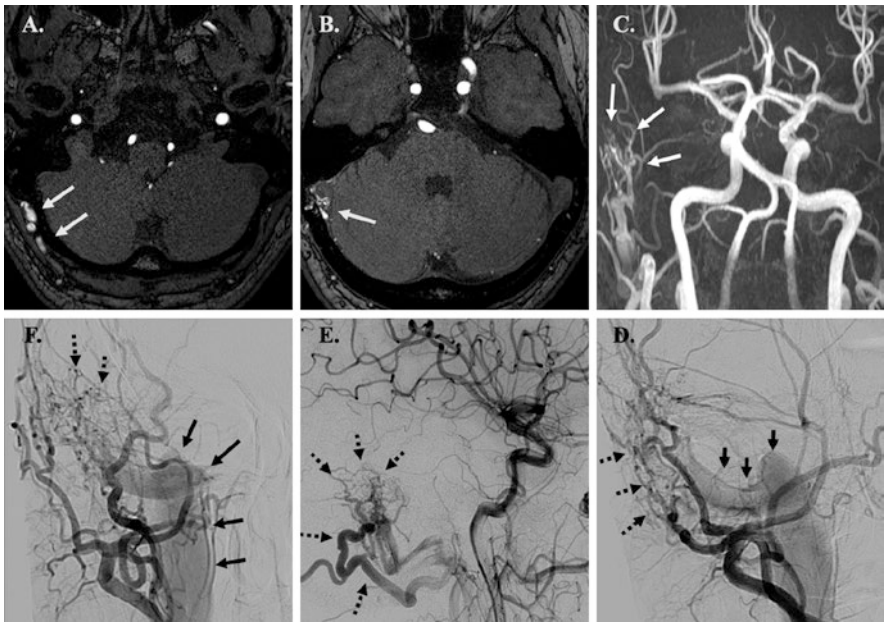

Fig. 2.6 (**a**, **b**) Axial 3D-TOF-MRA images showing dilated branches of the right occipital artery draining into the right sigmoid sinus (arrows) consistent with a dural AVF. (**c**) Coronal 3D-TOF-MRA MIP image showing asymmetrically hypertrophied extracranial vessels in the vicinity of the right sigmoid sinus (arrows). (**d**, **f**) Oblique, lateral, and frontal DSA images better illustrate the angioarchitecture of this dural AVF. The fistula is supplied by hypertrophied branches of the right occipital, posterior auricular, and middle meningeal arteries (dashed lines). Early venous drainage into a dilated right sigmoid sinus and internal jugular vein is also appreciated (solid black arrows). The high temporal resolution of DSA provides important hemodynamic information regarding flow through the lesion. Additionally, subtle cortical vein reflux that might otherwise be missed on CTA or MRA is more readily identified on DSA

Catheter DSA allows for accurate delineation of feeder artery anatomy, arteriovenous shunting, dural sinus and venous anatomy, and cortical vein reflux [65, 73, 74]. In addition to cortical vein reflux, catheter angiography identifies engorged leptomeningeal veins which are another imaging finding of venous congestion [73, 74]. Evaluation of dAVFs with CTA is difficult as these lesions often do not have a nidus. CTA features of dAVFs include the early opacification of a dural sinus, stenosis or thrombosis of a dural sinus, asymmetric enlargement of cortical veins, and the presence of enlarged medullary or pial veins [65, 75]. The presence of medullary or pial vein enhancement on CTA is reported to have the highest specificity for dural AVFs with associated cortical vein reflux with a specificity greater than 90% [75].

Historically, the evaluation of dAVFs with MRA was difficult given the lack of lesion nidus and the complex associated flow patterns. Technical improvements in TR-CE-MRA have made this technique a more viable imaging alternative for dAVF screening and evaluation [74]. Improvements in temporal resolution using techniques such as CENTRA k-space sampling have improved separation of arterial and venous phases, allowing for improved visualization of venous outflow [76]. In a small cohort, TRICKS-MRA has been shown to correctly identify (or exclude) and grade dAVFs relative to catheter DSA in more than 90% of cases [77].

Intracranial Vasculopathies

Intracranial vasculopathies represent an array of disease processes which affect the walls of intracranial arteries. These disease processes ultimately manifest as single or multifocal narrowing or irregularity on luminal imaging. These diseases include intracranial atherosclerotic disease (ICAD), reversible cerebral vasoconstriction syndrome (RCVS), infectious/inflammatory vasculitis, and Moyamoya disease (MMD). ICAD has a variety of appearances on luminal imaging. Early in the disease process, there is outward vessel wall remodeling with minimal or no luminal stenosis [78]. As ICAD progresses, eccentric luminal stenosis is frequently present [79–81]. ICAD most commonly involves arterial bifurcation points and more commonly involves proximal intracranial arteries (Fig. 2.7). Unlike ICAD, infectious/inflammatory vasculitis (Figs. 2.8 and 2.9) and RCVS will often present with concentric luminal stenoses that is thought to more commonly involve peripheral branches as compared to ICAD [81–83]. Luminal imaging features of RCVS include involvement of multiple vascular territories with a beaded appearance of medium to large cerebral vessels with multifocal areas of narrowing interspersed with normal caliber vessel segments [84]. RCVS may also present as diffuse luminal narrowing (Fig. 2.10). In cases of first-pass CE-MRA or 3D TOF-MRA with contrast, smooth concentric vessel enhancement may be appreciated at the site of stenosis in patients with underlying infectious/inflammatory vasculitis [85]. This enhancement is better visualized on dedicated vessel wall imaging (VWI) studies.

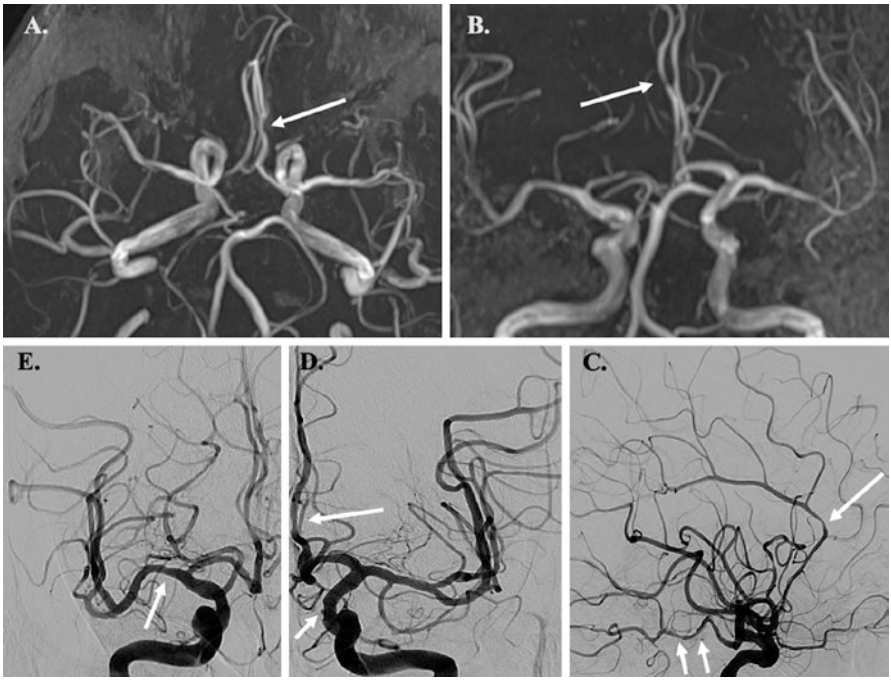

Fig. 2.7 (**a**, **b**) Axial and coronal 3D-TOF-MRA MIP images showing focal stenosis of the proximal left A2 segment (arrow). (**c**) Lateral DSA image of the left ICA highlights eccentric, multifocal narrowing of the left ACA and the left PCA (arrows). (**d**) Frontal DSA image of the left ICA shows eccentric narrowing of the supraclinoid ICA and proximal A2 segment (arrows). (**e**) Frontal DSA image of the right ICA with eccentric narrowing of the proximal M1 segment (arrow). The eccentric distribution of these multifocal stenoses within the proximal intracranial vasculature, closely associated with arterial branch points, is consistent with intracranial atherosclerotic disease (ICAD)

In the case of MMD, luminal imaging commonly demonstrates stenosis and occlusion of the carotid termini, proximal MCAs, and proximal ACAs with development of robust compensatory collateral vessels as the disease process progresses (Fig. 2.11), at least in the middle stages of disease evolution [80, 86]. True MMD commonly demonstrates concentric, smooth tapering until occlusion, whereas MMS caused by ICAD is more likely to have irregular occlusion and will more frequently involve other vascular territories with irregular, multifocal narrowing, although MMD may also involve the posterior circulation [86]. While MMD does not have to involve both sides equivalently at the time of detection, the patient will eventually develop bilateral steno-occlusive disease. This is not the case with many MMS processes. There is frequently proximal collapse of the ipsilateral cervical internal carotid artery in MMD secondary to downstream outflow obstruction.

Luminal imaging, such as DSA, provides information regarding the severity and distribution of luminal stenoses in patients with an underlying intracranial vascu-

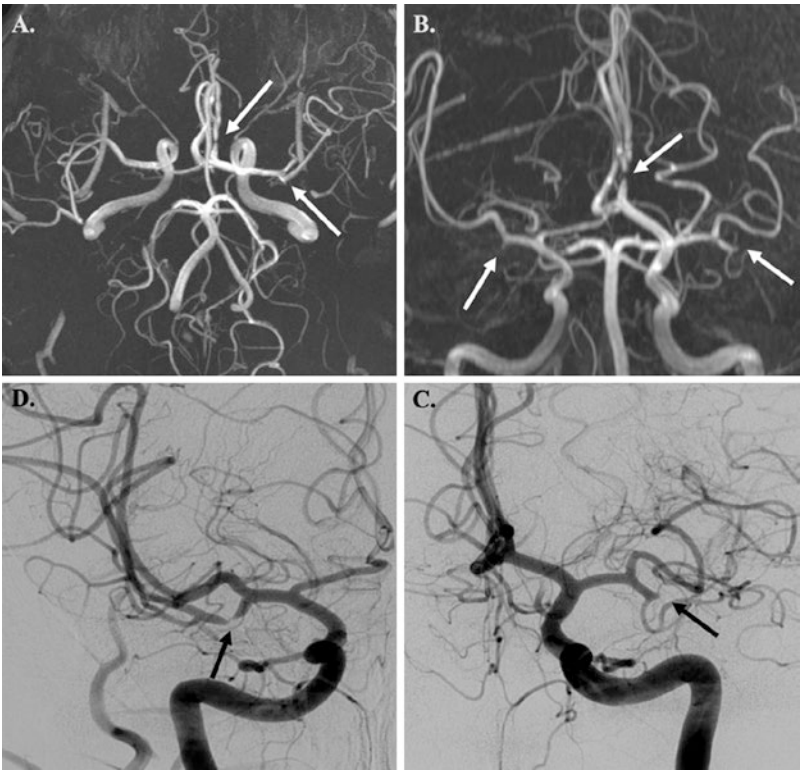

Fig. 2.8 (**a**) Axial 3D-TOF-MRA MIP shows occlusion of the inferior division of the left MCA and focal stenosis of the left A2 segment (arrows). (**b**) Coronal 3D-TOF-MRA MIP shows occlusion of the inferior divisions of the bilateral MCAs and high-grade left ACA stenosis (arrows). (**c**) Frontal DSA image of the left ICA demonstrates complete occlusion of the inferior division of the left MCA (arrow). (**d**) Frontal DSA image of the right ICA shows a high-grade, eccentric stenosis of the inferior division of the right MCA (arrow). MRA tends to overestimate the degree of luminal stenosis, as is evident in this case. Although the eccentric distribution of the stenosis is more commonly associated with ICAD, this patient had PCR-confirmed varicella-zoster virus (VZV) vasculitis

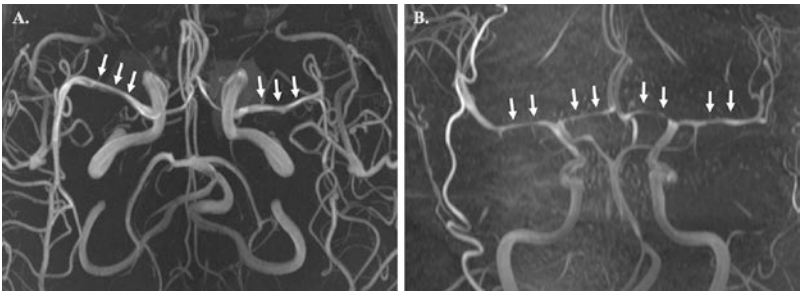

Fig. 2.9 (**a**) Axial 3D-TOF-MRA MIP image with diffuse narrowing of the bilateral M1 and proximal M2 segments (arrows). (**b**) Coronal 3D-TOF-MRA MIP image demonstrating severe diffuse narrowing of the bilateral M1 and A1 segments (arrows). This patient was found to have fungal meningitis complicated by severe vasculitis

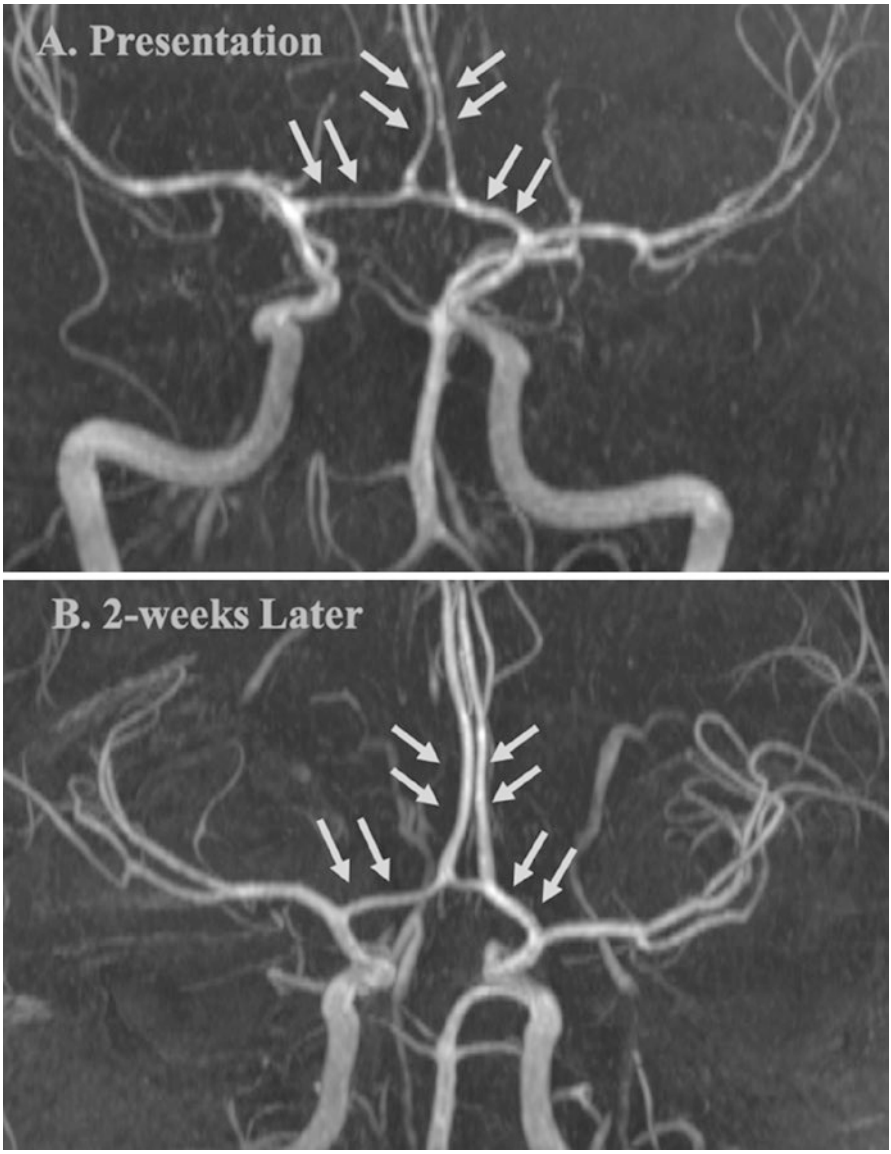

Fig. 2.10 (**a**) 3D-TOF-MRA demonstrates segmental narrowing of the bilateral A1 and A2 segments (arrows) at initial presentation. The affected arterial segments have a subtle beaded appearance. (**b**) Repeat MRA performed 2 weeks later illustrates marked improvement in vessel caliber (arrows). Although the luminal narrowing is nonspecific, the spontaneous improvement in the caliber of these arterial segments with time is consistent with reversible cerebral vasoconstriction syndrome (RCVS)

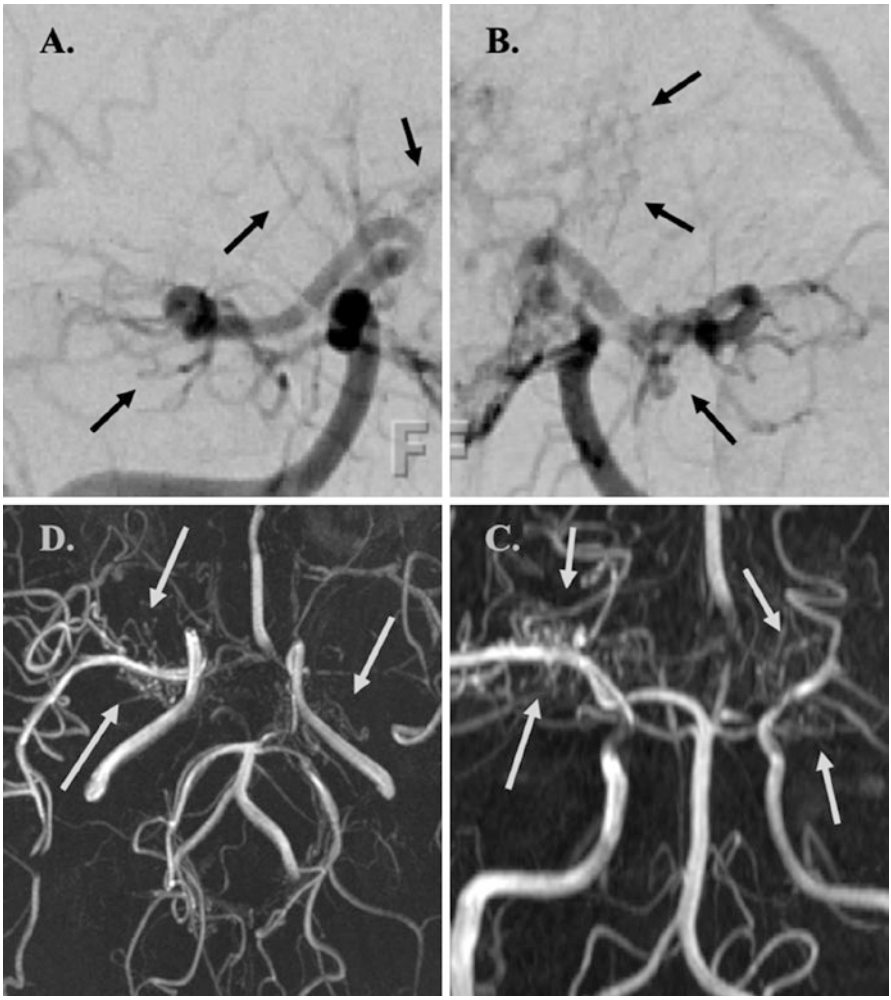

Fig. 2.11 (**a**, **b**) Frontal projection DSA images depicts steno-occlusive disease of the bilateral ICAs secondary to Moyamoya disease (MMD). There is occlusion of the terminal ICAs with development of robust compensatory basal ganglia perforators (arrows) giving the characteristic "puff of smoke" appearance associated with this disease process. (**c**, **d**) 3D-TOF-MRA MIP performed on a different patient again highlights steno-occlusive disease of the bilateral terminal ICAs with robust collateral vessel formation (arrows), compatible with MMD. MMD is a diagnosis of exclusion, reached only after other underlying vasculopathies are excluded. These include ICAD, infectious/inflammatory vasculopathy, or radiation-induced vasculopathy. If an underlying etiology for the luminal imaging abnormalities is identified, then a diagnosis of Moyamoya syndrome (MMS) is made. Unfortunately, luminal imaging has extreme difficulty discriminating between underlying vasculopathy etiologies

lopathy. However, these findings are not specific to any one disease process. The high spatial resolution of DSA allows for accurate evaluation of small peripheral arterial branches in addition to the circle of Willis and large proximal arterial segments [84, 87]. In cases of ICAD, the degree of luminal stenosis has proven helpful in predicting individual patient stroke risk [88, 89].

In most cases of intracranial vasculopathy, CTA and MRA will demonstrate segmental luminal narrowing of varying severity [84]. Although CT is sensitive to vascular calcifications, there is little impact of this finding in shaping one's differential diagnosis as these findings are most commonly related to senescence [90]. Multiple studies have demonstrated that it is difficult to confidently suggest an underlying etiology for multifocal intracranial stenoses based on luminal imaging findings alone [80, 81, 91] (Fig. 2.12). The accuracy of CTA in diagnosing ICAD has been reported to be less than 32%, whereas the accuracy with which it can diagnose intracranial vasculitis has been reported to be less than 15% [80].

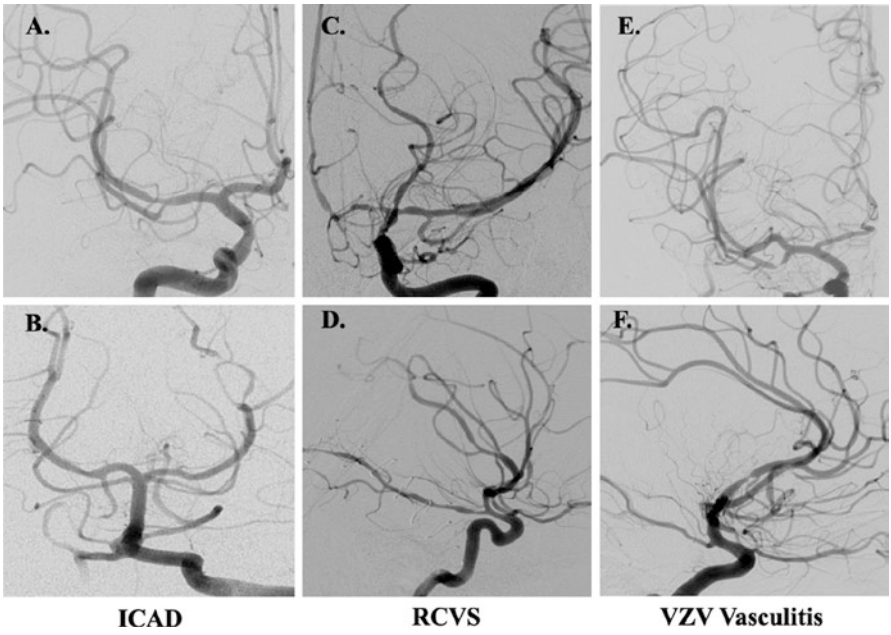

Fig. 2.12 (**a**, **b**) DSA images of the right ICA and posterior circulation, respectively, with multifocal luminal stenoses secondary to ICAD. (**c**, **d**) Oblique and lateral DSA images of the left ICA with multifocal stenoses secondary to RCVS. (**e**, **f**) Oblique and lateral DSA images of the left ICA with multifocal high-grade stenoses secondary to VZV vasculitis. Based on luminal imaging alone, it is nearly impossible to differentiate between these underlying etiologies. Advanced imaging techniques, such as dedicated MR vessel wall imaging (VWI), prove helpful in better differentiating causes for intracranial vasculopathy

Future Directions of Luminal Imaging

At present, luminal imaging provides limited information about the health of the vessel wall. Dedicated high spatial resolution vessel wall imaging (VWI) techniques that null intraluminal blood signal for improved vessel wall visualization may provide new insights into a multitude of cerebrovascular pathologies [92]. Moving forward, techniques that incorporate both luminal imaging and VWI acquisitions in the same sequence may prove to replace MR luminal imaging [91, 93–99]. Incorporation of VWI data into the luminal scan can help identify combinations of distinct imaging findings that can differentiate specific types of intracranial vasculopathies or better characterize disease risk [80, 81, 91, 100, 101].

Other new emerging imaging techniques will undoubtedly improve the quality of current luminal imaging. For instance, ultrashort echo time (UTE) MRA has the potential to reduce flow artifacts from turbulent flow and off-resonance artifacts from metallic implants [56]. In this technique, a short duration, spatially nonselective hard pulse for radiofrequency excitation, simultaneous gradient ramping and data acquisition, and k-space sampling with half radial projections are performed [56]. The development of simultaneous multislice (SMS) image acquisition techniques has the potential to accelerate image acquisition by a factor proportional to the number of slices/slabs simultaneously acquired [56, 102]. Incorporation of compressed sensing-sensitivity encoding (CS-SENSE) techniques, which rely on random undersampling of k-space, into MRA image acquisition algorithms represents another promising alternative for MRA acquisition acceleration that still preserves image quality [103]. The implementation of deep learning algorithms into imaging workflows and image processing has the potential to dramatically increase radiologist efficiency and image quality [56]. Implementation of intracranial artery feature extraction algorithms may provide quantitative vascular data that may better predict patient outcomes in the setting of intracranial vascular disease, including stroke and dementia [104].

References

1. Bechan RS, van Rooij SB, Sprengers ME, Peluso JP, Sluzewski M, Majoie CB, van Rooij WJ. CT angiography versus 3D rotational angiography in patients with subarachnoid hemorrhage. Neuroradiology. 2015;57(12):1239–46.
2. Chandra T, Pukenas B, Mohan S, Melhem E. Contrast-enhanced magnetic resonance angiography. Magn Reson Imaging Clin N Am. 2012;20(4):687–98.
3. Agid R, Andersson T, Almqvist H, Willinsky RA, Lee SK, ter Brugge KG, Farb RI, Soderman M. Negative CT angiography findings in patients with spontaneous subarachnoid hemorrhage: when is digital subtraction angiography still needed? AJNR Am J Neuroradiol. 2010;31(4):696–705.
4. Anderson GB, Ashforth R, Steinke DE, Findlay JM. CT angiography for the detection of cerebral vasospasm in patients with acute subarachnoid hemorrhage. AJNR Am J Neuroradiol. 2000;21(6):1011–5.

5. Aralasmak A, Akyuz M, Ozkaynak C, Sindel T, Tuncer R. CT angiography and perfusion imaging in patients with subarachnoid hemorrhage: correlation of vasospasm to perfusion abnormality. Neuroradiology. 2009;51(2):85–93.
6. Khosravani H, Mayer SA, Demchuk A, Jahromi BS, Gladstone DJ, Flaherty M, Broderick J, Aviv RI. Emergency noninvasive angiography for acute intracerebral hemorrhage. AJNR Am J Neuroradiol. 2013;34(8):1481–7.
7. Vogl TJ, Schulz B, Bauer RW, Stover T, Sader R, Tawfik AM. Dual-energy CT applications in head and neck imaging. AJR Am J Roentgenol. 2012;199(5 Suppl):S34–9.
8. Watanabe Y, Tsukabe A, Kunitomi Y, Nishizawa M, Arisawa A, Tanaka H, Yoshiya K, Shimazu T, Tomiyama N. Dual-energy CT for detection of contrast enhancement or leakage within high-density haematomas in patients with intracranial haemorrhage. Neuroradiology. 2014;56(4):291–5.
9. Dolati P, Eichberg D, Wong JH, Goyal M. The utility of dual-energy computed tomographic angiography for the evaluation of brain aneurysms after surgical clipping: a prospective study. World Neurosurg. 2015;84(5):1362–71.
10. Machida H, Tanaka I, Fukui R, Shen Y, Ishikawa T, Tate E, Ueno E. Dual-energy spectral CT: various clinical vascular applications. Radiographics. 2016;36(4):1215–32.
11. Deng K, Liu C, Ma R, Sun C, Wang XM, Ma ZT, Sun XL. Clinical evaluation of dual-energy bone removal in CT angiography of the head and neck: comparison with conventional bone-subtraction CT angiography. Clin Radiol. 2009;64(5):534–41.
12. Zhang LJ, Wu SY, Niu JB, Zhang ZL, Wang HZ, Zhao YE, Chai X, Zhou CS, Lu GM. Dual-energy CT angiography in the evaluation of intracranial aneurysms: image quality, radiation dose, and comparison with 3D rotational digital subtraction angiography. AJR Am J Roentgenol. 2010;194(1):23–30.
13. Zhang LJ, Wu SY, Poon CS, Zhao YE, Chai X, Zhou CS, Lu GM. Automatic bone removal dual-energy CT angiography for the evaluation of intracranial aneurysms. J Comput Assist Tomogr. 2010;34(6):816–24.
14. Alnemari A, Mansour TR, Bazerbashi M, Buehler M, Schroeder J, Gaudin D. Dynamic four-dimensional computed tomography angiography for neurovascular pathologies. World Neurosurg. 2017;105:1034 e1011-1034 e1018.
15. Kortman HG, Smit EJ, Oei MT, Manniesing R, Prokop M, Meijer FJ. 4D-CTA in neurovascular disease: a review. AJNR Am J Neuroradiol. 2015;36(6):1026–33.
16. Willems PW, Taeshineetanakul P, Schenk B, Brouwer PA, Terbrugge KG, Krings T. The use of 4D-CTA in the diagnostic work-up of brain arteriovenous malformations. Neuroradiology. 2012;54(2):123–31.
17. Smit EJ, Vonken EJ, Meijer FJ, Dankbaar JW, Horsch AD, van Ginneken B, Velthuis B, van der Schaaf I, Prokop M. Timing-invariant CT angiography derived from CT perfusion imaging in acute stroke: a diagnostic performance study. AJNR Am J Neuroradiol. 2015;36(10):1834–8.
18. Dehkharghani S, Bammer R, Straka M, Bowen M, Allen JW, Rangaraju S, Kang J, Gleason T, Brasher C, Nahab F. Performance of CT ASPECTS and collateral score in risk stratification: can target perfusion profiles be predicted without perfusion imaging? AJNR Am J Neuroradiol. 2016;37(8):1399–404.
19. Vagal A, Menon BK, Foster LD, Livorine A, Yeatts SD, Qazi E, d'Esterre C, Shi J, Demchuk AM, Hill MD, et al. Association between CT angiogram collaterals and CT perfusion in the interventional management of stroke III trial. Stroke. 2016;47(2):535–8.
20. van den Wijngaard IR, Boiten J, Holswilder G, Algra A, Dippel DW, Velthuis BK, Wermer MJ, van Walderveen MA. Impact of collateral status evaluated by dynamic computed tomographic angiography on clinical outcome in patients with ischemic stroke. Stroke. 2015;46(12):3398–404.
21. van Seeters T, Biessels GJ, Kappelle LJ, van der Schaaf IC, Dankbaar JW, Horsch AD, Niesten JM, Luitse MJ, Majoie CB, Vos JA, et al. CT angiography and CT perfusion improve prediction of infarct volume in patients with anterior circulation stroke. Neuroradiology. 2016;58(4):327–37.

22. Zhang S, Chen W, Tang H, Han Q, Yan S, Zhang X, Chen Q, Parsons M, Wang S, Lou M. The prognostic value of a four-dimensional CT angiography-based collateral grading scale for reperfusion therapy in acute ischemic stroke patients. PLoS One. 2016;11(8):e0160502.
23. Anzalone N, Scomazzoni F, Cirillo M, Righi C, Simionato F, Cadioli M, Iadanza A, Kirchin MA, Scotti G. Follow-up of coiled cerebral aneurysms at 3T: comparison of 3D time-of-flight MR angiography and contrast-enhanced MR angiography. AJNR Am J Neuroradiol. 2008;29(8):1530–6.
24. Ivancevic MK, Geerts L, Weadock WJ, Chenevert TL. Technical principles of MR angiography methods. Magn Reson Imaging Clin N Am. 2009;17(1):1–11.
25. Bremerich J, Bilecen D, Reimer P. MR angiography with blood pool contrast agents. Eur Radiol. 2007;17(12):3017–24.
26. Frydrychowicz A, Russe MF, Bock J, Stalder AF, Bley TA, Harloff A, Markl M. Comparison of gadofosveset trisodium and gadobenate dimeglumine during time-resolved thoracic MR angiography at 3T. Acad Radiol. 2010;17(11):1394–400.
27. Amarteifio E, Essig M, Bockler D, Attigah N, Schuster L, Demirel S. Comparison of gadofosveset (Vasovist((R))) with gadobenate dimeglumine (Multihance((R)))-enhanced MR angiography for high-grade carotid artery stenosis. J Neuroradiol. 2015;42(4):236–44.
28. Kau T, Gasser J, Celedin S, Rabitsch E, Eicher W, Uhl E, Hausegger KA. MR angiographic follow-up of intracranial aneurysms treated with detachable coils: evaluation of a blood-pool contrast medium. AJNR Am J Neuroradiol. 2009;30(8):1524–30.
29. Korosec FR, Frayne R, Grist TM, Mistretta CA. Time-resolved contrast-enhanced 3D MR angiography. Magn Reson Med. 1996;36(3):345–51.
30. Razek AA, Gaballa G, Megahed AS, Elmogy E. Time resolved imaging of contrast kinetics (TRICKS) MR angiography of arteriovenous malformations of head and neck. Eur J Radiol. 2013;82(11):1885–91.
31. Grist TM, Mistretta CA, Strother CM, Turski PA. Time-resolved angiography: past, present, and future. J Magn Reson Imaging. 2012;36(6):1273–86.
32. Lim RP, Shapiro M, Wang EY, Law M, Babb JS, Rueff LE, Jacob JS, Kim S, Carson RH, Mulholland TP, et al. 3D time-resolved MR angiography (MRA) of the carotid arteries with time-resolved imaging with stochastic trajectories: comparison with 3D contrast-enhanced Bolus-Chase MRA and 3D time-of-flight MRA. AJNR Am J Neuroradiol. 2008;29(10):1847–54.
33. Lim RP, Koktzoglou I. Noncontrast magnetic resonance angiography: concepts and clinical applications. Radiol Clin N Am. 2015;53(3):457–76.
34. Choi J, Seo H, Lim Y, Han Y, Park H. Sliding time of flight: sliding time of flight MR angiography using a dynamic image reconstruction method. Magn Reson Med. 2015;73(3):1177–83.
35. Miyazaki M, Akahane M. Non-contrast enhanced MR angiography: established techniques. J Magn Reson Imaging. 2012;35(1):1–19.
36. Kim HJ, Yoon DY, Kim ES, Lee HJ, Jeon HJ, Lee JY, Cho BM. Intraobserver and interobserver variability in CT angiography and MR angiography measurements of the size of cerebral aneurysms. Neuroradiology. 2017;59(5):491–7.
37. Dawkins AA, Evans AL, Wattam J, Romanowski CA, Connolly DJ, Hodgson TJ, Coley SC. Complications of cerebral angiography: a prospective analysis of 2,924 consecutive procedures. Neuroradiology. 2007;49(9):753–9.
38. Heit JJ, Pastena GT, Nogueira RG, Yoo AJ, Leslie-Mazwi TM, Hirsch JA, Rabinov JD. Cerebral angiography for evaluation of patients with CT angiogram-negative subarachnoid hemorrhage: An 11-year experience. AJNR Am J Neuroradiol. 2016;37(2):297–304.
39. Thiex R, Norbash AM, Frerichs KU. The safety of dedicated-team catheter-based diagnostic cerebral angiography in the era of advanced noninvasive imaging. AJNR Am J Neuroradiol. 2010;31(2):230–4.
40. Willinsky RA, Taylor SM, TerBrugge K, Farb RI, Tomlinson G, Montanera W. Neurologic complications of cerebral angiography: prospective analysis of 2,899 procedures and review of the literature. Radiology. 2003;227(2):522–8.

41. Citron SJ, Wallace RC, Lewis CA, Dawson RC, Dion JE, Fox AJ, Manzione JV, Payne CS, Rivera FJ, Russell EJ, et al. Quality improvement guidelines for adult diagnostic neuroangiography. Cooperative study between ASITN, ASNR, and SIR. J Vasc Interv Radiol. 2003;14(9 Pt 2):S257–62.
42. Brenner DJ, Hall EJ. Computed tomography--an increasing source of radiation exposure. N Engl J Med. 2007;357(22):2277–84.
43. Sodickson A, Baeyens PF, Andriole KP, Prevedello LM, Nawfel RD, Hanson R, Khorasani R. Recurrent CT, cumulative radiation exposure, and associated radiation-induced cancer risks from CT of adults. Radiology. 2009;251(1):175–84.
44. Cochran ST, Bomyea K, Sayre JW. Trends in adverse events after IV administration of contrast media. AJR Am J Roentgenol. 2001;176(6):1385–8.
45. McDonald JS, McDonald RJ, Carter RE, Katzberg RW, Kallmes DF, Williamson EE. Risk of intravenous contrast material-mediated acute kidney injury: a propensity score-matched study stratified by baseline-estimated glomerular filtration rate. Radiology. 2014;271(1):65–73.
46. McDonald JS, McDonald RJ, Tran CL, Kolbe AB, Williamson EE, Kallmes DF. Postcontrast acute kidney injury in pediatric patients: a cohort study. Am J Kidney Dis. 2018;72(6):811–8.
47. McDonald JS, McDonald RJ, Williamson EE, Kallmes DF, Kashani K. Post-contrast acute kidney injury in intensive care unit patients: a propensity score-adjusted study. Intensive Care Med. 2017;43(6):774–84.
48. McDonald RJ, McDonald JS, Bida JP, Carter RE, Fleming CJ, Misra S, Williamson EE, Kallmes DF. Intravenous contrast material-induced nephropathy: causal or coincident phenomenon? Radiology. 2013;267(1):106–18.
49. Davenport MS, Khalatbari S, Cohan RH, Dillman JR, Myles JD, Ellis JH. Contrast material-induced nephrotoxicity and intravenous low-osmolality iodinated contrast material: risk stratification by using estimated glomerular filtration rate. Radiology. 2013;268(3):719–28.
50. Davenport MS, Khalatbari S, Dillman JR, Cohan RH, Caoili EM, Ellis JH. Contrast material-induced nephrotoxicity and intravenous low-osmolality iodinated contrast material. Radiology. 2013;267(1):94–105.
51. Wallace RC, Karis JP, Partovi S, Fiorella D. Noninvasive imaging of treated cerebral aneurysms, part I: MR angiographic follow-up of coiled aneurysms. AJNR Am J Neuroradiol. 2007;28(6):1001–8.
52. Blackham KA, Passalacqua MA, Sandhu GS, Gilkeson RC, Griswold MA, Gulani V. Applications of time-resolved MR angiography. AJR Am J Roentgenol. 2011;196(5):W613–20.
53. Machet A, Portefaix C, Kadziolka K, Robin G, Lanoix O, Pierot L. Brain arteriovenous malformation diagnosis: value of time-resolved contrast-enhanced MR angiography at 3.0T compared to DSA. Neuroradiology. 2012;54(10):1099–108.
54. Zou Z, Ma L, Cheng L, Cai Y, Meng X. Time-resolved contrast-enhanced MR angiography of intracranial lesions. J Magn Reson Imaging. 2008;27(4):692–9.
55. Morita S, Masukawa A, Suzuki K, Hirata M, Kojima S, Ueno E. Unenhanced MR angiography: techniques and clinical applications in patients with chronic kidney disease. Radiographics. 2011;31(2):E13–33.
56. Edelman RR, Koktzoglou I. Noncontrast MR angiography: An update. J Magn Reson Imaging. 2019;49(2):355–73.
57. van Amerongen MJ, Boogaarts HD, de Vries J, Verbeek AL, Meijer FJ, Prokop M, Bartels RH. MRA versus DSA for follow-up of coiled intracranial aneurysms: a meta-analysis. AJNR Am J Neuroradiol. 2014;35(9):1655–61.
58. Agid R, Schaaf M, Farb R. CE-MRA for follow-up of aneurysms post stent-assisted coiling. Interv Neuroradiol. 2012;18(3):275–83.
59. Attali J, Benaissa A, Soize S, Kadziolka K, Portefaix C, Pierot L. Follow-up of intracranial aneurysms treated by flow diverter: comparison of three-dimensional time-of-flight MR angiography (3D-TOF-MRA) and contrast-enhanced MR angiography (CE-MRA) sequences with digital subtraction angiography as the gold standard. J Neurointerv Surg. 2016;8(1):81–6.

60. Boddu SR, Tong FC, Dehkharghani S, Dion JE, Saindane AM. Contrast-enhanced time-resolved MRA for follow-up of intracranial aneurysms treated with the pipeline embolization device. AJNR Am J Neuroradiol. 2014;35(11):2112–8.
61. Heit JJ, Gonzalez RG, Sabbag D, Brouwers HB, Ordonez Rubiano EG, Schaefer PW, Hirsch JA, Romero JM. Detection and characterization of intracranial aneurysms: a 10-year multidetector CT angiography experience in a large center. J Neurointerv Surg. 2016;8(11):1168–72.
62. Chen X, Liu Y, Tong H, Dong Y, Ma D, Xu L, Yang C. Meta-analysis of computed tomography angiography versus magnetic resonance angiography for intracranial aneurysm. Medicine (Baltimore). 2018;97(20):e10771.
63. Duarte Conde MP, de Korte AM, Meijer FJA, Aquarius R, Boogaarts HD, Bartels R, de Vries J. Subtraction CTA: An alternative imaging option for the follow-up of flow-diverter-treated aneurysms? AJNR Am J Neuroradiol. 2018;39(11):2051–6.
64. HaiFeng L, YongSheng X, YangQin X, Yu D, ShuaiWen W, XingRu L, JunQiang L. Diagnostic value of 3D time-of-flight magnetic resonance angiography for detecting intracranial aneurysm: a meta-analysis. Neuroradiology. 2017;59(11):1083–92.
65. Barreau X, Marnat G, Gariel F, Dousset V. Intracranial arteriovenous malformations. Diagn Interv Imaging. 2014;95(12):1175–86.
66. Grobovschek M, Himmer M, Wolfsgruber P, Weymayr F. Intracranial aneurysms and vascular malformations: diagnosis for therapy. A long-term study at a central hospital. A Neuroradiological approach. Part II: 2000-2008. The time of the beginning with newer diagnostic developments in CT, MR, DSA for endovascular intervention, microneurosurgery, radiotherapy. Neuroradiol J. 2011;24(6):889–94.
67. Spetzler RF, Martin NA. A proposed grading system for arteriovenous malformations. J Neurosurg. 1986;65(4):476–83.
68. Delgado Almandoz JE, Schaefer PW, Forero NP, Falla JR, Gonzalez RG, Romero JM. Diagnostic accuracy and yield of multidetector CT angiography in the evaluation of spontaneous intraparenchymal cerebral hemorrhage. AJNR Am J Neuroradiol. 2009;30(6):1213–21.
69. Derdeyn CP, Zipfel GJ, Albuquerque FC, Cooke DL, Feldmann E, Sheehan JP, Torner JC. Management of Brain Arteriovenous Malformations: a scientific statement for healthcare professionals from the American Heart Association/American Stroke Association. Stroke. 2017;48(8):e200–24.
70. Gross BA, Frerichs KU, Du R. Sensitivity of CT angiography, T2-weighted MRI, and magnetic resonance angiography in detecting cerebral arteriovenous malformations and associated aneurysms. J Clin Neurosci. 2012;19(8):1093–5.
71. Eddleman CS, Jeong HJ, Hurley MC, Zuehlsdorff S, Dabus G, Getch CG, Batjer HH, Bendok BR, Carroll TJ. 4D radial acquisition contrast-enhanced MR angiography and intracranial arteriovenous malformations: quickly approaching digital subtraction angiography. Stroke. 2009;40(8):2749–53.
72. Schubert T, Wu Y, Johnson KM, Wieben O, Maksimovic J, Mistretta C, Turski P. Time-of-arrival parametric maps and Virtual Bolus images derived from contrast-enhanced time-resolved radial magnetic resonance angiography improve the display of brain arteriovenous malformation vascular anatomy. Investig Radiol. 2016;51(11):706–13.
73. Reynolds MR, Lanzino G, Zipfel GJ. Intracranial Dural Arteriovenous Fistulae. Stroke. 2017;48(5):1424–31.
74. Gandhi D, Chen J, Pearl M, Huang J, Gemmete JJ, Kathuria S. Intracranial dural arteriovenous fistulas: classification, imaging findings, and treatment. AJNR Am J Neuroradiol. 2012;33(6):1007–13.
75. Lin YH, Wang YF, Liu HM, Lee CW, Chen YF, Hsieh HJ. Diagnostic accuracy of CTA and MRI/MRA in the evaluation of the cortical venous reflux in the intracranial dural arteriovenous fistula DAVF. Neuroradiology. 2018;60(1):7–15.
76. Nishimura S, Hirai T, Sasao A, Kitajima M, Morioka M, Kai Y, Omori Y, Okuda T, Murakami R, Fukuoka H, et al. Evaluation of dural arteriovenous fistulas with 4D contrast-enhanced MR angiography at 3T. AJNR Am J Neuroradiol. 2010;31(1):80–5.

77. Farb RI, Agid R, Willinsky RA, Johnstone DM, Terbrugge KG. Cranial dural arteriovenous fistula: diagnosis and classification with time-resolved MR angiography at 3T. AJNR Am J Neuroradiol. 2009;30(8):1546–51.
78. Mossa-Basha M, Wasserman BA. Low-grade carotid stenosis: implications of MR imaging. Neuroimaging Clin N Am. 2016;26(1):129–45.
79. Dieleman N, van der Kolk AG, van Veluw SJ, Frijns CJ, Harteveld AA, Luijten PR, Hendrikse J. Patterns of intracranial vessel wall changes in relation to ischemic infarcts. Neurology. 2014;83(15):1316–20.
80. Mossa-Basha M, de Havenon A, Becker KJ, Hallam DK, Levitt MR, Cohen WA, Hippe DS, Alexander MD, Tirschwell DL, Hatsukami T, et al. Added value of Vessel Wall magnetic resonance imaging in the differentiation of Moyamoya Vasculopathies in a non-Asian cohort. Stroke. 2016;47(7):1782–8.
81. Mossa-Basha M, Shibata DK, Hallam DK, de Havenon A, Hippe DS, Becker KJ, Tirschwell DL, Hatsukami T, Balu N, Yuan C. Added value of Vessel Wall magnetic resonance imaging for differentiation of nonocclusive intracranial Vasculopathies. Stroke. 2017;48(11):3026–33.
82. Bond KM, Nasr D, Lehman V, Lanzino G, Cloft HJ, Brinjikji W. Intracranial and Extracranial neurovascular manifestations of Takayasu arteritis. AJNR Am J Neuroradiol. 2017;38(4):766–72.
83. Mandell DM, Matouk CC, Farb RI, Krings T, Agid R, ter Brugge K, Willinsky RA, Swartz RH, Silver FL, Mikulis DJ. Vessel wall MRI to differentiate between reversible cerebral vasoconstriction syndrome and central nervous system vasculitis: preliminary results. Stroke. 2012;43(3):860–2.
84. Miller TR, Shivashankar R, Mossa-Basha M, Gandhi D. Reversible cerebral vasoconstriction syndrome, part 2: diagnostic work-up, imaging evaluation, and differential diagnosis. AJNR Am J Neuroradiol. 2015;36(9):1580–8.
85. Gounis MJ, van der Marel K, Marosfoi M, Mazzanti ML, Clarencon F, Chueh JY, Puri AS, Bogdanov AA Jr. Imaging inflammation in cerebrovascular disease. Stroke. 2015;46(10):2991–7.
86. Ahn SH, Lee J, Kim YJ, Kwon SU, Lee D, Jung SC, Kang DW, Kim JS. Isolated MCA disease in patients without significant atherosclerotic risk factors: a high-resolution magnetic resonance imaging study. Stroke. 2015;46(3):697–703.
87. Alexander MD, Cooke DL, Meyers PM, Amans MR, Dowd CF, Halbach VV, Higashida RT, Hetts SW. Lesion stability characteristics outperform degree of stenosis in predicting outcomes following stenting for symptomatic intracranial atherosclerosis. J Neurointerv Surg. 2016;8(1):19–23.
88. Chimowitz MI, Kokkinos J, Strong J, Brown MB, Levine SR, Silliman S, Pessin MS, Weichel E, Sila CA, Furlan AJ, et al. The Warfarin-Aspirin symptomatic intracranial disease study. Neurology. 1995;45(8):1488–93.
89. Kasner SE, Chimowitz MI, Lynn MJ, Howlett-Smith H, Stern BJ, Hertzberg VS, Frankel MR, Levine SR, Chaturvedi S, Benesch CG, et al. Predictors of ischemic stroke in the territory of a symptomatic intracranial arterial stenosis. Circulation. 2006;113(4):555–63.
90. Vos A, Van Hecke W, Spliet WG, Goldschmeding R, Isgum I, Kockelkoren R, Bleys RL, Mali WP, de Jong PA, Vink A. Predominance of nonatherosclerotic internal elastic Lamina calcification in the intracranial internal carotid artery. Stroke. 2016;47(1):221–3.
91. Mossa-Basha M, Hwang WD, De Havenon A, Hippe D, Balu N, Becker KJ, Tirschwell DT, Hatsukami T, Anzai Y, Yuan C. Multicontrast high-resolution vessel wall magnetic resonance imaging and its value in differentiating intracranial vasculopathic processes. Stroke. 2015;46(6):1567–73.
92. Lindenholz A, van der Kolk AG, Zwanenburg JJM, Hendrikse J. The use and pitfalls of intracranial vessel wall imaging: how we do it. Radiology. 2018;286(1):12–28.
93. Balu N, Zhou Z, Hippe DS, Hatsukami T, Mossa-Basha M, Yuan C. Accelerated multicontrast high isotropic resolution 3D intracranial vessel wall MRI using a tailored k-space undersampling and partially parallel reconstruction strategy. New York: Magma; 2019.

94. Chen S, Ning J, Zhao X, Wang J, Zhou Z, Yuan C, Chen H. Fast simultaneous noncontrast angiography and intraplaque hemorrhage (fSNAP) sequence for carotid artery imaging. Magn Reson Med. 2017;77(2):753–8.
95. Chen S, Zhao H, Li J, Zhou Z, Li R, Balu N, Yuan C, Chen H, Zhao X. Evaluation of carotid atherosclerotic plaque surface characteristics utilizing simultaneous noncontrast angiography and intraplaque hemorrhage (SNAP) technique. J Magn Reson Imaging. 2018;47(3):634–9.
96. Fan Z, Yu W, Xie Y, Dong L, Yang L, Wang Z, Conte AH, Bi X, An J, Zhang T, et al. Multicontrast atherosclerosis characterization (MATCH) of carotid plaque with a single 5-min scan: technical development and clinical feasibility. J Cardiovasc Magn Reson. 2014;16:53.
97. Li D, Zhao H, Chen X, Chen S, Qiao H, He L, Li R, Xu J, Yuan C, Zhao X. Identification of intraplaque haemorrhage in carotid artery by simultaneous non-contrast angiography and intraPlaque haemorrhage (SNAP) imaging: a magnetic resonance vessel wall imaging study. Eur Radiol. 2018;28(4):1681–6.
98. Qi H, Sun J, Qiao H, Chen S, Zhou Z, Pan X, Wang Y, Zhao X, Li R, Yuan C, et al. Carotid intraplaque hemorrhage imaging with quantitative vessel wall T1 mapping: technical development and initial experience. Radiology. 2018;287(1):276–84.
99. Shu H, Sun J, Hatsukami TS, Balu N, Hippe DS, Liu H, Kohler TR, Zhu W, Yuan C. Simultaneous noncontrast angiography and intraplaque hemorrhage (SNAP) imaging: comparison with contrast-enhanced MR angiography for measuring carotid stenosis. J Magn Reson Imaging. 2017;46(4):1045–52.
100. Lehman VT, Brinjikji W, Kallmes DF, Huston JR, Lanzino G, Rabinstein AA, Makol A, Mossa-Bosha M. Clinical interpretation of high-resolution vessel wall MRI of intracranial arterial diseases. Br J Radiol. 2016;89(1067):20160496.
101. Obusez EC, Hui F, Hajj-Ali RA, Cerejo R, Calabrese LH, Hammad T, Jones SE. High-resolution MRI vessel wall imaging: spatial and temporal patterns of reversible cerebral vasoconstriction syndrome and central nervous system vasculitis. AJNR Am J Neuroradiol. 2014;35(8):1527–32.
102. Schulz J, Boyacioglu R, Norris DG. Multiband multislab 3D time-of-flight magnetic resonance angiography for reduced acquisition time and improved sensitivity. Magn Reson Med. 2016;75(4):1662–8.
103. Vranic JE, Cross NM, Wang Y, Hippe DS, de Weerdt E, Mossa-Basha M. Compressed sensing-sensitivity encoding (CS-SENSE) accelerated brain imaging: reduced scan time without reduced image quality. AJNR Am J Neuroradiol. 2019;40(1):92–8.
104. Chen L, Mossa-Basha M, Sun J, Hippe DS, Balu N, Yuan Q, Pimentel K, Hatsukami TS, Hwang JN, Yuan C. Quantification of morphometry and intensity features of intracranial arteries from 3D TOF MRA using the intracranial artery feature extraction (iCafe): a reproducibility study. Magn Reson Imaging. 2019;57:293–302.

Chapter 3
Advanced Intracranial Vessel Wall Imaging and Future Directions

Noushin Yahyavi-Firouz-Abadi and Bruce Alan Wasserman

Introduction

Conventional angiographic techniques such as CT angiography, MR angiography, and digital subtraction angiography demonstrate luminal stenosis but are unable to characterize the underlying disease within the vessel wall. Depiction of the vessel wall abnormality improves the ability to distinguish vasculopathies with similar angiographic findings and can offer insight into risk and management of the underlying disease. Vessel wall visualization requires suppression of blood flow most commonly using black blood MRI (BBMRI) sequences [1]. Historically, two-dimensional (2-D) T1 or proton density black blood sequences were developed to characterize the vessel wall of carotid arteries driven partly by access to endarterectomy specimens for comparison with imaging [2, 3]. However, application of 2-D sequences for imaging intracranial vessels is challenging given the smaller size and tortuosity of these vessels. 2-D techniques have a non-isotropic resolution that results in overestimation of vessel wall thickness due to the small size of vessels compared to even the most optimized 2-D voxel size [4]. In addition, achieving contiguous 2-D slices orthogonal to the course of intracranial vessels can be very challenging due to the tortuosity of these vessels [5]. Isotropic 3-D vessel wall MRI (VWMRI) overcomes this challenge and enables characterization of the intracranial vessel wall with reduced partial volume averaging [6]. A detailed explanation of the 3-D high isotropic resolution black blood MRI technique and protocols has been previously reported [1, 7].

N. Yahyavi-Firouz-Abadi · B. A. Wasserman (✉)
Division of Neuroradiology, The Russell H. Morgan Department of Radiology and Radiological Sciences, Johns Hopkins University, Baltimore, MD, USA
e-mail: nyahyav1@jhmi.edu; bwasser@jhmi.edu

C. Yuan et al. (eds.), *Vessel Based Imaging Techniques*,
https://doi.org/10.1007/978-3-030-25249-6_3

In this chapter, we review the role of vessel wall MRI for evaluation of vasculopathies including atherosclerotic disease, vasculitis, reversible cerebral vasoconstriction syndrome (RCVS), dissection, and aneurysms. In addition, we review 4D flow MRI, 4D-CTA, and transcranial Doppler ultrasound.

Intracranial Vasa Vasorum

Vasa vasorum consist of networks of arteries, capillaries, and veins supplying oxygen and nutrients to the walls of larger blood vessels. Intracranial vessels are unique in the paucity of vasa vasorum found in their adventitia under normal conditions, thought to be a consequence of the surrounding cerebrospinal fluid environment [8]. Vasa vasorum may develop within intracranial arteries with age, predominantly at the proximal portions [9], and as a consequence of vascular diseases such as atherosclerosis, vasculitis, and aneurysms [8, 10]. Its development has been implicated in promoting inflammatory processes, which can progress to the inner layers [11] leading to the initiation and acceleration of intracranial atherosclerosis [8]. For example, there is a strong association between presence of vasa vasorum and atherosclerotic plaque particularly in thicker intracranial vessels [10]. The relative paucity of intracranial vasa vasorum offers an explanation for the lower frequency of intracranial atherosclerosis compared to coronary and carotid atherosclerosis and higher correlation of extracranial carotid and coronary atherosclerosis compared to intracranial and coronary atherosclerosis [12].

Given the unique features of intracranial vasa vasorum and its implication in intracranial vasculopathies, imaging detection of intracranial vasa vasorum may have an important role in disease diagnosis and prognostication. Intracranial vasa vasorum can be detected by contrast-enhanced MR and CT techniques and is evident by vessel wall enhancement [8, 13].

Intracranial Atherosclerotic Disease

Intracranial atherosclerotic disease (ICAD) is very prevalent and a major cause of ischemic stroke [14]. The estimated prevalence of symptomatic intracranial stenosis varies from 1 in 100,000 for whites to 15 in 100,000 in African Americans in population-based studies [15]. Autopsy studies have noted intracranial atherosclerotic disease to be present in as many as 23% and 80% of people in their 6th and 9th decades of life, respectively [15]. Traditional methods of diagnosing atherosclerosis have been based on measures of luminal narrowing which underestimates plaque burden because of compensatory dilatation (remodeling) to accommodate plaque formation especially early on [6]. In coronary arteries, outward (positive) remodeling can preserve the lumen at a plaque burden as high as 40% of the arterial lumen circumscribed by the internal elastic lamina based on plaque specimen analyses

[16]. Negative or inward remodeling results in luminal narrowing and may alter hemodynamics. Although outward remodeling limits the hemodynamic impact of the plaque, it may be associated with increased plaque vulnerability and clinical events as shown in coronary arteries [17, 18].

Imaging Intracranial Atherosclerotic Plaque

Vessel wall magnetic resonance imaging is an effective method for measurement of wall thickness and characterization of pathologic features of the carotid arteries [3] and intracranial vessels [1, 19]. 3D high isotropic resolution black blood MR imaging has made it possible to identify and characterize intracranial atherosclerotic disease [1, 20] and discriminating it from other vasculopathies [7, 21].

A US community-based population study (the Atherosclerosis Risk in Communities (ARIC) study) estimated the prevalence of having at least one intracranial atherosclerotic plaque to be 34.4% using VWMRI [22] which is higher than previous estimates of intracranial stenosis in population-based studies [15]. In the ARIC study, 10.8% of participants had ICAD with no detectable stenosis [22] which helped to explain the difference in prevalence estimates. Cross-sectional reliability estimates of VWMRI measurements of intracranial atherosclerotic plaque based on 102 repeat scans and 20 inter-reader and 29 intra-reader repeat readings have been shown to range from good to excellent for quantitative measurements (e.g., intracranial vessel lumen, wall thickness) and fair to good for qualitative measurements (plaque presence, ordinal stenosis) [20]. The high reliability is likely a reflection of the reproducibility of 3D imaging and the effect of adequate training for image interpretation, which was heavily emphasized in this study [20].

MR Features of Atherosclerotic Plaque and Identifying Culprit Plaque

Imaging features of atherosclerotic plaque on VWMRI are more challenging to detect in intracranial vessels compared to extracranial vessels due to the smaller size of intracranial vessels. This can result in partial volume averaging of plaque components, including lipid core, fibrous cap, calcification, intraplaque hemorrhage, and enhancement, resulting in a heterogeneous signal [19, 23]. Intracranial atherosclerotic plaques are eccentric often with irregular wall thickening and variable degrees of enhancement (Fig. 3.1) [19, 21, 24]. Although individual plaque components may not be readily visible due to resolution constraints, heterogeneous signal and intraplaque hemorrhage may be helpful discriminators from other lesions [19, 23]. If detected, the fibrous cap may present as a T2 hyperintense and enhancing band overlying a T2 hypointense lipid core [21]. This T2 hyperintense band and heterogeneous signal are typically absent in cases of vasculitis and RCVS [21]. Intracranial

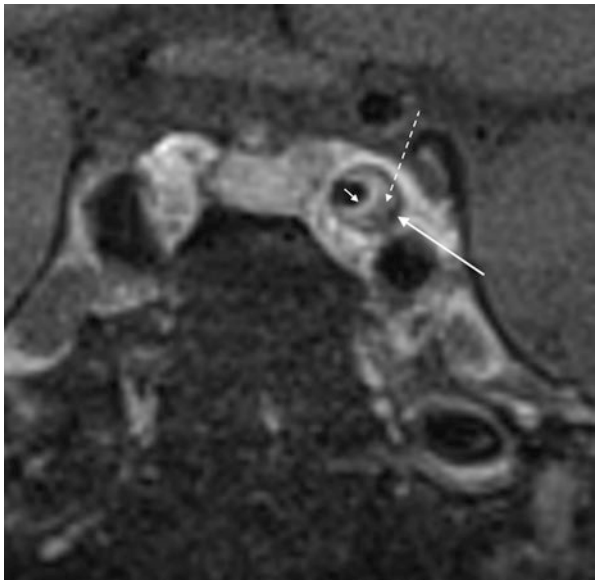

Fig. 3.1 Features of an atherosclerotic plaque involving the cavernous carotid artery with an enhancing fibrous cap (short arrow), lipid core (dotted arrow), and peripheral calcification (long arrow)

atherosclerotic plaque enhancement can vary in degree and, consequently, is not useful for discriminating from other vasculopathies. However, a high degree of enhancement might be useful for identifying lesions that are responsible for downstream ischemic infarcts (culprit plaques) likely reflecting inflammation, endothelial permeability, and neovascularity associated with increased macrophage infiltration and neovascularity as seen in postmortem specimens [25–29]. Therefore, plaque enhancement may be used as a marker for plaque instability and stroke risk assessment. In addition, recanalized vessels following treatment for thromboembolic disease demonstrate concentric vessel wall thickening and enhancement which is more robust in patients who underwent both mechanical thrombectomy and medical therapy than medical therapy alone [30].

VWMRI has been used to characterize vascular remodeling in extracranial carotid [31, 32] and intracranial arteries [6] and has enabled our ability to detect atherosclerosis with no luminal stenosis [33]. These non-stenotic lesions appear to be the strongest risk factor for white matter hyperintensities in patients without intracranial stenoses [34]. Luminal preservation in cervical internal carotid arteries has been shown to occur at plaque burdens up to 62% measured using MRI techniques [31, 32]. Intracranial arteries can also remodel to a high degree as a result of plaque formation with the posterior circulation having a higher capacity for positive remodeling than the anterior circulation [6]. Prevalence of positive remodeling in atherosclerotic plaques in stroke patients was shown to be 29.9% in the anterior circulation versus 54% in the posterior circulation, with lumen patency being maintained in the posterior circulation with plaque burdens up to approximately 55.3% [6]. This may be attributed to differences in hemodynamics (i.e., slower flow in the posterior circulation) and sparse sympathetic innervation of the vertebrobasilar system [6, 35, 36].

Another potential application of VWMRI is determining the location of atherosclerotic plaque relative to a branch artery. Although atherosclerotic plaques tend to arise from arterial wall opposite a branch artery ostium [5, 37, 38], some plaques arise close to the ostia and are associated with increased risk of infarction [38]. Angioplasty can push the atheromatous material from the treated artery to a branch resulting in acute stroke. Determining location of plaque relative to ostium may be useful in intracranial angioplasty risk assessment [39].

Vasculitis

Vasculitides are rare group of diseases defined by inflammation of the vessel wall [8]. Central nervous system vasculitis (CNSV) can be defined as any inflammatory vasculopathy that results in nonatheromatous intracranial vascular inflammation [40]. Primary CNSV is caused by direct involvement of vessels, while secondary vascular inflammation can result from infections, autoimmune processes, tumors, or other processes [40]. Although exact mechanism of involvement of vasa vasorum in vasculitis is not well established, higher prevalence of extracranial vasculitis suggests a role given higher density of vasa vasorum in extracranial arteries [8].

Conventional angiographic features of vasculitis are nonspecific and include multifocal luminal irregularity and stenosis that may overlap with a variety of intracranial vasculopathies such as atherosclerosis and RCVS. Intracranial VWMRI may help in distinguishing vasculitis from other etiologies of intracranial stenosis. Furthermore, some of small vessel vasculitides cannot be identified on catheter angiography [40]. Luminal narrowing is only detected on cerebral angiography in 25–43% of patients with biopsy-proven primary CNS angiitis [41, 42]. On VWMRI, intracranial vasculitis tends to present with segmental, concentric homogenous enhancement of the vessel wall and/or circumferential, peri-adventitial enhancement following a vessel segment (Fig. 3.2) [40]. Imaging features that are more suggestive of atherosclerosis such as calcification, fibrous cap and lipid core, or focal, non-circumferential wall thickening may help to exclude vasculitis [40]. Vasculitic lesions typically lack T2 hyperintensity, while ICAD lesions often demonstrate T2 hyperintensity or heterogeneous T2 signal [21]. It is important to note that there is overlap between ICAD and vasculitis as ICAD can demonstrate circumferential wall thickening and vasculitis can have eccentric enhancement [23, 43, 44]. Given the similarity and overlap of imaging findings and clinical manifestations between CNS vasculitis and atherosclerosis and the toxicity of immunosuppressive therapy, a biopsy may be needed for definitive diagnosis [40]. Because of the high false negative rate of biopsies for CNSV due to patchy and segmental involvement of vessels by this disease, VWMRI may be useful for guiding biopsies, and this has yielded higher success rates compared to biopsies guided by conventional imaging [40]. VWMRI should be acquired close to the time of biopsy to ensure the target is actively inflamed since vessel wall inflammation may be transient [40].

Fig. 3.2 VWMRI appearance of small vessel vasculitis in a patient with clinical and radiological diagnosis of small vessel vasculitis. Contrast-enhanced VWMRI demonstrates peri-adventitial enhancement of an inflamed segment of a vessel seen in long axis (arrow)

Pitfalls of VWMRI for vasculitis include inability to distinguish between transmural inflammation (e.g., primary CNSV) and perivascular inflammation (e.g., sarcoidosis) [40]. In addition, concentric wall thickening after thrombectomy may mimic vasculitis if patient's history is not known [30].

Reversible Cerebral Vasoconstriction Syndrome

Vasospasm results from smooth muscle shortening and increased wall redundancy that can result in a fivefold increase in wall thickness corresponding to 60% luminal narrowing [45, 46]. Arterial wall thickening is a feature of vasospasm on vessel wall imaging [7]. RCVS is characterized by noninflammatory reversible multifocal cerebral vasoconstriction associated with recurrent thunderclap headaches that resolve spontaneously within 3 months [47, 48]. It is an underdiagnosed entity and may lead to complications such as posterior reversible encephalopathy, subarachnoid hemorrhage, and ischemic infarcts [48, 49]. Timely distinction of RCVS from its top differential consideration, vasculitis, is essential since treatment strategies are very different. In particular, the appropriate management of vasculitis by steroids carries a significant morbidity [42].

VWMRI can be helpful to distinguish RCVS from CNSV. Both vasoconstriction and vasculitis result in vessel wall thickening and luminal narrowing, but CNSV tends to demonstrate more intense wall enhancement and moderate wall thickening.

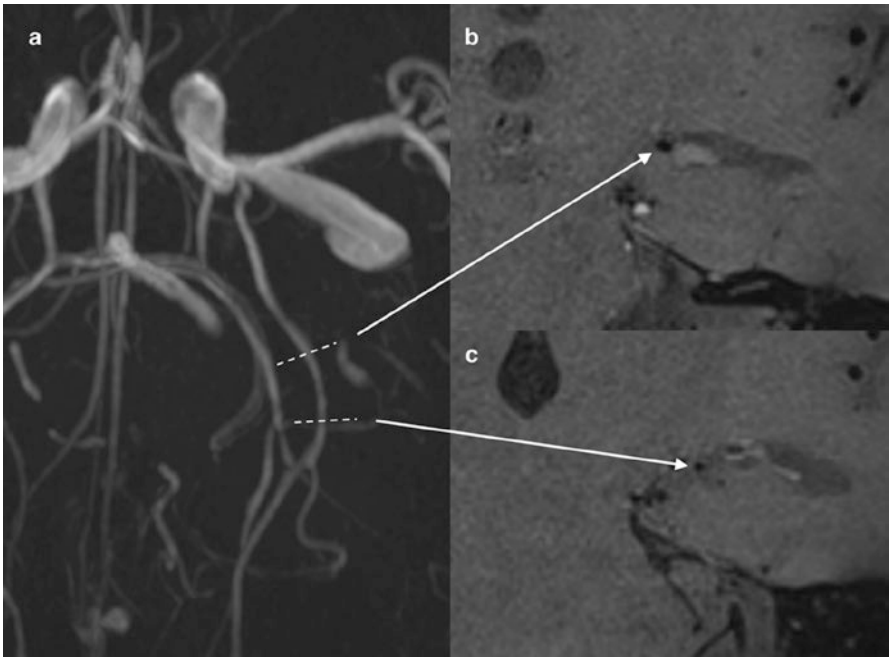

Fig. 3.3 VWMRI in a 5-year-old with RCVS. Time-of-flight MR angiography (**a**) demonstrates focal narrowing of duplicated left posterior cerebral artery. VWMRI shows cross-sectional appearance of normal segment of the vessel (**b**) compared to narrowed segment (**c**). No periadventitial or vessel wall enhancement in region of focal narrowing of the left posterior cerebral artery is seen (**c**)

In contrast, RCVS typically demonstrates little to no enhancement (Fig. 3.3), with only 31–47% of patients showing any enhancement with this disease [43, 44, 47]. However, the sensitivity of using a low degree of enhancement to diagnose RCVS is limited considering strong enhancement was seen in as many as a fourth of cases in one series [47]. The most reliable test for confirming this diagnosis remains follow-up imaging since wall enhancement in RCVS tends to resolve early, within 3 months [44].

Arterial Dissection

Arterial dissection results from an intimal tear with blood products tracking into the vessel wall. Vasa vasorum are implicated in the pathogenesis of intramural thrombus in arterial dissection [8]. Intracranial vessel wall dissection may result from extension of a dissection from extracranial arteries such as vertebral or carotid arteries or may be an isolated finding [7, 50]. VWMRI features of intracranial arterial dissection include intimal flap (curvilinear T2 hyperintensity) separating the true

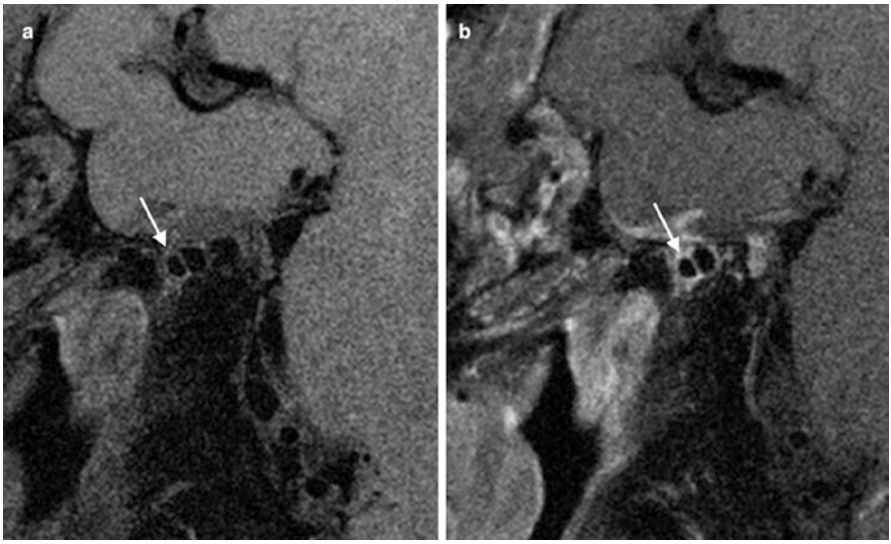

Fig. 3.4 Chronic arterial dissection of the horizontal petrous segment of the carotid artery. Non-contrast (**a**) and contrast-enhanced (**b**) VWMR images through the short axis of the artery demonstrate enhancement of the vessel wall and flap separating the false lumen (arrow) from the true lumen

lumen from the false lumen and eccentric arterial wall thickening with T1 hyperintense intramural hematoma (Fig. 3.4) [7, 50]. A study of dissecting aneurysms demonstrated improved detection of dissections using VWMRI compared to catheter angiography (42% vs 16%, respectively) [50]. Intramural hematoma evolves over time. Deoxyhemoglobin in acute intramural hematoma is iso-intense on T1-weighted images and may be detected using T2∗ or susceptibility-weighted imaging before conversion to methemoglobin which is T1 hyperintense [51]. In a study of dissecting aneurysms, 83% of intramural hematomas were detected on T1-weighted images, and 59% could be seen on T2-weighted images [50]. However, T1 hyperintensity in the wall is not specific to arterial dissection and can also be seen with intraplaque hemorrhage in ICAD lesions [23], so other features such as vascular calcification or a trauma history can be helpful for diagnosis.

Aneurysms

There is ongoing debate regarding the pathophysiology that underlies aneurysm growth and rupture. Vasa vasorum are reported to be present in large (4 mm or larger) saccular aneurysms and fusiform aneurysms and have been implicated in growth and rupture of these lesions [8]. Repetitive intramural hemorrhage from vasa vasorum and reabsorption of blood is believed to induce inflammation and

proliferation of microvessels that are prone to re-bleeding. This is postulated to result in enlargement and weakening/rupture of the aneurysm wall [52].

There is a growing body of evidence that supports the use of VWMRI for evaluating aneurysms [53, 54]. Contrast enhancement in the wall of unstable aneurysms has been reported and may be due to a loss of vasa vasorum integrity, intimal angiogenesis, and inflammatory activity [8, 55, 56]. Two recent histological studies of unruptured intracranial aneurysms revealed associations of aneurysm wall enhancement on VWMRI with higher macrophage infiltration, increased cellularity, neovascularization, and a thicker wall of the aneurysm [57, 58].

Retrospective studies have reported thick peripheral enhancement of ruptured aneurysms in the setting of subarachnoid hemorrhage, while unruptured aneurysms do not enhance [56, 59, 60]. It is noteworthy that in these retrospective studies, enhancement may represent inflammatory changes related to the rupture itself [23].

Aneurysm wall enhancement may also be a predictor of progression. In prospective studies of asymptomatic patients, enlarging or morphologically changing aneurysms demonstrate thick peripheral enhancement compared to little to no enhancement in stable asymptomatic aneurysms suggesting a potential role of VWMRI for treatment planning [60, 61]. Circumferential aneurysm wall enhancement >1 mm in thickness is shown to have the highest specificity and negative predictive value for differentiating between stable and unstable aneurysms [61]. In addition, a stronger degree of enhancement was associated with a higher clinical risk for rupture based on PHASES (population, hypertension, age, size, earlier subarachnoid hemorrhage, and size) score [62]. A meta-analysis of five retrospective and prospective studies with 492 subjects showed a significant and independent association of aneurysm wall enhancement with aneurysm rupture [63].

Potential use of VWMRI in detecting the source of hemorrhage in angiogram negative non-perimesencephalic subarachnoid hemorrhage has also been studied with no change in patient management [64]. Further investigation is warranted to understand the mechanism of aneurysm rupture and instability before contrast enhancement can be used as a marker for impending rupture.

4D Flow MRI

New applications of phase-contrast MRI have emerged to noninvasively evaluate blood flow qualitatively (flow visualization and direction) and quantitatively (velocity, pressure, wall shear stress) [65]. Hemodynamic parameters such as flow patterns, location of flow impact on aneurysm wall, size of impact zone, and wall shear stress (WSS) are of particular interest in assessing risk of aneurysm growth and rupture [66]. Low WSS and high oscillatory shear index are thought to initiate inflammatory cell-mediated remodeling in large aneurysms, while high WSS and positive WSS gradients can facilitate mural cell-mediated remodeling in small or secondary bleb aneurysms [66]. Both of these pathways may lead to aneurysm growth and rupture.

4D flow MRI has also been used to measure flow in arteriovenous malformations (AVM), specifically in arterial feeders along with arteries adjacent and contralateral to the AVM for a global hemodynamic evaluation for embolization planning [67, 68]. Velocity-derived flow-tracking cartography can help with functional assessment of the AVM with high reliability and good to excellent agreement with DSA for identification of shunt location and arterial feeders and evaluation of retrograde flow in dural venous sinuses or cortical veins [65]. Virtual MR flow-tracking cartography can classify dural arteriovenous fistulas (AVF) similar to catheter angiography (Cognard classification) providing risk stratification of bleeding based on assessment of venous drainage [69].

4D-CTA

In 4D CT angiography (4D-CTA), images are obtained throughout intravenous administration of contrast bolus using continuous or noncontinuous acquisition [70]. 4D-CTA is shown to be comparable to DSA in detecting and grading of cerebral AVMs [71, 72] and dural AVFs [73, 74]. In the work-up of acute ischemic stroke, 4D-CTA has been shown to be superior to conventional CTA for characterizing the extent and dynamics of collateral flow [75] and intracranial thrombus burden [76]. 4D-CTA has been comparable with DSA in discriminating antegrade flow from retrograde flow across an occluded vessel helping to predict rate of recanalization following intravenous thrombolysis which is correlated with antegrade flow [77]. Characterization of collateral flow also helps with prognostication of clinical outcome after ischemic stroke and rate of complications such as hemorrhagic transformation [70, 78].

Transcranial Doppler Sonography

Transcranial Doppler ultrasound (TCD) is a noninvasive ultrasound technique that can be used at the bedside to detect and localize intracranial arterial narrowing or occlusion. For detecting middle cerebral artery (MCA) occlusion, TCD has greater than a 90% sensitivity and its specificity approximates that of CTA [79]. TCD has lower sensitivity than CTA for detection of basilar or carotid terminus thrombus [79]. In addition to establishing patency, TCD can provide complementary information to CTA such as visualizing real-time embolization, presence of microemboli, and alternating flow signals indicative of steal phenomenon [79]. Furthermore, TCD can detect restenosis or re-occlusion after thrombolysis or thrombectomy [80]. Main drawbacks of its use are lack of adequate sonographic window through the temporal bone and limited availability of experienced technician or clinician [81].

Conclusions

In summary, the current literature supports an important role for intracranial vessel wall imaging in differentiating etiologies of intracranial vessel wall narrowing such as atherosclerosis, vasospasm, vasculitis, and arterial dissection. In addition, it can be useful for identification of non-stenotic lesions that would escape angiographic detection. Potential applications include risk stratification for atherosclerotic plaques and identifying actively inflamed lesions in vasculitis which could be useful for directing targeted biopsies of vessels. Future applications of VWMRI might also include risk stratification of aneurysms for rupture or growth. 4D flow technique is a useful adjunct for assessment of flow dynamics and rupture risk of aneurysms, AVMs, and dural arteriovenous fistulas and may be useful in treatment planning. Further investigations are warranted in larger samples for validation of clinical use of vessel wall MR and 4D MR/CT.

References

1. Qiao Y, Steinman DA, Qin Q, Etesami M, Schär M, Astor BC, et al. Intracranial arterial wall imaging using three-dimensional high isotropic resolution black blood MRI at 3.0 Tesla. J Magn Reson Imaging. 2011;34:22–30. https://doi.org/10.1002/jmri.22592.
2. Saba L, Yuan C, Hatsukami TS, Balu N, Qiao Y, DeMarco JK, et al. Carotid artery wall imaging: perspective and guidelines from the ASNR Vessel Wall Imaging Study Group and Expert Consensus Recommendations of the American Society of Neuroradiology. AJNR Am J Neuroradiol. 2018;39:E9–31. https://doi.org/10.3174/ajnr.A5488.
3. Wasserman BA, Smith WI, Trout HH, Cannon RO, Balaban RS, Arai AE. Carotid artery atherosclerosis: in vivo morphologic characterization with gadolinium-enhanced double-oblique MR imaging initial results. Radiology. 2002;223:566–73. https://doi.org/10.1148/radiol.2232010659.
4. Antiga L, Wasserman BA, Steinman DA. On the overestimation of early wall thickening at the carotid bulb by black blood MRI, with implications for coronary and vulnerable plaque imaging. Magn Reson Med. 2008;60:1020–8. https://doi.org/10.1002/mrm.21758.
5. Zhu XJ, Du B, Lou X, Hui FK, Ma L, Zheng BW, et al. Morphologic characteristics of atherosclerotic middle cerebral arteries on 3T high-resolution MRI. AJNR Am J Neuroradiol. 2013;34:1717–22. https://doi.org/10.3174/ajnr.A3573.
6. Qiao Y, Anwar Z, Intrapiromkul J, Liu L, Zeiler SR, Leigh R, et al. Patterns and implications of intracranial arterial remodeling in stroke patients. Stroke. 2016;47:434–40. https://doi.org/10.1161/STROKEAHA.115.009955.
7. Mandell DM, Mossa-Basha M, Qiao Y, Hess CP, Hui F, Matouk C, et al. Intracranial vessel wall MRI: principles and expert consensus recommendations of the American Society of Neuroradiology. AJNR Am J Neuroradiol. 2017;38:218–29. https://doi.org/10.3174/ajnr.A4893.
8. Portanova A, Hakakian N, Mikulis DJ, Virmani R, Abdalla WMA, Wasserman BA. Intracranial vasa vasorum: insights and implications for imaging. Radiology. 2013;267:667–79. https://doi.org/10.1148/radiol.13112310.
9. Connolly ES, Huang J, Goldman JE, Holtzman RN. Immunohistochemical detection of intracranial vasa vasorum: a human autopsy study. Neurosurgery. 1996;38:789–93.
10. Takaba M, Endo S, Kurimoto M, Kuwayama N, Nishijima M, Takaku A. Vasa vasorum of the intracranial arteries. Acta Neurochir. 1998;140:411–6.

11. Maiellaro K, Taylor WR. The role of the adventitia in vascular inflammation. Cardiovasc Res. 2007;75:640–8. https://doi.org/10.1016/j.cardiores.2007.06.023.
12. Bae H-J, Yoon B-W, Kang D-W, Koo J-S, Lee S-H, Kim K-B, et al. Correlation of coronary and cerebral atherosclerosis: difference between extracranial and intracranial arteries. Cerebrovasc Dis. 2006;21:112–9. https://doi.org/10.1159/000090209.
13. Qiao Y, Etesami M, Astor BC, Zeiler SR, Trout HH, Wasserman BA. Carotid plaque neovascularization and hemorrhage detected by MR imaging are associated with recent cerebrovascular ischemic events. AJNR Am J Neuroradiol. 2012;33:755–60. https://doi.org/10.3174/ajnr.A2863.
14. Wong LKS. Global burden of intracranial atherosclerosis. Int J Stroke. 2006;1:158–9. https://doi.org/10.1111/j.1747-4949.2006.00045.x.
15. Suri MFK, Johnston SC. Epidemiology of intracranial stenosis. J Neuroimaging. 2009;19(S1):11S–6S. https://doi.org/10.1111/j.1552-6569.2009.00415.x.
16. Glagov S, Weisenberg E, Zarins CK, Stankunavicius R, Kolettis GJ. Compensatory enlargement of human atherosclerotic coronary arteries. N Engl J Med. 1987;316:1371–5. https://doi.org/10.1056/NEJM198705283162204.
17. Varnava AM, Mills PG, Davies MJ. Relationship between coronary artery remodeling and plaque vulnerability. Circulation. 2002;105:939–43.
18. White AJ, Duffy SJ, Walton AS, Ng JF, Rice GE, Mukherjee S, et al. Matrix metalloproteinase-3 and coronary remodelling: implications for unstable coronary disease. Cardiovasc Res. 2007;75:813–20. https://doi.org/10.1016/j.cardiores.2007.05.003.
19. Qiao Y, Zeiler SR, Mirbagheri S, Leigh R, Urrutia V, Wityk R, et al. Intracranial plaque enhancement in patients with cerebrovascular events on high-spatial-resolution MR images. Radiology. 2014;271:534–42. https://doi.org/10.1148/radiol.13122812.
20. Qiao Y, Guallar E, Suri FK, Liu L, Zhang Y, Anwar Z, et al. MR imaging measures of intracranial atherosclerosis in a population-based study. Radiology. 2016;280:860–8. https://doi.org/10.1148/radiol.2016151124.
21. Mossa-Basha M, Hwang WD, De Havenon A, Hippe D, Balu N, Becker KJ, et al. Multicontrast high-resolution vessel wall magnetic resonance imaging and its value in differentiating intracranial vasculopathic processes. Stroke. 2015;46:1567–73. https://doi.org/10.1161/STROKEAHA.115.009037.
22. Qiao Y, Suri FK, Zhang Y, Liu L, Gottesman R, Alonso A, et al. Racial differences in prevalence and risk for intracranial atherosclerosis in a US Community-Based Population. JAMA Cardiol. 2017;2:1341–8. https://doi.org/10.1001/jamacardio.2017.4041.
23. Kontzialis M, Wasserman BA. Intracranial vessel wall imaging: current applications and clinical implications. Neurovasc Imaging. 2016;2:4. https://doi.org/10.1186/s40809-016-0014-5.
24. Swartz RH, Bhuta SS, Farb RI, Agid R, Willinsky RA, Terbrugge KG, et al. Intracranial arterial wall imaging using high-resolution 3-tesla contrast-enhanced MRI. Neurology. 2009;72:627–34. https://doi.org/10.1212/01.wnl.0000342470.69739.b3.
25. Chen XY, Wong KS, Lam WWM, Zhao H-L, Ng HK. Middle cerebral artery atherosclerosis: histological comparison between plaques associated with and not associated with infarct in a postmortem study. Cerebrovasc Dis. 2008;25:74–80. https://doi.org/10.1159/000111525.
26. Mazighi M, Labreuche J, Gongora-Rivera F, Duyckaerts C, Hauw J-J, Amarenco P. Autopsy prevalence of proximal extracranial atherosclerosis in patients with fatal stroke. Stroke. 2009;40:713–8. https://doi.org/10.1161/STROKEAHA.108.514349.
27. Labadzhyan A, Csiba L, Narula N, Zhou J, Narula J, Fisher M. Histopathologic evaluation of basilar artery atherosclerosis. J Neurol Sci. 2011;307:97–9. https://doi.org/10.1016/j.jns.2011.05.004.
28. Aoki S, Shirouzu I, Sasaki Y, Okubo T, Hayashi N, Machida T, et al. Enhancement of the intracranial arterial wall at MR imaging: relationship to cerebral atherosclerosis. Radiology. 1995;194:477–81. https://doi.org/10.1148/radiology.194.2.7824729.
29. Kerwin WS, Oikawa M, Yuan C, Jarvik GP, Hatsukami TS. MR imaging of adventitial vasa vasorum in carotid atherosclerosis. Magn Reson Med. 2008;59:507–14. https://doi.org/10.1002/mrm.21532.

30. Power S, Matouk C, Casaubon LK, Silver FL, Krings T, Mikulis DJ, et al. Vessel wall magnetic resonance imaging in acute ischemic stroke: effects of embolism and mechanical thrombectomy on the arterial wall. Stroke. 2014;45:2330–4. https://doi.org/10.1161/STROKEAHA.114.005618.
31. Astor BC, Sharrett AR, Coresh J, Chambless LE, Wasserman BA. Remodeling of carotid arteries detected with MR imaging: atherosclerosis risk in communities carotid MRI study. Radiology. 2010;256:879–86. https://doi.org/10.1148/radiol.10091162.
32. Babiarz LS, Astor B, Mohamed MA, Wasserman BA. Comparison of gadolinium-enhanced cardiovascular magnetic resonance angiography with high-resolution black blood cardiovascular magnetic resonance for assessing carotid artery stenosis. J Cardiovasc Magn Reson. 2007;9:63–70. https://doi.org/10.1080/10976640600843462.
33. Lee WJ, Choi HS, Jang J, Sung J, Kim T-W, Koo J, et al. Non-stenotic intracranial arteries have atherosclerotic changes in acute ischemic stroke patients: a 3T MRI study. Neuroradiology. 2015;57:1007–13. https://doi.org/10.1007/s00234-015-1566-9.
34. Kim TH, Choi JW, Roh HG, Moon W-J, Moon SG, Chun YI, et al. Atherosclerotic arterial wall change of non-stenotic intracranial arteries on high-resolution MRI at 3.0T: correlation with cerebrovascular risk factors and white matter hyperintensity. Clin Neurol Neurosurg. 2014;126:1–6. https://doi.org/10.1016/j.clineuro.2014.08.010.
35. Beausang-Linder M, Bill A. Cerebral circulation in acute arterial hypertension--protective effects of sympathetic nervous activity. Acta Physiol Scand. 1981;111:193–9. https://doi.org/10.1111/j.1748-1716.1981.tb06724.x.
36. Chatzizisis YS, Coskun AU, Jonas M, Edelman ER, Feldman CL, Stone PH. Role of endothelial shear stress in the natural history of coronary atherosclerosis and vascular remodeling: molecular, cellular, and vascular behavior. J Am Coll Cardiol. 2007;26(49):2379–93. https://doi.org/10.1016/j.jacc.2007.02.059.
37. Huang B, Yang W-Q, Liu X-T, Liu H-J, Li P-J, Lu H-K. Basilar artery atherosclerotic plaques distribution in symptomatic patients: a 3.0T high-resolution MRI study. Eur J Radiol. 2013;82:e199–203. https://doi.org/10.1016/j.ejrad.2012.10.031.
38. Xu W-H, Li M-L, Gao S, Ni J, Zhou L-X, Yao M, et al. Plaque distribution of stenotic middle cerebral artery and its clinical relevance. Stroke. 2011;42:2957–9. https://doi.org/10.1161/STROKEAHA.111.618132.
39. Jiang W-J, Yu W, Ma N, Du B, Lou X, Rasmussen PA. High resolution MRI guided endovascular intervention of basilar artery disease. J Neurointerv Surg. 2011;3:375–8. https://doi.org/10.1136/jnis.2010.004291.
40. Zeiler SR, Qiao Y, Pardo CA, Lim M, Wasserman BA. Vessel wall MRI for targeting biopsies of intracranial vasculitis. AJNR Am J Neuroradiol. 2018;39:2034–6. https://doi.org/10.3174/ajnr.A5801.
41. Hajj-Ali RA, Singhal AB, Benseler S, Molloy E, Calabrese LH. Primary angiitis of the CNS. Lancet Neurol. 2011;10:561–72. https://doi.org/10.1016/S1474-4422(11)70081-3.
42. Salvarani C, Brown RD, Calamia KT, Christianson TJH, Weigand SD, Miller DV, et al. Primary central nervous system vasculitis: analysis of 101 patients. Ann Neurol. 2007;62:442–51. https://doi.org/10.1002/ana.21226.
43. Mossa-Basha M, Shibata DK, Hallam DK, De Havenon A, Hippe DS, Becker KJ, et al. Added value of vessel wall MRI for differentiation of non-occlusive intracranial vasculopathies. Stroke. 2017;48:3026–33. https://doi.org/10.1161/STROKEAHA.117.018227.
44. Obusez EC, Hui F, Hajj-Ali RA, Cerejo R, Calabrese LH, Hammad T, et al. High-resolution MRI vessel wall imaging: spatial and temporal patterns of reversible cerebral vasoconstriction syndrome and central nervous system vasculitis. AJNR Am J Neuroradiol. 2014;35:1527–32. https://doi.org/10.3174/ajnr.A3909.
45. Findlay JM, Weir BK, Kanamaru K, Espinosa F. Arterial wall changes in cerebral vasospasm. Neurosurgery. 1989;25:736–45. discussion 745-746
46. Mandell DM, Matouk CC, Farb RI, Krings T, Agid R, terBrugge K, et al. Vessel wall MRI to differentiate between reversible cerebral vasoconstriction syndrome and central nervous system vasculitis: preliminary results. Stroke. 2012;43:860–2. https://doi.org/10.1161/STROKEAHA.111.626184.

47. Chen C-Y, Chen S-P, Fuh J-L, Lirng J-F, Chang F-C, Wang Y-F, et al. Vascular wall imaging in reversible cerebral vasoconstriction syndrome - a 3-T contrast-enhanced MRI study. J Headache Pain. 2018;19:74. https://doi.org/10.1186/s10194-018-0906-7.
48. Ducros A, Boukobza M, Porcher R, Sarov M, Valade D, Bousser M-G. The clinical and radiological spectrum of reversible cerebral vasoconstriction syndrome. A prospective series of 67 patients. Brain. 2007;130:3091–101. https://doi.org/10.1093/brain/awm256.
49. Singhal AB, Hajj-Ali RA, Topcuoglu MA, Fok J, Bena J, Yang D, et al. Reversible cerebral vasoconstriction syndromes: analysis of 139 cases. Arch Neurol. 2011;68:1005–12. https://doi.org/10.1001/archneurol.2011.68.
50. Wang Y, Lou X, Li Y, Sui B, Sun S, Li C, et al. Imaging investigation of intracranial arterial dissecting aneurysms by using 3 T high-resolution MRI and DSA: from the interventional neuroradiologists' view. Acta Neurochir. 2014;156:515–25. https://doi.org/10.1007/s00701-013-1989-1.
51. Kim T-W, Choi HS, Koo J, Jung SL, Ahn K-J, Kim B-S, et al. Intramural hematoma detection by susceptibility-weighted imaging in intracranial vertebral artery dissection. Cerebrovasc Dis. 2013;36:292–8. https://doi.org/10.1159/000354811.
52. Krings T, Piske RL, Lasjaunias PL. Intracranial arterial aneurysm vasculopathies: targeting the outer vessel wall. Neuroradiology. 2005;47:931–7. https://doi.org/10.1007/s00234-005-1438-9.
53. Park JK, Lee CS, Sim KB, Huh JS, Park JC. Imaging of the walls of saccular cerebral aneurysms with double inversion recovery black-blood sequence. J Magn Reson Imaging. 2009;30:1179–83. https://doi.org/10.1002/jmri.21942.
54. Kleinloog R, Korkmaz E, Zwanenburg JJM, Kuijf HJ, Visser F, Blankena R, et al. Visualization of the aneurysm wall: a 7.0-tesla magnetic resonance imaging study. Neurosurgery. 2014;75:614–22 . discussion 622. https://doi.org/10.1227/NEU.0000000000000055.
55. Scanarini M, Mingrino S, Giordano R, Baroni A. Histological and ultrastructural study of intracranial saccular aneurysmal wall. Acta Neurochir. 1978;43:171–82.
56. Nagahata S, Nagahata M, Obara M, Kondo R, Minagawa N, Sato S, et al. Wall enhancement of the intracranial aneurysms revealed by magnetic resonance vessel wall imaging using three-dimensional turbo spin-echo sequence with motion-sensitized driven-equilibrium: a sign of ruptured aneurysm? Clin Neuroradiol. 2016;26:277–83. https://doi.org/10.1007/s00062-014-0353-z.
57. Shimonaga K, Matsushige T, Ishii D, Sakamoto S, Hosogai M, Kawasumi T, et al. Clinicopathological insights from vessel wall imaging of unruptured intracranial aneurysms. Stroke. 2018;49:2516–9. https://doi.org/10.1161/STROKEAHA.118.021819.
58. Hudson Joseph S, Mario Z, Daichi N, Kung David K, Pascal J, Samaniego Edgar A, et al. Magnetic resonance vessel wall imaging in human intracranial aneurysms. Stroke. 2019;50:e1. https://doi.org/10.1161/STROKEAHA.118.023701.
59. Matouk CC, Mandell DM, Günel M, Bulsara KR, Malhotra A, Hebert R, et al. Vessel wall magnetic resonance imaging identifies the site of rupture in patients with multiple intracranial aneurysms: proof of principle. Neurosurgery. 2013;72:492–6 . discussion 496. https://doi.org/10.1227/NEU.0b013e31827d1012.
60. Edjlali M, Gentric J-C, Régent-Rodriguez C, Trystram D, Hassen WB, Lion S, et al. Does aneurysmal wall enhancement on vessel wall MRI help to distinguish stable from unstable intracranial aneurysms? Stroke. 2014;45:3704–6. https://doi.org/10.1161/STROKEAHA.114.006626.
61. Edjlali M, Guédon A, Ben Hassen W, Boulouis G, Benzakoun J, Rodriguez-Régent C, et al. Circumferential thick enhancement at vessel wall MRI has high specificity for intracranial aneurysm instability. Radiology. 2018;289:181–7. https://doi.org/10.1148/radiol.2018172879.
62. Hartman JB, Watase H, Sun J, Hippe DS, Kim L, Levitt M, et al. Intracranial aneurysms at higher clinical risk for rupture demonstrate increased wall enhancement and thinning on multicontrast 3D vessel wall MRI. Br J Radiol. 2019; https://doi.org/10.1259/bjr.20180950.

63. Wang X, Zhu C, Leng Y, Degnan AJ, Lu J. Intracranial aneurysm wall enhancement associated with aneurysm rupture: a systematic review and meta-analysis. Acad Radiol. 2018; https://doi.org/10.1016/j.acra.2018.05.005.
64. Coutinho JM, Sacho RH, Schaafsma JD, Agid R, Krings T, Radovanovic I, et al. High-resolution vessel wall magnetic resonance imaging in angiogram-negative non-perimesencephalic subarachnoid hemorRHAGE. Clin Neuroradiol. 2017;27:175–83. https://doi.org/10.1007/s00062-015-0484-x.
65. Edjlali M, Roca P, Gentric J-C, Trystram D, Rodriguez-Régent C, Nataf F, et al. Advanced technologies applied to physiopathological analysis of central nervous system aneurysms and vascular malformations. Diagn Interv Imaging. 2014;95:1187–93. https://doi.org/10.1016/j.diii.2014.05.003.
66. Meng H, Tutino VM, Xiang J, Siddiqui A. High WSS or low WSS? Complex interactions of hemodynamics with intracranial aneurysm initiation, growth, and rupture: toward a unifying hypothesis. AJNR Am J Neuroradiol. 2014;35:1254–62. https://doi.org/10.3174/ajnr.A3558.
67. Ansari SA, Schnell S, Carroll T, Vakil P, Hurley MC, Wu C, et al. Intracranial 4D flow MRI: toward individualized assessment of arteriovenous malformation hemodynamics and treatment-induced changes. AJNR Am J Neuroradiol. 2013;34:1922–8. https://doi.org/10.3174/ajnr.A3537.
68. Wasserman BA, Lin W, Tarr RW, Haacke EM, Müller E. Cerebral arteriovenous malformations: flow quantitation by means of two-dimensional cardiac-gated phase-contrast MR imaging. Radiology. 1995;194:681–6. https://doi.org/10.1148/radiology.194.3.7862962.
69. Edjlali M, Roca P, Rabrait C, Trystram D, Rodriguez-Régent C, Johnson KM, et al. MR selective flow-tracking cartography: a postprocessing procedure applied to four-dimensional flow MR imaging for complete characterization of cranial dural arteriovenous fistulas. Radiology. 2014;270:261–8. https://doi.org/10.1148/radiol.13130507.
70. Kortman HGJ, Smit EJ, Oei MTH, Manniesing R, Prokop M, Meijer FJA. 4D-CTA in neurovascular disease: a review. AJNR Am J Neuroradiol. 2015;36:1026–33. https://doi.org/10.3174/ajnr.A4162.
71. Wang H, Ye X, Gao X, Zhou S, Lin Z. The diagnosis of arteriovenous malformations by 4D-CTA: a clinical study. J Neuroradiol. 2014;41:117–23. https://doi.org/10.1016/j.neurad.2013.04.004.
72. Willems PWA, Taeshineetanakul P, Schenk B, Brouwer PA, Terbrugge KG, Krings T. The use of 4D-CTA in the diagnostic work-up of brain arteriovenous malformations. Neuroradiology. 2012;54:123–31. https://doi.org/10.1007/s00234-011-0864-0.
73. Willems PWA, Brouwer PA, Barfett JJ, terBrugge KG, Krings T. Detection and classification of cranial dural arteriovenous fistulas using 4D-CT angiography: initial experience. AJNR Am J Neuroradiol. 2011;32:49–53. https://doi.org/10.3174/ajnr.A2248.
74. Fujiwara H, Momoshima S, Akiyama T, Kuribayashi S. Whole-brain CT digital subtraction angiography of cerebral dural arteriovenous fistula using 320-detector row CT. Neuroradiology. 2013;55:837–43. https://doi.org/10.1007/s00234-013-1181-6.
75. Frölich AMJ, Wolff SL, Psychogios MN, Klotz E, Schramm R, Wasser K, et al. Time-resolved assessment of collateral flow using 4D CT angiography in large-vessel occlusion stroke. Eur Radiol. 2014;24:390–6. https://doi.org/10.1007/s00330-013-3024-6.
76. Frölich AMJ, Schrader D, Klotz E, Schramm R, Wasser K, Knauth M, et al. 4D CT angiography more closely defines intracranial thrombus burden than single-phase CT angiography. AJNR Am J Neuroradiol. 2013;34:1908–13. https://doi.org/10.3174/ajnr.A3533.
77. Frölich AMJ, Psychogios MN, Klotz E, Schramm R, Knauth M, Schramm P. Antegrade flow across incomplete vessel occlusions can be distinguished from retrograde collateral flow using 4-dimensional computed tomographic angiography. Stroke. 2012;43:2974–9. https://doi.org/10.1161/STROKEAHA.112.668889.
78. Tan IYL, Demchuk AM, Hopyan J, Zhang L, Gladstone D, Wong K, et al. CT angiography clot burden score and collateral score: correlation with clinical and radiologic outcomes in acute middle cerebral artery infarct. AJNR Am J Neuroradiol. 2009;30:525–31. https://doi.org/10.3174/ajnr.A1408.

79. Tsivgoulis G, Sharma VK, Lao AY, Malkoff MD, Alexandrov AV. Validation of transcranial Doppler with computed tomography angiography in acute cerebral ischemia. Stroke. 2007;38:1245–9. https://doi.org/10.1161/01.STR.0000259712.64772.85.
80. Brunser AM, Mansilla E, Hoppe A, Olavarría V, Sujima E, Lavados PM. The role of TCD in the evaluation of acute stroke. J Neuroimaging. 2016;26:420–5. https://doi.org/10.1111/jon.12334.
81. Kilburg C, McNally JS, de Havenon A, Taussky P, Kalani MYS, Park MS. Advanced imaging in acute ischemic stroke. Neurosurg Focus. 2017;42:E10. https://doi.org/10.3171/2017.1.FOCUS16503.

Part II
Carotid Artery

Chapter 4
Atherosclerosis of the Carotid Artery

Matthijs F. Jansen, Esther Lutgens, and Mat J. A. P. Daemen

Pathogenesis of Atherosclerosis

Atherosclerosis is a two-faced disease. While it has one of the longest incubation periods known to man, its main complications, myocardial infarction and ischemic stroke, happen suddenly and often without prior warning. The earliest signs of disease, fatty streak lesions, can already be found in the first decade of life in the aorta and will develop in the coronary arteries in the second decade [1]. These lesions form after the arterial endothelium is activated by an injurious stimulus, such as low shear stress, turbulent flow, or oxidative stress. Both low shear stress and turbulent flow are present at arterial bifurcations, including the bifurcation of the internal and

M. F. Jansen
Department of Medical Biochemistry, Amsterdam Cardiovascular Sciences (ACS), Amsterdam UMC, University of Amsterdam, Amsterdam, The Netherlands

Department of Cardiology, Amsterdam UMC, VU Medical Center, Amsterdam, The Netherlands
e-mail: m.f.jansen@amc.uva.nl

E. Lutgens
Department of Medical Biochemistry, Amsterdam Cardiovascular Sciences (ACS), Amsterdam UMC, University of Amsterdam, Amsterdam, The Netherlands

Institute for Cardiovascular Prevention (IPEK), Ludwig Maximilians University, Munich, Germany
e-mail: e.lutgens@amc.uva.nl

Mat J. A. P. Daemen (✉)
Department of Pathology, Amsterdam Cardiovascular Sciences (ACS), Amsterdam UMC, University of Amsterdam, Amsterdam, The Netherlands
e-mail: m.j.daemen@amsterdamumc.nl

C. Yuan et al. (eds.), *Vessel Based Imaging Techniques*,
https://doi.org/10.1007/978-3-030-25249-6_4

external carotid artery, causing a high incidence of atherosclerotic plaques at sites like these [2].

Due to the activation of the endothelium, lipid components, most notably low-density lipoproteins (LDL), start accumulating in the subendothelial space. Once trapped in the subendothelial space, the lipid particles are altered, most importantly by lipid oxidation as a result of exposure to the oxidative waste of vascular cells. The oxidation of LDL particles leads to the formation of oxidized LDL (oxLDL), the most potent early stimulator of the inflammatory process driving atherosclerosis [3]. The activated endothelium also starts attracting immune cells by expressing cell adhesion molecules and secreting chemokines, a process that is also propagated by immune cells, mostly macrophages, already present in the plaque [4, 5].

The extent and speed of atherosclerotic plaque buildup are modulated by the severity of dyslipidemia as well as severity of the inflammatory response, and both are correlated with incidence of cardiovascular disease [6]. Many factors play a role in the severity of the inflammatory response in atherosclerosis; some of the most notable are mechanical forces [2], sex hormones [7], chronic inflammatory diseases [8], metabolic syndrome/obesity [9], (epi)genetics [10, 11], and diabetes mellitus [12].

Lipids

More than a century ago, the German pathologist Rudolf Virchow discovered that cholesterol was present in atherosclerotic plaques. In the 1950s, the Framingham Heart Study firmly established high lipid levels as a risk factor for atherosclerosis [13]. Lipid-lowering statins (inhibitors of HMG-CoA reductase) are very successful in reducing cardiovascular risk [14]. PCSK9 inhibitors are a new class of drugs, capable of dramatically lowering lipids in combination with statins, resulting in the further lowering of cardiovascular risk [15, 16]. The importance of lipids is also evident in mouse models, where, besides a knockout of genes such as apolipoprotein E (ApoE) or the LDL receptor (LDLR), a lipid-rich diet is needed to induce significant atherosclerosis.

Intracellular cholesterol homeostasis is the cumulative result of three simultaneous processes: (1) intracellular synthesis; (2) uptake from plasma lipoproteins, most importantly via LDL; and (3) reverse cholesterol transport by high-density lipoproteins (HDL). Cholesterol levels are sensed by the LXR (liver X receptor), a nuclear receptor which stimulates cholesterol transport toward the liver, biliary excretion, and possibly reduction in cholesterol synthesis. Contrary to the function of LXR, sterol regulatory element-binding protein 1c and 2 (SREBP-1c and SREBP-2) increase lipogenesis, cholesterol synthesis, and cholesterol uptake. Mice lacking the LXR gene feature a higher expression of SREBP-2, as well as several cholesterol-related genes such as HMG-CoA synthase and HMG-CoA reductase [17]. These properties make increasing LXR or decreasing SREBP interesting new therapeutic targets.

Low-Density Lipoproteins

Low-density lipoproteins are a large contributor to cardiovascular risk, and lowering LDL is one of the most effective ways for risk reduction [14]. In patients, both in clinics and clinical trials, plasma levels of LDL are generally not measured directly due to high costs; instead, LDL-C is determined using the Friedewald equation (LDL-C = Total cholesterol - HDL - triglycerides). In most situations, LDL and LDL-C correlate well; however, in certain situations, most notably hypertriglyceridemia, the LDL-C value can deviate from the actual LDL concentration [18]. In health, cells upregulate the LDL receptor (LDLR) when in need of cholesterol, which is required for cell growth, steroid/hormone synthesis, and the structural integrity of cell membranes. Circulating LDL particles bind to the LDL receptor and are then transported into the cell via endocytosis. At higher plasma levels of LDL, the LDLR will become saturated. When the amount of circulating LDL exceeds the ability of the liver to catabolize LDL, receptor-independent uptake of LDL will occur, especially at sites where the endothelium has become activated, ultimately leading to the formation of foam cells and fatty streaks [18]. After binding to LDL and internalizing it, the LDLR is able to be reused on the cell membrane. The enzyme PSCK9 inactivates the LDLR, making it unable to be reused. Inhibiting the PSCK9 enzyme severely lowers plasma LDL-C levels [15, 16].

Oxidized LDL

When entering the vessel wall, LDL is modified via a variety of mechanisms. The most relevant mechanism is the oxidation of LDL by reactive oxygen species (ROS). While non-modified LDL binds to the LDLR, oxLDL binds to scavenger receptors including CD36, SR(A), and LOX-1 that are mostly expressed by macrophages [3]. OxLDL is a potent activator of macrophages, ultimately leading to the formation of foam cells. The presence of oxLDL upregulates the LOX-1 receptor while downregulating the LDLR, initiating a positive feedback loop where more LDL is oxidized and then taken up via LOX-1 [18].

Triglycerides

Like LDL, triglycerides have been shown to be an important risk factor for cardiovascular disease in the Framingham Heart Study [13]. In humans, triglycerides are transported via very low-density lipoproteins (VLDL) [18]. Pharmacological inhibition of triglycerides has not been as successful as LDL lowering. However, some recent studies have shown that in patients on statins with high triglycerides, triglyceride lowering reduces major adverse cardiovascular events (MACE) [19].

HDL

HDL is the smallest of the lipoprotein family. HDL acts as a reverse carrier of cholesterol, as it is able to uptake cholesterol from cells. HDL is important for the recycling of cholesterol back to the liver and the delivery of cholesterol toward hormone-producing organs [19]. As higher levels of HDL are correlated with lower incidence of adverse cardiovascular events in the general population, HDL was thought of as a promising new therapeutic target [13]. However, this has come under scrutiny in recent years as more in-depth examinations of population data show no other associations between HDL and cardiovascular events, except for an increased risk when HDL levels are very low. Furthermore, in Mendelian randomization studies, it was shown that genetically high HDL does not protect against cardiovascular events [20]. Ultimately, increasing HDL through various pharmacological methods in cardiovascular patients does not result in the lowering of cardiovascular risk [20, 21].

Inflammation

Monocytes

Among the first cells recruited to the activated endothelium are monocytes. Monocytes are short-lived mononuclear phagocytes, which differentiate into macrophages once they infiltrate into the vessel wall. Monocytes are recruited to the site of the plaque by the secretion of chemokines such as CCL2 and CCL5 by the endothelium. The endothelial cells express the adhesion molecules P-, L-, and E-selectin, ICAM-1, and VCAM-1, to which the monocyte adheres. After adhering to the vessel wall, the monocytes start rolling along the activated endothelium and subsequently enter the subendothelial space, either via para-endothelial or trans-endothelial migration [4, 5].

In mice, two general subpopulations of monocytes have been described: the inflammatory Ly6C^{high} monocyte, which is preferentially recruited toward inflamed tissue, and the patrolling Ly6C^{low} monocytes which are homed toward non-inflamed tissues. In murine atherosclerosis, inflammatory (Ly6C^{high}) monocytes are preferentially recruited toward the vessel wall and have been shown to aggravate atherosclerosis [22–24]. In humans, three major monocyte subsets have been described. Similar to mice, human monocytes can be divided into inflammatory CD14++CD16- expressing monocytes (classical monocytes) and anti-inflammatory CD14+CD16++ expressing monocytes (nonclassical monocytes). Additionally, in humans, an intermediate CD14^{++}CD16^{+}CCR2^{+}-expressing subset (intermediate monocytes) can be identified. Functionally, CD14++CD16- monocytes (classicals) support inflammation and phagocytosis, CD14^{++}CD16^{+}CCR2^{+} monocytes (intermediates) are pro-inflammatory, and CD14+CD16++ monocytes (nonclassicals) are aimed toward

restoration of homeostasis (healing) [5, 25]. In humans, both higher levels of classical monocytes and intermediate monocytes have been shown to correlate with a higher incidence of cardiovascular disease [24, 26, 27].

When monocytes migrate over the endothelial barrier toward the intima, they come into contact with colony-stimulating factors, most importantly macrophage colony-stimulating factor (M-CSF) and granulocyte-macrophage colony-stimulating factor (GM-CSF) secreted by endothelial cells, vascular smooth muscle cells (vSMC), and macrophages. These factors initiate the differentiation of monocytes into macrophages [28].

Macrophages

In healthy tissue, the most notable macrophage functions are phagocytosis (the uptake of solid particles or pathogens), efferocytosis (the uptake and clearance of apoptotic cells), tissue remodeling, and chemoattraction. All of these processes are impaired in the atherosclerotic plaque.

Like monocytes, macrophages can be divided into different subtypes. Which subtype a macrophage becomes is mostly determined by the environment and stimuli the macrophage is exposed to. At the extremes, macrophages can be divided into the pro-inflammatory M1- and the anti-inflammatory M2 macrophage. M1 macrophages are induced by Th1 cytokines and excrete pro-inflammatory cytokines like TNF, IL-6, IL-1β, and IL-12. Sustained M1 activation results in tissue damage and eventually impaired wound healing. The anti-inflammatory M2 macrophages are induced by Th2 cytokines and excrete anti-inflammatory cytokines like IL-10 and TGF-β. Functionally M2 macrophages scavenge debris and promote the resolution of inflammation, most importantly by clearing apoptotic cells (efferocytosis) and the dampening of immune responses, ultimately promoting tissue repair and healing [29].

It is important to note however that the M1 vs. M2 division is a simplified concept. Between the M1 and M2 phenotypes, a spectrum of other macrophage phenotypes can be identified, each with a different or yet undetermined function. In experimental mouse models of atherosclerosis, the M1 subtype and the plaque-specific M4 subtype are pro-inflammatory and pro-atherogenic. An increase of these macrophage subtypes inside the murine atherosclerotic plaque is correlated with larger and more vulnerable plaques. The other macrophage subtypes, the M2 phenotype and the plaque-specific M(hb) and Mhem phenotypes, have been shown to be anti-inflammatory and anti-atherogenic in murine atherosclerosis. The Mox phenotype that has been identified fairly recently is currently not well understood [30]. Through phagocytosis, macrophages take up oxLDL, an important step in the progression of atherosclerosis. Via scavenging receptors CD36, SR (A), and LOX-1, oxLDL is transported into the macrophage, where it is transformed into cholesteryl esters by the enzyme acetyl-CoA acetyltransferase (ACAT1).

Foam Cells

The excessive accumulation of cholesteryl esters in the endoplasmic reticulum of the macrophage induces its transformation to a foam cell (named after its foamy appearance on histology) [3]. Furthermore, the phagocytosis of cholesterol crystals activates the NLRP3 inflammasome, which in turn induces an enhanced secretion of IL-1β. The inhibition of IL-1β via the monoclonal antibody canakinumab has been shown to reduce cardiovascular events in patients [31, 32].

It is currently unknown which specific macrophage phenotype is the precursor of the foam cell. However, several studies have shown that the M2 phenotypes are more prone to differentiate into a foam cell.

The transformation of a macrophage into a foam cell induces various apoptotic pathways that ultimately lead to its demise. In advanced atherosclerosis, efferocytosis is impaired, leading to the formation of "post-apoptotic" foam cells that ultimately undergo secondary necrosis. This process is one of the main drivers of the formation of the necrotic core and a major cause of enhanced and sustained inflammation in the plaque [33].

Neutrophils

Neutrophils are short-lived phagocytic cells. Even though few neutrophils can be found in advanced atherosclerotic plaques, their importance in atherosclerosis is not to be underestimated. The degree of hypercholesterolemia-induced neutrophilia is positively correlated with atherosclerotic plaque size in experimental models and associated with plaque vulnerability in humans [34]. In both health and atherosclerosis, neutrophils work in conjunction with macrophages. Macrophages improve neutrophil survival through secretion of growth factors such as G-CSF, GM-CSF, and TNF. In turn, neutrophils attract monocytes toward the plaque and improve endothelial permeability, ultimately aiding and increasing monocyte infiltration into the atherosclerotic plaque [35]. Neutrophils, co-localized with macrophages, can be found at the cap of the atherosclerotic plaque. There, neutrophils release granule proteins, matrix metalloproteinases, and cathepsins. These factors are potent determinants of atherogenesis in experimental animal models, and many of them have been correlated with vulnerable plaques [36, 37].

T Cells

T cells play a central role in cell-mediated immunity. These immune cells are defined by T cell receptor (TCR) on their cell surface. Antigen-presenting cells (APCs, DCs, macrophages, and B cells) present antigens via MHC II to the TCR,

causing the T cell to become activated after simultaneous interaction of co-stimulatory molecules with their ligands, though it is also possible for T cell activation to be antigen independent.

Several subtypes of T cells have been identified, the T-helper cell (Th), the cytotoxic T cell (Tc), and the regulatory T cell (Treg). Like macrophages, T cells can somewhat switch between these subtypes depending on environmental cues it encounters.

T-helper cells (Th cells) are defined by the expression of CD4 and functions as an assistant to other immune cells. Most importantly, it induces activation of B cells, macrophages, and cytotoxic T cells and maturation of B cells. In general, there are two subtypes of Th-cells, Th1 and Th2. The Th1 subtype is considered pro-inflammatory; the Th2 is more anti-inflammatory. The balance between Th1 and Th2 levels plays a role in several diseases, like psoriasis (Th cell population skewed toward Th1) and asthma (Th-cell population skewed toward Th2) [38, 39].

T cells are recruited toward the vessel wall via mechanisms similar to macrophage recruitment and make up about 10% of the total cell populace in an atherosclerotic plaque. About 70% of these T cells are T-helper (CD4+) cells, the remaining fraction mostly being cytotoxic (CD8+) T cells [40]. In the vessel wall, T cells become activated in response to antigens and start to produce inflammatory agents (e.g., IFN-γ).The antigen that triggers the immune response and induces T cell proliferation and polarization is most likely atherosclerosis-specific antigens such as (the ApoB100 part of) LDL [41].

The majority of CD4+ T cells, and thus the majority of T cells, are of the Th1 subset. This subset has been extensively described as pro-atherogenic. Through the production of IFN-γ, T cells recruit macrophages and other T cells toward the atherosclerotic plaque, causing an increase in the secretion of Th1-promoting cytokines, an increased lipid uptake by macrophages, and an increase in foam cell formation, ultimately leading to an increased plaque growth and vulnerability. The positive feedback loop where Th1 cells recruit other Th1 cells is a major contributor to plaque progression. In patients suffering from cardiovascular disease, higher levels of Th1 cells have been found [42–44].

Th2 cells support antibody production of B cells via secretion of IL-4, IL-5, IL-10, and IL-13. While the Th2 subtype is increased in hyperlipidemia, the Th2 subtype is rare in atherosclerotic lesions. The role of Th2 cells in atherosclerosis is still poorly understood and seemingly contradictory. While IL-5 and IL-13 clearly protect against atherosclerosis, the prototypic Th2 cytokine IL-4 doesn't protect against atherosclerosis [42–44].

Regulatory T cells comprise around 5% of CD4+ T cells in the peripheral blood in humans. An overall protective role of regulatory T cells is suggested in both murine and human atherosclerosis studies. In mice, depletion of regulatory T cells aggravated atherosclerosis, suggesting that regulatory T cells limit plaque inflammation and thus disease progression. The mechanism of this action has not yet been identified. In humans, relatively low levels of regulatory T cells were found in atherosclerotic plaques, which might play a role in the persistent inflammation in these lesions. Moreover, compared to stable plaques, in rupture-prone plaques, fewer

regulatory T cells can be found. Together, this data suggests a protective role of regulatory T cells in atherosclerosis [45].

In early atherosclerosis, few cytotoxic (CD8+) T cells are present in the atherosclerotic plaque. However, they appear to be the dominating immune cell in advanced human plaques. In these lesions, CD8+ T cells concentrate around shoulder regions and fibrous caps. Furthermore, in murine atherosclerosis, CD8+ T cells have a pro-atherogenic effect. CD8+ T lymphocytes most likely promote the development of vulnerable atherosclerotic plaques by inducing apoptosis of macrophages, smooth muscle cells, and endothelial cells that in turn leads to secondary necrosis and necrotic core formation [46].

B Cells

B cells are known for their ability to produce antigens and are identified by the presence of a B cell receptor on their cell membrane. Besides antigen production, B cells are also able to serve as antigen-presenting cells and can activate both CD4+ and CD8+ T cells. Furthermore, they can promote chemokine production, produce a variety of cytokines (e.g., IFN-γ, IL-2, IL-12, IL-4, IL-6, and IL-10), promote leukocyte recruitment, and polarize T cells. Mature B cells can be divided into two categories: the B1 subtype, which is innate, T cell independent and produces polyreactive natural IgM antibodies, and the B2 subtype, which is important in adaptive immunity, as it is able to produce specific IgG antibodies tailored to a specific antigen and T cell dependent. Natural IgM antibodies against oxLDL, produced by B1 cells, are protective against atherosclerosis. In murine atherosclerosis, IL-5 mediates the production of the anti-oxLDL IgM antibodies. In contrast to the IgM antibodies produced by B1 cells, IgG antibodies against oxLDL promote atherosclerosis. This is evident in mice lacking B2 cells, as those have decreased plaque formation. Conversely, an increase in B2 cells increased plaque formation. This correlates with the fact that increased titers of anti-oxLDL antibodies are associated with an increase in adverse cardiovascular events [47].

Progression Toward the Advanced Plaque

As defined by histology, different stages of plaque development can be distinguished [48, 49]. As noted above, atherosclerotic lesions start developing around the second decade of life. The first detectable abnormalities in the vessel wall are intimal xanthomas (or fatty streaks). These lesions show accumulation of foam cells in the vessel wall, without the presence of a necrotic core or fibrous cap. Both human and animal research suggest that most of these lesions regress [50, 51].

While intimal xanthomas are detectable in children, the majority of advanced atherosclerotic lesions seem to originate from intimal thickening [52]. Intimal

thickening refers to the accumulation of smooth muscle cells (SMCs) in the intima, without the presence of lipid, macrophages, or foam cells. From normal intima thickening, pathological intimal thickening can develop. The lesions are characterized by a proteoglycan-rich matrix containing smooth muscle cells, perhaps a few macrophages and other immune cells, with small areas of lipid accumulation but with minimal or no evidence of a lipid core or necrosis. These lesions seem especially prone to erosion (see below).

Both intimal xanthomas and lesions with (pathological) intimal thickening can develop into a fibrous cap atheroma. These atherosclerotic plaques are characterized by a fibrous cap, overlaying a well-developed necrotic core. The fibrous cap is an overlay of connective tissue, consisting of smooth muscle cells and collagen in a proteoglycan matrix. This fibrous cap separates the blood from the highly thrombogenic necrotic core, which consists of a core of necrotic cells, surrounded by macrophages. When the necrotic core increases in size, increasingly large amount of extracellular lipids and cholesterol crystals will accumulate in it and form one or several large masses, also called the lipid core. Depending on the thickness of the fibrous cap, plaques can be quantified as thick-cap fibroatheromas or thin-cap fibroatheromas. The cut-off value distinguishing between these two plaques is different per vascular bed. In carotid plaques, plaques with a cap thinner than 165–200 μm are considered thin-capped [53, 54], while in coronary atherosclerosis, this cut-off value is 65 μm [55].

Thick-capped fibroatheromas rarely rupture but can erode (see below). Conversely, thin-cap fibroatheromas are very prone to rupture; most ruptured coronary plaques found during an autopsy study of >200 deceased patients had a cap thinner than 65 μm [48].

Ultimately, plaques can develop into stable fibrocalcific plaques. While these plaques can still cause clinical symptoms due to a reduction of lumen size, they will not cause acute ischemic syndromes. These plaques usually cause significant stenosis, are collagen-rich, and have large calcified areas. They contain few inflammatory cells, though a necrotic core may be present [48].

It is very important to note that progression of atherosclerotic disease is not a linear process. During the lifespan of an atherosclerotic plaque, its fibrous cap thickness can increase or decrease, and the plaque can regress all together or progress into a fibrocalcific plaque, making a previously dangerous (vulnerable) plaque suddenly stable or vice versa [56].

The Vulnerable Plaque

As atherosclerotic disease progresses, plaques will cause ischemic syndromes via three main mechanisms:

1. Plaque rupture: rupture of the fibrous cap overlaying the plaque, exposing the highly thrombogenic lipid core to blood, which immediately starts clotting, ultimately resulting in a thromboembolic stenosis or even occlusion of the vessel.

2. Plaque erosion: typically, the endothelial layer is absent in these plaques, resulting in the exposure of smooth muscle cells and extracellular matrix to blood, resulting inocclusion precipitated largely by the thrombus or distal embolization.
3. Calcified nodule: a relatively rare occurrence where calcifications protrude into the lumen, which are correlated with ischemic stroke [57–59].

Plaque Rupture

In a histopathological study of carotid endarterectomy, 67% of stroke patients had a thrombus at the endarterectomy site, compared to 27% in asymptomatic individuals. Plaque rupture was the most common cause of thrombus formation in both cases (64% of cases in stroke patients, compared to 25% of asymptomatic patients) [53]. Similar numbers are seen in coronary atherosclerosis, where about 60% of acute myocardial infarctions are due to plaque rupture. However, it should be noted that carotid plaque composition has changed over the years, as a decrease in percentage of carotid plaques with vulnerable characteristics has been observed. The same phenomenon can be observed in coronary atherosclerosis, where a decrease in plaque rupture and concurrent increase in plaque erosion has been observed. These changes over time are possibly due to the increased statin use and decreased tobacco use in recent years [60].

Plaques vulnerable to rupture (vulnerable plaques) have several histological characteristics, first identified in postmortem studies in patients who died from myocardial infarction. These plaques have a large lipid core (>40% of the total plaque area), a large necrotic core, intra-plaque neovascularization, intra-plaque hemorrhages, inflammatory cell infiltration into the fibrous cap, and, most importantly, a thin fibrous cap [1]. These same characteristics are of importance in carotid atherosclerosis, with one notable difference [61]. In carotid vulnerable plaques, intra-plaque hemorrhage (IPH) is especially predictive of future carotid atherosclerosis progression and stroke [62, 63]. Advanced lesions often show IPH, and it is postulated that micro-hemorrhages within the plaque occur from microvessels, originating from the adventitial vasa vasorum or from neovessels arising from the luminal endothelium. Both IPH and plaque rupture are associated with an increased density in microvessels [62].

Plaque rupture occurs when the shear stress pulling on the fibrous cap exceeds the tensile strength of this fibrous cap. In the carotid artery, retrospective studies determined that caps thinner than <165 μm [53] or <200 μm [54] are prone to rupture. These plaques are termed thin-cap fibroatheromas (TCFA). In coronary atherosclerosis, the threshold for rupture prone plaques is lower (65 μm [55]), most likely due to differences in flow and vessel diameter. The coronary threshold and the importance of the thin cap in coronary plaque rupture have been confirmed by

in vivo intravascular imaging in patients [64]. In carotid atherosclerosis, no prospective studies determining the usefulness and/or accuracy of these values have been performed yet.

Thinning of the fibrous cap is induced by two concurrent mechanisms. Macrophages and foam cells inside the plaque induce tissue remodeling, especially fibrous cap thinning, via the secretion of several proteolytic enzymes such as plasminogen activators, cathepsins, and matrix metalloproteinase) [65]. Furthermore, smooth muscle cells (SMC) are gradually lost in the thinning fibrous cap due to SMC apoptosis. At the site of cap rupture, SMCs are usually absent. Both of these processes are most apparent at the shoulder regions of a plaque, which is probably why this is the region with the thinnest fibrous cap [66].

In both coronary and carotid atherosclerosis, rupture of a thin fibrous cap can sometimes be induced by a trigger, such as alcohol or coffee consumption, heavy meals, cigarette smoking, anger, anxiety, work stress, industrial accidents, war and terror attacks, earthquakes, and sporting events [67]. These triggers likely cause activation of the sympathetic nervous system, resulting in an increased heart rate and higher blood pressure and possibly increased platelet reactivity. It should be noted that some studies indicate that plaque rupture caused by these triggers would have happened a few weeks later anyway [66].

Plaque Erosion

About 35% of myocardial infarctions are due to plaque erosion, a number that is seemingly rising in the last decade [60]. These numbers might be lower in carotid atherosclerosis, being the underlying mechanism in about 10% of stroke or TIA patients, though it should be noted that this study was performed with a low number of patients in an older database [68]. Plaque erosion occurs when the endothelial cell layer overlying the fibrous cap disappears, thus exposing the thrombotic extracellular matrix to the blood, ultimately leading to clot formation. As no identifying morphological features of plaque prone to erosion have been identified, characterizing these plaques has proven difficult [57].

In regions of disturbed flow, toll-like receptor 2 (TLR2) is activated on endothelial cells. Ligation of TLR2 induces the production of IL-8, promoting neutrophil adhesion and recruitment. In vitro, co-incubation of endothelial cells with TLR2 agonists and neutrophils promotes endothelial cell death. This combination of factors might also lead to the loss of endothelial cells in vivo, ultimately resulting in the exposure of the fibrous cap to the blood. This exposure activates platelets, causing them to release pro-inflammatory mediators (further aggravating the process leading to endothelial cell death) and to release blockers of fibrinolysis (increase the durability of clots) and causing them to adhere to the exposed fibrous cap, leading to the initiation of thrombus formation [69].

Calcified Nodules

About 6–7% of carotid thrombosis is thought to be caused by calcified nodules, though it should be noted that this number is derived from a low number of cases [53]. This number is slightly lower in coronary atherosclerosis [58]. First introduced by Virmani et al., calcified nodules refer to a rare type of thrombosis caused by extruding calcified nodules into the vessel lumen [48]. These calcified nodules are more often present in older individuals and tortuous arteries. In coronary atherosclerosis, calcified nodules identified by IVUS in the PROSPECT trial were unlikely to cause adverse cardiovascular events during a 3-year follow-up [57].

Atherosclerosis in the Carotid Artery

Atherosclerotic plaques have different morphologies in every vascular bed, mostly due to the differences in anatomy and/or hemodynamics between the vascular beds. The carotid artery can be subdivided into several distinct regions. The left common carotid artery (CCA) directly stems from the aortic arch, the right CCA stems from the brachiocephalic artery, which in turn stems from the aortic arch. On both sides, the CCA bifurcates into two arteries, the internal and the external carotid artery. Both internal carotid arteries, together with the basilar artery, supply the circle of Willis. The external carotid arteries supply the neck, face, and eyes. At the bifurcation of the CCA, a widening of the artery occurs called the bulb (Fig. 4.1). This unique aspect of the CCA aggravates the already disturbed, turbulent flow at the bifurcation [70].

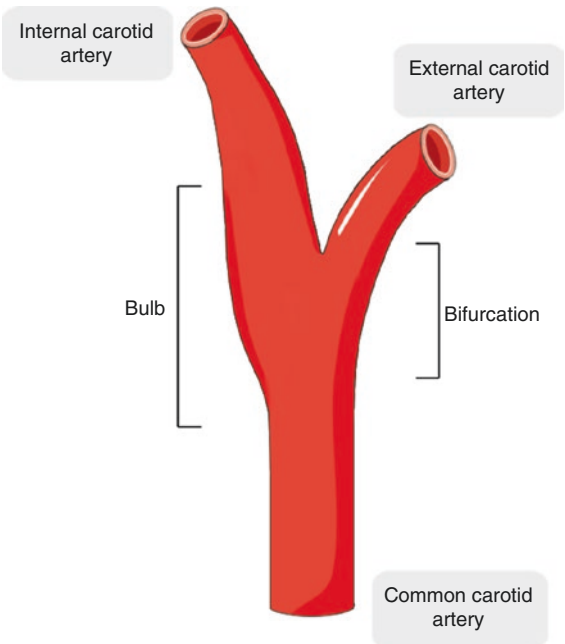

Fig. 4.1 The carotid artery

The disturbed flow around the bifurcation and bulb aggravates the formation of atherosclerotic plaques. When observing plaque size in carotid endarterectomy, the largest, most restricting, plaques form around the base or midsection of the internal carotid artery [71]. Furthermore, when observing atherosclerotic plaques using MRI, the common carotid artery showed outward remodeling, while at the bifurcation and internal carotid artery, the more malign inward remodeling was observed [70].

Carotid Artery Versus Coronary Artery Atherosclerosis

Carotid and coronary atherosclerosis overlap in many key areas but also differ in many other aspects (see Table 4.1). Systemic factors, like blood lipid levels, are similar in coronary and carotid atherosclerosis for obvious reasons. The hemodynamic environment however is very different in the two vascular beds.

The amount of flow through the carotid artery is mostly determined during the systolic phase. In contrast, flow thorough coronary arteries is only present during the diastolic phase, as the smaller coronary vessels are closed by the ventricular

Table 4.1 Differences between carotid and coronary atherosclerosis

Feature		Carotid artery	Coronary artery
ANATOMY	Collateral circulation	Well developed (circle of Willis)	Developed in response to flow deficit
	Other factors	Carotid artery bulb aggravates non-laminar shear stress	Blood flow only during diastole
Plaque features	Thin-cap cut-off	Thin cap: <165–200 μm	Thin cap: <65 μm
	Plaque hemorrhaging	Important predictor for stroke	Weaker correlation with ACS
Plaque pathology	Thrombosis	Distal embolization	Local thrombosis causing obstruction
	Plaque rupture	Frequent	Frequent (ca. 60%), associated with STEMI
	Erosion	Rare (10%)	Infrequent (35%), associated with NSTEMI
	Calcified nodules	Rare (6–7%)	Rare (5%)
Risk factors	Hypertension	Both high diastolic and high systolic pressure are a risk factor	High systolic pressure is a risk factor
	Inflammation (CRP)	Risk factor	Risk factor
Therapy	Blood pressure therapy	Effective (more effective in stroke prevention than in ACS prevention)	Effective (more effective in stroke prevention than in ACS prevention)
	Anti-lipid therapy	Effective (but no reduction in IMT)	Effective (plaque regression with very low lipids)
	Reduction of inflammation	Likely effective (one trial showing benefit)	Probably not effective (one trial showing no benefit)

pressure during the systolic phase. While blood pressure influences the increase of both coronary and carotid atherosclerosis, changes in blood pressure affect stroke incidence more than the incidence of myocardial infarction [72]. Due to the carotid bulb, the maximum area at the carotid bifurcation is much higher than the maximum area in the common carotid area, leading to slower blood flow and low, non-laminar shear stress. This phenomenon is not present in the coronary arteries [73].

While carotid artery plaques develop later in life, as compared to lesions in the coronary circulation, the morphology of carotid atherosclerosis is somewhat similar to that of coronary atherosclerosis [74]; however, some notable differences exist.

The mean fibrous cap thickness is about 3× as thick in ruptured carotid plaques (165–200 μm [53, 54]) as compared to ruptured coronary plaques (65 μm [64]), most likely due to the stronger pull, and thus earlier rupture, on the fibrous cap caused by different hemodynamics in the carotid artery. Intra-plaque hemorrhage is more frequent and larger in the carotid artery, as compared to the coronary artery. These changes are thought to be due to the higher pressure and flow in the vasa vasorum of carotid plaques [73]. Possibly secondary to these differences, calcified nodules are more frequent in carotid atherosclerosis, while plaque erosion is rarer in carotid atherosclerosis, as compared to coronary atherosclerosis [73].

In general, myocardial infarction is caused by local thrombosis at the site of the atherosclerotic plaque. Conversely, distal embolization appears to be the most prevalent mechanism causing ischemic events by carotid atherosclerosis. Only when the intracranial collateral network (circle of Willis) is incomplete or obstructed, carotid artery occlusion can lead to cerebral ischemia [74].

While the relation between complete blockage of the carotid artery and brain ischemia is obvious, the correlation between embolization and cerebral ischemia is clouded by confounders. Many risk factors for carotid atherosclerosis (hypertension, smoking, etc.) also increase risk of atrial fibrillation (AF) [75, 76]. While AF is an important risk factor for ischemic stroke, it is not for carotid atherosclerosis [77]. This interaction makes it harder to interpret whether an increase in the incidence ischemic stroke is due to more vulnerable carotid plaques, due to the presence of atrial fibrillation, or both.

In patients with atherosclerotic stenosis of the carotid artery of >50%, who experienced ischemic symptoms (amaurosis fugax or TIA), carotid endarterectomy reduces stroke risk by about 75% [78], suggesting that the problematic emboli often originate in the carotid plaque. It should be noted that these trials are more than 10 years old, and, as stated above, carotid artery plaque composition has changed since. As such, the beneficial effects of carotid endarterectomy could be lower today. However, no newer trials comparing optimal medical treatment to carotid endarterectomy in symptomatic patients have been performed.

In asymptomatic carotid artery stenosis, the benefit of carotid endarterectomy is less clear as asymptomatic patients have a low long-term risk for stroke. Furthermore, the benefit of carotid endarterectomy compared to medical therapy has not been well established in asymptomatic patients, as there is a likely relationship between

vascular dementia and the extent of carotid atherosclerosis [79]. There is a clear association between the extent of carotid atherosclerosis and signs of brain ischemia on MRI [80]. Furthermore, the extent of carotid artery atherosclerosis is associated with cognitive impairment. However, the effect of carotid endarterectomy in halting cognitive impairment is unclear [81]. It should be noted that none of these studies exclude patients with AF, meaning that the exact role of carotid atherosclerosis in vascular dementia should still be viewed with some uncertainty.

Logically, the risk of major adverse cardiovascular events increases with the number of arterial systems affected by atherosclerosis [82]. For example, patients presenting with symptomatic ischemic disease in one cardiovascular system at baseline had a 25% risk of recurrent major adverse cardiovascular event (MACE) after 3 years, compared to a 45% risk of MACE after 3 years in patients with symptomatic disease in three cardiovascular systems [83].

Furthermore, the extent of atherosclerosis in the carotid artery correlates with the extent of the disease in the coronary circulation. Increasing carotid intima-media thickness is well correlated with risk of ischemic stroke and correlates almost as well with risk of myocardial infarction [84]. Moreover, a significant portion of symptomatic stroke patients has subclinical coronary atherosclerosis [85]. Lastly, carotid plaque phenotype as measured by MRI might be an excellent predictor of future coronary artery disease [86]. This overlap suggests that the development of atherosclerosis is influenced by systemic parameters; however, due to local anatomy and hemodynamic parameters, differences between vascular beds are present.

Risk Factors in Carotid Atherosclerosis

Of the two types of stroke, ischemic and hemorrhagic, only ischemic stroke is correlated with carotid atherosclerosis. Stroke caused by carotid atherosclerosis is invoked by either of the two mechanisms, thrombosis or embolization. In thrombotic stroke, the carotid artery is (almost) completely occluded. When the anatomy of the circle of Willis is incomplete, the resulting flow deficit cannot be compensated by the collateral circulation, culminating in cerebral ischemia. In thromboembolic stroke, the dominant cause of stroke in carotid atherosclerosis, emboli that form at various sites, gets stuck in the cerebral vascular network, leading to a blockage of that artery. Clinical symptoms are dependent on the size of the embolus and which the artery is blocked by the thrombus. About 15–20% of all ischemic stroke occurrences are thought to be due to carotid atherosclerosis [87]. Furthermore, the extent of carotid artery atherosclerosis is likely associated with cognitive impairment and signs of brain ischemia on MRI [80, 81].

It should be noted that the risk of stroke, especially in asymptomatic patients with carotid stenosis >50%, has drastically decreased over the last 40 years, most likely due to much improved pharmacological interventions [88].

Lipids

Unfavorable lipid profiles (high LDL-C, high triglycerides, low HDL) correlate with atherosclerosis in any vessel. In the carotid artery, unfavorable lipid profiles are associated with carotid intima-media thickness and a vulnerable plaque composition [89–91]. Surprisingly however, levels of total cholesterol and low-density lipoprotein (LDL-C) cholesterol appear unrelated to incidence of stroke in the Framingham Heart Study [92].

Ultimately, lowering lipid levels is effective in the prevention of stroke. In a variety of large statin trials, designed to study the reduction of major adverse cardiovascular events in general, the incidence of ischemic stroke was lower in statin-treated patients. Furthermore, more aggressive treatment further decreased stroke risk [14]. In both the FOURIER and the SPIRE trials, designed to study the effect of anti-PSCK9 antibodies on lipid levels and reduction of cardiovascular events on top of statins, treatment with the anti-PSCK9 antibodies severely lowered lipids and lowered ischemic stroke risk [15, 16].

Hypertension

Hypertension, most importantly systolic and pulse pressure, is a risk factor in all cardiovascular diseases. In carotid atherosclerosis, both a higher carotid intima-media thickness and vulnerable carotid plaque composition are highly correlated with blood pressure [90, 91]. Furthermore, hypertension is one of the largest contributors to risk of ischemic stroke [77]. Though it should be noted that atrial fibrillation, another large contributor to stroke risk, is also correlated with hypertension. Pharmacological reduction of blood pressure toward baseline is effective in reducing stroke risk, though debate is still ongoing about optimal pressure targets [92–94].

Smoking

It is well known that the smoking of tobacco is a major contributor to atherosclerotic plaque initiation, development, and ultimately its complications, such as stroke and myocardial infarction. Smokers have an unfavorable lipid profile (LDL-C, triglycerides, and total cholesterol are higher) and more inflammation (LDL-C, triglycerides, and total cholesterol are higher) and are more prone to thrombosis. Furthermore, they have decreased vascular function due to reduce nitric oxide (NO) production, increased in adhesion molecules on endothelial cells, and eventual endothelial dysfunction [95, 96]. Together, these effects lead to a more vulnerable plaque, which has more atheroma, a smaller fibrous cap, and more plaque hemorrhage. In carotid

atherosclerosis, smoking is correlated with a higher carotid intima-media thickness and vulnerable carotid plaque composition [90, 91].Ultimately, stroke risk is increased by tobacco and is estimated to cause about 15% of all strokes per year. Cessation of smoking is highly effective, as it decreases stroke risk back to baseline after 2–4 years [97].

Obesity

Obesity is a growing epidemic, with 76% of people being overweight and 25% being obese in the United States. Obesity is associated with many risk factors of cardiovascular disease but also separately with atherosclerosis. It is associated with hypertension, diabetes, and metabolic syndrome and a higher risk of coronary artery disease. In carotid atherosclerosis, higher body weight is associated with increased intima-media thickness and high-risk plaque characteristics [90, 91]. Moreover, for each 1-unit increase in BMI, there is a 4% increased risk of ischemic stroke. It should be noted that obesity increases risk of atrial fibrillation by the same amount [98].

Diabetes

Intracellular hyperglycemia, caused by diabetes mellitus, induces excessive reactive oxygen species (ROS) production in the atherosclerotic plaque, leading to increased oxidation of lipids and increased inflammation, most notably via activation of the NLRP3 inflammasome [99]. It has been shown that diabetes mellitus is an independent and modifiable risk factor for ischemic stroke. Interestingly, risk for stroke is higher in younger patients suffering from diabetes mellitus. Even prediabetes has been linked to an increase in the risk of ischemic stroke [100]. Older glucose-lowering drugs have already been successful in lowering cardiovascular risk, and several new drugs have shown promising results in reducing cardiovascular events, including stroke [101].

Inflammation (High hsCRP Levels)

High-sensitive C-reactive protein (hsCRP) is a marker of inflammation, being produced downstream of IL-1β and IL-6. Higher levels of hsCRP are associated with acute coronary syndromes and ischemic stroke [102]. And, like in coronary atherosclerosis, hsCRP is associated with a more advanced plaque in the carotid artery [103]. In a primary prevention setting, treating patients with a high hsCRP at baseline with atorvastatin (the JUPITER trial) reduces incidence of ischemic

stroke. In high-risk populations, this correlation is not present, probably because these patients have maximal benefit of statins therapy regardless of hsCRP [104]. However, in the CANTOS trial, reduction of inflammation via canakinumab (an IL-1β inhibitor) on top of statin did reduce hsCRP, but not stroke incidence [32].

Conclusion

The formation of an atherosclerotic plaque is a complex process, involving a variety of lipids and immune and nonimmune cells. While the disease is similar in the carotid and coronary arteries, some large differences are present between the two, due to the hemodynamic variations and different disease etiologies of stroke and myocardial infarction. A plethora of risk factors is involved in carotid plaque formation and subsequent stroke risk, with hypertension and lipid levels being the most prominent risk factors.

References

1. Lusis AJ. Atherosclerosis. Nature. 2000;407:233–41.
2. Kwak BR, Bäck M, Bochaton-Piallat ML, et al. Biomechanical factors in atherosclerosis: mechanisms and clinical implications. Eur Heart J. 2014;35:3013–20.
3. Chistiakov DA, Melnichenko AA, Myasoedova VA, Grechko AV, Orekhov AN. Mechanisms of foam cell formation in atherosclerosis. J Mol Med. 2017;95:1153–65.
4. Bäck M, Weber C, Lutgens E. Regulation of atherosclerotic plaque inflammation. J Intern Med. 2015;278:462–82.
5. Gerhardt T, Ley K. Monocyte trafficking across the vessel wall. Cardiovasc Res. 2015;107:321–30.
6. Ridker PM, Danielson E, Fonseca FA, Genest J, Gotto AM Jr, Kastelein JJ, Koenig W, Libby P, Lorenzatti AJ, MacFadyen JG, Nordestgaard BG, Shepherd J, Willerson JT, Glynn RJ. Rosuvastatin to prevent vascular events in men and women with elevated C-reactive protein. N Engl J Med. 2008;359:2195–207.
7. Boese AC, Kim SC, Yin K-J, Lee J-P, Hamblin MH. Sex differences in vascular physiology and pathophysiology: estrogen and androgen signaling in health and disease. Am J Physiol Heart Circ Physiol. 2017; https://doi.org/10.1152/ajpheart.00217.2016.
8. Arida A, Protogerou AD, Kitas GD, Sfikakis PP. Systemic inflammatory response and atherosclerosis: the paradigm of chronic inflammatory rheumatic diseases. Int J Mol Sci. 2018;19:1–27.
9. Kachur S, Morera R, De Schutter A, Lavie CJ. Cardiovascular risk in patients with prehypertension and the metabolic syndrome. Curr Hypertens Rep. 2018; https://doi.org/10.1007/s11906-018-0801-2.
10. Wierda RJ, Geutskens SB, Jukema JW, Quax PHA, van den Elsen PJ. Epigenetics in atherosclerosis and inflammation. J Cell Mol Med. 2010;14:1225–40.
11. Schunkert H, von Scheidt M, Kessler T, Stiller B, Zeng L, Vilne B. Genetics of coronary artery disease in the light of genome-wide association studies. Clin Res Cardiol. 2018;107:2–9.
12. Einarson TR, Acs A, Ludwig C, Panton UH. Prevalence of cardiovascular disease in type 2 diabetes: a systematic literature review of scientific evidence from across the world in 2007-2017. Cardiovasc Diabetol. 2018;17:1–19.

13. Mahmood SS, Levy D, Vasan RS, Wang TJ. The Framingham Heart Study and the epidemiology of cardiovascular disease: a historical perspective. Lancet. 2014;383:999–1008.
14. Navarese EP, Robinson JG, Kowalewski M, Kołodziejczak M, Andreotti F, Bliden K, Tantry U, Kubica J, Raggi P, Gurbel PA. Association between baseline LDL-C level and total and cardiovascular mortality after LDL-C lowering a systematic review and meta-analysis. JAMA. 2018;319:1566–79.
15. Sabatine MS, Giugliano RP, Keech AC, et al. Evolocumab and clinical outcomes in patients with cardiovascular disease. N Engl J Med. 2017;376:1713–22.
16. Ridker PM, Revkin J, Amarenco P, et al. Cardiovascular efficacy and safety of Bococizumab in high-risk patients. N Engl J Med. 2017;376:1527–39.
17. Bełtowski J. Liver X receptors (LXR) as therapeutic targets in dyslipidemia. Cardiovasc Ther. 2008;26:297–316.
18. Helkin A, Stein JJ, Lin S, Siddiqui S, Maier KG, Gahtan V. Dyslipidemia part 1 - review of lipid metabolism and vascular cell physiology. Vasc Endovasc Surg. 2016;50:107–18.
19. Bhatt DL, Steg PG, Miller M, et al. Cardiovascular risk reduction with icosapent ethyl for hypertriglyceridemia. N Engl J Med. 2019;308:11–22.
20. März W, Kleber ME, Scharnagl H, Speer T, Zewinger S, Ritsch A, Parhofer KG, von Eckardstein A, Landmesser U, Laufs U. HDL cholesterol: reappraisal of its clinical relevance. Clin Res Cardiol. 2017;106:663–75.
21. AIM-HIGH Investigators, Boden WE, Probstfield JL, Anderson T, Chaitman BR, Desvignes-Nickens P, Koprowicz K, McBride R, Teo K, Weintraub W. Niacin in patients with low HDL cholesterol levels receiving intensive statin therapy. N Engl J Med. 2011;365:2255–67.
22. Hanna RN, Shaked I, Hubbeling HG, et al. NR4A1 (Nur77) deletion polarizes macrophages toward an inflammatory phenotype and increases atherosclerosis. Circ Res. 2012;110:416–27.
23. Hamers AAJ, Vos M, Rassam F, Marincovic G, Kurakula K, Van Gorp PJ, De Winther MPJ, Gijbels MJJ, De Waard V, De Vries CJM. Bone marrow-specific deficiency of nuclear receptor Nur77 enhances atherosclerosis. Circ Res. 2012;110:428–38.
24. Libby P, Nahrendorf M, Swirski FK. Monocyte heterogeneity in cardiovascular disease. Semin Immunopathol. 2013;5:553–62.
25. Wong KL, Tai JJY, Wong WC, Han H, Sem X, Yeap WH, Kourilsky P, Wong SC. Gene expression profiling reveals the defining features of the classical, intermediate, and nonclassical human monocyte subsets. Blood. 2011; https://doi.org/10.1182/blood-2010-12-326355.
26. Cignarella A, Tedesco S, Cappellari R, Fadini GP. The continuum of monocyte phenotypes: experimental evidence and prognostic utility in assessing cardiovascular risk. J Leukoc Biol. 2018;103:1021–8.
27. Zawadaa AM, Rogaceva KS, Schirmer SH, Sester M, Böhm M, Flisera D, Heine GH. Monocyte heterogeneity in human cardiovascular disease. Immunobiology. 2012;217:1273–84.
28. Di Gregoli K, Johnson JL. Role of colony-stimulating factors in atherosclerosis. Curr Opin Lipidol. 2012;23:412–21.
29. Gordon S, Martinez FO. Alternative activation of macrophages: mechanism and functions. Immunity. 2010;32:593–604.
30. Colin S, Chinetti-gbaguidi G, Staels B. Macrophage phenotypes in atherosclerosis. Immunol Rev. 2014;262:153–66.
31. Duewell P, Kono H, Rayner KJ, et al. NLRP3 inflammasomes are required for atherogenesis and activated by cholesterol crystals. Nature. 2010;464:1357–61.
32. Ridker PM, Everett BM, Thuren T, et al. Antiinflammatory therapy with Canakinumab for atherosclerotic disease. N Engl J Med. 2017; https://doi.org/10.1056/NEJMoa1707914.
33. Maguire EM, Pearce SWA, Xiao Q. Foam cell formation: a new target for fighting atherosclerosis and cardiovascular disease. Vasc Pharmacol. 2018; https://doi.org/10.1016/j.vph.2018.08.002.
34. Drechsler M, Megens RTA, Van Zandvoort M, Weber C, Soehnlein O. Hyperlipidemia-triggered neutrophilia promotes early atherosclerosis. Circulation. 2010;122:1837–45.
35. Prame Kumar K, Nicholls AJ, Wong CHY. Partners in crime: neutrophils and monocytes/macrophages in inflammation and disease. Cell Tissue Res. 2018;371:551–65.

36. Myasoedova VA, Chistiakov DA, Grechko AV, Orekhov AN. Matrix metalloproteinases in pro-atherosclerotic arterial remodeling. J Mol Cell Cardiol. 2018;123:159–67.
37. Silvestre-Roig C, De Winther MP, Weber C, Daemen MJ, Lutgens E, Soehnlein O. Atherosclerotic plaque destabilization: mechanisms, models, and therapeutic strategies. Circ Res. 2014;114:214–26.
38. Mehta NN, Yu Y, Pinnelas R, Krishnamoorthy P, Shin DB, Troxel AB, Gelfand JM. Attributable risk estimate of severe psoriasis on major cardiovascular events. Am J Med. 2011;124:775.e1-6.
39. Liu C-L, Zhang J-Y, Shi G-P. Interaction between allergic asthma and atherosclerosis. Transl Res. 2016;174:5–22.
40. Jonasson L, Holm J, Skalli O, Bondjers G, Hansson GK. Regional accumulations of T cells, macrophages, and smooth muscle cells in the human atherosclerotic plaque. Arteriosclerosis. 1986;6:131–8.
41. Hermansson A, Johansson DK, Ketelhuth DFJ, Andersson J, Zhou X, Hansson GK. Immunotherapy with tolerogenic apolipoprotein B-100-loaded dendritic cells attenuates atherosclerosis in hypercholesterolemic mice. Circulation. 2011;123:1083–91.
42. Hedrick CC. Lymphocytes in atherosclerosis. Arterioscler Thromb Vasc Biol. 2015;35:253–7.
43. Legein B, Temmerman L, Biessen EAL, Lutgens E. Inflammation and immune system interactions in atherosclerosis. Cell Mol Life Sci. 2013;70:3847–69.
44. Hansson GK, Hermansson A. The immune system in atherosclerosis. Nat Immunol. 2011;12:204–12.
45. Bullenkamp J, Dinkla S, Kaski JC, Dumitriu IE. Targeting T cells to treat atherosclerosis: Odyssey from bench to bedside. Eur Hear J Cardiovasc Pharmacother. 2016;2:194–9.
46. Kyaw T, Peter K, Li Y, Tipping P, Toh BH, Bobik A. Cytotoxic lymphocytes and atherosclerosis: significance, mechanisms and therapeutic challenges. Br J Pharmacol. 2017;174:3956–72.
47. Sage AP, Tsiantoulas D, Binder CJ, Mallat Z. The role of B cells in atherosclerosis. Nat Rev Cardiol. 2018; https://doi.org/10.1038/s41569-018-0106-9.
48. Virmani R, Kolodgie FD, Burke AP, Farb A, Schwartz SM. Lessons from sudden coronary death: a comprehensive morphological classification scheme for atherosclerotic lesions. Arterioscler Thromb Vasc Biol. 2000;20:1262–75.
49. Stary HC, Chandler AB, Dinsmore RE, Fuster V, Glagov S, Insull W, Rosenfeld ME, Schwartz CJ, Wagner WD, Wissler RW. A definition of advanced types of atherosclerotic lesions and a histological classification of atherosclerosis. A report from the Committee on Vascular Lesions of the Council on Arteriosclerosis, American Heart Association. Circulation. 1995;92:1355–74.
50. Armstrong ML, Heistad DD, Megan MB, Lopez JA, Harrison DG. Reversibility of atherosclerosis. Cardiovasc Clin. 1990;20:113–26.
51. Strong JP, Malcom GT, McMahan CA, Tracy RE, Newman WP, Herderick EE, Cornhill JF. Prevalence and extent of atherosclerosis in adolescents and young adults: implications for prevention from the Pathobiological Determinants of Atherosclerosis in Youth Study. JAMA. 1999;281:727–35.
52. Kim DN, Schmee J, Lee KT, Thomas WA. Atherosclerotic lesions in the coronary arteries of hyperlipidemic swine. Part 1. Cell increases, divisions, losses and cells of origin in first 90 days on diet. Atherosclerosis. 1987;64:231–42.
53. Mauriello A, Sangiorgi GM, Virmani R, et al. A pathobiologic link between risk factors profile and morphological markers of carotid instability. Atherosclerosis. 2010;208:572–80.
54. Redgrave JN, Gallagher P, Lovett JK, Rothwell PM. Critical cap thickness and rupture in symptomatic carotid plaques: the oxford plaque study. Stroke. 2008;39:1722–9.
55. Burke AP, Farb A, Malcom GT, Liang YH, Smialek J, Virmani R. Coronary risk factors and plaque morphology in men with coronary disease who died suddenly. N Engl J Med. 1997;336:1276–82.
56. Stone GW, Maehara A, Lansky AJ, et al. A prospective natural-history study of coronary atherosclerosis. N Engl J Med. 2011;364:226–35.

57. Falk E, Nakano M, Bentzon JF, Finn AV, Virmani R. Update on acute coronary syndromes: the pathologists' view. Eur Heart J. 2013;34:719–28.
58. Paprottka KJ, Saam D, Rübenthaler J, Schindler A, Sommer NN, Paprottka PM, Clevert DA, Reiser M, Saam T, Helck A. Prevalence and distribution of calcified nodules in carotid arteries in correlation with clinical symptoms. Radiol Med. 2017;122:449–57.
59. Diethrich EB, Pauliina Margolis M, Reid DB, Burke A, Ramaiah V, Rodriguez-Lopez JA, Wheatley G, Olsen D, Virmani R. Virtual histology intravascular ultrasound assessment of carotid artery disease: the Carotid Artery Plaque Virtual Histology Evaluation (CAPITAL) study. J Endovasc Ther. 2007;14:676–86.
60. Pasterkamp G, Den Ruijter HM, Libby P. Temporal shifts in clinical presentation and underlying mechanisms of atherosclerotic disease. Nat Rev Cardiol. 2016;14:21–9.
61. Howard DPJ, Van Lammeren GW, Rothwell PM, Redgrave JN, Moll FL, De Vries JPPM, De Kleijn DPV, Den Ruijter HM, De Borst GJ, Pasterkamp G. Symptomatic carotid atherosclerotic disease: correlations between plaque composition and ipsilateral stroke risk. Stroke. 2015;46:182–9.
62. Kolodgie FD, Yahagi K, Mori H, Romero ME, Trout HH, Finn AV, Virmani R. High-risk carotid plaque: lessons learned from histopathology. Semin Vasc Surg. 2017;30:31–43.
63. Gupta A, Baradaran H, Schweitzer AD, Kamel H, Pandya A, Delgado D, Dunning A, Mushlin AI, Sanelli PC. Carotid plaque MRI and stroke risk: a systematic review and meta-analysis. Stroke. 2013;44:3071–7.
64. Yonetsu T, Jang I-K. Advances in intravascular imaging: new insights into the vulnerable plaque from imaging studies. Korean Circ J. 2018;48:1–15.
65. Ketelhuth DFJ, Bäck M. The role of matrix metalloproteinases in atherothrombosis. Curr Atheroscler Rep. 2011;13:162–9.
66. Bentzon JF, Otsuka F, Virmani R, Falk E. Mechanisms of plaque formation and rupture. Circ Res. 2014;114:1852–66.
67. Mittleman MA, Mostofsky E. Physical, psychological and chemical triggers of acute cardiovascular events: preventive strategies. Circulation. 2011;124:346–54.
68. Spagnoli LG, Mauriello A, Sangiorgi G, Fratoni S, Bonanno E, Schwartz RS, Piepgras DG, Pistolese R, Ippoliti A, Holmes DR. Extracranial thrombotically active carotid plaque as a risk factor for ischemic stroke. JAMA. 2004;292:1845–52.
69. Quillard T, Franck G, Mawson T, Folco E, Libby P. Mechanisms of erosion of atherosclerotic plaques. Curr Opin Lipidol. 2017;28:434–41.
70. Watase H, Sun J, Hippe DS, et al. Carotid artery remodeling is segment specific. Arterioscler Thromb Vasc Biol. 2018;38:927–34.
71. Clagett GP, Robinowitz M, Youkey JR, Fisher DF, Fry RE, Myers SI, Lee EL, Collins GJ, Virmani R. Morphogenesis and clinicopathologic characteristics of recurrent carotid disease. J Vasc Surg. 1986;3:10–23.
72. Verdecchia P, Reboldi G, Angeli F, Trimarco B, Mancia G, Pogue J, Gao P, Peter S, Teo K, Yusuf S. Systolic and diastolic blood pressure changes in relation with myocardial infarction and stroke in patients with coronary artery disease. Hypertension. 2015;65:108–14.
73. Morbiducci U, Kok AM, Kwak BR, Stone PH, Steinman DA, Wentzel JJ. Atherosclerosis at arterial bifurcations: evidence for the role of haemodynamics and geometry. Thromb Haemost. 2016;115:484–92.
74. Jashari F, Ibrahimi P, Nicoll R, Bajraktari G, Wester P, Henein MY. Coronary and carotid atherosclerosis: similarities and differences. Atherosclerosis. 2013;227:193–200.
75. Chamberlain AM, Agarwal SK, Folsom AR, Duval S, Soliman EZ, Ambrose M, Eberly LE, Alonso A. Smoking and incidence of atrial fibrillation: results from the Atherosclerosis Risk in Communities (ARIC) study. Heart Rhythm. 2011;8:1160–6.
76. Dzeshka MS, Shantsila A, Shantsila E, Lip GYH. Atrial fibrillation and hypertension. Hypertension. 2017;70:854–61.
77. O'Donnell MJ, Chin SL, Rangarajan S, et al. Global and regional effects of potentially modifiable risk factors associated with acute stroke in 32 countries (INTERSTROKE): a case-control study. Lancet. 2016;388:761–75.

78. Rothwell PM, Eliasziw M, Gutnikov SA, Warlow CP, Barnett HJM, Carotid Endarterectomy Trialists Collaboration. Endarterectomy for symptomatic carotid stenosis in relation to clinical subgroups and timing of surgery. Lancet. 2004;363:915–24.
79. Meschia JF, Klaas JP, Brown RD, Brott TG. Evaluation and management of atherosclerotic carotid stenosis. Mayo Clin Proc. 2017;92:1144–57.
80. Moroni F, Ammirati E, Magnoni M, D'Ascenzo F, Anselmino M, Anzalone N, Rocca MA, Falini A, Filippi M, Camici PG. Carotid atherosclerosis, silent ischemic brain damage and brain atrophy: a systematic review and meta-analysis. Int J Cardiol. 2016;223:681–7.
81. Wang T, Mei B, Zhang J. Atherosclerotic carotid stenosis and cognitive function. Clin Neurol Neurosurg. 2016;146:64–70.
82. Rothwell PM, Villagra R, Gibson R, Donders RCJM, Warlow CP. Evidence of a chronic systemic cause of instability of atherosclerotic plaques. Lancet. 2000;355:19–24.
83. Alberts MJ, Bhatt DL, Mas JL, et al. Three-year follow-up and event rates in the international REduction of Atherothrombosis for Continued Health Registry. Eur Heart J. 2009;30:2318–26.
84. Lorenz MW, Markus HS, Bots ML, Rosvall M, Sitzer M. Prediction of clinical cardiovascular events with carotid intima-media thickness: a systematic review and meta-analysis. Circulation. 2007;115:459–67.
85. Yoo J, Yang JH, Choi BW, et al. The frequency and risk of preclinical coronary artery disease detected using multichannel cardiac computed tomography in patients with ischemic stroke. Cerebrovasc Dis. 2012;33:286–94.
86. Hamada S, Kashiwazaki D, Yamamoto S, Akioka N, Kuwayama N, Kuroda S. Impact of plaque composition on risk of coronary artery diseases in patients with carotid artery stenosis. J Stroke Cerebrovasc Dis. 2018;27:3599–604.
87. Chaturvedi S, Bruno A, Feasby T, Holloway R, Benavente O, Cohen SN. Carotid endarterectomy — an evidence-based review. Report of the Therapeutics and Technology Assessment AAN. 2005; https://doi.org/10.1212/01.wnl.0000176036.07558.82.
88. Marquardt L, Geraghty OC, Mehta Z, Rothwell PM. Low risk of ipsilateral stroke in patients with asymptomatic carotid stenosis on best medical treatment: a prospective, population-based study. Stroke. 2010;41:11–7.
89. el-Barghouti N, Elkeles R, Nicolaides A, Geroulakos G, Dhanjil S, Diamond J. The ultrasonic evaluation of the carotid intima-media thickness and its relation to risk factors of atherosclerosis in normal and diabetic population. Int Angiol. 1997;16:50–4.
90. Wang X, Dalmeijer GW, den Ruijter HM, et al. Clustering of cardiovascular risk factors and carotid intima-media thickness: the USE-IMT study. PLoS One. 2017;12:e0173393.
91. Pletsch-Borba L, Selwaness M, van der Lugt A, Hofman A, Franco OH, Vernooij MW. Change in carotid plaque components: a 4-year follow-up study with serial MR imaging. JACC Cardiovasc Imaging. 2018;11:184–92.
92. Kannel WB, Wolf PA. Peripheral and cerebral atherothrombosis and cardiovascular events in different vascular territories: insights from the Framingham Study. Curr Atheroscler Rep. 2006;8:317–23.
93. Kannel WB. Hypertension: reflections on risks and prognostication. Med Clin North Am. 2009;93:541–58.
94. Feigin VL, Roth GA, Naghavi M, et al. Global burden of stroke and risk factors in 188 countries, during 1990–2013: a systematic analysis for the Global Burden of Disease Study 2013. Lancet Neurol. 2016;15:913–24.
95. Csordas A, Bernhard D. The biology behind the atherothrombotic effects of cigarette smoke. Nat Rev Cardiol. 2013;10:219–30.
96. Messner B, Bernhard D. Smoking and cardiovascular disease: mechanisms of endothelial dysfunction and early atherogenesis. Arterioscler Thromb Vasc Biol. 2014;34:509–15.
97. Boehme AK, Esenwa C, Elkind MSV. Stroke risk factors, genetics, and prevention. Circ Res. 2017;120:472–95.

98. Mandviwala T, Khalid U, Deswal A. Obesity and cardiovascular disease: a risk factor or a risk marker? Curr Atheroscler Rep. 2016; https://doi.org/10.1007/s11883-016-0575-4.
99. Yuan T, Yang T, Chen H, Fu D, Hu Y, Wang J, Yuan Q, Yu H, Xu W, Xie X. New insights into oxidative stress and inflammation during diabetes mellitus-accelerated atherosclerosis. Redox Biol. 2019;20:247–60.
100. Chen R, Ovbiagele B, Feng W, Carolina S, Carolina S. Diabetes and stroke: epidemiology, pathophysiology, pharmaceuticals and outcome. Am J Med Sci. 2017;351:380–6.
101. Paneni F, Lüscher TF. Cardiovascular protection in the treatment of Type 2 diabetes: a review of clinical trial results across drug classes. Am J Cardiol. 2017;120:S17–27.
102. Emerging Risk Factors Collaboration, Kaptoge S, Di Angelantonio E, Lowe G, Pepys MB, Thompson SG, Collins R, Danesh J. C-reactive protein concentration and risk of coronary heart disease, stroke, and mortality: an individual participant meta-analysis. Lancet. 2010;375:132–40.
103. Lombardo A, Biasucci LM, Lanza GA, Coli S, Silvestri P, Cianflone D, Liuzzo G, Burzotta F, Crea F, Maseri A. Inflammation as a possible link between coronary and carotid plaque instability. Circulation. 2004;109:3158–63.
104. Heart Protection Study Collaborative Group, Emberson J, Bennett D, Link E, Parish S, Danesh J, Armitage J, Collins R. C-reactive protein concentration and the vascular benefits of statin therapy: an analysis of 20,536 patients in the Heart Protection Study. Lancet. 2011;377:469–76.

Chapter 5
Current Imaging Approaches and Challenges in the Assessment of Carotid Artery Disease

Krishnan Ravindran, Waleed Brinijiki, J. Kevin DeMarco, and John Huston III

MR Angiography in Vessel Wall Imaging of the Internal Carotid Artery

Introduction

MRI has historically been the most well-established imaging modality for carotid plaque characterization due to its high signal-to-noise ratio and its establishment as the gold standard for carotid plaque imaging when compared to histological gold standards. Both intraplaque hemorrhage and lipid-rich necrotic core can be detected with high sensitivity and specificity on MRI and, importantly, good inter-observer agreement. Its noninvasive nature, lack of radiation exposure, and high soft tissue contrast enable detailed visualization of plaque morphology. There are a wide variety of pulse sequences available for plaque characterization with MRI. Fast spin echo (FSE) is the most commonly used technique as it allows for T1-, T2-, and proton density (PD)-weighted imaging. Gradient echo imaging with or without inversion recovery preparatory pulses is another technique for rapid imaging acquisition which has high reliability to detect plaque hemorrhage and lipid-rich necrotic core on T1-weighted images. This method uses FSE sequences with double inversion recovery preparatory pulses, thus resulting in a high amount of contrast between the dark vessel lumen and the vessel wall.

K. Ravindran · W. Brinijiki (✉) · J. Huston III
Department of Radiology, Mayo Clinic, Rochester, MN, USA
e-mail: Brinjikji.Waleed@mayo.edu; jhuston@mayo.edu

J. K. DeMarco (✉)
Department of Radiology, Walter Reed National Military Medical Center, Bethesda, MD, USA

Department of Radiology, Uniformed Services University of the Health Sciences, Bethesda, MD, USA

C. Yuan et al. (eds.), *Vessel Based Imaging Techniques*,
https://doi.org/10.1007/978-3-030-25249-6_5

Fat suppression is absolutely essential for characterization of plaque morphology. This method is needed to suppress signal of subcutaneous fat resulting in a high degree of contrast between plaque components, the carotid wall and surrounding tissues. Administration of gadolinium-based contrast aids delineation of plaque morphology and differentiation of core from fibrous cap on T1 sequences [1]. Contrast enhancement is believed to be associated with plaque inflammation and neovascularization [2]. Neovascularity is seen in nearly 100% of contrast-enhancing areas and the histological presence of macrophage infiltration in nearly 90% of post-contrast-enhancing regions [3]. MRI findings correlate strongly with histopathological findings of plaque morphology and have high specificity/sensitivity and inter-observer agreement [4]. Antibody-coated superparamagnetic iron oxide particles have also been used as an alternative potential contrast agent and shown to reflect histological plaque inflammation and endothelial activation [5].

Intraplaque Hemorrhage

MRI is excellent at detecting intraplaque hemorrhage [6, 7]. Intraplaque hemorrhage is often located diffusely in the plaque and colocalizes with lipid-rich necrotic core. Intraplaque hemorrhage is optimally evaluated on T1-weighted and fat-/flow-suppressed sequences as hemoglobin products induce T1 shortening [8, 9]. Black-blood sequences using T1-weighted imaging with fat saturation or MPRAGE-type sequences demonstrate plaque hemorrhage as T1 hyperintense with signal intensities at least 50% higher than the adjacent sternocleidomastoid muscle. These sequences suppress flow artifact near the carotid bifurcation, though increasing the time for examination. Plaque hemorrhage can easily be identified using both surface coil imaging techniques and large field-of-view MPRAGE imaging using standard head and neck coils. The sensitivity of specificity of plaque hemorrhage identification using surface coils is about 98% compared to histological gold standard, while the sensitivity of plaque hemorrhage identification of surface coils compared to MPRAGE imaging is well over 90%. Figure 5.1 shows an example of intraplaque hemorrhage.

Plaque hemorrhage signal intensities can change over time. Fresh plaque hemorrhage is hyperintense on T1-weighted images and hypointense/isointense on T2-weighted images and PD-weighted images. Both hemorrhage and lipid-rich core may exhibit high T1 signal. These can be distinguished on T1-weighted time-of-flight (TOF) sequences, with hemorrhage typically appearing hyperintensing on both T1 and TOF. Proton density-weighted sequences are also used, though plaque hemorrhage appearance on this sequence is more variable. In a study of 26 patients undergoing TOF and T1- and T2-weighted imaging prior to endarterectomy, MRI was able to differentiate intraplaque hemorrhage from juxtaluminal hemorrhage with near 100% accuracy [10]. Recent plaque hemorrhage is hyperintense on all contrast weightings. In a study of 42 plaques with recent intraplaque hemorrhage, Yim and colleagues demonstrated the presence of a peripheral rim of high signal intensity (“halo sign”) around the carotid on maximum intensity project images of

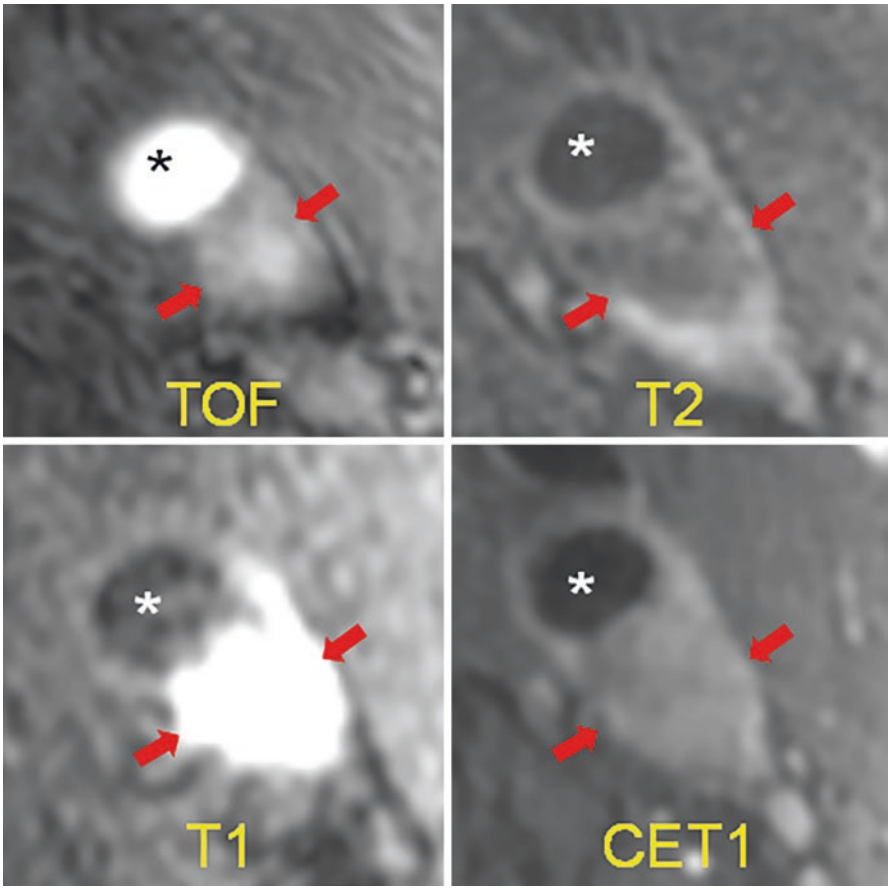

Fig. 5.1 Example of intraplaque hemorrhage on surface coil MRI at 3T. Time of flight (TOF) shows a widely patent lumen (∗) with a large plaque associated with positive remodeling, which is T1 hyperintense (arrows). On T2, the lumen (∗) is widely patent, and there is T2 hypointensity within the plaque. On MPRAGE, we see the patent lumen (∗) with marked T1 hyperintensity in the carotid plaque consistent with hemorrhage. On the contrast-enhanced T1 weighted image (CET1), the plaque is again seen with minimal internal enhancement but robust enhancement of the adventitia. (*J* jugular vein)

TOF MRI [11]. The negative predictive value of this halo sign on TOF MR angiography was 95%. The T1 hyperintensity of plaque hemorrhage can last for months to years following the initial event. However, older plaque hemorrhage has been reported to appear hypointense on all contrast weightings [12].

In asymptomatic individuals with 50–70% carotid stenosis, the presence of intraplaque hemorrhage on MRI was associated with a markedly increased risk of cerebrovascular events [13] (hazard ratio 3.59, 95% confidence interval 2.48–4.71, $p < 0.001$). In a further meta-analysis of 689 patients undergoing carotid MRI, the event rate for cerebrovascular events was 17.8% per year, compared to 2.4% in patients without MRI-visible intraplaque hemorrhage [14].

Lipid-Rich Necrotic Core

Lipid-rich necrotic core is best identified on MRI black-blood vessel wall imaging. Lipid-rich necrotic core is identified using a combination of T1 fat-saturated black-blood imaging with and without contrast. Lipid-rich necrotic core consists of a hypointense plaque on T1 fat-saturated imaging with an associated internal hypointense/non-enhancing region. Unlike plaque hemorrhage, necrotic core typically appears hyperintense on T1-weighted sequences but isointense on TOF images. The lack of internal enhancement indicates necrotic lipid which is not vascularized. The sensitivity and specificity of surface coil imaging at 3T in identification of LRNC are also over 95% when compared to histological controls. When compared to a surface coil exam, imaging of carotid plaques with standard head and neck coils has a sensitivity and specificity of about 85–90% for identification of lipid-rich necrotic core. Unlike ultrasound, MRI is able to distinguish lipid-rich core from hemorrhage and calcification with high sensitivity and specificity. Single-sequence T1-weighted turbo field echo (TFE) MRI has been shown to be as good, if not superior, to multi-sequence MRI in quantifying lipid-rich necrotic core with inter-reader reproducibility above 0.90 [15]. Contrast-enhanced MRI importantly allows discrimination of fibrous cap from necrotic core; given the avascular nature of the core, it displays minimal contrast enhancement, while the surrounding fibrous tissue has been shown to display strong enhancement [16]. In this study, the authors further identified a subset of lesions that hyper-enhanced with contrast administration, which was histologically corroborated with the presence of plaque neovascularization. Use of high-resolution contrast-enhanced MRI furthermore enables in vivo quantification of fibrous cap length and area [17]. T2-weighted sequences have been suggested to overestimate lipid core volume [18]. Moreover, the presence of hemorrhage within the lipid-rich necrotic core may result in T2 hyperintensity and make delineation of fibrous cup and necrotic core difficult. On high-resolution contrast-enhanced MRI, hemorrhage showed minimal enhancement making lipid-rich necrotic core delineation easier. Figure 5.2 shows an example of lipid-rich necrotic core.

MRI Plaque Features and Prognosis

Plaque enhancement with gadolinium visualized using 3T MRI is strongly associated with plaque vulnerability and cerebrovascular ischemic events, independent of wall thickness and degree of stenosis [19]. Indeed, MRI biomarkers of carotid plaque show stronger association with the presence of clinical symptoms than degree of luminal stenosis [1]. In a meta-analysis of nine studies (779 patients) assessing plaque characteristics and clinical prognosis, incidence of future transient ischemic attack or stroke was more than three times higher with the presence of either intraplaque hemorrhage or lipid-rich necrotic core [20]. Taken together, these results suggest characterization of plaque morphology and composition using MRI

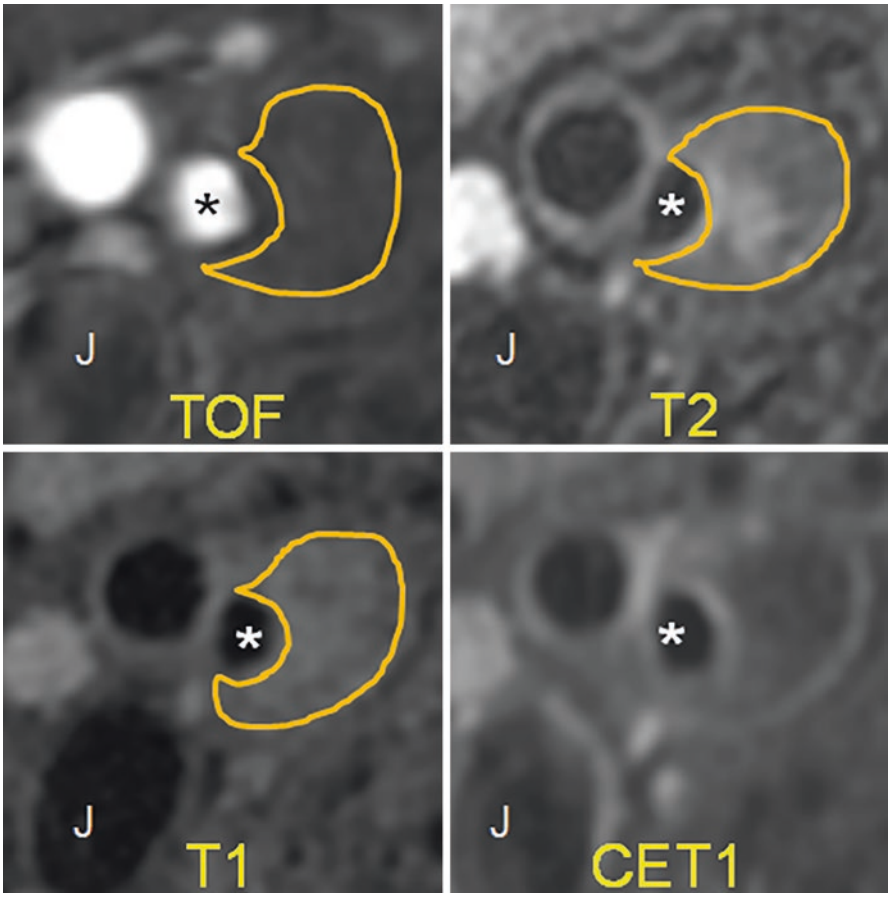

Fig. 5.2 Example of lipid-rich necrotic core. TOF shows a patent carotid artery lumen (∗). There is a large plaque with positive remodeling, which does not have any internal hyperintensity. On T2, there is some internal hyperintensity, but for the most part, the plaque is hypointense. On the T1 fat-saturated image, we see internal hypointensity. On the contrast-enhanced T1 image (CET1), there is peripheral enhancement of the plaque and no internal enhancement. This is characteristic of lipid-rich necrotic core

techniques may indeed provide greater information for risk stratification than quantitative stenosis measurement.

MRI Summary

MRI is highly specific and sensitive for plaque morphology, and features of plaque vulnerability on MRI correlate well with risk of future cerebrovascular events across several studies. Literature assessing the role of multiple contrast-weighted MRI in

evaluating carotid plaque has substantially increased. Expense and availability remain limiters in certain populations. Importantly, MRI findings also corroborate very strongly with histological findings, suggesting MRI with multiple contrast weightings may be an important tool for selecting candidate patients for intervention. Notably, plaque morphology findings may not be fully concordant with MR angiographic stenosis, particularly in predicting risk of future transient ischemic attacks or stroke.

CT Angiography in Vessel Wall Imaging of the Carotid Artery

Introduction

Multi-detector row CT angiography (CTA) is an easy and rapid imaging modality to detect extracranial carotid stenosis. The role of CTA to evaluate carotid vessel wall abnormality is less clear. Compared with the robust, extensive literature describing the MR imaging characteristics of vulnerable carotid plaque features, there is less literature and less consensus on the vulnerable plaque detection using CTA. Carotid CT vessel wall imaging (VWI) to detect various components in the soft plaque has been limited by overlapping Hounsfield units (HU) and blurring/blooming effect of extensive plaque calcifications (CA). Nevertheless, exciting new research indicates that vulnerable plaque features can be detected using CTA. We will review the CTA appearance of lipid-rich necrotic core (LRNC) which is associated with the American Heart Association lesion type IV/V (AHA-LT4/5). Next, we look at multiple different techniques that have been proposed to detect intraplaque hemorrhage (IPH) seen in American Heart Association lesion type VI (AHA-LT6) plaques. Lastly, we will look at research evaluating the ability of CTA to measure fibrous cap and/or identify fissured fibrous cap.

Lipid-Rich Necrotic Core

Carotid CTA can differentiate between soft tissue and calcified plaque. The use of simple Hounsfield units (HU) to detect LRNC on carotid CTA has led to inconsistent results. Some of the initial poor correlation of CTA-detected LRNC and histology was probably related to partial volume artifacts due to the use of single-slice CTA with thick axial images. Even with the use of more modern multi-detector CT (MDCT) scanners with thinner axial slices, partial volume effects still limit the detection of smaller LRNC regions. Also, extensive carotid plaque CA can lead to blurring/blooming which limits detection of adjacent soft tissue plaque including LRNC. Recent post-processing algorithms can mitigate both the blurring and partial volume effects to more accurately detect and quantify carotid plaque LRNC.

Initial studies comparing the detection of LRNC on CTA with histological evaluation of carotid endarterectomy specimens (CEA) utilized a single-slice spiral CT

scanner with axial images reconstructed every 1.5 mm. In a review of 55 patients undergoing CEA who underwent single-slice spiral CTA preoperatively, there was a statistically significant decrease in HU density measurements with increasing plaque lipid but with high standard deviation of these values [21]. The authors concluded that analysis of plaque attenuation does not give useful information concerning plaque composition.

In a subsequent study in 15 symptomatic patients with severe carotid stenosis who underwent a carotid CTA just prior to CEA using a 16-slice MDCT scanner with axial images reconstructed at 0.6 mm intervals, the measured attenuation value of LRNC was 25 HU ± 19 HU with a cutoff of 60 HU to differentiate between LRNC and fibrous tissue [22]. However, the regression plots showed good correlation of LRNC size measured on CTA compared with CEA specimen histology ($R^2 = 0.77$) only in mildly calcified carotid plaques (0–10%). The authors hypothesized that the lack of correlation between LRNC HU measurements in more densely CA plaque and histology could be explained by the blooming effect of CA on CTA.

Wintermark et al. described their comparison of eight patients with recent TIA who underwent preoperative 16-section MDCT carotid angiography with postoperative microCT and histological evaluation of the CEA specimen [23]. Despite using more modern preoperative CT scanners with 0.5 mm thick reconstructed axial images on their in vivo carotid CTA, there was a significant overlap in HU measurements between fibrous tissue and LRNC. The authors did note that if they restricted the analysis to large LRNC (>5 pixels in diameter), there was a greater concordance between CTA and histology ($\kappa = 0.796$, $P < 0.001$).

In a more recent study of 51 patients with suspected ischemic stroke or transient ischemic attack (TIA) who underwent MDCT carotid angiography and multicontrast carotid plaque MRI within 14 days of the event, a significantly lower HU was detected in plaque containing LRNC or plaque with IPH contained in the LRNC region compared to fibrous plaque [24].

Very recently a new post-processing algorithm using lumen boundary to detect and mitigate blurring and partial volume effects and fit a patient-specific point spread function to the original CTA data has been developed to more accurately measure LRNC and CA [25]. When comparing the preoperative carotid CTA using multiple modern MDCT scanners in 31 consecutive patients scheduled for CEA with postoperative specimen histology, there were a high correlation and low bias between the in vivo software analysis and ex vivo histopathological quantitative measurements of LRNC as well as low reader variability even in the presence of extensive plaque CA (Fig. 5.3).

In summary, there were initial conflicting results when comparing the detection and quantification of LRNC using simple HU measurements on carotid CTA compared with histological evaluation of carotid CEA specimens. As the research and technology have evolved, it now appears that the combination of modern MDCT scanners and a recent post-processing algorithm to mitigate blurring and partial volume effects is now possible to measure carotid plaque LRNC with high correlation and low bias compared with histology.

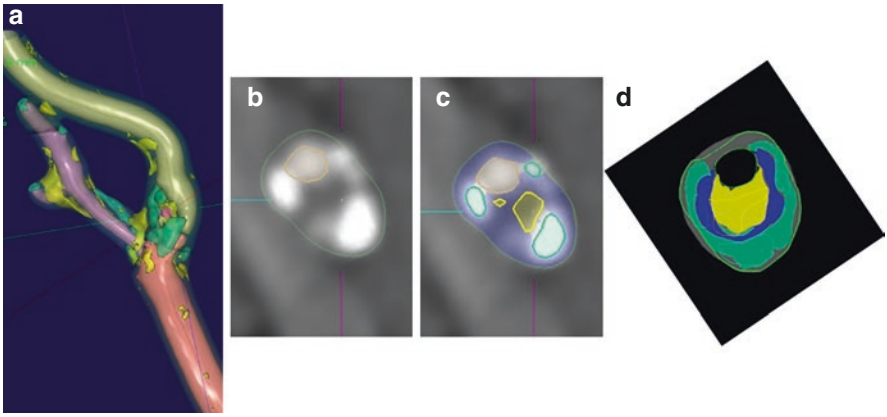

Fig. 5.3 Example of severe stenosis internal carotid artery. (**a**) Three-dimensional segmentation of lumen, vessel wall, and plaque components performed. (**b**) Magnified raw CT angiographic oblique axial image at the level of maximum stenosis shown as green line in part **a**. (**c**) Same level with the segmentation results superimposed (residual lumen outlined by dashed line, yellow outline = LRNC, green outline = calcifications). (**d**) Overlay of regions derived from CT angiography and histologic examination. Histologic sections are shown in solid colors, and results of software analysis are shown in outline. (Yellow = LRNC, green = calcification, blue = fibrosis post-processing using vascuCAP, Elucid Bioimaging Inc., Wenham, MA. ClinicalTrials.gov Identifier: NCT02143102. Images courtesy of Andrew Buckler and Samantha St. Pierre)

Intraplaque Hemorrhage

The literature suggests that accurate detection and quantification of IPH with carotid CTA is even more difficult than LRNC quantification. We will review the research to detect IPH with direct HU measurements as well as indirect detection using general plaque morphology to imply the presence of IPH.

Adjuk et al. analyzed the HU measurements of carotid plaque in the preoperative carotid CTA obtained with a 16-row MDCT scanner in 2 studies of 31 and 50 patients with CEA specimen correlation. They obtained three measurements using a 2 mm diameter region of interest on the 0.7 mm thick axial image in the visually lowest attenuated portion of the plaque and record the lowest of the 3 measurements for comparison with histology. Some of these low attenuation regions were adjacent to CA. Using 33.8 HU as the IPH cutoff value, CTA had 100% sensitivity and 64.7–70.4% specificity to detect IPH.

In a comparison of 167 patients with suspected carotid stenosis who underwent a 4-row or 64-row MDCT carotid angiogram and 1.5T MRA with magnetization-prepared rapid acquisition gradient echo (MPRAGE) sequence using an 8-channel large field-of-view neurovascular coil obtained within 3 weeks, the mean HU for MRI+ IPH was higher (47 HU) compared with MRI- IPH (43 HU). However, significant overlap between distributions of plaque densities limited the value of mean plaque density for prediction of IPH [26].

In the previously described comparison of 8 patients with recent TIA who underwent preoperative 16-section MDCT carotid angiography with postoperative microCT and histological evaluation of the CEA specimen, the authors found the HU measurements of IPH to be higher than fibrous tissue with a cutoff value of 72 HU [23]. As with LRNC and fibrous tissue in the same study, the authors found significant overlap between the HU measurements of IPH and fibrous tissue which limits the value of HU to determine various plaque components. The authors did note that by restricting their analysis to large (>5 pixel) IPH, there was a greater concordance between CTA and histology ($\kappa = 0.712$, $P = 0.102$).

In a more recent publication of 91 patients undergoing preoperative carotid CTA using a 16-row MDCT scanner with 0.6 mm slice thickness, a low average value (18.4 HU) was found for IPH. Using a threshold of 25 HU, IPH presence was detected with a sensitivity of 93.2% and a specificity of 92.7% compared with histopathological evaluation of the CEA specimen [27].

There is an almost equal number of publications demonstrating that IPH has simple HU measurements lower than or higher than fibrous tissue using either histological validation or comparison with MPRAGE. There is no clear way to reconcile these discrepant findings. IPH detection on MDCT carotid angiography using the newly developed post-processing algorithm to mitigate blurring and partial volume effects is an area of current research.

Given the discrepancies in using simple HU to detect IPH, other authors have exploited indirect findings on carotid CTA to detect IPH and/or AHA-LT6 plaques which in part can contain IPH. To date, CTA is not able to reliably identify complicated AHA-TL6 plaques, which are characterized by fibrous cap rupture, attached thrombus, or plaque hemorrhage. Multi-contrast MRI using dedicated carotid plaque surface coils has been shown to accurately identify AHA-LT6 plaques which are closely associated with an increased clinical risk of stroke.

Trelles et al. reported a study of 51 patients with suspected stroke/TIA who underwent multi-contrast carotid MRI with dedicated surface coils and MDCT carotid angiography within 14 days of the event/hospitalization [24]. The maximum soft plaque component thickness proved the best discriminating factor to predict AHA-LT6 by MR imaging, with a receiver operating characteristic area under the curve of 0.89. The optimal sensitivity and specificity for detection of AHA-LT6 by MR imaging was achieved with a soft plaque component thickness threshold of 4.4 mm (sensitivity, 0.65; specificity, 0.94; positive predictive value, 0.75; and negative predictive value, 0.9).

Eisenmenger et al. took a different approach to find an indirect sign of IPH [28]. Because adventitial inflammation is highly associated with IPH and chronic inflammation is associated with calcification, they undertook a retrospective study of 96 patients who underwent a multi-contrast carotid MRI with dedicated surface coils and MDCT carotid angiography within 1 month of each other to determine whether adventitial calcification with internal soft plaque (rim sign) could aid in carotid IPH prediction. A positive rim sign was defined as adventitial calcification (<2-mm thick) with internal soft plaque (≥2-mm thickness). Their final model included the rim sign (prevalence ratio = 11.9, $P < .001$) and

maximum soft plaque thickness (prevalence ratio = 1.2, $P = .06$). This model had excellent intraplaque hemorrhage prediction (area under the curve = 0.94), outperforming the rim sign alone, maximum soft plaque thickness, NASCET stenosis, and ulceration (area under the curve = 0.88, 0.86, 0.77, and 0.63, respectively; $P < .001$).

In summary, there are conflicting results using simple HU to detect IPH. The potential to use the recently described post-processing algorithm to mitigate blurring and reduce partial volume effects to improve IPH detection/quantification is an active area of research. Currently, the best recommendation is to use indirect findings such as the rim sign and maximum thickness of soft tissue plaque to suggest the presence of IPH and/or AHA-LT6 plaque.

Fissured Fibrous Cap

Wintermark et al. developed an automated carotid plaque classification algorithm to identify LRNC and IPH which showed good correlation with histology only when larger LRNC and IPH were considered. They also reported the linear regression between CTA and histology examination was excellent for mean minimal and mean maximal fibrous cap thickness [23]. This technique has not been validated in a separate set of patients. Saba et al. evaluated diffuse plaque enhancement when manually comparing pre-contrast and post-contrast carotid CTA to predict the presence of a fissured fibrous cap [27]. They demonstrated that both plaque neovascularization and fissured fibrous cap were associated with plaque enhancement. Histologic analysis showed that the presence of fissured fibrous cap is associated with a larger contrast plaque enhancement compared with the contrast plaque enhancement of plaques without fissured fibrous cap. The authors noted the increased radiation dose required to calculate the contrast enhancement and hypothesized that future radiation reduction techniques could help make the approach more suitable for clinical use.

CTA Summary

General wisdom says that CT is best to evaluate high-contrast structures (bone, lung, etc.) and MR is best to detect low-contrast soft tissue abnormalities. The extensive literature detailing MR techniques to identify carotid plaque characteristics and the prognostic significance of MR plaque features as well as using MR plaque findings to monitor medical therapy effectiveness supports this general wisdom. Recent research now indicates that CTA can also be used to detect LRNC with high correlation and low bias compared with histology. Even without the use of this new post-processing algorithm, there appears to be value in reviewing the source

axial CTA images to measure the thickness of soft tissue plaque and describe low attenuation regions within the soft tissue plaque to suggest the presence of vulnerable plaque including LRNC. The role of CTA to detect IPH and fibrous cap abnormalities is less clear. Given the ubiquitous use of CTA to evaluate carotid disease, there may be value to include LRNC detection in the routine workup of patients with suspected carotid stenosis. Put another way, do not just report carotid stenosis on CTA neck exams. Despite the new research, there are no randomized controlled trials or even natural history cohort studies to clarify the role of CTA-detected LRNC to predict future ipsilateral stroke/TIA. The role of carotid CTA to evaluate the change in LRNC volume with changes in medical therapy has not been tested, and the impact of multiple CTA exams with its radiation dose needs to be taken into consideration.

Ultrasound Carotid Plaque Imaging

Introduction

Duplex ultrasound is the most widely available noninvasive imaging modality for assessment of carotid plaque. Carotid ultrasound allows for real-time assessment of both plaque morphological characteristics and blood flow. Increasing evidence supports characterization of plaque morphology using ultrasound in risk stratification of patients with both asymptomatic and symptomatic carotid disease, as highlighted in meta-analyses [29, 30]. Established techniques such as B-mode ultrasound as well as newer generation technologies such as contrast-enhanced ultrasound and three-dimensional ultrasound provide extensive information surrounding plaque morphology that may be used for prognostication and interventional consideration.

Techniques

Grayscale ultrasound morphological features of carotid plaques include echogenicity, surface characteristics, and the presence of plaque ulceration. Grayscale ultrasonography can be used to identify non-calcified hypoechoic plaque regions which have been shown to be an independent risk factor for stroke [31]. B-mode ultrasonography allows delineation of vessel wall and is used to assess plaque echogenicity with strong histopathologic correlation [1, 32]. Grayscale carotid plaque echogenicity has been originally stratified into four types by Gray-Weale and colleagues: purely hypoechoic (type I), hypoechoic with small hyperechoic areas (type II), hyperechoic with small hypoechoic areas (type III), and hyperechoic (type IV) [33]. Echolucency is strongly correlated with plaque vulnerability and stroke risk in patients with asymptomatic carotid stenosis; in a 2015 meta-analysis of seven

studies comprising 7557 patients, the relative risk of future ipsilateral stroke with echolucent plaque was 2.31, independent of stenosis degree (95% confidence interval 1.58–3.39, $p < 0.0001$) [29]. A meta-analysis of 23 studies comprising 6706 carotid plaques showed echolucency to occur nearly four times as frequently in symptomatic plaques compared to asymptomatic plaques [30]. In an attempt to standardize images and mitigate inter-observer variability, the median grayscale content of each plaque following normalization of pixel brightness using blood column and adventitia has been used by certain study authors [34]. Others have extended this concept by quantifying the specific pixel intensities of various plaque components on B-mode images, including fibrous tissue, blood, calcium, and lipid and then mapped these to normalized carotid plaque images, termed pixel distribution analysis [35]. This analysis demonstrates symptomatic plaques to have larger quantities of calcium, intraplaque hemorrhage, and lipid, compared to asymptomatic plaques.

B-mode carotid ultrasound is highly specific for identification of plaque surface ulceration though ultrasound-visible ulceration is not always a widespread feature of symptomatic plaques. Additionally, substantial variability exists in the incidence of plaque ulceration as detected on ultrasound [36]. Pulse and color Doppler ultrasound allow for quantification of several flow parameters including peak systolic velocity, end-diastolic velocity, and performance of spectral waveform analysis for assessment of luminal stenosis. While this technique is inexpensive and portable and provides direct information regarding flow, this modality is operator-dependent and is associated with inconsistent inter-observer agreement. Moreover, the correlation of duplex ultrasonography with angiographically determined stenosis is poor [37]. Doppler ultrasound assessment of plaque vulnerability has lower specificity and sensitivity compared to black-blood fat-suppressed MRI sequences; it has been suggested that ultrasound may not be sufficient to identify LRNC vs fibrous plaque for surgical decision-making [38, 39].

Contrast-enhanced ultrasound (CEUS) is a relatively novel technique that utilizes intravenous microbubble contrast agent to assess vessel lumen, intraplaque morphology, and, in particular, neovascularization. Microbubbles are produced from an inert gas and can be contained within a hydrophobic shell for stability [35]. Importantly, microbubble contrast is not nephrotoxic and is associated with minimal side effects. Ultrasound pulses are used to suppress tissue signal, thereby amplifying signal from contrast bubbles. Following injection, microbubbles move into the vasa vasorum and intraplaque microvessels. The vasa vasorum is identified by the presence of echogenic microbubbles in the adventitial layer, while intraplaque vessels are identified by movement of microbubbles from adventitia to plaque core. Thus, plaque and intima-media interface appear hypoechoic, while lumen and wall appear enhanced. Both expanded vasa vasorum and intraplaque neovascularization are associated with advanced lesions.

Plaque enhancement with microbubble contrast is markedly higher in symptomatic plaques and associated with increased cardiovascular events, though not always histologically corroborative with plaque morphology [40–42]. Uniquely, CEUS allows for visualization of plaque heterogeneity both spatially and temporally with-

out exposure to ionizing radiation (Johri et al. 2017). Intraplaque vessel size as determined by CEUS has also recently been significantly associated with carotid plaque histology (Amamoto Cerebovasc Dis 2018). Persisting plaque enhancement following contrast administration is suggested to reflect increased intraplaque inflammatory cells, which phagocytize microbubbles and adhere to adjacent endothelium, termed "late-phase enhancement" [43]. Though an informative technique, CEUS is similarly operator-dependent and contraindicated in several conditions, including acute heart failure, unstable angina, and right-to-left cardiac shunts [44].

Three-dimensional (3-D) ultrasound is another novel technique that has garnered interest in recent years. Though two-dimensional B-mode images are readily obtainable, the single slice provides limited information. Importantly, 3-D imaging mitigates the inherent operator dependence of two-dimensional ultrasonography. Segmented image acquisition is performed longitudinally along the plaque, bounded by vessel wall; these images are then stacked and collated to produce volume -rendered reconstructions. In small preliminary studies, 3-D ultrasound has shown excellent specificity for the evaluation of stenosis and for measurement of plaque volume [45, 46]. Volumetric quantification allows plaque components to be identified based on tissue volumes, including hemorrhage, lipid, and calcium. Plaque composition is furthermore readily characterized using 3-D protocols, and plaque volume changes as small as 5% are detectable [35, 47]. However, 3-D ultrasound is more time-consuming than traditional two-dimensional ultrasound. Inter- and intra-observer reliabilities are substantially lower than compared to conventional ultrasound.

Ultrasound elastography is another technique that has been used in other organs, namely, breast and thyroid, and has recently been applied to carotid plaque imaging. This modality takes advantage of radial and longitudinal displacement of the plaque in response to artery pulsation and enables plaque motion to be tracked using registration and visualized displacement vectors [35]. Elastography analysis enables determination of strain and translation in both axial and longitudinal axes. Carotid plaque elasticity has been corroborated with intraplaque neovascularization as seen on CEUS [48]. Furthermore, axial strain and translation have been reported to be higher in vulnerable, neovascularized plaques with corollary MRI [49, 50]. These results suggest a potential role for quantitative analysis of plaque morphology through measurement of displacement parameters.

Poor signal-to-noise and moderate spatial resolutions make intraplaque hemorrhage difficult to distinguish from lipid-rich necrotic core on ultrasound. On B-mode imaging, the necrotic core can appear hypoechoic in appearance, also known as a juxtaluminal black area. Histologically, this region correlates with a lipid core that is adjacent to the vessel lumen. A juxtaluminal black area of 8 mm^2 has been shown to be highly prevalent in symptomatic plaques and independently associated with neurological symptoms [51]. Furthermore, in the analysis of 1121 patients with asymptomatic carotid stenosis, the juxtaluminal black area was linearly associated with future stroke rate, with 0.4% risk in patients with area less than 4 mm^2 and 5% risk in patients with area greater than 10 mm [2, 52]. In this study, the juxtaluminal black area was defined as an area of pixels with grayscale value less than 25 without an evident echogenic cap (grayscale greater than 25).

Ultrasound Summary

Ultrasound has remained the workhorse imaging modality for carotid plaque imaging, though the technique is limited by operator dependence, non-optimal spatial and contrast resolution, and inter-observer variability. Unlike other modalities, however, ultrasonography is inexpensive, widely available and does not pose risk of radiation exposure or contrast nephrotoxicity. Importantly, Doppler ultrasound remains a key modality for real-time assessment of flow and carotid stenosis. Newer generation improvements to ultrasonography include administration of microbubble contrast and three-dimensional image acquisition. These techniques allow for improved assessment of plaque vulnerability via intraplaque neovascularization with markedly higher inter-observer reliability. The utility of carotid ultrasonography in selecting patients for carotid endarterectomy based on degree of stenosis and plaque characteristics, however, remains to be determined.

Disclaimer The views expressed in this chapter are those of the author and do not reflect the official policy of the Department of Army/Navy/Air Force, Department of Defense, or US Government.

The identification of specific products or scientific instrumentation does not constitute endorsement or implied endorsement on the part of the author, DoD, or any component agency.

References

1. Brinjikji W, Lehman VT, Huston J 3rd, et al. The association between carotid intraplaque hemorrhage and outcomes of carotid stenting: a systematic review and meta-analysis. J Neurointerv Surg. 2017;9(9):837–42.
2. Kerwin WS, O'Brien KD, Ferguson MS, Polissar N, Hatsukami TS, Yuan C. Inflammation in carotid atherosclerotic plaque: a dynamic contrast-enhanced MR imaging study. Radiology. 2006;241(2):459–68.
3. Millon A, Mathevet JL, Boussel L, et al. High-resolution magnetic resonance imaging of carotid atherosclerosis identifies vulnerable carotid plaques. J Vasc Surg. 2013;57(4):1046–1051.e1042.
4. den Hartog AG, Bovens SM, Koning W, et al. Current status of clinical magnetic resonance imaging for plaque characterisation in patients with carotid artery stenosis. Eur J Vasc Endovasc Surg. 2013;45(1):7–21.
5. Chan JM, Monaco C, Wylezinska-Arridge M, Tremoleda JL, Gibbs RG. Imaging of the vulnerable carotid plaque: biological targeting of inflammation in atherosclerosis using iron oxide particles and MRI. Eur J Vasc Endovasc Surg. 2014;47(5):462–9.
6. Chu B, Kampschulte A, Ferguson MS, et al. Hemorrhage in the atherosclerotic carotid plaque: a high-resolution MRI study. Stroke. 2004;35(5):1079–84.
7. Moody AR, Murphy RE, Morgan PS, et al. Characterization of complicated carotid plaque with magnetic resonance direct thrombus imaging in patients with cerebral ischemia. Circulation. 2003;107(24):3047–52.
8. Moody AR. Magnetic resonance direct thrombus imaging. J Thromb Haemost. 2003;1(7):1403–9.
9. Singh N, Moody AR, Roifman I, Bluemke DA, Zavodni AE. Advanced MRI for carotid plaque imaging. Int J Cardiovasc Imaging. 2016;32(1):83–9.

10. Kampschulte A, Ferguson MS, Kerwin WS, et al. Differentiation of intraplaque versus juxtaluminal hemorrhage/thrombus in advanced human carotid atherosclerotic lesions by in vivo magnetic resonance imaging. Circulation. 2004;110(20):3239–44.
11. Yim YJ, Choe YH, Ko Y, et al. High signal intensity halo around the carotid artery on maximum intensity projection images of time-of-flight MR angiography: a new sign for intraplaque hemorrhage. J Magn Reson Imaging. 2008;27(6):1341–6.
12. Chu B, Hatsukami TS, Polissar NL, et al. Determination of carotid artery atherosclerotic lesion type and distribution in hypercholesterolemic patients with moderate carotid stenosis using noninvasive magnetic resonance imaging. Stroke. 2004;35(11):2444–8.
13. Singh N, Moody AR, Gladstone DJ, et al. Moderate carotid artery stenosis: MR imaging-depicted intraplaque hemorrhage predicts risk of cerebrovascular ischemic events in asymptomatic men. Radiology. 2009;252(2):502–8.
14. Saam T, Hetterich H, Hoffmann V, et al. Meta-analysis and systematic review of the predictive value of carotid plaque hemorrhage on cerebrovascular events by magnetic resonance imaging. J Am Coll Cardiol. 2013;62(12):1081–91.
15. Cappendijk VC, Heeneman S, Kessels AG, et al. Comparison of single-sequence T1w TFE MRI with multisequence MRI for the quantification of lipid-rich necrotic core in atherosclerotic plaque. J Magn Reson Imaging. 2008;27(6):1347–55.
16. Yuan C, Kerwin WS, Ferguson MS, et al. Contrast-enhanced high resolution MRI for atherosclerotic carotid artery tissue characterization. J Magn Reson Imaging. 2002;15(1):62–7.
17. Cai J, Hatsukami TS, Ferguson MS, et al. In vivo quantitative measurement of intact fibrous cap and lipid-rich necrotic core size in atherosclerotic carotid plaque: comparison of high-resolution, contrast-enhanced magnetic resonance imaging and histology. Circulation. 2005;112(22):3437–44.
18. Serfaty JM, Chaabane L, Tabib A, Chevallier JM, Briguet A, Douek PC. Atherosclerotic plaques: classification and characterization with T2-weighted high-spatial-resolution MR imaging-- an in vitro study. Radiology. 2001;219(2):403–10.
19. Qiao Y, Etesami M, Astor BC, Zeiler SR, Trout HH, Wasserman BA. Carotid plaque neovascularization and hemorrhage detected by MR imaging are associated with recent cerebrovascular ischemic events. AJNR Am J Neuroradiol. 2012;33(4):755–60.
20. Gupta A, Baradaran H, Schweitzer AD, et al. Carotid plaque MRI and stroke risk: a systematic review and meta-analysis. Stroke. 2013;44(11):3071–7.
21. Walker LJ, Ismail A, McMeekin W, Lambert D, Mendelow AD, Birchall D. Computed tomography angiography for the evaluation of carotid atherosclerotic plaque: correlation with histopathology of endarterectomy specimens. Stroke. 2002;33(4):977–81.
22. de Weert TT, Ouhlous M, Meijering E, et al. In vivo characterization and quantification of atherosclerotic carotid plaque components with multidetector computed tomography and histopathological correlation. Arterioscler Thromb Vasc Biol. 2006;26(10):2366–72.
23. Wintermark M, Jawadi SS, Rapp JH, et al. High-resolution CT imaging of carotid artery atherosclerotic plaques. AJNR Am J Neuroradiol. 2008;29(5):875–82.
24. Trelles M, Eberhardt KM, Buchholz M, et al. CTA for screening of complicated atherosclerotic carotid plaque--American Heart Association type VI lesions as defined by MRI. AJNR Am J Neuroradiol. 2013;34(12):2331–7.
25. Sheahan M, Ma X, Paik D, et al. Atherosclerotic plaque tissue: noninvasive quantitative assessment of characteristics with software-aided measurements from conventional CT angiography. Radiology. 2018;286(2):622–31.
26. JM UK-I, Fox AJ, Aviv RI, et al. Characterization of carotid plaque hemorrhage: a CT angiography and MR intraplaque hemorrhage study. Stroke. 2010;41(8):1623–9.
27. Saba L, Francone M, Bassareo PP, et al. CT attenuation analysis of carotid intraplaque hemorrhage. AJNR Am J Neuroradiol. 2018;39(1):131–7.
28. Eisenmenger LB, Aldred BW, Kim SE, et al. Prediction of carotid intraplaque hemorrhage using adventitial calcification and plaque thickness on CTA. AJNR Am J Neuroradiol. 2016;37(8):1496–503.

29. Gupta A, Kesavabhotla K, Baradaran H, et al. Plaque echolucency and stroke risk in asymptomatic carotid stenosis: a systematic review and meta-analysis. Stroke. 2015;46(1):91–7.
30. Brinjikji W, Rabinstein AA, Lanzino G, et al. Ultrasound characteristics of symptomatic carotid plaques: a systematic review and meta-analysis. Cerebrovasc Dis. 2015;40(3–4):165–74.
31. Polak JF, Shemanski L, O'Leary DH, et al. Hypoechoic plaque at US of the carotid artery: an independent risk factor for incident stroke in adults aged 65 years or older. Cardiovascular Health Study. Radiology. 1998;208(3):649–54.
32. Reiter M, Horvat R, Puchner S, et al. Plaque imaging of the internal carotid artery - correlation of B-flow imaging with histopathology. AJNR Am J Neuroradiol. 2007;28(1):122–6.
33. Gray-Weale AC, Graham JC, Burnett JR, Byrne K, Lusby RJ. Carotid artery atheroma: comparison of preoperative B-mode ultrasound appearance with carotid endarterectomy specimen pathology. J Cardiovasc Surg. 1988;29(6):676–81.
34. el-Barghouty N, Nicolaides A, Bahal V, Geroulakos G, Androulakis A. The identification of the high risk carotid plaque. Eur J Vasc Endovasc Surg. 1996;11(4):470–8.
35. Cires-Drouet RS, Mozafarian M, Ali A, Sikdar S, Lal BK. Imaging of high-risk carotid plaques: ultrasound. Semin Vasc Surg. 2017;30(1):44–53.
36. Nakamura T, Tsutsumi Y, Shimizu Y, Uchiyama S. Ulcerated carotid plaques with ultrasonic echolucency are causatively associated with thromboembolic cerebrovascular events. J Stroke Cerebrovasc Dis. 2013;22(2):93–9.
37. Beach KW, Leotta DF, Zierler RE. Carotid Doppler velocity measurements and anatomic stenosis: correlation is futile. Vasc Endovasc Surg. 2012;46(6):466–74.
38. Arai D, Yamaguchi S, Murakami M, et al. Characteristics of carotid plaque findings on ultrasonography and black blood magnetic resonance imaging in comparison with pathological findings. Acta Neurochir Suppl. 2011;112:15–9.
39. Watanabe Y, Nagayama M, Suga T, et al. Characterization of atherosclerotic plaque of carotid arteries with histopathological correlation: vascular wall MR imaging vs. color Doppler ultrasonography (US). J Magn Reson Imaging. 2008;28(2):478–85.
40. Vavuranakis M, Sigala F, Vrachatis DA, et al. Quantitative analysis of carotid plaque vasa vasorum by CEUS and correlation with histology after endarterectomy. VASA Zeitschrift fur Gefasskrankheiten. 2013;42(3):184–95.
41. Xiong L, Deng YB, Zhu Y, Liu YN, Bi XJ. Correlation of carotid plaque neovascularization detected by using contrast-enhanced US with clinical symptoms. Radiology. 2009;251(2):583–9.
42. Staub D, Patel MB, Tibrewala A, et al. Vasa vasorum and plaque neovascularization on contrast-enhanced carotid ultrasound imaging correlates with cardiovascular disease and past cardiovascular events. Stroke. 2010;41(1):41–7.
43. Owen DR, Shalhoub J, Miller S, et al. Inflammation within carotid atherosclerotic plaque: assessment with late-phase contrast-enhanced US. Radiology. 2010;255(2):638–44.
44. Ten Kate GL, van den Oord SC, Sijbrands EJ, et al. Current status and future developments of contrast-enhanced ultrasound of carotid atherosclerosis. J Vasc Surg. 2013;57(2):539–46.
45. Landry A, Spence JD, Fenster A. Measurement of carotid plaque volume by 3-dimensional ultrasound. Stroke. 2004;35(4):864–9.
46. Bucek RA, Reiter M, Dirisamer A, et al. Three-dimensional color Doppler sonography in carotid artery stenosis. AJNR Am J Neuroradiol. 2003;24(7):1294–9.
47. Hossain MM, AlMuhanna K, Zhao L, Lal BK, Sikdar S. Semiautomatic segmentation of atherosclerotic carotid artery wall volume using 3D ultrasound imaging. Med Phys. 2015;42(4):2029–43.
48. Zhang Q, Li C, Zhou M, et al. Quantification of carotid plaque elasticity and intraplaque neovascularization using contrast-enhanced ultrasound and image registration-based elastography. Ultrasonics. 2015;62:253–62.

49. Huang C, Pan X, He Q, et al. Ultrasound-based carotid elastography for detection of vulnerable atherosclerotic plaques validated by magnetic resonance imaging. Ultrasound Med Biol. 2016;42(2):365–77.
50. Roy Cardinal MH, Heusinkveld MHG, Qin Z, et al. Carotid artery plaque vulnerability assessment using noninvasive ultrasound elastography: validation with MRI. AJR Am J Roentgenol. 2017;209(1):142–51.
51. Griffin MB, Kyriacou E, Pattichis C, et al. Juxtaluminal hypoechoic area in ultrasonic images of carotid plaques and hemispheric symptoms. J Vasc Surg. 2010;52(1):69–76.
52. Kakkos SK, Griffin MB, Nicolaides AN, et al. The size of juxtaluminal hypoechoic area in ultrasound images of asymptomatic carotid plaques predicts the occurrence of stroke. J Vasc Surg. 2013;57(3):609–618.e601; discussion 617-608.

Chapter 6
Advanced Carotid Vessel Wall Imaging and Future Directions

Jie Sun and Thomas S. Hatsukami

Introduction

Within the circulatory system, the extracranial carotid artery bifurcation is one of the most common sites for developing atherosclerotic plaques. In an imaging study of middle-aged males and females, carotid atherosclerosis was seen in 31% of the participants, which was more common than atherosclerosis in the aorta or coronary arteries and only behind iliofemoral atherosclerosis [1]. Most individuals with carotid atherosclerosis are not aware of its presence as the disease is often asymptomatic, even when there is already substantial luminal stenosis. However, prognostic evaluation of carotid plaque in high-risk individuals is clinically significant given its potential pathophysiological consequences, including intraluminal thrombosis, artery-to-artery thromboembolism, and in the late stage, severe luminal stenosis, all of which may lead to brain infarction and/or hypoperfusion. Because of the high prevalence of carotid atherosclerosis in the general population, carotid artery disease is a major source for neurological ischemic events, accountable for about 41,000 ischemic stroke incidences annually in the USA alone [2]. The burden of asymptomatic brain infarctions and/or hypoperfusion is often less recognized but expected to be >10-fold higher than that of ischemic strokes, which is increasingly recognized as a major contributor to cognitive impairment and dementia [3]. Furthermore, as a local manifestation of systemic atherosclerosis, carotid atherosclerosis is often evaluated for improving cardiovascular risk assessment and monitoring response to medical treatment, given that carotid lesions are less challenging

J. Sun
Department of Radiology, University of Washington, Seattle, WA, USA
e-mail: sunjie@uw.edu

T. S. Hatsukami (✉)
Department of Surgery, University of Washington, Seattle, WA, USA
e-mail: tomhat@uw.edu

C. Yuan et al. (eds.), *Vessel Based Imaging Techniques*,
https://doi.org/10.1007/978-3-030-25249-6_6

to image and characterize compared to atherosclerotic lesions in other deep-seated, small-caliber arteries.

In contrast to luminal imaging techniques that grade the severity of carotid atherosclerosis according to its impact on lumen diameter or area, vessel wall imaging with magnetic resonance imaging (MRI) allows for direct visualization of carotid plaque morphology and tissue composition, as well as pathological activities at the cellular level when contrast agents are used. MRI of carotid atherosclerosis has been rapidly evolving in the past two decades. Images with diagnostic image quality at 0.6–0.8 mm spatial resolution can now be achieved on all major platforms by modifying commercially available pulse sequences. This wave of technical development in the past two decades has been primarily driven by an unmet clinical need in the selection of patients with carotid disease for carotid revascularization. Since the early 1990s, several landmark clinical trials evaluated the efficacy of carotid endarterectomy (CEA) in a broad spectrum of patient populations. The North American Symptomatic Carotid Endarterectomy Trial (NASCET) compared CEA to medical treatment alone in patients with transient ischemic attack or nondisabling ischemic stroke within the previous 6 months. There was clear evidence of a net benefit in patients with high-grade stenosis (70–99%) but not in patients with moderate or mild stenosis [4]. The number needed to treat to prevent 1 ischemic stroke in 5 years was 6 and 15 in the groups with high and moderate stenosis, respectively. Nonetheless, the risk under medical therapy alone in patients with <70% stenosis was still considerable at about 20% over 5 years in the mild-to-moderate stenosis group. Compared to studies on symptomatic patients, clinical trials that evaluated the efficacy of CEA in asymptomatic patients documented a more moderate benefit using stenosis severity to guide patient selection [5]. These clinical trials highlighted the limitations of luminal stenosis-based carotid disease risk assessment. Two decades later, it has become more challenging to decide on the best treatment for individual patients based on luminal stenosis due to the changing landscape in clinical management of carotid artery disease, including improvements in optimal medical therapy, reduced perioperative complication rates of carotid revascularization, and new approaches to carotid artery stenting (CAS). Since carotid vessel wall imaging may allow for more precise risk estimation than luminal stenosis assessment by characterizing key pathophysiological processes, it has potential to revise existing guidelines on indications for carotid revascularization.

Evidence on the Capabilities of Carotid Vessel Wall Imaging

Early studies of CEA specimens have established the role of plaque rupture in the pathogenesis of ischemic strokes from carotid plaque. In a histopathological study of 269 carotid plaques obtained en bloc from surgical endarterectomy, Spagnoli et al. [6] found that thrombotically active plaque associated with high inflammatory infiltrate was observed in 74% of patients with stroke, 35% of patients with transient

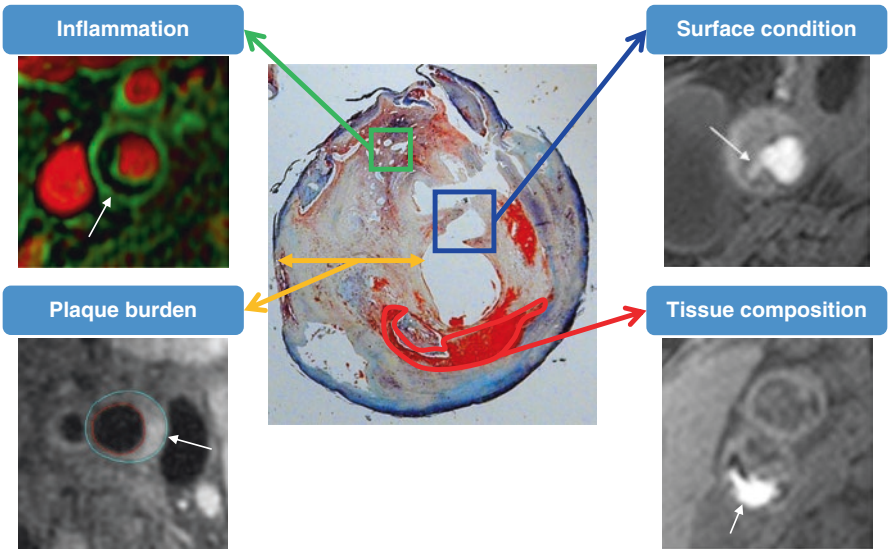

Fig. 6.1 Carotid plaque morphology: accessible information with MRI. Carotid plaques are heterogeneous at various levels. With different protocols, MRI allows us to noninvasively evaluate carotid plaque burden, tissue composition, surface condition, and inflammatory activities

ischemic attack, and 15% of asymptomatic patients. Intraluminal thrombi were associated with cap rupture in 90% of the cases and erosion in the remaining 10% of cases in the group with stroke [6]. The exact mechanisms of plaque rupture are still not fully understood. A variety of imaging modalities have been proposed for identification of specific carotid characteristics that were associated with risk of plaque rupture in histopathological studies [7], such as large necrotic core, thin fibrous cap, intraplaque hemorrhage, and inflammatory cell infiltration. Tissue echogenicity on ultrasound has been leveraged to identify carotid plaques with a large necrotic core [8]. Fluorodeoxyglucose positron emission tomography has been used to study carotid plaque inflammation [9]. Nonetheless, of the noninvasive vessel wall imaging techniques currently available, MRI holds the greatest promise for identification of high-risk carotid plaques because of its rich contrast mechanisms that allow assessment of plaque burden, tissue composition, luminal surface condition, and inflammatory activities (Fig. 6.1), which will be discussed in the following sections.

Plaque Burden

The carotid vessel wall expands at the origin of the internal carotid artery to form the carotid bulb, where atherosclerosis tends to build up due to the presence of low wall shear stress. During plaque development, there can also be various degrees of

expansive remodeling of the vessel wall [10]. As such, a significant amount of atherosclerosis could already exist before there is appreciable luminal stenosis. Large plaque burden is known to be associated with increased risk for plaque rupture [11]. As a marker of systemic atherosclerosis, carotid plaque burden was strongly associated with coronary calcium score and may improve the prediction of cardiovascular events beyond conventional risk factors [12, 13].

Accurate measurement of carotid plaque burden requires clear delineation of lumen and outer wall boundaries. High spatial resolution is necessary to minimize partial volume averaging [14]. Duivenvoorden et al. [15] compared different in-plane resolutions of carotid MRI varying from 0.65 mm to 0.20 mm at 3 mm slice thickness performed on the same subjects. Mean wall area measured on images with lower resolution was larger than those measured on images with higher resolution. When a phased-array surface coil is available, images are typically acquired with 2 mm slice thickness and 0.5–0.6 mm in-plane resolution in 2D carotid MRI and with 0.6–0.8 mm isotropic resolution in 3D carotid MRI [16–18], which have been shown to provide good signal-to-noise within clinically acceptable scan times. In addition to high spatial resolution, sufficient blood and fat suppression are also essential in achieving diagnostic image quality. Blood suppression in cardiovascular MR can be implemented using inflow saturation, double inversion recovery (DIR), or motion sensitization. As the flow pattern near the carotid artery bifurcation can be very complex, inflow saturation is rarely adequate. DIR is flow direction dependent and often used in 2D carotid MRI. However, flow artifacts may still arise from recirculating flow which has not outflowed from the imaging slice at the second inversion pulse. Motion-sensitized driven equilibrium (MSDE) preparation has been shown to provide more complete flow suppression compared to inflow saturation and DIR [19]. MSDE preparation allows flow direction-independent blood suppression in a large imaging slab and, thus, has been frequently used in 3D carotid MRI.

Mean/maximum wall area and mean/maximum wall thickness are common measurements of carotid plaque burden, which are usually obtained by segmenting lumen and total vessel area on cross-sectional images. Multiple studies have evaluated the precision and accuracy of these measurements by carotid MRI. Despite minor methodological differences, previous studies consistently showed excellent inter-observer and inter-scan reproducibility of carotid wall measurements [16, 20–22]. The coefficient of variation for repeated scans, an indicator of measurement errors, was <10% for most carotid wall measurements, which was smaller compared to similar measurements by B-mode ultrasound [15]. Of note, measurement precision is influenced by image quality and spatial resolution. At the same image quality, larger carotid plaques are expected to be associated with smaller measurement errors, which may have implications for planning pharmaceutical trials using imaging endpoints [23]. Furthermore, wall area measurements typically have smaller measurement errors than wall thickness measurements.

The accuracy of MRI measurements of carotid plaque burden has also been established. In patients who underwent CEA, Luo et al. [24] demonstrated a high agreement between in vivo MRI measurements of carotid plaque burden and cor-

responding ex vivo MRI measurements (Pearson's correlation coefficient >0.90). The correlations between minimum lumen area, maximum wall area, and wall volume were weak, suggesting that these measurements provide different information of carotid plaque burden.

Plaque Tissue Composition

Plaque tissue composition plays an essential role in the pathogenesis of atherothrombotic complications. Ruptured plaques frequently harbor large necrotic cores, intraplaque hemorrhages, and speckle calcifications [25]. As substantial heterogeneity in tissue composition exists among carotid plaques with the same level of luminal stenosis, it is expected that noninvasive imaging of carotid plaque composition would allow for improved prediction of clinical risk. Common plaque components, besides fibrous tissue, include extracellular lipids, necrotic tissue, calcification, and intraplaque hemorrhage. MRI is unique for imaging plaque composition in that it allows differentiation between all common plaque components. Indeed, its capability of accurately classifying all common plaque components has led to multiple studies demonstrating that carotid MRI is able to not only detect lipid core presence but also quantitatively measure lipid core area or percent area [26, 27]. Furthermore, MRI is currently considered the only imaging modality that is capable of detecting intraplaque hemorrhage, a characteristic feature of high-risk carotid plaque.

Early work by Toussaint et al. [28] showed that water but not lipids gave the predominant signal in lipid core and that the lipid core and collagenous cap could be differentiated based on T2 contrast. By using CEA specimens, Yuan et al. [29] showed that multi-contrast carotid MRI, which included T1, T2, proton density, and 3D time of flight (TOF), was able to detect lipid-rich necrotic core with and without intraplaque hemorrhage with high accuracy. Subsequent work by Yuan et al. [30] and Wasserman et al. [31] suggested that gadolinium contrast enhancement may further improve the discrimination between lipid core and fibrous tissue. Using histological analysis as the reference standard, Trivedi et al. [26], Cai et al. [27], and Saam et al. [32] evaluated the capability of multi-contrast MRI in quantifying the lipid-rich necrotic core in patients undergoing CEA. A high agreement was seen between multi-contrast MRI (either with or without gadolinium contrast) and histology in quantifying the lipid-rich necrotic core, measured as a percentage of total wall area. When available, combining pre- and post-contrast images is preferred to T2-weighted images for quantifying lipid-rich necrotic core as gadolinium contrast-enhanced images not only afford a higher agreement with histological analysis but also improve the intra- and inter-observer reproducibility [27, 33]. With reference to pre-contrast images, the lipid core is measured as nonenhanced or little enhanced areas on post-contrast images. When gadolinium contrast-enhanced images are not available, T2-weighted images should be used for measuring lipid core complemented by information from other contrast weightings such as the presence of intra-

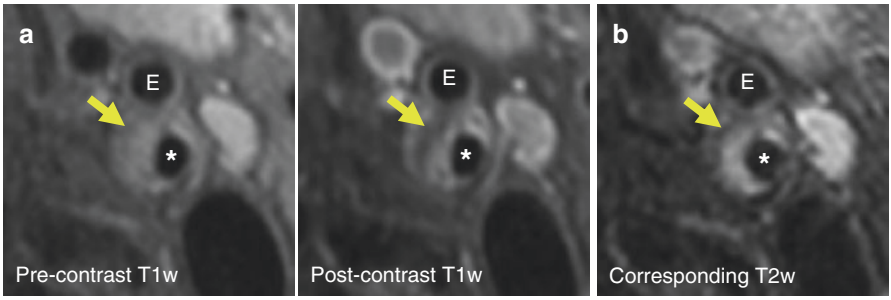

Fig. 6.2 Lipid-rich necrotic core detection by combining pre- and post-contrast images. (**a**) Because of presence of neovasculature and expanded extravascular space, fibrous tissue in carotid plaque enhances after gadolinium contrast injection. The lipid-rich necrotic core (arrow) is detected as areas with no or little enhancement on post-contrast T1w-TSE images when compared with pre-contrast T1w-TSE. (**b**) Cholesterols and cholesterol esters constitute the main lipid content of carotid plaque, which shorten T2 of water molecules. Thus, the lipid-rich necrotic core is detected as hypointense areas on T2w-TSE, which is used as an alternative when post-contrast images are not available. ∗indicates lumen of internal carotid artery; E, external carotid artery; T1w-TSE, T1-weighted turbo spin echo; T2w-TSE, T2-weighted turbo spin echo

plaque hemorrhage (Fig. 6.2). While lipid core areas are typically hypointense on T2-weighted images, intraplaque hemorrhage frequently exists within lipid-rich necrotic core and sometimes results in hyperintense signals on T2-weighted images.

Intraplaque hemorrhage is a common finding in advanced carotid plaques. The degradation of red blood cells produces methemoglobin, which reduces the T1 relaxation time of surrounding water molecules and generates a hyperintense signal on T1-weighted images. Moody et al. [34] studied 63 patients scheduled for CEA using a heavily T1-weighted magnetization-prepared 3D gradient echo (MP-RAGE) sequence. T1 hyperintensity was observed in 40 (63.5%) cases, with an 84% sensitivity and 84% specificity for intraplaque hemorrhage seen on histology. Several other studies have since evaluated the performance of heavily T1-weighted MP-RAGE sequence with optimized contrast and/or improved spatial resolution for detecting intraplaque hemorrhage [35–37]. Notably, Ota et al. [38] showed that MP-RAGE provided better tissue contrast between intraplaque hemorrhage and background tissue and achieved a higher agreement with histological analysis when compared to T1-weighted fast spin echo and TOF. When MP-RAGE is not available, the source images of the pre-contrast scan in contrast-enhanced MR angiography and TOF images can be used to detect intraplaque hemorrhage [39], which may be particularly handy in the clinical setting.

Luminal Surface Condition

The typical vulnerable plaque in the coronary artery is described as thin-cap fibroatheroma. Virmani et al. [25] measured fibrous cap thickness of ruptured coronary plaques and found that mean cap thickness at the site of rupture was 23 ± 19 um,

with 95% of the cases measuring <65 um. Therefore, the fibrous cap overlying the necrotic core is considered thin in coronary arteries if it is <65 um in histology. Compared to coronary plaques, carotid plaques can rupture when the fibrous cap is thicker or less infiltrated by inflammatory cells, which is likely explained by the different hemodynamic conditions between carotid and coronary arteries. Redgrave et al. [40] studied fibrous cap thickness in 428 CEA plaques. The median minimum cap thickness was 150 um (interquartile range: 80, 210), and the median representative cap thickness was 300 um (interquartile range: 200, 500). The optimal cutoff values for discriminating ruptured from nonruptured plaques were minimum cap thickness <200 um and representative cap thickness <500 um. Further, fibrous cap rupture leads to fissure or ulceration, which are important features to identify as they increase the ipsilateral risk of cerebral embolism and the risk of cardiovascular events in general [41]. Another luminal surface condition that is of particular relevance is calcified nodule, which is seen more frequently in carotid plaques than in coronary plaques [42].

Characterizing the fibrous cap has typically relied on endovascular imaging techniques such as optical coherence tomography. Because of limited spatial resolution of carotid MRI, it is challenging to directly measure the thickness of fibrous cap. Nonetheless, it is possible to classify carotid plaques into those with thick, thin, or ruptured fibrous cap based on carotid MRI findings. Thick fibrous cap appears as a dark band between white lumen and gray wall on 3D TOF [43]. On T2-weighted or contrast-enhanced images, fibrous cap is distinguishable from the underlying necrotic core and considered to be thick if it is readily visible. On the other hand, absence of the dark band between the white lumen and gray wall on 3D TOF and lack of fibrous cap signal on T2-weighted or contrast-enhanced images indicate the presence of thin fibrous cap. Fibrous cap rupture is considered if there is juxtaluminal hyperintense signal on 3D TOF, which indicates the presence of fissure or ulceration. In a study of 22 patients undergoing CEA, classification of fibrous cap by 3D TOF showed a high agreement with histological findings (89% agreement; kappa, 0.83 [95%CI, 0.67, 1.0]) [43]. Calcified nodule appears hypointense on all MRI contrast weightings and protrudes into the lumen. As calcified nodules may be indistinguishable from carotid lumen on black-blood images, its detection usually requires comparing lumen morphology between bright- and black-blood images.

Plaque Inflammation and Neovasculature

Atherosclerosis has been recognized as an inflammatory disease. Although most studies focused on coronary atherosclerosis or animal models, there is also clear evidence on the role of inflammation in carotid atherosclerosis progression. T lymphocytes and macrophages were abundant in symptomatic carotid plaques and closely associated with plaque rupture [6]. Redgrave et al. [7] and Peeters et al. [44] found that inflammatory cells and proinflammatory cytokines tended to decrease with time after ischemic stroke but persisted after transient ischemic attack, while smooth muscle cell content increased with time after ischemic stroke, suggesting a

possible healing process after ischemic stroke but not after transient ischemic attack. Plaque neovascularization has been described in the early stages of plaque development and may alleviate hypoxia as the carotid wall thickens [45, 46]. However, it is likely a major contributor to plaque progression and rupture given its associations with intraplaque hemorrhage and plaque inflammation [47–49]. Electron microscopy studies revealed the compromised structural integrity and leucocyte infiltration of intraplaque microvessels [50], which supports plaque neovasculature as a route for intraplaque hemorrhage and plaque inflammation.

Imaging plaque inflammation and neovasculature with carotid MRI requires contrast agent. Initially developed in cancer imaging, dynamic contrast-enhanced MRI (DCE-MRI) uses clinically available gadolinium contrast to study the amount and permeability of microvessels (Fig. 6.3). Kerwin et al. [51] developed a DCE-MRI protocol that was suitable to image plaque neovasculature in carotid stenosis. Histological validation in CEA patients showed that pharmacokinetic parameters from DCE-MRI of carotid plaque (K^{trans}, transfer constant; v_p, fractional plasma volume) were associated with not only microvessel density but also macrophage content [52, 53]. In plaques with predominantly

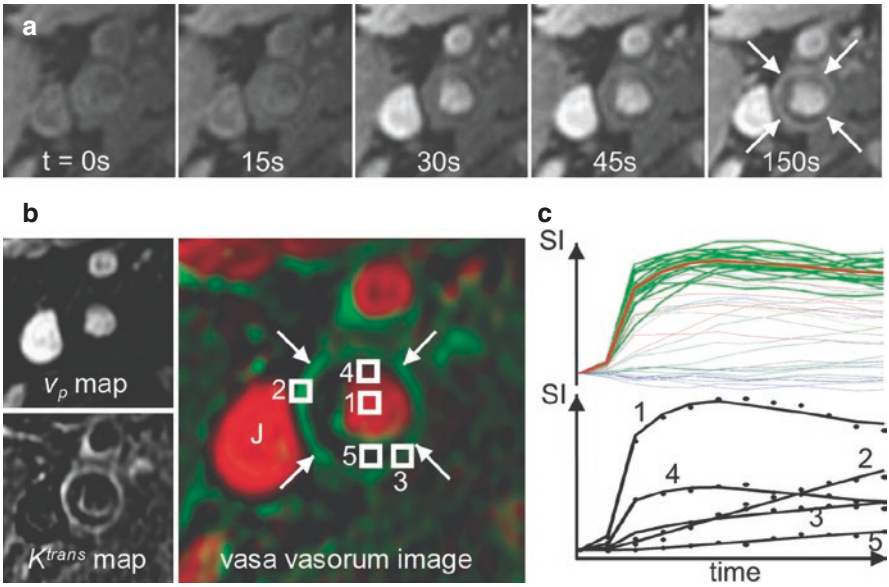

Fig. 6.3 Dynamic contrast-enhanced MRI for probing plaque inflammation and neovasculature. (**a**) Original DCE-MR images of different time points show the dynamic enhancement process of a carotid plaque (arrows). (**b**) Pharmacokinetic modeling generates K^{trans} and v_p maps, which are fused in the color-coded vasa vasorum image. J, jugular vein. (**c**) Top graph shows signal-intensity-versus-time curves for all pixels in the 2 cm^2 region for the set of blood curves extracted by the clustering algorithm (green lines) and their average (red line). Bottom graph shows typical fitting results for the kinetic model with corresponding points in (**b**), including a pixel in the lumen (1), adventitial pixels with high (2) and low (3) K^{trans}, a pixel with partial volume of the lumen (4), and an interior plaque pixel (5). (Adapted with permission from Kerwin et al. [55])

necrotic tissue, DCE-MRI measurements of the plaque area can be influenced by plaque composition [54]. On the other hand, the adventitia is a thickened layer of fibrous tissue and rich in neovasculature, which makes it an appealing imaging target for studying plaque neovasculature [55–57]. Several studies have evaluated the scan-rescan reproducibility of DCE-MRI of carotid plaque. Gaens et al. [53] found that the Patlak model is preferred in DCE-MRI analysis, with which the coefficient of variation was 16% for K^{trans} and 26% for v_p. In a multicenter study, Chen et al. [58] reported a coefficient of variation of 25% for K^{trans} and 62% for v_p. The lower reproducibility of v_p indicated that it is more vulnerable to flow signal contamination than K^{trans}. The subset of larger plaques showed an improved reproducibility for v_p, with a coefficient of variation of 28%. Besides pharmacokinetic modeling, DCE-MRI data can also be analyzed for empirical parameters of the enhancement-versus-time curve such as area under the curve [59, 60]. Compared to pharmacokinetic parameters, area under the curve is influenced by other factors besides plaque neovasculature. Qiao et al. [61] showed that adventitial enhancement on post-contrast T1-weighted images may also provide information about plaque neovasculature, which could be useful to classify patients when DCE-MRI data are not available.

Another approach to plaque inflammation is to use ultrasmall superparamagnetic iron oxide particles (USPIOs) as MRI contrast agent to directly image macrophages. Kooi et al. [62] studied the potential of USPIO-enhanced MRI for measuring plaque inflammation in 11 patients undergoing CEA. After at least 24 hours post USPIO injection, histological and electron microscopical analyses of plaques demonstrated that USPIOs were primarily found in plaque macrophages and could lead to signal changes on T2∗-weighted images. Trivedi et al. [63] found that 24–36 hours post USPIO injection was the optimal time window for detecting signal changes, with which USPIO-enhanced MRI may be a sensitive way to detect carotid plaque inflammation [64].

Evidence on the Applications of Carotid Vessel Wall Imaging

As novel information on carotid atherosclerotic plaque becomes increasingly assessible with vessel wall MRI techniques, there have come along new opportunities to optimize clinical diagnosis and management in patients with carotid artery disease or other atherosclerotic cardiovascular diseases. It is worth mentioning that the clinical value of vessel wall MRI usually depends on the strength and nature of the association between an imaging feature and the risk of atherothrombosis. Once an imaging biomarker is successfully developed, it is essential to elucidate its relationship with clinical events or their surrogates, including the evolution of imaging biomarkers prior to or after clinical events. Imaging biomarkers that are strongly implicated in the pathogenesis of clinical events may be useful for identifying the culprit lesion in clinical diagnosis, selecting patients at higher risk for stroke for CEA or CAS, and monitoring disease progression or therapeutic response at the lesion level.

To Identify the Culprit Lesion

In patients who present with neurological ischemic events, carotid atherosclerosis is currently considered to be the culprit lesion if the degree of luminal stenosis exceeds 50%, as specified in the TOAST classification [65]. While stenosis severity is an indicator of the likelihood of a carotid plaque to be accountable for ipsilateral thromboembolic events, the presence of stenosis itself is not a surrogate for atherothrombosis. Clinically, it is not uncommon to encounter cases in which only mild carotid stenosis (<50%) is found ipsilateral to brain infarct(s). In a retrospective study, Cheung et al. [66] studied 217 patients referred for carotid vessel wall imaging due to neurological ischemic symptoms who had <50% carotid stenosis on Doppler ultrasound or TOF MR angiography. Intraplaque hemorrhage, detected as hyperintense signals on MP-RAGE, was found in 13% (31 out of 233) of carotid arteries ipsilateral to neurological ischemic symptoms compared to 7% (14 out of 201) of contralateral carotid arteries ($p < 0.05$, Fisher's exact test).

Freilinger et al. [67] interrogated the hypothesis that complicated, nonstenotic carotid plaques may contribute to clinical events previously classified as cryptogenic strokes. Thirty-two consecutive patients with ischemic stroke of undetermined etiology in the anterior circulation after extensive clinical workup were scanned with a multi-contrast carotid MRI protocol to detect complicated plaques (AHA Type VI) in the ipsilateral or contralateral carotid artery, defined as the presence of fibrous cap rupture, intraplaque hemorrhage, or mural thrombus. The mean time interval between qualifying stroke and carotid MRI was 5.8 ± 4.1 days. AHA Type VI plaques were found in 12 (37.5%) of carotid arteries ipsilateral to cryptogenic stroke, whereas none was found on the contralateral side ($p = 0.001$, McNemar's test). The most common diagnostic feature was intraplaque hemorrhage (75%), followed by fibrous cap rupture (50%) and luminal thrombus (33%). This proof-of-concept study provided evidence that a substantial proportion of anterior circulation ischemic strokes previously classified as cryptogenic may be due to artery-to-artery thromboembolism from nonstenotic carotid plaques.

Similar findings have been reported by Gupta et al. [68] and Singh et al. [69]. Gupta et al. [68] used TOF for detecting intraplaque hemorrhage, which is less sensitive than MP-RAGE but more readily available in routine MR angiography studies of cervical arteries. A total of 119 (35.3%) patients were classified as having stroke of undetermined origin according to the TOAST criteria among 337 consecutive patients diagnosed with ischemic stroke. Twenty-seven cases, which had only unilateral anterior circulation infarct(s) and available TOF images during inpatient admission, were selected for analysis. Six (22.2%) patients were found to have high-intensity signals in the nonstenotic carotid artery ipsilateral to brain infarct(s), while none had high-intensity signals consistent with intraplaque hemorrhage on the contralateral side ($p = 0.01$, McNemar's test). The study by Singh et al. [69] examined 35 consecutive patients with embolic strokes of undetermined origin with MP-RAGE. Ipsilateral and contralateral intraplaque hemorrhage was found in seven (20.0%) and three (8.6%) patients ($p = 0.005$ for difference), respectively. The three

patients with intraplaque hemorrhage contralateral to stroke also had intraplaque hemorrhage on the ipsilateral side.

Despite these promising results, there remains a pressing need for large-scale, multicenter studies with standardized imaging protocols to determine the diagnostic features that can be incorporated into clinical diagnosis workup. Intraplaque hemorrhage is not rare even in asymptomatic patients. Silent fibrous cap rupture is also much more common than clinical events, which may stay unhealed for years. Residual luminal thrombus may provide the "smoking gun" evidence for recent thromboembolism from carotid atherosclerosis. However, the reliable detection of luminal thrombus remains challenging.

To Select Patients at Higher Risk for Stroke for Carotid Revascularization

In the clinical decision-making of carotid revascularization versus medical therapy alone, future risk of carotid-source ischemic stroke needs to be evaluated and compared to surgical risk including periprocedural stroke and myocardial infarction on an individual basis. As mentioned in the introduction section, multiple randomized clinical trials comparing CEA versus medical therapy alone have shown an unmet need for identifying which individual patients are at high risk for future stroke and, therefore, could benefit from prophylactic surgical intervention, among asymptomatic patients as well as symptomatic patients with mild-to-moderate carotid stenosis. These clinical trials were conducted during a period when clinical assessment of carotid atherosclerosis was largely limited to measuring luminal stenosis on angiography, which provided limited information on plaque characteristics. As carotid vessel wall imaging makes it possible to identify and quantify a variety of plaque characteristics, certain plaque features that are associated with neurological ischemic events have been shown in prospective, longitudinal studies to predict future risk of ipsilateral ischemic stroke. To date, evidence on the independent predictive value of plaque characteristics is most abundant for carotid plaque composition and luminal surface condition. Thus, vessel wall imaging information may help further classify carotid artery disease beyond stenosis severity.

In one of the earliest investigations using carotid MRI, Takaya et al. [70] followed 154 patients with asymptomatic 50–79% stenosis for an average of 38.2 months. Baseline plaque characteristics, including thin/ruptured fibrous cap (38% of cases; HR, 17.0; 95% CI, 2.2, 132), intraplaque hemorrhage (28% of cases; HR, 5.2; 95% CI, 1.6, 17.3), larger %lipid core area (HR, 1.6 per 10% increase; 95% CI, 1.2, 2.0), and greater maximal wall thickness (HR, 1.6 per 1 mm increase; 95% CI, 1.1, 2.3), were predictive of subsequent ipsilateral stroke or transient ischemic attack. Kwee et al. [71] showed that these plaque characteristics, including thin/rupture fibrous cap (HR, 5.8; 95% CI, 1.9, 17.3), intraplaque hemorrhage (HR, 3.5; 95% CI, 1.1, 11.9), and lipid core (HR, 3.2; 95% CI, 1.1, 9.5), were also predic-

tive of recurrent stroke in 126 symptomatic patients with 30–69% stenosis. Compared to lipid core and/or fibrous cap status, there has been more abundant evidence on the prognostic value of intraplaque hemorrhage, thanks to its straightforward detection on heavily T1-weighted MRI. Three independent meta-analyses have been published on this topic, which highlighted the great potential of MRI-detected plaque characteristics for identifying high-risk patients [72–74]. Recently, Gupta et al. [75] conducted a cost-effectiveness analysis concerning asymptomatic carotid stenosis (50–89%), which compared two management strategies: (1) intensive medical therapy in which patients undergo CEA if there is substantial stenosis progression (≥90%) and (2) intensive medical therapy plus MRI-based patient stratification in which those with intraplaque hemorrhage on carotid MRI undergo CEA. MRI-based patient stratification was found to be cost-efficient for identifying asymptomatic patients with carotid stenosis who are likely to benefit from CEA.

Given these promising results, vessel wall imaging will likely play a major role in stratifying patients with mild-to-moderate stenosis to optimize outcomes of carotid artery disease in the near future. MRI of intraplaque hemorrhage can be readily incorporated into clinical protocols, and presence of intraplaque hemorrhage was strongly associated with increased risk of ischemic stroke, particularly in symptomatic patients [73]. Further optimizing the approach to imaging-based patient stratification is of high clinical significance since the majority of total ischemic strokes occur in patients with mild-to-moderate stenosis due to the vast population affected. However, prospective data from large-scale, multicenter studies remain scarce. While patients without intraplaque hemorrhage appear to have minimal risk for future stroke, the heterogeneous outcomes in patients with intraplaque hemorrhage remain to be understood.

To Choose Between CEA and CAS

CEA is a well-established technique that provides long-lasting prevention of ipsilateral stroke in patients with high-risk carotid artery disease. The perioperative risk for major surgical complications, including stroke, myocardial infarction, and death, is small but not negligible. CAS is less invasive than CEA and does not require general anesthesia [76]. Several randomized clinical trials have compared CEA and CAS in patients without high surgical risk. The composite event rate, which included both perioperative major events and long-term ipsilateral strokes, was similar between CEA and CAS. However, the overall stroke rate was higher with CAS (OR, 1.50; 95% CI, 1.22, 1.84), which was attributed to a higher perioperative risk of embolic stroke during CAS compared to CEA [77]. Current clinical guidelines by the Society for Vascular Surgery recommend CEA as the first-line treatment for most patients who require carotid revascularization. CAS is an alternative to CEA for selected anatomic or medical reasons. CAS mechanically disrupts carotid plaque during stent deployment, which is considered a major source for distal emboli as supported by intraoperative transcranial Doppler monitoring. As

such, carotid plaque composition (and its thrombogenicity) may serve as a risk factor for perioperative embolization in the setting of carotid artery stenting.

Carotid plaques with intraplaque hemorrhage have large lipid-rich necrotic core, which is highly thrombogenic. Yoshimura et al. [78] tested the hypothesis that high-intensity signal on preoperative TOF-MRA, indicative of large intraplaque hemorrhage, is associated with increased risk of postoperative ipsilateral ischemic lesions on diffusion-weighted images. A total of 112 patients undergoing CAS were studied. High-intensity signal was present in 38 (33.9%) patients. After CAS, new ischemic lesions on diffusion-weighted images ipsilateral to CAS were found in 51 patients, which were more frequently seen in patients with high-intensity signal plaque (65.8% versus 35.1%, $p = 0.002$). Using the MP-RAGE sequence, Chung et al. [79] also examined whether intraplaque hemorrhage is a significant risk factor for cerebral embolism during CAS. Intraplaque hemorrhage was detected in 43 (45.7%) patients. New ipsilateral ischemic lesions on postoperative diffusion-weighted images were found in 9 (20.9%) and 16 (31.4%) patients with and without intraplaque hemorrhage ($p = 0.35$). There have been a number of other studies on this topic [80–83]. All evaluated intraplaque hemorrhage as a risk factor for periprocedural cerebral embolization, whereas some also evaluated other variables such as plaque volume, remodeling index, and tumor necrosis factor α. The techniques that were used to detect intraplaque hemorrhage varied substantially between studies. Recently, Brinjikji et al. [84] performed a meta-analysis on the association between intraplaque hemorrhage on pre-surgery MRI and clinical outcomes after CAS. Nine studies with a total of 491 patients were included. The composite outcome of stroke, myocardial infarction, and death within 30 days was 8.1% (13/160) in the intraplaque hemorrhage group and 2.1% (5/239) in the non-intraplaque hemorrhage group (OR, 4.45; 95% CI, 1.61, 12.30). The rate of new ipsilateral ischemic lesions on diffusion-weighted imaging was 49.7% (75/161) in the intraplaque hemorrhage group and 33.6% (81/241) in the non-intraplaque hemorrhage group (OR, 2.01; 95% CI, 1.31, 3.09) [84].

Overall, existing data support that high-risk carotid plaques, when disrupted during CAS, are more likely to lead to distal embolization and postprocedural stroke. How this pathophysiological association can be used clinically to optimize treatment selection for individual patients, such as switching to CEA or a different type of protection device (e.g., proximal protection, flow reversal), remains to be explored.

To Monitor Therapeutic Response

Imaging measurements of carotid atherosclerosis are often used to evaluate the efficacy of medical therapies. Because of the large sample size and long follow-up that are needed to power a clinical trial using cardiovascular events as the primary endpoint, the development of new anti-atherosclerosis therapies is usually prolonged and expensive. Surrogate endpoints by vessel wall imaging may greatly expedite the

drug development process by dramatically reducing sample size and shorten study duration that are needed to demonstrate drug efficacy. As a noninvasive, ionizing radiation-free technique that provides a spectrum of quantitative measurements from plaque morphology to inflammatory activity, carotid MRI is ideally suited for monitoring therapeutic response. Importantly, MRI measurements of carotid atherosclerosis have shown excellent test-retest reproducibility in previous studies. Duivenvoorden et al. [15] compared common carotid mean wall thickness by MRI and common carotid intima-media thickness by ultrasound. Measurements were repeated 3 times within 3 weeks in 45 subjects, consisting of 15 healthy younger volunteers, 15 older volunteers, and 15 patients with 30–70% carotid stenosis. The coefficient of variation, which indicates measurement errors, was 6.9% for mean wall thickness by MRI and 12.8% for intima-media thickness by ultrasound. Other carotid wall measurements, such as mean wall area, showed similar measurement errors as mean wall thickness. Because of the smaller size, plaque components have larger measurement errors compared to wall thickness or area measurements. Nonetheless, plaque composition may tend to change earlier and/or more dramatically than plaque size under treatment, as studies have documented significant changes in carotid plaque composition before significant changes in carotid plaque size were observed [85, 86].

A number of carotid MRI studies have evaluated the effects of statin therapy on carotid wall. In one of the earliest investigations, Corti et al. [87] studied 32 carotid plaques and found a reduction in wall area but not in lumen area after 1-year simvastatin treatment. The ORION study was the first to evaluate changes in carotid plaque composition under statin therapy using multi-contrast vessel wall MRI. In the ORION study, Underhill et al. [85] studied 33 subjects with 16–79% carotid stenosis by ultrasound and elevated LDL cholesterol. After 2 years of statin therapy, there was a reduction in lipid core volume but not in carotid wall volume. Zhao et al. [85] performed a serial imaging study over 3 years in 33 subjects with documented necrotic core at baseline, which shed light onto the time course of plaque lipid depletion under lipid-lowering treatment. There was a significant reduction in necrotic core size in Year 1, whereas the reduction in wall volume was not apparent until Year 2.

Beyond cost saving via reducing sample size and shortening study duration, imaging-based clinical trials provide some other benefits, including clarifying the mechanisms of experimental agents and revealing heterogeneous responses to treatment at the individual level. Interestingly, different plaque phenotypes responded differently to the same lipid-lowering strategy. Intraplaque hemorrhage plaques were less likely to have lipid depletion than non-intraplaque hemorrhage plaques under intensive statin therapy, indicating a need for more aggressive or targeted treatment in patients with intraplaque hemorrhage [88]. Eventually, understanding atherosclerotic plaque progression or regression under various medical treatments may facilitate the pursuit of optimal medical therapy for individual patients. To this end, highly robust methods will be needed. Certain measurement errors may be acceptable (do not affect pathophysiological associations) in research that investigates disease mechanisms at the group level but may be unacceptable in the management of individual patients.

Future Perspectives

Validation of New Carotid Vessel Wall Imaging Techniques

Despite the established capabilities and expanding applications of traditional vessel wall imaging techniques, carotid MRI is an evolving field with tremendous opportunities in the coming years. New imaging techniques have been developed to overcome certain limitations of the traditional techniques so that imaging biomarkers of carotid plaque morphology and activities may be measured more accurately and reproducibly. As such, comparison with traditional techniques may not be sufficient. Further validation against CEA specimens is helpful to demonstrate if these new techniques bring about new or more detailed information on carotid plaques compared to traditional vessel wall MRI techniques.

Diffusion-weighted vessel wall imaging has been proposed as an alternative to T2-weighted imaging for measuring the lipid-rich necrotic core, but traditional diffusion-weighted imaging sequences may not be ideal for vessel wall MRI [89–91]. Xie et al. [92] developed a diffusion-weighted turbo spin echo sequence and demonstrated in a pilot study that the in vivo ADC value of lipid-rich necrotic core was significantly lower than that of fibrous tissue ($0.60 \pm 0.16 \times 10^{-3}$ mm^2/s vs. $1.27 \pm 0.29 \times 10^{-3}$ mm^2/s, $p < 0.01$). Moreover, high-resolution T2 mapping has been developed as a more quantitative approach to lipid core quantification in carotid arteries [93–96], in which lipid core can be measured by pixel-level classification of T2 maps. Chai et al. [97] studied the performance of T2 maps for quantifying lipid core by using histological analysis. Dual T2 thresholds were used to detect lipid cores with and without intraplaque hemorrhage. A high correlation was seen between T2 mapping and histology in measuring percent lipid core area ($r = 0.83$, $p < 0.001$).

Similarly, a number of new techniques have been developed to further improve intraplaque hemorrhage detection and/or provide additional information beyond MP-RAGE. Zhu et al. [98] developed a 3D spoiled gradient-recalled echo sequence with inversion recovery and multiple echoes (3D SHINE). In addition to intraplaque hemorrhage detection, 3D SHINE allows classification of intraplaque hemorrhages based on T2$*$ estimated from the multi-echo acquisition. Wang et al. [99] introduced phase-sensitive image reconstruction so that both intraplaque hemorrhage (positive signal) and lumen (negative signal) have high contrast compared to the background static tissue, described as simultaneous non-contrast angiography and intraplaque hemorrhage (SNAP) imaging. Because of the high contrast between intraplaque hemorrhage and lumen, juxtaluminal intraplaque hemorrhage can be better characterized on SNAP than on MP-RAGE (Fig. 6.4). Fan et al. [100] developed a 3D spoiled segmented fast low angle shot readout with 3 different contrast weightings (heavily T1-weighted, gray blood, T2-weighted) acquired in an interleaved fashion (MATCH). The resulting co-registered images can be used not only for detecting intraplaque hemorrhage but also for measuring other plaque components. Qi et al. [101] developed a high-resolution vessel wall T1 mapping tech-

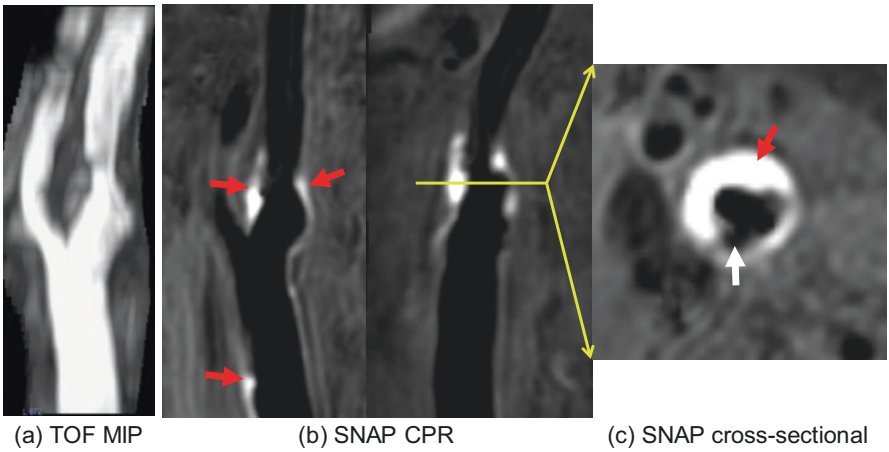

Fig. 6.4 Intraplaque hemorrhage detection by SNAP (Simultaneous Non-contrast Angiography and intraPlaque hemorrhage imaging). (**a**) TOF maximum intensity projection shows stenosis in the internal carotid artery. (**b**) Two SNAP curved-planar reformations illustrate the distribution of intraplaque hemorrhage (red arrows). (**c**) Cross-sectional SNAP image at the level of yellow line shows the presence of intraplaque hemorrhage (red arrow) and ulceration (white arrow)

nique by adopting efficient radial data acquisition and sliding window image reconstruction (GOAL-SNAP). Compared to T1-weighted imaging, T1 mapping may generate highly reproducible, quantitative measurements of intraplaque hemorrhage for serial imaging studies.

Moreover, there have also been multiple exciting developments of new DCE-MRI protocols for carotid vessel wall imaging, which have potential to improve the usability and precision of pharmacokinetic parameters given the 3D imaging capability, improved spatial/time resolution, and T1-based quantification of gadolinium contrast [102–105].

Clinical Translation of Carotid Vessel Wall Imaging

Although a number of carotid vessel wall imaging measurements have been shown to predict ipsilateral neurological ischemic events, there remains a critical need to clarify the key steps in carotid atherosclerosis progression that lead to symptomatic carotid plaques. With a wide spectrum of imaging measurements that provide carotid plaque information at various levels, it is critical to leverage the capabilities of vessel wall MRI to bridge our knowledge gap between imaging biomarkers (and their progression) and clinical events [106]. Furthermore, previous studies on the various applications of vessel wall imaging are primarily single-center investigations of limited sample size. Despite promising results from these studies, multicenter collaborative studies are needed to establish specific clinical values of vessel

wall imaging in these applications. To this end, standardized imaging protocols and data collection schemes are warranted in the future so that it is possible to pool large-scale data from multiple institutions [107]. In doing so, the study results will also be more generalizable to the broad cardiovascular community.

Summary

In the past two decades, abundant evidence has accumulated on the capabilities of vessel wall MRI in characterizing carotid plaques in terms of carotid plaque burden, tissue composition, luminal surface condition, and plaque inflammation and neovascularization. Carotid plaque characteristics by vessel wall imaging have been shown to be associated with the pathophysiology of clinical complications independently of luminal stenosis. As such, carotid vessel wall imaging affords the potential to optimize individual patient care by providing complementary information to traditional angiography techniques in clinical decision-making. Despite promising results from pioneering translational research that highlighted potential clinical values of vessel wall imaging in making etiology-level diagnosis, improving risk stratification and treatment selection, and evaluating therapeutic response in clinical management of carotid disease, achieving the full potential of vessel wall imaging awaits establishment of key biomarkers, standardization of imaging protocols, and large-scale conclusive studies.

References

1. Fernandez-Friera L, Penalvo JL, Fernandez-Ortiz A, Ibanez B, Lopez-Melgar B, Laclaustra M, Oliva B, Mocoroa A, Mendiguren J, Martinez DVV, Garcia L, Molina J, Sanchez-Gonzalez J, Guzman G, Alonso-Farto JC, Guallar E, Civeira F, Sillesen H, Pocock S, Ordovas JM, Sanz G, Jimenez-Borreguero LJ, Fuster V. Prevalence, vascular distribution, and multiterritorial extent of subclinical atherosclerosis in a middle-aged cohort: the PESA (Progression of Early Subclinical Atherosclerosis) Study. Circulation. 2015;131:2104–13.
2. Flaherty ML, Kissela B, Khoury JC, Alwell K, Moomaw CJ, Woo D, Khatri P, Ferioli S, Adeoye O, Broderick JP, Kleindorfer D. Carotid artery stenosis as a cause of stroke. Neuroepidemiology. 2013;40:36–41.
3. Johnston SC, O'Meara ES, Manolio TA, Lefkowitz D, O'Leary DH, Goldstein S, Carlson MC, Fried LP, Longstreth WJ. Cognitive impairment and decline are associated with carotid artery disease in patients without clinically evident cerebrovascular disease. Ann Intern Med. 2004;140:237–47.
4. Barnett HJ, Taylor DW, Eliasziw M, Fox AJ, Ferguson GG, Haynes RB, Rankin RN, Clagett GP, Hachinski VC, Sackett DL, Thorpe KE, Meldrum HE, Spence JD. Benefit of carotid endarterectomy in patients with symptomatic moderate or severe stenosis. North American Symptomatic Carotid Endarterectomy Trial Collaborators. N Engl J Med. 1998;339:1415–25.
5. Halliday A, Mansfield A, Marro J, Peto C, Peto R, Potter J, Thomas D. Prevention of disabling and fatal strokes by successful carotid endarterectomy in patients without recent neurological symptoms: randomised controlled trial. Lancet. 2004;363:1491–502.

6. Spagnoli LG, Mauriello A, Sangiorgi G, Fratoni S, Bonanno E, Schwartz RS, Piepgras DG, Pistolese R, Ippoliti A, Holmes DR. Extracranial thrombotically active carotid plaque as a risk factor for ischemic stroke. JAMA. 2004;292:1845–52.
7. Redgrave J, Lovett JK, Gallagher PJ, Rothwell PM. Histological assessment of 526 symptomatic carotid plaques in relation to the nature and timing of ischemic symptoms – the Oxford plaque study. Circulation. 2006;113:2320–8.
8. AbuRahma AF, Wulu JT, Crotty B. Carotid plaque ultrasonic heterogeneity and severity of stenosis. Stroke. 2002;33:1772–5.
9. Tawakol A, Migrino RQ, Bashian GG, Bedri S, Vermylen D, Cury RC, Yates D, LaMuraglia GM, Furie K, Houser S, Gewirtz H, Muller JE, Brady TJ, Fischman AJ. In vivo 18F-fluorodeoxyglucose positron emission tomography imaging provides a noninvasive measure of carotid plaque inflammation in patients. J Am Coll Cardiol. 2006;48:1818–24.
10. Watase H, Sun J, Hippe DS, Balu N, Li F, Zhao X, Mani V, Fayad ZA, Fuster V, Hatsukami TS, Yuan C. Carotid artery remodeling is segment specific: an in vivo study by vessel wall magnetic resonance imaging. Arterioscler Thromb Vasc Biol. 2018;38(4):927–34.
11. Narula J, Nakano M, Virmani R, Kolodgie FD, Petersen R, Newcomb R, Malik S, Fuster V, Finn AV. Histopathologic characteristics of atherosclerotic coronary disease and implications of the findings for the invasive and noninvasive detection of vulnerable plaques. J Am Coll Cardiol. 2013;61:1041–51.
12. Sillesen H, Muntendam P, Adourian A, Entrekin R, Garcia M, Falk E, Fuster V. Carotid plaque burden as a measure of subclinical atherosclerosis: comparison with other tests for subclinical arterial disease in the High Risk Plaque BioImage study. J Am Coll Cardiol Img. 2012;5:681–9.
13. Baber U, Mehran R, Sartori S, Schoos MM, Sillesen H, Muntendam P, Garcia MJ, Gregson J, Pocock S, Falk E, Fuster V. Prevalence, impact, and predictive value of detecting subclinical coronary and carotid atherosclerosis in asymptomatic adults: the BioImage study. J Am Coll Cardiol. 2015;65:1065–74.
14. Antiga L, Wasserman BA, Steinman DA. On the overestimation of early wall thickening at the carotid bulb by black blood MRI, with implications for coronary and vulnerable plaque imaging. Magn Reson Med. 2008;60:1020–8.
15. Duivenvoorden R, de Groot E, Elsen BM, Lameris JS, van der Geest RJ, Stroes ES, Kastelein JJ, Nederveen AJ. In vivo quantification of carotid artery wall dimensions: 3.0-Tesla MRI versus B-mode ultrasound imaging. Circ Cardiovasc Imaging. 2009;2:235–42.
16. Saam T, Hatsukami TS, Yarnykh VL, Hayes CE, Underhill H, Chu BC, Takaya N, Cai JM, Kerwin WS, Xu DX, Polissar NL, Neradilek B, Hamar WK, Maki J, Shaw DW, Buck RJ, Wyman B, Yuan C. Reader and platform reproducibility for quantitative assessment of carotid atherosclerotic plaque using 1.5T Siemens, Philips, and General Electric scanners. J Magn Reson Imaging. 2007;26:344–52.
17. Balu N, Yarnykh VL, Chu B, Wang J, Hatsukami T, Yuan C. Carotid plaque assessment using fast 3D isotropic resolution black-blood MRI. Magn Reson Med. 2011;65:627–37.
18. Fan Z, Zhang Z, Chung YC, Weale P, Zuehlsdorff S, Carr J, Li D. Carotid arterial wall MRI at 3T using 3D variable-flip-angle turbo spin-echo (TSE) with flow-sensitive dephasing (FSD). J Magn Reson Imaging. 2010;31:645–54.
19. Wang J, Yarnykh VL, Hatsukami T, Chu B, Balu N, Yuan C. Improved suppression of plaque-mimicking artifacts in black-blood carotid atherosclerosis imaging using a multislice motion-sensitized driven-equilibrium (MSDE) turbo spin-echo (TSE) sequence. Magn Reson Med. 2007;58:973–81.
20. Alizadeh DR, Doornbos J, Tamsma JT, Stuber M, Putter H, van der Geest RJ, Lamb HJ, de Roos A. Assessment of the carotid artery by MRI at 3T: a study on reproducibility. J Magn Reson Imaging. 2007;25:1035–43.
21. Vidal A, Bureau Y, Wade T, Spence JD, Rutt BK, Fenster A, Parraga G. Scan-rescan and intra-observer variability of magnetic resonance imaging of carotid atherosclerosis at 1.5 T and 3.0 T. Phys Med Biol. 2008;53:6821–35.
22. Syed MA, Oshinski JN, Kitchen C, Ali A, Charnigo RJ, Quyyumi AA. Variability of carotid artery measurements on 3-Tesla MRI and its impact on sample size calculation for clinical research. Int J Cardiovasc Imaging. 2009;25:581–9.

23. Sun J, Zhao XQ, Balu N, Hippe DS, Hatsukami TS, Isquith DA, Yamada K, Neradilek MB, Canton G, Xue Y, Fleg JL, Desvigne-Nickens P, Klimas MT, Padley RJ, Vassileva MT, Wyman BT, Yuan C. Carotid magnetic resonance imaging for monitoring atherosclerotic plaque progression: a multicenter reproducibility study. Int J Cardiovasc Imaging. 2015;31:95–103.
24. Luo Y, Polissar N, Han C, Yarnykh V, Kerwin WS, Hatsukami TS, Yuan C. Accuracy and uniqueness of three in vivo measurements of atherosclerotic carotid plaque morphology with black blood MRI. Magn Reson Med. 2003;50:75–82.
25. Virmani R, Kolodgie FD, Burke AP, Farb A, Schwartz SM. Lessons from sudden coronary death – a comprehensive morphological classification scheme for atherosclerotic lesions. Arterioscler Thromb Vasc Biol. 2000;20:1262–75.
26. Trivedi RA, U-King-Im JM, Graves MJ, Horsley J, Goddard M, Kirkpatrick PJ, Gillard JH. MRI-derived measurements of fibrous-cap and lipid-core thickness: the potential for identifying vulnerable carotid plaques in vivo. Neuroradiology. 2004;46:738–43.
27. Cai JM, Hatsukami TS, Ferguson MS, Kerwin WS, Saam T, Chu BC, Takaya N, Polissar NL, Yuan C. In vivo quantitative measurement of intact fibrous cap and lipid-rich necrotic core size in atherosclerotic carotid plaque: comparison of high-resolution, contrast-enhanced magnetic resonance imaging and histology. Circulation. 2005;112:3437–44.
28. Toussaint JF, Southern JF, Fuster V, Kantor HL. T-2-weighted contrast for NMR characterization of human atherosclerosis. Arterioscler Thromb Vasc Biol. 1995;15:1533–42.
29. Yuan C, Mitsumori LM, Ferguson MS, Polissar NL, Echelard D, Ortiz G, Small R, Davies JW, Kerwin WS, Hatsukami TS. In vivo accuracy of multispectral magnetic resonance imaging for identifying lipid-rich necrotic cores and intraplaque hemorrhage in advanced human carotid plaques. Circulation. 2001;104:2051–6.
30. Yuan C, Kerwin WS, Ferguson MS, Polissar N, Zhang SX, Cai JM, Hatsukami TS. Contrast-enhanced high resolution MRI for atherosclerotic carotid artery tissue characterization. J Magn Reson Imaging. 2002;15:62–7.
31. Wasserman BA, Smith WI, Trout HH, Cannon RO, Balaban RS, Arai AE. Carotid artery atherosclerosis: in vivo morphologic characterization with gadolinium-enhanced double-oblique MR imaging–initial results. Radiology. 2002;223:566–73.
32. Saam T, Ferguson MS, Yarnykh VL, Takaya N, Xu D, Polissar NL, Hatsukami TS, Yuan C. Quantitative evaluation of carotid plaque composition by in vivo MRI. Arterioscler Thromb Vasc Biol. 2005;25:234–9.
33. Takaya N, Cai JM, Ferguson MS, Yarnykh VL, Chu BC, Saam T, Polissar NL, Sherwood J, Cury RC, Anders RJ, Broschat KO, Hinton D, Furie KL, Hatsukami TS, Yuan C. Intra- and interreader reproducibility of magnetic resonance imaging for quantifying the lipid-rich necrotic core is improved with gadolinium contrast enhancement. J Magn Reson Imaging. 2006;24:203–10.
34. Moody AR, Murphy RE, Morgan PS, Martel AL, Delay GS, Allder S, MacSweeney ST, Tennant WG, Gladman J, Lowe J, Hunt BJ. Characterization of complicated carotid plaque with magnetic resonance direct thrombus imaging in patients with cerebral ischemia. Circulation. 2003;107:3047–52.
35. Zhu DC, Ferguson MS, DeMarco JK. An optimized 3D inversion recovery prepared fast spoiled gradient recalled sequence for carotid plaque hemorrhage imaging at 3.0 T. Magn Reson Imaging. 2008;26:1360–6.
36. Bitar R, Moody AR, Leung G, Symons S, Crisp S, Butany J, Rowsell C, Kiss A, Nelson A, Maggisano R. In vivo 3D high-spatial-resolution MR imaging of intraplaque hemorrhage. Radiology. 2008;249:259–67.
37. Cappendijk VC, Cleutjens K, Heeneman S, Schurink G, Welten R, Kessels A, van Suylen RJ, Daemen M, van Engelshoven J, Kooi ME. In vivo detection of hemorrhage in human atherosclerotic plaques with magnetic resonance imaging. J Magn Reson Imaging. 2004;20:105–10.
38. Ota H, Yarnykh VL, Ferguson MS, Underhill HR, DeMarco JK, Zhu DC, Oikawa M, Dong L, Zhao XH, Collar A, Hatsukami TS, Yuan C. Carotid intraplaque hemorrhage imaging at 3.0-T MR imaging: comparison of the diagnostic performance of three T1-weighted sequences. Radiology. 2010;254:551–63.

39. Qiao Y, Etesami M, Malhotra S, Astor BC, Virmani R, Kolodgie FD, Trout HR, Wasserman BA. Identification of intraplaque hemorrhage on MR angiography images: a comparison of contrast-enhanced mask and time-of-flight techniques. AJNR Am J Neuroradiol. 2011;32:454–9.
40. Redgrave JN, Gallagher P, Lovett JK, Rothwell PM. Critical cap thickness and rupture in symptomatic carotid plaques: the oxford plaque study. Stroke. 2008;39:1722–9.
41. Rothwell PM, Villagra R, Gibson R, Donders RC, Warlow CP. Evidence of a chronic systemic cause of instability of atherosclerotic plaques. Lancet. 2000;355:19–24.
42. Virmani R, Ladich ER, Burke AP, Kolodgie FD. Histopathology of carotid atherosclerotic disease. Neurosurgery. 2006;59:S219–27, S3–S13.
43. Hatsukami TS, Ross R, Polissar NL, Yuan C. Visualization of fibrous cap thickness and rupture in human atherosclerotic carotid plaque in vivo with high-resolution magnetic resonance imaging. Circulation. 2000;102:959–64.
44. Peeters W, Hellings WE, de Kleijn DPV, de Vries JPPM, Moll FL, Vink A, Pasterkamp G. Carotid atherosclerotic plaques stabilize after stroke: insights into the natural process of atherosclerotic plaque stabilization. Arterioscler Thromb Vasc Biol. 2009;29:128–33.
45. Fleiner M, Kummer M, Mirlacher M, Sauter G, Cathomas G, Krapf R, Biedermann BC. Arterial neovascularization and inflammation in vulnerable patients: early and late signs of symptomatic atherosclerosis. Circulation. 2004;110:2843–50.
46. Jeziorska M, Woolley DE. Neovascularization in early atherosclerotic lesions of human carotid arteries: its potential contribution to plaque development. Hum Pathol. 1999;30:919–25.
47. Nikkari ST, O'Brien KD, Ferguson M, Hatsukami T, Welgus HG, Alpers CE, Clowes AW. Interstitial collagenase (MMP-1) expression in human carotid atherosclerosis. Circulation. 1995;92:1393–8.
48. O'Brien KD, McDonald TO, Chait A, Allen MD, Alpers CE. Neovascular expression of E-selectin, intercellular adhesion molecule-1, and vascular cell adhesion molecule-1 in human atherosclerosis and their relation to intimal leukocyte content. Circulation. 1996;93:672–82.
49. Moreno PR, Purushothaman KR, Fuster V, Echeverri D, Truszczynska H, Sharma SK, Badimon JJ, O'Connor WN. Plaque neovascularization is increased in ruptured atherosclerotic lesions of human aorta: implications for plaque vulnerability. Circulation. 2004;110:2032–8.
50. Sluimer JC, Kolodgie FD, Bijnens A, Maxfield K, Pacheco E, Kutys B, Duimel H, Frederik PM, van Hinsbergh V, Virmani R, Daemen M. Thin-walled microvessels in human coronary atherosclerotic plaques show incomplete endothelial junctions relevance of compromised structural integrity for intraplaque microvascular leakage. J Am Coll Cardiol. 2009;53:1517–27.
51. Kerwin W, Hooker A, Spilker M, Vicini P, Ferguson M, Hatsukami T, Yuan C. Quantitative magnetic resonance imaging analysis of neovasculature volume in carotid atherosclerotic plaque. Circulation. 2003;107:851–6.
52. Kerwin WS, O'Brien KD, Ferguson MS, Polissar N, Hatsukami TS, Yuan C. Inflammation in carotid atherosclerotic plaque: a dynamic contrast-enhanced MR imaging study. Radiology. 2006;241:459–68.
53. Gaens ME, Backes WH, Rozel S, Lipperts M, Sanders SN, Jaspers K, Cleutjens JP, Sluimer JC, Heeneman S, Daemen MJ, Welten RJ, Daemen JW, Wildberger JE, Kwee RM, Kooi ME. Dynamic contrast-enhanced MR imaging of carotid atherosclerotic plaque: model selection, reproducibility, and validation. Radiology. 2013;266:271–9.
54. Chen H, Cai J, Zhao X, Underhill H, Ota H, Oikawa M, Dong L, Yuan C, Kerwin WS. Localized measurement of atherosclerotic plaque inflammatory burden with dynamic contrast-enhanced MRI. Magn Reson Med. 2010;64:567–73.
55. Kerwin WS, Oikawa M, Yuan C, Jarvik GP, Hatsukami TS. MR imaging of adventitial vasa vasorum in carotid atherosclerosis. Magn Reson Med. 2008;59:507–14.
56. Sun J, Song Y, Chen H, Kerwin WS, Hippe DS, Dong L, Chen M, Zhou C, Hatsukami TS, Yuan C. Adventitial perfusion and intraplaque hemorrhage: a dynamic contrast-enhanced MRI study in the carotid artery. Stroke. 2013;44:1031–6.
57. van Hoof RH, Voo SA, Sluimer JC, Wijnen NJ, Hermeling E, Schreuder FH, Truijman MT, Cleutjens JP, Daemen MJ, Daemen JH, van Oostenbrugge RJ, Mess WH, Wildberger JE, Heeneman S, Kooi ME. Vessel wall and adventitial DCE-MRI parameters demonstrate simi-

lar correlations with carotid plaque microvasculature on histology. J Magn Reson Imaging. 2017;46(4):1053–9.
58. Chen H, Sun J, Kerwin WS, Balu N, Neradilek MB, Hippe DS, Isquith D, Xue Y, Yamada K, Peck S, Yuan C, O'Brien KD, Zhao XQ. Scan-rescan reproducibility of quantitative assessment of inflammatory carotid atherosclerotic plaque using dynamic contrast-enhanced 3T CMR in a multi-center study. J Cardiovasc Magn Reson. 2014;16:51.
59. Calcagno C, Cornily JC, Hyafil F, Rudd J, Briley-Saebo KC, Mani V, Goldschlager G, Machac J, Fuster V, Fayad ZA. Detection of neovessels in atherosclerotic plaques of rabbits using dynamic contrast enhanced MRI and 18F-FDG PET. Arterioscler Thromb Vasc Biol. 2008;28:1311–7.
60. Calcagno C, Vucic E, Mani V, Goldschlager G, Fayad ZA. Reproducibility of black blood dynamic contrast-enhanced magnetic resonance imaging in aortic plaques of atherosclerotic rabbits. J Magn Reson Imaging. 2010;32:191–8.
61. Qiao Y, Etesami M, Astor BC, Zeiler SR, Trout HR, Wasserman BA. Carotid plaque neovascularization and hemorrhage detected by MR imaging are associated with recent cerebrovascular ischemic events. Am J Neuroradiol. 2012;33:755–60.
62. Kooi ME, Cappendijk VC, Cleutjens KB, Kessels AG, Kitslaar PJ, Borgers M, Frederik PM, Daemen MJ, van Engelshoven JM. Accumulation of ultrasmall superparamagnetic particles of iron oxide in human atherosclerotic plaques can be detected by in vivo magnetic resonance imaging. Circulation. 2003;107:2453–8.
63. Trivedi RA, U-King-Im JM, Graves MJ, Cross JJ, Horsley J, Goddard MJ, Skepper JN, Quartey G, Warburton E, Joubert I, Wang L, Kirkpatrick PJ, Brown J, Gillard JH. In vivo detection of macrophages in human carotid atheroma: temporal dependence of ultrasmall superparamagnetic particles of iron oxide-enhanced MRI. Stroke. 2004;35:1631–5.
64. Trivedi RA, Mallawarachi C, U-King-Im JM, Graves MJ, Horsley J, Goddard MJ, Brown A, Wang L, Kirkpatrick PJ, Brown J, Gillard JH. Identifying inflamed carotid plaques using in vivo USPIO-enhanced MR imaging to label plaque macrophages. Arterioscler Thromb Vasc Biol. 2006;26:1601–6.
65. Adams HJ, Bendixen BH, Kappelle LJ, Biller J, Love BB, Gordon DL, Marsh ER. Classification of subtype of acute ischemic stroke. Definitions for use in a multicenter clinical trial. TOAST. Trial of Org 10172 in Acute Stroke Treatment. Stroke. 1993;24:35–41.
66. Cheung HM, Moody AR, Singh N, Bitar R, Zhan J, Leung G. Late stage complicated atheroma in low-grade stenotic carotid disease: MR imaging depiction--prevalence and risk factors. Radiology. 2011;260:841–7.
67. Freilinger TM, Schindler A, Schmidt C, Grimm J, Cyran C, Schwarz F, Bamberg F, Linn J, Reiser M, Yuan C, Nikolaou K, Dichgans M, Saam T. Prevalence of nonstenosing, complicated atherosclerotic plaques in cryptogenic stroke. J Am Coll Cardiol Img. 2012;5:397–405.
68. Gupta A, Gialdini G, Lerario M, Baradaran H, Giambrone A, Navi B, Marshall R, Iadecola C, Hooman K. Magnetic resonance angiography detection of abnormal carotid artery plaque in patients with cryptogenic stroke. J Am Heart Assoc. 2015;4:e2012.
69. Singh N, Moody AR, Panzov V, Gladstone DJ. Carotid intraplaque hemorrhage in patients with embolic stroke of undetermined source. J Stroke Cerebrovasc Dis. 2018;27(7):1956–9.
70. Takaya N, Yuan C, Chu BC, Saam T, Underhill H, Cai JM, Tran N, Polissar NL, Isaac C, Ferguson MS, Garden GA, Cramer SC, Maravilla KR, Hashimoto B, Hatsukami TS. Association between carotid plaque characteristics and subsequent ischemic cerebrovascular events: a prospective assessment with MRI – initial results. Stroke. 2006;37:818–23.
71. Kwee RM, van Oostenbrugge RJ, Mess WH, Prins MH, van der Geest RJ, Ter Berg JW, Franke CL, Korten AG, Meems BJ, van Engelshoven JM, Wildberger JE, Kooi ME. MRI of carotid atherosclerosis to identify TIA and stroke patients who are at risk of a recurrence. J Magn Reson Imaging. 2013;37:1189–94.
72. Saam T, Hetterich H, Hoffmann V, Yuan C, Dichgans M, Poppert H, Koeppel T, Hoffmann U, Reiser MF, Bamberg F. Meta-analysis and systematic review of the predictive value of carotid plaque hemorrhage on cerebrovascular events by magnetic resonance imaging. J Am Coll Cardiol. 2013;62:1081–91.

73. Hosseini AA, Kandiyil N, Macsweeney ST, Altaf N, Auer DP. Carotid plaque hemorrhage on magnetic resonance imaging strongly predicts recurrent ischemia and stroke. Ann Neurol. 2013;73:774–84.
74. Gupta A, Baradaran H, Schweitzer AD, Kamel H, Pandya A, Delgado D, Dunning A, Mushlin AI, Sanelli PC. Carotid plaque MRI and stroke risk: a systematic review and meta-analysis. Stroke. 2013;44:3071–7.
75. Gupta A, Mushlin AI, Kamel H, Navi BB, Pandya A. Cost-effectiveness of carotid plaque MR imaging as a stroke risk stratification tool in asymptomatic carotid artery stenosis. Radiology. 2015;277:763–72.
76. Yadav JS, Wholey MH, Kuntz RE, Fayad P, Katzen BT, Mishkel GJ, Bajwa TK, Whitlow P, Strickman NE, Jaff MR, Popma JJ, Snead DB, Cutlip DE, Firth BG, Ouriel K. Protected carotid-artery stenting versus endarterectomy in high-risk patients. N Engl J Med. 2004;351:1493–501.
77. Brott TG, Hobson RW, Howard G, Roubin GS, Clark WM, Brooks W, Mackey A, Hill MD, Leimgruber PP, Sheffet AJ, Howard VJ, Moore WS, Voeks JH, Hopkins LN, Cutlip DE, Cohen DJ, Popma JJ, Ferguson RD, Cohen SN, Blackshear JL, Silver FL, Mohr JP, Lal BK, Meschia JF. Stenting versus endarterectomy for treatment of carotid-artery stenosis. N Engl J Med. 2010;363(1):11–23.
78. Yoshimura S, Yamada K, Kawasaki M, Asano T, Kanematsu M, Takamatsu M, Hara A, Iwama T. High-intensity signal on time-of-flight magnetic resonance angiography indicates carotid plaques at high risk for cerebral embolism during stenting. Stroke. 2011;42:3132–7.
79. Chung GH, Jeong JY, Kwak HS, Hwang SB. Associations between cerebral embolism and carotid intraplaque hemorrhage during protected carotid artery stenting. AJNR Am J Neuroradiol. 2016;37(4):686–91.
80. Yamada K, Yoshimura S, Kawasaki M, Enomoto Y, Asano T, Hara A, Minatoguchi S, Iwama T. Embolic complications after carotid artery stenting or carotid endarterectomy are associated with tissue characteristics of carotid plaques evaluated by magnetic resonance imaging. Atherosclerosis. 2011;215:399–404.
81. Tanemura H, Maeda M, Ichikawa N, Miura Y, Umeda Y, Hatazaki S, Toma N, Asakura F, Suzuki H, Sakaida H, Matsushima S, Taki W. High-risk plaque for carotid artery stenting evaluated with 3-dimensional T1-weighted gradient echo sequence. Stroke. 2013;44:105–10.
82. Maruyama D, Fukuda K, Kataoka H, Morita Y, Nishimura K, Kawamura Y, Iihara K. Evaluation of carotid artery outward remodeling by T1-weighted magnetic resonance imaging in carotid endarterectomy and stenting. J Vasc Surg. 2015;61:1464–71.
83. Lin C, Tang X, Shi Z, Zhang L, Yan D, Niu C, Zhou M, Wang L, Fu W, Guo D. Serum tumor necrosis factor α levels are associated with new ischemic brain lesions after carotid artery stenting. J Vasc Surg. 2018;68(3):771–8.
84. Brinjikji W, Lehman VT, Huston JR, Murad MH, Lanzino G, Cloft HJ, Kallmes DF. The association between carotid intraplaque hemorrhage and outcomes of carotid stenting: a systematic review and meta-analysis. J Neurointerv Surg. 2017;9:837–42.
85. Zhao XQ, Dong L, Hatsukami T, Phan BA, Chu B, Moore A, Lane T, Neradilek MB, Polissar N, Monick D, Lee C, Underhill H, Yuan C. MR imaging of carotid plaque composition during lipid-lowering therapy: a prospective assessment of effect and time course. J Am Coll Cardiol Img. 2011;4:977–86.
86. Underhill HR, Yuan C, Zhao XQ, Kraiss LW, Parker DL, Saam T, Chu B, Takaya N, Liu F, Polissar NL, Neradilek B, Raichlen JS, Cain VA, Waterton JC, Hamar W, Hatsukami TS. Effect of rosuvastatin therapy on carotid plaque morphology and composition in moderately hypercholesterolemic patients: a high-resolution magnetic resonance imaging trial. Am Heart J. 2008;155:581–4.
87. Corti R, Fuster V, Fayad ZA, Worthley SG, Helft G, Smith D, Weinberger J, Wentzel J, Mizsei G, Mercuri M, Badimon JJ. Lipid lowering by simvastatin induces regression of human atherosclerotic lesions: two years' follow-up by high-resolution noninvasive magnetic resonance imaging. Circulation. 2002;106:2884–7.
88. Sun J, Balu N, Hippe DS, Xue Y, Dong L, Zhao X, Li F, Xu D, Hatsukami TS, Yuan C. Subclinical carotid atherosclerosis: short-term natural history of lipid-rich necrotic core–a multicenter study with MR imaging. Radiology. 2013;268:61–8.

89. Qiao Y, Ronen I, Viereck J, Ruberg FL, Hamilton JA. Identification of atherosclerotic lipid deposits by diffusion-weighted imaging. Arterioscler Thromb Vasc Biol. 2007;27:1440–6.
90. Young VE, Patterson AJ, Sadat U, Bowden DJ, Graves MJ, Tang TY, Priest AN, Skepper JN, Kirkpatrick PJ, Gillard JH. Diffusion-weighted magnetic resonance imaging for the detection of lipid-rich necrotic core in carotid atheroma in vivo. Neuroradiology. 2010;52:929–36.
91. Kim SE, Treiman GS, Roberts JA, Jeong EK, Shi X, Hadley JR, Parker DL. In vivo and ex vivo measurements of the mean ADC values of lipid necrotic core and hemorrhage obtained from diffusion weighted imaging in human atherosclerotic plaques. J Magn Reson Imaging. 2011;34:1167–75.
92. Xie Y, Yu W, Fan Z, Nguyen C, Bi X, An J, Zhang T, Zhang Z, Li D. High resolution 3D diffusion cardiovascular magnetic resonance of carotid vessel wall to detect lipid core without contrast media. J Cardiovasc Magn Reson. 2014;16:67.
93. Biasiolli L, Lindsay AC, Chai JT, Choudhury RP, Robson MD. In-vivo quantitative T2 mapping of carotid arteries in atherosclerotic patients: segmentation and T2 measurement of plaque components. J Cardiovasc Magn Reson. 2013;15:69.
94. Coolen BF, Poot DH, Liem MI, Smits LP, Gao S, Kotek G, Klein S, Nederveen AJ. Three-dimensional quantitative T1 and T2 mapping of the carotid artery: sequence design and in vivo feasibility. Magn Reson Med. 2016;75:1008–17.
95. Yuan J, Usman A, Reid SA, King KF, Patterson AJ, Gillard JH, Graves MJ. Three-dimensional black-blood T2 mapping with compressed sensing and data-driven parallel imaging in the carotid artery. Magn Reson Imaging. 2017;37:62–9.
96. Qi H, Sun J, Qiao H, Zhao X, Guo R, Balu N, Yuan C, Chen H. Simultaneous T1 and T2 mapping of the carotid plaque (SIMPLE) with T2 and inversion recovery prepared 3D radial imaging. Magn Reson Med. 2018;80(6):2598–608.
97. Chai JT, Biasiolli L, Li L, Alkhalil M, Galassi F, Darby C, Halliday AW, Hands L, Magee T, Perkins J, Sideso E, Handa A, Jezzard P, Robson MD, Choudhury RP. Quantification of lipid-rich core in carotid atherosclerosis using MRI T2 mapping – relation to clinical presentation. J Am Coll Cardiol Img. 2017;10:747–56.
98. Zhu DC, Vu AT, Ota H, DeMarco JK. An optimized 3D spoiled gradient recalled echo pulse sequence for hemorrhage assessment using inversion recovery and multiple echoes (3D SHINE) for carotid plaque imaging. Magn Reson Med. 2010;64:1341–51.
99. Wang J, Bornert P, Zhao H, Hippe DS, Zhao X, Balu N, Ferguson MS, Hatsukami TS, Xu J, Yuan C, Kerwin WS. Simultaneous noncontrast angiography and intraPlaque hemorrhage (SNAP) imaging for carotid atherosclerotic disease evaluation. Magn Reson Med. 2013;69:337–45.
100. Fan Z, Yu W, Xie Y, Dong L, Yang L, Wang Z, Conte AH, Bi X, An J, Zhang T, Laub G, Shah PK, Zhang Z, Li D. Multi-contrast atherosclerosis characterization (MATCH) of carotid plaque with a single 5-min scan: technical development and clinical feasibility. J Cardiovasc Magn Reson. 2014;16:53.
101. Qi H, Sun J, Qiao H, Chen S, Zhou Z, Pan X, Wang Y, Zhao X, Li R, Yuan C, Chen H. Carotid intraplaque hemorrhage imaging with quantitative vessel wall T1 mapping: technical development and initial experience. Radiology. 2018;287:276–84.
102. Calcagno C, Robson PM, Ramachandran S, Mani V, Kotys-Traughber M, Cham M, Fischer SE, Fayad ZA. SHILO, a novel dual imaging approach for simultaneous HI-/LOw temporal (Low-/Hi-spatial) resolution imaging for vascular dynamic contrast enhanced cardiovascular magnetic resonance: numerical simulations and feasibility in the carotid arteries. J Cardiovasc Magn Reson. 2013;15:42.
103. Mendes J, Parker DL, McNally S, DiBella E, Bolster BJ, Treiman GS. Three-dimensional dynamic contrast enhanced imaging of the carotid artery with direct arterial input function measurement. Magn Reson Med. 2014;72:816–22.
104. Qi H, Huang F, Zhou Z, Koken P, Balu N, Zhang B, Yuan C, Chen H. Large coverage black-bright blood interleaved imaging sequence (LaBBI) for 3D dynamic contrast-enhanced MRI of vessel wall. Magn Reson Med. 2018;79(3):1334–44.

105. Wang N, Christodoulou AG, Xie Y, Wang Z, Deng Z, Zhou B, Lee S, Fan Z, Chang H, Yu W, Li D. Quantitative 3D dynamic contrast-enhanced (DCE) MR imaging of carotid vessel wall by fast T1 mapping using Multitasking. Magn Reson Med. 2019;81:2302–14.
106. Saba L, Saam T, Jager HR, Yuan C, Hatsukami TS, Saloner D, Wasserman BA, Bonati LH, Wintermark M. Imaging biomarkers of vulnerable carotid plaques for stroke risk prediction and their potential clinical implications. Lancet Neurol. 2019;18(6):559–72.
107. Saba L, Yuan C, Hatsukami TS, Balu N, Qiao Y, DeMarco JK, Saam T, Moody AR, Li D, Matouk CC, Johnson MH, Jager HR, Mossa-Basha M, Kooi ME, Fan Z, Saloner D, Wintermark M, Mikulis DJ, Wasserman BA. Carotid artery wall imaging: perspective and guidelines from the ASNR vessel wall imaging study group and expert consensus recommendations of the American Society of Neuroradiology. AJNR Am J Neuroradiol. 2018;39(2):E9–E31.

Part III
Peripheral Artery Disease

Chapter 7
Peripheral Artery Disease: An Overview

Mary M. McDermott

Lower extremity peripheral artery disease (PAD), defined as atherosclerotic obstruction of the lower extremity arteries, now affects 8.5 million men and women in the United States and more than 200 million people worldwide [1, 2]. Atherosclerotic obstruction in the lower extremity arteries limits oxygen delivery to lower extremity skeletal muscle during walking activity, and in cases of extremely severe PAD, oxygen delivery can be limited at rest. Thus, people with PAD have difficulty walking long distances, due to inadequate oxygenation of lower extremity muscle during exercise, and patients with extremely severe PAD can develop critical limb ischemia including gangrene. Most patients with PAD will not develop critical limb ischemia, but have difficulty walking more than short distances due to ischemia of their limbs with walking. Consistent with this phenomenon, people with PAD have significantly greater functional impairment and higher rates of mobility loss, compared to people without PAD [3–5]. In addition, people with PAD typically have atherosclerotic blockages in the coronary and cerebrovascular arteries [6]. Therefore, people with PAD also have an increased risk of coronary ischemic events, stroke, and mortality, compared to people without PAD [7, 8]. Major therapeutic goals for people with PAD consist of improving walking ability and preventing cardiovascular events. This chapter describes the epidemiology of PAD, diagnosis of PAD, and clinical consequences of PAD. Therapeutic approaches to PAD are briefly summarized. The Table 7.1 provides a brief summary of risk factors, diagnosis, prognosis, and treatment for PAD.

M. M. McDermott (✉)
Northwestern University Feinberg School of Medicine, Chicago, IL, USA
e-mail: mdm608@northwestern.edu

C. Yuan et al. (eds.), *Vessel Based Imaging Techniques*,
https://doi.org/10.1007/978-3-030-25249-6_7

Table 7.1 Overview of peripheral artery disease

Characteristic	Evidence
Risk factors	Older age, diabetes, and cigarette smoking are the strongest risk factors for PAD. Hypertension, hyperlipidemia, and inflammation are also risk factors for PAD
Diagnosis	Ankle brachial index <0.90 is a widely accepted and noninvasive method for diagnosing PAD
Symptoms	Intermittent claudication is considered the most classical symptom of PAD. However, most people with PAD are either asymptomatic or report exertional leg symptoms other than claudication
Treatment	Treatment should focus on preventing cardiovascular events by prescribing antiplatelet therapy and a potent statin and by treating hypertension. Walking exercise improves mobility and prevents functional decline in PAD
Prognosis	People with PAD are at increased risk of cardiovascular events and all-cause mortality, compared to those without PAD. Most patients with PAD experience decline in walking endurance over time, although only a relatively small minority will ever develop critical limb ischemia

Epidemiology and Risk Factors for PAD

Older age is a major risk factor for PAD and the prevalence of PAD increases markedly with increasing age. PAD is uncommon in people younger than age 50 but affects as many as 20% of people age 80 and older [6, 8, 9]. PAD will be increasingly common as the population survives to older ages with chronic diseases. In addition to older age, traditional atherosclerotic disease risk factors, such as diabetes mellitus, cigarette smoking, hypertension, dyslipidemia, and increased inflammation are risk factors for PAD. Cigarette smoking and diabetes mellitus are particularly important risk factors for PAD [8, 10, 11]. For example, cigarette smoking and diabetes are stronger risk factors for PAD than for coronary artery disease [8, 9].

People who currently smoke have a 2.0- to 3.4-fold higher risk of PAD compared to people who never smoked [8]. Furthermore, there is a dose-dependent association between cigarette smoking and risk of PAD. Among male participants in the Health Professionals Follow-Up Study, men who smoked the most cigarettes had a 12.9-fold higher risk of developing PAD compared to men who had never smoked [12]. Smoking cessation reduces the risk of PAD, but smokers remain at increased risk for PAD for up to 20 years after quitting smoking, compared to individuals who never smoked cigarettes [8, 12]. Epidemiologic evidence shows that diabetes mellitus is associated with a 1.9–4.0-fold increased risk of PAD, even after adjustment for other potential confounders [8]. Some evidence suggests that more severe diabetes is associated with higher risk of PAD [8]. In addition, people with PAD who have diabetes are at higher risk of amputation and mortality compared to people with PAD who do not have diabetes. One report described that among people with PAD, those with diabetes had a fivefold higher risk of an amputation, compared to

those without diabetes [13]. Among people with PAD, those who have diabetes also tend to have more distal lower extremity atherosclerosis compared to those without diabetes [13, 14]. Hypertension, hyperlipidemia, and inflammation are also significant and independent risk factors for PAD [8, 12].

The prevalence of PAD is similar between men and women over age 65 [6, 15], but African-Americans have a higher prevalence of PAD compared to Caucasians, independent of differences in cardiovascular risk factors between African-Americans and Caucasians [6, 7]. For example, the Cardiovascular Health Study of 5084 community-dwelling men and women age 65 and older in the United States reported that nonwhite race (primarily African-American race) was associated with a 2.1-fold higher prevalence of PAD compared to Caucasians [15]. In the Women's Health and Aging Study, 328 of 933 community-dwelling women age 65 and older with mobility impairment had PAD. Those with PAD had a significantly higher prevalence of African-American participants, compared to those without PAD (36.3% vs. 24.8%) [16]. In summary, there are not significant differences in the prevalence of PAD between older men and women, but African-Americans have a higher prevalence, compared to Caucasians.

Symptoms and Diagnosis of Peripheral Artery Disease

The most classical symptom of PAD is intermittent claudication, defined as exertional calf pain that begins with walking activity, resolves within 10 minutes of rest, and does not begin while at rest [17, 18]. In people with PAD, exertional calf pain due to ischemia is caused by insufficient oxygen supply during walking activity. Symptoms resolve with rest, when the flow of oxygen-rich arterial blood is sufficient to meet oxygen requirements. Although intermittent claudication is considered the most classical symptom of PAD, most people with PAD have atypical leg symptoms other than classical intermittent claudication, and many people with PAD are asymptomatic – i.e., they have no exertional leg symptoms [3–5, 15, 16]. In patients identified from a community-dwelling setting with objectively documented PAD, approximately 60% report no exertional leg symptoms, and approximately 10% report classical exertional leg symptoms, with the remainder reporting exertional leg symptoms other than classical intermittent claudication [15]. In patients identified in a clinical practice setting, approximately 30% to 50% are asymptomatic and approximately 25 to 30% have classical symptoms of intermittent claudication [3–5]. Reasons for the range of leg symptoms and high prevalence of asymptomatic disease among people with PAD remain unclear. However, nearly 60% of people with asymptomatic PAD developed exertional leg symptoms during a 6-minute walk test [19], suggesting that many people with PAD restrict activity to avoid leg symptoms and subsequently become asymptomatic. People with PAD who report exertional leg symptoms other than intermittent claudication have a higher prevalence of diabetes, peripheral neuropathy, and spinal stenosis [3], suggesting that comorbid diseases may influence symptoms experienced during walking activity by people with PAD.

Only a small proportion of patients with PAD develop critical limb ischemia, the manifestation of end-stage PAD that may lead to amputation if not reversed. In one study, approximately 2.5% of patients with PAD developed rest pain or gangrene per year [8]. However, rates of progression to critical limb ischemia may be highest during the year after PAD is diagnosed [8], perhaps because severe PAD is more likely to be diagnosed than mild PAD.

Diagnosing PAD

Although symptoms of PAD are myriad and many people with PAD report no leg symptoms, PAD can be noninvasively diagnosed with the ankle brachial index (ABI), a ratio of Doppler-recorded systolic pressures in the lower and upper extremities. A normal ABI is 1.10–1.40 [20]. An ABI < 0.90 is reasonably sensitive and highly specific for a diagnosis of PAD [20, 21].

The ABI can be performed in the outpatient setting by measuring Doppler-recorded systolic pressures in the right and left brachial arteries and in the dorsalis pedis and posterior tibial arteries in each lower extremity. In healthy people without PAD, arterial pressures increase with greater distance away from the heart. This phenomenon results in higher systolic pressures at the ankle compared to the brachial arteries in people without lower extremity arterial obstruction. Therefore, people without lower extremity atherosclerosis typically have an ABI value ≥1.10 and <1.40, and an ABI < 0.90 is consistent with significant lower extremity atherosclerosis [20–24]. Lijmer et al. reported that an ABI < 0.91 had a sensitivity of 79% and a specificity of 96% for PAD in approximately 100 limbs, based on a comparison of the ABI value with angiographic study of the lower extremities [21]. The relatively low sensitivity of ABI < 0.90 occurs because some patients with PAD have medial calcinosis of their distal lower extremity arteries, resulting in ABI values above 1.10 even in the presence of significant lower extremity arterial obstruction [20]. Lower ABI values are indicative of more severe PAD. An ABI value <0.50 indicates severe PAD, while a value of 0.50–0.90 indicates mild to moderate PAD. People with an ABI value of 0.91–1.09 typically have mild PAD, and ABI values in this range are associated with higher rates of mobility loss and increased cardiovascular mortality rates, compared to people with ABI values of 1.10–1.40.

The ABI should be performed with the patient lying supine, after at least a 5-minute rest period. Appropriately sized blood pressure cuffs are placed over each brachial artery and at each ankle. At the ankle, the blood pressure cuff bladder should be positioned so that the artery marker is directly over the posterior tibial artery. Patients should be instructed not to talk during the examination, since talking can alter the systolic pressures during the test. A handheld Doppler is used to locate each artery before each arterial pressure measurement. Blood pressures are typically measured sequentially starting with the right upper extremity and them moving to the right lower extremity, left lower extremity, and the left upper extremity. In the lower extremities, the dorsalis pedis and the posterior tibial pressure are each mea-

sured. The probe should be positioned so that it detects the strongest signal from the artery prior to cuff inflation. Accurate ABI measurement consists of inflating the cuff sphygmomanometer to at least 20 mm above the systolic pressure and deflating the pressure no faster than 2 mm/second. The systolic pressure at which the pulse reappears is measured and recorded for each artery and used to calculate the ABI.

Calculating the ABI

An ABI may be calculated for each lower extremity artery, by dividing the lower extremity artery's pressure by the highest of the brachial artery pressures. The ABI is typically calculated for each leg, by dividing the highest of the two pressures in each leg by the highest of the left vs. right brachial artery pressures. The highest pressure in each leg is traditionally used to calculate the ABI for each leg, because the highest pressure represents the greatest arterial pressure reaching the foot. This information is useful when estimating the degree to which overall perfusion is compromised for each leg. However, it has been demonstrated that the ABI calculation using the average of the dorsalis pedis and posterior tibial artery pressures correlates most closely with functional impairment in people with PAD [24]. Using the lowest of the dorsalis pedis and posterior tibial pressures to calculate the ABI in each leg maximizes sensitivity of the ABI for the diagnosis of PAD [25] but is associated with lower specificity.

Association of PAD with Increased Risk of Mortality and Cardiovascular Events

It is well established that people with PAD have higher rates of all-cause mortality and cardiovascular events, compared to people without PAD [2, 26]. This association has been demonstrated in multiple observational studies both from community-dwelling settings and from medical center settings. To illustrate the association of the ABI with all-cause and cardiovascular mortality, the ABI Collaboration team of investigators combined data from 16 population-based observational studies that collected data on ABI and subsequent occurrence of cardiovascular events and mortality [26]. The meta-analysis included 24,955 men and 23,339 women with ABI values and 480,325 person years of follow-up [26]. Among men, cardiovascular mortality rates at 10-year follow-up were 18.7% for men with ABI < 0.90 vs. 4.4% for men with a normal ABI value (hazard ratio (HR) = 4.2, 95% confidence interval (CI) = 3.3–5.4) [26]. For women, cardiovascular mortality rates at 10-year follow-up were 12.6% among women with ABI < 0.90 and 4.1% in women with a normal ABI (HR = 3.5, 95% CI = 2.4–5.1) [26]. When men and women were stratified by Framingham Risk Score (FRS), an ABI < 0.90 was associated with an approximately twofold increased risk of 10-year all-cause mortality, cardiovascular

mortality, and coronary event rate, compared to normal ABI values. These and other data demonstrate that the ABI is both an important diagnostic tool for detecting PAD and also an important prognostic tool with regard to future cardiovascular risk. An advantage of the ABI compared to other measures of PAD is that it is a simple, noninvasive, and relatively inexpensive test. However, the ABI may be insensitive to detecting PAD when lower extremity arteries are affected by medial calcinosis, which is common in older people and in people with diabetes.

PAD and Lower Extremity Functional Impairment

Because PAD blocks oxygenated blood perfusion of lower extremity skeletal muscle during walking activity, oxygen requirements during activity exceed oxygen supply to lower extremity muscle, resulting in ischemic leg symptoms and/or weakness of the lower extremities on exertion. Consistent with this phenomenon, people with PAD have greater functional impairment, poorer physical activity levels, and higher rates of mobility loss than people without PAD [3–5, 16, 27–29]. These associations were demonstrated in the Walking and Leg Circulation Study (WALCS), in which 726 men and women age 55 and older with and without PAD underwent functional testing at baseline and were followed longitudinally with annual study visits, to document changes in mobility and walking performance over time [3, 27]. At baseline, compared to individuals with a normal ABI value, those with ABI < 0.50 were 11.7 times more likely to be unable to walk for 6 minutes without stopping, and those with an ABI of 0.70–0.90 were 2.7 times more likely to be unable to walk for 6 minutes without stopping [16]. At 5-year follow-up, participants with severe PAD in the WALCS cohort were 4.2 times more likely, and those with mild PAD were 3.2 times more likely to develop mobility loss, defined as the inability to walk ¼ mile or walk up 1 flight of stairs without assistance, compared to people without PAD [28]. These associations were independent of age, comorbidities, and other confounders. Furthermore, functional impairment and functional decline occurs even among people with PAD who report no exertional leg symptoms [3–5, 29]. The fact that many patients with PAD restrict their physical activity or slow their walking speed to avoid exertional ischemic leg symptoms is likely to further contribute to functional impairment and decline in people with PAD.

Therapeutic Interventions for People with PAD

Therapeutic strategies for people with PAD should focus on preventing cardiovascular events and improving functional impairment and preventing functional decline. Over the past 25 years, greater progress has been made in preventing cardiovascular events than in improving walking impairment or preventing mobility loss in people with PAD. Quitting smoking is associated with lower rates of critical

limb ischemia and cardiovascular event rates. Therefore, all patients with PAD who continue to smoke cigarettes should be helped to quit smoking. Clinical practice guidelines for people with PAD recommend antiplatelet therapy and treatment with a potent statin to prevent cardiovascular events [30]. Some evidence suggests that clopidogrel is more efficacious than aspirin for preventing cardiovascular events in people with PAD [31]. Recent evidence supports prescription of low-dose rivaroxaban (2.5 mg twice daily) in combination with low-dose aspirin in patients who have PAD and concomitant coronary artery disease and are high risk for cardiac and ischemic limb events [31]. Recent evidence suggests that adding vorapaxar to aspirin or clopidogrel can prevent progression to ischemic limb events including critical limb ischemia or acute limb ischemia [31].

Therapeutic Interventions for Improving Functional Performance and Preventing Functional Decline

Few medical therapies have been identified that improve walking performance in people PAD. In 2019, only two medications, cilostazol and pentoxifylline, have been FDA approved for treating PAD-associated ischemic symptoms. However, benefits from cilostazol are modest, improving treadmill walking performance by only approximately 25–40% [32, 33]. Side effects are common and include palpitations, dizziness, headaches, and diarrhea [32, 33]. In one study, 20% of patients discontinued cilostazol within 3 months [30]. Pentoxifylline does not improve walking performance meaningfully more than placebo, and the most recent clinical practice guidelines recommend against using pentoxifylline, due to lack of efficacy [30].

Supervised treadmill exercise is currently considered the most effective medical therapy for improving walking performance in people with PAD [34]. Based on consistent clinical trial evidence, demonstrating improved treadmill walking performance in response to supervised treadmill exercise interventions, in 2017, the Centers for Medicare and Medicaid Services (CMS) published a decision memorandum describing their intent to cover supervised exercise therapy for symptomatic peripheral artery disease. CMS now pays for up to three exercise sessions per week lasting 30–60 minutes per session for a duration of 12 weeks [34]. The exercise must take place in a hospital or outpatient hospital setting and must be delivered by qualified personnel trained with training in exercise therapy for patients with PAD. While the CMS decision to cover supervised exercise should increase access to this effective intervention, many patients with PAD find it burdensome to travel for supervised exercise three times weekly [35]. Furthermore, gains from supervised exercise may be lost, 6 months after completion of a supervised exercise program [36]. Alternative approaches to help patients with PAD adhere to walking exercise regimens are needed.

Home-based walking exercise avoids the time, effort, and cost associated with travel to a medical center for supervised exercise. For these reasons, home-based walking exercise has the potential to be more accessible and acceptable to patients

with PAD than supervised exercise programs. However, not all home-based exercise interventions have been effective [37, 38]. Recent evidence suggests that effective home-based exercise interventions require incorporation of behavioral methods and occasional medical center visits, to encourage adherence to the walking exercise program at home.

Conclusion

PAD is common, affecting approximately 10–15% of men and women age 65 and older. PAD will be increasingly common as the population lives longer with chronic disease. PAD is frequently underdiagnosed, in part because patients with PAD often report no exertional leg symptoms or have leg symptoms that are not consistent with classical intermittent claudication. The therapeutic approach to PAD consists of medical therapies to prevent cardiovascular events and exercise interventions to improve walking ability and prevent mobility loss. While the recent CMS determination to cover supervised exercise for people with PAD should increase access to this therapy, effective home-based exercise strategies that do not require frequent travel to a hospital-based exercise center are needed to maximize uptake of exercise activity by people with PAD.

References

1. Fowkes FG, Rudan D, Rudan I, Aboyans V, Denenberg JO, McDermott MM, et al. Comparison of global estimates of prevalence and risk factors for peripheral artery disease in 2000 and 2010: a systematic review and analysis. Lancet. 2013;382(9901):1329–40.
2. Benjamin EJ, Blaha MJ, Chiuve SE, Cushman M, Das SR, Deo R, et al. Heart disease and stroke statistics—2017 update: a report from the American Heart Association. Circulation. 2017;135:e146–603.
3. McDermott MM, Greenland P, Liu K, Guralnik JM, Criqui MH, Dolan NC, et al. Leg symptoms in peripheral arterial disease: associated clinical characteristics and functional impairment. JAMA. 2001;286(13):1599–606.
4. McDermott MM, Applegate WB, Bonds DE, Buford TW, Church T, Espeland MA, et al. Ankle brachial index values, leg symptoms, and functional performance among community-dwelling older men and women in the lifestyle interventions and independence for elders study. J Am Heart Assoc. 2013;2(6):e000257.
5. McDermott MM. Lower extremity manifestations of peripheral artery disease: the pathophysiologic and functional implications of leg ischemia. Circ Res. 2015;116(9):1540–50.
6. McDermott MM, Liu K, Criqui MH, Ruth K, Goff D, Saad MF, et al. Ankle-brachial index and subclinical cardiac and carotid disease: the multi-ethnic study of atherosclerosis. Am J Epidemiol. 2005;162(1):33–41.
7. Criqui MH, McClelland RL, McDermott MM, Allison MA, Blumenthal RS, Aboyans V, et al. The ankle-brachial index and incident cardiovascular events in the MESA (Multi-ethnic study of atherosclerosis). J Am Coll Cardiol. 2010;56(18):1506–12.
8. Criqui MH, Aboyans V. Epidemiology of peripheral artery disease. Circ Res. 2015;116(9):1509–26.

9. Allison MA, Ho E, Denenberg JO, Langer RD, Newman AB, Fabsitz RR, et al. Ethnic-specific prevalence of peripheral arterial disease in the United States. Am J Prev Med. 2007;32(4):328–33.
10. Fowkes FG, Housley E, Riemersma RA, Macintyre CC, Cawood EH, Prescott RJ, et al. Smoking, lipids, glucose intolerance, and blood pressure as risk factors for peripheral atherosclerosis compared with ischemic heart disease in the Edinburgh artery study. Am J Epidemiol. 1992;135(4):331–40.
11. Kannel WB. Risk factors for atherosclerotic cardiovascular outcomes in different arterial territories. J Cardiovasc Risk. 1994;1(4):333–9.
12. Joosten MM, Pai JK, Bertoia ML, Rimm EB, Spiegelman D, Mittleman MA, et al. Associations between conventional cardiovascular risk factors and risk of peripheral artery disease. JAMA. 2012;308(16):1660–7.
13. Jude EB, Oyibo SO, Chalmers N, Boulton AJ. Peripheral arterial disease in diabetic and non-diabetic patients: a comparison of severity and outcome. Diabetes Care. 2001;24(8):1433–7.
14. Haltmayer M, Mueller T, Horvath W, Luft C, Poelz W, Haidinger D. Impact of atherosclerotic risk factors on the anatomical distribution of peripheral arterial disease. Int Angiol. 2001;20(3):200–7.
15. Newman AB, Siscovick DS, Manolio TA, Polak J, Fried LP, Borhani NO, et al. Ankle-arm index as a measure of atherosclerosis in the Cardiovascular Health Study(CHS) Collaborative Research Group. Circulation. 1993;88(3):837–45.
16. McDermott MM, Fried L, Simonsick E, Ling S, Guralnik JM. Asymptomatic peripheral arterial disease is independently associated with impaired lower extremity functioning: the Women's Health and Aging Study. Circulation. 2000;101(9):1007–12.
17. Rose GA. The diagnosis of ischemic heart pain and intermittent claudication in field surveys. Bull World Health Organ. 1962;27:645–58.
18. Criqui MH, Denenberg JO, Bird CE, Fronek A, Klauber MR, Langer RD. The correlation between symptoms and non-invasive test results in patients referred for peripheral arterial disease testing. Vasc Med. 1996;1(1):65–71.
19. McDermott MM, Greenland P, Liu K, Guralnik JM, Celic L, Criqui MH, et al. The ankle brachial index is associated with leg function and physical activity: the Walking and Leg Circulation Study. Ann Intern Med. 2002;136(12):873–83.
20. Aboyans V, Criqui MH, Abraham P, Allison MA, Creager MA, Diehm C, et al. Measurement and interpretation of the ankle-brachial index: a scientific statement from the American Heart Association. Circulation. 2012;126(24):2890–909.
21. Lijmer JG, Hunink MGM, van den Dungen JL, Smit AJ. ROC analyses of noninvasive tests for peripheral arterial disease. Ultrasound Med Biol. 1996;22(4):391–8.
22. Guo X, Li J, Paang W, Zhao M, Luo Y, Sun Y, et al. Sensitivity and specificity of ankle-brachial index for detecting angiographic stenosis of peripheral arteries. Circ J. 2008;72(4):605–10.
23. Ouriel K, McDonnell AE, Metz CE, Zarinss CK. Critical evaluation of stress testing in the diagnosis of peripheral vascular disease. Surgery. 1982;91(6):686–93.
24. McDermott MM, Criqui MH, Liu K, Guralnik JM, Greenland P, Martin GJ, et al. Lower ankle/brachial index, as calculated by averaging the dorsalis pedis and posterior tibial pressure, and lower extremity functioning in peripheral arterial disease. J Vasc Surg. 2000;32(6):1164–71.
25. Nead KT, Cooke JP, Olin JW, Leeper NJ. Alternative ankle-brachial index method identifies additional at-risk individuals. J Am Coll Cardiol. 2013;62(6):553–9.
26. Ankle Brachial Index Collaboration, Fowkes FG, Murray GD, Butcher I, Heald CL, Lee RJ, et al. Ankle brachial index combined with Framingham Risk Score to predict cardiovascular events and mortality: a meta-analysis. JAMA. 2008;300(2):197–208.
27. McDermott MM, Liu K, Greenland P, Guralnik JM, Criqui MH, Chan C, et al. Functional decline in peripheral arterial disease: associations with the ankle brachial index and leg symptoms. JAMA. 2004;292(4):453–61.
28. McDermott MM, Guralnik JM, Tian L, Liu K, Ferrucci L, Liao Y, et al. Associations of borderline and low normal ankle-brachial index values with functional decline at 5-year follow-up: the WALCS (Walking and Leg Circulation Study). J Am Coll Cardiol. 2009;53(12):1056–62.

29. McDermott MM, Ferrucci L, Liu K, Guralnik JM, Tian L, Liao Y, et al. Leg symptom categories and rates of mobility decline in peripheral artery disease. J Am Geriatr Soc. 2010;58(7):1256–62.
30. Gerhard-Herman MD, Gornik HL, Barrett C, Barshes NR, Corriere MA, Drachman DE, et al. 2016 AHA/ACC guideline on the management of patients with peripheral artery disease: executive summary: a report of the American College of Cardiology/American Heart Association task force on clinical practice guidelines. Circulation. 2017;135:e686–785.
31. Hess CN, Hiatt WR. Antithrombotic therapy for peripheral artery disease in 2018. JAMA. 2018;319(22):2329–30.
32. McDermott MM. Exercise rehabilitation for peripheral artery disease: a review. J Cardiopulm Rehabil Prev. 2018;38(2):63–9.
33. McDermott MM. Medical management of functional impairment in peripheral artery disease: a review. Prog Cardiovasc Dis. 2018;60(6):586–92.
34. McDermott MM. Exercise training for intermittent claudication. J Vasc Surg. 2017;66(5):1612–20.
35. Harwood AE, Smith GE, Cayton T, Broadbent E, Chetter IC. A systematic review of the uptake and adherence rates to supervised exercise programs in patients with intermittent claudication. Ann Vasc Surg. 2016;34:280–9.
36. McDermott MM, Kibbe MR, Guralnik JM, Ferrucci L, Criqui MH, Domanchuk K, et al. Durability of benefits from supervised treadmill exercise in patients with peripheral artery disease. J Am Heart Assoc. 2019;8(1):e009380.
37. McDermott MM, Spring B, Berger JS, Treat-Jacobson D, Conte MS, Creager MA, et al. Effect of a home-based exercise intervention of wearable technology and telephone coaching on walking performance in peripheral artery disease: the HONOR Randomized Clinical Trial. JAMA. 2018;319(16):1665–76.
38. McDermott MM, Ferrucci L, Tian L, Guralnik JM, Lloyd-Jones D, Kibbe MR, et al. Effect of granulocyte-macrophage colony-stimulating factor with or without supervised exercise on walking performance in patients with peripheral artery disease: the PROPEL randomized clinical trial. JAMA. 2017;318(21):2089–98.

Chapter 8
Current Imaging Approaches and Challenges in the Assessment of Peripheral Artery Disease

Liisa L. Bergmann and Christopher J. François

Introduction

The current standard of care for imaging peripheral artery wall pathology predominantly focuses on quantifying the vascular lumen size using digital subtraction angiography (DSA), computed tomography angiography (CTA), and magnetic resonance angiography (MRA). In larger, central vessels, magnetic resonance can also be used to measure velocity and volume of flow. Velocity of blood flow can also be measured using Doppler ultrasound (US), in addition to visualizing vessel size with grayscale US; however, vascular wall calcifications create artifacts that limit visualization of intraluminal flow. US is highly user dependent, and even when a skilled technician is available, the examination of the arterial system of an extremity is time-consuming. Interestingly, calcium possibly poses the greatest challenge in visualizing extremity vessel walls and lumens, as it may result in imaging artifacts in other modalities also.

This chapter will review standard peripheral artery imaging paradigms, focusing on peripheral arterial disease and acute limb ischemia, the most common and emergent peripheral vessel wall diseases in the United States, respectively. Conventional standard imaging paradigms and their benefits and limitations will be discussed, predominantly in the context of these common conditions.

L. L. Bergmann · C. J. François (✉)
Cardiovascular Imaging Section, Department of Radiology, University of Wisconsin School of Medicine and Public Health, Madison, WI, USA
e-mail: CFrancois@uwhealth.org

C. Yuan et al. (eds.), *Vessel Based Imaging Techniques*,
https://doi.org/10.1007/978-3-030-25249-6_8

Peripheral Arterial Disease and Acute Limb Ischemia

Background

Approximately 8.5 million Americans (7.2%) age 40 years or older are estimated to have peripheral arterial disease (PAD), defined as a low ankle-brachial index (<0.9) in 6.5 million and ABI > 0.9 after revascularization therapy or false-negative ABI > 0.9 in an additional 2 million [1, 2]. Based on 2003–2008 nationwide ICD coding from large employers, Medicare and Medicaid, the incidence of PAD in adults over 40 years old was over 12% [2, 3]. At least 1.6 million (approximately 25% of patients with low ABI) of these are estimated to have severe PAD, with ABI < 0.7 [1, 2]. Approximately 1.3% of American adults over 40 years of age have critical limb ischemia [2, 3], the most severe presentation of PAD.

The etiology of peripheral arterial disease is atherosclerosis, due to hardening and thickening of arterial walls. This process is exacerbated by smoking, diabetes mellitus, and hypertension, especially in the arterioles. Ultimately vessel lumens narrow so that blood flow becomes turbulent. Emboli may acutely and completely obstruct already narrowed arteries. The most severe presentation is acute limb ischemia (ALI), also known as a cold limb, when a vessel lumen is sufficiently obstructed so that blood flow approaches zero.

Acute limb ischemia is most commonly caused by complete arterial occlusion [4] associated with PAD; however, there are other causes. In a young and otherwise healthy person, cystic adventitial disease may cause ALI with markedly decreased or absent peripheral pulses. Trauma and prolonged exposure are usually clinically obvious. In traumatic posterior dislocation of the knee, the popliteal artery and distal pulses must be carefully evaluated. Patients with total venous outflow occlusion, an uncommon cause of ALI, usually present with the precursor to venous gangrene, known as “phlegmasia cerulea dolens,” or swollen, dusky blue, and painful extremity; the presence of peripheral pulses readily excludes arterial occlusion as the etiology [4].

Ankle-Brachial Index and Ultrasound

Ankle-brachial index, toe brachial index, and handheld Doppler can be used at the bedside to support a diagnosis of ALI [4]. Thermographic (infrared camera) attachments for multiple brands of smartphones are commercially available to the general public, for the cost of approximately US $200.00, and provide another option for noninvasive bedside evaluation of distal extremity perfusion [5]. Although all of the bedside evaluations in this paragraph may aid in prompt clinical diagnosis of ALI, they are all insufficient for arterial mapping and interventional planning. Despite its wide availability, the role of ultrasound and Doppler is limited in ALI for several

reasons. Even when a skilled user is available, the exam of the arterial system of an extremity is rather time-consuming. Also vascular calcifications will prevent visualization of intraluminal flow due to artifact.

Catheter Angiography

When there is high clinical suspicion for ALI, catheter angiography, also known as x-ray angiography (XA) and digital subtraction angiography (DSA) which are used interchangeably throughout this chapter, remains the gold standard, because of its high resolution and because diagnosis and treatment are possible in the same procedure. The American College of Radiology (ACR) recommends DSA when there is an intermediate level of suspicion of an acutely obstructed artery [4]. Despite its widespread availability, XA poses multiple risks to the patient. There is the possibility of iodinated contrast injury to the kidneys, which can be decreased by patient selection. The invasive nature of XA, even when the diagnostic portion of the procedure ultimately demonstrates no need for interventional treatment, poses the risk of numerous complications, including but not limited to hemorrhage, pseudoaneurysm, dissection, subcutaneous hematoma, and infection. Additionally, exposure to ionizing radiation poses both risks of deterministic injury and increased risk of cancer over the patient's lifetime.

Computed Tomography Angiography

Computed tomography angiography (CTA) is also commonly used for diagnostic imaging in acute limb ischemia and/or peripheral arterial disease due to its wide availability and rapid acquisition times (Fig. 8.1). ACR guidelines indicate that CTA is usually appropriate to evaluate the sudden onset of a cold, painful limb, the same as magnetic resonance angiography (MRA) without and with contrast [4]. Clinical peripheral CTA typically consists of an initial non-contrast acquisition to assist with identification of calcified plaques that can be difficult to distinguish from enhancing lumen on the angiographic images. The CTA acquisition is performed during the first-pass of intravenous contrast through the peripheral arteries, scanning from cephalad to caudal. Timing of image acquisition can be based on real-time tracking of the contrast bolus or based on a test bolus scan performed prior to the CTA to determine the arrival of contrast in the peripheral arteries.

Despite its frequent use, CTA is imperfect and does pose some risk to patients. Calcified atherosclerosis can lead to difficulties in diagnosis in CTA (Fig. 8.2), specifically the overestimation of calcium plaque size and underestimation of vessel lumen size due to calcium blooming artifact, which is predominantly partial volume averaging artifact with some influence from motion artifact. Iodinated contrast

Fig. 8.1 CTA runoff including abdominal aorta, pelvic arteries, and arteries in the lower extremities can typically be performed in less than 20 seconds of scan time

necessary for this examination is associated with the risk of contrast nephropathy. Also, each exposure to ionizing radiation brings with it a slightly increased risk of stoichiometric effects, including cancer.

Magnetic Resonance Angiography

Appropriate catheters and guidewires for magnetic resonance image-guided intravascular procedures are under development [6, 7]; however until these are widely available, magnetic resonance imaging will continue to be used predominantly for diagnostic imaging in PAD and ALI. Magnetic resonance angiography (MRA)

Fig. 8.2 Calcified plaque can limit the diagnostic quality of CTA. Calcified plaques (solid arrows) in the superficial femoral arteries appear to cause severe bilateral stenosis. Non-calcified plaque (dashed arrows) do not cause blooming artifact

without and with IV contrast in suspected limb ischemia is considered usually appropriate, according to the ACR appropriateness criteria [4].

In a 2013 meta-analysis, no significant difference in sensitivity or specificity was found when comparing CTA to contrast-enhanced (CE) MRA [8]; this was especially true when dedicated additional CE MRA imaging of the calf was performed. In the acute setting, however, the use of MRA may be restricted by the lack of availability of an MR technician and/or MRI table time. Assuming a technician and the magnet itself are available, radiologists may consider non-contrast-enhanced MRA as well as a post-contrast T1-weighted MRA. T2-weighted magnetic resonance imaging without, or prior to, contrast would demonstrate some secondary signs of acute limb ischemia, such as soft tissue edema.

High-temporal and high-spatial resolution time-resolved contrast-enhanced MRA techniques are widely used clinically [9]. These sequences were developed in the late 1990s [10, 11]. Clinically, these time-resolved contrast-enhanced MRA sequences are used to acquire high-resolution vascular images in the calves (Fig. 8.3a) followed by traditional 3D contrast-enhanced MRA in the pelvis (Fig. 8.3b) and thighs (Fig. 8.3c). This approach is often referred to as a "hybrid" peripheral MRA technique and results in consistent high-quality arterial imaging without venous contamination [12, 13].

The ACR notes that MRA without IV contrast is "sometimes appropriate," particularly in patients with estimated glomerular filtration rate (eGFR) of <30 mL/min [4]. However, no unconfounded case of nephrogenic systemic fibrosis (NSF) was found in over 1400 high-risk inpatients who received gadobenate dimeglumine (MultiHance) [14]. Also, there was no case of NSF in 401 patients with decreased renal function, 303 of whom were dependent on dialysis, after administration of gadobenate dimeglumine [15]. Since 2008, only one case of NSF has been reported

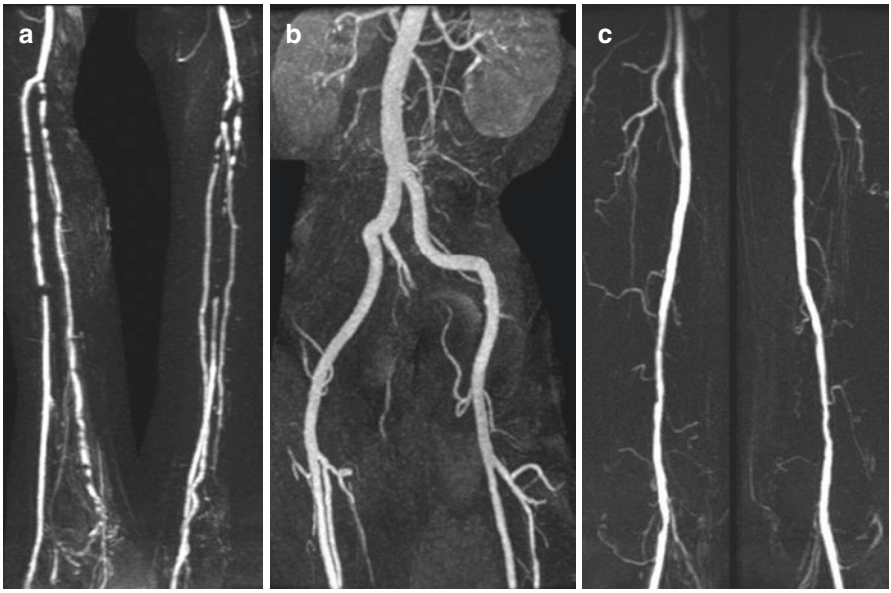

Fig. 8.3 Hybrid peripheral MRA approach consists of (**a**) time-resolved contrast-enhanced (CE) MRA in the calves followed by (**b**) 3D CE MRA in the pelvis and (**c**) 3D CE MRA in the thighs

with any gadolinium-based contrast agent, and this was in a patient with normal eGFR [16]. American College of Radiology classifies gadolinium-based contrast agents (GBCAs) as follows: Group I GBCAs are associated with the greatest number of NSF cases; Group II GBCAs are associated with few, if any, unconfounded cases of NSF; and Group III GBCAs have limited data however are also associated with few, if any, unconfounded cases of NSF [17].

Concern for nephrogenic systemic fibrosis (NSF) after gadolinium-based contrast administration heightened interest in non-contrast MRA sequences. Non-contrast-enhanced (NE) MRA eliminates the exceedingly low possibility of NSF; however, our institution has identified zero cases of NSF since gadodiamide was removed from the gadolinium-based contrast agent (GBCA) formulary [18]. NE MRA also eliminates gadolinium retention and any as-of-yet-unknown associated risks [19, 20]. Patient preference may be to avoid GBCAs due to recent lay press coverage of gadolinium deposition and new symptoms following GBCA exposure, the US Food and Drug Administration issuance of a new class warning regarding the occurrence of gadolinium deposition, and the European Medicines Agency recommending suspension of use of some GBCAs [21, 22]. NE MRA has greatly improved in the last decade; however, challenges still remain.

The limitations of NE MRA sequences commercially available in 2011 were well summarized by Hodnett et al. [23]. Gated 2D time-of-flight imaging requires excessive scan time and results in less than ideal image quality often due to artifacts attributed to in-plane flow. Subtraction techniques are unfortunately highly sensitive to patient motion and require precise timing of systolic imaging during the peak velocity of blood flow for the vessel segment being images, “which is both patient-

and operator-dependent" [23]. Electrocardiogram (ECG)-gated 3D half-Fourier fast spin echo (FSE) is one such subtraction technique, with which Lim et al. were technically successful just over half the time [24, 25]. Fan et al. explored flow-sensitive dephasing (FSD)-prepared balanced steady-state free precession (SSFP); however this also requires long imaging time and image subtraction, both of which increase sensitivity to motion artifacts [26].

As described in multiple 2011 publications, Hodnett et al. explored the use of quiescent-interval single-shot (QISS) MRA, which was not commercially available at the time [23, 27, 28]. QISS NE MRA at 1.5 Tesla has demonstrated high diagnostic accuracy compared with DSA and improved visualization of heavily calcified arteries in the lower extremities when compared to CTA [29]. In 3 Tesla magnetic fields, NE QISS MRA demonstrated similar sensitivity and specificity to CTA overall; however, NE QISS MRA sensitivity was significantly higher than CTA in heavily calcified segments [30]. These various MR sequences are described in more detail below.

In 2011, QISS, MRA images of the arteries from the aortic bifurcation to the feet were obtained in approximately 6 minutes. These two-dimensional images were obtained sequentially via ECG-gated balanced steady-state free precession acquisition [27]. Each thin-slice two-dimensional image is obtained during diastole, after electromagnetic pulses eliminate signal from soft tissue in the slice as well as from anticipated venous inflow. Imaged arterial signal intensity thus depends only upon arterial inflow time, making heart rate and arrhythmias essentially irrelevant. Hodnett et al. found this technique interchangeable with MRA with contrast and with DSA due to similar results for all three modalities attributed to short table time, motion insensitivity, and lack of adjustments required for each patient [23, 27].

Liu et al. provide an excellent summary of the current challenges facing the three main non-contrast-enhanced (NE) MRA techniques: quiescent-interval single-shot (QISS), described above; flow-sensitive dephasing (FSD)-prepared balanced steady-state free precession (SSFP), referred to simply as FSD SSFP; and non-contrast angiography of the arteries and veins sampling perfection with application-optimized contrast by using different flip angle evaluation, called [31].

Ward et al. compared QISS and NATIVE SPACE to contrast-enhanced MRA, time-resolved in the calf only, at 1.5 Tesla, and found QISS to have greater specificity and image quality than NATIVE SPACE [32]. Also, poor quality of multiple NATIVE SPACE images resulted in two of two reading radiologists to incorrectly identify segmental occlusion which was not present on QISS or contrast-enhanced MRA. CE MRA technique included "time-resolved coronal fast low angle shot-based sequence (TWIST – time-resolved angiography with interleaved stochastic trajectories) … [and] stepping table MRA for the remainder of the peripheral vascular system" [32].

Hansmann compared QISS at 3 T to contrast-enhanced MRA and also to digital subtraction angiography [33]. Similar to Ward's methodology, CE MRA was obtained with time-resolution only in the calf. Due to time-consuming shimming, QISS acquisition time at 3 T was markedly increased to approximately 18 minutes. Motion artifact was attributed to this increased imaging time. QISS imaging was as sensitive to stenosis greater than 50% as contrast-enhanced MRA, however, and in several instances better correlated with DSA.

Zhang et al. [34] compared NE MRA to contrast-enhanced CE MRA obtained at 3.0 T magnetic field strength. NE MRA images were obtained using a flow-sensitive dephasing (FSD) technique that depends on magnitude subtraction of two images obtained sequentially via ECG-gated, 3D balanced SSFP acquisition. Dark artery measurements were obtained during systole and bright artery measurement obtained during diastole, when relatively slow arterial flow results in what is similar to a high T2 signal intensity. The images were obtained over 4–5 minutes. Magnitude subtraction of the two images results in easy visualization of the arteries, without venous contamination and without much visualization of the soft tissues. Aside from the relatively longer table time, dark artery image dependence on univector arterial flow velocity resulted in artifact resembling stenosis in vessel segments oriented transversely. Contrast-enhanced MRA images were obtained using 3D gradient-echo (fast low-angle shot, or FLASH) sequence in three coronal images both prior to and following intravenous contrast administration after contrast arrived in the abdominal aorta as measured using a 2D gradient-echo sequence. These images were obtained in approximately 1 minute; however, they were not time-resolved and were found to have venous contamination. Non-contrast-enhanced MRA overestimated stenoses in comparison to contrast MRA.

Liu et al. compared imaging of calf vessels using non-contrast-enhanced (NE) MRA also using FSD 3D SSFP acquisition at 1.5 T to contrast-enhanced (CE) MRA [35] and at 3.0 T to CE MRA as well as DSA [31]. In both studies, CE MRA were obtained using the same sequences as Zhang et al. [34], again which were not time-resolved. Similarly, NE MRA overestimated stenoses compared to CE MRA, and similarly, venous contamination was sometimes problematic in CE MRA images.

Zhang et al. [36] also compared two NE MRA sequences of the calf arteries, FSD SSFP and QISS, with contrast-enhanced MRA at 1.5 T. ECG-gated QISS required about 4-minute acquisition time, only slightly less than FSD SSFP acquisition time. FSD SSFP had slightly higher specificity than QISS, but otherwise the two NE MRA sequences had similar sensitivity and negative predictive value for stenosis greater than 50%. CE MRA was approximately 1-minute acquisition time.

In summary, although much progress has been made in non-contrast-enhanced MRA of the peripheral arteries, at present we continue to favor MRA with contrast over non-contrast-enhanced MRA FSD SSFP sequence, due to decreased time of acquisition, decreased motion-artifact sensitivity, and lack of heart rate and arrhythmia dependence. The addition of time-resolution contrast-enhanced MRA would reduce or eliminate venous contamination noted in contrast-enhanced MRA obtained using 3D gradient-echo (fast low-angle shot, FLASH) sequence.

The Challenges Facing Current Imaging Paradigms

Like any medical test, ideally every imaging test ordered would be appropriate to the relevant diagnostic question, after a thorough patient interview and physical examination. The ideal imaging test would minimize risk to the patients – this

would require it to be noninvasive and expose a patient to minimal or no ionizing radiation. The test would be reliable with rapid and consistent results.

In peripheral arterial disease, an ideal imaging test would clearly demonstrate vessel wall thickness, vessel wall elasticity, and direction, rate, and volume of intraluminal flow. Also, improved means of visualizing the perfusion of adjacent tissue would be helpful to clinical decision-making. Finally, an ideal test would provide information that enables us to predict future progression of disease, even in an asymptomatic patient.

In peripheral arterial disease, we currently prefer MRA without and with contrast, including time-resolved imaging. CTA with iodinated contrast remains a reliable and fast diagnostic option; however, this poses increased risk to the kidneys and ionizing radiation exposure relative to contrast-enhanced MRA. There is ongoing improvement of non-contrast-enhanced MRA for clinical evaluation of peripheral arterial disease. Techniques for evaluating microvasculature in peripheral arterial disease that are not yet commonly used in the clinical setting include contrast-enhanced ultrasound, contrast-enhanced MRI perfusion imaging, non-contrast-enhanced blood-oxygen-level-dependent (BOLD) and arterial spin labeling (ASL) MRI, and magnetic resonance spectroscopy with 31-phosphorus [37, 38].

References

1. Centers for Disease, C. and Prevention. Lower extremity disease among persons aged > or =40 years with and without diabetes--United States, 1999-2002. MMWR Morb Mortal Wkly Rep. 2005;54(45):1158–60.
2. Benjamin EJ, et al. Heart disease and stroke statistics-2018 update: a report from the American Heart Association. Circulation. 2018;137(12):e67–e492.
3. Nehler MR, et al. Epidemiology of peripheral arterial disease and critical limb ischemia in an insured national population. J Vasc Surg. 2014;60(3):686–95 e2.
4. Weiss CR, et al. ACR appropriateness criteria((R)) sudden onset of cold, painful leg. J Am Coll Radiol. 2017;14(5s):S307–s313.
5. Theuma F, Cassar K. The use of smartphone-attached thermography camera in diagnosis of acute lower limb ischemia. J Vasc Surg. 2018;67(4):1297.
6. Barkhausen J, et al. White paper: interventional MRI: current status and potential for development considering economic perspectives, Part 1: general application. Rofo. 2017;189(7):611–23.
7. Sedaghat F, Tuncali K. Enabling technology for MRI-guided intervention. Top Magn Reson Imaging. 2018;27(1):5–8.
8. Jens S, et al. Diagnostic performance of computed tomography angiography and contrast-enhanced magnetic resonance angiography in patients with critical limb ischaemia and intermittent claudication: systematic review and meta-analysis. Eur Radiol. 2013;23(11):3104–14.
9. Hadizadeh DR, et al. High temporal and high spatial resolution MR angiography (4D-MRA). Rofo. 2014;186(9):847–59.
10. Korosec FR, et al. Time-resolved contrast-enhanced 3D MR angiography. Magn Reson Med. 1996;36(3):345–51.
11. Frayne R, et al. MR angiography with three-dimensional MR digital subtraction angiography. Top Magn Reson Imaging. 1996;8(6):366–88.

12. Pereles FS, et al. Accuracy of stepping-table lower extremity MR angiography with dual-level bolus timing and separate calf acquisition: hybrid peripheral MR angiography. Radiology. 2006;240(1):283–90.
13. Hansmann J, et al. Impact of time-resolved MRA on diagnostic accuracy in patients with symptomatic peripheral artery disease of the calf station. AJR Am J Roentgenol. 2013;201(6):1368–75.
14. Bruce R, et al. Incidence of nephrogenic systemic fibrosis using gadobenate dimeglumine in 1423 patients with renal insufficiency compared with gadodiamide. Investig Radiol. 2016;51(11):701–5.
15. Nandwana SB, et al. Gadobenate dimeglumine administration and nephrogenic systemic fibrosis: is there a real risk in patients with impaired renal function? Radiology. 2015;276(3):741–7.
16. Lohani S, et al. A unique case of nephrogenic systemic fibrosis from gadolinium exposure in a patient with normal eGFR. BMJ Case Rep. 2017;2017:bcr–2017.
17. ACR Committee on Drugs and Contrast Media. ACR manual on contrast media, version 10.3. 2018.
18. Reeder SB, Rowley HA, Sadowski EA. Updated NSF screening procedure at the University of Wisconsin. 2016; University of Wisconsin School of Medicine and Public Health: Department of Radiology. p. 1.
19. McDonald RJ, et al. Gadolinium retention: a research roadmap from the 2018 NIH/ACR/RSNA workshop on gadolinium chelates. Radiology. 2018;289(2):517–34.
20. Lyapustina T, et al. Evaluating the patient with reported gadolinium-associated illness. J Med Toxicol. 2019;15(1):36–44.
21. FDA Drug Safety Communication: FDA warns that gadolinium-based contrast agents (GBCAs) are retained in the body; requires new class warnings. 2018.
22. European Medicines Agency's final opinion confirms restrictions on use of linear gadolinium agents in body scans. 2017.
23. Hodnett PA, et al. Peripheral arterial disease in a symptomatic diabetic population: prospective comparison of rapid unenhanced MR angiography (MRA) with contrast-enhanced MRA. AJR Am J Roentgenol. 2011;197(6):1466–73.
24. Miyazaki M, Akahane M. Non-contrast enhanced MR angiography: established techniques. J Magn Reson Imaging. 2012;35(1):1–19.
25. Lim RP, et al. 3D nongadolinium-enhanced ECG-gated MRA of the distal lower extremities: preliminary clinical experience. J Magn Reson Imaging. 2008;28(1):181–9.
26. Fan Z, et al. 3D noncontrast MR angiography of the distal lower extremities using flow-sensitive dephasing (FSD)-prepared balanced SSFP. Magn Reson Med. 2009;62(6):1523–32.
27. Hodnett PA, et al. Evaluation of peripheral arterial disease with nonenhanced quiescent-interval single-shot MR angiography. Radiology. 2011;260(1):282–93.
28. Hodnett PA, et al. Evaluation of peripheral arterial disease with nonenhanced quiescent-interval single-shot MR angiography. Radiology. 2017;282(2):614.
29. Varga-Szemes A, et al. Accuracy of noncontrast quiescent-interval single-shot lower extremity MR angiography versus CT angiography for diagnosis of peripheral artery disease: comparison with digital subtraction angiography. JACC Cardiovasc Imaging. 2017;10(10 Pt A):1116–24.
30. Wu G, et al. The diagnostic value of non-contrast enhanced quiescent interval single shot (QISS) magnetic resonance angiography at 3T for lower extremity peripheral arterial disease, in comparison to CT angiography. J Cardiovasc Magn Reson. 2016;18(1):71.
31. Liu J, et al. Image quality and stenosis assessment of non-contrast-enhanced 3-T magnetic resonance angiography in patients with peripheral artery disease compared with contrast-enhanced magnetic resonance angiography and digital subtraction angiography. PLoS One. 2016;11(11):e0166467.
32. Ward EV, et al. Comparison of quiescent inflow single-shot and NATIVE SPACE for nonenhanced peripheral MR angiography. J Magn Reson Imaging. 2013;38(6):1531–8.
33. Hansmann J, et al. Nonenhanced ECG-gated quiescent-interval single shot MRA: image quality and stenosis assessment at 3 tesla compared with contrast-enhanced MRA and digital subtraction angiography. J Magn Reson Imaging. 2014;39(6):1486–93.

34. Zhang N, et al. Noncontrast MR angiography (MRA) of infragenual arteries using flow-sensitive dephasing (FSD)-prepared steady-state free precession (SSFP) at 3.0 Tesla: comparison with contrast-enhanced MRA. J Magn Reson Imaging. 2016;43(2):364–72.
35. Liu X, et al. Detection of infragenual arterial disease using non-contrast-enhanced MR angiography in patients with diabetes. J Magn Reson Imaging. 2014;40(6):1422–9.
36. Zhang N, et al. Non-contrast enhanced MR angiography (NCE-MRA) of the calf: a direct comparison between flow-sensitive dephasing (FSD) prepared Steady-State Free Precession (SSFP) and Quiescent-Interval Single-Shot (QISS) in patients with diabetes. PLoS One. 2015;10(6):e0128786.
37. Aschwanden M, et al. Assessing the end-organ in peripheral arterial occlusive disease-from contrast-enhanced ultrasound to blood-oxygen-level-dependent MR imaging. Cardiovasc Diagn Ther. 2014;4(2):165–72.
38. Pollak AW, Kramer CM. MRI in lower extremity peripheral arterial disease: recent advancements. Curr Cardiovasc Imaging Rep. 2013;6(1):55–60.

Chapter 9
Advanced Peripheral Artery Vessel Wall Imaging and Future Directions

Adrián I. Löffler and Christopher M. Kramer

In the field of peripheral arterial disease (PAD), the ankle-brachial index (ABI) is considered the gold standard imaging modality for initial screening or diagnosis of lower extremity PAD based on current clinical practice guidelines [1]. While the ABI is an excellent study for diagnosing peripheral arterial occlusion, it has limited utility for assessing arterial wall disease. Being able to directly measure plaque and peripheral arterial remodeling in arterial walls may be better suited for defining disease burden. It is widely recognized that PAD is more complicated than a flow-limiting process and that atheromatous plaque is a nidus for inflammation with consequent risk of plaque rupture [2]. A recent histopathologic study has suggested that atherothromboembolic disease is a primary feature of PAD [3]. We will review the current imaging techniques presently used for vessel wall imaging including intravascular ultrasound (IVUS), fluoro-deoxy-glucose positron emission tomography/computed tomography (FDG-PET/CT), and magnetic resonance imaging (MRI).

Intravascular Ultrasound (IVUS)

IVUS is an imaging technique that uses a transducer or probe attached to a catheter that generates real-time ultrasound waves and provides a 360-degree cross-sectional view of arteries [4]. Whereas angiography portrays only a 2D profile of the lumen,

A. I. Löffler
Division of Cardiovascular Medicine, University of Virginia Health System, Charlottesville, VA, USA
e-mail: al2ys@virginia.edu

C. M. Kramer (✉)
Division of Cardiovascular Medicine and Department of Radiology and Medical Imaging, University of Virginia Health System, Charlottesville, VA, USA
e-mail: ckramer@virginia.edu

C. Yuan et al. (eds.), *Vessel Based Imaging Techniques*,
https://doi.org/10.1007/978-3-030-25249-6_9

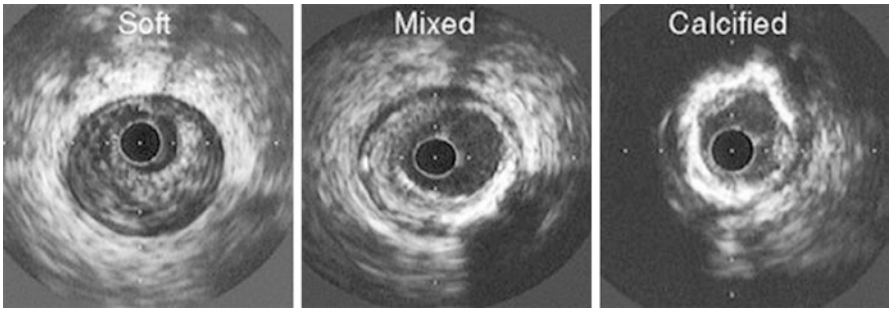

Fig. 9.1 Atheroma morphology by IVUS. Soft (left), mixed fibrous and calcified (center), and heavily calcified atheromas (right) are illustrated. (From Nissen and Yock [5]; with permission from Wolters Kluwer Health, Inc.)

ultrasound allows for real-time cross-sectional image acquisition of vessel wall atheromatous plaques, intimal thickening, media and adventitia (Fig. 9.1) [5]. IVUS can also be used to define plaque morphology (i.e., soft, fibrous, calcified, or mixed) and identify presence or absence of a lipid core in the plaque [6]. IVUS has been studied for measuring regression or regression of atherosclerosis and restenosis after percutaneous interventions [4, 7–9]. IVUS historically was the gold standard for quantitative and qualitative evaluation of the vascular wall and lumen [10]. However, IVUS is not suitable in the peripheral vasculature as approximately 50% of vessel segments aren't quantifiable due to extensive vessel wall calcifications resulting in dorsal echo extinction [10]. Another limitation is its invasiveness and higher costs as it requires an invasive peripheral angiogram.

Computed Tomography Angiography (CTA) and FDG-Positron Emission Tomography/CT (FDG-PET/CT)

CTA has the advantage of higher spatial resolution compared to ultrasound. Since the arrival of multidetector scanners and multiple cross-sectional imaging allowing for rapid acquisition times, the use of CTA has grown. CTA also allows for three-dimensional (3D) imaging of the peripheral arterial tree which can be useful when planning revascularization strategies. CTA has shown to be effective in identifying >50% stenotic lesions in PAD with a sensitivity of 95% and specificity of 96% [11]. The presence of dense focal calcifications in the arterial wall can lead to overestimation of the degree of stenosis [12]. Other limitations of CTA include the need for iodinated contrast and ionizing radiation exposure.

FDG-PET/CT can be used to evaluate atherosclerotic plaque composition in the superficial femoral artery [13]. PET utilizes positron-emitting radiotracers that encounter electrons in neighboring tissues that lead to annihilation reactions resulting in emission of gamma photons which are detected by scintillation detectors on the scanner. The regions of tracer uptake detected by PET need to be co-registered

with CT (PET/CT) or MRI (PET/MRI) to link the region of uptake with an anatomical location. The advantage of PET is that it can directly measure the metabolic processes within plaque [2]. Different radiotracers can be used to target and measure the distinct metabolic features of atherogenesis such as macrophage-mediated inflammatory change (^{18}F-fluorodeoxyglucose), hypoxia (^{18}F-fluoromisonidazole), and microcalcification (^{18}F-sodium fluoride) [2]. Figure 9.2 shows a highly calcified superficial femoral artery (SFA) on CT with the uptake of ^{18}F-sodium fluoride (^{18}F-NaF) on PET in the calcified plaque region of the vessel.

^{18}F-fluorodeoxyglucose (FDG) is the mainstay radioligand in PET imaging and thus has been the most commonly used radiotracer in atherosclerosis. FDG is an analogue of glucose which accumulates intracellularly via glucose transporter member (GLUT) 1 and 3 in proportion to demand for glucose. GLUT 1 and 3 are upregulated during atherogenesis due to hypoxia within the plaque core [2]. A small study of 20 patients underwent PET/CT of the iliac, femoral, and carotid arteries 90 minutes after ^{18}F-FDG administration with repeat imaging 2 weeks later [14].

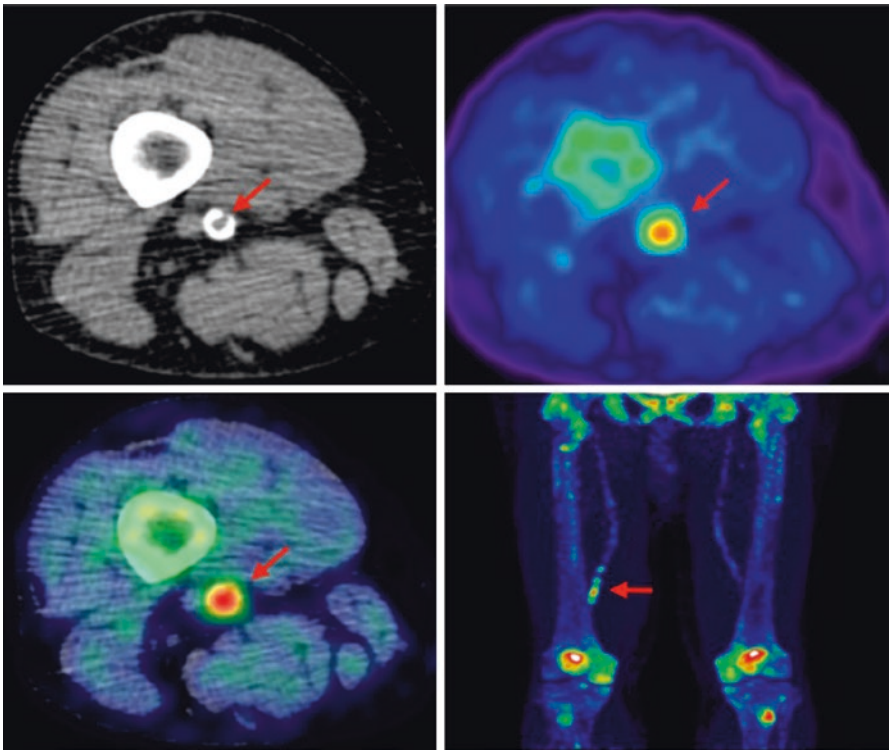

Fig. 9.2 Lower limb ^{18}F-NaF imaging: non-contrast CT (*top left*) with a rim of calcification of the vessel, ^{18}F-NaF PET (*top right*), and fused ^{18}F-NaF PET/CT (*bottom left*) of the superficial femoral artery (*arrow*) at the level of the adductor canal, demonstrating significant vessel uptake in this symptomatic patient. In addition, there is prominent uptake seen in the vessel at the same level on the coronal image (*bottom right*). (Reprinted from Evans et al. [2], page 7; http://creativecommons.org/licenses/by/4.0/; no changes were made)

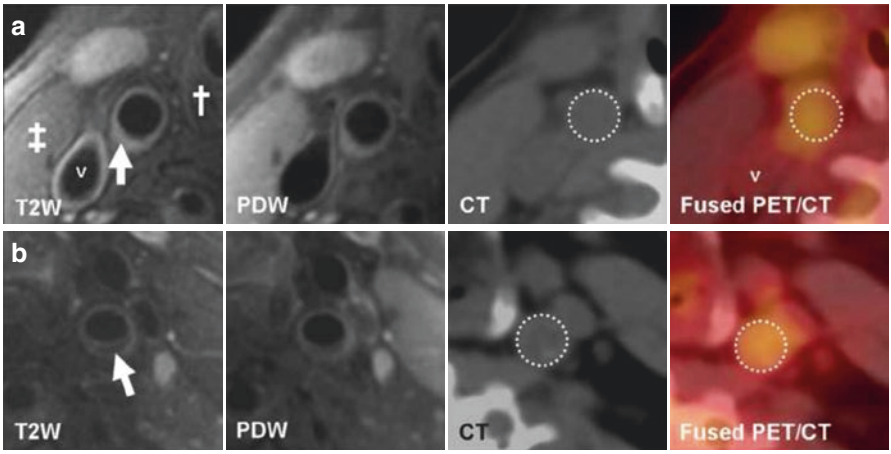

Fig. 9.3 (Reprinted from Silvera et al. [15]; with permission from Elsevier) (**a**) Transverse MR and FDG-PET/CT images demonstrating a collagen rich plaque of the right common carotid artery. The T2-weighted (T2W) image demonstrates the right common carotid artery (white arrow), the jugular vein ("v"), the sterno-cleido-mastoid muscle (‡) and the thyroid cartilage (†). Carotid artery wall appears hyperintense on T2W (white arrow) and on proton density weighted (PDW) images. CT confirms the absence of calcification in the artery wall. The right common carotid artery is displayed on the computed tomography (CT) and on the fused positron emission tomography/CT (PET/CT) images (white dashed circle). (**b**) Transverse MR images and corresponding FDG-PET/CT images indicate a carotid artery lipid-rich necrotic core plaque, hypointense on T2W (white arrow) and on PDW images. CT image demonstrates the absence of calcification. The white dashed circle demonstrates FDG uptake into the entire artery section on the PET/CT image

This demonstrated excellent reproducibility of ^{18}F-FDG uptake as a marker of inflammation within vessel wall plaque. This technique along with complementary MRI has been used to classify plaque into three different groups, collagen, lipid-rich necrotic core, and calcium, as shown in Fig. 9.3 [15].

Magnetic Resonance Imaging (MRI)

Contrast-Enhanced Techniques

Contrast-enhanced magnetic resonance angiography and CT angiography are both useful for diagnosing and assessing PAD; however, they don't provide information on arterial remodeling and can underestimate the extent of atherosclerosis [16]. Furthermore, contrast agents limit the use of both of these modalities in certain patients, including those with advanced chronic kidney disease. Below we will summarize different MRI techniques that have been developed for arterial wall assessment.

MRI has the advantage of lack of radiation exposure and thus can be used for serial arterial wall assessments. Technical advances have enabled improved spatial

resolution which permits imaging of structures smaller than 1 mm in diameter with MRI [10]. This paved the path for new studies using MRI for noninvasive assessment of atherosclerotic plaque in vivo [17, 18]. Meissner et al. studied high-resolution MRI in the femoral arterial segments of patients with PAD and compared it to IVUS [10]. MRI was performed at 1.5 T with a three-dimensional (3D) time-of-flight sequence with in-plane resolution of 0.78 × 0.49 mm^2. When compared with IVUS, they demonstrated precise assessment of cross-sectional lumen area and

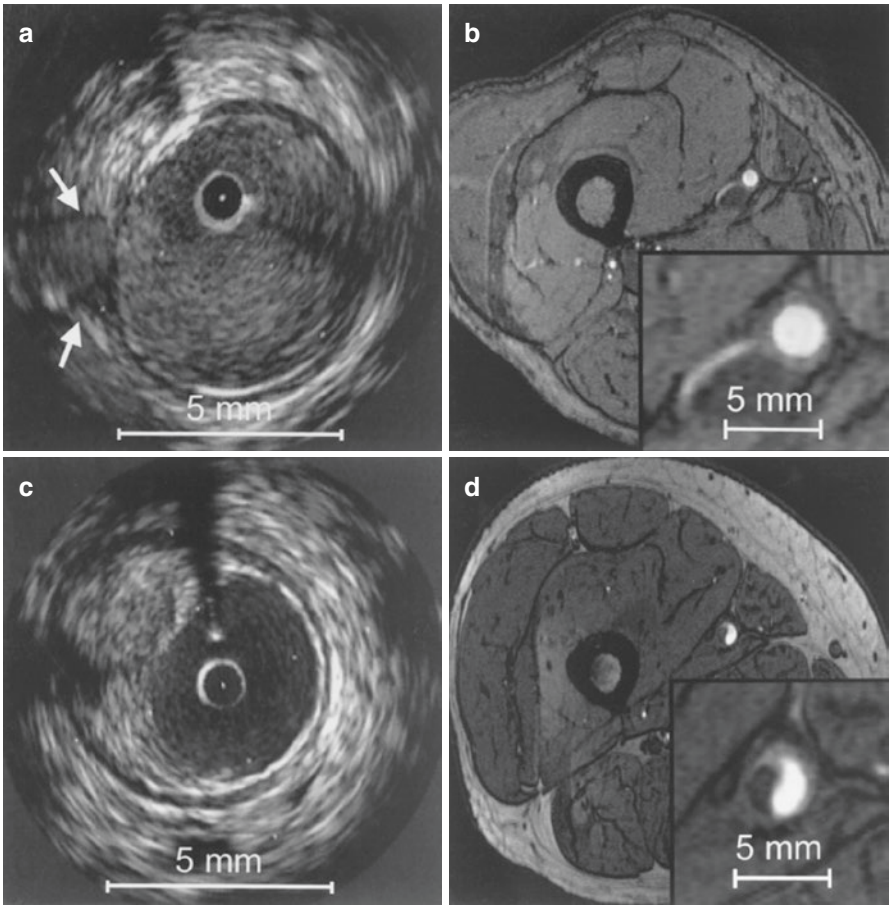

Fig. 9.4 Correlation between IVUS and axial high-resolution (HR) 3D time-of-flight MR images in two different vessel segments. Insets in each MR image represent magnified views of the distal superficial femoral artery. HR MR images are acquired at a slice thickness of 2 mm with an in-plane resolution of 0.78 ′ 0.49 mm^2, with no interslice gap. (**a**) IVUS visualization of a vessel segment with a side branch (white arrows); (**b**) corresponding HR MR image. The course of the side branch can be clearly followed. (**c**) IVUS visualization of a vessel wall segment with characteristic plaque formation. (**d**) corresponding HR MR image. The hypointense plaque can be clearly differentiated from the hyperintense lumen. (Reprinted from Meissner et al. [10]; with permission from Elsevier.)

extent of calcification in PAD. Figure 9.4 demonstrates how hypointense plaque can be clearly differentiated from the hyperintense lumen. This technique however does require gadolinium contrast for 3D contrast-enhanced angiography to allow for exact position of the MR imaging slices. This would preclude patients with stage 4 or 5 chronic kidney disease or allergic reactions to gadolinium from undergoing this technique.

Non-contrast-Enhanced Techniques

More recent advances in MRI techniques in PAD have focused on non-contrast sequences [19]. The SFA is a suitable vessel for high-resolution MR plaque imaging as it is the most common site of lower extremity atherosclerosis [20, 21]. The SFA also is not influenced by artifacts from systolic and diastolic changes such as coronary arteries, carotid arteries, and the thoracic aorta. Its anatomical position allows for use of high-resolution coil systems with associated high spatial resolution. SFA occlusion and plaque burden are associated with reduced ABIs and 6-minute walk distance [21–23].

Multiple plaque imaging techniques described below utilize turbo (fast) spin echo sequences as this is an efficient way to increase the speed of basic spin echo imaging. Preparation pulses can be added prior to imaging sequence in order to change image contrast, such as fat suppression, "black blood" contrast, T1 contrast enhancement, etc.

"Black-blood" two-dimensional (2D) fast spin echo (FSE) MRI approaches, where blood signal is suppressed using a double inversion recovery (DIR) pulse, are suitable for arterial wall imaging, but these approaches tend to be very time-consuming [24–26]. 3D FSE sequences were effective in reducing partial volume-averaging effects by allowing contiguous acquisition of thin sections however suffered from T2-induced signal decay and long scan times [27, 28]. More recently SPACE (sampling perfection with application optimized contrasts using different flip angle evolution) has been developed which uses a single-slab 3D turbo spin echo (TSE) sequence with variable refocusing flip angles and spatially nonselective radiofrequency (RF) refocusing pulses [16, 29]. These modifications allow for greater efficiency over the previous 3D FSE by allowing more echoes to be acquired following each RF pulse excitation. This sequence also dephases flowing blood and suppresses the blood signal without the need for DIR preparation, permitting the use of thicker 3D slabs and efficient coverage of larger vascular territories. Mihai G. et al. used T1-weighted SPACE and compared it to contrast-enhanced MR angiography (CE-MRA) in aorta, iliac, and SFA arteries assessment in patients with PAD [16]. Quantitative comparison of lumen areas with T1-weighted SPACE and CE-MRA had strong correlation ($r > 0.9$; $P < 0.001$). Furthermore, SPACE allows for visualization of the vessel wall remodeling and atherosclerosis burden, which is an advantage over the conventional CE-MRA as shown in Fig. 9.5.

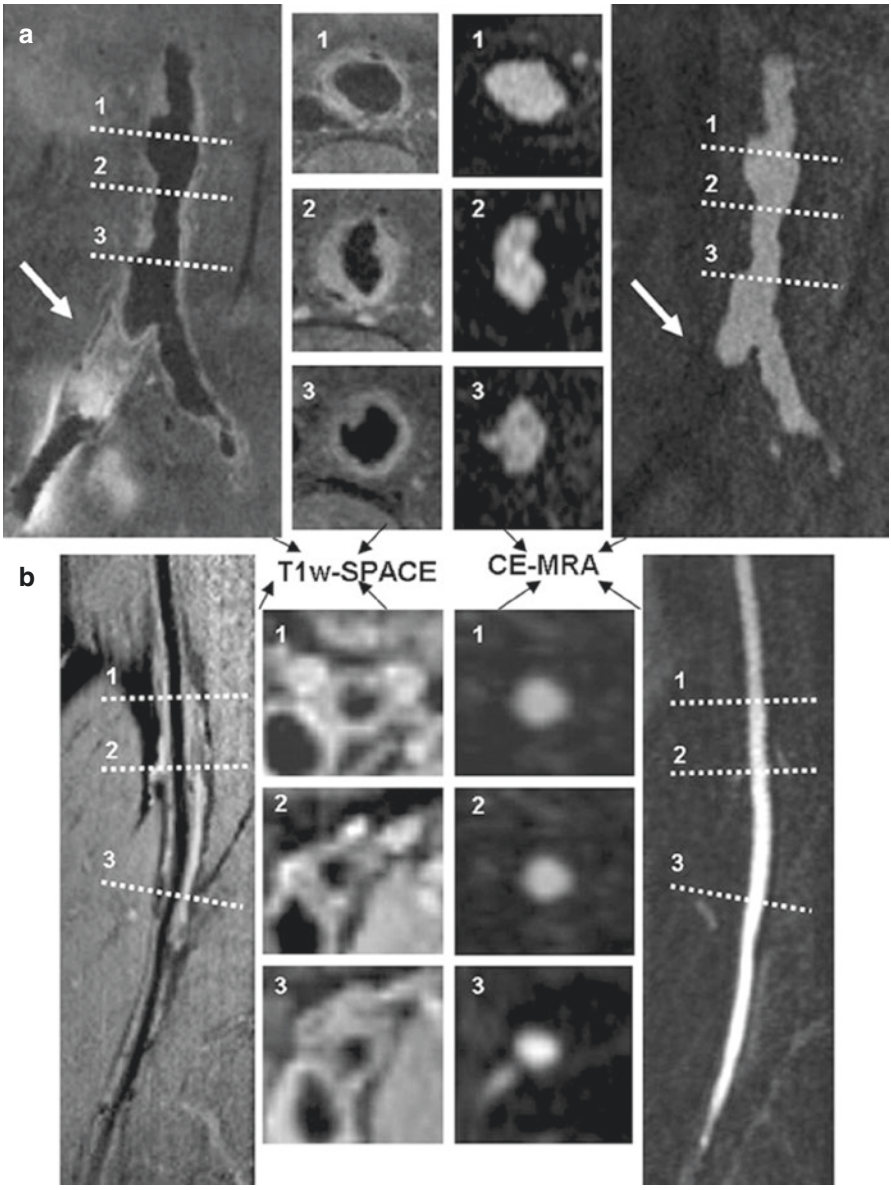

Fig. 9.5 (**a**, **b**) Use of T1w-SPACE (left, **a** and **b**) and CE-MRA (right, **a** and **b**) to assess disease in a patient with PAD. The 3D SPACE (left) and MPR CE-MRA (right) images of abdominal aorta (**a**) and SFA (**b**) segments demonstrate luminal stenosis and atherosclerosis in a 63-year-old patient with PAD. ABI was 0.82 on the right lower extremity. Arrows depict total right iliac occlusion (**a**, right and left). Observe the almost normal looking SFA lumen in the sagittal reconstruct of CE-MRA (**b**, left). The 3D SPACE sagittal and transversal reconstructed images (right) show wall thickening suggestive of uniform plaque buildup. Note: Dotted lines on sagittal reconstructed images show position/orientation of transversal MPR images. (Reprinted from Mihai et al. [16]; with permission from John Wiley and Sons)

Isbell D.C. et al. studied the use of MRI for SFA plaque volume quantification [30]. This technique uses multi-slice TSE pulse sequences with fat presaturation. Blood flow is suppressed creating a dark lumen. Imaging slices begin above the femoral bifurcation and continue through the adductor canal. With each individual slice, cross-sectional area (CSA) of the vessel wall is measured. The volume for each slice can be derived by multiplying the CSA by the slice thickness. Total SFA plaque volume is then calculated by adding the volume of all the individual slices. This technique has been shown to have excellent intra-observer ($r = 0.997$), inter-observer ($r = 0.987$), and test-retest ($r = 0.996$) reliability and reproducibility. This is ideal for the study and validation of pharmacologic therapies for PAD. Statin and ezetimibe used in statin-naïve patients with PAD showed no progression of SFA plaque volume using MRI [31]. PCSK9 inhibitors are newer cholesterol reducing agents that have been shown to reduced LDL cholesterol up to 70% in patients on statins or intolerant to statins [32, 33]. A recent study has also shown they can improve cardiovascular outcomes [34]. A current randomized controlled trial is underway seeing if a PCSK9 inhibitor (alirocumab) can reduce SFA plaque volume, measured by MRI, in PAD patients (NCT 02959047).

MRI techniques have also been studied in PAD plaque characteristic imaging. The proximal SFA is identified and imaged with bright-blood 2D time-of-flight images and proton density-weighted images. Additional T1- and T2-weighted TSE images are acquired for plaque characterization. Readers trace the outer boundary and the lumen of each cross-sectional image as shown in Fig. 9.6 [35]. Plaque area, wall thickness, and lumen area are then quantified. Lipid-rich necrotic core (LRNC) without hemorrhage is identified by isointense on proton density-weighted and time-of-flight images, hypointense on T2-weighted images, and isointense or slightly hyperintense on T1-weighed images. Intraplaque hemorrhage is characterized as hyperintense on time-of-flight and T1-weighted images and can be either hyperintense or hypointense on T1-weighted and proton density images based on the stage of hemorrhage. LRNC plaque and intraplaque hemorrhage have been identified as high-risk plaque and have been identified in the proximal SFA of <25% of adults with PAD [35]. PAD patients with LRNC in the SFA have higher rates of clinical PAD events independent of ABI [36]. LRNC however does not predict higher mobility loss in PAD which appears to be more impacted by greater plaque quantity and smaller luminal area in the SFA [37].

In summary, vessel wall imaging for PAD has been mainly studied using IVUS, FDG-PET/CT, and MRI. MRI has largely replaced IVUS for plaque assessment in PAD due to the limitation of IVUS in calcified plaques. MRI techniques summarized above have been used to validate pharmacologic therapies for PAD in clinical trials but aren't widely utilized in the clinical setting as of yet. These new techniques set the stage for larger clinical trials studying SFA plaque characteristics and outcomes.

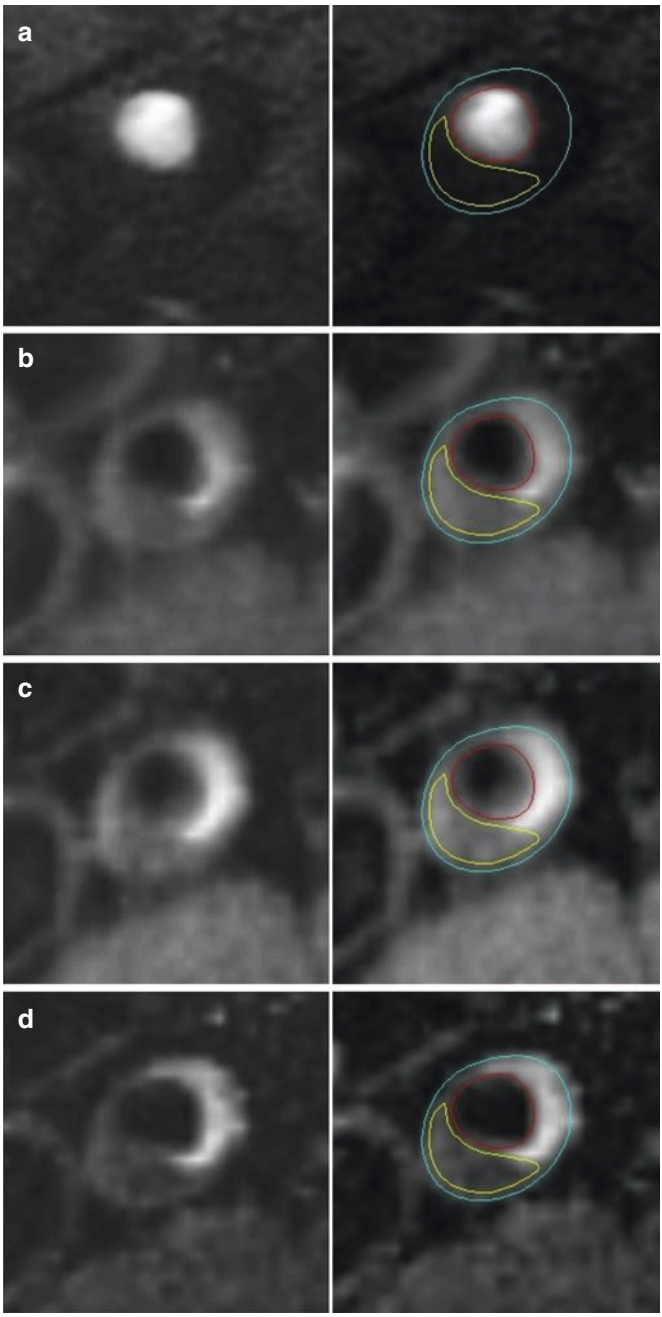

Fig. 9.6 MRI images of the proximal superficial femoral artery (SFA) from a participant in the Walking and Leg Circulation Study III cohort. Imaging sequence is time of flight (**a**), T1 (**b**), proton density (**c**), and T2 (**d**). Panels on the left are the original images, and panels on the right include the traced contours for the plaque composition analysis. The blue contour delineates the outer boundary of the SFA, the red contour delineates the lumen, and the yellow contour delineates the lipid-rich necrotic core. (Reprinted from Polonsky et al. [35]; with permission from Elsevier)

References

1. Gerhard-Herman MD, Gornik HL, Barrett C, Barshes NR, Corriere MA, Drachman DE, et al. 2016 AHA/ACC guideline on the management of patients with lower extremity peripheral artery disease: a report of the American College of Cardiology/American Heart Association task force on clinical practice guidelines. Circulation. 2017;135(12):e726–79.
2. Evans NR, Tarkin JM, Chowdhury MM, Warburton EA, Rudd JH. PET imaging of atherosclerotic disease: advancing plaque assessment from anatomy to pathophysiology. Curr Atheroscler Rep. 2016;18(6):30–016-0584-3.
3. Narula N, Dannenberg AJ, Olin JW, Bhatt DL, Johnson KW, Nadkarni G, et al. Pathology of peripheral artery disease in patients with critical limb ischemia. J Am Coll Cardiol. 2018;72(18):2152–63.
4. Makris GC, Chrysafi P, Little M, Patel R, Bratby M, Wigham A, et al. The role of intravascular ultrasound in lower limb revascularization in patients with peripheral arterial disease. Int Angiol. 2017;36(6):505–16.
5. Nissen SE, Yock P. Intravascular ultrasound: novel pathophysiological insights and current clinical applications. Circulation. 2001;103(4):604–16.
6. Niwamae N, Kumakura H, Kanai H, Araki Y, Kasama S, Sumino H, et al. Intravascular ultrasound analysis of correlation between plaque-morphology and risk factors in peripheral arterial disease. Ann Vasc Dis. 2009;2(1):27–33.
7. Weissman NJ, Sheris SJ, Chari R, Mendelsohn FO, Anderson WD, Breall JA, et al. Intravascular ultrasonic analysis of plaque characteristics associated with coronary artery remodeling. Am J Cardiol. 1999;84(1):37–40.
8. van Lankeren W, Gussenhoven EJ, Qureshi A, van der Lugt A. Intravascular ultrasound and histology in in vitro assessment of iliac artery angioplasty. Cardiovasc Intervent Radiol. 1999;22(1):50–5.
9. Schwarzenberg H, Muller-Hulsbeck S, Gluer CC, Steffens JC, Heller M. Evaluation of maximum neointima proliferation and plaque morphology in iliac self-expanding nitinol stents with intravascular sonography. AJR Am J Roentgenol. 1998;171(6):1627–30.
10. Meissner OA, Rieger J, Rieber J, Klauss V, Siebert U, Tato F, et al. High-resolution MR imaging of human atherosclerotic femoral arteries in vivo: validation with intravascular ultrasound. J Vasc Interv Radiol. 2003;14(2 Pt 1):227–31.
11. Met R, Bipat S, Legemate DA, Reekers JA, Koelemay MJ. Diagnostic performance of computed tomography angiography in peripheral arterial disease: a systematic review and meta-analysis. JAMA. 2009;301(4):415–24.
12. Lawrence JA, Kim D, Kent KC, Stehling MK, Rosen MP, Raptopoulos V. Lower extremity spiral CT angiography versus catheter angiography. Radiology. 1995;194(3):903–8.
13. Pollak AW, Norton PT, Kramer CM. Multimodality imaging of lower extremity peripheral arterial disease: current role and future directions. Circ Cardiovasc Imaging. 2012;5(6):797–807.
14. Rudd JH, Myers KS, Bansilal S, Machac J, Pinto CA, Tong C, et al. Atherosclerosis inflammation imaging with 18F-FDG PET: carotid, iliac, and femoral uptake reproducibility, quantification methods, and recommendations. J Nucl Med. 2008;49(6):871–8.
15. Silvera SS, Aidi HE, Rudd JH, Mani V, Yang L, Farkouh M, et al. Multimodality imaging of atherosclerotic plaque activity and composition using FDG-PET/CT and MRI in carotid and femoral arteries. Atherosclerosis. 2009;207(1):139–43.
16. Mihai G, Chung YC, Kariisa M, Raman SV, Simonetti OP, Rajagopalan S. Initial feasibility of a multi-station high resolution three-dimensional dark blood angiography protocol for the assessment of peripheral arterial disease. J Magn Reson Imaging. 2009;30(4):785–93.
17. Skinner MP, Yuan C, Mitsumori L, Hayes CE, Raines EW, Nelson JA, et al. Serial magnetic resonance imaging of experimental atherosclerosis detects lesion fine structure, progression and complications in vivo. Nat Med. 1995;1(1):69–73.
18. Yuan C, Beach KW, Smith LH Jr, Hatsukami TS. Measurement of atherosclerotic carotid plaque size in vivo using high resolution magnetic resonance imaging. Circulation. 1998;98(24):2666–71.

19. Mathew RC, Kramer CM. Recent advances in magnetic resonance imaging for peripheral artery disease. Vasc Med. 2018;23(2):143–52.
20. Hyvarinen S. Arteriographic findings of claudication patients. Ann Clin Res. 1984;16(Suppl 41):1–45.
21. McDermott MM, Liu K, Carroll TJ, Tian L, Ferrucci L, Li D, et al. Superficial femoral artery plaque and functional performance in peripheral arterial disease: walking and leg circulation study (WALCS III). JACC Cardiovasc Imaging. 2011;4(7):730–9.
22. Li F, McDermott MM, Li D, Carroll TJ, Hippe DS, Kramer CM, et al. The association of lesion eccentricity with plaque morphology and components in the superficial femoral artery: a high-spatial-resolution, multi-contrast weighted CMR study. J Cardiovasc Magn Reson. 2010;12:37–429X-12-37.
23. McDermott MM, Liu K, Carr J, Criqui MH, Tian L, Li D, et al. Superficial femoral artery plaque, the ankle-brachial index, and leg symptoms in peripheral arterial disease: the walking and leg circulation study (WALCS) III. Circ Cardiovasc Imaging. 2011;4(3):246–52.
24. Botnar RM, Stuber M, Kissinger KV, Kim WY, Spuentrup E, Manning WJ. Noninvasive coronary vessel wall and plaque imaging with magnetic resonance imaging. Circulation. 2000;102(21):2582–7.
25. Simonetti OP, Finn JP, White RD, Laub G, Henry DA. "Black blood" T2-weighted inversion-recovery MR imaging of the heart. Radiology. 1996;199(1):49–57.
26. Edelman RR, Chien D, Kim D. Fast selective black blood MR imaging. Radiology. 1991;181(3):655–60.
27. Luk-Pat GT, Gold GE, Olcott EW, Hu BS, Nishimura DG. High-resolution three-dimensional in vivo imaging of atherosclerotic plaque. Magn Reson Med. 1999;42(4):762–71.
28. Crowe LA, Gatehouse P, Yang GZ, Mohiaddin RH, Varghese A, Charrier C, et al. Volume-selective 3D turbo spin echo imaging for vascular wall imaging and distensibility measurement. J Magn Reson Imaging. 2003;17(5):572–80.
29. Mugler JP 3rd, Bao S, Mulkern RV, Guttmann CR, Robertson RL, Jolesz FA, et al. Optimized single-slab three-dimensional spin-echo MR imaging of the brain. Radiology. 2000;216(3):891–9.
30. Isbell DC, Meyer CH, Rogers WJ, Epstein FH, DiMaria JM, Harthun NL, et al. Reproducibility and reliability of atherosclerotic plaque volume measurements in peripheral arterial disease with cardiovascular magnetic resonance. J Cardiovasc Magn Reson. 2007;9(1):71–6.
31. West AM, Anderson JD, Meyer CH, Epstein FH, Wang H, Hagspiel KD, et al. The effect of ezetimibe on peripheral arterial atherosclerosis depends upon statin use at baseline. Atherosclerosis. 2011;218(1):156–62.
32. Blom DJ, Hala T, Bolognese M, Lillestol MJ, Toth PD, Burgess L, et al. A 52-week placebo-controlled trial of evolocumab in hyperlipidemia. N Engl J Med. 2014;370(19):1809–19.
33. Robinson JG, Farnier M, Krempf M, Bergeron J, Luc G, Averna M, et al. Efficacy and safety of alirocumab in reducing lipids and cardiovascular events. N Engl J Med. 2015;372(16):1489–99.
34. Sabatine MS, Giugliano RP, Keech AC, Honarpour N, Wiviott SD, Murphy SA, et al. Evolocumab and clinical outcomes in patients with cardiovascular disease. N Engl J Med. 2017;376(18):1713–22.
35. Polonsky TS, Liu K, Tian L, Carr J, Carroll TJ, Berry J, et al. High-risk plaque in the superficial femoral artery of people with peripheral artery disease: prevalence and associated clinical characteristics. Atherosclerosis. 2014;237(1):169–76.
36. McDermott MM, Kramer CM, Tian L, Carr J, Guralnik JM, Polonsky T, et al. Plaque composition in the proximal superficial femoral artery and peripheral artery disease events. JACC Cardiovasc Imaging. 2017;10(9):1003–12.
37. McDermott MM, Carroll T, Carr J, Yuan C, Ferrucci L, Guralnik JM, et al. Femoral artery plaque characteristics, lower extremity collaterals, and mobility loss in peripheral artery disease. Vasc Med. 2017;22(6):473–81.

Part IV
Aorta

Chapter 10
Imaging Approaches for Aortic Disease

Muhannad Aboud Abbasi, Ashitha Pathrose, Ali Mostafa Serhal, and James Carr

Introduction

Aortic diseases are a significant cause of morbidity and mortality that can potentially result in catastrophic clinical consequences if a diagnosis is delayed. Therefore, prompt and accurate assessment is paramount to safe patient care and appropriate clinical outcomes. Aortic diseases can broadly be divided into valvular, aneurysmal, dissection-related, atherosclerotic, trauma-related, and congenital. The goal of this chapter is to outline common disease processes that affect the aorta, with emphasis on the strengths and limitations of the different imaging modalities, which are currently in use.

Overview of Imaging Techniques

The imaging options available for assessment of the thoracic aorta include plain radiography, transthoracic echocardiography (TTE), transesophageal echocardiography (TEE), computed tomography (CT), computed tomography angiography (CTA), magnetic resonance imaging (MRI), and aortography. Imaging modalities used for the abdominal aorta include ultrasonography (US), CT, CTA, MRI, and catheter angiography.

M. A. Abbasi (✉) · A. Pathrose · A. M. Serhal · J. Carr
Department of Radiology, Northwestern Memorial Hospital, Chicago, IL, USA
e-mail: ashitha.pathrose@northwestern.edu; ali.serhal@northwestern.edu; jcarr@northwestern.edu

C. Yuan et al. (eds.), *Vessel Based Imaging Techniques*,
https://doi.org/10.1007/978-3-030-25249-6_10

Plain Radiography

Plain radiography has limited use for assessing the thoracic aorta and is mostly utilized as an initial screening tool. Signs such as an abnormal aortic contour or widening of the aortic silhouette in a suggestive clinical scenario raise the clinical suspicion for aortic dissection or other aortic pathologies. CXRs have a sensitivity of 64% and a specificity of 86% for acute aortic syndromes [1]. However, radiographs alone are not sensitive enough to exclude aortic pathology or blunt aortic injury when it is clinically suspected [2, 3].

Echocardiography

Transthoracic echocardiography is a noninvasive imaging technique that is widely used in clinical practice due to its rapid availability and portability. It is highly effective in the evaluation of the proximal aorta, the aortic valve, left ventricular morphology and function, and suspected pericardial effusions. However, due to limited acoustic windows and reduced anatomic coverage, it is not considered the first-line imaging technique for the entire aorta and often demands further evaluation with TEE, CT/CTA, and MRI. Compared to TTE, TEE is a more sensitive and specific modality, offering superior visualization of the posterior cardiac structures and is particularly effective at assessing diseases of the aortic root. TEE has high sensitivity in the evaluation of suspected acute aortic pathology (dissection, transection, and intramural hematoma), suspected prosthetic valve dysfunction (thrombus, pannus ingrowth, vegetation, or regurgitation), and screening for left atrial thrombus in patients with atrial fibrillation or atrial flutter [4–6]. However, since TEE provides limited anatomic coverage of the aortic arch and descending thoracic aorta, it is mainly reserved for evaluating diseases at the aortic root, such as aneurysms and dissections. Since TEE is a portable modality, it is particularly useful for evaluating sick patients in the intensive care unit or emergency department, who cannot be transferred for more advanced imaging with CT or MR. TEE is also an invasive procedure with possible morbidity [7], albeit small, and is therefore mostly used for exclusion of aortic root pathology.

Ultrasonography

Ultrasound is the examination of choice for initial workup of abdominal aortic pathologies. It has a sensitivity of nearly 100% in the diagnosis of abdominal aortic aneurysms (AAA) [8]. Ultrasonography is largely preferred for screening and monitoring because of its relatively low cost, widespread availability, and noninvasive

nature. It is accurate to within 0.3 cm in estimating aneurysm diameter on serial scans with little interobserver variation [9]. However, limitations include suboptimal image quality in patients who are obese or who have excessive bowel gas. Furthermore, US cannot reliably identify the presence of periaortic disease or the proximal and distal extent of an aneurysm. It also has limited ability in determining the patency of the visceral vasculature, the relationship of an aneurysm with respect to renal vessels, or the presence of iliac aneurysms. As a result, US alone cannot fully provide the necessary information required in the preoperative evaluation of a patient undergoing elective aneurysm repair.

Contrast-enhanced ultrasound (CEUS) is an evolving complementary imaging technique useful for real-time characterization of macrovascular pathologies like aortic dissection, ruptures, and endoleaks following endovascular repair of AAA, as well as microvascular pathologies like aortitis. This technique uses microbubbles containing inert gases as ultrasonographic contrast agents, making them safe for patients with impaired renal function [10, 11].

Computed Tomography and Computed Tomography Angiography

The speed and ease of CT acquisitions render this technique of choice for diagnosing acute and chronic aortic pathologies, such as intramural hematomas, aneurysms, traumatic injuries, atherosclerosis, and dissections. Multi-detector row CT (MDCT) has become one of the most widely used imaging modalities for the assessment of aortic diseases. Its major advantages are excellent spatial and temporal resolution, widespread availability, and ability to image the entire aorta (i.e., thoracic and abdominal aorta) within seconds. By markedly shortening the scan time, respiratory motion artifacts are limited, and the dose of iodinated contrast can be reduced [12]. It also enables easy visualization of the aortic lumen and wall, resulting in precise and reproducible measurements of aortic diameter. Current scanners with higher rows of detectors allow acquisition of isotropic volumetric datasets, which can be reconstructed in any plane for optimal display and measurement [13].

The typical CT protocol for assessing the aorta includes a non-contrast CT initially followed by an arterial phase CT angiogram. A delayed post-contrast CT may be indicated in certain conditions such as dissection and vasculitis. In an acute non-traumatic scenario, the non-contrast scan is essential for detecting acute aortic wall intramural hematomas, which appears as a curvilinear hyperdense region in aortic wall. A relatively thick 5 mm slice can be more useful than thinner sections due to relatively decreased image noise and increased contrast, which enables the appreciation of the high-density rim of an acute intramural hematoma [14]. A contrast-enhanced CT angiogram (CTA), timed to the arterial phase, is the mainstay for evaluating the thoracic and abdominal aorta. Nonionic iodinated contrast agents are preferably injected from the right arm to minimize artifacts from the

Table 10.1 ECG-gated thoracic CTA protocol

Pre-contrast (Y/N)	Yes	
CTA (contrast)	mAs	120 care dose
	IV contrast (injection rate)	70 cc (4 cc/s)
	Slice thickness	2 mm
	Collimator	192 × 0.6
	Rotation time	0.25
	Pitch	3.2
	kV	80–120 kV (90 ref. care kV)
Delayed post-contrast	Indicated for assessment of vasculitis	

dense contrast in the innominate veins. Triggering the scan by automated bolus tracking in the aortic lumen will usually provide reliable aortic enhancement. A delayed post-contrast venous-phase CTA is used for the assessment of dissection or inflammatory diseases (e.g., vasculitis). Table 10.1 outlines a typical thoracic CTA protocol.

Newer approaches to CT imaging of the aorta include dual-energy CT (DECT) that uses both low-energy (i.e., 80–100 kVp tube potential) and high-energy (140 kVp) photons when acquiring data – this is becoming more widely available for aortic imaging. It can be used for quantifying aortic calcification, thus enabling identification of patients at risk for adverse cardiovascular events [15]. Alternatively, it can be employed to subtract calcification from the aortic wall to allow improved visualization of the mural contours, thereby facilitating more accurate measurements of aortic dimensions. Spectral detector CT (SDCT) is also a new technique in which multiple spectrally distinct attenuation datasets are acquired, enabling differentiation of tissues with varying attenuation at different photon energies. SDCT aids in artifact reduction, increasing intravascular contrast in suboptimally enhanced contrast studies and differentiating delayed slow flow from the thrombus [16]. Single-source dual-layer detector CT which involves the use of a single-source scanner that discriminates DECT data at the detector level and photon-counting detector CT that uses a polychromatic x-ray energy beam to acquire DECT data are other novel CT techniques that hold promise.

Various post-processing image visualization techniques can also be used for CTA including multiplanar reconstruction (MPR), maximum intensity projection (MIP), 3D volume rendering (3D-VR), and curved planar reformation (CPR).

The main disadvantages of CTA are the need for contrast administration and ionizing radiation exposure. Iodinated contrast agents (ICA) may cause allergic reactions and need cautious use in patients with nephropathy. The administration of ICA may cause contrast-induced nephropathy (CIN), especially in those with pre-existing renal impairment. The incidence of CIN in the general population is up to 6%; however, studies indicate that up to 50% of patients with pre-existing nephropathy are at risk of developing CIN [17]. Ionizing radiation exposure from CT may limit its use, especially in young patients who may require serial follow-up imaging [18]. Dramatic decreases in radiation exposure have been observed recently from

using various dose reduction techniques, including prospective ECG triggering, ECG-based tube current modulation, lower peak kilovoltage (kVp), and iterative reconstruction algorithms [19, 20].

Compared to other modalities such as TTE and MRI, CT lacks flow assessment capabilities, which are useful in assessing aortic insufficiency and shunts. Cardiac motion artifacts mainly affect the aortic root in non-ECG-gated CTA and are more frequently present with heart rates of 65 bpm or more. ECG gating reduces motion artifacts from cardiac and aortic movement at the cost of an increase in radiation dose; however this technique is still preferentially used for imaging the thoracic aorta [21], whereas non-ECG-gated CTA is preferred for imaging the abdominal aorta [22]. Retrospective ECG gating is rarely used in the thoracic aorta due to greater radiation exposure [23] but may be used in clinical situations where there is concomitant aortic valve disease (e.g., infective endocarditis).

Magnetic Resonance Imaging

Magnetic resonance imaging (MRI) is a versatile modality for imaging a variety of aortic diseases, providing precise information about anatomy and pathology, as well as flow and functional data, all from the same protocol. The combination of targeted sequences, multiplanar imaging, and lack of ionizing radiation with MRI makes it particularly useful for the assessment of a diverse range of aortic conditions, especially in younger patients. The major drawback of using MRI is its limited availability in an acute setting and when there are implanted metallic devices adjacent to the aorta, such as stents, embolization coils, or occlusion devices, which often cause artifacts which preclude adequate evaluation. Table 10.2 summarizes the common sequences employed in different clinical scenarios affecting the thoracic and abdominal aorta.

Table 10.2 Clinical indications for different MRA sequences

	Acute aortic syndromes	Thoracic aortic aneurysm	Congenital abnormalities	Vasculitis
bSSFP	+	+	+	+
Cine bSSFP		+ (AV valve)	+ (AV valve)	
TR-MRA	+	+	+	+
CE-MRA	+	+	+	+
PC-MRA		+ (AV valve)	+ (AV valve)	
Pre-contrast VIBE	+			+
Post-contrast VIBE	+			+ (delayed post-contrast for inflammation)
NC-MRA	+	+	+	+

Plus sign (+) indicates sequence is performed for clinical suspicion

MRI Techniques

Balanced Steady-State Free Precession

Balanced steady-state free precession (bSSFP) techniques are gradient echo techniques that are widely used for cine imaging of the heart. These sequences are primarily T2 weighted and produce a high signal from blood without the need for a contrast agent. The contrast-to-noise ratio depends on the T2/T1 relaxation differences of the tissues, which at short repetition times (TR) is high for blood and soft tissues, thus improving the overall image quality. There are different strategies for implementing the bSSFP technique: as a single shot (electrocardiographically (ECG)-triggered 2D acquisition), as cine (breath-hold ECG-triggered segmented k-space acquisition), as real-time cine (which does not require breath-holding or ECG triggering but with lower spatial and temporal resolution), or as a 3D sequence (nonselective radiofrequency pulse with segmented acquisition to obtain isotropic 3D data with very high spatial resolution) for imaging the coronary arteries and thoracic aorta.

Black-Blood Imaging

Black-blood imaging (BB) enables evaluation of blood vessel walls and is useful for the evaluation of a variety of pathologies, including acute aortic syndromes, atherosclerosis, vasculitis, and neoplasms. A flow-sensitive double inversion recovery (DIR) technique is used to null signal from flowing blood [24]. This technique uses two 180° inversion recovery pulses in close succession to null the signal of flowing blood, helping to visualize the walls of the blood vessels. The first 180° inversion recovery pulse is spatially nonselective which inverts the magnetization in the entire tissue volume, including the blood signal, while the succeeding reversion 180° pulse is spatially selective and regenerates the magnetization for imaging [25]. Vectorcardiogram (VCG)-gated proton density-weighted 2D fast spin-echo (FSE) sequence is the most commonly used pulse sequence. VCG gating increases imaging time; however, it significantly reduces motion artifact. Single-shot FSE (SSFSE) sequences are much faster and allow for image acquisition in either a single breath-hold or during free breathing. T1-weighted BB images with fat saturation are recommended in an acute setting, to help in the diagnosis of aortic wall hematomas [26]. T2-weighted BB imaging with fat saturation helps to evaluate edema in inflammatory disorders [27].

T1-Weighted Gradient Echo Fat-Saturated Imaging

T1-weighted gradient echo fat-saturated (GRE-FS) imaging before and after contrast injection is used routinely in evaluating several thoracic pathologies. Precontrast T1 GRE-FS is useful in demonstrating intramural hematomas, which

appears as a bright T1-hyperintense region within the aortic wall. The entire thoracic aorta is imaged in axial and either coronal or sagittal orientations before and after contrast injection. Delayed post-contrast GRE-FS may be used to assess contrast enhancement of the aortic wall in conditions such as vasculitis.

Contrast-Enhanced MRA

Time-Resolved MRA (TR-MRA)

Advanced gradient strength with modern MRI systems allows shorter acquisition times per 3D acquisition volume, enabling contrast-enhanced MRA (CE-MRA) to be implemented with sub-second temporal resolution [28]. This is achieved using a combination of acceleration strategies, i.e., short TR, parallel imaging, and view sharing (e.g., TWIST). When these strategies are used in combination, the aorta can be imaged with acquisition speeds of 1–2 frames per second, allowing evaluation of high-flow vascular lesions, such as shunts and dissections. In its most basic implementation, TR-MRA can be used as a timing bolus acquisition for planning the higher-resolution CE-MRA.

Conventional CE-MRA

Conventional CE-MRA is the most widely used technique for a comprehensive evaluation of the thoracic aorta. It is a timed, single-phase acquisition, which provides better spatial resolution than TR-MRA, particularly in the z-direction, and produces better depiction of more subtle abnormalities, such as penetrating aortic ulcers. The basic pulse sequence for conventional CE-MRA is also a standard 3D GRE acquisition. Gadolinium contrast is injected through a cannula placed in an antecubital vein. The contrast transit time is calculated from the sub-second TR-MRA, which is used for bolus timing. Images are acquired during breath-holding. Image subtraction is employed to enhance contrast, and subtracted 3D sets are calculated from the raw data which are subjected to MIP and volume-rendering post-processing algorithms. ECG gating is used for CE-MRA of the thoracic aorta to provide artifact-free images of the aortic root in particular, similar to CTA [29, 30].

Phase-Contrast MRA (PC-MRA)

Phase-contrast MRA (PC-MRA) is a velocity-sensitive imaging technique that is most useful where there is high suspicion for vascular stenoses, such as in coarctation. This technique depends on velocity differences or phase shifts in moving blood

(i.e., protons) to produce image contrast in flowing blood. Phase shifts from moving spins are generated by applying magnetic field gradients with alternating opposing polarities. The velocity-encoding (VENC) variable controls the amplitude of the magnetic gradient and is adjusted up or down depending on the amplitude of the velocity being measured. PC-MRA can be implemented as a 2D or 3D acquisition. 2D PC-MRA is useful when the region to be assessed is clearly visible so that the imaging slice can be accurately placed. 4D flow MRI combines tri-directional VENC with a 3D spatial acquisition potentially allowing vascular flow patterns to be visualized and measured from a single 3D acquisition [31]. This technique allows assessment of complex vascular hemodynamics with MRI in large aneurysms or congenital heart diseases. Disadvantages of this technique include long acquisition times and complex time-consuming post-processing. This technique is described in greater detail in a subsequent chapter.

Non-contrast MRA

Non-contrast MRA (NC-MRA) techniques are increasingly being used routinely, particularly in "at risk" patients, such as those with renal failure or pediatric patients. NC-MRA of the thoracic aorta incorporates several techniques including bSSFP which produces bright blood signal determined by T2/T1 ratio and FSE which relies on an ECG-gated 3D partial-Fourier FSE sequence, which is triggered to systole and diastole [32]. bSSFP can be implemented as a 2D or 3D acquisition. 2D SSFP is a rapid free-breathing technique that is useful in acutely ill patients and reserved for excluding serious pathology such as aortic dissection [33]. 3D SSFP has a longer acquisition time (typically 3–4 minutes with respiratory gating) and facilitates accurate orthogonal measurement of aortic aneurysms. FSE approaches depend on the timing of acquisition to different parts of the cardiac cycle adding complexity and consequent error to the imaging protocol.

Positron Emission Tomography-Computed Tomography (PET-CT) or Nuclear Imaging

Although PET-CT has been established as a standard imaging modality in the evaluation of malignancy, growing evidence suggests that PET-CT images have many advantages in the evaluation of aortic disease as well, especially acute aortic syndromes, aortic aneurysms, atherosclerotic lesions, aortitis, and aortic tumors [34]. Elevated uptake of fluorine-2-deoxy-D-glucose (FDG) has been correlated with the development and progression of both thoracic and abdominal aneurysms in a number of clinical studies [35–39]. Other radiotracers targeting matrix metalloproteinases, mitochondrial translocator proteins, and endothelial cell adhesion molecules

are being investigated for clinical utility in identifying the progression of disease in aortic aneurysms [40]. FDG PET/CT imaging of atherosclerosis allows for the in vivo visualization of vascular inflammation, which can help evaluate plaque vulnerability and predict clinical events. It is also useful in diagnosis, differential diagnosis, and the identification of target sites for biopsy in aortitis. Moreover, it is helpful for evaluating disease extent and activity, predicting prognostic outcomes, monitoring response to therapy, and evaluating therapeutic effectiveness [34].

Abnormalities of the Thoracic Aorta

Acute Aortic Syndromes

Acute aortic syndrome (AAS) comprises of three overlapping clinical entities: aortic dissection, intramural hematoma, and penetrating atherosclerotic ulcer [41].

Aortic Dissection

Aortic dissection is the most common type of AAS [42, 43]. It is a potentially life-threatening condition that occurs secondary to an aortic intimal tear which allows blood to propagate into the media and separate the layers of the aorta, forming a false lumen which is separated from the true lumen by an intimal flap [44]. Although the true incidence of aortic dissection is difficult to define, a recent population study has suggested that the incidence of aortic dissection is up to 4.6 cases per 100,000 people per year [45]. The most important risk factor for the development of aortic dissection is uncontrolled hypertension. Other risk factors include increased age, cocaine abuse, bicuspid aortic valve, connective tissue disorders, and aortic surgery or infection.

Aortic dissections are most commonly classified according to the anatomical extent based on the DeBakey and Stanford classifications. The Stanford classification divides dissection into those affecting ascending aortic (Type A) (Figs. 10.1 and 10.2), which is a surgical emergency, and those that do not involve the ascending aorta (Type B) (Figs. 10.3 and 10.4) which can be managed medically if patients are hemodynamically stable with no signs of end-organ damage.

Urgent and definitive imaging of the thoracic aorta using echocardiography, MDCT, CTA, or MRA is recommended in all patients with suspected aortic dissection [46]. The role of imaging in dissection is to confirm the diagnosis, classify, evaluate the false lumen, and determine branch involvement as well as the extent of involvement. Table 10.3 summarizes the American College of Radiology (ACR) imaging recommendations for aortic dissection [47]. ACR recommends CTA of the chest and abdomen as the definitive test in most patients with acute aortic dissection.

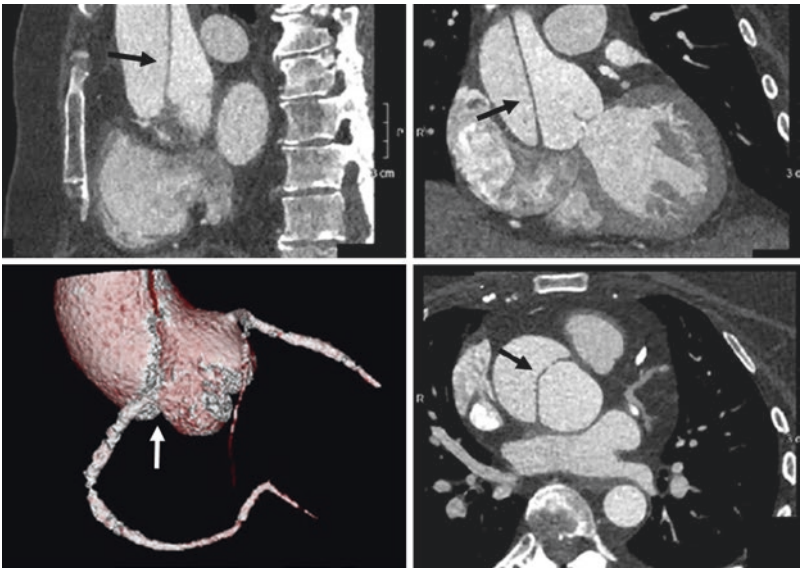

Fig. 10.1 A 61-year-old female presenting with chest pain. ECG-gated CTA of the thoracic aorta depicting a Type A aortic dissection (black arrows) which extends from the root to the ascending aorta. Note the extension of the dissection flap into the ostium of the right coronary artery depicted on the volume-rendering image (white arrow)

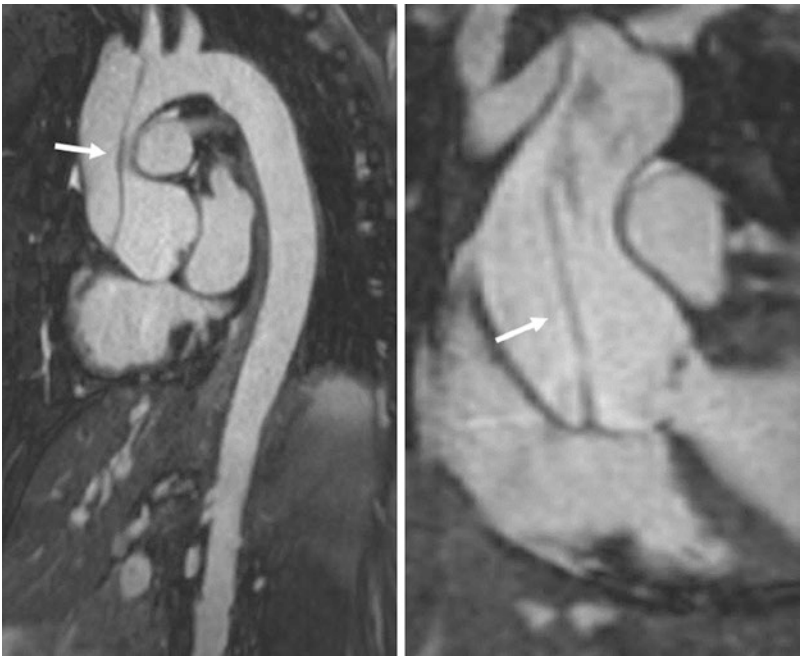

Fig. 10.2 This is the same patient from above. The sagittal and coronal contrast-enhanced MRA of the aorta demonstrates a Type A dissection with the flap extending from the root into the mid-aortic arch (arrows)

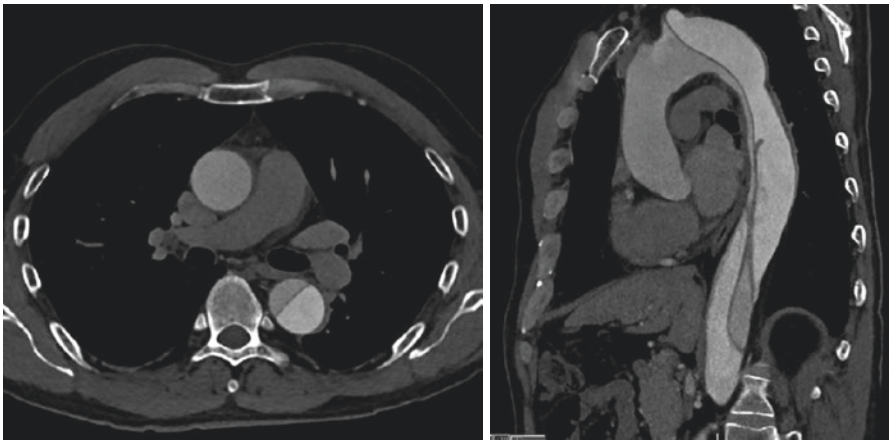

Fig. 10.3 A 59-year-old man with history of Type B aortic dissection, conservatively managed to date. Axial and sagittal reformats of an ECG-gated thoracic CTA demonstrating a Type B aortic dissection arising from the lesser curvature extending to the origin of the left subclavian artery and extending to the common iliac arteries bilaterally (not shown)

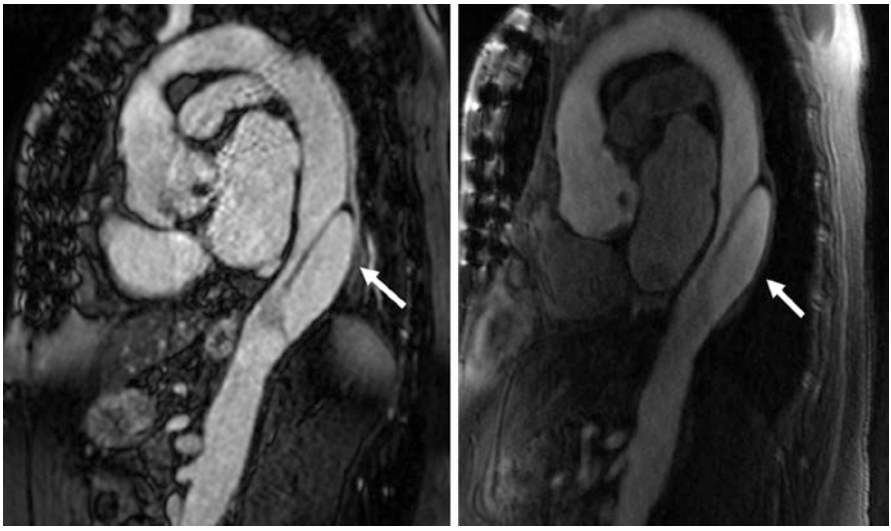

Fig. 10.4 A 61-year-old female with a history of chronic type dissection following a motor vehicle accident 2 years prior. Sagittal bSSFP MRA (**a**) and CE-MRA (**b**) of the thoracic aorta demonstrating a Type B aortic dissection involving the mid-descending thoracic aorta and extending to the bilateral common iliac arteries (not shown). The false lumen is enlarged and partially thrombosed proximally

Table 10.3 The American College of Radiology (ACR) imaging recommendations for aortic dissection

Imaging modality	Comments
CXR	Done mainly to rule out other pathology. Non-specific findings, low negative predictive value
CTA chest and abdomen with contrast	Rapid, cost-effective, safe, and minimally invasive modality. Information provided on the intimal flap, entry/reentry site, branch vessel involvement, and other diagnoses. Considered the gold standard at many centers
Angiography	Invasive, high contrast, and radiation burden. Used rarely when the branch vessel involvement is not determined from CTA. Still required in the definitive preoperative evaluation of coronaries if other examinations were suboptimal
MRA chest and abdomen with or without contrast	Used in hemodynamically stable patients, those with contraindications to contrast, those with uncertain diagnosis or suspicion for a chronic dissection. Newer imaging sequences may allow quicker imaging. Information provided by non-contrast ECG- and respiratory-gated MRA is comparable to contrast-enhanced MRA, making it an appealing alternative in those with nephropathy
Echocardiography	Bedside, rapid, widely available. TEE is recommended if skilled operator and reader are present and if the hemodynamic stability of patient precludes CTA or MRA. Sensitivity is similar to that of MRA and CTA. Can assess coexisting coronary artery involvement. TTE not recommended due to low sensitivity in detecting distal dissections
FDG-PET/CT skull base to mid-thigh	May be recommended in distinguishing acute from chronic dissection in certain clinical scenarios, if available

However, if the patient is hemodynamically stable, has contraindications to ICA, or has had a significant number of previous CTAs for similar symptoms, an MRA of the chest and abdomen with or without contrast is a reasonable diagnostic alternative. A CXR should be ordered in any patient with acute chest pain to look for other causes (e.g., pneumothorax), if it does not delay the definitive diagnostic test. In the case of an aortic dissection, a widening of the mediastinum on CXR can be initially suggestive in the correct clinical context but cannot be used to exclude an aortic dissection as it is highly non-specific, with approximately 1/3 of the patients showing no abnormalities [48]. Echocardiography has the advantage of being easily accessible; however, it does not produce images of the entire aorta, particularly the descending aorta, and is not widely recommended. TEE may be preferentially used to exclude Type A dissection in very ill patients who are unfit to undergo CTA or MRA.

CTA is considered the first-line test for assessing aortic dissection as it provides an accurate assessment of the entire aorta in the chest and abdomen within seconds and at high spatial resolution. CTA can accurately distinguish the true from the false lumen and assesses the extent of the dissection and involvement of aortic branches. A pre-contrast scan of the upper thorax is considered an essential part of the clinical scan protocol in order to exclude intramural hematoma, which may be a precursor for dissection. Additionally, a delayed venous-phase CT acquisition (40–60 seconds

post-contrast injection) is usually included to allow visualization of a slow filling false lumen in aortic dissection.

MRA is usually reserved for patients with a contraindication to CT. MRA has high sensitivity and specificity for detection of dissection and is used as a first-line test or alternative to CTA [28]. The MRA protocol for dissection includes bSSFP, pre- and post-contrast GRE-FS, TR-MRA, CE-MRA, and delayed-phase post-contrast GRE-FS. bSSFP has been shown to be highly accurate for diagnosis and classification of aortic dissection in sick patients who cannot hold their breath [33]. Breath-hold cine SSFP or non-ECG-triggered real-time SSFP can be used to evaluate aortic insufficiency and hemopericardium in Type A dissections. In chronic aortic dissections which become aneurysmally dilated, 4D flow MRI may be very useful for identifying the site of fenestration between true and false lumen [49].

Intramural Hematoma (IMH)

IMH, which is bleeding into the aortic wall, can result from microscopic tears within the aortic intima, hemorrhage of vasa vasorum into the medial layer of the aorta, or from penetrating atherosclerotic ulcers. IMH usually occurs in patients with diffuse atherosclerosis, most commonly in the descending aorta. It may propagate in an antegrade or retrograde direction similar to dissection and progress to dissection in up to 50% of cases. Imaging relies on demonstrating blood within the aortic wall. MRI is ideally suited to making this diagnosis due to its sensitivity for detection of blood products. Intramural blood, which appears as a T1-hyperintense rim within the aortic wall, is detected on pre-contrast T1 GRE-FS or using black-blood FSE techniques (Fig. 10.5). Non-contrast CTA is included in all CTA protocols for assessing an IMH. Extensive IMH conforming to the false lumen of a typical dissection is sometimes termed a non-communicating dissection as false lumen may have thrombosed or is extremely slow to fill.

Penetrating Atherosclerotic Ulcer

Penetrating aortic ulcer (PAU) is a chronic aortic condition, defined as an atherosclerotic lesion that penetrates the internal elastic lamina through the media and is associated with hematoma formation within the aortic wall. PAUs are more frequent in elderly men with hypertension, tobacco use, and coronary artery disease [50]. Initially, these atheromatous ulcers are confined to the intimal layer and are usually asymptomatic. If untreated, the lesions progress to deep atheromatous ulcers that penetrate through the elastic lamina into the media, and patients present with acute chest pain radiating to the interscapular region. It is usually located in the descending aorta and is rarely observed in the ascending aorta. PAU is considered a prelude to IMH and aortic dissection [28]. PAUs are well depicted either on MRA

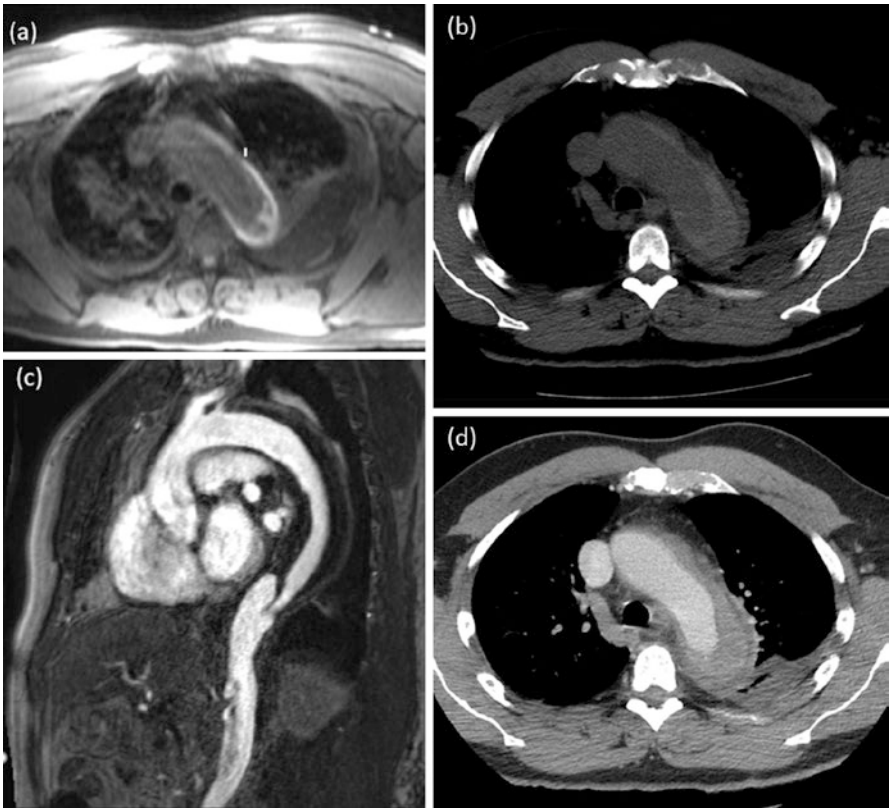

Fig. 10.5 MRA and CTA images of a 59-year-old male patient with intramural hematoma. Axial T1 VIBE image (**a**) demonstrates a crescent-shaped hyperintensity in the distal aortic arch with corresponding hyperdensity on the non-contrast CT image (**b**). The intramural hematoma demonstrates hypodensity on the sagittal contrast-enhanced MRA (**c**) and the axial post-contrast CT scan (**d**)

post-contrast T1 GRE-FS images as a protrusion from the lumen in acute or subacute disease or on conventional CE-MRA and on CTA as a contrast-filled outpouching with jagged margins on an aortic wall with severe underlying atherosclerotic disease (Fig. 10.6) [51].

Thoracic Aortic Aneurysm

Thoracic aortic aneurysms (TAA) are a relatively common and important pathologic entity which predispose to lethal clinical consequences such as rupture or dissection if left undiagnosed [52]. The incidence of TAA is estimated to be up to 7.6 cases per 100,000 person-years [45]. Many risk factors have been implicated in

Fig. 10.6 Non-contrast MRA (navigator balanced SSFP) in a 55-year-old male patient referred for arch abnormality identified on transesophageal echocardiogram; axial slice demonstrates the outpouching from the lateral aspect of the arch with partial thrombus consistent with a penetrating atherosclerotic ulcer (arrow)

the development of TAA, the most common being chronic atherosclerosis, hypertension, smoking, and hyperlipidemia [53–55]. TAAs are clinically silent and most commonly discovered as an incidental finding when conducting thoracic imaging for other unrelated conditions. When present, symptoms may be subtle and include stridor or hoarseness due to the compressive effect of an enlarging aneurysm or dyspnea and fatigue secondary to aortic root involvement and resulting aortic regurgitation causing heart failure.

TAAs are most commonly classified based on the aortic segment they involve and their shape. TAAs are more common in the aortic root and ascending aorta (60%) when compared to the descending aorta (40%). Most TAAs are fusiform in shape (involving a continuous segment of the vessel), whereas a saccular aneurysm (arising in an eccentric manner from aortic wall) suggests a mycotic aneurysm or pseudoaneurysm [56, 57]. By definition, a TAA is diagnosed when the aortic diameter is greater than 5 cm in the ascending aorta and 4 cm in the descending aorta [58]. Gender, age, and the location in the thoracic aorta all dictate if an aortic segment is considered aneurysmal. Women typically have smaller aortic diameters than men. Diameters that are considered normal also increase with increasing age and larger body masses [59, 60]. Therefore, it is more accurate to calculate values normalized to body surface area. The normal diameters of the thoracic aorta in adults are as follows: 3.5–3.7 cm for females and 3.6–3.9 cm for males at the aortic root,

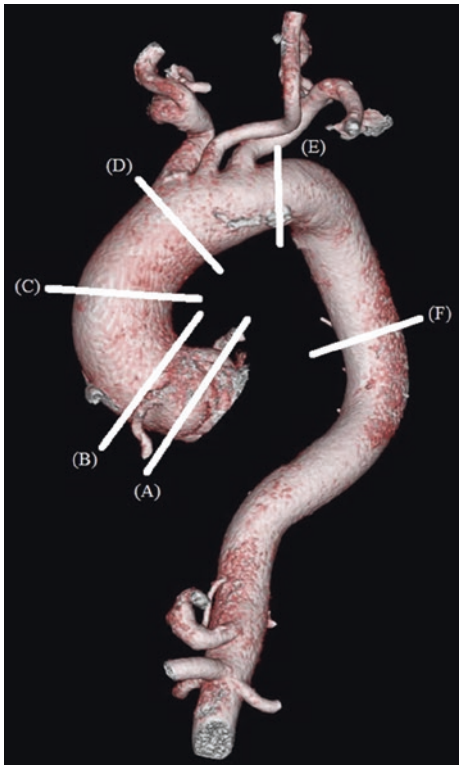

Fig. 10.7 Volume-rendered CTA of a thoracic aortic aneurysm. (A) Sinus of Valsalva: 47 × 44 × 41 mm. (B) Sino-tubular junction: 43 × 41 mm. (C) Mid-ascending aorta: 49 × 47 mm. (D) Proximal aortic arch: 41 × 40 mm. (E) Distal aortic arch: 31 × 29 mm. (F) Lower descending thoracic aorta: 28 × 27 mm

around 2.85 cm for both genders at the mid-ascending aorta, and 2.45–2.6 cm for females and 2.4–3.0 cm for males at the mid-descending aorta [61]. Figure 10.7 depicts a volume-rendered image of a thoracic aortic aneurysm with standardized measurements taken at six anatomical locations.

TAAs can have variable expansion rates based upon current diameter, location within the aorta, and the etiology [28, 52, 62]. The size and rate of expansion of the TAA will determine the urgency for surgical intervention [61, 63]. Rarely, a TAA may rupture, particularly if it is over 5.5 cm in size, which leads to significant morbidity and mortality. Therefore, prompt and accurate assessment is paramount to appropriate clinical outcomes. Symptomatic TAAs require urgent surgical intervention, while asymptomatic TAAs can be serially monitored with imaging and risk factor control. Long-term surveillance is necessary to evaluate the development of symptoms, size of aneurysm, and development of complications. The preferred imaging modality is based on the location of the aneurysm. Ideally, consistency using the same modality for follow-up is preferred to have an accurate assessment of aneurysmal diameter [64]. Current guidelines recommend imaging 6 months after the initial diagnosis to monitor for rapid aneurysmal expansion and stability. If imaging shows instability or rapid expansion, best practice would be surgical intervention or more frequent imaging. Table 10.4 outlines the guidelines for TAA surveillance and recommended management [61].

Table 10.4 Guidelines for thoracic aortic aneurysm surveillance and recommended management

Aneurysmal description	Size and frequency of monitoring
Aortic root/ascending aortic aneurysm (sporadic/degenerative)	3.5–4.5 cm: annual CTA or MRA 4.5–5.4 cm: biannual CTA or MRA Over 5.4 cm: surgical intervention -If aortic valvular disease present concomitant TTE is recommended
Aortic root/ascending aortic aneurysm (genetically mediated/connective tissue disease)	3.5–4.0 cm: annual CTA or MRA 4.0–5.0 cm: biannual CTA or MRA Over 5.0 cm: surgical intervention -If aortic valvular disease present concomitant TTE is recommended
Descending aortic aneurysm	4.0–5.0 cm: annual CTA or MRA 5.0–6.0 cm: annual CT or MRA Over 6.0 cm: surgical intervention

Table 10.5 The American College of Radiology recommendations for imaging thoracic aortic aneurysms

Imaging modality	Comments
CXR	Helpful to exclude other thoracic pathology, but findings such as a widened mediastinum or tortuous aorta on CXR are not sensitive or specific to TAA
CTA chest with contrast	Provides an excellent anatomic assessment including branch involvement and pre- and postoperative assessment. ECG-gated CTA has provided the ability to minimize cardiac motion artifacts, particularly at the aortic root. More appropriate than MRA if the patient is hemodynamically unstable. Limited in follow-up by high radiation and contrast burden
MRA chest with or without contrast	Allows for excellent assessment and follow-up of TAA size, shape, extent, and diameters with no radiation exposure. Although ECG- and navigator-gated CE-MRA is currently the gold standard to evaluate TAA, an NC-MRA using bSSFP is an acceptable alternative to CE-MRA in those with nephropathy. More appropriate than CT for aneurysms involving the aortic sinus and in patients who required follow-up for known TAAs to limit radiation exposure
Echocardiography	Rapid, widely available modality which is particularly useful in unstable patients, may be useful for initial workup for TAA. Transthoracic echocardiography allows for adequate assessment of the aortic root; however, it provide limited assessment of the ascending and descending aorta. It also may be limited in obese patients or patients with an abnormal thoracic wall secondary to surgery or comorbid chronic obstructive pulmonary disease. Therefore, should be followed up with CTA or MRA.

TTE, ECG-gated CTA, and MRA are the most commonly used modalities in the diagnosis and surveillance of TAA [65]. The modality used is dictated by the clinical context as well as the availability and expertise at each institution. Table 10.5 summarizes the ACR recommendations for imaging TAAs [66]. TTE is useful in the assessment of aneurysms of the aortic root. The proximal ascending aorta and the descending aorta are not visualized with enough detail to obtain

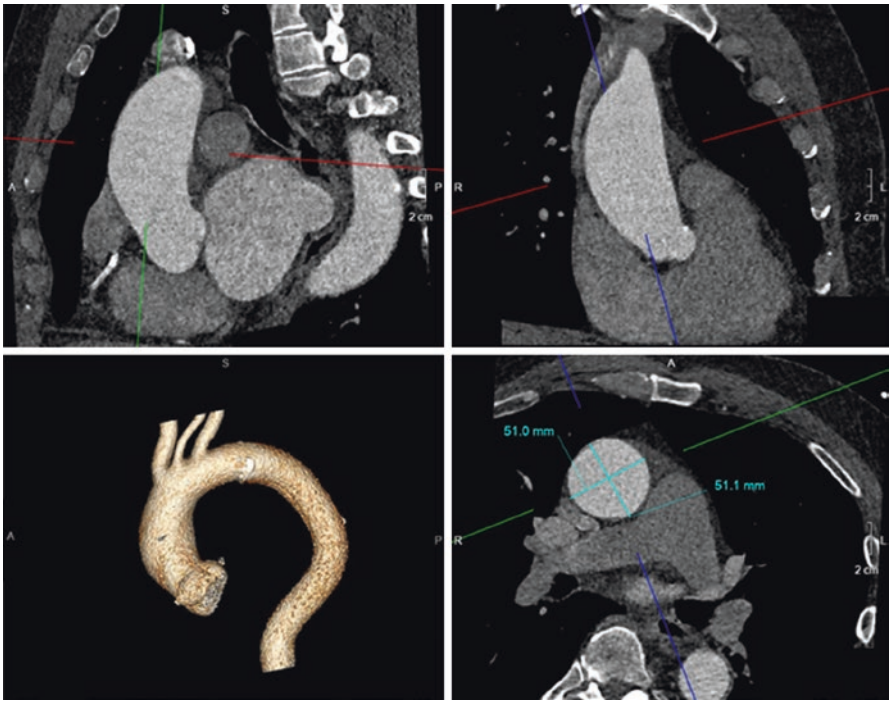

Fig. 10.8 ECG-gated CTA of the thoracic aorta in a 59-year-old patient for routine follow-up of a thoracic aortic aneurysm. Cross-sectional measurements of the ascending aorta were performed using a double oblique technique using the sagittal and coronal reformats in order to obtain orthogonal measurements. The mid-ascending aorta measures 51 × 51.1 mm

accurate measurements for diagnosis or follow-up. Therefore, if TAA is detected with TTE, it is imperative to further assess and characterize the aneurysm with either CTA or MRA. TEE is not typically used in clinical practice to diagnosis TAA due to its invasive nature and inability to assess the distal ascending aorta and proximal arch [61].

ECG-gated CTA (Fig. 10.8) is most commonly used to evaluate TAAs, given its rapid acquisition, wide availability, and submillimeter diagnostic accuracy [67]. ECG gating to diastole minimizes artifact due to cardiac motion and possible erroneous measurements, which is particularly necessary when assessing mobile structures like the aortic root and ascending arch [68]. Patients who require serial imaging for follow-up of TAAs are exposed to higher amounts of radiation over time when using CTA. This has been reduced with prospective ECG gating and low kV techniques. The downside to this technique is that the cusp motion and aortic valve morphology cannot be adequately assessed, as imaging throughout the whole cardiac cycle (retrospective gating) is required to assess moving structures. Also, the risk of contrast-induced nephropathy is always of concern, particularly in patients with renal insufficiency.

CE-MRA is also useful as a first-line test for diagnosing and assessing TAAs, as it can depict the exact diameters, the morphology, and extent of an aneurysm. Cine

imaging sequences obtained by PC-MRA provide an accurate assessment of concomitant aortic valve function by evaluation of valve morphology and cusp motion, which is helpful in assessing the degree of regurgitation or stenosis in patients with coexisting BAV or if the aortic root is involved in the TAA. Importantly, CE-MRA does not involve ionizing radiation and therefore may be more desirable for younger patients with TAAs who require serial follow-up (Fig. 10.9). Similar to CTA, ECG gating to diastole is preferred when assessing TAAs with CE-MRA to produce high-quality accurate artifact-free images of the thoracic aorta. Although gadolinium contrast is helpful for thoracic aortic evaluation, it is not always necessary when evaluating TAA with MRA, particularly if assessing aortic diameter. NC-MRA using bSSFP technique may serve as a suitable alternative to CE-MRA in patients with renal insufficiency or allergy to gadolinium. Additionally, repeated gadolinium contrast administrations when following up TAA with CE-MRA may be undesirable, particularly due to recent emerging concerns about gadolinium brain deposition [69].

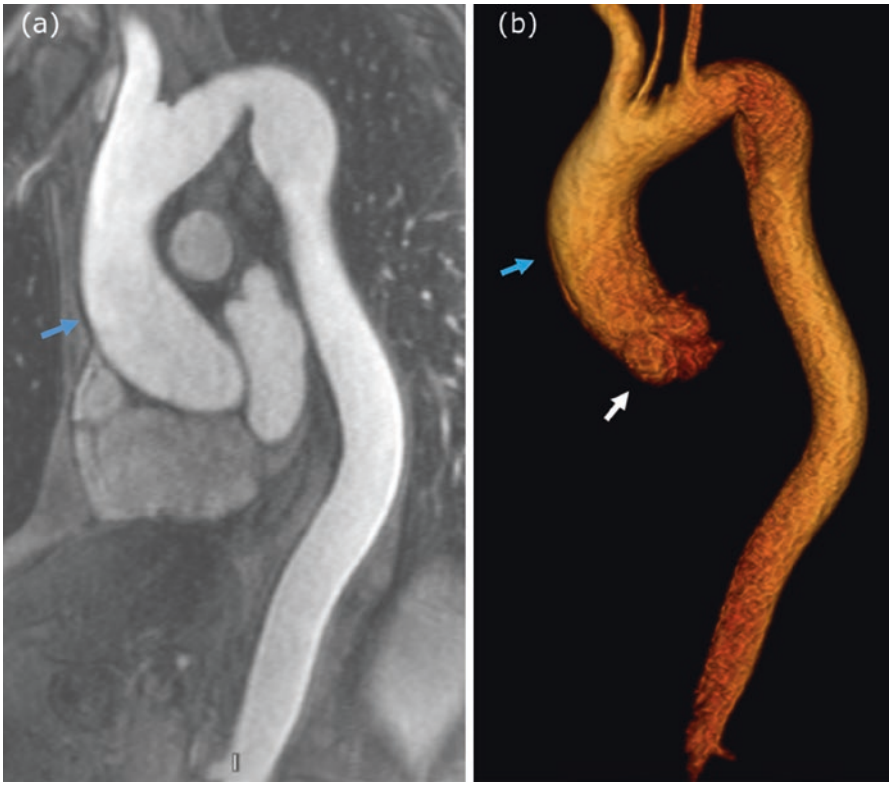

Fig. 10.9 A 61-year-old male who presents for a routine follow-up for a thoracic aortic aneurysm. Sagittal contrast-enhanced MRA (**a**) and a volume rendering (**b**) of a thoracic aortic aneurysm with a maximum measurement of 4.8 cm at the sinus of Valsalva (white arrow in **b**) and 4.5 cm at the mid-ascending aorta level (blue arrows)

Newer techniques such as 4D flow MRI may provide additional information about flow patterns in TAAs (e.g., vortical flow) as well as additional quantitative parameters such as wall shear stress [70], which may contribute to aneurysmal expansion.

Traumatic Aortic Injuries

Traumatic aortic injuries (TAI) are one of the most common causes of death in road traffic accidents with aortic transection accounting for 18% of all deaths from motor vehicle accidents [71]. Table 10.6 outlines the Society for Vascular Surgery criteria of traumatic aortic injuries (TAI). TAI are classified into Grade 1 (intimal tear), Grade 2 (intramural hematoma or large intimal flap), Grade 3 (pseudoaneurysm), and Grade 4 (aortic ruptures) (Fig. 10.10) [72]. The morbidity and mortality are historically around 85% if the injury is left untreated [73], and a high index of suspicion and careful evaluation is needed for an accurate diagnosis. A newer classification system known as the Harborview criteria classifies aortic injury into mild, moderate, and severe. No intervention and possible follow-up imaging are indicated in mild aortic injury if an intimal tear (<10 mm) is present; if the injury is moderate (intimal tear >10 mm), a semi-elective repair is indicated; and in severe injury (including rupture, active bleeding, and large left subclavian hematoma; >15 mm), immediate repair is indicated [74]. Proposed mechanisms include rapid acceleration or deceleration, shearing forces, osseous pinch, and hydrostatic forces or water hammer phenomenon [75]. Contrast-enhanced MDCT is the preferred imaging technique for evaluation of patients with multiple trauma; injuries to several organ systems can be detected in a matter of minutes. A traumatic aortic transection (aortic rupture) is a devastating condition that usually affects patients involved in high-energy blunt trauma such as road traffic accidents. The most common area is at the aortic isthmus distal to the left subclavian artery origin. For survivors, prompt imaging is crucial to guide emergency management. Contrast-enhanced computed tomographic angiography (CE-CTA) of the chest and TEE are the gold standard imaging modalities for diagnosis of this potentially fatal condition [61]. CE-CTA is highly sensitive and specific and therefore recommended for the hemodynamically stable patient [76], while TEE is employed in the hemodynamically unstable patient [77]. It is recommended that all patients with TAI should undergo a follow-up CTA 6 weeks post-injury.

Table 10.6 The Society for Vascular Surgery criteria of traumatic aortic injuries with indicated management

Classification grade	Description of injury (and indicated management)
Grade 1	Intimal tear (medical management; low-dose aspirin)
Grade 2	Intramural hematoma/large intimal flap (medical management or by thoracic endovascular repair; TAVER)
Grade 3	Pseudoaneurysm (urgent TEVAR)
Grade 4	Rupture (emergency TEVAR)

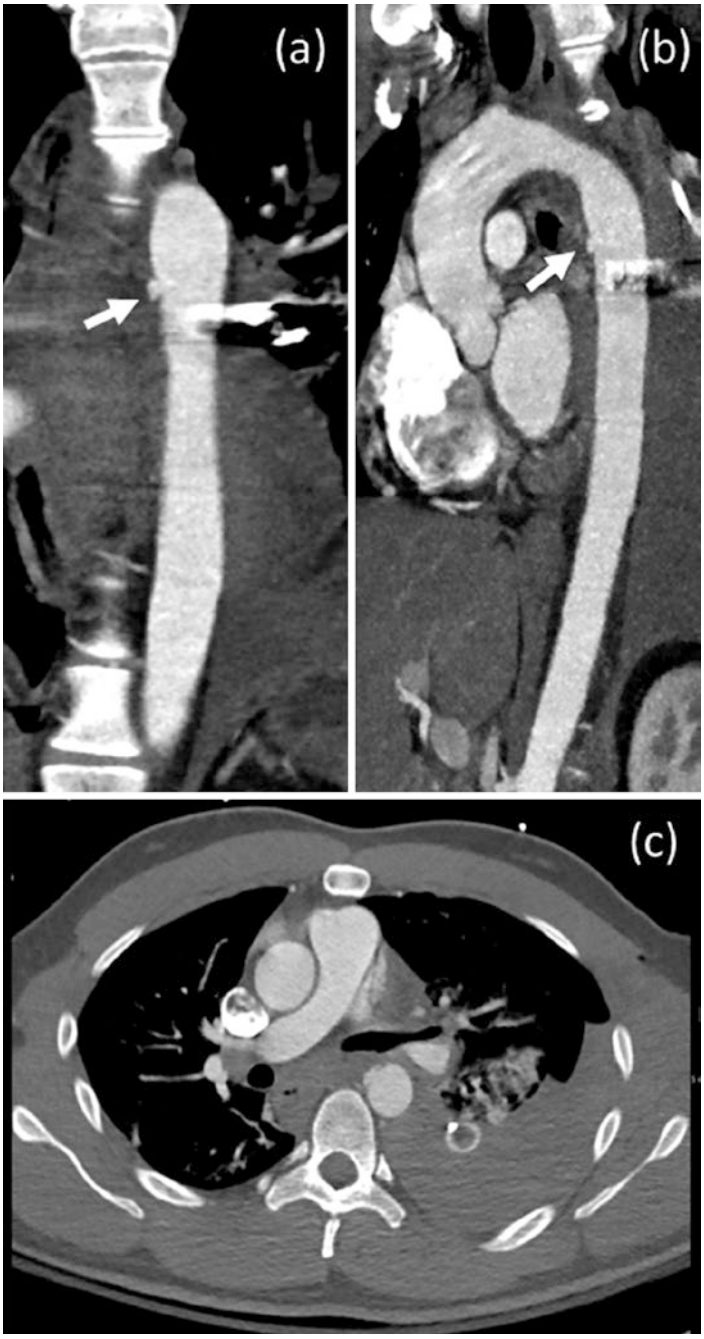

Fig. 10.10 A 27-year-old male patient who suffered a chest gunshot wound. These are coronal (**a**), sagittal (**b**), and axial (**c**) CTA images which demonstrate aortic injury in the anterior aspect of the proximal descending aorta (arrow). Note the presence of a large left hemothorax and a chest tube in situ (black arrow). Metal artifact from the restrained bullet can be seen

Vasculitis

Vasculitis is an umbrella term that refers to a group of disorders causing inflammation of the blood vessels. This chapter will focus on large vessel vasculitis (LVV) which is the most common type of primary vasculitis affecting the aorta and its major branches. LVV is comprised of giant cell arteritis (GCA) and Takayasu's arteritis (TAK). A broad range of noninvasive imaging modalities and techniques have superseded conventional angiography and biopsy in diagnosing and monitoring the progression of these two conditions, as they are associated with lower complication rates and provide information about vessel wall morphology and active pathology [78, 79].

Takayasu's Arteritis (TAK)

TAK is an idiopathic granulomatous patchy vasculitis which affects the aorta and its main branches. The disease is more common in younger patients under the age of 50, in women more than men (10:1), and is more prevalent in the Asian population [80]. Symptoms are highly variable based on the vascular territory involved, but most patients who present acutely are either in the acute pre-pulseless phase and have nonspecific constitutional symptoms such as muscle pain, weight loss, low-grade fever, and fatigue. Patients who present in the more chronic pulseless phase usually have more severe symptoms such as renovascular hypertension or limb ischemia secondary to the inflammation causing stenosis of affected vessels. A severe inflammatory phase can destroy the media and lead to the development of TAA [81]. Classification of TAK (I-V) is based on the extent of aortic and main branch involvement [82].

The most recent 2018 EULAR guidelines recommend CE-MRA as the initial modality in evaluating mural inflammation and luminal structural associated with TAK such as stenosis, occlusion, or aneurysm development (Fig. 10.11) [79]. Using CE-MRA in TAK minimizes radiation exposure to patients, who are typically young. A recent study indicated that CE-MRA had a sensitivity and specificity approaching 100% when compared to conventional angiography [83]. CTA and/or PET are used as an acceptable alternative (Figs. 10.12 and 10.13) [79]. Findings on MRA and CTA that indicate acute active disease include wall thickening and enhancement. The aortic valve may be involved and show signs of stenosis or regurgitation. In the chronic phase, diffuse distal narrowing may be appreciated with aneurysmal formation [84]. US does not allow for adequate assessment for the thoracic aorta; therefore, it is not typically used. One small study indicated that CTA had a specificity and sensitivity approaching 100% when compared to conventional angiography [85].

Giant Cell Arteritis (GCA)

GCA is a granulomatous vasculitis that affects medium to large elastic arteries, particularly in the aorta and temporal branch of the extracranial carotid artery, giving it the commonly known name of temporal arteritis. The disease is uncommon before

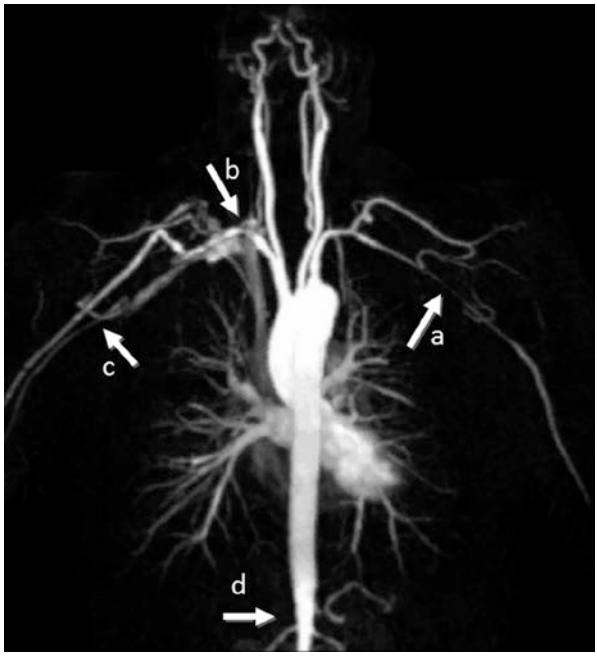

Fig. 10.11 Single image from a coronal time-resolved MRA of the chest in a 38-year-old female patient with suspected Takayasu arteritis. There is a long-segment stenosis in the left axillary artery (a), multifocal stenosis in the right subclavian artery (b), and the occlusion in the right axillary artery (c). In the limit of the field of view, note the circumference of the infrarenal aorta (d)

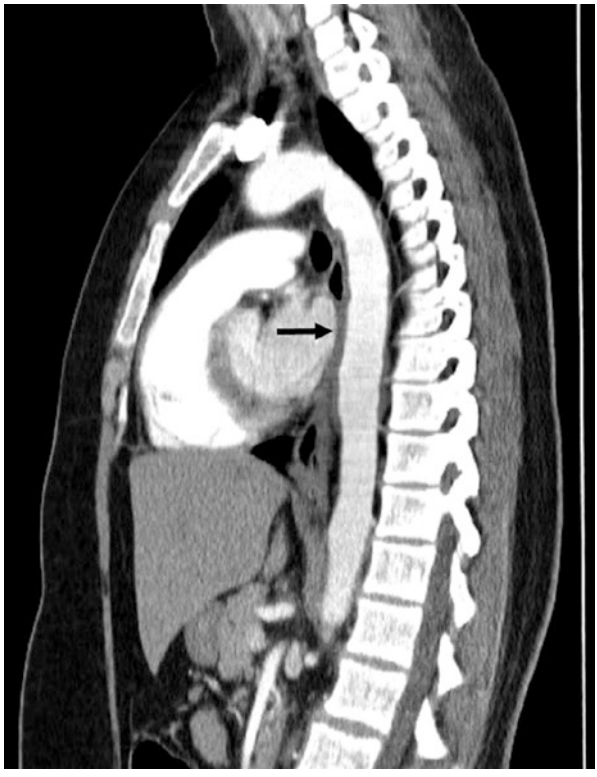

Fig. 10.12 This arterial phase CTA of the aorta in a patient with known Takayasu arteritis. There is circumferential wall thickening in the mid-thoracic aorta and extending to the arch

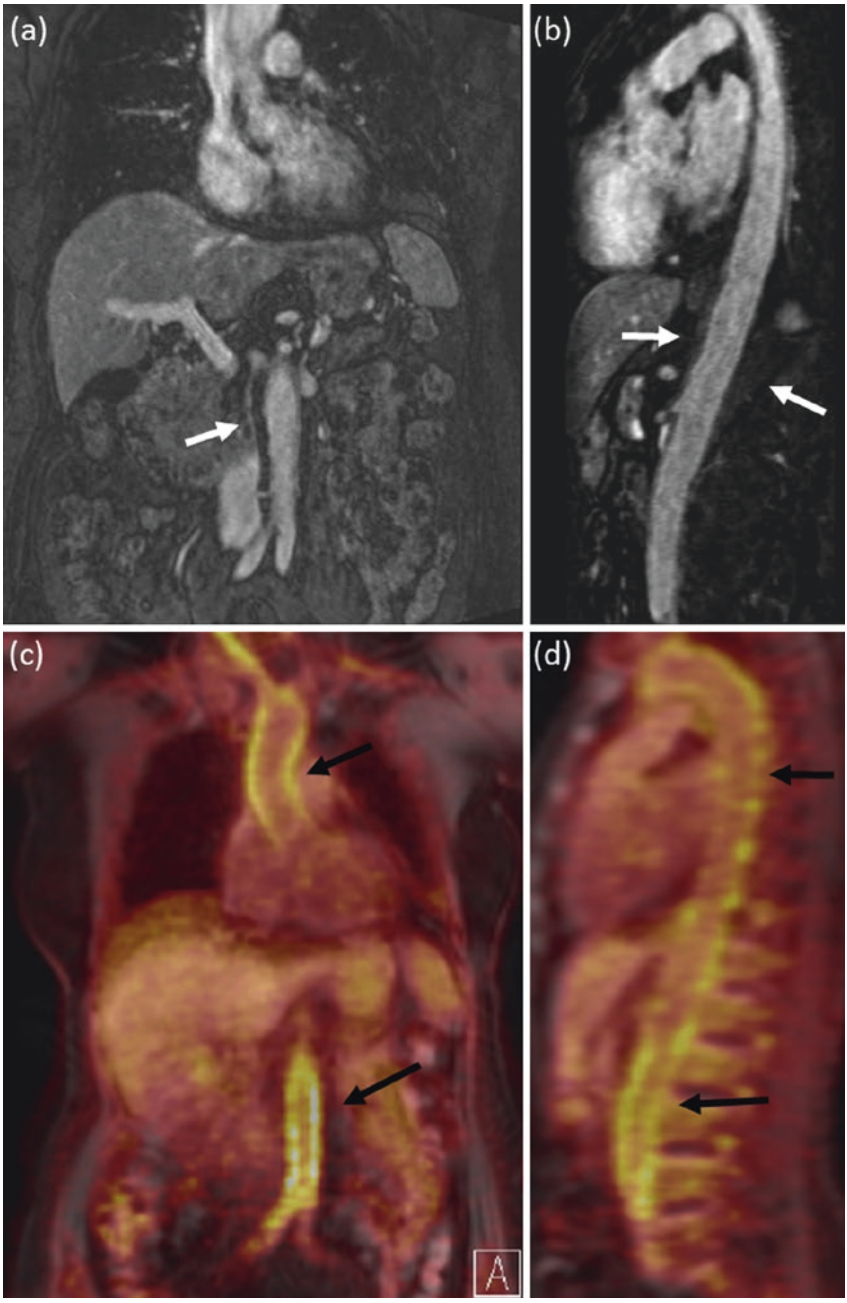

Fig. 10.13 Images from a whole body PET/MR of a 76-year-old female patient with polymyalgia rheumatic and suspicion for vasculitis. Coronal (**a**) and sagittal (**b**) MRA demonstrates circumferential narrowing of the aortic wall demonstrating low signal intensity (white arrows). Corresponding coronal (**c**) and sagittal (**d**) images from fused PET/MR demonstrate significant 18-FDG uptake in the aortic wall in the chest and abdomen concerning for vasculitis

the age of 50 and tends to occur more commonly in females and in patients of northern European descent [86]. Patients may have non-specific clinical findings, the most suggestive being jaw claudication, a temporal headache, and scalp tenderness.

US has very limited ability to assess LV-GCA affecting the thoracic aorta, and therefore in clinical practice, MRA, PET, and/or CTA are employed to assess for LV-GCA. CE-MRA is the modality of choice for evaluating LV-GCA [79]. Specific MRI protocols and sequences used can detect the presence and extent of structural lesions such as aortic wall thickening and occlusive/stenotic lesions with high accuracy. In addition, the contrast enhancement of the arterial wall suggests active mural inflammation [87, 88]. PET can also be used to assess GCA, with FDG uptake seen in regions of active inflammation, and has the advantage of evaluating other sinister pathologies such as cancer and infection in patients with non-specific constitutional and systemic symptoms. Nevertheless, PET is a costly modality, which is not widely available and exposes patients to radiation. Furthermore, inexperienced readers may misinterpret atherosclerotic disease as LV-GCA. Missing structural information such as wall thickness and obstruction can be overcome by combining PET and CT [89]. The choice of imaging for long-term surveillance of the disease activity and assessment of structural damage is an individual decision based on specific clinical situations, local expertise, and availability of modalities.

Congenital Abnormalities of the Aorta

A large number of congenital abnormalities can affect the thoracic aorta such aortic coarctation (Fig. 10.14), patent ductus arteriosus (PDA), aortic hypoplasia, right-sided aortic arch, aberrant subclavian artery, and double aortic arch. These conditions are best assessed using CE-MRA [90, 91]. Cine images of the heart should always be included when assessing for congenital aorta abnormalities to detect coexisting cardiac defects. 3D steady-state MRA can be used to evaluate the complex vasculature in congenital heart disease, and flow pattern can be visualized using 4D flow MRI. Anomalies of the aortic arch are classified into three groups based on Edwards' hypothetical model: Group 1 (double arch anomalies), Group 2 (left aortic arch anomalies), and Group 3 (right aortic arch anomalies) [92]. As these anomalies may be associated with congenital heart disease, comprehensive imaging using volume-rendered CTA and MRA is indicated to obtain important preoperative information and assess the relationship of the arch to the esophagus and trachea [93].

Abdominal Aorta

Abdominal aortic aneurysm (AAA) is defined as an abnormal focal or segmental dilatation of the abdominal aorta to 50% more than the proximal un-diseased segment or diameter of greater than 3 cm [94]. It is the most common area of arterial aneurysm [95]. It tends to affect people of older age, males more than females (4:1),

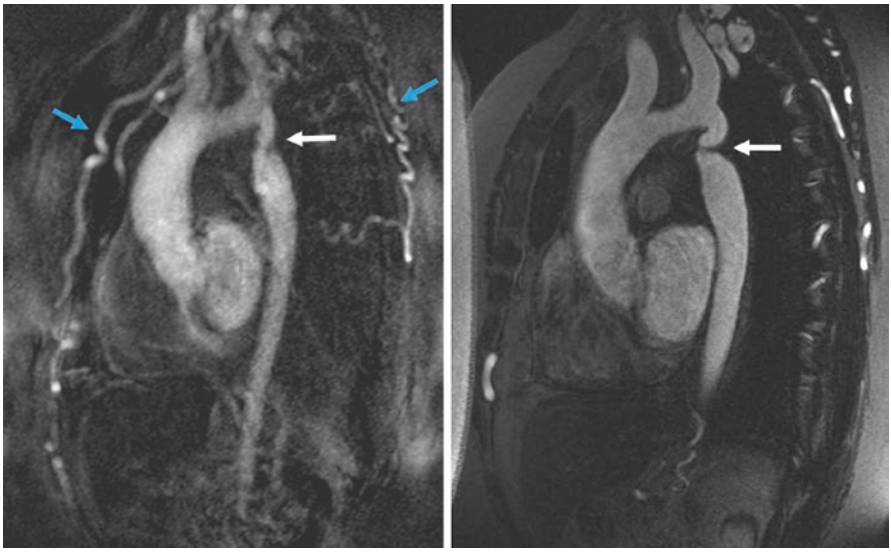

Fig. 10.14 Sagittal MRA images of the aorta in a 52-year-old female demonstrating focal post-ductal coarctation and over 90% stenosis of the lumen (white arrows). There are prominent collaterals in the chest wall (blue arrows). This patient also had a bicuspid aortic valve

and Caucasians [96]. The main risk factors for AAA rupture are a large diameter (>5.5 cm), rate of expansion (1 cm/year), and most importantly current tobacco usage, as it has been proven to be the most detrimental risk factor leading to degeneration of the aortic wall [97]. Most patients are asymptomatic and are diagnosed when abdominal imaging is conducted for other reasons. When symptomatic, patients classically present with abdominal pain radiating to back or flank, and occasionally symptoms of ischemia occur in the lower extremities secondary to thromboembolism.

Currently, abdominal x-ray (AXR), US, MDCT, and MRA are used to assess the abdominal aorta. In clinical practice, US and MDCT are the most commonly used modalities as they are highly sensitive and specific for establishing a diagnosis of AAA [98]. Each modality is recommended under differing clinical conditions depending upon the clinical presentation and hemodynamic stability of the patient.

Lateral AXR views may show curvilinear calcification of the abdominal aorta, but both opposing aortic walls need to be calcified and viewed before the diagnosis of AAA can be made. A tortuous, calcified aorta can mimic AAA, and unless both walls can be seen clearly calcified, the diagnosis of AAA cannot be made.

US is the most commonly employed initial imaging modality in an asymptomatic patient, as it provides a noninvasive, inexpensive assessment of the abdominal aorta without the use of potentially nephrotoxic contrast and the exposure to radiation. US has a sensitivity and specificity approaching 100% in detecting non-leaking AAAs [96, 99]. The limitation of US is technician and equipment-dependency [100]. Furthermore, US may not always provide an accurate visualization of the

abdominal aorta in up to 3% of patients, due to air in the overlying loops of bowel or patient obesity [96, 101]. When the US images are adequate or when a preoperative assessment is required, another imaging modality should be used, which is typically abdominal MDCT.

Abdominal MDCT is used in the acute setting in a symptomatic patient to determine if an aneurysm is leaking, has ruptured, or is enlarging rapidly or if the symptoms present could be related to other abdominal pathology [54, 102–104]. Abdominal MDCT is necessary for preoperative planning as it provides an anatomical assessment of the proximal and distal extent of the aneurysm and involvement of the major branch vessels in relation to the aortic bifurcation, which determines the suitability for endovascular (EVAR) repair [54, 102–104]. If there is a concern for contrast-induced nephropathy, a non-contrast MDCT scan may be sufficient to provide diagnostic information about aortic dimensions. Disadvantages of MDCT are the potential to overestimate the aortic diameter, greater cost, and the cumulative risk of radiation with repeated scans in patients with known AAA [8]. To avoid overestimation of the aortic diameter on CT, measurements should be obtained perpendicular to the centerline which can be achieved using semiautomated software or orthogonal measurements [105, 106]. CT scan findings consistent with ruptured aneurysm include para-aortic fat stranding, retroperitoneal hemorrhage or hematoma, indistinct aortic wall, and extravasation of intravenous contrast outside the aorta. Signs that indicate a contained leak or imminent rupture include the draped aorta sign, hyperdense crescent sign, thrombus fissuration, and a tangential calcium sign. Most importantly, a 5 mm increase of aneurysm diameter in a 6-month period, or a diameter of >7 cm are also considered urgent indications for surgical repair due to impending rupture.

MRA is not commonly used in the initial evaluation of AAA but may play a role in selected patients, such as in those with chronic kidney disease in whom iodinated contrast administration is contraindicated [107]. Similar to MDCT, MRA provides a reliable assessment of morphology and size of the aneurysm which guides management decisions and aids in preoperative assessment [108]. Furthermore, it can assess the presence of atheroma or thrombus and involvement of the side branches. Compared to MDCT, there is contradictory evidence regarding which modality is more sensitive to employ in assessing postoperative complication surveillance particularly post-EVAR endoleaks. CTA is the preferred modality due to its reproducibility and lack of impact of metal in stent grafts on image quality. MRA has also been shown to be sensitive for detecting post-EVAR endoleaks [109, 110]. Figure 10.15 shows an infrarenal abdominal aortic aneurysm on CTA. However, MRA is more susceptible to motion artifacts than MDCT, because a patient must remain still for a longer period than with MDCT. Additionally, MRA may be susceptible to metal artifacts from adjacent stent grafts. Table 10.7 outlines the classification of endoleaks occurring post-EVAR, most preferred imaging modality for detection and suggested management [111, 112].

Catheter arteriography has some utility in patients with significant contraindications to both CTA and MRA, although it is inadequate alone for pre-procedural planning.

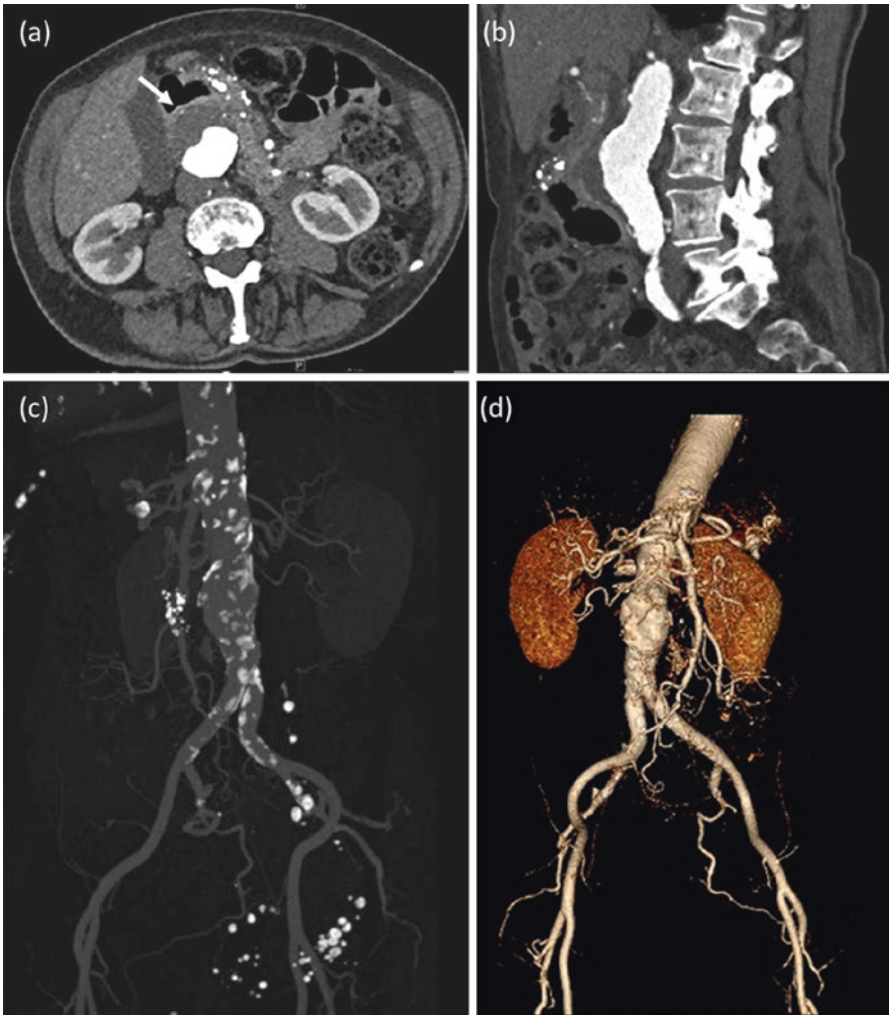

Fig. 10.15 Axial (**a**), sagittal (**b**), and volume rendered (**c**) and (**d**) images from a CTA of the abdomen and pelvis in an 88-year-old female demonstrate an infrarenal abdominal aortic aneurysm with a maximum dimension of 4.3 cm. There is a partial thrombus in the aneurysm lumen anteriorly (arrow)

Mycotic Aneurysm

A mycotic aortic aneurysm (MAA) is a specific type of aneurysm which causes focal dilation of the aorta secondary to an infection, usually in the setting of bacteremia [113]. High suspicion is required as symptoms are relatively non-specific, and prompt imaging is essential to confirm the diagnosis. Multi-detector CT angiography (MD-CTA) provides a prompt 3D reconstruction with high resolution making it the imaging modality of choice. Recently, advances in CE-MRA have

Table 10.7 Classification of endoleaks occurring post-EVAR with recommended imaging and treatment

	Definition and treatment	Imaging modality of choice
Type 1	A leak occurring at the end of a graft. Most common post-thoracic aneurysm repair. Subclassified in 1a (proximal leak) and 1b (distal leak). Urgent intervention required	Triple-phased CT angiography; may show hyper-attenuation due to acute hemorrhage. Contrast usually collects in the center of the sac
Type 2 (retroleak)	Retrograding flow through a collateral branch vessel, most commonly lumbar and inferior mesenteric branches. Most common after AAA repair. Subclassified into IIa (single vessel) and IIb (two or more vessels). Surveillance; most resolve spontaneously and require no intervention	Dual-energy and triple-phased CT angiography. Delayed phase particularly sensitive in detection of endoleak
Type 3	A leak secondary to mechanical failure of the graft and a defect in the graft fabric. Subclassified into IIIa (separation of the modular components) and IIIb (fracture in endograft). Rare; urgent intervention required	Multiphase CT angiography; arterial phase particularly sensitive in detection of endoleak
Type 4	Increased porosity graft; no treatment required	None usually required
Type 5 (endotension)	Is not considered a true leak and is defined as continuous expansion of the aneurysm sac greater than 5 mm, without an evident leak site on imaging; may relate to a low-flow endoleak. Often requires intervention	Debatable; MR angiography and contrast-enhanced ultrasound may be more accurate than CTA for postoperative endoleak

rendered it a valid alternative to MD-CTA [114, 115]. Periaortic changes are also helpful in diagnosing MAAs. Earlier signs include arterial wall irregularity and periaortic edema or gas, which can progress to periaortic mass or stranding. Periaortic soft tissue inflammation may appear as a homogeneous contrast-enhancing mass on CT, which can develop into heterogenous attenuation with tissue necrosis.

Conclusion

Aortic diseases cause significant morbidity and mortality and therefore require prompt and accurate evaluation. Advancements in imaging, especially CT and MRI, have contributed to a more accurate and effective diagnosis and follow-up in patients, resulting in improved clinical outcomes. As a result, both CT and MRI are the main imaging modalities used for assessing aortic diseases. Newer techniques, such as dual-energy CT and 4D flow MRI, promise to produce improved characterization of aortic pathology and may help predict which patients are more likely to progress. An understanding of the widely used imaging techniques and their characteristic imaging findings plays an integral part in the successful diagnosis and management of affected patients [56].

References

1. von Kodolitsch Y, Nienaber CA, Dieckmann C, Schwartz AG, Hofmann T, Brekenfeld C, Nicolas V, Berger J, Meinertz T. Chest radiography for the diagnosis of acute aortic syndrome. Am J Med. 2004;116(2):73–7.
2. Braverman AC. Acute aortic dissection: clinician update. Circulation. 2010;122(2):184–8. https://doi.org/10.1161/circulationaha.110.958975.
3. Mirvis SE, Bidwell JK, Buddemeyer EU, Diaconis JN, Pais SO, Whitley JE, Goldstein LD. Value of chest radiography in excluding traumatic aortic rupture. Radiology. 1987;163(2):487–93. https://doi.org/10.1148/radiology.163.2.3562831.
4. Sordelli C, Severino S, Ascione L, Coppolino P, Caso P. Echocardiographic assessment of heart valve prostheses. J Cardiovasc Echogr. 2014;24(4):103–13. https://doi.org/10.4103/2211-4122.147201.
5. Patil TA, Nierich A. Transesophageal echocardiography evaluation of the thoracic aorta. Ann Card Anaesth. 2016;19(Supplement):S44–55. https://doi.org/10.4103/0971-9784.192623.
6. Meredith EL, Masani ND. Echocardiography in the emergency assessment of acute aortic syndromes. Eur J Echocardiogr. 2009;10(1):i31–9. https://doi.org/10.1093/ejechocard/jen251.
7. Cote G, Denault A. Transesophageal echocardiography-related complications. Can J Anaesth. 2008;55(9):622–47. https://doi.org/10.1007/bf03021437.
8. Sparks AR, Johnson PL, Meyer MC. Imaging of abdominal aortic aneurysms. Am Fam Physician. 2002;65(8):1565–70.
9. Sternbergh WC 3rd, Gonze MD, Garrard CL, Money SR. Abdominal and thoracoabdominal aortic aneurysm. Surg Clin North Am. 1998;78(5):827–43, ix.
10. Rafailidis V, Partovi S, Dikkes A, Nakamoto DA, Azar N, Staub D. Evolving clinical applications of contrast-enhanced ultrasound (CEUS) in the abdominal aorta. Cardiovasc Diagn Ther. 2018;8(Suppl 1):S118–s130. https://doi.org/10.21037/cdt.2017.09.09.
11. Li X, Staub D, Rafailidis V, Al-Natour M, Kalva S, Partovi S. Contrast-enhanced ultrasound of the abdominal aorta – current status and future perspectives. VASA. 2019;48(2):115–25. https://doi.org/10.1024/0301-1526/a000749.
12. Brink JA, Heiken JP, Forman HP, Sagel SS, Molina PL, Brown PC. Hepatic spiral CT: reduction of dose of intravenous contrast material. Radiology. 1995;197(1):83–8. https://doi.org/10.1148/radiology.197.1.7568859.
13. Guo K, Lath N, Tan JL. Imaging: Echo, CT and MRI. In: Niwa K, Kaemmerer H, editors. Aortopathy. Tokyo: Springer Japan; 2017. p. 75–111. https://doi.org/10.1007/978-4-431-56071-5_6.
14. Gutschow SE, Walker CM, Martínez-Jiménez S, Rosado-de-Christenson ML, Stowell J, Kunin JR. Emerging concepts in intramural hematoma imaging. Radiographics. 2016;36(3):660–74. https://doi.org/10.1148/rg.2016150094.
15. Fuentes-Orrego JM, Pinho D, Kulkarni NM, Agrawal M, Ghoshhajra BB, Sahani DV. New and evolving concepts in CT for abdominal vascular imaging. Radiographics. 2014;34(5):1363–84. https://doi.org/10.1148/rg.345130070.
16. Hu D, Yu T, Duan X, Peng Y, Zhai R. Determination of the optimal energy level in spectral CT imaging for displaying abdominal vessels in pediatric patients. Eur J Radiol. 2014;83(3):589–94. https://doi.org/10.1016/j.ejrad.2013.10.016.
17. Parfrey P. The clinical epidemiology of contrast-induced nephropathy. Cardiovasc Intervent Radiol. 2005;28(Suppl 2):S3–11.
18. Brenner DJ, Hall EJ. Computed tomography — an increasing source of radiation exposure. N Engl J Med. 2007;357(22):2277–84. https://doi.org/10.1056/NEJMra072149.
19. Poll LW, Cohnen M, Brachten S, Ewen K, Modder U. Dose reduction in multi-slice CT of the heart by use of ECG-controlled tube current modulation ("ECG pulsing"): phantom measurements. RoFo. 2002;174(12):1500–5. https://doi.org/10.1055/s-2002-35945.

20. Leschka S, Stolzmann P, Schmid FT, Scheffel H, Stinn B, Marincek B, Alkadhi H, Wildermuth S. Low kilovoltage cardiac dual-source CT: attenuation, noise, and radiation dose. Eur Radiol. 2008;18(9):1809–17. https://doi.org/10.1007/s00330-008-0966-1.
21. Schernthaner RE, Stadler A, Beitzke D, Homolka P, Weber M, Lammer J, Czerny M, Loewe C. Dose modulated retrospective ECG-gated versus non-gated 64-row CT angiography of the aorta at the same radiation dose: comparison of motion artifacts, diagnostic confidence and signal-to-noise-ratios. Eur J Radiol. 2012;81(4):e585–90. https://doi.org/10.1016/j.ejrad.2011.06.053.
22. Beeres M, Schell B, Mastragelopoulos A, Herrmann E, Kerl JM, Gruber-Rouh T, Lee C, Siebenhandl P, Bodelle B, Zangos S, Vogl TJ, Jacobi V, Bauer RW. High-pitch dual-source CT angiography of the whole aorta without ECG synchronisation: initial experience. Eur Radiol. 2012;22(1):129–37. https://doi.org/10.1007/s00330-011-2257-5.
23. Wu W, Budovec J, Foley WD. Prospective and retrospective ECG gating for thoracic CT angiography: a comparative study. Am J Roentgenol. 2009;193(4):955–63. https://doi.org/10.2214/AJR.08.2158.
24. Brown R, Nguyen TD, Spincemaille P, Cham MD, Choi G, Winchester PA, Prince MR, Wang Y. Effect of blood flow on double inversion recovery vessel wall MRI of the peripheral arteries: quantitation with T2 mapping and comparison with flow-insensitive T2-prepared inversion recovery imaging. Magn Reson Med. 2010;63(3):736–44. https://doi.org/10.1002/mrm.22227.
25. Francois CJ, Carr JC. MRI of the thoracic aorta. Magn Reson Imaging Clin N Am. 2007;15(4):639–51, vii. https://doi.org/10.1016/j.mric.2007.08.011.
26. Holloway BJ, Rosewarne D, Jones RG. Imaging of thoracic aortic disease. Br J Radiol. 2011;84(special_issue_3):S338–54. https://doi.org/10.1259/bjr/30655825.
27. Stojanovska J, Rodriguez K, Mueller GC, Agarwal PP. MR imaging of the thoracic aorta. Magn Reson Imaging Clin N Am. 2015;23(2):273–91. https://doi.org/10.1016/j.mric.2015.01.004.
28. Ward E, Carr JC. Thoracic aorta. In: Carr JC, Carroll TJ, editors. Magnetic resonance angiography: principles and applications. New York: Springer New York; 2012. p. 239–52. https://doi.org/10.1007/978-1-4419-1686-0_18.
29. Bireley WR 2nd, Diniz LO, Groves EM, Dill K, Carroll TJ, Carr JC. Orthogonal measurement of thoracic aorta luminal diameter using ECG-gated high-resolution contrast-enhanced MR angiography. J Magn Reson Imaging. 2007;26(6):1480–5. https://doi.org/10.1002/jmri.21085.
30. Groves EM, Bireley W, Dill K, Carroll TJ, Carr JC. Quantitative analysis of ECG-gated high-resolution contrast-enhanced MR angiography of the thoracic aorta. AJR Am J Roentgenol. 2007;188(2):522–8. https://doi.org/10.2214/ajr.05.1467.
31. Bock J, Frydrychowicz A, Lorenz R, Hirtler D, Barker AJ, Johnson KM, Arnold R, Burkhardt H, Hennig J, Markl M. In vivo noninvasive 4D pressure difference mapping in the human aorta: phantom comparison and application in healthy volunteers and patients. Magn Reson Med. 2011;66(4):1079–88. https://doi.org/10.1002/mrm.22907.
32. Miyazaki M, Lee VS. Nonenhanced MR angiography. Radiology. 2008;248(1):20–43. https://doi.org/10.1148/radiol.2481071497.
33. Pereles FS, McCarthy RM, Baskaran V, Carr JC, Kapoor V, Krupinski EA, Finn JP. Thoracic aortic dissection and aneurysm: evaluation with nonenhanced true FISP MR angiography in less than 4 minutes. Radiology. 2002;223(1):270–4. https://doi.org/10.1148/radiol.2231010966.
34. Kim J, Song H-C. Role of PET/CT in the evaluation of aortic disease. Chonnam Med J. 2018;54(3):143–52. https://doi.org/10.4068/cmj.2018.54.3.143.
35. Kotze CW, Menezes LJ, Endozo R, Groves AM, Ell PJ, Yusuf SW. Increased metabolic activity in abdominal aortic aneurysm detected by 18F-fluorodeoxyglucose (18F-FDG) positron emission tomography/computed tomography (PET/CT). J Vasc Surg. 2009;50(1):237. https://doi.org/10.1016/j.jvs.2009.05.036.
36. Truijers M, Kurvers HA, Bredie SJ, Oyen WJ, Blankensteijn JD. In vivo imaging of abdominal aortic aneurysms: increased FDG uptake suggests inflammation in the aneurysm wall. J Endovasc Ther. 2008;15(4):462–7. https://doi.org/10.1583/08-2447.1.

37. Reeps C, Essler M, Pelisek J, Seidl S, Eckstein HH, Krause BJ. Increased 18F-fluorodeoxyglucose uptake in abdominal aortic aneurysms in positron emission/computed tomography is associated with inflammation, aortic wall instability, and acute symptoms. J Vasc Surg. 2008;48(2):417–23; discussion 424. https://doi.org/10.1016/j.jvs.2008.03.059.
38. Kotze CW, Groves AM, Menezes LJ, Harvey R, Endozo R, Kayani IA, Ell PJ, Yusuf SW. What is the relationship between (1)(8)F-FDG aortic aneurysm uptake on PET/CT and future growth rate? Eur J Nucl Med Mol Imaging. 2011;38(8):1493–9. https://doi.org/10.1007/s00259-011-1799-8.
39. Courtois A, Nusgens BV, Hustinx R, Namur G, Gomez P, Somja J, Defraigne JO, Delvenne P, Michel JB, Colige AC, Sakalihasan N. 18F-FDG uptake assessed by PET/CT in abdominal aortic aneurysms is associated with cellular and molecular alterations prefacing wall deterioration and rupture. J Nucl Med. 2013;54(10):1740–7. https://doi.org/10.2967/jnumed.112.115873.
40. Singh P, Almarzooq Z, Salata B, Devereux RB. Role of molecular imaging with positron emission tomographic in aortic aneurysms. J Thorac Dis. 2017;9(Suppl 4):S333–42. https://doi.org/10.21037/jtd.2017.04.18.
41. Vilacosta I, Aragoncillo P, Cañadas V, San Román JA, Ferreirós J, Rodríguez E. Acute aortic syndrome: a new look at an old conundrum. Heart. 2009;95(14):1130. https://doi.org/10.1136/hrt.2008.153650.
42. LeMaire SA, Russell L. Epidemiology of thoracic aortic dissection. Nat Rev Cardiol. 2011;8(2):103–13. https://doi.org/10.1038/nrcardio.2010.187.
43. Clouse WD, Hallett JW Jr, Schaff HV, Spittell PC, Rowland CM, Ilstrup DM, Melton LJ 3rd. Acute aortic dissection: population-based incidence compared with degenerative aortic aneurysm rupture. Mayo Clin Proc. 2004;79(2):176–80.
44. Criado FJ. Aortic dissection: a 250-year perspective. Tex Heart Inst J. 2011;38(6):694–700.
45. McClure RS, Brogly SB, Lajkosz K, Payne D, Hall SF, Johnson AP. Epidemiology and management of thoracic aortic dissections and thoracic aortic aneurysms in Ontario, Canada: a population-based study. J Thorac Cardiovasc Surg. 2018;155(6):2254–2264.e2254. https://doi.org/10.1016/j.jtcvs.2017.11.105.
46. Kienzl D, Prosch H, Topker M, Herold C. Imaging of non-cardiac, non-traumatic causes of acute chest pain. Eur J Radiol. 2012;81(12):3669–74. https://doi.org/10.1016/j.ejrad.2011.02.042.
47. Gomes AS, Bettmann MA, Boxt LM, Grollman J, Henkin RE, Higgins CB, Kelley MJ, Needleman L, Pagan-Marin H, Polak JF, Stanford W. Acute chest pain--suspected aortic dissection. American College of Radiology. ACR Appropriateness Criteria. Radiology. 2000;215(Suppl):1–5.
48. Hagan PG, Nienaber CA, Isselbacher EM, et al. The international registry of acute aortic dissection (irad): new insights into an old disease. JAMA. 2000;283(7):897–903. https://doi.org/10.1001/jama.283.7.897.
49. Allen BD, Aouad PJ, Burris NS, Rahsepar AA, Jarvis KB, François CJ, Barker AJ, Malaisrie SC, Carr JC, Collins JD, Markl M. Detection and hemodynamic evaluation of flap fenestrations in type B aortic dissection with 4D flow MRI: comparison with conventional MRI and CT angiography. Radiol Cardiothorac Imaging. 2019;1(1):e180009. https://doi.org/10.1148/ryct.2019180009.
50. Romero J, Shah A, Korniyenko A. A blind spot in the eye of imaging technology: penetrating atheromatous ulcer. Hell J Cardiol. 2013;54(4):322–5.
51. Mohiaddin RH, McCrohon J, Francis JM, Barbir M, Pennell DJ. Contrast-enhanced magnetic resonance angiogram of penetrating aortic ulcer. Circulation. 2001;103(4):e18–9. https://doi.org/10.1161/01.CIR.103.4.e18.
52. Kuzmik GA, Sang AX, Elefteriades JA. Natural history of thoracic aortic aneurysms. J Vasc Surg. 2012;56(2):565–71. https://doi.org/10.1016/j.jvs.2012.04.053.
53. Bickerstaff LK, Pairolero PC, Hollier LH, Melton LJ, Van Peenen HJ, Cherry KJ, Joyce JW, Lie JT. Thoracic aortic aneurysms: a population-based study. Surgery. 1982;92(6):1103–8.

54. Isselbacher EM. Thoracic and abdominal aortic aneurysms. Circulation. 2005;111(6):816–28. https://doi.org/10.1161/01.cir.0000154569.08857.7a.
55. Reed D, Reed C, Stemmermann G, Hayashi T. Are aortic aneurysms caused by atherosclerosis? Circulation. 1992;85(1):205–11.
56. Lee W-K, Mossop PJ, Little AF, Fitt GJ, Vrazas JI, Hoang JK, Hennessy OF. Infected (mycotic) aneurysms: spectrum of imaging appearances and management. Radiographics. 2008;28(7):1853–68. https://doi.org/10.1148/rg.287085054.
57. Kalisz K, Rajiah P. Radiological features of uncommon aneurysms of the cardiovascular system. World J Radiol. 2016;8(5):434–48. https://doi.org/10.4329/wjr.v8.i5.434.
58. Munden RF, Carter BW, Chiles C, MacMahon H, Black WC, Ko JP, McAdams HP, Rossi SE, Leung AN, Boiselle PM, Kent MS, Brown K, Dyer DS, Hartman TE, Goodman EM, Naidich DP, Kazerooni EA, Berland LL, Pandharipande PV. Managing incidental findings on thoracic CT: mediastinal and cardiovascular findings. A white paper of the ACR Incidental Findings Committee. J Am Coll Radiol. 2018;15(8):1087–96. https://doi.org/10.1016/j.jacr.2018.04.029.
59. Vriz O, Aboyans V, D'Andrea A, Ferrara F, Acri E, Limongelli G, Della Corte A, Driussi C, Bettio M, Pluchinotta FR, Citro R, Russo MG, Isselbacher E, Bossone E. Normal values of aortic root dimensions in healthy adults. Am J Cardiol. 2014;114(6):921–7. https://doi.org/10.1016/j.amjcard.2014.06.028.
60. Campens L, Demulier L, De Groote K, Vandekerckhove K, De Wolf D, Roman MJ, Devereux RB, De Paepe A, De Backer J. Reference values for echocardiographic assessment of the diameter of the aortic root and ascending aorta spanning all age categories. Am J Cardiol. 2014;114(6):914–20. https://doi.org/10.1016/j.amjcard.2014.06.024.
61. Hiratzka LF, Bakris GL, Beckman JA, Bersin RM, Carr VF, Casey DE, Eagle KA, Hermann LK, Isselbacher EM, Kazerooni EA, Kouchoukos NT, Lytle BW, Milewicz DM, Reich DL, Sen S, Shinn JA, Svensson LG, Williams DM. 2010 ACCF/AHA/AATS/ACR/ASA/SCA/SCAI/SIR/STS/SVM guidelines for the diagnosis and management of patients with thoracic aortic disease. Circulation. 2010;121(13):e266–369. https://doi.org/10.1161/CIR.0b013e3181d4739e.
62. Chau KH, Elefteriades JA. Natural history of thoracic aortic aneurysms: size matters, plus moving beyond size. Prog Cardiovasc Dis. 2013;56(1):74–80. https://doi.org/10.1016/j.pcad.2013.05.007.
63. Erbel R, Aboyans V, Boileau C, Bossone E, Bartolomeo RD, Eggebrecht H, Evangelista A, Falk V, Frank H, Gaemperli O, Grabenwoger M, Haverich A, Iung B, Manolis AJ, Meijboom F, Nienaber CA, Roffi M, Rousseau H, Sechtem U, Sirnes PA, Allmen RS, Vrints CJ, Guidelines ESCCfP. 2014 ESC guidelines on the diagnosis and treatment of aortic diseases: document covering acute and chronic aortic diseases of the thoracic and abdominal aorta of the adult. The Task Force for the Diagnosis and Treatment of Aortic Diseases of the European Society of Cardiology (ESC). Eur Heart J. 2014;35(41):2873–926. https://doi.org/10.1093/eurheartj/ehu281.
64. Mani K, Wanhainen A. Accurate and reproducible diameter measurement is essential in surveillance and treatment of thoracic aortic aneurysms. Eur J Vasc Endovasc Surg. 2014;47(1):27. https://doi.org/10.1016/j.ejvs.2013.10.004.
65. Cikach F, Desai MY, Roselli EE, Kalahasti V. Thoracic aortic aneurysm: how to counsel, when to refer. Cleve Clin J Med. 2018;85(6):481–92. https://doi.org/10.3949/ccjm.85a.17039.
66. Bennett SJ, Dill KE, Hanley M, Ahmed O, Desjardins B, Gage KL, Ginsburg M, Khoynezhad A, Oliva IB, Steigner ML, Strax R, Verma N, Rybicki FJ. ACR appropriateness criteria((R)) suspected thoracic aortic aneurysm. J Am Coll Radiol. 2018;15(5s):S208–s214. https://doi.org/10.1016/j.jacr.2018.03.031.
67. Bhave NM, Nienaber CA, Clough RE, Eagle KA. Multimodality imaging of thoracic aortic diseases in adults. JACC Cardiovasc Imaging. 2018;11(6):902–19. https://doi.org/10.1016/j.jcmg.2018.03.009.
68. Agarwal PP, Chughtai A, Matzinger FRK, Kazerooni EA. Multidetector CT of thoracic aortic aneurysms. Radiographics. 2009;29(2):537–52. https://doi.org/10.1148/rg.292075080.

69. Guo BJ, Yang ZL, Zhang LJ. Gadolinium deposition in brain: current scientific evidence and future perspectives. Front Mol Neurosci. 2018;11:335. https://doi.org/10.3389/fnmol.2018.00335.
70. Stankovic Z, Allen BD, Garcia J, Jarvis KB, Markl M. 4D flow imaging with MRI. Cardiovasc Diagn Ther. 2014;4(2):173–92. https://doi.org/10.3978/j.issn.2223-3652.2014.01.02.
71. Greendyke RM. Traumatic rupture of aorta: special reference to automobile accidents. JAMA. 1966;195(7):527–30. https://doi.org/10.1001/jama.1966.03100070071021.
72. Azizzadeh A, Keyhani K, Miller CC 3rd, Coogan SM, Safi HJ, Estrera AL. Blunt traumatic aortic injury: initial experience with endovascular repair. J Vasc Surg. 2009;49(6):1403–8. https://doi.org/10.1016/j.jvs.2009.02.234.
73. Parmley Loren F, Mattingly Thomas W, Manion William C, Jahnke Edward J. Nonpenetrating traumatic injury of the aorta. Circulation. 1958;17(6):1086–101. https://doi.org/10.1161/01.CIR.17.6.1086.
74. Heneghan RE, Aarabi S, Quiroga E, Gunn ML, Singh N, Starnes BW. Call for a new classification system and treatment strategy in blunt aortic injury. J Vasc Surg. 2016;64(1):171–6. https://doi.org/10.1016/j.jvs.2016.02.047.
75. Cullen EL, Lantz EJ, Johnson CM, Young PM. Traumatic aortic injury: CT findings, mimics, and therapeutic options. Cardiovasc Diagn Ther. 2014;4(3):238–44. https://doi.org/10.3978/j.issn.2223-3652.2014.06.02.
76. Fox N, Schwartz D, Salazar JH, Haut ER, Dahm P, Black JH, Brakenridge SC, Como JJ, Hendershot K, King DR, Maung AA, Moorman ML, Nagy K, Petrey LB, Tesoriero R, Scalea TM, Fabian TC. Evaluation and management of blunt traumatic aortic injury: a practice management guideline from the Eastern Association for the Surgery of Trauma. J Trauma Nurs. 2015;22(2):99–110. https://doi.org/10.1097/JTN.0000000000000118.
77. Hainer C, Bockler D, Bernhard M, Scheuren K, Stein KM, Rauch H, Martin E, Weigand MA. [Blunt traumatic aortic injury: importance of transesophageal echocardiography]. Anaesthesist. 2008;57(3):262–8. https://doi.org/10.1007/s00101-008-1334-x.
78. Prieto-Gonzalez S, Arguis P, Cid MC. Imaging in systemic vasculitis. Curr Opin Rheumatol. 2015;27(1):53–62. https://doi.org/10.1097/bor.0000000000000130.
79. Dejaco C, Ramiro S, Duftner C, Besson FL, Bley TA, Blockmans D, Brouwer E, Cimmino MA, Clark E, Dasgupta B, Diamantopoulos AP, Direskeneli H, Iagnocco A, Klink T, Neill L, Ponte C, Salvarani C, Slart RHJA, Whitlock M, Schmidt WA. EULAR recommendations for the use of imaging in large vessel vasculitis in clinical practice. Ann Rheum Dis. 2018;77(5):636. https://doi.org/10.1136/annrheumdis-2017-212649.
80. Johnston SL, Lock RJ, Gompels MM. Takayasu arteritis: a review. J Clin Pathol. 2002;55(7):481–6.
81. Numano F, Okawara M, Inomata H, Kobayashi Y. Takayasu's arteritis. Lancet (London, England). 2000;356(9234):1023–5. https://doi.org/10.1016/s0140-6736(00)02701-x.
82. Nastri MV, Baptista LP, Baroni RH, Blasbalg R, de Avila LF, Leite CC, de Castro CC, Cerri GG. Gadolinium-enhanced three-dimensional MR angiography of Takayasu arteritis. Radiographics. 2004;24(3):773–86. https://doi.org/10.1148/rg.243035096.
83. Yamada I, Nakagawa T, Himeno Y, Kobayashi Y, Numano F, Shibuya H. Takayasu arteritis: diagnosis with breath-hold contrast-enhanced three-dimensional MR angiography. J Magn Reson Imaging. 2000;11(5):481–7.
84. Sueyoshi E, Sakamoto I, Uetani M. MRI of Takayasu's arteritis: typical appearances and complications. Am J Roentgenol. 2006;187(6):W569–75. https://doi.org/10.2214/AJR.05.1093.
85. Yamada I, Nakagawa T, Himeno Y, Numano F, Shibuya H. Takayasu arteritis: evaluation of the thoracic aorta with CT angiography. Radiology. 1998;209(1):103–9. https://doi.org/10.1148/radiology.209.1.9769819.
86. Watts RA. 2. Epidemiology of giant cell arteritis: a critical review. Rheumatology. 2014;53(suppl_2):i1–2. https://doi.org/10.1093/rheumatology/keu183.
87. Bley TA, Weiben O, Uhl M, Vaith P, Schmidt D, Warnatz K, Langer M. Assessment of the cranial involvement pattern of giant cell arteritis with 3T magnetic resonance imaging. Arthritis Rheum. 2005;52(8):2470–7. https://doi.org/10.1002/art.21226.

88. Bley TA, Uhl M, Carew J, Markl M, Schmidt D, Peter HH, Langer M, Wieben O. Diagnostic value of high-resolution MR imaging in giant cell arteritis. AJNR Am J Neuroradiol. 2007;28(9):1722–7. https://doi.org/10.3174/ajnr.A0638.
89. Puppo C, Massollo M, Paparo F, Camellino D, Piccardo A, Shoushtari Zadeh Naseri M, Villavecchia G, Rollandi GA, Cimmino MA. Giant cell arteritis: a systematic review of the qualitative and semiquantitative methods to assess vasculitis with 18F-fluorodeoxyglucose positron emission tomography. Biomed Res Int. 2014;2014:574248. https://doi.org/10.1155/2014/574248.
90. Soler R, Rodriguez E, Requejo I, Fernandez R, Raposo I. Magnetic resonance imaging of congenital abnormalities of the thoracic aorta. Eur Radiol. 1998;8(4):540–6. https://doi.org/10.1007/s003300050430.
91. Russo V, Renzulli M, La Palombara C, Fattori R. Congenital diseases of the thoracic aorta. Role of MRI and MRA. Eur Radiol. 2006;16(3):676–84. https://doi.org/10.1007/s00330-005-0027-y.
92. Crawford T. An atlas of vascular rings and related malformations of the aortic arch system. J Clin Pathol. 1964;17(5):579–80.
93. Priya S, Thomas R, Nagpal P, Sharma A, Steigner M. Congenital anomalies of the aortic arch. Cardiovasc Diagn Ther. 2018;8(Suppl 1):S26–44. https://doi.org/10.21037/cdt.2017.10.15.
94. Keisler B, Carter C. Abdominal aortic aneurysm. Am Fam Physician. 2015;91(8):538–43.
95. Chaikof EL, Brewster DC, Dalman RL, Makaroun MS, Illig KA, Sicard GA, Timaran CH, Upchurch GR Jr, Veith FJ, Society for Vascular Surgery. The care of patients with an abdominal aortic aneurysm: the Society for Vascular Surgery practice guidelines. J Vasc Surg. 2009;50(4 Suppl):S2–49. https://doi.org/10.1016/j.jvs.2009.07.002.
96. Chaikof EL, Dalman RL, Eskandari MK, Jackson BM, Lee WA, Mansour MA, Mastracci TM, Mell M, Murad MH, Nguyen LL, Oderich GS, Patel MS, Schermerhorn ML, Starnes BW. The Society for Vascular Surgery practice guidelines on the care of patients with an abdominal aortic aneurysm. J Vasc Surg. 2018;67(1):2–77.e72. https://doi.org/10.1016/j.jvs.2017.10.044.
97. Norman PE, Curci JA. Understanding the effects of tobacco smoke on the pathogenesis of aortic aneurysm. Arterioscler Thromb Vasc Biol. 2013;33(7):1473–7. https://doi.org/10.1161/ATVBAHA.112.300158.
98. Mohler ER, Gornik HL, Gerhard-Herman M, Misra S, Olin JW, Zierler RE. ACCF/ACR/AIUM/ASE/ASN/ICAVL/SCAI/SCCT/SIR/SVM/SVS 2012 appropriate use criteria for peripheral vascular ultrasound and physiological testing Part I: arterial ultrasound and physiological testing. A report of the American College of Cardiology Foundation Appropriate Use Criteria Task Force, American College of Radiology, American Institute of Ultrasound in Medicine, American Society of Echocardiography, American Society of Nephrology, Intersocietal Commission for the Accreditation of Vascular Laboratories, Society for Cardiovascular Angiography and Interventions, Society of Cardiovascular Computed Tomography, Society for Interventional Radiology, Society for Vascular Medicine, and Society for Vascular Surgery. J Am Coll Cardiol. 2012;60(3):242–76. https://doi.org/10.1016/j.jacc.2012.02.009.
99. Concannon E, McHugh S, Healy DA, Kavanagh E, Burke P, Clarke Moloney M, Walsh SR. Diagnostic accuracy of non-radiologist performed ultrasound for abdominal aortic aneurysm: systematic review and meta-analysis. Int J Clin Pract. 2014;68(9):1122–9. https://doi.org/10.1111/ijcp.12453.
100. Chiu KW, Ling L, Tripathi V, Ahmed M, Shrivastava V. Ultrasound measurement for abdominal aortic aneurysm screening: a direct comparison of the three leading methods. Eur J Vasc Endovasc Surg. 2014;47(4):367–73. https://doi.org/10.1016/j.ejvs.2013.12.026.
101. Beales L, Wolstenhulme S, Evans JA, West R, Scott DJ. Reproducibility of ultrasound measurement of the abdominal aorta. Br J Surg. 2011;98(11):1517–25. https://doi.org/10.1002/bjs.7628.
102. Siegel CL, Cohan RH, Korobkin M, Alpern MB, Courneya DL, Leder RA. Abdominal aortic aneurysm morphology: CT features in patients with ruptured and nonruptured aneurysms. AJR Am J Roentgenol. 1994;163(5):1123–9. https://doi.org/10.2214/ajr.163.5.7976888.

103. Litmanovich D, Bankier AA, Cantin L, Raptopoulos V, Boiselle PM. CT and MRI in diseases of the aorta. AJR Am J Roentgenol. 2009;193(4):928–40. https://doi.org/10.2214/ajr.08.2166.
104. Ten Bosch JA, Teijink JA, Willigendael EM, Prins MH. Endovascular aneurysm repair is superior to open surgery for ruptured abdominal aortic aneurysms in EVAR-suitable patients. J Vasc Surg. 2010;52(1):13–8. https://doi.org/10.1016/j.jvs.2010.02.014.
105. Chaikof EL, Blankensteijn JD, Harris PL, White GH, Zarins CK, Bernhard VM, Matsumura JS, May J, Veith FJ, Fillinger MF, Rutherford RB, Kent KC. Reporting standards for endovascular aortic aneurysm repair. J Vasc Surg. 2002;35(5):1048–60.
106. Mora C, Marcus C, Barbe C, Ecarnot F, Long A. Measurement of maximum diameter of native abdominal aortic aneurysm by angio-CT: reproducibility is better with the semi-automated method. Eur J Vasc Endovasc Surg. 2014;47(2):139–50. https://doi.org/10.1016/j.ejvs.2013.10.013.
107. Ernst CB. Abdominal aortic aneurysm. N Engl J Med. 1993;328(16):1167–72. https://doi.org/10.1056/nejm199304223281607.
108. Pitton MB, Schweitzer H, Herber S, Schmiedt W, Neufang A, Kalden P, Thelen M, Duber C. MRI versus helical CT for endoleak detection after endovascular aneurysm repair. AJR Am J Roentgenol. 2005;185(5):1275–81. https://doi.org/10.2214/AJR.04.0729.
109. Habets J, Zandvoort HJ, Reitsma JB, Bartels LW, Moll FL, Leiner T, van Herwaarden JA. Magnetic resonance imaging is more sensitive than computed tomography angiography for the detection of endoleaks after endovascular abdominal aortic aneurysm repair: a systematic review. Eur J Vasc Endovasc Surg. 2013;45(4):340–50. https://doi.org/10.1016/j.ejvs.2012.12.014.
110. Venkataraman S, Semelka RC, Weeks S, Braga L, Vaidean G. Assessment of aorto-iliac disease with magnetic resonance angiography using arterial phase 3-D gradient-echo and interstitial phase 2-D fat-suppressed spoiled gradient-echo sequences. J Magn Reson Imaging. 2003;17(1):43–53. https://doi.org/10.1002/jmri.10235.
111. Partovi S, Trischman T, Rafailidis V, Ganguli S, Rengier F, Goerne H, Rajiah P, Staub D, Patel IJ, Oliveira G, Ghoshhajra B. Multimodality imaging assessment of endoleaks post-endovascular aortic repair. Br J Radiol. 2018;91(1087):20180013. https://doi.org/10.1259/bjr.20180013.
112. Guo Q, Zhao J, Huang B, Yuan D, Yang Y, Zeng G, Xiong F, Du X. A systematic review of ultrasound or magnetic resonance imaging compared with computed tomography for endoleak detection and aneurysm diameter measurement after endovascular aneurysm repair. J Endovasc Ther. 2016;23(6):936–43. https://doi.org/10.1177/1526602816664878.
113. Deipolyi AR, Rho J, Khademhosseini A, Oklu R. Diagnosis and management of mycotic aneurysms. Clin Imaging. 2016;40(2):256–62. https://doi.org/10.1016/j.clinimag.2015.11.011.
114. Czum JM, Corse WR, Ho VB. MR angiography of the thoracic aorta. Magn Reson Imaging Clin N Am. 2005;13(1):41–64, v. https://doi.org/10.1016/j.mric.2004.12.009.
115. McGuigan EA, Sears ST, Corse WR, Ho VB. MR angiography of the abdominal aorta. Magn Reson Imaging Clin N Am. 2005;13(1):65–89, v–vi. https://doi.org/10.1016/j.mric.2004.12.010.

Part V
Coronary Artery

Chapter 11
Pathophysiology of Coronary Artery Disease

Hiroyuki Jinnouchi, Frank D. Kolodgie, Maria Romero, Renu Virmani, and Aloke V. Finn

Introduction

Despite many and continued advances in medical therapies and diagnostic imaging modalities and greater understanding of the molecular mechanisms of atherosclerosis, coronary artery disease (CAD) remains the major cause of morbidity and mortality throughout the world. Deaths from cardiovascular disease (CVD) reached a total of 17.3 million worldwide in 2012 and are expected to rise up to 23.6 million by 2030 [1]. Atherosclerosis is a mutifactorial disease and includes well-known risk factors like hypertension, hyperlipidemia, diabetes mellitus, smoking, and family history. In addition, recently high-sensitivity C-reactive protein, homocysteine, high fibrinogen, Lp(a), and LpPLa2 have been recognized as biomarkers associated with atherosclerosis. The American Heart Association (AHA) has suggested adding health metrics like physical activity, healthy diet, and body mass index (BMI) in addition to blood pressure, total cholesterol, blood glucose, and smoking. Understanding the morphologic features of the atherosclerotic disease as well as its background can result in better comprehension of the disease. It is thought that most acute coronary syndromes (ACS) are the result of luminal thrombosis, although not all are associated with occlusive diseases. There are three main causes of coronary thrombosis such as plaque rupture, erosion, and calcified nodule [2]. Based on the autopsy studies, the majority of thrombosis occurs from plaque rupture (55–65%), followed by erosion (30–35%) and, least frequent, calcified nodule (2–7%) [2]. In a recent systematic worldwide review of published autopsy series of the causes of coronary thrombosis, plaque rupture

H. Jinnouchi · F. D. Kolodgie · M. Romero · R. Virmani · A. V. Finn (✉)
CVPath Institute Inc., Gaithersburg, MD, USA
e-mail: HJinnouchi@CVPath.org; fkolodgie@cvpath.org; mromero@CVPath.org; rvirmani@cvpath.org; afinn@cvpath.org

C. Yuan et al. (eds.), *Vessel Based Imaging Techniques*,
https://doi.org/10.1007/978-3-030-25249-6_11

occurred in 73% which is higher than our data and is likely due to the inclusion of cases of acute myocardial infarction and those with known coronary artery disease. Our data is different because we have only included cases of sudden coronary death without a known history of coronary artery disease, with a mean age of 50 years. Also, individuals from hospital-based autopsies are usually older (>60 years) than those dying suddenly [3]. In addition to age distribution, plaque rupture is more common in AMI patients (79%) as compared to individuals who have died suddenly (65%) and to our knowledge does not equate the hospital. Also, the incidence of erosion is lower in AMI patients (25%) than individuals dying of sudden coronary death (35%) [2, 4].

This chapter will focus on the structural characteristic of plaque progression and mode of presentation, i.e., acute coronary syndrome versus stable angina.

The Classification of Atherosclerosis

It is important to understand how atherosclerosis progresses and what lesion constitutes atherosclerosis and to determine the various stages of lesion progression. In the mid-1990s, Stary et al. under the auspices of the American Heart Association defined early and advanced lesions of atherosclerosis in two separate publications [5, 6]. The first consensus document classified the stages of early atherosclerosis into three different numerical categories: initial lesion is the first microscopic and chemical detection of lipid deposits, Type I; fatty streak (FS) is the gross visibility of yellow color streaks, Type II; and transition or intermediate lesion is the transition to a fibroatheroma, Type III. In a separate manuscript, the definition of advanced lesions of atherosclerosis was described as fibroatheroma with well-defined region of necrotic core in the intima, Type IV; fibroatheroma or atheroma with a thick layer of fibrous connective tissue is Type V; and complicated plaques with surface defects, and/or hematoma-hemorrhage, and/or thrombosis are Type VI. At this time, other causes of coronary thrombosis, i.e., erosion and calcified nodule, did not weigh in at all in this classification.

Our laboratory with the largest registry of human autopsy cases of patients dying from sudden coronary death worldwide reported that this numeric nomenclature was not enough. For example, it was not appreciated that the precursor lesion of plaque rupture was a thin-cap fibroatheroma and that erosion and calcified nodule were other causes of coronary thrombosis. The atherosclerosis process is considered too complicated to be classified into numerical groups. These problems encouraged us to modify the AHA classification. In our modified AHA classification published in 2000, AHA types I–IV lesions were replaced by descriptive terminology, i.e., adaptive intimal thickening (AIT), intimal xanthoma (FS), pathologic intimal thickening, and fibroatheroma [2], which were later divided into early and late fibroatheroma. AHA types V and VI were discarded since these classifications did not show other types of coronary thrombosis such as erosion and calcified nodule and stabilized plaque like healed plaque, chronic total occlusion, and fibrocalcific

and fibrous plaques [7]. Stary wrote editorial review in which he modified the AHA classification but still did not acknowledge the existence of plaque erosion and calcified nodule [8].

Intimal Thickening and Fatty Streaks

The earliest stage in the arterial wall is called intimal thickening (AHA Type I), consisting of smooth muscle cells in an extracellular matrix and a lack of lipid deposition. Intimal thickening is observed in most arteries (e.g., coronary, carotid, abdominal, and descending aorta and iliac artery) [9] (Fig. 11.1). It is thought that intimal thickening is a physiological response to blood flow rather than atherosclerotic progression. However, in the autopsy studies enrolling neonates, adolescents, and young adults, intimal masses located in near branch points might be precursors

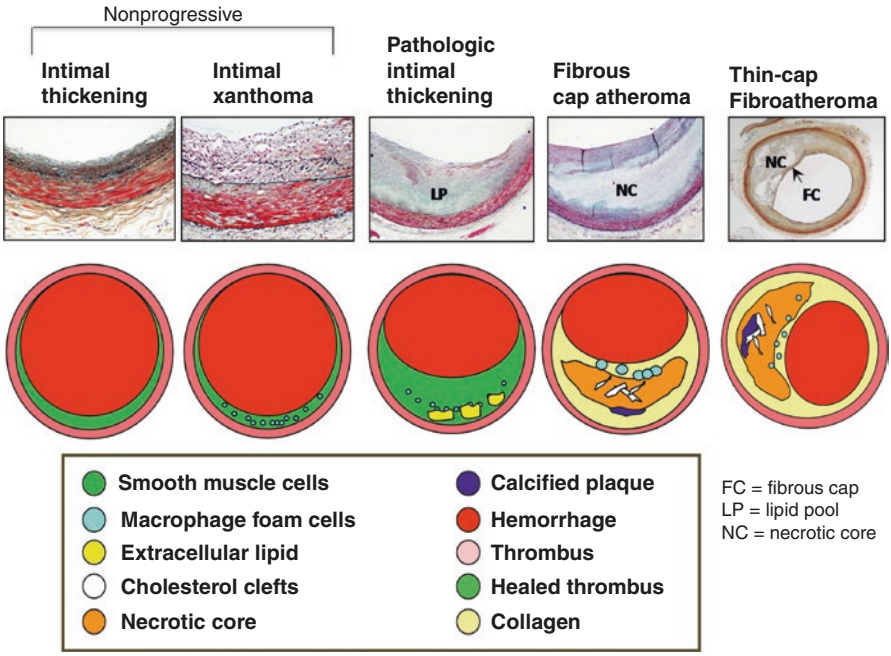

Fig. 11.1 Development of human coronary atherosclerosis. The two nonprogressive lesions are intimal thickening or intimal xanthoma (foam cell collections known as fatty streaks, AHA Type II). Pathological intimal thickening (AHA Type III, transitional lesions) is the first of progressive plaques marked by an acellular lipid pool rich in proteoglycan; inflammation when present is typically confined to the most luminal aspect of this plaque. Fibroatheromas are lesions with areas of necrosis characterized by cellular debris and cholesterol monohydrate with varying degrees of calcification or hemorrhage. Finally, thin-cap fibroatheroma or vulnerable plaques are recognized by their relatively large necrotic cores and thin fibrous caps. (Reproduced with permission from Virmani et al. [2])

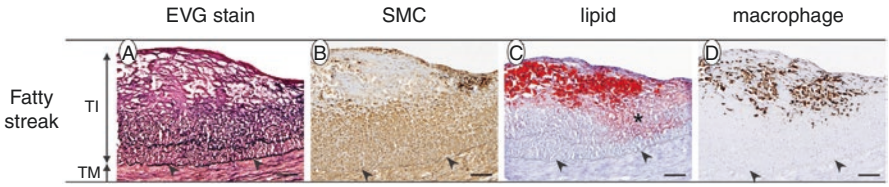

Fig. 11.2 Histology of fatty streak consists of foamy macrophage infiltration of the intima with variable smooth muscle cells and proteoglycan-collagen matrix deposition. (**a**) EVG stain: elastic fibers were stained in black. (**b**) SMC: SMCs immunostained with anti-α-SMA/HHF35. (**c**) Lipid: extracellular and intracellular lipids stained with Sudan IV stain. Extracellular lipids in the fatty streak are indicated by an asterisk. (**d**) Macrophage: macrophages immunostained with an anti-CD68 antibody. Arrowheads indicate internal elastic lamina. Bars represent 100 μm. TI, tunica intima; TM, tunica media. (Reprinted from Nakagawa et al. [14], with permission from Elsevier)

to high-risk plaques that may eventually with plaque progression lead to thrombosis since the intimal masses enlarge with advancing age [10, 11]. Nakagawa and Nakashima reported an intermediate stage between AIT and FS which they called as fatty infiltration, but there is an absence of macrophages which we believe is similar to PIT without macrophages.

Intimal xanthoma (AHA Type II), which is called FS, is a lesion with infiltrating lipid-laden cells such as macrophages or SMC, the latter to a lesser extent within the intima [12–14] (Figs. 11.1 and 11.2). This lesion has been shown to regress especially in the thoracic aorta and the right coronary artery in young individuals in the study "Pathobiological Determinants of Atherosclerosis in Youth (PDAY)" reported by McGill et al. [15]. Therefore, it is believed that intimal xanthoma is atherosclerosis-prone lesion rather than the progressive atherosclerotic lesion.

Pathologic Intimal Thickening

Pathological intimal thickening (PIT, AHA Type III lesion) is considered as the earliest lesion of progressive atherosclerosis which consists of SMCs within extracellular matrix composed of proteoglycan within the lipid pool, which is located near the media [16] (Fig. 11.1). There is a relative absence of viable SMCs within the area of the lipid pool. The extracellular matrix consists of hyaluronan and proteoglycans such as versican along with lipid deposition. The PIT lesion also shows the presence of proteoglycans biglycan and decorin surrounding the SMCs. The SMCs in the intima in the region of the lipid pool undergo apoptosis near the media, and in the late phases, there is loss of SMC and accumulation of basement membrane (BM) as demonstrated by periodic acid-Schiff (PAS) stain and by transmission electron microscopy. Structural changes in the glycosaminoglycan chain of proteoglycans, i.e., versican and biglycan, are the initial proatherogenic proteoglycans which bind the atherogenic lipoproteins [17, 18]. On the other hand, enrichment in decorin in the neointima of the internal thoracic artery is observed which

may play a role that results in the resistance to the development of atherosclerosis [19]. As PIT lesions become more advanced, macrophages begin to accumulate toward the lumen with eventual infiltration into the lipid pool converting the latter to a necrotic core. PIT lesions with macrophages are considered as a more advanced lesion. Specific protein expressed in the lipid pools may initiate the macrophages accumulate in PIT lesions, although the specific proteins remain unknown.

Free cholesterol is seen as fine crystalline structures (devoid of lipids) in paraffin-embedded sections within the area of lipid pool to varying degree; however, they are never excessive. The origin of free cholesterol in early phases is likely derived from dying macrophages and SMC; however the exact processes involved remain unknown [20]. Accumulation of extracellular lipid within the area of lipid pools is derived from the circulating plasma lipoprotein [21, 22]. In some experimental studies, intrinsic phenotypic changes of smooth muscle cells were observed in the initial stage of plaque formation which may contribute to SMC apoptosis rather than intrinsic role of SMC (i.e., cell-cell interactions or the microenvironment of the plaque) [23, 24]. In the setting of hyperlipidemia (cholesterol-rich), SMCs undergo apoptosis in vitro likely through Bcl-2 and Bax genes. However, function of phagocytosis is reduced in the presence of hyperlipidemia, leading to necrosis of apoptotic SMCs and leakage of intracellular IL-1. IL-1 acts on the surrounding viable SMCs and induces them to secrete IL-6 and monocyte chemotactic protein (MCP-1) which provoke the progression of atherosclerosis [25].

Microcalcifications ($\geq$0.5 μm and typically <15 μm) are another feature in the PIT lesions, which can be identified by anionic stains such as von Kossa's or alizarin red stains. It is likely that microcalcifications coalesce and form fragmented calcification; this may also involve collagen which acts as a scaffold, enhancing aggregation of microvesicles. The mechanisms that lead to microcalcification remain controversial with one group in favoring microvesicles as the mechanism of calcification and on the other related to apoptosis as the underlying mechanism with late coalescence. Most calcification in the early stages of PIT is microcalcification; however, fragmented calcification may be observed in a minority of cases.

Fibroatheroma

Fibroatheroma is the more advanced lesion of atherosclerosis and is distinguished from PIT lesions by the presence of an acellular necrotic core (AHA Type IV) [2] (Fig. 11.1). At this phase there is an absence or decrease in hyaluronan and proteoglycan such as versican and biglycan with the absence of collagen in the area of the necrotic core. Fibroatheromas are classified into two types, "early" and "late," on the basis of the relative absence of matrix molecules. Early fibroatheroma show some presence of hyaluronan, versican, and biglycan and other matrix proteins due to the infiltrating macrophages within the lipid pool, which is converting to necrotic core by the focal loss of matrix. The late necrotic core is devoid of any matrix and no longer stains for hyaluronan, proteoglycans, and collagen

matrix as identified by specific stains for proteoglycans, hyaluronan, and Sirius red stain. Matrix metalloproteinases (MMPs) released by macrophages are responsible for the breakdown of proteoglycan and collagen. Also, apoptotic cell death of macrophages and free apoptotic bodies are abundant within the area of necrotic core, which has been described by Ira Tabas as a "grave yard" of macrophages [26]. In addition to the deficiency of extracellular matrix (ECM), the necrotic core in late fibroatheroma exhibits more cholesterol clefts, calcification, intraplaque hemorrhage, and surrounding neoangiogenesis as compared to early fibroatheroma [27].

The most distinguishing feature of late fibroatheroma is the accumulation of free cholesterol. Acyl coenzyme A (ACAT1) esterifies free cholesterol and stores esterified cholesterol in macrophages [28]. Macrophage ACAT1 deficiency has been shown in mice to lead to an increase in atherosclerotic lesion area including free cholesterol accumulation in hyperlipidemic mice. Therefore, it is thought that ACAT1 is deficient in macrophages in the setting of advance atherosclerotic lesions. Also, accumulation of free cholesterol along with macrophage death is believed to contribute to the development toward late fibroatheroma [28, 29]. We have shown that red blood cells membranes, which are richest in free cholesterol of all cell membranes, are likely another source of free cholesterol present within the human necrotic core.

Thin-Cap Fibroatheroma

Late fibroatheromas are usually characterized by having a thick fibrous cap composed mainly of type I and III collagen, proteoglycans, and interspersed SMCs. Fibrous cap plays an important role in harboring necrotic core away from the flowing blood. As the lesion becomes more advanced, the fibrous cap can undergo thinning and is referred to as a thin-cap fibroatheroma (TCFA) although the precise mechanism still remains unknown. It is unknown whether the fibrous cap may begin as a thin cap or is converted from a thick to thin cap. The thinning of the fibrous cap is thought to result from ECM degradation by MMPs and ADAMTS (a disintegrin and metalloproteinase with thrombospondin motifs) family, along with a deficiency in repair mechanism [30]. Although the MMPs and TIMPs in monocytes/macrophages secrete several types of extracellular proteases, which include serine proteases, cathepsins, and metalloproteinases, it is likely that overproduction of MMPs is what leads to cap thinning. The TCFA generally has large necrotic core along with intact thin fibrous cap consisting mostly of type I collagen with coexisting inflammatory cells such as macrophages and lymphocytes of varying degree. Generally, there is the absence or decrease of SMCs within the thin fibrous cap of TCFA lesions due to SMC apoptosis. We have defined thin cap as $\leq$65 μm based upon the thickness of ruptured cap. The ruptured caps measured 23 ± 19 μm considering 95% confidence interval of the cap; we calculated a cap thickness below $\leq$65 μm defining a TCFA [31]. The necrotic core was also measured and was found to be lesser in

TCFA than in plaque rupture (25 ± 15% vs. 35 ± 20%, respectively) [32]. Narula et al. showed the best discriminators of TCFA besides cap thickness were macrophage infiltration and necrotic core size [32].

Plaque Rupture

Plaque rupture (PR) is defined by the presence of the disruption of thin fibrous cap along with an overlying thrombus and underlying necrotic core (Fig. 11.3). Generally, more than 30% of total plaque area is occupied by a necrotic core in plaque ruptures [2, 33, 34]. The thin fibrous cap is composed of Type I collagen with few SMCs, and the cap is infiltrated with macrophages and T lymphocytes as described above (Fig. 11.1). Due to discontinuity of the fibrous cap, the flowing blood comes in contact with the highly thrombogenic necrotic core leading to a luminal thrombus,

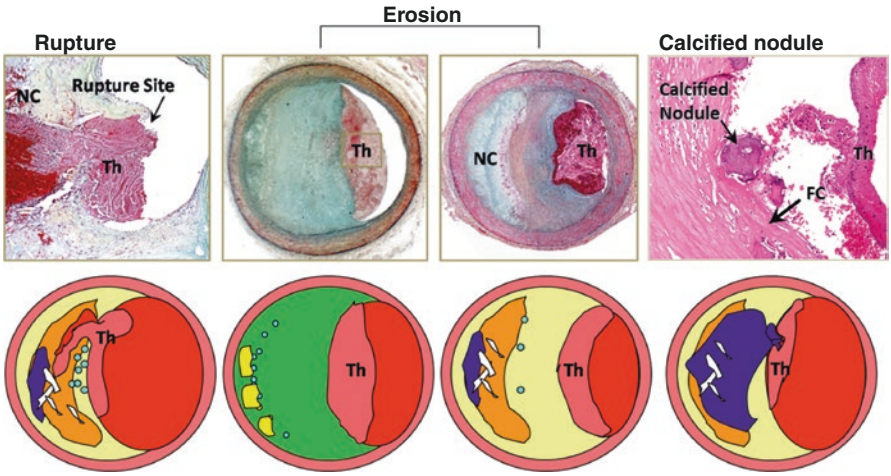

Fig. 11.3 Atherosclerotic lesions with luminal thrombi. Coronary plaque features responsible for acute thrombosis comprise three different morphologies: rupture, erosion, and calcified nodules. Ruptured plaques are thin fibrous cap atheromas with luminal thrombi (Th). These lesions usually have an extensive necrotic core (NC) containing large numbers of cholesterol crystals and a thin fibrous cap (<65 μm) infiltrated by foamy macrophages and T lymphocytes. The fibrous cap is thinnest at the site of rupture and consists of a few collagen bundles and rare smooth muscle cells. The luminal thrombus is in communication with the lipid-rich necrotic core. Erosions occur over lesions rich in smooth muscle cells and proteoglycans. Luminal thrombi overlie areas lacking surface endothelium. The deep intima of the eroded plaque often shows extracellular lipid pools, but necrotic cores are uncommon; when present, the necrotic core does not communicate with the luminal thrombus. Inflammatory infiltrate is usually absent but, if present, is sparse and consists of macrophages and lymphocytes. Calcified nodules are plaques with luminal thrombi showing calcific nodules protruding into the lumen through a disrupted thin fibrous cap. There is absence of an endothelium at the site of the thrombus, and inflammatory cells (macrophages and T lymphocytes) are absent. (Reproduced with permission from Virmani et al. [2])

which may or may not be occlusive. The thrombus is composed of aggregated platelets (so-called white thrombus). If the lumen is obstructed, the thrombus propagates proximal to the obstruction site, consisting of layers of fibrin (line of Zahn) separated by red blood cells (so-called red thrombus). Furthermore, the extent of organization can determine the duration of the thrombus. As the thrombus organized by monocyte infiltration which release growth factors attracting smooth muscle and endothelial cells. The SMCs proliferate and deposit extracellular matrix consisting of proteoglycans and collagen, while endothelial cells proliferate to form microchannels. Once thrombi begin to organize, they fail to respond to thrombolytic therapy.

While the precise mechanism of PR has not been fully understood, presumably one potential mechanism of disruption of cap is likely weakness of the cap infiltrated by macrophages that release MMPs promoting degradation of collagen, proteoglycans, and elastin. Also, T lymphocytes release interferon gamma which decrease the number of SMCs and their ability to form new collagen.

Recent studies have shown that MMP may play an important role in fibrous cap disruption in plaque ruptures. Type I collagen provides most of the tensile strength to the fibrous cap [35]. Collagenases, such as MMP-1, MMP-8, and MMP-13, result in proteolytic breaks in collagen types I, II, and III, whereas the continued degradation of the interstitial collagens results from the gelatinases MMP-2 and MMP-9 [36–40]. Atheromatous lesions express more MMP-1, MMP-2, MMP-3, MMP-9, and MMP-13 in carotid plaques in diabetic and nondiabetic patients, without significant differences, except for MMP-2 showing greater expression in nondiabetics. However, differences were seen between symptomatic and asymptomatic individuals with greater expression of MMP-1and MMP-9 in those without diabetes. Similarly endogenous antagonists to MMPs, i.e., tissue inhibitors of metalloproteinases (TIMPS), are present in diabetic and nondiabetic, with no differences between them; however, symptomatic individuals had greater expression of TIMP-1 [40, 41]. Galis et al. have reported higher expression of MMP-1, MMP-3, and MMP-9; positive macrophages in shoulder region were found in the sites with collagenase-cleaved Type I collagen. Other proteinases such as the cathepsin family (cathepsins S and K) and the inhibitor cystatin C are associated with degrading extracellular matrix [42]. However, these proteinases have a capability of a strong elastolytic activity, leading to matrix remodeling and migration and proliferation of cells [36]. Collagenolysis is most likely the major trigger of plaque rupture. In addition to the importance of both collagenolysis and elastolysis, additional local factors such as flow dynamics and vasospasm and cap calcium can also contribute to rupture events.

Plaque ruptures not only result in symptomatic but also asymptomatic events [43]. Most symptomatic events occur secondary to severe narrowing which is observed in over 70% of cases of plaque rupture in individuals dying of sudden coronary death. However, approximately 30% of plaque ruptures occur in lesions that are less severely narrowed (<75% x-sectional area narrowing) [44]. In a previous study reported by Mann and Davies, healed plaque ruptures in the plaques with <50% diameter stenosis were observed in 18.6% of lesions, whereas those with ≥51% luminal stenosis were in 73.2% ($P < 0.001$) [45] (Fig. 11.4). Also, in our

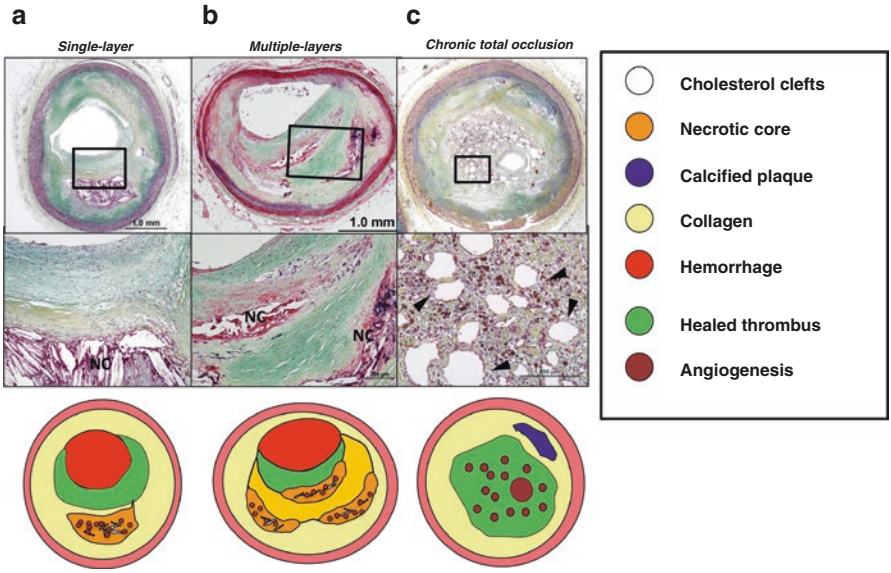

Fig. 11.4 Episodic rupture and healing can lead to chronic total occlusion. Histological and schematic images are shown for (**a**) single-layer healed plaque rupture, (**b**) multiple-layer healed plaque rupture, and (**c**) chronic total occlusion. Arrowheads indicate neoangiogenesis. Abbreviation: NC, necrotic core. (Histological image in panel (**a**) reprinted with permission from Nature Publishing Group © Otsuka et al. [61]. Histological image in panel (**c**) reprinted from Yahagi et al. [62], with permission from Elsevier)

autopsy study, 61% of victims who suffered from sudden coronary death had healed plaque ruptures [43]. As the number of healed plaque rupture increased so did the luminal stenosis increase. Plaque ruptures without a previous healed rupture are not common. Only 11% of plaque ruptures were virgin ruptures in individuals with sudden death [43]. Also, the incidence of healed plaque ruptures was greatest in individuals with stable plaque with healed myocardial infarction followed by acute plaque rupture and was least in those with stable plaque without healed infarction (2.0 ± 1.4, 1.5 ± 1.2, and 1.1 ± 1.4, respectively) [43].

Plaque Hemorrhage

An elaborate vascular network of intraplaque vasa vasorum (Vv) is frequently observed in atherosclerotic plaques, consisting of arterioles and capillaries. Vv are located in the adventitia in normal coronary arteries, and as the plaque enlarged, they enter the intima through media [46]. Vv are significantly increased when the luminal stenosis exceeds 25% [47], and it has been reported that plaques below 0.35 mm in thickness are avascular but beyond 0.35 mm are vascularized. It has been reported that 70% of Vv originate from the adventitial, whereas the

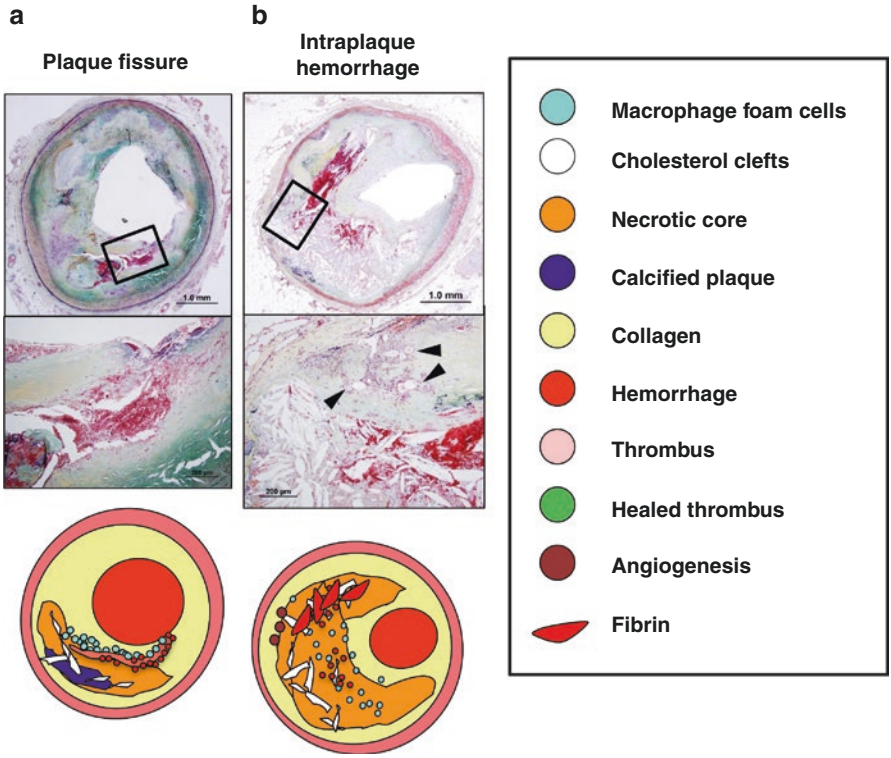

Fig. 11.5 Plaque morphologies that can lead to necrotic core expansion. Histological and schematic images are shown for (**a**) plaque fissure and (**b**) intraplaque hemorrhage. Arrowheads indicate neoangiogenesis. (Reprinted from Yahagi et al. [7], with permission from Elsevier)

remaining 30% are luminal in origin [47]. In 1928, Boyed et al. were the first to describe the existence of intraplaque hemorrhages, and Davies et al. reported that plaque hemorrhages coexisting in plaque fissures [48] (Fig. 11.5). In the 1980s, Virmani and Roberts reported that 10% of epicardial coronary artery segments in patients dying with coronary heart disease showed intraplaque hemorrhage [49]. Also, in the same study, they described that 4% of them showed the presence of iron. Later, we reported that intraplaque hemorrhages provoked macrophage infiltration and accelerated plaque progression. Hemorrhage is an important source of free cholesterol within plaques [27]. We showed that intraplaque hemorrhage in sudden coronary death victims as assessed by glycophorin A staining increased as plaques progressed and was highest in TCFA and this correlated with increase in necrotic core as well as with increase in macrophage infiltration. Furthermore, imaging studies have shown that anticoagulation therapy increases the risk of intraplaque hemorrhage [50]. Intraplaque hemorrhage in coronary arteries is most frequently observed in patients treated with oral anticoagulants (61%) as compared to those on antiplatelet inhibitors (53%) or without any such therapy (46%).

Density of intraplaque microvessels was highest in plaques of patients on platelet inhibitors ($P < 0.05$). Also, large intraplaque hemorrhages were associated with oral anticoagulant therapy [51].

Plaque Erosion

Plaque erosion is defined as the presence of an acute thrombus which is directly in contact with the underlying intima that is mainly composed of SMCs and proteoglycan-collagen matrix without endothelial cells at the interphase of thrombus and underlying plaque (Fig. 11.3). The underlying plaque in erosions is composed of either PIT or fibroatheroma, with majority of cases showing fibroatheromas (84%). Most erosion lesions show fragmented calcification when it is present (23%). The intimal plaque in erosion lesions is rich in versican, hyaluronan, and Type III collagen unlike rupture or stable plaques which typically have abundant type I collagen and biglycan and decorin [44, 52]. Also, CD44, a cell-surface glycoprotein (homing cell adhesion molecule) involved in cell-cell interaction, was localized along the plaque/thrombus interphase in erosions, whereas in rupture and stable plaque, it is mostly confined to inflammatory cells. A selective accumulation of versican, hyaluronan, and CD44 in plaque erosion implicates an involvement of these molecules in the de-endothelialization and platelet aggregation. And also, hyaluronan is able to provoke polymerization of fibrin, which may promote SMCs migration and plaque progression. Typically, the plaque erosion lesions are eccentric, with less severe narrowing from underlying plaque as compared to plaque ruptures and stable plaques. We have demonstrated that the culprit site of plaque erosions showed minimal inflammation consisting of few or absent macrophages and lymphocytes [2, 44]. Although inflammation at the site of erosion was reported by van der Wal et al. [53], we have rarely observed excessive inflammation in cases with erosion.

Plaque erosion is the second most frequent cause of coronary thrombosis in patients dying from acute myocardial infarction or sudden coronary death, with rupture being the most frequent [2, 31]. The risk factors for plaque erosions are different from those of rupture [31]. Of men dying from sudden coronary death, those with rupture had higher plasma total cholesterol (TC), lower high-density lipoprotein cholesterol (HDL-C), and higher TC/HDL-C ratio than plaque erosion [31]. On the other hand, only TC correlated with plaque rupture in women [54]. Smoking was the only important factor for plaque erosion in women with coronary disease who died suddenly [54]. In our sudden coronary death registry, plaque erosion is more frequent in females, especially those less than 50 years and who have less severe stenosis, less calcification, and less plaque burden and thrombus than rupture [54]. Also, women who smoke are more likely to have myocardial infarction than men who smoke [55]. More than 80% of thrombi are plaque erosion in young women, whereas the main cause of thrombosis is rupture in women who are older than 50 years old.

In our autopsy study, distal embolization was more common in plaque erosion (71%) than plaque rupture (42%) [56]. Kramer et al. reported that 88% of coronary thrombi in erosions demonstrate late stages of healing, defined as >24 hours duration of thrombus. On the other hand, only 54% of plaque rupture showed late stage of healing [57]. Also, even later healing stage of 7 days duration occurs in 46% in plaque erosion, whereas only 9% of rupture. Ferrante G et al. reported that density of myeloperoxidase-positive cells is higher in plaque erosion than plaque rupture [58]. Moreover, living patients with plaque erosion show higher circulating myeloperoxidase levels as compared to plaque rupture, suggesting there is the possibility that inflammatory biomarkers may help differentiate rupture from erosion. However, large prospective clinical studies are needed to confirm the differences between erosion and rupture using the imaging modalities (i.e., optical coherence tomography).

Calcified Nodule

Calcified nodule is the least frequent cause of coronary thrombi and exists only in the setting of highly calcified coronary disease (Fig. 11.3). Calcified nodule consists of fragments of pieces of calcium with disrupted intima and an overlying thrombus. The eruptive calcified nodule is usually eccentric and protrudes into the lumen. Calcified nodule typically shows lack of endothelium in the area of the nodules of calcium; the luminal surface shows the presence of a white thrombi consisting mainly of platelet which is usually nonocclusive. Although the mechanisms of calcified nodule are not fully understood, there is abundant fibrin within the area of calcified spicules with a coexisting few osteoclasts and inflammatory cells. The arteries that harbor calcified nodule show the presence of sheets of calcium, and we believe that the sheets of calcium crack and break which is usually observed in highly tortuous arteries [2]. Nodular calcification is said to be present when nodules of calcium do not disrupt the luminal surface of the plaque. Medial disruption is common in both but is more frequent in those with nodular calcification. Both these entities are observed in older individuals, diabetics, and patients with chronic kidney disease and especially in those on dialysis. The highest prevalence of nodular calcification is in the mid-right coronary or tortuous left anterior descending coronary arteries.

It is not possible with IVUS imaging to distinguish calcified nodule from nodular calcification due to poor resolution. Recently OCT studies have been able to identify calcified nodule. Jia et al. defined OCT-calcified nodule as having a disrupted fibrous cap over a calcified plaque characterized by protruding calcification with extensive calcium both proximal and distal to the lesion. In patients presenting with acute coronary syndrome, the prevalence of calcified nodule was 7.9% in patients, and its incidence was more common in older patients [59]. The more recent OCT study published in 2017 evaluated 889 de novo culprit lesions in 889 patients (48% ACS and 52% with stable angina) [60]. Calcified nodules were most

frequently observed in the ostia or mid-right coronary artery. Significant predicators for the presence of calcified nodule by multivariate analysis were seen in patients on hemodialysis, in-lesion angiographic tortuosity angle, and maximum arc of calcium by OCT.

In patients presenting with stable angina, there is usually severe underlying narrowing (>75% cross-sectional area narrowing) by fibrocalcific plaque or healed plaque ruptures, and both these lesions demonstrate the highest degree of calcification. In patients presenting with acute coronary syndrome, there is either a luminal thrombus from rupture, erosion, or calcified nodule or there is sudden enlargement of the plaque from intraplaque hemorrhage that may occur in vulnerable or non-vulnerable plaques. Luminal narrowing is usually severer in ruptures than in erosions and is very variable in calcified nodules.

Conclusion

Plaque rupture is characterized by the presence of disrupted thin cap that is infiltrated by macrophages and T lymphocytes allowing a direct contact of the necrotic core to the circulating blood that leads to luminal thrombus. Plaque erosion is another cause of coronary thrombus, but its incidence is much less than rupture. Lesions of plaque erosion are rich in SMCs and proteoglycan-collagen matrix with an absence of endothelial cells at the site of the thrombus. Calcified nodule is the least frequent mechanism of coronary thrombus and must be distinguished from nodular calcification with the former having disruption of the fibrous cap and the presence of a luminal thrombus. The calcified nodule shows fragments of calcification within which protrude into the lumen and are separated by fibrin. Stable angina patients usually demonstrate the presence of fibrocalcific plaque or healed plaque rupture in the presence of severe luminal narrowing. While unstable plaques are usually seen in acute coronary syndromes and constitute vulnerable plaque with hemorrhage and lesions with luminal thrombi. Understanding the mechanism of the three different causes of coronary thrombosis is crucial in order to better treat these modalities in patients presenting with acute coronary syndromes and stable angina.

References

1. Laslett LJ, Alagona P Jr, Clark BA 3rd, Drozda JP Jr, Saldivar F, Wilson SR, Poe C, Hart M. The worldwide environment of cardiovascular disease: prevalence, diagnosis, therapy, and policy issues: a report from the American college of cardiology. J Am Coll Cardiol. 2012;60:S1–49.
2. Virmani R, Kolodgie FD, Burke AP, Farb A, Schwartz SM. Lessons from sudden coronary death: a comprehensive morphological classification scheme for atherosclerotic lesions. Arterioscler Thromb Vasc Biol. 2000;20:1262–75.
3. Falk E, Nakano M, Bentzon JF, Finn AV, Virmani R. Update on acute coronary syndromes: the pathologists' view. Eur Heart J. 2013;34:719–28.

4. Arbustini E, Dal Bello B, Morbini P, Burke AP, Bocciarelli M, Specchia G, Virmani R. Plaque erosion is a major substrate for coronary thrombosis in acute myocardial infarction. Heart. 1999;82:269–72.
5. Stary HC, Blankenhorn DH, Chandler AB, Glagov S, Insull W Jr, Richardson M, Rosenfeld ME, Schaffer SA, Schwartz CJ, Wagner WD, et al. A definition of the intima of human arteries and of its atherosclerosis-prone regions. A report from the Committee on Vascular Lesions of the Council on Arteriosclerosis, American Heart Association. Arterioscler Thromb. 1992;12:120–34.
6. Stary HC, Chandler AB, Dinsmore RE, Fuster V, Glagov S, Insull W Jr, Rosenfeld ME, Schwartz CJ, Wagner WD, Wissler RW. A definition of advanced types of atherosclerotic lesions and a histological classification of atherosclerosis. A report from the Committee on Vascular Lesions of the Council on Arteriosclerosis, American Heart Association. Arterioscler Thromb Vasc Biol. 1995;15:1512–31.
7. Yahagi K, Kolodgie FD, Otsuka F, Finn AV, Davis HR, Joner M, Virmani R. Pathophysiology of native coronary, vein graft, and in-stent atherosclerosis. Nat Rev Cardiol. 2016;13:79–98.
8. Stary HC. Natural history and histological classification of atherosclerotic lesions: an update. Arterioscler Thromb Vasc Biol. 2000;20:1177–8.
9. Nakashima Y, Chen YX, Kinukawa N, Sueishi K. Distributions of diffuse intimal thickening in human arteries: preferential expression in atherosclerosis-prone arteries from an early age. Virchows Arch. 2002;441:279–88.
10. McGill HC Jr, McMahan CA, Tracy RE, Oalmann MC, Cornhill JF, Herderick EE, Strong JP. Relation of a postmortem renal index of hypertension to atherosclerosis and coronary artery size in young men and women. Pathobiological determinants of atherosclerosis in youth (pday) research group. Arterioscler Thromb Vasc Biol. 1998;18:1108–18.
11. Ikari Y, McManus BM, Kenyon J, Schwartz SM. Neonatal intima formation in the human coronary artery. Arterioscler Thromb Vasc Biol. 1999;19:2036–40.
12. Fan J, Watanabe T. Inflammatory reactions in the pathogenesis of atherosclerosis. J Atheroscler Thromb. 2003;10:63–71.
13. Aikawa M, Rabkin E, Okada Y, Voglic SJ, Clinton SK, Brinckerhoff CE, Sukhova GK, Libby P. Lipid lowering by diet reduces matrix metalloproteinase activity and increases collagen content of rabbit atheroma: a potential mechanism of lesion stabilization. Circulation. 1998;97:2433–44.
14. Nakagawa K, Nakashima Y. Pathologic intimal thickening in human atherosclerosis is formed by extracellular accumulation of plasma-derived lipids and dispersion of intimal smooth muscle cells. Atherosclerosis. 2018;274:235–42.
15. McGill HC Jr, McMahan CA, Herderick EE, Tracy RE, Malcom GT, Zieske AW, Strong JP. Effects of coronary heart disease risk factors on atherosclerosis of selected regions of the aorta and right coronary artery. Pday research group. Pathobiological determinants of atherosclerosis in youth. Arterioscler Thromb Vasc Biol. 2000;20:836–45.
16. Hixson JE, McMahan CA, McGill HC Jr, Strong JP. Apo B insertion/deletion polymorphisms are associated with atherosclerosis in young black but not young white males. Pathobiological Determinants of Atherosclerosis in Youth (PDAY) Research Group. Arterioscler Thromb. 1992;12:1023–9.
17. Nakashima Y, Fujii H, Sumiyoshi S, Wight TN, Sueishi K. Early human atherosclerosis: accumulation of lipid and proteoglycans in intimal thickenings followed by macrophage infiltration. Arterioscler Thromb Vasc Biol. 2007;27:1159–65.
18. Nakashima Y, Wight TN, Sueishi K. Early atherosclerosis in humans: role of diffuse intimal thickening and extracellular matrix proteoglycans. Cardiovasc Res. 2008;79:14–23.
19. Merrilees MJ, Beaumont B, Scott LJ. Comparison of deposits of versican, biglycan and decorin in saphenous vein and internal thoracic, radial and coronary arteries: correlation to patency. Coron Artery Dis. 2001;12:7–16.
20. Tulenko TN, Chen M, Mason PE, Mason RP. Physical effects of cholesterol on arterial smooth muscle membranes: evidence of immiscible cholesterol domains and alterations in bilayer width during atherogenesis. J Lipid Res. 1998;39:947–56.

21. Hoff HF, Bradley WA, Heideman CL, Gaubatz JW, Karagas MD, Gotto AM Jr. Characterization of low density lipoprotein-like particle in the human aorta from grossly normal and atherosclerotic regions. Biochim Biophys Acta. 1979;573:361–74.
22. Smith EB, Slater RS. The microdissection of large atherosclerotic plaques to give morphologically and topographically defined fractions for analysis. 1. The lipids in the isolated fractions. Atherosclerosis. 1972;15:37–56.
23. Bennett MR, Evan GI, Schwartz SM. Apoptosis of human vascular smooth muscle cells derived from normal vessels and coronary atherosclerotic plaques. J Clin Invest. 1995;95:2266–74.
24. Perales S, Alejandre MJ, Palomino-Morales R, Torres C, Iglesias J, Linares A. Effect of oxysterol-induced apoptosis of vascular smooth muscle cells on experimental hypercholesterolemia. J Biomed Biotechnol. 2009;2009:456208.
25. Clarke MC, Talib S, Figg NL, Bennett MR. Vascular smooth muscle cell apoptosis induces interleukin-1-directed inflammation: effects of hyperlipidemia-mediated inhibition of phagocytosis. Circ Res. 2010;106:363–72.
26. Tabas I. Macrophage death and defective inflammation resolution in atherosclerosis. Nat Rev Immunol. 2010;10:36–46.
27. Kolodgie FD, Gold HK, Burke AP, Fowler DR, Kruth HS, Weber DK, Farb A, Guerrero LJ, Hayase M, Kutys R, Narula J, Finn AV, Virmani R. Intraplaque hemorrhage and progression of coronary atheroma. N Engl J Med. 2003;349:2316–25.
28. Tabas I. Cholesterol and phospholipid metabolism in macrophages. Biochim Biophys Acta. 2000;1529:164–74.
29. Tabas I, Marathe S, Keesler GA, Beatini N, Shiratori Y. Evidence that the initial up-regulation of phosphatidylcholine biosynthesis in free cholesterol-loaded macrophages is an adaptive response that prevents cholesterol-induced cellular necrosis. Proposed role of an eventual failure of this response in foam cell necrosis in advanced atherosclerosis. J Biol Chem. 1996;271:22773–81.
30. Newby AC. Metalloproteinase expression in monocytes and macrophages and its relationship to atherosclerotic plaque instability. Arterioscler Thromb Vasc Biol. 2008;28:2108–14.
31. Burke AP, Farb A, Malcom GT, Liang YH, Smialek J, Virmani R. Coronary risk factors and plaque morphology in men with coronary disease who died suddenly. N Engl J Med. 1997;336:1276–82.
32. Narula J, Nakano M, Virmani R, Kolodgie FD, Petersen R, Newcomb R, Malik S, Fuster V, Finn AV. Histopathologic characteristics of atherosclerotic coronary disease and implications of the findings for the invasive and noninvasive detection of vulnerable plaques. J Am Coll Cardiol. 2013;61:1041–51.
33. Narula J, Garg P, Achenbach S, Motoyama S, Virmani R, Strauss HW. Arithmetic of vulnerable plaques for noninvasive imaging. Nat Clin Pract Cardiovasc Med. 2008;5(Suppl 2):S2–10.
34. Kolodgie FD, Burke AP, Farb A, Gold HK, Yuan J, Narula J, Finn AV, Virmani R. The thin-cap fibroatheroma: a type of vulnerable plaque: the major precursor lesion to acute coronary syndromes. Curr Opin Cardiol. 2001;16:285–92.
35. Libby P. Molecular bases of the acute coronary syndromes. Circulation. 1995;91:2844–50.
36. Dollery CM, Owen CA, Sukhova GK, Krettek A, Shapiro SD, Libby P. Neutrophil elastase in human atherosclerotic plaques: production by macrophages. Circulation. 2003;107:2829–36.
37. Herman MP, Sukhova GK, Libby P, Gerdes N, Tang N, Horton DB, Kilbride M, Breitbart RE, Chun M, Schonbeck U. Expression of neutrophil collagenase (matrix metalloproteinase-8) in human atheroma: a novel collagenolytic pathway suggested by transcriptional profiling. Circulation. 2001;104:1899–904.
38. Libby P. Coronary artery injury and the biology of atherosclerosis: inflammation, thrombosis, and stabilization. Am J Cardiol. 2000;86:3J–8J; discussion 8J–9J.
39. Libby P. Inflammation in atherosclerosis. Nature. 2002;420:868–74.
40. Sukhova GK, Schonbeck U, Rabkin E, Schoen FJ, Poole AR, Billinghurst RC, Libby P. Evidence for increased collagenolysis by interstitial collagenases-1 and -3 in vulnerable human atheromatous plaques. Circulation. 1999;99:2503–9.

41. Libby P. Changing concepts of atherogenesis. J Intern Med. 2000;247:349–58.
42. Sukhova GK, Shi GP, Simon DI, Chapman HA, Libby P. Expression of the elastolytic cathepsins s and k in human atheroma and regulation of their production in smooth muscle cells. J Clin Invest. 1998;102:576–83.
43. Burke AP, Kolodgie FD, Farb A, Weber DK, Malcom GT, Smialek J, Virmani R. Healed plaque ruptures and sudden coronary death: evidence that subclinical rupture has a role in plaque progression. Circulation. 2001;103:934–40.
44. Farb A, Burke AP, Tang AL, Liang TY, Mannan P, Smialek J, Virmani R. Coronary plaque erosion without rupture into a lipid core. A frequent cause of coronary thrombosis in sudden coronary death. Circulation. 1996;93:1354–63.
45. Mann J, Davies MJ. Mechanisms of progression in native coronary artery disease: role of healed plaque disruption. Heart (British Cardiac Society). 1999;82:265–8.
46. Williams JK, Heistad DD. Structure and function of vasa vasorum. Trends Cardiovasc Med. 1996;6:53–7.
47. Kumamoto M, Nakashima Y, Sueishi K. Intimal neovascularization in human coronary atherosclerosis: its origin and pathophysiological significance. Hum Pathol. 1995;26:450–6.
48. Boyle JJ. Heme and haemoglobin direct macrophage mhem phenotype and counter foam cell formation in areas of intraplaque haemorrhage. Curr Opin Lipidol. 2012;23:453–61.
49. Virmani R, Roberts WC. Extravasated erythrocytes, iron, and fibrin in atherosclerotic plaques of coronary arteries in fatal coronary heart disease and their relation to luminal thrombus: frequency and significance in 57 necropsy patients and in 2958 five mm segments of 224 major epicardial coronary arteries. Am Heart J. 1983;105:788–97.
50. Pasterkamp G, van der Steen AF. Intraplaque hemorrhage: an imaging marker for atherosclerotic plaque destabilization? Arterioscler Thromb Vasc Biol. 2012;32:167–8.
51. Li X, Vink A, Niessen HW, Kers J, de Boer OJ, Ploegmakers HJ, Tijssen JG, de Winter RJ, van der Wal AC. Total burden of intraplaque hemorrhage in coronary arteries relates to the use of coumarin-type anticoagulants but not platelet aggregation inhibitors. Virchows Arch. 2014;465(6):723–9.
52. Kolodgie FD, Burke AP, Farb A, Weber DK, Kutys R, Wight TN, Virmani R. Differential accumulation of proteoglycans and hyaluronan in culprit lesions: insights into plaque erosion. Arterioscler Thromb Vasc Biol. 2002;22:1642–8.
53. van der Wal AC, Becker AE, van der Loos CM, Das PK. Site of intimal rupture or erosion of thrombosed coronary atherosclerotic plaques is characterized by an inflammatory process irrespective of the dominant plaque morphology. Circulation. 1994;89:36–44.
54. Burke AP, Farb A, Malcom GT, Liang Y, Smialek J, Virmani R. Effect of risk factors on the mechanism of acute thrombosis and sudden coronary death in women. Circulation. 1998;97:2110–6.
55. Njolstad I, Arnesen E, Lund-Larsen PG. Smoking, serum lipids, blood pressure, and sex differences in myocardial infarction. A 12-year follow-up of the Finnmark study. Circulation. 1996;93:450–6.
56. Schwartz RS, Burke A, Farb A, Kaye D, Lesser JR, Henry TD, Virmani R. Microemboli and microvascular obstruction in acute coronary thrombosis and sudden coronary death: relation to epicardial plaque histopathology. J Am Coll Cardiol. 2009;54:2167–73.
57. Kramer MC, Rittersma SZ, de Winter RJ, Ladich ER, Fowler DR, Liang YH, Kutys R, Carter-Monroe N, Kolodgie FD, van der Wal AC, Virmani R. Relationship of thrombus healing to underlying plaque morphology in sudden coronary death. J Am Coll Cardiol. 2010;55:122–32.
58. Ferrante G, Nakano M, Prati F, Niccoli G, Mallus MT, Ramazzotti V, Montone RA, Kolodgie FD, Virmani R, Crea F. High levels of systemic myeloperoxidase are associated with coronary plaque erosion in patients with acute coronary syndromes: a clinicopathological study. Circulation. 2010;122:2505–13.
59. Jia H, Abtahian F, Aguirre AD, Lee S, Chia S, Lowe H, Kato K, Yonetsu T, Vergallo R, Hu S, Tian J, Lee H, Park SJ, Jang YS, Raffel OC, Mizuno K, Uemura S, Itoh T, Kakuta T, Choi SY, Dauerman HL, Prasad A, Toma C, McNulty I, Zhang S, Yu B, Fuster V, Narula J,

Virmani R, Jang IK. In vivo diagnosis of plaque erosion and calcified nodule in patients with acute coronary syndrome by intravascular optical coherence tomography. J Am Coll Cardiol. 2013;62:1748–58.
60. Lee T, Mintz GS, Matsumura M, Zhang W, Cao Y, Usui E, Kanaji Y, Murai T, Yonetsu T, Kakuta T, Maehara A. Prevalence, predictors, and clinical presentation of a calcified nodule as assessed by optical coherence tomography. JACC Cardiovasc Imaging. 2017;10:883–91.
61. Otsuka F, et al. Clinical classification of plaque morphology in coronary disease. Nat Rev Cardiol. 2014;11(7):379–89.
62. Yahagi K, et al. Sex differences in coronary artery disease: pathological observations. Atherosclerosis. 2015;239(1):260–7.

Chapter 12
Current Imaging Approaches and Challenges in the Assessment of Coronary Artery Disease

Mateus Diniz Marques and João Augusto Costa Lima

Introduction

For many decades, coronary angiography was the gold standard for the study of coronary artery diseases. Angiography allows a two-dimensional assessment of the coronary lumen, a vessel silhouette. Important components of the atherosclerotic process in the coronary vessel wall are not evaluated by angiography, such as positive remodeling, plaque composition, plaque extension, or diffuse atherosclerosis. Currently, evaluating the cardiovascular risk based on diagnosing coronary stenosis by angiography is not enough for both the diagnosis and the therapeutic definition in coronary artery disease (CAD). The new paradigm is evaluating the coronary artery wall. We know that acute coronary events are caused mainly by plaques with small degrees of stenosis, but with vulnerability characteristics that are hardly diagnosed by angiography.

Several diagnostic methods have been used to evaluate the characteristics of arterial walls in order to identify early stages of CAD and features that are able to predict plaque vulnerability. Many characteristics are evaluated in coronary artery wall. Some of the most clinically valuable characteristics are plaque burden, plaque volume, plaque extension, plaque high-risk features and contents, and signs of inflammation. Currently, there is no diagnostic method capable to accurately evaluate all these characteristics at the same time. Therefore, the combination of methods to

M. D. Marques
Federal University of Santa Maria, Santa Maria, Brazil
e-mail: mdmarques@ufsm.br

J. A. C. Lima (✉)
Johns Hopkins Hospital, Baltimore, MD, USA

Radiology and Epidemiology at the Johns Hopkins School of Medicine, Baltimore, MD, USA
e-mail: jlima@jhmi.edu

C. Yuan et al. (eds.), *Vessel Based Imaging Techniques*,
https://doi.org/10.1007/978-3-030-25249-6_12

achieve a complete diagnosis is necessary. Based on the clinical history, a reasonable approach is to choose a method that provides the best answer to the clinical decision-making. In this chapter, we will cover clinically available techniques for evaluating the coronary artery wall, its related diseases, and limitations of each technique.

Invasive Diagnostic Methods to Assess Coronary Wall

In order to better evaluate the coronary atherosclerosis, new diagnostic techniques such as intravascular ultrasound (IVUS) and optical coherence tomography (OCT) arose to complement the angiography exams. Both techniques corroborate and enrich coronary lumen assessment providing additional and valuable information regarding the coronary wall.

Intravascular Ultrasound

The first reports about the use of IVUS appeared in the end of the 1980s. Since then, its use has become increasingly commonplace and technological advances made it increasingly clinically useful. Initially, IVUS exams used gray-scale technique to assess the coronary wall characteristics. This technique had several limitations which compromised its diagnostic accuracy. Current acquisition and processing technologies such as the backscattered ultrasound waves using radio frequency allow accurate analysis of coronary wall. IVUS enables plaque composition discrimination (necrotic core, fibrous tissue, fibrofatty tissue, and dense calcium) as well as determining characteristics of high-risk plaques [1–3]. These diagnostic abilities allow us to use IVUS in monitoring the evolution of atherosclerosis over time and therapeutic response manifested by regression in plaque volume [4, 5].

An important clinical use of IVUS is diagnosing vulnerable plaques. Some plaque vulnerability characteristics assessed by IVUS are the thin-cap fibroatheroma (TCFA), positive remodeling, large plaque burden, and small luminal area. The PROSPECT study showed that in patients with acute coronary syndrome (ACS) plaques with vulnerability signs had increased risk of major acute coronary events (MACE) even in non-culprit lesions [6].

Another quite common clinical use of IVUS is during percutaneous coronary intervention (PCI). IVUS findings help before, during, and after procedure completion. IVUS can be used to choose the most appropriate technique and materials to be used during the PCI. It helps to confirm angiography findings and accurately reports the degree of coronary stenosis, plaque extension, plaque components, coronary ostium involvement, and vessel size. After the procedure, IVUS evaluates minimal lumen area, stent malapposition, stent edge, dissection, and tissue prolapse that may be determinant of future complications such as restenosis and stent

thrombosis [2]. Metanalyses focused on comparing IVUS-guided PCI with procedures guided exclusively by angiography showed better immediate and late angiographic results (greater post-minimal lumen diameter, lower restenosis, and revascularization requirement) as well as reduction in MACE [7, 8]. Currently, there is an increasing use of IVUS during PCI, especially when implanting drug eluting stents, where the risks of thrombosis and restenosis are significantly higher if there is stent malapposition. The IVUS-guided PCI is recommended for cases with increased complexity (complex lesions, chronic occlusion, bifurcations with ostium involvement, extensive plaques, or left main artery involvement) or to assess stent failure [9].

Limitations

Despite its excellent diagnostic capacity, IVUS usage to cardiovascular evaluation in general population is restricted for its invasive nature. IVUS exams must be performed in a hemodynamic laboratory, with a trained team and executed by a highly experienced hemodynamicist. All exams use iodinated contrast and need ionizing radiation to precisely locate the target vessel or lesion to be studied. Additionally, longer examination time and extra materials increase the costs, limiting its use in the cardiologic diagnostic practice.

Concerning image quality, IVUS has some limitations evaluating plaques with a great amount of calcification, impairing the visualization behind calcium. Additionally, some plaque structures may exhibit very similar echogenicity characteristics making it impossible to differentiate them, for example, thrombi and lipid component [2]. Finally, IVUS resolution is insufficient to measure the thickness of the fibrous cap; consequently TCFA is defined based on the identification of the necrotic core compressing the lumen.

Optical Coherence Tomography

Usually OCT is considered an alternative or complement to IVUS. Its great advantage comparing to IVUS is its spatial resolution (10–15 mc vs 100–150 mcm). The excellent resolution allows OCT to evaluate the atheroma layer in detail, being the only method capable of measuring in vivo the thickness of the layer and objectively defining TCFA (<65 mcm). Additionally, OCT allows the evaluation of the integrity of the cap, classifying culprit lesions as disrupted fibrous cap (with lipid predominance or calcified nodule) and intact fibrous cap [10]. In patients with ACS, those whose culprit lesion has uninterrupted fibrous cap instead of disrupted have a better prognosis over time, with a lower incidence of death, heart attack, and hospitalization [11].

There are several plaque vulnerability features besides TCFA which can be evaluated accurately by OCT such as plaque composition, macrophages wall infiltrate,

microcalcifications, neovascularization, and thrombus. All those features are usual findings in patients with ACS [12–14].

Like IVUS, OCT has been used in planning, guiding, and following PCI. As well as IVUS-guided procedures, using OCT showed to reduce the risk of cardiac death or acute myocardial infarction compared to the angiography-guided procedures [15]. Its excellent spatial resolution allows an excellent plaque characterization, identifying stent malapposition, stent edge, dissection, tissue prolapse, and thrombus [15, 16]. However, the assessment of lumen size after the procedure (minimal lumen area) measured by OCT is significantly lower than that measured by IVUS. This may result in a suboptimal stent expansion in OCT-guided procedures, increasing the chances of late complications such as stent thrombosis or restenosis [16]. The indications for OCT-guided PCI still need stronger randomized controlled trials to support them and should be restricted to cases with greater complexity or with stent failure suspicion [9].

Limitations

OCT imaging requires the use of contrast media to displace blood from the vessel lumen on the segment to be examined. This significantly increase the amount of contrast usually used in angiography. Another limitation imposed by red blood cells is the inability of OCT to visualize red thrombus.

The main disadvantage of OCT comparing to IVUS is the reduced image deep penetration (1–2 mm), making it impossible to fully evaluate plaque composition and the voluminous plaque necrotic core [13]. Reduced deep analysis limits the ability of assessing positive remodeling by OCT, an important plaque vulnerable feature perfectly evaluated by IVUS [13]. Recently, the advent of catheters with the two intracoronary imaging modalities IVUS and OCT promises to associate the high resolution of the OCT to evaluate the cap thickness with the best IVUS image depth for assessing the necrotic core and plaque burden. The combination of both would fully evaluate coronary plaque without dispensing the invasive approach, contrast media usage, and ionizing radiation exposure.

Noninvasive Diagnostic Methods to Assess Coronary Wall

Magnetic Resonance

The first high-resolution magnetic resonance imaging study (MRI) of human arteries was published by Martin et al. in 1995 [17]. Martin studied segments of the carotid, femoral, and aortic arteries and compared MRI findings with histological exams [17]. This study contributed significantly to developing arterial wall imaging techniques to reproduce such images in vivo and stimulated researchers to pursue

studying coronary artery walls by MRI. The use of MRI for the evaluation of coronary arteries became clinically feasible after the advent of the latest-generation scanners, allowing faster acquisition sequences and better image quality. Coronary wall evaluation by MRI is safe and noninvasive, does not expose the patient to ionizing radiation, and often does not need any form of contrast medium. These features make coronary wall MRI a promising diagnostic tool for the large-scale evaluation of suspected or known CAD individuals as well as evaluating coronary involvement of inflammatory pathologies.

After a long period of technological advances with emerging new-generation scanners and improvements of MRI sequences, in 2000 Fayad et al. [18] and Botnar et al. [19] published their studies on the use of MRI for the evaluation of coronary artery wall in vivo. They used T2-weighted sequences to assess the coronary artery wall characteristics without the use of contrast media. Coronary segments with atherosclerotic plaques by angiography showed greater vessel area and wall thickness on MRI compared to normal segments in the same patients [18, 19]. These findings boosted the use of MRI to assess coronary wall features in different clinical scenarios.

Coronary MRI demonstrated to be able to identify atherosclerosis in early stages, before significant luminal reduction is established (<50% stenosis). Segments with atherosclerosis presented increased wall thickness and increased wall area compared to healthy coronary segments on angiography [20]. MRI outer vessel area and plaque burden showed good correlation with IVUS [21]. However, coronary wall thickness assessed by MRI demonstrated low correlation with IVUS [22]. Besides identifying atherosclerotic plaques, an important role of MRI is identifying high-risk plaques and their vulnerable features. These plaques are characterized by a large lipid core, positive remodeling, a thin fibrous cap, and a high-inflammatory component being prone to rupture.

In order to assess high-risk plaques, different MRI techniques are available. The measurement of vessel wall signal intensity using T1-weighted three-dimensional black-blood gradient sequences without contrast-medium injection was validated in carotid arteries. High-intensity signal (HIS) in the carotid wall was associated with a high-risk plaque, intraplate thrombus, or hemorrhage assessed by histological exams [23–25]. This approach was used in patients with significant coronary stenosis (>70%), and HIS plaques had a high frequency of ultrasound attenuation, low CT density, and a high incidence of transient slow flow phenomena [26, 27]. Furthermore, the location of HIS in the coronary lumen or intrawall was also related to important features of plaque vulnerability [27]. Masumoto et al. [28] compared OCT findings in patients with angina pectoris and showed that thrombus and intimal vasculature were associated with intraluminal HIS. In contrast, intrawall HIS was associated with macrophage infiltration and absence of calcification [28].

Another non-contrast MRI ability is to identify methemoglobin in coronary wall using T1-weighted black-blood sequences. Methemoglobin is visualized in acute thrombus and intraplaque hemorrhages [26, 29], an important plaque vulnerability feature present in patients ongoing acute coronary syndrome [30, 31].

These combined techniques allow non-enhanced MRI to assess coronary wall thickness, vascular remodeling, plaque burden, and intraplaque hemorrhage or thrombus. These characteristics are known as vulnerable plaque features with significant clinical impact. Patients with HIS plaques have higher probability of MACE [32].

Beyond these non-contrast techniques, MRI can also evaluate coronary artery wall through images acquired after contrast injection (gadolinium). The technique shares the same principles of late gadolinium enhancement for evaluation of myocardial fibrosis. The pathophysiological pathway is based on the theory that there is a rupture of the cell membrane and the expansion of extracellular space by collagen in the fibrosis process. Providing gadolinium is an extracellular contrast, enlarged extracellular space will increase the contrast amount in those areas and extend the contrast wash out time. Late images acquired after gadolinium injection will enhance in fibrotic regions. Histological study of carotid plaques demonstrated that contrast enhancement was associated with neovascularization of the fibrous cap, increased endothelial permeability, and infiltration of inflammatory cells [33].

Early reports using T1-weighted images demonstrated that coronary wall contrast enhancement is strongly associated with vascular remodeling and atherosclerosis severity [29, 34]. Coronary wall enhanced areas by MRI correspond predominantly to mixed plaques by computed tomography angiography (CTA) [34]. In the setting of chronic coronary artery disease, contrast uptake in the coronary wall might be associated with neovascularization, endothelial permeability, and infiltration of inflammatory cells [29, 34].

Patients with ACS had significantly greater contrast uptake in the coronary wall of culprit lesions [35, 36]. However, long-term follow-up of these patients showed that the enhancement decreased 3 months after reperfusion [35]. This finding suggests that edema and the inflammatory process present in ACS have a significant role in this phenomenon and that enhancement of the coronary wall may be a surrogate biomarker of plaque activity and/or vulnerability [35, 36].

Delayed enhancement MRI can be useful for the evaluation of coronary wall involvement in several inflammatory diseases. Puntmann et al. [37] showed that patients with systemic lupus erythematosus at clinical remission have a higher signal intensity measured by contrast noise ratio on the coronary wall compared to control subjects [37]. In another study of the same group, they demonstrated that patients with systemic lupus erythematosus presented contrast enhancement in a diffuse pattern while patients with CAD had a regional distribution, but both had contrast noise ratio values higher than control patients [38]. In Takayasu's arteritis, the delay enhancement of the coronary wall seems to have the same distribution as segments with CAD [39].

Limitations

The image acquisition of coronary arteries is a challenge for any noninvasive imaging method, especially MRI. Some of the reasons for that lie in the fact that coronary arteries have reduced caliber and tortuous trajectory and are subjected to heart

and respiratory movements. New-generation scanners with optimized sequences allow faster exams, minimizing cardiac cycle and respiratory movement artifacts while maintaining adequate image quality. Another variable that compromises coronary MRI quality is the distance between MRI coil, positioned on the thoracic wall, and the coronary arteries. The greater the distance, the lower the noise signal ratio and worse image quality. Finally, the maximum spatial resolution obtained by the MRI (0.65 × 0.65 mm) is insufficient compared to those available by the IVUS (<0.1 mm) or even CTA (0.35 × 0.35 × 0.35 mm). MRI resolution allows a satisfactory analysis only for segments with greater caliber and restricting its evaluation to the proximal or middle coronary segments [40].

Computed Tomography Angiography

Computed tomography angiography has raised as an emerging diagnostic tool in the evaluation of coronary arteries in the past years. Coronary CTA allows the evaluation of several cardiac structures in a single acquisition such as the coronary arteries lumen, coronary wall, coronary adjacent structures (pericoronary fat and pericardium), myocardial perfusion, and functional and anatomical heart structures. These evaluations are possible using a single contrast-medium injection. The overall assessment of heart structure and function became possible by the evolution of scanners and the reconstruction algorithms. New equipment with a larger number of detectors (up to 320 detectors) and dual source energy scanners significantly improved spatial and temporal resolution, as well as reducing radiation exposure and the need of larger volumes of iodinated contrast [41].

In order to evaluate coronary arteries wall, it is necessary to inject iodinated contrast through a peripheral venous. The image acquisition technique for evaluating the coronary wall follows the same protocol as conventional CTA, allowing combined analysis of coronary lumen and coronary wall (Fig. 12.1). The identification of coronary stenosis location is of great importance while interpreting CTA exams focused on coronary wall analysis, driving the examiner to the specific segment to be studied. Coronary wall analysis requires a combined interpretation, using a subjective visual analysis and objective measurements performed semiautomatically (Figs. 12.1 and 12.2). Visually, the examiner identifies several complex features such as TCFA, napkin ring signal, positive remodeling, and major cap disruption. Ideally, objective measurement should always be added, including mean plaque attenuation, determining plaque components based on its attenuation range, plaque overall volume, as well as volume of each plaque components. Objective measurements are semiautomatic by using commercially validated software [42, 43]. The combined analysis allows the characterization of plaques as non-calcified, mixed, or calcified, as well as it highlights important features of plaque vulnerability (Fig. 12.1).

Although there have been technological advances, the first stages of atherosclerosis, which comprise the diffuse thickening of the intima with macrophage infil-

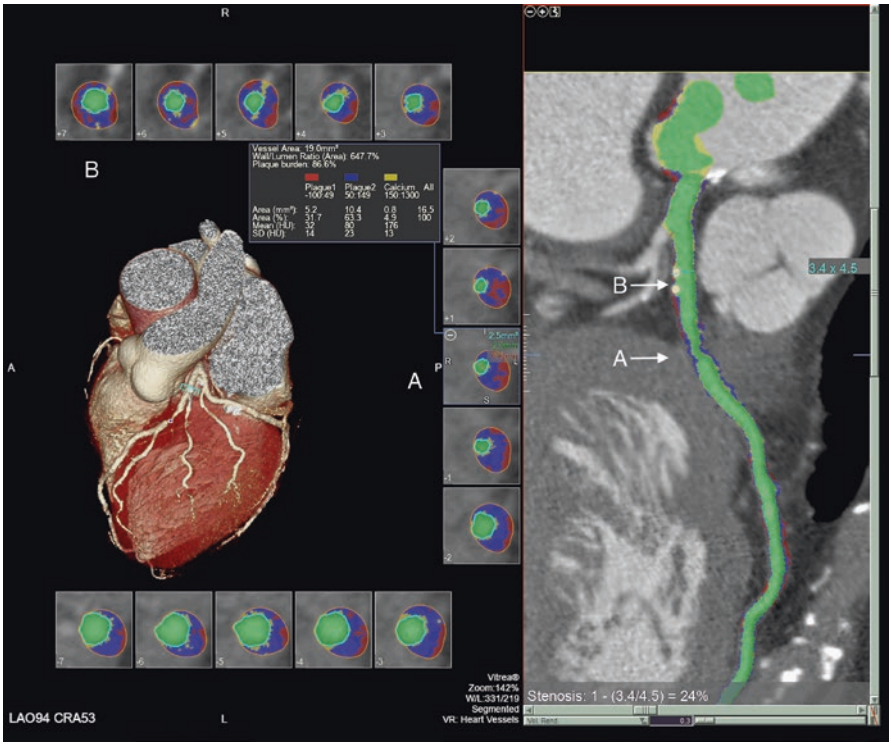

Fig. 12.1 Coronary computed tomography angiography with simultaneous visualization of the three-dimensional anatomy of the heart and coronary arteries, visualization of the coronary artery lumen in curved multiplanar reconstruction, and transverse images of the coronary artery with lumen and artery wall visualization. Cross-sectional analysis of the artery allows the evaluation of the characteristics of each slice and identification of segments with lumen stenosis (A) as well as segments apparently normal to angiography (B) but with atherosclerotic involvement identified by tomography

trates and the formation of the fatty strains [44], are not visible in current clinical computed tomography scanners available [45]. However, it is well known that exactly on these early stages of atherosclerosis, the plaques are more susceptible to rupture. Positive remodeling is an early atherosclerotic feature well identified by CTA, which is commonly associated with large necrotic-core plaques, hemorrhage, and TCFA [46, 47]. Unfortunately, not all plaque disruption features can be clearly identified by CTA. However, some valuable findings such as increased plaque volume, low plaque attenuation, and positive remodeling are well documented by CTA [48, 49]. These findings are well correlated with angiographic findings [48] and are present in up to 40% of patients considered to be clinically stable, representing silent disrupted plaques. These cases are difficult to be identified by the traditional cardiovascular risk assessment and are precisely the target patient of primary cardiovascular prevention [49].

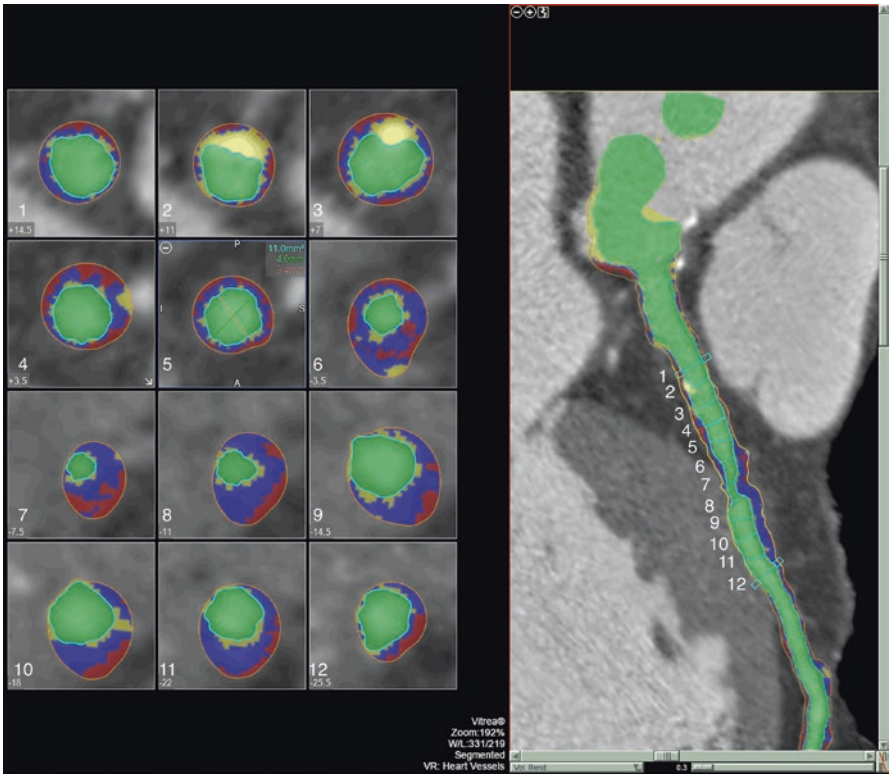

Fig. 12.2 Coronary computed tomography angiography with visualization of the luminography and several transversal sections of the artery. Tomography allows semiautomatic identification of early stages of atherosclerosis, with maintenance of lumen diameter (Section 1). Different components of the plaque are discriminated by color groups, based on the density expressed in Hounsfield units (Sections 2–4). Characteristics such as positive remodeling can be demonstrated in the transversal sections (Sections 10, 11)

CTA demonstrated good discriminatory accuracy between lipid-rich and fibrous-rich plaques. The plaque mean attenuation assessed by CTA was validated with histology on cadaver coronaries. The tissue attenuation measurement discriminated the predominant plaque component and was able to differentiate several stages of coronary atherosclerosis [50]. Structures with lower attenuation values on CTA are predominantly composed by lipids, while higher attenuation values are associated with fibrocalcific composition [51, 52] (Fig. 12.1). Predominantly lipid or mixed plaques are more vulnerable to rupture. Plaque composition analysis by coronary CTA is considered reliable and has good correlation with gold standard methods such as IVUS and OCT [53–56]. However, defining plaques as lipid-rich or fibrous-rich based on semiautomatic attenuation measures has some pitfalls. There is some attenuation overlap among those structures and the contrast enhancement can influence attenuation values affecting the accuracy of these classifications. In order to

overcome these limitations, some authors proposed that the best way to discriminate plaque components would be using quantitative histograms [51, 52].

The CONFIRM study showed that plaques classified as at early stages of coronary atherosclerosis and without significant stenosis should be treated with statins in order to prevent future cardiovascular events. Participants without CAD by CTA had no benefit on using statins [52]. Interpreting CTA focused on the coronary wall allows us to classify patients as individuals with normal coronary arteries, patients with CAD but with nonobstructive plaques and patients with CAD and obstructive plaques. Individuals with obstructive plaques obviously have worse prognosis. However, patients with nonobstructive plaques carry a worse prognosis when compared to individuals whose coronary walls are free of atherosclerosis by CTA [57, 58]. These results highlight the role of subclinical CAD on cardiovascular outcomes, requiring our attention to identifying and adequately treat these individuals. Despite usually being asymptomatic, these individuals are at higher risk compared to others with similar cardiovascular risk profile but without any coronary artery atherosclerotic involvement [57, 58]. These individuals can easily be identified by CTA, unlike via using ischemia testing methods or even angiography.

Identifying coronary plaques, even in subclinical stages, is extremely important for both therapeutic purposes and risk stratification. However, defining plaque characteristics may contain even more valuable information. A major contribution of CTA to risk stratification for ACS is identifying high-risk plaques.

TCFA plaques represent a major plaque complexity feature with high rupture probability and highly associated with ACS. Usually, those plaques have hemorrhage and calcification that can be visualized as bands separating the contrast-enhanced coronary lumen from the necrotic core on CTA [45, 52, 59, 60]. The difference between TCFA and ruptured plaques is based on the cap integrity and thrombus absence in TCFA. Incomplete visualization of the layer or cap discontinuation highly suggests rupture of a TCFA. However, CTA does not have enough spatial resolution to accurately evaluate rupture of a TCFA. This evaluation is restricted to methods with spatial resolution (<65 mic), like OCT [61]. Another plaque vulnerability feature assessed by CTA is the so-called napkin ring signal. This signal corresponds to a rim-like enhance with greater attenuation surrounding a low attenuation area. Napkin ring signal is visualized in mixed or non-calcified plaques and is associated with an increased risk of coronary events [62]. Plaques classified as TCFA by OCT usually present napkin ring signal, positive remodeling, and lower attenuation on CTA [59].

Vulnerable plaques represent an independent risk factor for future cardiac events even in clinically stable patients. Those plaques increase events risk in patients with significant coronary stenosis (>70%) [63] but also when they are identified in patients with mild CAD, with nonobstructive plaques (<50% stenosis) [64]. Several studies demonstrated that high-risk plaque features assessed by CTA (plaque burden, napkin ring signal, low attenuation, positive remodeling) are useful to refine the cardiovascular risk assessment [65–67]. For example, the presence of two or more high-risk plaque features is an independent predictor of all-cause mortality and ACS at a follow-up of 2 years (Hazard ratio 1.98) [68]. Among the high-risk

plaque features, it is not clear which one is the most harmful. Recently, Feuchtner et al. [69] showed that in a follow-up of 8 years, low attenuation plaque and napkin ring signal were the major predictors of MACE, overcoming the degree of stenosis and other traditional risk factors. Additionally, they confirmed previous findings that a negative CTA determines a great prognosis [69].

The role of CTA plaque analysis in cardiovascular risk assessment was studied in patients with acute chest pain evaluated in the emergency department. Plaque high-risk features (positive remodeling, spotty calcium, or napkin ring sign) represented an independent risk factor for the diagnosis of ACS, regardless of the degree of coronary stenosis or traditional cardiovascular risk factors [70].

Although the main use of CTA is focused on atherosclerotic disease, CTA offers great utility in the evaluation of other coronary diseases, especially coronary involvement of systemic inflammatory diseases. Takayasu's arteritis is one of the most frequent and shows some typical features by CTA. The disease presents coronary involvement in approximately 50% of the patients and presents one of the following presentation patterns: type 1, stenosis or occlusion in the ostia or proximal coronary segments; type 2, focal involvement of the coronary arteries with spared areas or diffuse arteritis; and type 3, coronary aneurysm [71, 72].

Other inflammatory diseases such as Kawasaki arteritis and Behçet's disease may also present cardiac involvement, usually manifested as myocardial ischemia secondary to thrombotic aneurysms and occlusions [71]. Immunoglobulin IgG4-related arteritis rarely involves coronary arteries and presents as wall calcifications and intimal thickening [71]. Another vasculitis, the coronary periarteritis, is a rare disease that can manifest itself through inflammatory infiltration leading to intimal fibrosis and coronary aneurysm. CTA images can identify diffuse or focal nodal lesions on the coronary wall or rings with soft attenuation surrounding coronary arteries [73].

Limitations

The main negative aspects of CTA that limit its universal use as the first-line cardiovascular risk stratification tool are the need for iodinated contrast media and exposure to ionizing radiation. The advent of new-generation scanners minimized the radiation exposure to values pretty acceptable (1.5–5 msV) and decreased the need for iodinated contrast volume [41]. Besides that, CTA has some particular challenges to overcome in order to provide a good imaging quality. CTA is subject to movement artifacts secondary to respiration or heart rate variability, especially in patients with arrhythmias or very high cardiac frequencies. Again, new-generation scans virtually overcome these artifacts. Scanners with larger number of detectors increased the cover area and allow a complete volumetric acquisition of the heart in a single heart beat decreasing the time of acquisition and minimizing artifacts [61]. Despite these advances, several facilities recommend heart rate control aiming values lower than 65 beats per minute before scanning. Often it is necessary preparation using oral or injectable negative chronotropic drugs.

Despite technical advances, best spatial resolution scanners commercially available are not able to accurately characterize certain plaque components associated with higher risk such as microcalcifications, intima ulceration, and plaque hemorrhages. Identifying these require images with higher spatial resolution that are available only for invasive methods such as OCT and IVUS. The limited spatial resolution of CTA compared to IVUS and OCT may also result in overestimation of calcified plaque areas and luminal stenosis on this segment. It can also underestimate the area of low attenuation lesions such as soft tissue plaque [61].

Finally, CTA may not be accurate in distinguishing structures with similar densities due to some attenuation overlap. The dual source of energy scanners minimized this limitation, acquiring the images with tube voltages of 80 and 140 kvp, improving the capacity of differentiation between calcified and non-calcified plaques [74, 75].

References

1. Mehta SK, McCrary JR, Frutkin AD, Dolla WJ, Marso SP. Intravascular ultrasound radiofrequency analysis of coronary atherosclerosis: an emerging technology for the assessment of vulnerable plaque. Eur Heart J. 2007;28(11):1283–8.
2. Hassan A, Dohi T, Daida H. Current use of intravascular ultrasound in coronary artery disease. Clin Med Insights Ther. 2016;8:CMT.S18472.
3. Garcia-Garcia HM, Mintz GS, Lerman A, Vince DG, Margolis MP, van Es GA, et al. Tissue characterisation using intravascular radiofrequency data analysis: recommendations for acquisition, analysis, interpretation and reporting. EuroIntervention. 2009;5(2):177–89.
4. Nissen SE, Tuzcu EM, Schoenhagen P, Crowe T, Sasiela WJ, Tsai J, et al. Statin therapy, LDL cholesterol, C-reactive protein, and coronary artery disease. N Engl J Med. 2005;352(1):29–38.
5. Tsujita K, Sugiyama S, Sumida H, Shimomura H, Yamashita T, Yamanaga K, et al. Impact of dual lipid-lowering strategy with ezetimibe and atorvastatin on coronary plaque regression in patients with percutaneous coronary intervention: the multicenter randomized controlled PRECISE-IVUS trial. J Am Coll Cardiol. 2015;66(5):495–507.
6. Stone GW, Maehara A, Lansky AJ, de Bruyne B, Cristea E, Mintz GS, et al. A prospective natural-history study of coronary atherosclerosis. N Engl J Med. 2011;364(3):226–35.
7. Parise H, Maehara A, Stone GW, Leon MB, Mintz GS. Meta-analysis of randomized studies comparing intravascular ultrasound versus angiographic guidance of percutaneous coronary intervention in pre-drug-eluting stent era. Am J Cardiol. 2011;107(3):374–82.
8. Jang JS, Song YJ, Kang W, Jin HY, Seo JS, Yang TH, et al. Intravascular ultrasound-guided implantation of drug-eluting stents to improve outcome: a meta-analysis. JACC Cardiovasc Interv. 2014;7(3):233–43.
9. Windecker S, Kolh P, Alfonso F, Collet JP, Cremer J, Falk V, et al. 2014 ESC/EACTS guidelines on myocardial revascularization: the Task Force on Myocardial Revascularization of the European Society of Cardiology (ESC) and the European Association for Cardio-Thoracic Surgery (EACTS) developed with the special contribution of the European Association of Percutaneous Cardiovascular Interventions (EAPCI). Eur Heart J. 2014;35(37):2541–619.
10. Jia H, Abtahian F, Aguirre AD, Lee S, Chia S, Lowe H, et al. In vivo diagnosis of plaque erosion and calcified nodule in patients with acute coronary syndrome by intravascular optical coherence tomography. J Am Coll Cardiol. 2013;62(19):1748–58.
11. Yonetsu T, Lee T, Murai T, Suzuki M, Matsumura A, Hashimoto Y, et al. Plaque morphologies and the clinical prognosis of acute coronary syndrome caused by lesions with intact fibrous cap diagnosed by optical coherence tomography. Int J Cardiol. 2016;203:766–74.

12. Koskinas KC, Ughi GJ, Windecker S, Tearney GJ, Raber L. Intracoronary imaging of coronary atherosclerosis: validation for diagnosis, prognosis and treatment. Eur Heart J. 2016;37(6):524–35a–c.
13. Tearney GJ, Regar E, Akasaka T, Adriaenssens T, Barlis P, Bezerra HG, et al. Consensus standards for acquisition, measurement, and reporting of intravascular optical coherence tomography studies: a report from the International Working Group for Intravascular Optical Coherence Tomography Standardization and Validation. J Am Coll Cardiol. 2012;59(12):1058–72.
14. Jang IK, Tearney GJ, MacNeill B, Takano M, Moselewski F, Iftima N, et al. In vivo characterization of coronary atherosclerotic plaque by use of optical coherence tomography. Circulation. 2005;111(12):1551–5.
15. Prati F, Di Vito L, Biondi-Zoccai G, Occhipinti M, La Manna A, Tamburino C, et al. Angiography alone versus angiography plus optical coherence tomography to guide decision-making during percutaneous coronary intervention: the Centro per la Lotta contro l'Infarto-Optimisation of Percutaneous Coronary Intervention (CLI-OPCI) study. EuroIntervention. 2012;8(7):823–9.
16. Waksman R, Kitabata H, Prati F, Albertucci M, Mintz GS. Intravascular ultrasound versus optical coherence tomography guidance. J Am Coll Cardiol. 2013;62(17 Suppl):S32–40.
17. Martin AJ, Gotlieb AI, Henkelman RM. High-resolution MR imaging of human arteries. J Magn Reson Imaging. 1995;5(1):93–100.
18. Fayad ZA, Fuster V, Fallon JT, Jayasundera T, Worthley SG, Helft G, et al. Noninvasive in vivo human coronary artery lumen and wall imaging using black-blood magnetic resonance imaging. Circulation. 2000;102(5):506–10.
19. Botnar RM, Stuber M, Kissinger KV, Kim WY, Spuentrup E, Manning WJ. Noninvasive coronary vessel wall and plaque imaging with magnetic resonance imaging. Circulation. 2000;102(21):2582–7.
20. Kim WY, Stuber M, Bornert P, Kissinger KV, Manning WJ, Botnar RM. Three-dimensional black-blood cardiac magnetic resonance coronary vessel wall imaging detects positive arterial remodeling in patients with nonsignificant coronary artery disease. Circulation. 2002;106(3):296–9.
21. He Y, Zhang Z, Dai Q, Zhou Y, Yang Y, Yu W, et al. Accuracy of MRI to identify the coronary artery plaque: a comparative study with intravascular ultrasound. J Magn Reson Imaging. 2012;35(1):72–8.
22. Gerretsen S, Kessels AG, Nelemans PJ, Dijkstra J, Reiber JH, van der Geest RJ, et al. Detection of coronary plaques using MR coronary vessel wall imaging: validation of findings with intravascular ultrasound. Eur Radiol. 2013;23(1):115–24.
23. Moody AR, Murphy RE, Morgan PS, Martel AL, Delay GS, Allder S, et al. Characterization of complicated carotid plaque with magnetic resonance direct thrombus imaging in patients with cerebral ischemia. Circulation. 2003;107(24):3047–52.
24. Takaya N, Yuan C, Chu B, Saam T, Polissar NL, Jarvik GP, et al. Presence of intraplaque hemorrhage stimulates progression of carotid atherosclerotic plaques: a high-resolution magnetic resonance imaging study. Circulation. 2005;111(21):2768–75.
25. Sun J, Underhill HR, Hippe DS, Xue Y, Yuan C, Hatsukami TS. Sustained acceleration in carotid atherosclerotic plaque progression with intraplaque hemorrhage: a long-term time course study. JACC Cardiovasc Imaging. 2012;5(8):798–804.
26. Keegan J. Coronary artery wall imaging. J Magn Reson Imaging. 2015;41(5):1190–202.
27. Kawasaki T, Koga S, Koga N, Noguchi T, Tanaka H, Koga H, et al. Characterization of hyperintense plaque with noncontrast T(1)-weighted cardiac magnetic resonance coronary plaque imaging: comparison with multislice computed tomography and intravascular ultrasound. JACC Cardiovasc Imaging. 2009;2(6):720–8.
28. Matsumoto K, Ehara S, Hasegawa T, Sakaguchi M, Otsuka K, Yoshikawa J, et al. Localization of coronary high-intensity signals on T1-weighted MR imaging: relation to plaque morphology and clinical severity of angina pectoris. JACC Cardiovasc Imaging. 2015;8(10):1143–52.

29. Maintz D, Ozgun M, Hoffmeier A, Fischbach R, Kim WY, Stuber M, et al. Selective coronary artery plaque visualization and differentiation by contrast-enhanced inversion prepared MRI. Eur Heart J. 2006;27(14):1732–6.
30. Jansen CH, Perera D, Makowski MR, Wiethoff AJ, Phinikaridou A, Razavi RM, et al. Detection of intracoronary thrombus by magnetic resonance imaging in patients with acute myocardial infarction. Circulation. 2011;124(4):416–24.
31. Ehara S, Hasegawa T, Nakata S, Matsumoto K, Nishimura S, Iguchi T, et al. Hyperintense plaque identified by magnetic resonance imaging relates to intracoronary thrombus as detected by optical coherence tomography in patients with angina pectoris. Eur Heart J Cardiovasc Imaging. 2012;13(5):394–9.
32. Noguchi T, Kawasaki T, Tanaka A, Yasuda S, Goto Y, Ishihara M, et al. High-intensity signals in coronary plaques on noncontrast T1-weighted magnetic resonance imaging as a novel determinant of coronary events. J Am Coll Cardiol. 2014;63(10):989–99.
33. Kerwin WS, O'Brien KD, Ferguson MS, Polissar N, Hatsukami TS, Yuan C. Inflammation in carotid atherosclerotic plaque: a dynamic contrast-enhanced MR imaging study. Radiology. 2006;241(2):459–68.
34. Yeon SB, Sabir A, Clouse M, Martinezclark PO, Peters DC, Hauser TH, et al. Delayed-enhancement cardiovascular magnetic resonance coronary artery wall imaging: comparison with multislice computed tomography and quantitative coronary angiography. J Am Coll Cardiol. 2007;50(5):441–7.
35. Ibrahim T, Makowski MR, Jankauskas A, Maintz D, Karch M, Schachoff S, et al. Serial contrast-enhanced cardiac magnetic resonance imaging demonstrates regression of hyperenhancement within the coronary artery wall in patients after acute myocardial infarction. JACC Cardiovasc Imaging. 2009;2(5):580–8.
36. Jansen CHP, Perera D, Wiethoff AJ, Phinikaridou A, Razavi RM, Rinaldi A, et al. Contrast-enhanced magnetic resonance imaging for the detection of ruptured coronary plaques in patients with acute myocardial infarction. PLoS One. 2017;12(11):e0188292.
37. Puntmann VO, D'Cruz D, Taylor PC, Hussain T, Indermuhle A, Butzbach B, et al. Contrast enhancement imaging in coronary arteries in SLE. JACC Cardiovasc Imaging. 2012;5(9):962–4.
38. Varma N, Hinojar R, D'Cruz D, Arroyo Ucar E, Indermuehle A, Peel S, et al. Coronary vessel wall contrast enhancement imaging as a potential direct marker of coronary involvement: integration of findings from CAD and SLE patients. JACC Cardiovasc Imaging. 2014;7(8):762–70.
39. Schneeweis C, Schnackenburg B, Stuber M, Berger A, Schneider U, Yu J, et al. Delayed contrast-enhanced MRI of the coronary artery wall in takayasu arteritis. PLoS One. 2012;7(12):e50655.
40. Kuo YS, Kelle S, Lee C, Hinojar R, Nagel E, Botnar R, et al. Contrast-enhanced cardiovascular magnetic resonance imaging of coronary vessel wall: state of art. Expert Rev Cardiovasc Ther. 2014;12(2):255–63.
41. Achenbach S. Coronary CT angiography-future directions. Cardiovasc Diagn Ther. 2017;7(5):432–8.
42. Oberoi S, Meinel FG, Schoepf UJ, Nance JW, De Cecco CN, Gebregziabher M, et al. Reproducibility of noncalcified coronary artery plaque burden quantification from coronary CT angiography across different image analysis platforms. AJR Am J Roentgenol. 2014;202(1):W43–9.
43. Ovrehus KA, Schuhbaeck A, Marwan M, Achenbach S, Norgaard BL, Botker HE, et al. Reproducibility of semi-automatic coronary plaque quantification in coronary CT angiography with sub-mSv radiation dose. J Cardiovasc Comput Tomogr. 2016;10(2):114–20.
44. Hansson GK. Inflammation, atherosclerosis, and coronary artery disease. N Engl J Med. 2005;352(16):1685–95.
45. Henzler T, Porubsky S, Kayed H, Harder N, Krissak UR, Meyer M, et al. Attenuation-based characterization of coronary atherosclerotic plaque: comparison of dual source and dual energy CT with single-source CT and histopathology. Eur J Radiol. 2011;80(1):54–9.
46. Ohayon J, Finet G, Gharib AM, Herzka DA, Tracqui P, Heroux J, et al. Necrotic core thickness and positive arterial remodeling index: emergent biomechanical factors for evaluating the risk of plaque rupture. Am J Physiol Heart Circ Physiol. 2008;295(2):H717–27.

47. Schoenhagen P, Ziada KM, Kapadia SR, Crowe TD, Nissen SE, Tuzcu EM. Extent and direction of arterial remodeling in stable versus unstable coronary syndromes: an intravascular ultrasound study. Circulation. 2000;101(6):598–603.
48. Madder RD, Chinnaiyan KM, Marandici AM, Goldstein JA. Features of disrupted plaques by coronary computed tomographic angiography: correlates with invasively proven complex lesions. Circ Cardiovasc Imaging. 2011;4(2):105–13.
49. Bilolikar AN, Goldstein JA, Madder RD, Chinnaiyan KM. Plaque disruption by coronary computed tomographic angiography in stable patients vs. acute coronary syndrome: a feasibility study. Eur Heart J Cardiovasc Imaging. 2016;17(3):247–59.
50. Becker CR, Nikolaou K, Muders M, Babaryka G, Crispin A, Schoepf UJ, et al. Ex vivo coronary atherosclerotic plaque characterization with multi-detector-row CT. Eur Radiol. 2003;13(9):2094–8.
51. Schlett CL, Maurovich-Horvat P, Ferencik M, Alkadhi H, Stolzmann P, Scheffel H, et al. Histogram analysis of lipid-core plaques in coronary computed tomographic angiography: ex vivo validation against histology. Investig Radiol. 2013;48(9):646–53.
52. Marwan M, Taher MA, El Meniawy K, Awadallah H, Pflederer T, Schuhback A, et al. In vivo CT detection of lipid-rich coronary artery atherosclerotic plaques using quantitative histogram analysis: a head to head comparison with IVUS. Atherosclerosis. 2011;215(1):110–5.
53. Obaid DR, Calvert PA, Brown A, Gopalan D, West NEJ, Rudd JHF, et al. Coronary CT angiography features of ruptured and high-risk atherosclerotic plaques: correlation with intravascular ultrasound. J Cardiovasc Comput Tomogr. 2017;11(6):455–61.
54. Obaid DR, Calvert PA, Gopalan D, Parker RA, Hoole SP, West NE, et al. Atherosclerotic plaque composition and classification identified by coronary computed tomography: assessment of computed tomography-generated plaque maps compared with virtual histology intravascular ultrasound and histology. Circ Cardiovasc Imaging. 2013;6(5):655–64.
55. Wieringa WG, Lexis CP, Lipsic E, van der Werf HW, Burgerhof JG, Hagens VE, et al. In vivo coronary lesion differentiation with computed tomography angiography and intravascular ultrasound as compared to optical coherence tomography. J Cardiovasc Comput Tomogr. 2017;11(2):111–8.
56. Dey D, Schepis T, Marwan M, Slomka PJ, Berman DS, Achenbach S. Automated three-dimensional quantification of noncalcified coronary plaque from coronary CT angiography: comparison with intravascular US. Radiology. 2010;257(2):516–22.
57. Min JK, Shaw LJ, Devereux RB, Okin PM, Weinsaft JW, Russo DJ, et al. Prognostic value of multidetector coronary computed tomographic angiography for prediction of all-cause mortality. J Am Coll Cardiol. 2007;50(12):1161–70.
58. Hadamitzky M, Taubert S, Deseive S, Byrne RA, Martinoff S, Schomig A, et al. Prognostic value of coronary computed tomography angiography during 5 years of follow-up in patients with suspected coronary artery disease. Eur Heart J. 2013;34(42):3277–85.
59. Kashiwagi M, Tanaka A, Kitabata H, Tsujioka H, Kataiwa H, Komukai K, et al. Feasibility of noninvasive assessment of thin-cap fibroatheroma by multidetector computed tomography. JACC Cardiovasc Imaging. 2009;2(12):1412–9.
60. Motoyama S, Sarai M, Harigaya H, Anno H, Inoue K, Hara T, et al. Computed tomographic angiography characteristics of atherosclerotic plaques subsequently resulting in acute coronary syndrome. J Am Coll Cardiol. 2009;54(1):49–57.
61. Saremi F, Achenbach S. Coronary plaque characterization using CT. AJR Am J Roentgenol. 2015;204(3):W249–60.
62. Maurovich-Horvat P, Schlett CL, Alkadhi H, Nakano M, Otsuka F, Stolzmann P, et al. The napkin-ring sign indicates advanced atherosclerotic lesions in coronary CT angiography. JACC Cardiovasc Imaging. 2012;5(12):1243–52.
63. Motoyama S, Ito H, Sarai M, Kondo T, Kawai H, Nagahara Y, et al. Plaque characterization by coronary computed tomography angiography and the likelihood of acute coronary events in mid-term follow-up. J Am Coll Cardiol. 2015;66(4):337–46.
64. Conte E, Annoni A, Pontone G, Mushtaq S, Guglielmo M, Baggiano A, et al. Evaluation of coronary plaque characteristics with coronary computed tomography angiography in patients

with non-obstructive coronary artery disease: a long-term follow-up study. Eur Heart J Cardiovasc Imaging. 2017;18(10):1170–8.
65. Hell MM, Motwani M, Otaki Y, Cadet S, Gransar H, Miranda-Peats R, et al. Quantitative global plaque characteristics from coronary computed tomography angiography for the prediction of future cardiac mortality during long-term follow-up. Eur Heart J Cardiovasc Imaging. 2017;18(12):1331–9.
66. Nadjiri J, Hausleiter J, Jahnichen C, Will A, Hendrich E, Martinoff S, et al. Incremental prognostic value of quantitative plaque assessment in coronary CT angiography during 5 years of follow up. J Cardiovasc Comput Tomogr. 2016;10(2):97–104.
67. Tesche C, Plank F, De Cecco CN, Duguay TM, Albrecht MH, Varga-Szemes A, et al. Prognostic implications of coronary CT angiography-derived quantitative markers for the prediction of major adverse cardiac events. J Cardiovasc Comput Tomogr. 2016;10(6):458–65.
68. Yamamoto H, Kihara Y, Kitagawa T, Ohashi N, Kunita E, Iwanaga Y, et al. Coronary plaque characteristics in computed tomography and 2-year outcomes: the PREDICT study. J Cardiovasc Comput Tomogr. 2018;12(5):436–43.
69. Feuchtner G, Kerber J, Burghard P, Dichtl W, Friedrich G, Bonaros N, et al. The high-risk criteria low-attenuation plaque <60 HU and the napkin-ring sign are the most powerful predictors of MACE: a long-term follow-up study. Eur Heart J Cardiovasc Imaging. 2017;18(7):772–9.
70. Puchner SB, Liu T, Mayrhofer T, Truong QA, Lee H, Fleg JL, et al. High-risk plaque detected on coronary CT angiography predicts acute coronary syndromes independent of significant stenosis in acute chest pain: results from the ROMICAT-II trial. J Am Coll Cardiol. 2014;64(7):684–92.
71. Jeon CH, Kim YK, Chun EJ, Kim JA, Yong HS, Doo KW, et al. Coronary artery vasculitis: assessment with cardiac multi-detector computed tomography. Int J Cardiovasc Imaging. 2015;31(Suppl 1):59–67.
72. Kang EJ, Kim SM, Choe YH, Lee GY, Lee KN, Kim DK. Takayasu arteritis: assessment of coronary arterial abnormalities with 128-section dual-source CT angiography of the coronary arteries and aorta. Radiology. 2014;270(1):74–81.
73. Zhou Z, Xu L, Zhang N, Wang H, Liu W, Sun Z, et al. CT coronary angiography findings in non-atherosclerotic coronary artery diseases. Clin Radiol. 2018;73(2):205–13.
74. Tanami Y, Ikeda E, Jinzaki M, Satoh K, Nishiwaki Y, Yamada M, et al. Computed tomographic attenuation value of coronary atherosclerotic plaques with different tube voltage: an ex vivo study. J Comput Assist Tomogr. 2010;34(1):58–63.
75. Barreto M, Schoenhagen P, Nair A, Amatangelo S, Milite M, Obuchowski NA, et al. Potential of dual-energy computed tomography to characterize atherosclerotic plaque: ex vivo assessment of human coronary arteries in comparison to histology. J Cardiovasc Comput Tomogr. 2008;2(4):234–42.

Chapter 13
Advanced Coronary Artery Vessel Wall Imaging and Future Directions

Yibin Xie, Damini Dey, and Debiao Li

Coronary artery disease (CAD) remains a menacing health threat in the industrialized countries despite recent decline in mortality. The majority of myocardial infarctions or sudden coronary deaths are caused by coronary plaque disruption and subsequent thrombotic occlusion, a process occurs suddenly after years of indolent atherosclerosis progression. Angiographic techniques that focus primarily on lumen narrowing have proven inadequate in accurately assessing lesion-specific risk as the majority of culprit plaques do not manifest significant stenosis. The composition and surface conditions of atherosclerotic plaques vary during different disease stages. Several types of lesion morphology, such as thin-cap fibroatheroma, are associated with weakened structure and predisposition for rupture. Plaques that are prone to rupture are referred to as "vulnerable" or "high risk." Imaging techniques that are capable of directly detecting high-risk plaque features are highly desirable as they could potentially improve lesion-specific risk stratification and help guide therapeutic decision-making.

To address the unmet clinical needs for more precise lesion characterization, coronary vessel wall imaging is an active research area that is currently undergoing

Y. Xie (✉)
Biomedical Imaging Research Institute, Cedars-Sinai Medical Center, Los Angeles, CA, USA
e-mail: Yibin.Xie@cshs.org

D. Dey
Biomedical Imaging Research Institute, Cedars-Sinai Medical Center, Los Angeles, CA, USA

Department of Medicine, University of California, Los Angeles, Los Angeles, CA, USA
e-mail: Damini.Dey@cshs.org

D. Li
Biomedical Imaging Research Institute, Cedars-Sinai Medical Center, Los Angeles, CA, USA

Department of Medicine, University of California, Los Angeles, Los Angeles, CA, USA

Department of Bioengineering, University of California, Los Angeles, Los Angeles, CA, USA
e-mail: Debiao.Li@cshs.org

C. Yuan et al. (eds.), *Vessel Based Imaging Techniques*,
https://doi.org/10.1007/978-3-030-25249-6_13

continuous development. Existing techniques are being improved to achieve better spatial resolution and diagnostic accuracy. Imaging time and complexity are being reduced and robustness being improved. New biomarkers and contrast mechanisms are being explored and validated. In this chapter we will briefly review the recent advances in noninvasive coronary vessel wall imaging techniques and discuss the trend toward comprehensive imaging solutions that consist of high-risk morphology, plaque burden, and pathophysiological activities. Additional discussions on coronary vessel wall imaging may also be found in the recent review articles on this topic [1–5].

New Advances in Coronary Vessel Wall MRI

Positive Remodeling and Plaque Burden The majority of atherosclerotic plaques develop in the arteries by growing outward, in a process termed "positive remodeling," without compromising the arterial lumen. The disease status in such cases is typically underdiagnosed as conventional angiographic images can only delineate vascular lumen. Coronary vessel wall MRI has been successfully applied to evaluate plaque burden in several clinical studies [6, 8, 9]. The most commonly used pulse sequence for evaluating plaque burden in patients is 2D black-blood imaging based on double inversion recovery (DIR) [8–11]. The blood nulling effect of DIR is typically sufficient for vessel wall imaging. However, a considerable number of exams were unsuccessful due to technical failures [6, 9, 12]. One of the major challenges of this technique is to coincide the optimal inversion time and the optimal data acquisition window during which cardiac motion is at the minimum. To relax such timing constraint, Abd-Elmoniem et al. designed a time-resolved acquisition scheme with spiral imaging and utilized phase-sensitive reconstruction to enhance the vessel wall contrast [13]. This technique (TRAPD) was successfully applied to 26 patients with increased risk of CAD and demonstrated improved success rate of 95% compared with 75% of the conventional DIR technique [14]. Recently, Ginami et al. further extended this approach by incorporating radial imaging with golden angle and k-t SENSE reconstruction to allow a flexible retrospective selection of the number of frames, frame duration, and position within the cardiac cycle. Due to the nature of 2D cross-sectional slices, conventional technique provides limited anatomical coverage and is prone to measurement bias caused by oblique slice placement. Andia et al. designed a subtraction-based method which interleaves T2 preparation pulses to address the limitations of 2D imaging [15]. As the image contrast is generated completely based on the T2 relaxation differences between blood and vessel wall, the resultant coronary vessel wall images are flow-independent. This technique demonstrated promising results of 3D whole-heart vessel wall images (Fig. 13.1). However, subtraction error between the two image sets and incomplete fat suppression may still occur. The same group later introduced nonrigid respiratory motion correction into the subtraction vessel wall imaging technique to reduce the scan time [16]. Alternatively, Xie et al. proposed a 3D

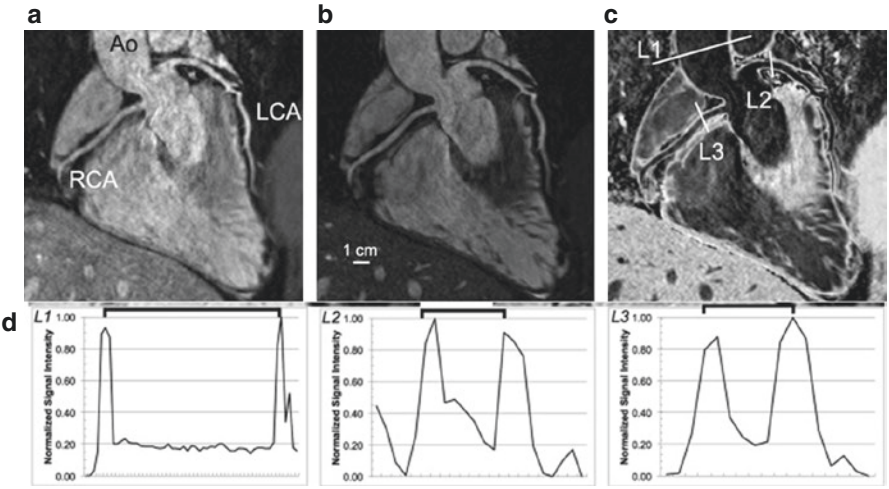

Fig. 13.1 Reformatted images of a whole-heart vessel wall imaging using the i-T2prep acquisition. (**a**, **b**) The T2prep(−) and T2prep(+) acquisitions. (**c**) The aortic, LCA, and RCA vessel wall in weighted subtracted images. (**d**) The normalized pixel intensity of a profile across the vessel at the level of ascending aorta, LCA, and RCA. Ao ascending aorta, LCA left coronary artery, and RCA right coronary artery. (Reproduced from Andia et al. with permission [15])

black-blood coronary vessel wall imaging method based on DIR with local in-plane reinversion combined with interleaved gray-blood images [17]. This technique (cDIG) showed excellent vessel wall morphology along with gray-blood images which may also be useful for identifying calcified nodules thus improving plaque delineation.

Intra-plaque Hemorrhage and T1 Hyperintensity Intra-plaque hemorrhage (IPH) is a known high-risk plaque feature that is associated with plaque progression and a predictor for future major adverse cardiovascular events [18, 19]. Existing data from autopsy studies and animal experiments suggest that IPH plays an important role in leukocyte infiltration and the enlargement of lipid core [18, 20]. Methemoglobin is the intermediate product in the process of hemoglobin breakdown which is present in the acute to subacute phases of IPH. It is a strong paramagnetic substance that markedly shortens T1; therefore, it can be visualized as regions of hyperintensity on T1-weighted black-blood techniques [21]. This technique has been well developed and validated to detect IPH in larger arteries such the carotid arteries [22]. Kawasaki et al. performed a comprehensive study comparing high-intensity plaques (HIPs) on T1-weighted black-blood images with plaque morphology on CT and intravascular ultrasound [23]. Increased frequency of adverse plaque characteristics was observed in HIPs, including higher positive remodeling, ultrasound attenuation, and spotty calcium. In another study comparing HIPs on MRI with CT plaque findings, Oei et al. observed significantly lower CT density in HIPs, suggesting a probable association between HIPs and IPH [24]. Notably, there was no correlation of plaque signal intensity with the degree of stenosis. The prognostic

value of T1-weighted coronary MRI has been investigated by Noguchi et al. in a longitudinal study that followed 568 patients with suspected or known CAD for a median of 55 months [25]. Using plaque to myocardium signal ratio (PMR), the researchers found that patients with HIPs (PMR >1.4) experienced significantly higher rate of coronary events. The calculation of PMR is a simplified way to normalize plaque signal intensity and reduce the impact from coil sensitivity variations. The presence of HIP was determined as an independent predictor with a hazard ratio of 3.56. The same group recently applied the technique to 48 patients before and after 12 months of intensive statin therapy and observed significant decrease in PMR from 1.38 to 1.11, indicating a potential role of the technique for quantitative assessment of therapeutic effects [26].

The most widely used T1-weighted black-blood protocol for assessing coronary IPH is based on inversion recovery 3D gradient-echo sequence with fat suppression [21]. Cartesian 3D acquisition with a transverse slab is commonly configured to cover the proximal, mid, and some distal segments of all major coronary artery branches. Cardiac and respiratory gating are typically required to reduce motion artifacts. Compounded by the relative high resolution needed for imaging coronary arteries, this protocol often results in unpredictable and prolonged scan time depending on the respiratory pattern. A considerable number of patients have to be excluded due to poor image quality in a recent clinical study [25]. Moreover, T1-weighted contrast heavily attenuates the signal of background tissue, such as myocardium, which makes it difficult to identify the location of plaque signal. Therefore, an additional bright-blood angiographic scan is required for providing anatomical reference, which further prolongs the study. Xie et al. proposed a new approach for coronary T1-weighted imaging which interleaved black-blood and bright-blood acquisition, providing exactly co-registered T1-weighted images and anatomical reference [27] (Fig. 13.2). This technique (CATCH) was developed based on radial sampling and retrospective motion compensation which accepted data from all breathing phases, allowing two- to threefold acceleration compared with conventional respiratory gated approaches. Whole-heart evaluation with fine isotropic resolution can be achieved with a scan of approximately 10 minutes. Ginami et al. incorporated T2-prepration and phase-sensitive inversion recovery (PSIR) reconstruction to a similar interleaving scheme, which improved the image contrast of the reference bright-blood images. Even though the scan time remained relatively long (18 minutes), the resultant bright-blood images are equivalent to a conventional non-contrast MR angiography and can be potentially used for evaluating lumen status.

Although there is strong clinical evidence supporting the prognostic value of T1-weighted coronary imaging, the pathophysiological nature of plaque hyperintensity remains an active topic for research. Early study by Jansen et al. demonstrated in a small group of patients with acute coronary syndrome ($N = 18$) that coronary hyperintensity could result from intracoronary thrombus, which contains T1-shortening methemoglobin similar to IPH [28]. Ehara et al. also demonstrated the association between T1 hyperintensity and thrombus using intracoronary OCT as the reference [29]. Matsumoto et al. further investigated the relationship between

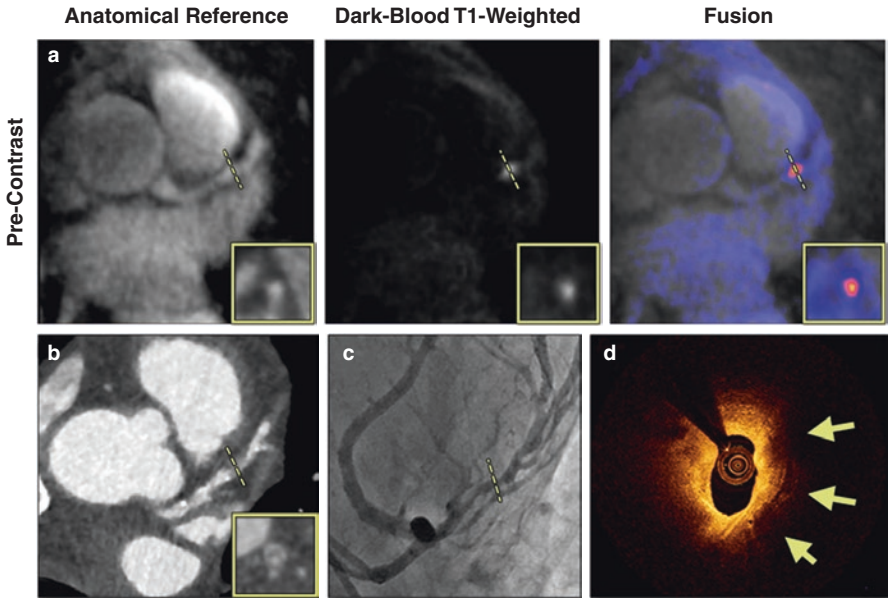

Fig. 13.2 A case of suspected CAD patient with a HIP on non-contrast CATCH images. (**a**) Non-contrast T1-weighted, anatomical reference and fusion images. (**b**) Computed tomography angiography. (**c**) X-ray angiography. (**d**) Optical coherence tomography cross-sectional image at the corresponding location of the coronary hyperintensive plaque. Arrows point to signal-poor regions, suggesting a large lipid pool. Dotted lines represent the location and orientation of the cross-sectional images at the lesion which are shown in boxes. LAD left anterior descending. (Reproduced from Xie et al. with permission [27])

the localization of T1 hyperintensity, such as intrawall or intralumenal, and the type of plaque morphology on OCT. Intrawall HIPs were associated with macrophage accumulation and absence of calcification, whereas intralumenal HIPs were associated with thrombus and intimal vasculature [30]. Xie et al. demonstrated that PMR is positively associated with the amount of high-risk plaque features including lipid core, macrophages, and cholesterol crystals as observed on OCT [27]. This result was later independently supported by a larger study of 106 patients with angina pectoris from which the investigators observed a stepwise increase in PMR of the culprit lesions in proportion to the accumulation of the number of adverse plaque characteristics [31]. In vivo validation of T1-weighted imaging for detecting coronary IPH is difficult due to the lack of gold standard for IPH. A recent study applied T1-weighted imaging to ex vivo coronary and carotid plaque specimens collected during endarterectomy surgery. Compared with histological analysis, T1-weighted imaging demonstrated sensitivity and specificity of 95.0% and 92.1%, respectively, for detecting IPH [32].

Contrast Enhancement of Vessel Wall Gadolinium-based contrast-enhanced MRI (CE-MRI) is routinely used to boost the blood signal and improve the visibility of lumen for MR angiography. Alternatively, recent studies also demonstrated

its capability to evaluate tissue properties of vessel wall and plaques, such as inflammation, neovascularization, and fibrosis. Compared with angiographic applications for which imaging is usually performed during arterial phase, vessel wall imaging typically requires sufficient delay after injection, e.g., 1 hour, to allow renal filtration and the washout of contrast media from healthy tissue. In one of the earliest attempts of CE-MRI for coronary vessel wall imaging, Maintz et al. studied nine patients with coronary artery disease confirmed by X-ray angiography. Using multidetector CT angiography as the reference, the investigators found that the majority of coronary plaques enhanced on CE-MRI (11 out of 13) were mixed plaques with partial calcification [21]. Further investigation using CT angiography and invasive coronary angiography as reference showed that coronary vessel enhancement is more prevalent in lesions that were calcified and with higher degree of lumen stenosis [33].

Contrast uptake in vessel wall is generally considered as the result of increased blood supply to the vascular bed as well as increased permeability of endothelium, both of which are associated with active inflammation. On the other hand, the "delayed enhancement" appearance is attributed to increased extracellular space with reduced washout kinetics, which are associated with fibrosis commonly found in recurrent or chronic inflammation [34]. Varma et al. investigated the feasibility of visual and quantitative assessment of vessel wall CE-MRI of atherosclerotic plaques in CAD and subclinical coronary vasculitis in systematic lupus erythematosus (SLE). The study showed that coronary vessel wall enhancement was prevalent in both diseases compared with controls that showed little signs of vessel wall uptake. Notably, the enhancement pattern appeared different for the two groups, with CAD patients showing patchy enhancement concentrated to the areas of minimal lumen diameter whereas SLE patients showing more diffused enhancement. Extensive coronary vessel wall enhancement was also observed in patients with Takayasu arteritis which is a type of chronic inflammatory disease of the aorta and its branches [35].

Vascular uptake of conventional gadolinium-based contrast media is nonspecific which does not indicate a specific disease characteristic. New contrast agents are being developed to bind to specific molecular targets relevant to vessel wall pathophysiology which could open new doors for better understanding molecular events in plaque formation and progression. One of the early examples is fibrin-binding gadolinium agent designed to detect coronary thrombosis [36]. Recently, new gadolinium-based molecular agent has been developed to target elastin, which is overly expressed during plaque development. This type of contrast media has shown improved visualization of plaque burden and coronary vessel wall remodeling after injury compared with conventional gadolinium agents [37, 38]. Notably, a newly developed contrast agent that selectively binds to serum albumin has been approved for use in human (gadofosveset trisodium, product name: Ablavar) [39]. Originally designed as blood pool agent for angiography, its use has been extended to probing endothelial permeability and neovascularization [40]. Preliminary data from 25 patients diagnosed with acute coronary syndromes showed that CE-MRI based on this agent was able to identify culprit coronary lesions in 9 of 11 segments and

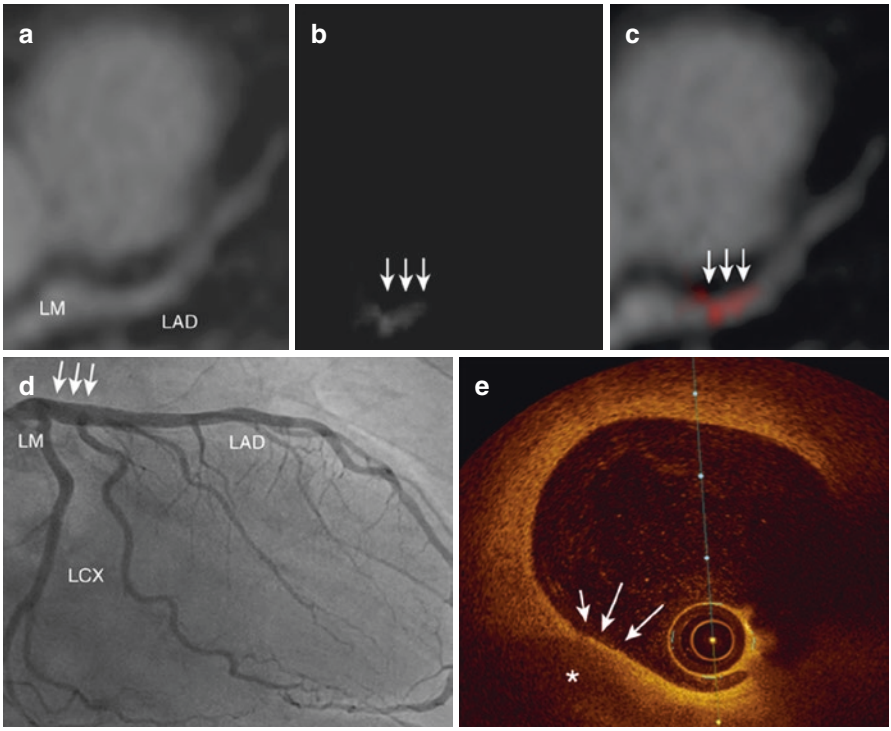

Fig. 13.3 A case of gadofosveset-enhanced MRI of a 63-year-old patient with chest pain. (**a**) MR angiography shows the course of the LM and LAD. (**b**) Gadofosveset-enhanced MRI demonstrates contrast enhancement in the left main artery (white arrows). (**c**) Fusion of MR angiography and vessel wall imaging sequence. (**d**) X-ray coronary angiography shows no signs of significant luminal narrowing in the entire coronary artery tree. (**e**) OCT reveals a thin-cap fibroatheroma (white arrows) with a large lipid core (asterisk) in the proximal LAD, correlating with the location of increased signal enhancement on gadofosveset-enhanced MRI. LM left main, LAD left anterior descending. (Reproduced from Engel et al. with permission [41])

exclude culprit coronary lesions in 162 of 195 segments, corresponding to sensitivity and specificity of 82% and 83%, respectively (Fig. 13.3) [41].

Vasomotion and Endothelial Functions Vasomotion is an important physiological function of the arteries that is often impaired by atherosclerosis. Stress imaging of coronary artery vasomotion is performed commonly in the catheterization laboratory. MRI-based vasomotor evaluation is an emerging alternative that can be performed noninvasively. The pioneering work by Pepe et al. successfully demonstrated the use of 2D spoiled gradient-echo sequence for imaging the cross-sectional view of coronary arteries before and after pharmacological vasodilation induced by sublingual nitroglycerin [42]. Terashima et al. showed the feasibility of a similar protocol in 12 patients who also underwent X-ray angiography, with the MRI measurements showing low interobserver variability (<5%) and good correlation with X-ray angiography ($r = 0.98$) [43]. Hays et al. replaced the pharmacological stressor

with the use of isometric handgrip, which allowed the evaluation of endothelial-dependent vasomotor response [44]. The study on 20 healthy subjects and 17 patients with CAD demonstrated that coronary artery area increased in healthy adults with stress but decreased in CAD patients. MRI has also been used to quantify coronary vessel wall distensibility, which is defined as the ratio of lumen diameter or area between diastole and systole [45]. This technique was applied to a group of heart transplant recipients and showed that coronary distensibility was correlated with wall thickness [46].

In summary, recent developments in MRI-based coronary vessel wall imaging have demonstrated its feasibility for evaluating various important disease characteristics including morphology, tissue properties, and functions. The existing protocols typically requires ECG gating and/or respiratory navigator. Due to the limitations in motion sensitivity, spatial resolution, coverage, and imaging time, data quality is often not sufficient in a considerable proportion of patients. Recent developments in motion compensation and fast imaging techniques showed promises to improve upon or eliminate these shortcomings, but additional clinical experience and data are needed to sufficiently validate the claims. Further technical improvements are still required to allow applications in patients with more challenging imaging conditions such as arrhythmia or the presence of stents or metal implants. Last but not least, it is important to improve the portability and availability of the new techniques and standardize study protocols in order to facilitate the clinical translation.

New Advances in Coronary Vessel Wall CTA

Technological Advances in CT In recent years, there have been significant advances in CT hardware and software, which have expanded the clinical utility of CT for cardiovascular imaging. Imaging of the coronary arteries is challenging due to their small dimensions, tortuosity, and continuous motion. Cardiovascular CT needs full synchronization with the electrocardiogram (ECG) signal and high temporal resolution to "freeze" cardiac motion. A general technical improvement for CT scanners is that gantry rotation times have been decreased by the manufacturers to address the requirement of high temporal resolution for clinical cardiac CT. Concurrently, there has been an effort to increase the spatial resolution, as well as the z-coverage to facilitate faster scanning of the heart. For low (<60 beats/min) and regular heart rates, single-heartbeat scans can be performed. Major advances in current CT hardware have been highlighted in a recent review article [47].

Coronary Calcium Scoring Coronary calcium scoring with non-contrast CT is used worldwide for cardiovascular risk stratification and provides a measure of global coronary atherosclerotic burden. It is a simple and low-cost test, without the use of premedication or contrast, and with a uniformly low attendant radiation burden [48–50]. To date, several follow-up studies have reported that the total coronary artery calcium measured by non-contrast CT predicts cardiovascular events [51–65], beyond standard cardiovascular risk indices.

Coronary CT Angiography (CTA) Coronary CT angiography (CTA) has recently emerged as a noninvasive diagnostic test in selected stable but symptomatic patients with suspected CAD [66–71]. Current clinical interpretation of CTA relies on visual assessment of stenosis grade, plaque type, and presence of high-risk plaque features [72, 73]. Invasive coronary angiography is the gold standard for the diagnosis of obstructive stenosis. CTA has, to date, shown high accuracy and sensitivity for detecting coronary artery stenoses when compared to invasive coronary angiography [67–71]. In particular, CTA has shown very high negative predictive value for obstructive stenoses (range 89–99% in multicenter studies) in patients with symptoms that suggest the presence of coronary artery disease [67–71].

In the last decade, numerous large-scale randomized, controlled trials have established the efficacy of CTA as a diagnostic test in clinical care. In the prospective, randomized PROMISE trial with 10,003 patients, performance of CTA was equivalent to stress testing when used as an initial test for suspected CAD, with similar event rates between stress testing and the CTA group at 2-year follow-up (3.3% vs. 3.0%) [74]. In the prospective, randomized SCOT-HEART trial, 4146 patients with suspected CAD were randomly assigned to standard care alone (typically, stress testing) or standard care plus CTA [75]; in this trial, CTA was shown to clarify the diagnosis, enable appropriate treatment, and significantly improve patient outcomes [76].

Plaque Imaging Current clinical interpretation of CTA relies on subjective visual assessment of stenosis grade or the detection of obstructive disease (≥50% stenosis). Beyond stenosis, CTA also permits noninvasive assessment of *atherosclerotic plaque* (including plaque burden and composition) and outward coronary artery remodeling [77–81]. Studies have shown that coronary plaque volume and remodeling quantified from CTA correlate strongly with invasive intravascular ultrasound (IVUS) [79, 82–86]. In a blinded comparison between CTA and IVUS by Dey et al., NCP volumes measured using standardized semiautomated software showed excellent per-plaque correlation ($r = 0.94$), with no significant differences compared to IVUS measurements [84].

Coronary CTA Plaque Features for Prediction of Adverse Cardiovascular Outcomes Features of plaque vulnerability measured by CT have been reported to include low-attenuation or low-density plaque (*LAP*)—with attenuation values ≤30 Hounsfield units (HU)—corresponding to the necrotic core and positive or outward remodeling [81, 87–90]. The napkin-ring sign has also been shown to be a CT signature of high-risk coronary atherosclerotic plaque [89, 91, 92].

Kristensen et al. measured CT plaque volumes with a semiautomated method in a study of 312 patients who presented with non-ST-segment elevation myocardial infarction at baseline. They showed that major adverse cardiac events (MACE) were associated with a higher amount of noncalcified plaque (NCP) in nonobstructive coronary lesions [93]. Semiautomated plaque measurements have been shown to improve prediction of future acute coronary syndrome (ACS) over conventional CTA assessment [receiver operator characteristic area under curve (AUC) 0.79 vs. 0.64, $p < 0.05$] [94].

A study by Motoyama et al. investigated whether *visually assessed plaque characteristics by CTA* can predict midterm likelihood of future ACS over mean 3.9 years

of follow-up [95]. The presence of LAP, positive remodeling, and severe stenosis by CTA (≥70%)—defined as high-risk plaque features—were visually assessed in 3158 patients undergoing CTA. ACS occurred in 88 patients and was significantly more frequent in patients with severe stenosis; CTA-verified high-risk plaque was an independent predictor of ACS. However, the cumulative number of patients suffering ACS was similar for patients with and without visually identified high-risk plaques [95]; this was primarily attributed to the diffuse nature of atherosclerosis.

In studies with comprehensive *quantitative plaque analysis*, low-density NCP burden has been shown to improve prediction of future adverse cardiac events, *even in diffuse atherosclerosis* [94, 96]. Figure 13.4 shows an example of standardized

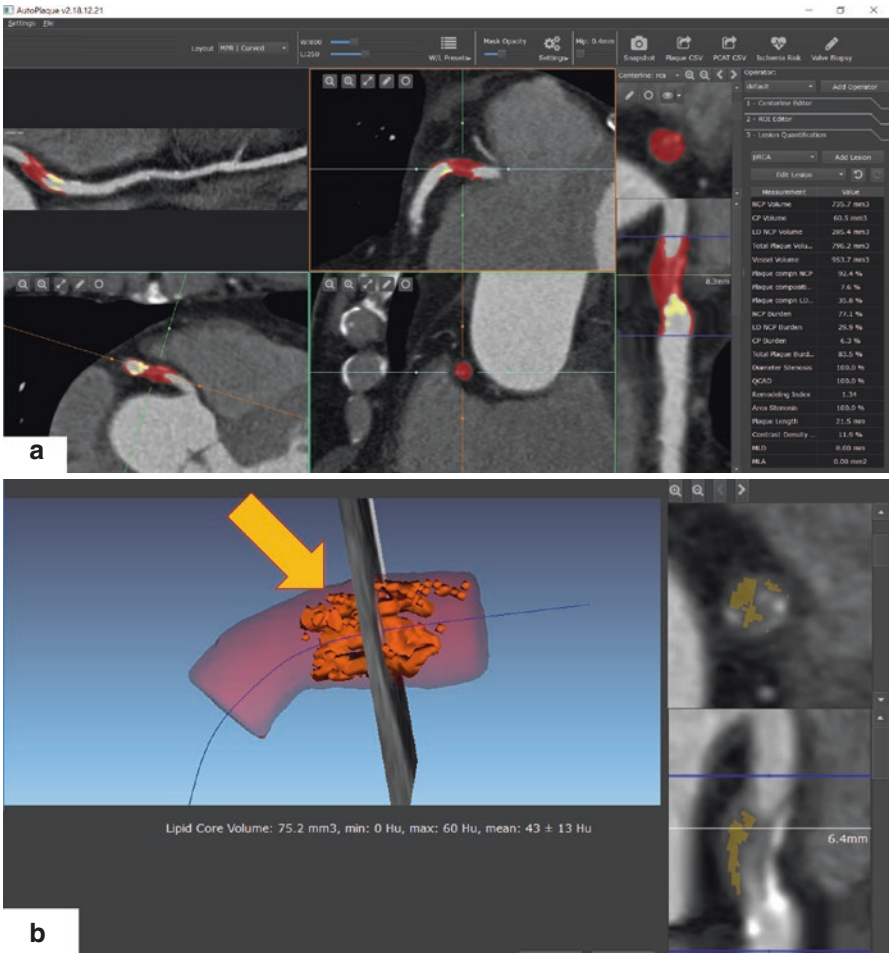

Fig. 13.4 Example of semiautomated quantification of high-risk coronary plaque with large NCP burden, lipid core, and coronary artery remodeling, in a 66-year-old male patient undergoing CTA. (**a**) Standardized quantification of plaque and stenosis, red overlay shows noncalcified plaque, and yellow overlay shows calcified plaque. (**b**) Detailed view showing lipid core or low-density noncalcified plaque. Arrow shows 3D view of lipid core, shown in yellow overlay in cross-sectional view

semiautomated quantification of high-risk coronary plaque, with large NCP, lipid core, and coronary artery remodeling, in a 66-year-old male patient. Using such standardized semiautomated approach, Hell et al. have investigated whether quantitative global per-patient plaque characteristics from coronary CTA can predict subsequent cardiac death, during 5-year midterm follow-up. In this study, low-density noncalcified plaque, noncalcified plaque (NCP), and total plaque volumes as well as contrast density difference (a measure of luminal contrast kinetics) were the strongest independent predictors of future cardiac death, even when adjusted for segment involvement score [96]. In another recent matched case-control cohort of patients with ACS, quantitative plaque evaluation including lowest-density plaque composition identified high-risk patients above and beyond stenosis severity and total plaque burden [97].

Plaque Progression for Prediction of Adverse Cardiovascular Outcomes Intravascular imaging studies have demonstrated that the lesions likely to result in MACE have modest luminal stenosis and large plaque burden but evolve voluminously to result in significant stenosis at the time of ACS [7, 98, 99]. The prognostic importance of plaque progression has also been highlighted in the CTA study by Motoyama et al. [95]. Serial CTA was performed in 449 patients, and plaque progression was visually assessed as any increase in stenosis grade [95]; plaque progression detected by serial CTA was found to be an independent predictor of ACS.

New data using standardized quantitative software show that a per-patient low-density lipoprotein (LDL) cholesterol decrease of 10% or greater is related to beneficial changes in the amount and composition of noncalcified plaque by serial CTA performed 1 year or more apart [100]. Recently, it has also been shown in a multicenter registry that statin therapy causes slower progression of total plaque volume, along with increased calcification and reduction of high-risk plaque features by CTA [101].

Plaque and Lesion-Specific Ischemia It is known that stenosis does not equate ischemia, and significant stenosis in CTA often does not indicate hemodynamic significance. Low-density NCP—which has been shown to be of prognostic importance—has also been shown to be an imaging biomarker which predicts lesion-specific ischemia by invasive FFR [102, 103]. In the multicenter NXT trial, low-density NCP provided independent and incremental discrimination of ischemia beyond stenosis severity [102].

Plaque and Machine Learning The feasibility and accuracy of machine learning to predict all-cause mortality at 5-year follow-up were evaluated in the CONFIRM registry (10,030 patients). All available clinical and visually assessed CTA measures were objectively evaluated. Machine learning risk score combining clinical and CTA data exhibited a significantly higher AUC (0.79) for the prediction of death, compared to established risk indices and visual CTA assessment of stenosis and plaque [104]. Machine learning has also been applied to predict lesion-specific ischemia. In the NXT trial (254 patients), machine learning combination of clinical data and quantitative stenosis and plaque features exhibited higher AUC compared to pretest likelihood of coronary artery disease or quantitative CTA metrics for

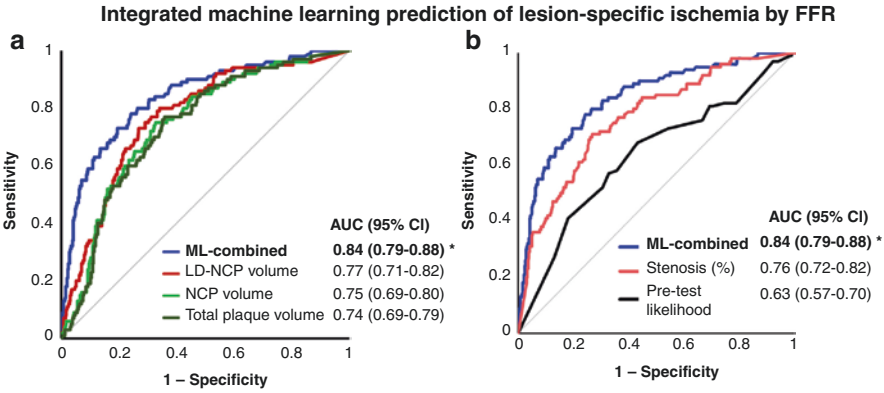

Fig. 13.5 Prediction of lesion-specific ischemia by the integrated ischemia risk score by machine learning (ML-combined) and plaque metrics. (**a**) ML-combined vs. quantitative plaque volumes (LD-NCP, NCP, and total plaque volume). (**b**) ML-combined vs. quantitative stenosis and pretest likelihood of coronary artery disease. ML-combined had a significantly higher AUC compared to individual quantitative CTA plaque measures or the pretest likelihood. (Reproduced from Dey et al. with permission [105])

predicting ischemia (ML 0.84 vs. best clinical score 0.63, CTA stenosis 0.76, low-density noncalcified plaque volume 0.77, $p < 0.006$) [105] (Fig. 13.5). Contrast density difference had the highest information gain to identify lesion-specific ischemia [105].

Pericoronary Adipose Tissue Recent coronary CTA studies indicate that there is a direct interaction between pericoronary adipose tissue (PCAT) and coronary vasculature [106–112]. While it is known that pericoronary and epicardial fat are metabolically active and function as a source of several adipokines (cell signaling proteins emitted by adipose tissue), recent studies suggest that inflammatory signaling is bi-directional and may also occur from atheroma in the vessel wall to perivascular adipocytes (fat cells) [113]. In particular, PCAT density measured from CTA was shown to detect vascular inflammation by histology in patients undergoing cardiac surgery. This histological validation has supported the finding that vascular inflammation inhibits adipocyte maturation and lipid accumulation in PCAT, resulting in a reduced size of adipocytes and increasing PCAT density as measured from CTA [113]. In lower risk patients, PCAT density measured from CTA also predicted cardiac death in a dual-center cohort of stable patients [114]. Goeller et al. have shown that PCAT density measured from CTA differentiates culprit plaques in patients with their first ACS and is a potential marker of high-risk plaque [115].

In summary, coronary CTA allows plaque characterization over the coronary tree. Several studies have now shown that quantitative CTA measures (such as low-density NNCP, NCP, positive remodeling, and contrast density difference) improve prediction of both lesion-specific ischemia and adverse cardiovascular events. The evidence to date indicates that quantitative PCAT and CTA plaque biomarkers may be a valuable tool to identify high-risk plaque, initiate, and guide future prevention strategies.

New Advances in Coronary Vessel Wall PET

Coronary Vascular Inflammation 18F-Fluorodeoxyglucose (18F-FDG) PET has been used to detect active inflammation in large arterial beds such as aorta and carotid arteries, showing strong correlation with the presence of macrophages [116–118]. 18F-FDG uptake in the coronary vessel wall was first shown by Alexanderson et al. who reported a case with a soft plaque on the left main [119]. A prospective study by Rogers et al. demonstrated the feasibility of 18F-FDG localization in inflamed coronary vessel wall [120]. In patients who received coronary stents, culprit lesions showed markedly higher 18F-FDG uptake compared with stable lesions. One of the major challenges of applying 18F-FDG PET in the coronary arteries is the high uptake by the myocardium, which uses glucose (18F-FDG analog) as the primary energy source. Any uptake in the coronary arteries 18F-FDG is often obscured by signal from left ventricle. Williams et al. designed a dietary preparation consisting of a low-carbohydrate, high-fat meal and a vegetable oil drink, which proved a feasible way to reduce myocardial 18F-FDG uptake [121]. Alternatively, new PET tracers specifically designed for targeting inflammation are under development, such as 68Ga-DOTATATE and 18F-fluorodeoxymannose [122, 123].

Coronary Microcalcification 18F-Sodium fluoride has been proposed as an alternative tracer to 18F-FDG for imaging coronary vessel wall due to its low uptake in myocardium and preferential binding to vascular regions of microcalcification [124]. 18F-Sodium fluoride uptake was associated with multiple adverse features on IVUS and CT angiography, including lipid core and positive remodeling [125]. In a prospective clinical trial of 40 patients with myocardial infarction or stable angina, Joshi et al. showed that 18F-sodium fluoride was capable of accurately localizing the culprit lesions in over 90% of the patients (Fig. 13.6) [126]. A prospective multicenter trial (the PREFFIR study) is ongoing to further investigate the

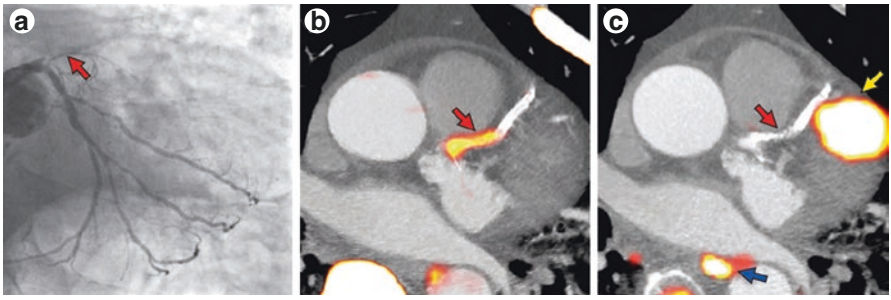

Fig. 13.6 Focal 18F-fluoride and 18F-fluorodeoxyglucose uptake in patients with myocardial infarction. (**a**) Patient with acute ST-segment elevation myocardial infarction with proximal occlusion (red arrow) of the left anterior descending artery on invasive coronary angiography. (**b**) Intense focal 18F-fluoride (18F-NaF, tissue-to-background ratios, culprit 2.27 versus reference segment 1.09 [108% increase]) uptake (yellow-red) at the site of the culprit plaque (red arrow) on the combined PET/CT. (**c**) Corresponding 18F-FDG PET/CT image showing no uptake at the site of the culprit plaque (18F-FDG, tissue-to-background ratios, 1.63 versus reference segment 1.91 [15% decrease]). (Reproduced from Joshi et al. with permission [126])

prognostic value of 18F-fluoride for improving risk stratification following myocardial infarction.

Advanced Motion Compensation and PET/MR Another major limitation of coronary vessel wall imaging with PET is the complex combination of cardiac and respiratory motion. Compounded by the relatively low spatial resolution of PET, previous protocols are not capable of precisely localizing focal uptake within the coronary circulation. Gated acquisition and retrospective motion correction were proposed which showed reduced image noise and increased target-to-background ratios [127]. Recently, the advent of hybrid PET/MR scanners not only reduces the radiation doses associated with the conventional PET/CT systems but also opens new possibilities of improving the motion compensation for PET [128–130]. However, additional technical developments are required in achieving an accurate and reliable MR attenuation correction (MRAC) to realize the full potential of such new platform [131].

In summary, the feasibility of coronary vessel wall imaging with PET has been demonstrated. Important disease activities such as inflammation and active calcification are accessible with the existing approaches. Current clinical evidence supports PET's strong value in lesion risk stratification. Recent advances in motion compensation and hybrid PET/MR systems are addressing the two most significant drawbacks of imprecise localization and high radiation dose.

References

1. Xie Y, Pang J, Yang Q, Li D. Magnetic resonance imaging of coronary arteries: latest technical innovations and clinical experiences. Cardiovasc Innov Appl. 2016;2(1):85–99.
2. Xie Y, Jin H, Zeng M, Li D. Coronary artery plaque imaging. Curr Atheroscler Rep. 2017;19(9):37.
3. Dweck MR, Puntman V, Vesey AT, Fayad ZA, Nagel E. MR imaging of coronary arteries and plaques. J Am Coll Cardiol Img. 2016;9(3):306–16.
4. Tarkin JM, Dweck MR, Evans NR, Takx RA, Brown AJ, Tawakol A, et al. Imaging atherosclerosis. Circ Res. 2016;118(4):750–69.
5. Adamson PD, Newby DE. Non-invasive imaging of the coronary arteries. Eur Heart J. 2018;0:1–11.
6. Miao C, Chen S, Macedo R, Lai S, Liu K, Li D, et al. Positive remodeling of the coronary arteries detected by magnetic resonance imaging in an asymptomatic population: MESA (Multi-Ethnic Study of Atherosclerosis). J Am Coll Cardiol. 2009;53(18):1708–15.
7. Stone GW, Maehara A, Lansky AJ, de Bruyne B, Cristea E, Mintz GS, et al. A prospective natural-history study of coronary atherosclerosis. N Engl J Med. 2011;364(3):226–35.
8. Macedo R, Chen S, Lai S, Shea S, Malayeri AA, Szklo M, et al. MRI detects increased coronary wall thickness in asymptomatic individuals: the multi-ethnic study of atherosclerosis (MESA). J Magn Reson Imaging. 2008;28(5):1108–15.
9. Terashima M, Nguyen PK, Rubin GD, Meyer CH, Shimakawa A, Nishimura DG, et al. Right coronary wall CMR in the older asymptomatic advance cohort: positive remodeling and associations with type 2 diabetes and coronary calcium. J Cardiovasc Magn Reson. 2010;12:75.
10. Fayad ZA, Fuster V, Fallon JT, Jayasundera T, Worthley SG, Helft G, et al. Noninvasive in vivo human coronary artery lumen and wall imaging using black-blood magnetic resonance imaging. Circulation. 2000;102(5):506–10.

11. Botnar RM, Stuber M, Kissinger KV, Kim WY, Spuentrup E, Manning WJ. Noninvasive coronary vessel wall and plaque imaging with magnetic resonance imaging. Circulation. 2000;102(21):2582–7.
12. Kim WY, Stuber M, Kissinger KV, Andersen NT, Manning WJ, Botnar RM. Impact of bulk cardiac motion on right coronary MR angiography and vessel wall imaging. J Magn Reson Imaging. 2001;14(4):383–90.
13. Abd-Elmoniem KZ, Weiss RG, Stuber M. Phase-sensitive black-blood coronary vessel wall imaging. Magn Reson Med. 2010;63(4):1021–30.
14. Abd-Elmoniem KZ, Gharib AM, Pettigrew RI. Coronary vessel wall 3-T MR imaging with time-resolved acquisition of phase-sensitive dual inversion-recovery (TRAPD) technique: initial results in patients with risk factors for coronary artery disease. Radiology. 2012;265(3):715–23.
15. Andia ME, Henningsson M, Hussain T, Phinikaridou A, Protti A, Greil G, et al. Flow-independent 3D whole-heart vessel wall imaging using an interleaved T2-preparation acquisition. Magn Reson Med. 2013;69(1):150–7.
16. Cruz G, Atkinson D, Henningsson M, Botnar RM, Prieto C. Highly efficient nonrigid motion-corrected 3D whole-heart coronary vessel wall imaging. Magn Reson Med. 2017;77(5):1894–908.
17. Xie G, Bi X, Liu J, Yang Q, Natsuaki Y, Conte AH, et al. Three-dimensional coronary dark-blood interleaved with gray-blood (cDIG) magnetic resonance imaging at 3 tesla. Magn Reson Med. 2016;75(3):997–1007.
18. Hellings WE, Peeters W, Moll FL, Piers SR, van Setten J, Van der Spek PJ, et al. Composition of carotid atherosclerotic plaque is associated with cardiovascular outcome: a prognostic study. Circulation. 2010;121(17):1941–50.
19. Virmani R, Burke AP, Farb A, Kolodgie FD. Pathology of the vulnerable plaque. J Am Coll Cardiol. 2006;47(8 Suppl):C13–8.
20. Virmani R, Kolodgie FD, Burke AP, Farb A, Schwartz SM. Lessons from sudden coronary death: a comprehensive morphological classification scheme for atherosclerotic lesions. Arterioscler Thromb Vasc Biol. 2000;20(5):1262–75.
21. Maintz D, Ozgun M, Hoffmeier A, Fischbach R, Kim WY, Stuber M, et al. Selective coronary artery plaque visualization and differentiation by contrast-enhanced inversion prepared MRI. Eur Heart J. 2006;27(14):1732–6.
22. Moody AR, Murphy RE, Morgan PS, Martel AL, Delay GS, Allder S, et al. Characterization of complicated carotid plaque with magnetic resonance direct thrombus imaging in patients with cerebral ischemia. Circulation. 2003;107(24):3047–52.
23. Kawasaki T, Koga S, Koga N, Noguchi T, Tanaka H, Koga H, et al. Characterization of hyperintense plaque with noncontrast T(1)-weighted cardiac magnetic resonance coronary plaque imaging: comparison with multislice computed tomography and intravascular ultrasound. J Am Coll Cardiol Img. 2009;2(6):720–8.
24. Oei ML, Ozgun M, Seifarth H, Bunck A, Fischbach R, Orwat S, et al. T1-weighted MRI for the detection of coronary artery plaque haemorrhage. Eur Radiol. 2010;20(12):2817–23.
25. Noguchi T, Kawasaki T, Tanaka A, Yasuda S, Goto Y, Ishihara M, et al. High-intensity signals in coronary plaques on noncontrast T1-weighted magnetic resonance imaging as a novel determinant of coronary events. J Am Coll Cardiol. 2014;63(10):989–99.
26. Noguchi T, Tanaka A, Kawasaki T, Goto Y, Morita Y, Asaumi Y, et al. Effect of intensive statin therapy on coronary high-intensity plaques detected by noncontrast T1-weighted imaging: the AQUAMARINE pilot study. J Am Coll Cardiol. 2015;66(3):245–56.
27. Xie Y, Kim YJ, Pang J, Kim JS, Yang Q, Wei J, et al. Coronary atherosclerosis T1-weighed characterization with integrated anatomical reference: comparison with high-risk plaque features detected by invasive coronary imaging. J Am Coll Cardiol Img. 2017;10(6):637–48.
28. Jansen CH, Perera D, Makowski MR, Wiethoff AJ, Phinikaridou A, Razavi RM, et al. Detection of intracoronary thrombus by magnetic resonance imaging in patients with acute myocardial infarction. Circulation. 2011;124(4):416–24.
29. Ehara S, Hasegawa T, Nakata S, Matsumoto K, Nishimura S, Iguchi T, et al. Hyperintense plaque identified by magnetic resonance imaging relates to intracoronary thrombus as

detected by optical coherence tomography in patients with angina pectoris. Eur Heart J Cardiovasc Imaging. 2012;13(5):394–9.
30. Matsumoto K, Ehara S, Hasegawa T, Sakaguchi M, Otsuka K, Yoshikawa J, et al. Localization of coronary high-intensity signals on T1-weighted MR imaging: relation to plaque morphology and clinical severity of angina pectoris. J Am Coll Cardiol Img. 2015;8(10):1143–52.
31. Matsumoto K, Ehara S, Hasegawa T, Nishimura S, Shimada K. The signal intensity of coronary culprit lesions on T1-weighted magnetic resonance imaging is directly correlated with the accumulation of vulnerable morphologies. Int J Cardiol. 2017;231:284–6.
32. Liu W, Xie Y, Wang C, Du Y, Nguyen C, Wang Z, et al. Atherosclerosis T1-weighted characterization (CATCH): evaluation of the accuracy for identifying intraplaque hemorrhage with histological validation in carotid and coronary artery specimens. J Cardiovasc Magn Reson. 2018;20(1):27.
33. Yeon SB, Sabir A, Clouse M, Martinezclark PO, Peters DC, Hauser TH, et al. Delayed-enhancement cardiovascular magnetic resonance coronary artery wall imaging: comparison with multislice computed tomography and quantitative coronary angiography. J Am Coll Cardiol. 2007;50(5):441–7.
34. Dill T, Ekinci O, Hansel J, Kluge A, Breidenbach C, Hamm CW. Delayed contrast-enhanced magnetic resonance imaging for the detection of autoimmune myocarditis and long-term follow-up. J Cardiovasc Magn Reson. 2005;7(2):521–3.
35. Schneeweis C, Schnackenburg B, Stuber M, Berger A, Schneider U, Yu J, et al. Delayed contrast-enhanced MRI of the coronary artery wall in takayasu arteritis. PLoS One. 2012;7(12):e50655.
36. Botnar RM, Buecker A, Wiethoff AJ, Parsons EC Jr, Katoh M, Katsimaglis G, et al. In vivo magnetic resonance imaging of coronary thrombosis using a fibrin-binding molecular magnetic resonance contrast agent. Circulation. 2004;110(11):1463–6.
37. Makowski MR, Wiethoff AJ, Blume U, Cuello F, Warley A, Jansen CH, et al. Assessment of atherosclerotic plaque burden with an elastin-specific magnetic resonance contrast agent. Nat Med. 2011;17(3):383–8.
38. von Bary C, Makowski M, Preissel A, Keithahn A, Warley A, Spuentrup E, et al. MRI of coronary wall remodeling in a swine model of coronary injury using an elastin-binding contrast agent. Circ Cardiovasc Imaging. 2011;4(2):147–55.
39. Phinikaridou A, Andia ME, Protti A, Indermuehle A, Shah A, Smith A, et al. Noninvasive magnetic resonance imaging evaluation of endothelial permeability in murine atherosclerosis using an albumin-binding contrast agent. Circulation. 2012;126(6):707–19.
40. Pedersen SF, Thrysoe SA, Paaske WP, Thim T, Falk E, Ringgaard S, et al. CMR assessment of endothelial damage and angiogenesis in porcine coronary arteries using gadofosveset. J Cardiovasc Magn Reson. 2011;13:10.
41. Engel LC, Landmesser U, Gigengack K, Wurster T, Manes C, Girke G, et al. Novel approach for in vivo detection of vulnerable coronary plaques using molecular 3-T CMR imaging with an albumin-binding probe. J Am Coll Cardiol Img. 2019;12(2):297–306.
42. Pepe A, Lombardi M, Takacs I, Positano V, Panzarella G, Picano E. Nitrate-induced coronary vasodilation by stress-magnetic resonance imaging: a novel noninvasive test of coronary vasomotion. J Magn Reson Imaging. 2004;20(3):390–4.
43. Terashima M, Meyer CH, Keeffe BG, Putz EJ, de la Pena-Almaguer E, Yang PC, et al. Noninvasive assessment of coronary vasodilation using magnetic resonance angiography. J Am Coll Cardiol. 2005;45(1):104–10.
44. Hays AG, Hirsch GA, Kelle S, Gerstenblith G, Weiss RG, Stuber M. Noninvasive visualization of coronary artery endothelial function in healthy subjects and in patients with coronary artery disease. J Am Coll Cardiol. 2010;56(20):1657–65.
45. Lin K, Lloyd-Jones DM, Liu Y, Bi X, Li D, Carr JC. Noninvasive evaluation of coronary distensibility in older adults: a feasibility study with MR angiography. Radiology. 2011;261(3):771–8.
46. Lin K, Lloyd-Jones DM, Taimen K, Liu Y, Bi X, Li D, et al. The detection of coronary stiffness in cardiac allografts using MR imaging. Eur J Radiol. 2014;83(8):1402–7.

47. Commandeur F, Goeller M, Dey D. Cardiac CT: technological advances in hardware, software, and machine learning applications. Curr Cardiovasc Imaging Rep. 2018;11(8):19.
48. Agatston AS, Janowitz WR, Hildner FJ, Zusmer NR, Viamonte M Jr, Detrano R. Quantification of coronary artery calcium using ultrafast computed tomography. J Am Coll Cardiol. 1990;15(4):827–32.
49. Callister T, Cooil B, Raya S, Lippolis N, Russo D, Raggi P. Coronary artery disease: improved reproducibility of calcium scoring with an electron-beam CT volumetric method. Radiology. 1998;208(3):807–14.
50. McCollough CH, Ulzheimer S, Halliburton SS, Shanneik K, White RD, Kalender WA. Coronary artery calcium: a multi-institutional, multimanufacturer international standard for quantification at cardiac CT. Radiology. 2007;243(2):527–38.
51. Arad Y, Goodman KJ, Roth M, Newstein D, Guerci AD. Coronary calcification, coronary disease risk factors, C-reactive protein, and atherosclerotic cardiovascular disease events: the St. Francis Heart Study. J Am Coll Cardiol. 2005;46(1):158–65.
52. Shaw L, Raggi P, Schisterman E, Berman D, Callister T. Prognostic value of cardiac risk factors and coronary artery calcium screening for all-cause mortality. Radiology. 2003;228(3):826–33.
53. Berman DS, Hachamovitch R, Shaw LJ, Friedman JD, Hayes SW, Thomson LE, et al. Roles of nuclear cardiology, cardiac computed tomography, and cardiac magnetic resonance: noninvasive risk stratification and a conceptual framework for the selection of noninvasive imaging tests in patients with known or suspected coronary artery disease. J Nucl Med. 2006;47(7):1107–18.
54. Arad Y, Spadaro LA, Goodman K, Newstein D, Guerci AD. Prediction of coronary events with electron beam computed tomography. J Am Coll Cardiol. 2000;36(4):1253–60.
55. Raggi P, Callister TQ, Cooil B, He ZX, Lippolis NJ, Russo DJ, et al. Identification of patients at increased risk of first unheralded acute myocardial infarction by electron-beam computed tomography. Circulation. 2000;101(8):850–5.
56. Park R, Detrano R, Xiang M, Fu P, Ibrahim Y, LaBree L, et al. Combined use of computed tomography coronary calcium scores and C-reactive protein levels in predicting cardiovascular events in nondiabetic individuals. Circulation. 2002;106(16):2073–7.
57. Shemesh J, Morag-Koren N, Goldbourt U, Grossman E, Tenenbaum A, Fisman EZ, et al. Coronary calcium by spiral computed tomography predicts cardiovascular events in high-risk hypertensive patients. J Hypertens. 2004;22(3):605–10.
58. Wong ND, Hsu JC, Detrano RC, Diamond G, Eisenberg H, Gardin JM. Coronary artery calcium evaluation by electron beam computed tomography and its relation to new cardiovascular events. Am J Cardiol. 2000;86(5):495–8.
59. Kondos GT, Hoff JA, Sevrukov A, Daviglus ML, Garside DB, Devries SS, et al. Electron-beam tomography coronary artery calcium and cardiac events: a 37-month follow-up of 5635 initially asymptomatic low- to intermediate-risk adults. Circulation. 2003;107(20):2571–6.
60. Greenland P, LaBree L, Azen SP, Doherty TM, Detrano RC. Coronary artery calcium score combined with Framingham score for risk prediction in asymptomatic individuals. JAMA. 2004;291(2):210–5.
61. LaMonte MJ, FitzGerald SJ, Church TS, Barlow CE, Radford NB, Levine BD, et al. Coronary artery calcium score and coronary heart disease events in a large cohort of asymptomatic men and women. Am J Epidemiol. 2005;162(5):421–9.
62. Taylor AJ, Bindeman J, Feuerstein I, Cao F, Brazaitis M, O'Malley PG. Coronary calcium independently predicts incident premature coronary heart disease over measured cardiovascular risk factors: mean three-year outcomes in the Prospective Army Coronary Calcium (PACC) project. J Am Coll Cardiol. 2005;46(5):807–14.
63. Vliegenthart R, Oudkerk M, Hofman A, Oei HH, van Dijck W, van Rooij FJ, et al. Coronary calcification improves cardiovascular risk prediction in the elderly. Circulation. 2005;112(4):572–7.
64. Becker A, Knez A, Becker C, Leber A, Anthopounou L, Boekstegers P, et al. [Prediction of serious cardiovascular events by determining coronary artery calcification measured by multi-slice computed tomography]. Dtsch Med Wochenschr. 2005;130(43):2433–8.

65. Detrano R, Guerci AD, Carr JJ, Bild DE, Burke G, Folsom AR, et al. Coronary calcium as a predictor of coronary events in four racial or ethnic groups. N Engl J Med. 2008;358(13):1336–45.
66. Taylor AJ, Cerqueira M, Hodgson JM, Mark D, Min J, O'Gara P, et al. ACCF/SCCT/ACR/AHA/ASE/ASNC/NASCI/SCAI/SCMR 2010 Appropriate Use Criteria for Cardiac Computed Tomography: A Report of the American College of Cardiology Foundation Appropriate Use Criteria Task Force, the Society of Cardiovascular Computed Tomography, the American College of Radiology, the American Heart Association, the American Society of Echocardiography, the American Society of Nuclear Cardiology, the North American Society for Cardiovascular Imaging, the Society for Cardiovascular Angiography and Interventions, and the Society for Cardiovascular Magnetic Resonance. J Am Coll Cardiol. 2010;56(22):1864–94.
67. Budoff MJ, Dowe D, Jollis JG, Gitter M, Sutherland J, Halamert E, et al. Diagnostic performance of 64-multidetector row coronary computed tomographic angiography for evaluation of coronary artery stenosis in individuals without known coronary artery disease: results from the prospective multicenter ACCURACY (Assessment by Coronary Computed Tomographic Angiography of Individuals Undergoing Invasive Coronary Angiography) Trial. J Am Coll Cardiol. 2008;52(21):1724–32.
68. Hausleiter J, Meyer T, Hadamitzky M, Zankl M, Gerein P, DorrLer K, et al. Non-invasive coronary computed tomographic angiography for patients with suspected coronary artery disease: the Coronary Angiography by Computed Tomography with the Use of a Submillimeter resolution (CACTUS) trial. Eur Heart J. 2007;28(24):3034–41.
69. Achenbach S, Ropers U, Kuettner A, Anders K, Pflederer T, Komatsu S, et al. Randomized comparison of 64-slice single- and dual-source computed tomography coronary angiography for the detection of coronary artery disease. J Am Coll Cardiol Cardiovasc Imaging. 2008;1(2):177–86.
70. Miller JM, Rochitte CE, Dewey M, Arbab-Zadeh A, Niinuma H, Gottlieb I, et al. Diagnostic performance of coronary angiography by 64-row CT. N Engl J Med. 2008;359(22):2324–36.
71. Meijboom WB, van Mieghem CAG, Mollet NR, Pugliese F, Weustink AC, van Pelt N, et al. 64-slice computed tomography coronary angiography in patients with high, intermediate, or low pretest probability of significant coronary artery disease. J Am Coll Cardiol. 2007;50:1469–75.
72. Abbara S, Blanke P, Maroules CD, Cheezum M, Choi AD, Han BK, et al. SCCT guidelines for the performance and acquisition of coronary computed tomographic angiography: a report of the society of Cardiovascular Computed Tomography Guidelines Committee: endorsed by the North American Society for Cardiovascular Imaging (NASCI). J Cardiovasc Comput Tomogr. 2016;10(6):435–49.
73. Cury RC, Abbara S, Achenbach S, Agatston A, Berman DS, Budoff MJ, et al. CAD-RADSTM coronary artery disease–reporting and data system. An expert consensus document of the Society of Cardiovascular Computed Tomography (SCCT), the American College of Radiology (ACR) and the North American Society for Cardiovascular Imaging (NASCI). Endorsed by the American College of Cardiology. J Cardiovasc Comput Tomogr. 2016;10(4):269–81.
74. Douglas PS, Hoffmann U, Patel MR, Mark DB, Al-Khalidi HR, Cavanaugh B, et al. Outcomes of anatomical versus functional testing for coronary artery disease. N Engl J Med. 2015;372(14):1291–300.
75. SCOT-HEART Investigators. CT coronary angiography in patients with suspected angina due to coronary heart disease (SCOT-HEART): an open-label, parallel-group, multicentre trial. Lancet. 2015;385(9985):2383–91.
76. Newby DE, Adamson PD, Berry C, Boon NA, Dweck MR, Flather M, et al. Coronary CT angiography and 5-year risk of myocardial infarction. N Engl J Med. 2018;379(10):924–33.
77. Achenbach S, Moselewski F, Ropers D, Ferencik M, Hoffmann U, MacNeill B, et al. Detection of calcified and noncalcified coronary atherosclerotic plaque by contrast-enhanced, submillimeter multidetector spiral computed tomography: a segment-based comparison with intravascular ultrasound. Circulation. 2004;109(1):14–7.

78. Achenbach S, Ropers D, Hoffmann U, MacNeill B, Baum U, Pohle K, et al. Assessment of coronary remodeling in stenotic and nonstenotic coronary atherosclerotic lesions by multidetector spiral computed tomography. J Am Coll Cardiol. 2004;43(5):842–7.
79. Leber AW, Becker A, Knez A, von Ziegler F, Sirol M, Nikolaou K, et al. Accuracy of 64-slice computed tomography to classify and quantify plaque volumes in the proximal coronary system: a comparative study using intravascular ultrasound. J Am Coll Cardiol. 2006;47(3):672–7.
80. Leber AW, Knez A, Becker A, Becker C, von Ziegler F, Nikolaou K, et al. Accuracy of multidetector spiral computed tomography in identifying and differentiating the composition of coronary atherosclerotic plaques: a comparative study with intracoronary ultrasound. J Am Coll Cardiol. 2004;43(7):1241–7.
81. Pundziute G, Schuijf JD, Jukema JW, Decramer I, Sarno G, Vanhoenacker PK, et al. Evaluation of plaque characteristics in acute coronary syndromes: non-invasive assessment with multi-slice computed tomography and invasive evaluation with intravascular ultrasound radiofrequency data analysis. Eur Heart J. 2008;29(19):2373–81.
82. Schepis T, Marwan M, Pflederer T, Seltmann M, Ropers D, Daniel WG, et al. Quantification of noncalcified coronary atherosclerotic plaques with Dual Source Computed Tomography: comparison to intravascular ultrasound. Heart. 2010;96:610–5.
83. Petranovic M, Soni A, Bezzera H, Loureiro R, Sarwar A, Raffel C, et al. Assessment of nonstenotic coronary lesions by 64-slice multidetector computed tomography in comparison to intravascular ultrasound: evaluation of nonculprit coronary lesions. J Cardiovasc Comput Tomogr. 2009;3(1):24–31.
84. Dey D, Schepis T, Marwan M, Slomka PJ, Berman DS, Achenbach S. Automated three-dimensional quantification of non-calcified coronary plaque from coronary CT angiography: comparison with intravascular ultrasound. Radiology. 2010;257(2):516–22.
85. Boogers MJ, Broersen A, van Velzen JE, de Graaf FR, El-Naggar HM, Kitslaar PH, et al. Automated quantification of coronary plaque with computed tomography: comparison with intravascular ultrasound using a dedicated registration algorithm for fusion-based quantification. Eur Heart J. 2012;33(8):1007–16.
86. Voros S, Rinehart S, Qian Z, Joshi P, Vazquez G, Fischer C, et al. Coronary atherosclerosis imaging by coronary CT angiography current status, correlation with intravascular interrogation and meta-analysis. JACC Cardiovasc Imaging. 2011;4(5):537–48.
87. Motoyama S, Sarai M, Harigaya H, Anno H, Inoue K, Hara T, et al. Computed tomographic angiography characteristics of atherosclerotic plaques subsequently resulting in acute coronary syndrome. J Am Coll Cardiol. 2009;54(1):49–57.
88. Motoyama S, Kondo T, Sarai M, Sugiura A, Harigaya H, Sato T, et al. Multislice computed tomographic characteristics of coronary lesions in acute coronary syndromes. J Am Coll Cardiol. 2007;50(4):319–26.
89. Pflederer T, Marwan M, Schepis T, Ropers D, Seltmann M, Muschiol G, Daniel WG, Achenbach S. Characterization of culprit lesions in acute coronary syndromes using coronary dual-source CT angiography. Atherosclerosis. 2010;211(2):437–44.
90. Puchner SB, Liu T, Mayrhofer T, Truong QA, Lee H, Fleg JL, et al. High-risk plaque detected on coronary CT angiography predicts acute coronary syndromes independent of significant stenosis in acute chest pain: results from the ROMICAT-II trial. J Am Coll Cardiol. 2014;64(7):684–92.
91. Maurovich-Horvat P, Hoffmann U, Vorpahl M, Nakano M, Virmani R, Alkadhi H. The napkin-ring sign: CT signature of high-risk coronary plaques? JACC Cardiovasc Imaging. 2010;3(4):440–4.
92. Narula J, Achenbach S. Napkin-ring necrotic cores: defining circumferential extent of necrotic cores in unstable plaques. JACC Cardiovasc Imaging. 2009;2(12):1436–8.
93. Kristensen TS, Kofoed KF, Kuhl JT, Nielsen WB, Nielsen MB, Kelbaek H. Prognostic implications of nonobstructive coronary plaques in patients with non-ST-segment elevation myocardial infarction: a multidetector computed tomography study. J Am Coll Cardiol. 2011;58(5):502–9.

94. Versteylen MO, Kietselaer BL, Dagnelie PC, Joosen IA, Dedic A, Raaijmakers RH, et al. Additive value of Semiautomated quantification of coronary artery disease using cardiac computed tomographic angiography to predict future acute coronary syndrome. J Am Coll Cardiol. 2013;61(22):2296–305.
95. Motoyama S, Ito H, Sarai M, Kondo T, Kawai H, Nagahara Y, et al. Plaque characterization by coronary computed tomography angiography and the likelihood of acute coronary events in mid-term follow-up. J Am Coll Cardiol. 2015;66(4):337–46.
96. Hell MM, Motwani M, Otaki Y, Cadet S, Gransar H, Miranda-Peats R, Valk J, PJ SL, Cheng V, Rozanski R, Tamarappoo BK, Hayes S, Achenbach S, Berman DS, Dey D, et al. Eur Heart J Cardiovasc Imaging. 2017;18(12):1331–9.
97. Chang HJ, Lin FY, Lee SE, Andreini D, Bax J, Cademartiri F, et al. Coronary atherosclerotic precursors of acute coronary syndromes. J Am Coll Cardiol. 2018;71(22):2511–22.
98. Moreno PR, Narula J. Thinking outside the lumen: fractional flow reserve versus intravascular imaging for major adverse cardiac event prediction. J Am Coll Cardiol. 2014;63(12):1141–4.
99. Ahmadi A, Leipsic J, Blankstein R, Taylor C, Hecht H, Stone GW, et al. Do plaques rapidly progress prior to myocardial infarction? The interplay between plaque vulnerability and progression. Circ Res. 2015;117(1):99–104.
100. Tamarappoo B, Otaki Y, Doris M, Arnson Y, Gransar HG, Hayes S, Friedman J, Thomson LEJ, Wang F, Rozanski A, Slomka PJ, Dey D, Berman DS. Improvement in LDL is associated with decrease in non-calcified plaque volume on coronary CTA as measured by automated quantitative software. J Cardiovasc Comput Tomogr. 2018;12(5):385–90.
101. Lee S-E, Chang H-J, Sung JM, Park H-B, Heo R, Rizvi A, et al. Effects of statins on coronary atherosclerotic plaques. JACC Cardiovasc Imaging. 2018;11:1475.
102. Gaur S, Ovrehus KA, Dey D, Leipsic J, Botker HE, Jensen JM, et al. Coronary plaque quantification and fractional flow reserve by coronary computed tomography angiography identify ischaemia-causing lesions. Eur Heart J. 2016;37(15):1220–7.
103. Diaz Zamudio M, Dey D, Schuhbaeck A, Nakazato R, Slomka PJ, Bermand DS, Achenbach S, Min JK, Doh JH, Koo BK. Automated quantitative plaque burden from coronary CT Angiography noninvasively predicts hemodynamic significance by fractional flow reserve in intermediate coronary lesions. Radiology. 2015;276(2):408–15.
104. Motwani M, Dey D, Berman DS, Germano G, Achenbach S, Al-Mallah MH, et al. Machine learning for prediction of all-cause mortality in patients with suspected coronary artery disease: a 5-year multicentre prospective registry analysis. Eur Heart J. 2017;38(7):500–7.
105. Dey D, Gaur S, Ovrehus KA, Slomka PJ, Betancur J, Goeller M, et al. Integrated prediction of lesion-specific ischaemia from quantitative coronary CT angiography using machine learning: a multicentre study. Eur Radiol. 2018;28:2655–64.
106. Mahabadi AA, Massaro JM, Rosito GA, Levy D, Murabito JM, Wolf PA, et al. Association of pericardial fat, intrathoracic fat, and visceral abdominal fat with cardiovascular disease burden: the Framingham Heart Study. Eur Heart J. 2009;30(7):850–6.
107. Mahabadi AA, Reinsch N, Lehmann N, Altenbernd J, Kalsch H, Seibel RM, et al. Association of pericoronary fat volume with atherosclerotic plaque burden in the underlying coronary artery: a segment analysis. Atherosclerosis. 2010;211(1):195–9.
108. Tamarappoo B, Dey D, Shmilovich H, Nakazato R, Gransar H, Cheng VY, et al. Increased pericardial fat volume measured from noncontrast CT predicts myocardial ischemia by SPECT. JACC Cardiovasc Imaging. 2010;3(11):1104–12.
109. Mazurek T, Zhang L, Zalewski A, Mannion JD, Diehl JT, Arafat H, et al. Human epicardial adipose tissue is a source of inflammatory mediators. Circulation. 2003;108:2460–6.
110. Shimabukuro M, Hirata Y, Tabata M, Dagvasumberel M, Sato H, Kurobe H, et al. Epicardial adipose tissue volume and adipocytokine imbalance are strongly linked to human coronary atherosclerosis. Arterioscler Thromb Vasc Biol. 2013;33(5):1077–84.
111. Bucerius J, Mani V, Wong S, Moncrieff C, Izquierdo-Garcia D, Machac J, et al. Arterial and fat tissue inflammation are highly correlated : a prospective 18F-FDG PET/CT study. Eur J Nucl Med Mol Imaging. 2014;41(5):934–45.

112. Gorter PM, van Lindert ASR, de Vos AM, Meijs MFL, van der Graaf Y, Doevendans PA, et al. Quantification of epicardial and peri-coronary fat using cardiac computed tomography; reproducibility and relation with obesity and metabolic syndrome in patients suspected of coronary artery disease. Atherosclerosis. 2008;197(2):896–903.
113. Antonopoulos AS, Sanna F, Sabharwal N, Thomas S, Oikonomou EK, Herdman L, et al. Detecting human coronary inflammation by imaging perivascular fat. Sci Transl Med. 2017;9(398).
114. Oikonomou EK, Marwan M, Desai MY, Mancio J, Alashi A, Hutt Centeno E, et al. Non-invasive detection of coronary inflammation using computed tomography and prediction of residual cardiovascular risk (the CRISP CT study): a post-hoc analysis of prospective outcome data. Lancet. 2018;392(10151):929–39.
115. Goeller M, Achenbach S, Cadet S, Kwan AC, Commandeur F, Slomka PJ, et al. Pericoronary adipose tissue computed tomography attenuation and high-risk plaque characteristics in acute coronary syndrome compared with stable coronary artery disease. JAMA Cardiol. 2018;3(9):858–63.
116. Rudd JH, Warburton EA, Fryer TD, Jones HA, Clark JC, Antoun N, et al. Imaging atherosclerotic plaque inflammation with [18F]-fluorodeoxyglucose positron emission tomography. Circulation. 2002;105(23):2708–11.
117. Rudd JH, Hyafil F, Fayad ZA. Inflammation imaging in atherosclerosis. Arterioscler Thromb Vasc Biol. 2009;29(7):1009–16.
118. Tawakol A, Migrino RQ, Hoffmann U, Abbara S, Houser S, Gewirtz H, et al. Noninvasive in vivo measurement of vascular inflammation with F-18 fluorodeoxyglucose positron emission tomography. J Nucl Cardiol. 2005;12(3):294–301.
119. Alexanderson E, Slomka P, Cheng V, Meave A, Saldana Y, Garcia-Rojas L, et al. Fusion of positron emission tomography and coronary computed tomographic angiography identifies fluorine 18 fluorodeoxyglucose uptake in the left main coronary artery soft plaque. J Nucl Cardiol. 2008;15(6):841–3.
120. Rogers IS, Nasir K, Figueroa AL, Cury RC, Hoffmann U, Vermylen DA, et al. Feasibility of FDG imaging of the coronary arteries: comparison between acute coronary syndrome and stable angina. J Am Coll Cardiol Img. 2010;3(4):388–97.
121. Williams G, Kolodny GM. Suppression of myocardial 18F-FDG uptake by preparing patients with a high-fat, low-carbohydrate diet. AJR Am J Roentgenol. 2008;190(2):W151–6.
122. Rominger A, Saam T, Vogl E, Ubleis C, la Fougere C, Forster S, et al. In vivo imaging of macrophage activity in the coronary arteries using 68Ga-DOTATATE PET/CT: correlation with coronary calcium burden and risk factors. J Nucl Med. 2010;51(2):193–7.
123. Tahara N, Mukherjee J, de Haas HJ, Petrov AD, Tawakol A, Haider N, et al. 2-deoxy-2-[18F]fluoro-D-mannose positron emission tomography imaging in atherosclerosis. Nat Med. 2014;20(2):215–9.
124. Dweck MR, Chow MW, Joshi NV, Williams MC, Jones C, Fletcher AM, et al. Coronary arterial 18F-sodium fluoride uptake: a novel marker of plaque biology. J Am Coll Cardiol. 2012;59(17):1539–48.
125. Joshi NV, Vesey A, Newby DE, Dweck MR. Will 18F-sodium fluoride PET-CT imaging be the magic bullet for identifying vulnerable coronary atherosclerotic plaques? Curr Cardiol Rep. 2014;16(9):521.
126. Joshi NV, Vesey AT, Williams MC, Shah AS, Calvert PA, Craighead FH, et al. 18F-fluoride positron emission tomography for identification of ruptured and high-risk coronary atherosclerotic plaques: a prospective clinical trial. Lancet. 2014;383(9918):705–13.
127. Rubeaux M, Joshi NV, Dweck MR, Fletcher A, Motwani M, Thomson LE, et al. Motion correction of 18F-NaF PET for imaging coronary atherosclerotic plaques. J Nucl Med. 2016;57(1):54–9.
128. Manber R, Thielemans K, Hutton BF, Barnes A, Ourselin S, Arridge S, et al. Practical PET respiratory motion correction in clinical PET/MR. J Nucl Med. 2015;56(6):890–6.

129. Kustner T, Schwartz M, Martirosian P, Gatidis S, Seith F, Gilliam C, et al. MR-based respiratory and cardiac motion correction for PET imaging. Med Image Anal. 2017;42:129–44.
130. Furst S, Grimm R, Hong I, Souvatzoglou M, Casey ME, Schwaiger M, et al. Motion correction strategies for integrated PET/MR. J Nucl Med. 2015;56(2):261–9.
131. Robson PM, Dey D, Newby DE, Berman D, Li D, Fayad ZA, et al. MR/PET imaging of the cardiovascular system. JACC Cardiovasc Imaging. 2017;10(10 Pt A):1165–79.

Part VI
Imaging Techniques

Chapter 14
Image Processing: What Is Needed and Unique for Vessel Wall Imaging?

Chun Yuan, Zach Miller, and William Kerwin

Introduction

This chapter focuses on the image processing needs for vessel wall imaging (VWI). While general image processing techniques can be applied to VWI, there are many unique aspects which need special attention. First, the size of vessels typically presents small targets for imaging, allowing only several pixels of coverage for a vessel wall. Second, vessel wall metrics extend beyond size and thickness to tissue composition. Third, comprehensive analysis of tissue composition requires processing of multimodality, multi-contrast, and/or contrast-enhanced data, which requires image registration. Finally, physicians are not yet well trained in reviewing VWI, although this is rapidly changing.

The Need for Image Processing

As established in previous chapters, vessel wall imaging (VWI) is capable of identifying and quantifying diseases of vasculature in both large and small vessels. Most commonly these are atherosclerosis, aneurysm, and Moyamoya, but the tools provided by imaging are applicable to other pathologies. Following image acquisition, image processing methods can be employed to identify significant locations and

C. Yuan (✉)
University of Washington, Seattle, WA, USA
e-mail: cyuan@uw.edu

Z. Miller · W. Kerwin
University of Washington Vascular Imaging Laboratory, Department of Radiology, Seattle, WA, USA
e-mail: zach1@uw.edu; bkerwin@uw.edu

C. Yuan et al. (eds.), *Vessel Based Imaging Techniques*,
https://doi.org/10.1007/978-3-030-25249-6_14

quantify disease extent and severity. This chapter will focus on image processing for vessel wall morphology and characterization of atherosclerosis, which remains the primary motivation for vessel wall imaging and the focus of the majority of image processing methods. Applications in other vascular diseases generally use methods originally developed for atherosclerosis.

While imaging acquisition methods are key to visualizing wall morphology and atherosclerotic plaques, image processing methods, most commonly applied after acquisition, are needed to identify plaques at risk of rupture, identify and analyze plaque components, and provide accurate measurement of plaque size, volume, morphology, and characteristics. They also enable rapid analysis of plaques and may provide us with automated methods of risk analysis for future vessel wall rupture or ischemic events.

As vessel stenosis measurements alone have been shown to be insufficient for accurate diagnoses of all plaques at risk of future events [1], the concept of "vulnerable plaques" (VP), i.e., plaques at higher risk of rupture or event due to constituents, morphology, or other factors, has emerged [2–4]. A series of foundational studies have established the corresponding appearance of these VP features on images [5]. A study by Underhill et al. [6] in particular provides a concise, comprehensive framework for risk analysis in the carotid artery and identifies the features of atherosclerosis which image processing methods should focus on. These are briefly summarized below.

As we know from previous chapters, the development of atherosclerotic plaques is complex [7]. Plaques may not only grow into the vessel lumen causing stenosis (narrowing), of the vessel, but also expand outward from the vessel lumen without impinging on luminal flow, a process referred to as "outward remodeling" [1]. Remodeling and its subsequent increase in overall plaque burden are thought to be important risk factors in cardiovascular events. Specific morphological measures that have also been shown to be associated with VP are plaque thickness (measured cross-sectionally from the thickest point of lumen to the outer wall boundary); normalized wall index (NWI), calculated as wall area divided by total vessel area and a measure of total plaque burden along the length of the vessel; and plaque eccentricity, a measure of the shape or "concentricity" of the plaque [8]. This concept has long been applied to coronary arteries [9]. Image processing is essential in providing efficient tools for identification and accurate measurement of these morphologies. Challenges for these morphological measurements include effective and accurate identification of luminal and outer wall boundaries—which may not be apparent because of flow artifacts, motion, and poorly marked border between vessel wall and surrounding tissues.

In addition to plaque size and morphological measures, certain constituents within the vessel wall have also been established to raise the risk severity of patients. A consensus summary based on carotid atherosclerosis identifies these high-risk components as intraplaque hemorrhage (IPH) and lipid-rich necrotic cores (LRNC), which may or may not be covered with a fibrous cap (FC) [10]. Underhill et al. developed a risk stratification system (see Fig. 14.1 for details) that can also be used to guide image processing approaches [6]. This system needs to use images acquired from multiple contrast weightings.

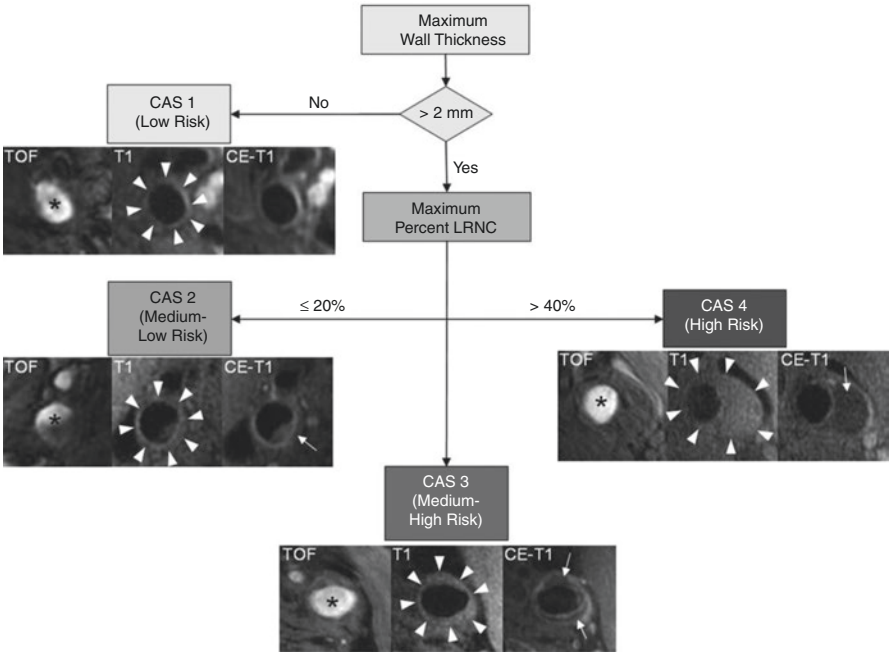

Fig. 14.1 Flow diagram of carotid artery scoring system from Underhill et al. Subjects with a maximum wall thickness >2 mm require additional evaluation. Further categorization of lesions can be determined by the size of the maximum percentage LRNC. Examples of matched cross-sectional images from three contrast weightings (TOF, T1WI, and CE-T1WI) for each category are provided. Images corresponding to CAS 1 (maximum wall thickness <2 mm) are from the left common carotid artery of a 69-year-old man imaged at MSU. The plaque in the CAS 2 (maximum percentage LRNC, ≤20%) example is from the right internal carotid artery of a 63-year-old man imaged at UW. There is a small LRNC (*arrow*) present on postcontrast imaging. Of note, there are also flow artifacts visible in the lumen—common artifacts in images distal to the bifurcation. The lesion in CAS 3 (maximum percentage LRNC, >20% and ≤40%) is from the left common carotid artery of a 65-year-old man imaged at AH. A noticeable LRNC (*arrows*) is present in both the anterior and posterior arterial walls. An example of a large LRNC (*arrow*) without IPH in the left common carotid artery of a 64-year-old man imaged at PLA is shown for CAS 4 (maximum percentage LRNC, >40%). Arrowheads indicate the outer wall boundary; asterisk indicates the lumen. (Reprinted with permission from Underhill et al. [6])

Plaque enhancement patterns during and after contrast application improve tissue contrast and are associated with plaque inflammation and neovasculature [11–13]. In particular, leakiness of neovasculature is in the vessel wall has been linked with VP [11]. Its measurement requires implementing kinetic modeling into vessel wall imaging to provide quantitative measures of contrast agent uptake and associated risk. Image processing techniques are clearly needed for this analysis.

Furthermore, size, tortuosity, length, vascular pathology, and pressure are different for each vascular bed. There is evidence that atherosclerosis progression and identifiers of VP may vary throughout vascular beds. However, for the purposes of image processing, the key assessments for vessels in terms of disease evaluation remain the same: identify lumen and outer wall boundaries, and then

define vessel wall morphology, plaque burden, distribution, and remodeling patterns, and identify regions of interest. Automated identification methods of lumen and outer wall boundaries can prepare image sets and enable plaque analysis and measurement that require human readers to be performed efficiently and relatively quickly.

Current Vessel Analysis Tools and What They Can Provide

Two well-known image processing techniques in vessel wall imaging are calcium scoring by CT and intima-media thickness (IMT) measurement by ultrasound. The first, calcium scoring based on CT imaging of coronary arteries, has shown that higher coronary calcium scores are predictive of patients with advanced coronary atheroma and are at higher risk for rupture [14]. This area has been much studied and confirms the initial findings investigating quantifying coronary calcium levels using CT [15]. The second, IMT as measured by ultrasound, has established that IMT measurements in the carotid artery are directly associated with increased risk of cardiovascular disease and progression [16, 17]. While CT and ultrasound both offer promising biomarkers for vessel disease, this chapter will focus on more recent MRI-based VWI processing techniques, which offer more comprehensive VWI information in multiple vascular beds.

Current and developing processing methods for identification, measurement, and analysis of all these vessel wall conditions are described below. A literature search for "vessel wall image processing" shows that many algorithms and methods have been attempted for vessel wall imaging; currently, however, only two software systems are both prevalent in peer-reviewed literature search and also used in multiple clinical studies and regulated drug trials. *VesselMASS RE*, developed by Medis, is a commercial software that has been used for vessel analysis in the Multi-Ethnic Study of Atherosclerosis [18, 19]. *CASCADE*, developed by the University of Washington Vascular Imaging Laboratory [20], is an academic software package which has been used in the ORION study CPC, AIM HIGH [21], and others [22–24].

Techniques for Image Processing

Although these two software suites offer different user interfaces and underlying algorithms for measurement, both have been validated, used in clinical trials, and rely on expert human review to confirm findings. After loading acquired MR images, multiple contrasts of image weightings will typically be displayed side by side, and overlying contours will be drawn (sometimes automatically) for vessel lumen, outer wall boundaries, and other regions of interest (Fig. 14.2). After confirmation by expert review, measurements are conducted based on drawn contours.

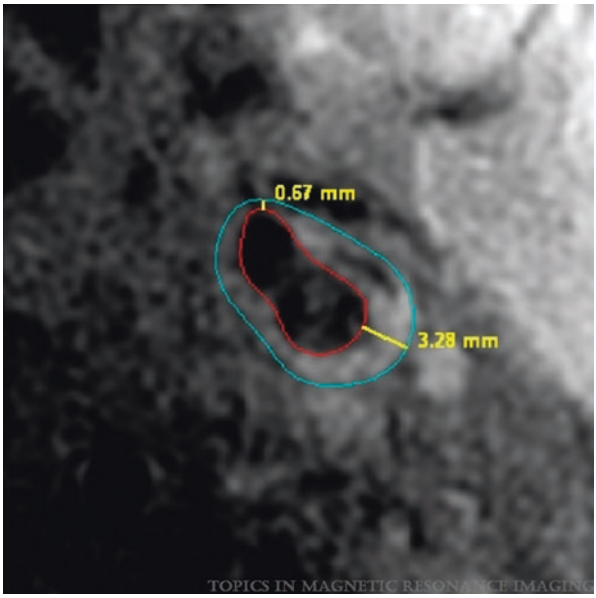

Fig. 14.2 Example of wall thickness measurement by CASCADE showing the minimal and maximal values detected. (Magnetic Resonance Imaging of Carotid Atherosclerosis: Plaque Analysis, Kerwin et al. [20]. Copyright © 2019 Wolters Kluwer Health, Inc. All rights reserved)

In order to achieve accurate vessel wall measurements, relevant parameters for vessel areas must first be captured, namely, area, wall thickness, normalized wall index, and plaque eccentricity, further described below.

Parameters

Area The capability of MRI to accurately define both luminal and adventitial boundaries for area measurement was first validated by a study that compared maximum wall areas measured from in vivo carotid MR images to images from corresponding ex vivo specimens in 1998 [56] and has since undergone a series of improvements for boundary detection [57], improved acquisition techniques, and establishing intra- and inter-reader reproducibility [40].

Vessel wall area, whether measured from lumen area, wall area, total vessel area, or area of a region of interest or plaque component, is typically measured by a number of pixels present inside the relevant contour. In the case of wall area, interior contours (i.e., the vessel lumen) may be subtracted from the outer wall. Due to vessel remodeling and varying morphology, vessel wall area measurements may represent a more accurate way of capturing total plaque burden and representative risk than clinically used measurements of vessel stenosis. A commonly reported used wall area measurement is normalized wall index, discussed in the following section.

Thickness Thickness is typically represented as maximum wall thickness (MaxWT) and is defined by the thickest point of the vessel wall in the imaging coverage. Measurements of arterial wall thickness have been shown to be effective at differentiating lesions with and without LRNC. For ipsilateral atherothrombotic risk [25], MaxWT was predictive of ipsilateral ischemic events (HR, 1.6; 95% CI, 1.1–2.3). In a recent cross-sectional study based on over 1000 subjects who had suffered TIA/stroke (CARE II), MaxWT was also found to be a strong discriminator to identify high-risk plaque as compared to stenosis measurement. On the other hand, if one is looking for a marker of generalized CV health/risk, mean wall thickness may also be useful. For example, in Mani et al. [26], subjects with prior MACE had higher mean wall thickness than those without. In MESA [19] the JHU group reported that MRI-measured mean wall thickness was associated with CVD outcomes.

Normalized Wall Index Normalized wall index (NWI) is calculated as wall area divided by total vessel area (wall area/(lumen + wall)area) ×100% and provides a measure of lesion burden that takes into account differences in the wall area for vessels of different diameters (i.e., the common, bulb, and internal carotid arteries). Saam et al. in a study published in 2007 [8] introduced this concept in carotid VWI and showed that a higher value for NWI is indicative of an artery with greater plaque burden. Since then, many studies have used this parameter in population-based studies [21] in different arteries and vascular beds, such as intracranial and peripheral arteries [27–29], and in comparisons of atherosclerosis burden between vascular beds [28–31].

Eccentricity Vessel wall eccentricity, a concept initiated in coronary artery atherosclerosis analysis [9], has been implicated as a key feature of VP and has been defined as minimum wall thickness divided by maximum wall thickness [32]. It is introduced based on considerations of vessel wall remodeling and the impact of hemodynamic forces. With 3D vessel wall lumen and outer wall boundaries identified, eccentricity can be easily measured, and revised definitions have been used in a number of studies [9]. A study by Mossa-Basha et al. applied it to intracranial vessels and found it to be an important indicator of atherosclerotic disease diagnosis [33]. Another study found it to be an important factor in looking at plaque distribution and structural stress [34]. A paper by Li et al. found that measures of plaque eccentricity are associated with preserved lumen size and advanced plaque features such as larger plaque burden, more lipid content, and increased calcification in femoral arteries [35].

Plaque Composition

Prior to measuring plaque composition, multi-contrast MR images are obtained, typically including black blood T1W and T2W and bright blood time-of-flight (TOF) sequences [36–40]. After acquisition, images must be registered to account for patient movement and coverage of sequence.

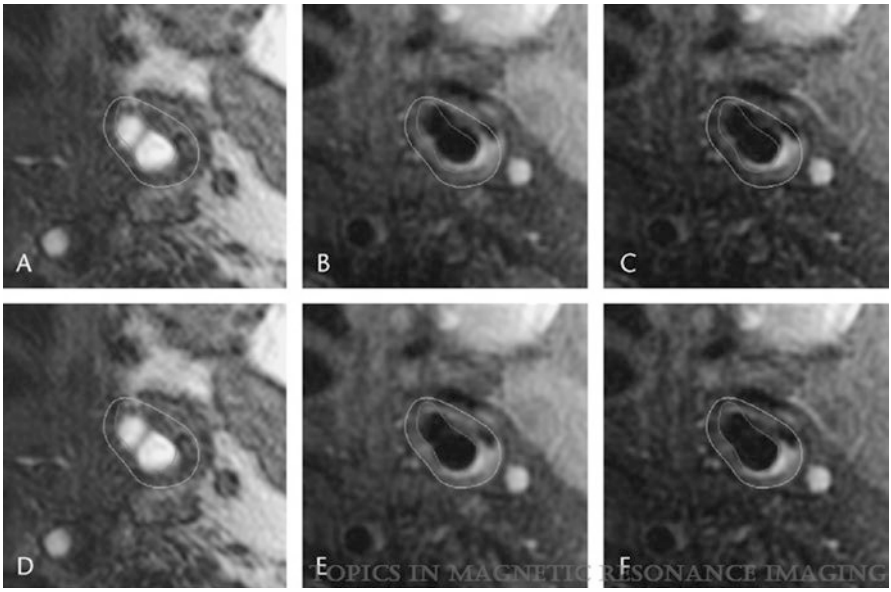

Fig. 14.3 Registration: lumen and wall boundaries mapped to TOF (**a**), PDW (**b**), and T2W (**c**) images show misalignment that is corrected by the registration algorithm (**d–f**). (Magnetic Resonance Imaging of Carotid Atherosclerosis: Plaque Analysis, Kerwin et al. [20]. Copyright © 2019 Wolters Kluwer Health, Inc. All rights reserved)

Once registered (Fig. 14.3), plaque components can be manually identified by trained reviewers, and different tissues, such as lipid-rich necrotic core (LRNC), intraplaque hemorrhage, loose matrix, and calcification, can be identified with their boundaries traced. Relative tissue areas and volumes can then be calculated. Presence of these tissues and their sizes have been used in many studies that assess their relationships with risk of clinical events and atherosclerosis progression and regression [36].

Advanced Features

Image Segmentation and MEPPS

A major tool in VWI processing is image segmentation—a method for separating components of the vessel wall or regions of interest seen on imaging for further analysis and measurement. This is a highly challenging area for MRI, as vessel segmentation requires multiple contrast weightings and image registration to accurately capture the parameters presented above. Additionally, human review, or manual segmentation, methods are often time-consuming and require

specialized training, making them clinically unviable. While many automatic image segmentation methods exist, few have been evaluated against human reviewers and histological ground truth.

Morphology-enhanced probabilistic plaque segmentation (MEPPS) is an automated image processing tool that was developed to mimic successful segmentation by trained human reviewers [41]. Unlike other segmentation methods, which typically derive segmented regions from the intensity values in different contrast-weighted images, MEPPS uses morphologic distribution information as an important factor. MEPPS was tested in 142 sets of multi-contrast MR images in patients undergoing carotid endarterectomy, and results were compared to the ground truth from corresponding histology of the excised carotid plaques for regions identified as necrotic core, calcification, loose matrix, and fibrous tissue. The results showed correlations (R^2) for the histology confirmed areas of 0.78, 0.83, 0.41, and 0.82, respectively. By comparison, manual review by trained reviewers blinded to histological results yielded correlations of 0.71, 0.76, 0.33, and 0.78, respectively.

Subsequently, MEPPS has been used in multiple clinical studies and trials. MEPPS also has the advantages of being relatively simple to use and does not introduce concerns of inter-reader variability. In a study by Kerwin et al., MEPPS was used to evaluate signal feature differences between two field strengths [42] to assess changes in plaque tissue over time [43] and to support the claim of plaque compositional changes in prospective trials of pharmaceutical treatments of atherosclerosis [21, 22, 42–46].

Dynamic Contrast Enhancement and K^{trans}

For the vessel image processing parameters listed in section “Introduction”, contrast-enhanced imaging is treated no differently than non-contrast and may be conducted using CASCADE or other tools. For quantitative measures of plaque inflammation and angiogenesis (i.e., neovasculature that may permeate atherosclerotic plaques) however, dynamic contrast-enhanced magnetic resonance imaging (DCE-MRI) coupled with pharmacokinetic modeling must be used. Following imaging with a 2D DCE acquisition protocol, a Kalman filter-based algorithm called the Kalman filtering, registration, and smoothing algorithm is applied to simultaneously filter noise and register image motion. Quantitative DCE-MR parameters related to perfusion characteristics may then be derived. The simplest of these is integrated area under a curve, consisting of the area under the signal intensity versus time curve (AUC) with different durations, a model-free approach that is highly reproducible. This method, however, suffers from a lack of physiologic meaning. Therefore, a more advanced approach using the Patlak model for pharmacokinetic modeling was developed by Kerwin et al. [47] and validated with histology. This method estimates K^{trans} (the transfer constant reflecting permeability of

neovessels) and v_p (the fractional plasma volume) for each pixel by linear fitting. Both K^{trans} and v_p have been correlated with histological features of inflammation and angiogenesis in multiple studies [11, 48].

Intracranial VWI Analysis

As outlined in the AJNR consensus paper of [49], VWI's application includes atherosclerosis, vasculitis, Moyamoya disease, radiation-induced arteriopathy, and arterial dissection. Both vessel morphology and tissue signal feature information, especially on postcontrast application, are critical for the accurate diagnosis. The role of image processing, especially 3D-based techniques, is important to assist in the analysis. To date, there has been limited report on specialized analysis packages addressing the special needs for ICA analysis.

The Future of Image Processing Methods in VWI

Vessel wall imaging is still a field going through rapid development in terms of image acquisition techniques and potential areas of clinical and research applications. Imaging processing will play a key role in this development. There are four areas worth consideration.

First is on simplified methods of plaque analysis and with specific targeted applications that can facilitate the clinical adaptation of VWI. We have discussed the usage of several software packages in this chapter, but they are designed more as a research tool for clinical trials with detailed vessel wall morphology and composition analysis as the main purpose. In many situations, effective simple methods may be more useful for clinical applications.

Second is on adopting the advancement in image acquisition techniques. An exciting new trend in VWI is the use of quantitative T1 and T2 mapping techniques for tissue characterization. In some sense, these techniques may reduce the need for image processing. But in reality, tissue maps will always need to be combined with proper imaging processing in order to provide usable data. In other words, image processing may need to be adopted as part of the quantitative imaging techniques.

Third is on the integration of different VWI techniques in imaging processing. The description of image processing techniques in this chapter is focused on MRI-based data acquisition and the needs to address multi-contrast analysis. VWI is a vast field that includes other imaging modalities, such as ultrasound, PET, and CT, each offering different aspects of information on the vessel wall, with different spatial resolution and viewing angles. Being able to integrate these data sets together will provide a comprehensive view of vascular maps. Furthermore, beyond anatomic

images, blood flow, vessel wall compliance and elastographic properties can now be assessed by imaging [50–54]. Effective integration of these data with 3D anatomic VWI will also be very useful and exciting.

Fourth is on training of physicians and professionals on how to use analysis tools that will be paramount to advancement of this field.

Finally, we will touch on the role of artificial intelligence (AI). AI provides an exciting opportunity in VWI from image acquisition to image quality improvement and image processing. A recent study by Li et al. [55] introduced an AI-based technique to sort carotid VWI into normal, diseased, or severely diseased categories automatically, within minutes of the original MRI data being acquired. The technique was developed based on over 300 carotid scans in subjects with varying levels of atherosclerosis.

In summary, image processing plays a key role in acquisition, registration, and qualitative and quantitative measurement of vessel wall imaging, without which assessments of vessel wall status and risk would not be possible.

References

1. Glagov S, Weisenberg E, Zarins CK, Stankunavicius R, Kolettis GJ. Compensatory enlargement of human atherosclerotic coronary arteries. N Engl J Med. 1987;316(22):1371–5. https://doi.org/10.1056/NEJM198705283162204.
2. Mann JM, Davies MJ. Vulnerable plaque. Relation of characteristics to degree of stenosis in human coronary arteries. Circulation. 1996;94(5):928–31.
3. Virmani R, Burke AP, Kolodgie FD, Farb A. Vulnerable plaque: the pathology of unstable coronary lesions. J Interv Cardiol. 2002;15(6):439–46.
4. Naghavi M, Libby P, Falk E, Casscells SW, Litovsky S, Rumberger J, Badimon JJ, Stefanadis C, Moreno P, Pasterkamp G, Fayad Z, Stone PH, Waxman S, Raggi P, Madjid M, Zarrabi A, Burke A, Yuan C, Fitzgerald PJ, Siscovick DS, de Korte CL, Aikawa M, Juhani Airaksinen KE, Assmann G, Becker CR, Chesebro JH, Farb A, Galis ZS, Jackson C, Jang IK, Koenig W, Lodder RA, March K, Demirovic J, Navab M, Priori SG, Rekhter MD, Bahr R, Grundy SM, Mehran R, Colombo A, Boerwinkle E, Ballantyne C, Insull W, Schwartz RS, Vogel R, Serruys PW, Hansson GK, Faxon DP, Kaul S, Drexler H, Greenland P, Muller JE, Virmani R, Ridker PM, Zipes DP, Shah PK, Willerson JT. From vulnerable plaque to vulnerable patient: a call for new definitions and risk assessment strategies: part I. Circulation. 2003;108(14):1664–72. https://doi.org/10.1161/01.CIR.0000087480.94275.97.
5. Underhill HR, Hatsukami TS, Fayad ZA, Fuster V, Yuan C. MRI of carotid atherosclerosis: clinical implications and future directions. Nat Rev Cardiol. 2010;7(3):165–73. https://doi.org/10.1038/nrcardio.2009.246.
6. Underhill HR, Hatsukami TS, Cai J, Yu W, DeMarco JK, Polissar NL, Ota H, Zhao X, Dong L, Oikawa M, Yuan C. A noninvasive imaging approach to assess plaque severity: the carotid atherosclerosis score. AJNR Am J Neuroradiol. 2010;31(6):1068–75. https://doi.org/10.3174/ajnr.A2007. PubMed PMID: 20093315; PMCID: PMC2885536.
7. Virmani R, Burke AP, Farb A, Kolodgie FD. Pathology of the unstable plaque. Prog Cardiovasc Dis. 2002;44(5):349–56.
8. Saam T, Yuan C, Chu B, Takaya N, Underhill H, Cai J, Tran N, Polissar NL, Neradilek B, Jarvik GP, Isaac C, Garden GA, Maravilla KR, Hashimoto B, Hatsukami TS. Predictors of carotid atherosclerotic plaque progression as measured by noninvasive magnetic resonance imaging.

Atherosclerosis. 2007;194(2):e34–42. https://doi.org/10.1016/j.atherosclerosis.2006.08.016. PubMed PMID: 16978632; PMCID: PMC2243074.
9. Mintz GS, Popma JJ, Pichard AD, Kent KM, Satler LF, Chuang YC, DeFalco RA, Leon MB. Limitations of angiography in the assessment of plaque distribution in coronary artery disease: a systematic study of target lesion eccentricity in 1446 lesions. Circulation. 1996;93(5):924–31.
10. Saba L, Yuan C, Hatsukami TS, Balu N, Qiao Y, DeMarco JK, Saam T, Moody AR, Li D, Matouk CC, Johnson MH, Jäger HR, Mossa-Basha M, Kooi ME, Fan Z, Saloner D, Wintermark M, Mikulis DJ, Wasserman BA, VWISGotASo N. Carotid artery wall imaging: perspective and guidelines from the ASNR vessel wall imaging study group and expert consensus recommendations of the American Society of Neuroradiology. AJNR Am J Neuroradiol. 2018;39(2):E9–E31. Epub 2018/01/11. https://doi.org/10.3174/ajnr.A5488.
11. Kerwin WS, O'Brien KD, Ferguson MS, Polissar N, Hatsukami TS, Yuan C. Inflammation in carotid atherosclerotic plaque: a dynamic contrast-enhanced MR imaging study. Radiology. 2006;241(2):459–68. PMCID: 16966482.
12. Wasserman BA, Casal SG, Astor BC, Aletras AH, Arai AE. Wash-in kinetics for gadolinium-enhanced magnetic resonance imaging of carotid atheroma. J Magn Reson Imaging. 2005;21(1):91–5. https://doi.org/10.1002/jmri.20228.
13. Owen DR, Shalhoub J, Miller S, Gauthier T, Doryforou O, Davies AH, Leen EL. Inflammation within carotid atherosclerotic plaque: assessment with late-phase contrast-enhanced US. Radiology. 2010;255(2):638–44. https://doi.org/10.1148/radiol.10091365.
14. Carr JJ. Calcium scoring for cardiovascular computed tomography: how, when and why? Radiol Clin N Am. 2019;57(1):1–12. https://doi.org/10.1016/j.rcl.2018.09.002.
15. Agatston AS, Janowitz WR, Hildner FJ, Zusmer NR, Viamonte M, Detrano R. Quantification of coronary artery calcium using ultrafast computed tomography. J Am Coll Cardiol. 1990;15(4):827–32.
16. O'Leary DH, Polak JF. Intima-media thickness: a tool for atherosclerosis imaging and event prediction. Am J Cardiol. 2002;90(10C):18L–21L.
17. O'Leary DH, Polak JF, Kronmal RA, Manolio TA, Burke GL, Wolfson SK. Carotid-artery intima and media thickness as a risk factor for myocardial infarction and stroke in older adults. Cardiovascular Health Study Collaborative Research Group. N Engl J Med. 1999;340(1):14–22. https://doi.org/10.1056/NEJM199901073400103.
18. Wasserman BA, Sharrett AR, Lai S, Gomes AS, Cushman M, Folsom AR, Bild DE, Kronmal RA, Sinha S, Bluemke DA. Risk factor associations with the presence of a lipid core in carotid plaque of asymptomatic individuals using high-resolution MRI: the multi-ethnic study of atherosclerosis (MESA). Stroke. 2008;39(2):329–35. Epub 2008/01/03. https://doi.org/10.1161/STROKEAHA.107.498634.
19. Zavodni AE, Wasserman BA, McClelland RL, Gomes AS, Folsom AR, Polak JF, Lima JA, Bluemke DA. Carotid artery plaque morphology and composition in relation to incident cardiovascular events: the Multi-Ethnic Study of Atherosclerosis (MESA). Radiology. 2014;271(2):381–9. Epub 2014/03/04. https://doi.org/10.1148/radiol.14131020. PubMed PMID: 24592924; PMCID: PMC4263652.
20. Kerwin W, Xu D, Liu F, Saam T, Underhill H, Takaya N, Chu B, Hatsukami T, Yuan C. Magnetic resonance imaging of carotid atherosclerosis: plaque analysis. Top Magn Reson Imaging. 2007;18(5):371–8. PMCID: 18025991.
21. Sun J, Zhao XQ, Balu N, Neradilek MB, Isquith DA, Yamada K, Cantón G, Crouse JR, Anderson TJ, Huston J, O'Brien K, Hippe DS, Polissar NL, Yuan C, Hatsukami TS. Carotid plaque lipid content and fibrous cap status predict systemic CV outcomes: the MRI Substudy in AIM-HIGH. JACC Cardiovasc Imaging. 2017;10(3):241–9. https://doi.org/10.1016/j.jcmg.2016.06.017. PubMed PMID: 28279371; PMCID: PMC5347460.
22. Underhill HR, Yuan C, Zhao XQ, Kraiss LW, Parker DL, Saam T, Chu B, Takaya N, Liu F, Polissar NL, Neradilek B, Raichlen JS, Cain VA, Waterton JC, Hamar W, Hatsukami TS. Effect of rosuvastatin therapy on carotid plaque morphology and composition in moderately hyper-

cholesterolemic patients: a high-resolution magnetic resonance imaging trial. Am Heart J. 2008;155(3):584–8. PMCID: 18294500.
23. Zhao XQ, Dong L, Hatsukami T, Phan BA, Chu B, Moore A, Lane T, Neradilek MB, Polissar N, Monick D, Lee C, Underhill H, Yuan C. MR imaging of carotid plaque composition during lipid-lowering therapy a prospective assessment of effect and time course. JACC Cardiovasc Imaging. 2011;4(9):977–86. https://doi.org/10.1016/j.jcmg.2011.06.013. PubMed PMID: 21920335; PMCID: PMC3638021.
24. O'Brien KD, Hippe DS, Chen H, Neradilek MB, Probstfield JL, Peck S, Isquith DA, Canton G, Yuan C, Polissar NL, Zhao XQ, Kerwin WS. Longer duration of statin therapy is associated with decreased carotid plaque vascularity by magnetic resonance imaging. Atherosclerosis. 2016;245:74–81. https://doi.org/10.1016/j.atherosclerosis.2015.11.032.
25. Takaya N, Yuan C, Chu B, Saam T, Underhill H, Cai J, Tran N, Polissar NL, Isaac C, Ferguson MS, Garden GA, Cramer SC, Maravilla KR, Hashimoto B, Hatsukami TS. Association between carotid plaque characteristics and subsequent ischemic cerebrovascular events: a prospective assessment with magnetic resonance imaging - initial results. Stroke. 2006;37:818–23.
26. Mani V, Muntner P, Gidding SS, Aguiar SH, El Aidi H, Weinshelbaum KB, Taniguchi H, van der Geest R, Reiber JH, Bansilal S, Farkouh M, Fuster V, Postley JE, Woodward M, Fayad ZA. Cardiovascular magnetic resonance parameters of atherosclerotic plaque burden improve discrimination of prior major adverse cardiovascular events. J Cardiovasc Magn Reson. 2009;11:10. Epub 2009/04/24. https://doi.org/10.1186/1532-429X-11-10. PubMed PMID: 19393089; PMCID: PMC2680849.
27. Zhou C, Qiao H, He L, Yuan C, Chen H, Zhang Q, Li R, Wang W, Du F, Li C, Zhao X. Characterization of atherosclerotic disease in thoracic aorta: a 3D, multicontrast vessel wall imaging study. Eur J Radiol. 2016;85(11):2030–5. Epub 2016/09/14. https://doi.org/10.1016/j.ejrad.2016.09.006.
28. Qiao Y, Guallar E, Suri FK, Liu L, Zhang Y, Anwar Z, Mirbagheri S, Xie YJ, Nezami N, Intrapiromkul J, Zhang S, Alonso A, Chu H, Couper D, Wasserman BA. MR Imaging Measures of Intracranial Atherosclerosis in a Population-based Study. Radiology. 2016;280(3):860–8. Epub 2016/03/29. https://doi.org/10.1148/radiol.2016151124. PubMed PMID: 27022858; PMCID: PMC5006718.
29. Cao Y, Sun Y, Zhou B, Zhao H, Zhu Y, Xu J, Liu X. Atherosclerotic plaque burden of middle cerebral artery and extracranial carotid artery characterized by MRI in patients with acute ischemic stroke in China: association and clinical relevance. Neurol Res. 2017;39(4):344–50. Epub 2017/01/30. https://doi.org/10.1080/01616412.2017.1281196.
30. Qiao H, He Q, Chen Z, Xu D, Huang L, He L, Jiang L, Li R, Luo J, Yuan C, Zhao X. Identification of early atherosclerotic lesions in carotid arteries with quantitative characteristics measured by 3D MRI. J Magn Reson Imaging. 2016;44(5):1270–6. Epub 2016/04/15. https://doi.org/10.1002/jmri.25264.
31. Xu Y, Li D, Yuan C, Zhou Z, He L, Li R, Cui Y, Li Q, Zheng Z, Zhao X. Association of severity between carotid and intracranial artery atherosclerosis. Ann Clin Transl Neurol. 2018;5(7):843–9. Epub 2018/06/04. https://doi.org/10.1002/acn3.590. PubMed PMID: 30009201; PMCID: PMC6043773.
32. von Birgelen C, Mintz GS, de Vrey EA, Kimura T, Popma JJ, Airiian SG, Leon MB, Nobuyoshi M, Serruys PW, de Feyter PJ. Atherosclerotic coronary lesions with inadequate compensatory enlargement have smaller plaque and vessel volumes: observations with three dimensional intravascular ultrasound in vivo. Heart. 1998;79(2):137–42. PubMed PMID: 9538305; PMCID: PMC1728616.
33. Mossa-Basha M, Shibata DK, Hallam DK, de Havenon A, Hippe DS, Becker KJ, Tirschwell DL, Hatsukami T, Balu N, Yuan C. Added value of vessel wall magnetic resonance imaging for differentiation of nonocclusive intracranial vasculopathies. Stroke. 2017;48(11):3026–33. Epub 2017/10/13. https://doi.org/10.1161/STROKEAHA.117.018227. PubMed PMID: 29030476; PMCID: PMC5687293.
34. Costopoulos C, Huang Y, Brown AJ, Calvert PA, Hoole SP, West NEJ, Gillard JH, Teng Z, Bennett MR. Plaque rupture in coronary atherosclerosis is associated with increased plaque

structural stress. JACC Cardiovasc Imaging. 2017;10(12):1472–83. Epub 2017/07/19. https://doi.org/10.1016/j.jcmg.2017.04.017. PubMed PMID: 28734911; PMCID: PMC5725311.
35. Li F, McDermott MM, Li D, Carroll TJ, Hippe DS, Kramer CM, Fan Z, Zhao X, Hatsukami TS, Chu B, Wang J, Yuan C. The association of lesion eccentricity with plaque morphology and components in the superficial femoral artery: a high-spatial-resolution, multi-contrast weighted CMR study. J Cardiovasc Magn Reson. 2010;12:37. Epub 2010/07/01. https://doi.org/10.1186/1532-429X-12-37. PubMed PMID: 20591197; PMCID: PMC2904754.
36. Yuan C, Kerwin WS, Yarnykh VL, Cai J, Saam T, Chu B, Takaya N, Ferguson MS, Underhill H, Xu D, Liu F, Hatsukami TS. MRI of atherosclerosis in clinical trials. NMR Biomed. 2006;19(6):636–54. https://doi.org/10.1002/nbm.1065.
37. Toussaint JF, LaMuraglia GM, Southern JF, Fuster V, Kantor HL. Magnetic resonance images lipid, fibrous, calcified, hemorrhagic, and thrombotic components of human atherosclerosis in vivo. Circulation. 1996;94(5):932–8.
38. Hatsukami TS, Ferguson MS, Beach KW, Gordon D, Detmer P, Burns D, Alpers C, Strandness DE. Carotid plaque morphology and clinical events. Stroke. 1997;28(1):95–100.
39. Cai JM, Hatsukami TS, Ferguson MS, Small R, Polissar NL, Yuan C. Classification of human carotid atherosclerotic lesions with in vivo multicontrast magnetic resonance imaging. Circulation. 2002;106(11):1368–73.
40. Saam T, Ferguson MS, Yarnykh VL, Takaya N, Xu D, Polissar NL, Hatsukami TS, Yuan C. Quantitative evaluation of carotid plaque composition by in vivo MRI. Arterioscler Thromb Vasc Biol. 2005;25(1):234–9.
41. Liu F, Xu D, Ferguson MS, Chu B, Saam T, Takaya N, Hatsukami TS, Yuan C, Kerwin WS. Automated in vivo segmentation of carotid plaque MRI with Morphology-Enhanced probability maps. Magn Reson Med. 2006;55(3):659–68; PMCID: 16470594.
42. Kerwin WS, Liu F, Yarnykh V, Underhill H, Oikawa M, Yu W, Hatsukami TS, Yuan C. Signal features of the atherosclerotic plaque at 3.0 Tesla versus 1.5 Tesla: impact on automatic classification. J Magn Reson Imaging. 2008;28(4):987–95.
43. Yoneyama T, Sun J, Hippe DS, Balu N, Xu D, Kerwin WS, Hatsukami TS, Yuan C. In vivo semi-automatic segmentation of multicontrast cardiovascular magnetic resonance for prospective cohort studies on plaque tissue composition: initial experience. Int J Cardiovasc Imaging. 2016;32(1):73–81. Epub 2015/07/14. https://doi.org/10.1007/s10554-015-0704-0. PubMed PMID: 26169389; PMCID: PMC4707978.
44. Underhill HR, Kerwin WS, Hatsukami TS, Yuan C. Automated measurement of mean wall thickness in the common carotid artery by MRI: a comparison to intima-media thickness by B-mode ultrasound. J Magn Reson Imaging. 2006;24(2):379–87. https://doi.org/10.1002/jmri.20636.
45. Liu W, Balu N, Sun J, Zhao X, Chen H, Yuan C, Zhao H, Xu J, Wang G, Kerwin WS. Segmentation of carotid plaque using multicontrast 3D gradient echo MRI. J Magn Reson Imaging. 2012;35(4):812–9. https://doi.org/10.1002/jmri.22886. PubMed PMID: 22127812; PMCID: PMC3298637.
46. Sun J, Zhao XQ, Balu N, Hippe DS, Hatsukami TS, Isquith DA, Yamada K, Neradilek MB, Cantón G, Xue Y, Fleg JL, Desvigne-Nickens P, Klimas MT, Padley RJ, Vassileva MT, Wyman BT, Yuan C. Carotid magnetic resonance imaging for monitoring atherosclerotic plaque progression: a multicenter reproducibility study. Int J Cardiovasc Imaging. 2015;31(1):95–103. https://doi.org/10.1007/s10554-014-0532-7. PubMed PMID: 25216871; PMCID: PMC4297722.
47. Kerwin W, Hooker A, Spilker M, Vicini P, Ferguson M, Hatsukami T, Yuan C. Quantitative magnetic resonance imaging analysis of neovasculature volume in carotid atherosclerotic plaque. Circulation. 2003;107(6):851–6.
48. Kerwin WS, Oikawa M, Yuan C, Jarvik GP, Hatsukami TS. MR imaging of adventitial vasa vasorum in carotid atherosclerosis. Magn Reson Med. 2008;59(3):507–14. PMCID: 18306402.
49. Mandell DM, Mossa-Basha M, Qiao Y, Hess CP, Hui F, Matouk C, Johnson MH, Daemen MJ, Vossough A, Edjlali M, Saloner D, Ansari SA, Wasserman BA, Mikulis DJ, VWISGotASo

N. Intracranial vessel wall MRI: principles and expert consensus recommendations of the American Society of Neuroradiology. AJNR Am J Neuroradiol. 2017;38(2):218–29. Epub 2016/07/28. https://doi.org/10.3174/ajnr.A4893.

50. Liu Z, Bai Z, Huang C, Huang M, Huang L, Xu D, Zhang H, Yuan C, Luo J. Inter-operator reproducibility of carotid elastography for identification of vulnerable atherosclerotic plaques. IEEE Trans Ultrason Ferroelectr Freq Control. 2019;66:505. Epub 2018/12/19. https://doi.org/10.1109/TUFFC.2018.2888479.
51. Di Leo N, Venturini L, de Soccio V, Forte V, Lucchetti P, Cerone G, Alagna G, Caratozzolo M, Messineo D, Di Gioia C, Di Marzo L, Fresilli D, De Vito C, Pugliese G, Cantisani V, D'Ambrosio F. Multiparametric ultrasound evaluation with CEUS and shear wave elastography for carotid plaque risk stratification. J Ultrasound. 2018;21(4):293–300. Epub 2018/10/31. https://doi.org/10.1007/s40477-018-0320-7. PubMed PMID: 30378007; PMCID: PMC6237715.
52. Cloutier G, Cardinal MR, Ju Y, Giroux MF, Lanthier S, Soulez G. Carotid plaque vulnerability assessment using ultrasound elastography and echogenicity analysis. AJR Am J Roentgenol. 2018;211(4):847–55. Epub 2018/08/30. https://doi.org/10.2214/AJR.17.19211.
53. Huang C, He Q, Huang M, Huang L, Zhao X, Yuan C, Luo J. Non-invasive identification of vulnerable atherosclerotic plaques using texture analysis in ultrasound carotid elastography: an in vivo feasibility study validated by magnetic resonance imaging. Ultrasound Med Biol. 2017;43(4):817–30. Epub 2017/01/30. https://doi.org/10.1016/j.ultrasmedbio.2016.12.003.
54. Andrews JPM, Fayad ZA, Dweck MR. New methods to image unstable atherosclerotic plaques. Atherosclerosis. 2018;272:118–28. Epub 2018/03/14. https://doi.org/10.1016/j.atherosclerosis.2018.03.021.
55. Li Chen, Huilin Zhao, Niranjan Balu, Xihai Zhao, Rui Li, Jianrong Xu, Thomas Hatsukami, Jenq-Neng Hwang, Chun Yuan editors. Carotid artery localization and lesion classification on 3D-MERGE MRI using neural network and object tracking methods. ISMRM, Paris; 2018.
56. Yuan C, Beach KW, Smith LH Jr, Hatsukami TS. Measurement of atherosclerotic carotid plaque size in vivo using high resolution magnetic resonance imaging. Circulation. 1998;98(24):2666–71.
57. Zhang S, Cai J, Luo Y, Han C, Polissar NL, Hatsukami TS, Yuan C. Measurement of carotid wall volume and maximum area with contrast-enhanced 3D MR imaging: initial observations. Radiology. 2003;228(1):200–5.

Chapter 15
Vessel Wall Imaging in the Era of Artificial Intelligence

Niranjan Balu, Zechen Zhou, and Chun Yuan

Introduction

Artificial intelligence (AI) in medicine typically uses advanced computational algorithms to perform diagnosis comparable to doctors or domain experts, by mathematically modeling human intelligence, or neural structure or activities. It is beginning to be widely used in several fields of radiology such as in cancer, neuro and cardiovascular.

In this chapter, we will discuss AI methods that can learn and establish data-driven models particularly using deep neural networks to accomplish various imaging and analysis tasks, such as imaging acceleration, image quality enhancement, and image analysis for vessel wall imaging (VWI).

Vessel wall of arteries can be imaged by only a few imaging modalities since it requires high spatial resolution and high contrast to distinguish the vessel wall from surrounding tissues. So far, magnetic resonance imaging (MRI) is the most comprehensive noninvasive modality for VWI in various vasculatures [1, 2]. Ultrasound can also allow for noninvasive vessel wall images but only in certain locations such as in the carotid arteries. In addition, invasive imaging from the luminal side of vessels is possible with intravascular ultrasound or optical coherence tomography. However, these imaging schemes are typically limited to some short segments of the arteries at specific locations. Therefore, the opportunities for AI applications are greater for MRI and ultrasound owing to the larger number of datasets available for training.

N. Balu
University of Washington, Department of Radiology, Seattle, WA, USA

Z. Zhou
Philips Research North America, Cambridge, MA, USA

C. Yuan (✉)
University of Washington, Seattle, WA, USA
e-mail: cyuan@uw.edu

C. Yuan et al. (eds.), *Vessel Based Imaging Techniques*,
https://doi.org/10.1007/978-3-030-25249-6_15

Currently, the role of AI in VWI is still in its infancy. We will briefly discuss several examples of AI-based techniques for VWI in two aspects. From vessel wall MRI acquisition perspective, AI methods can provide new opportunities for image acquisition optimization to improve the image quality and reduce acquisition time. On the other hand, AI methods can provide more accurate and clinically oriented post-processing tools to offer various pathways for MRI and ultrasound vessel wall image analysis.

Vessel Wall MRI Acquisition

Vessel wall MRI usually requires high-resolution, large coverage, and black-blood (BB) imaging features in sequences design to meet the clinical needs for atherosclerotic plaque detection. High-resolution is required to accurately evaluate the vessel wall condition and stratify the disease stages. Atherosclerosis is a systemic disease of vessel walls. Therefore, screening the entire vascular bed requires a large coverage imaging scheme. Furthermore, BB imaging techniques ensure good image contrast between lumen and vessel wall, and enable more accurate plaque burden measurements. However, these imaging requirements increase the challenges for obtaining diagnostic image quality for clinical application. To achieve high-resolution imaging, there are inevitable signal-to-noise ratio (SNR) penalties during data acquisition. This SNR loss will be further aggravated when large coverage BB imaging techniques [3, 4] are applied. In addition, the high-resolution large coverage MRI scan requires a long data acquisition time that might pose further challenges in clinical settings, as some patients may have difficulties to keep still for a long time which may further degrade the image quality due to motion. In this section, we discuss the application of AI methods to enhance image quality and accelerate imaging acquisition.

Adequate SNR level and image sharpness are essential factors to detect the presence of small plaques and ensure the accuracy of morphological measurements such as vessel wall thickness and plaque burden. AI methods can retrospectively enhance the image quality in several aspects, including reduction of noise and artifact levels and improvement of image sharpness. These requirements for retrospective image quality enhancement are closely related to the state-of-the-art image restoration problems, such as image denoising and super-resolution. With the recent advent of supervised deep learning methods, properly trained deep convolutional neural networks (CNN) can further boost the image restoration performance while significantly reducing the processing time by using the more advanced graphic processing unit (GPU) hardware. In the image denoising task, the deep CNN approach can outperform other competing methods by 0.2 dB to 0.6 dB of Peak SNR (PSNR) measurements [5]. Also, this trained denoising CNN model has demonstrated good generalization capability to tackle several other image restoration tasks. In addition, some recent studies [6–8] have explored efficient neural network architectures and effective optimization objectives for single image super-resolution task to achieve

0.9–1.1 dB PSNR improvements on more accurate estimation of structural boundaries and detailed textures compared to conventional methods. However, application of these new AI-based image post-processing methods to vessel wall image quality enhancement requires further investigation to demonstrate its clinical value and benefits.

AI methods can also be used to further optimize the VWI data acquisition scheme. Coupled with an AI-based super-resolution method to restore high-frequency components, VWI MRI sequences can be designed to improve the SNR level when acquiring low-frequency components during sacrificing certain SNR level when high-frequency components acquisition. After the scan, the AI-based super-resolution method can be used to restore the high-frequency components. Turbo spin echo (TSE) imaging with variable flip angle (VFA) refocusing pulse train [9, 10] is such an example of a VWI sequence that can provide a trade-off between SNR level and the imaging point spread function (PSF) for one specific tissue type. However, due to the limitations in the sequence design strategy, other tissues may experience different signal evolutions leading to various PSF profiles or blurring effects. Even for one specific tissue, considering the scan efficiency and voxel size required for VWI, the SNR penalty might not be well compensated at 3.0 T to achieve an ideal PSF especially for long echo train lengths. Therefore, the combination of a SNR-priority VFA design scheme and the super-resolution post-processing may provide a better trade-off across scan efficiency, PSF, and SNR for BB 3D TSE acquisitions. A recent study [11] has demonstrated sharper delineation of intracranial vessel wall and plaque boundaries using this approach as illustrated in Fig. 15.1. Also, AI methods can provide new ways of sequence optimization via reinforcement learning. Traditional sequence optimization requires expertise to intuitively build the sequence from some basic modules and perform parametric optimization to achieve the best performance. A recent study [12] demonstrated the feasibility of AI agent learning from the canonical pulse

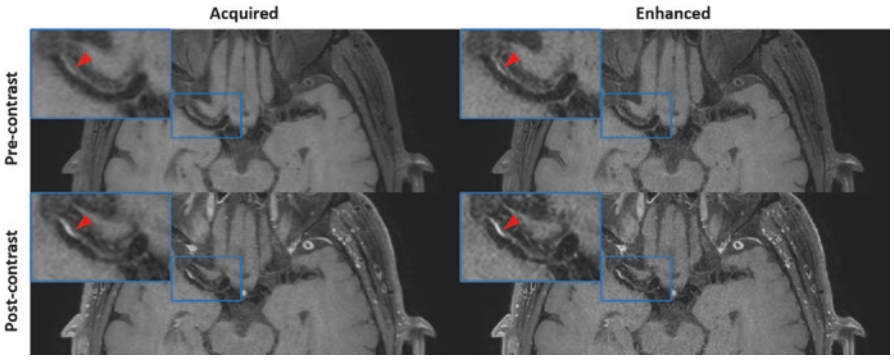

Fig. 15.1 An example of convolutional neural network (CNN)-based image enhancement from a patient acquired with optimized 3D T1-weighted TSE sequence. For both pre- and post-contrast images, CNN-enhanced results can provide clearer definition of the intracranial vessel wall and atherosclerotic plaque (as shown by red arrows) at the right middle cerebral artery

sequence to generate non-intuitive pulse sequences that can produce signals approximating Fourier spatial encoding. Further development of this AI-based sequence optimization method has the potential to provide more robust and better imaging sequences for VWI.

AI methods can also play an important role in imaging acceleration and help reduce the scan time and potential motion-related problems. One approach relies on deep learning-based super-resolution technique to estimate unacquired high-frequency components from the fully sampled low-frequency k-space and obtain a spatially interpolated image with an improved resolution. A recent work [13] demonstrated the feasibility of high-resolution image retrieval from its 4× downsampled image by using a 3D densely connected neural network model for intracranial vessel wall imaging that can result in 4-fold acceleration. The other approach to achieving imaging acceleration relies on the compressed sensing theory. A tailored deep neural network can represent the image in a more appropriate transformed sparse domain, so that the partially incoherent sampled k-space can more accurately restore the artifact free image than using universal or learned sparse transforms with shallow architectures [14–17]. In comparison to traditional imaging acceleration methods, deep learning-based image reconstruction approach may better preserve the natural appearance of MR images and, thus, pathologies. Compared to traditional image reconstruction, AI-based reconstruction has significantly reduced image reconstruction times thereby enabling an easier translation of this technique into the existing clinical workflow.

Vessel Wall Imaging Analysis

As described in the chapter for vessel wall image analysis, VWI analysis can be used for many purposes from screening to full comprehensive vascular analysis, to diagnose different vascular pathologies, and it can be applied in various different imaging modalities. AI methods may play important roles in all aspects of analysis.

MRI Vessel Wall Analysis

VWI and analysis are important for the differential diagnosis of diseases such as vasculitis, atherosclerosis, and arteriosclerosis. We will discuss atherosclerotic plaque analysis in detail in this section.

Both identification and quantification of plaque components have been shown to predict clinical outcomes. Plaque components such as lipid-rich necrotic core (LRNC), calcification, intraplaque hemorrhage (IPH), loose matrix, fibrous cap, and fibrous tissue can be identified using vessel wall MRI. The presence of intraplaque

hemorrhage in the carotid arteries is associated with stroke or transient ischemic attacks in the ipsilateral side [18]. Plaques with large LRNC, IPH, and a disrupted fibrous cap are deemed to be at higher risk for events [19, 20]. Moreover, plaque composition is also known to affect the progression of disease. For example, the presence of IPH is known to stimulate plaque progression in the same artery [21]. Quantitative measurements of the vessel wall were instrumental in describing such clinical associations. Combination of qualitative and quantitative information from plaque analysis form the basis of risks scores [19].

VWI provides a rich but complex set of images particularly in the case of MRI where multiple contrast weightings of the same anatomical location are produced. Information from these image weightings has to be combined for interpretation of the vessel wall composition. While such interpretation is common in radiology, the challenges for this application are the small size and variable plaque composition within a small region of plaque. While manual review is workable for plaque component identification, quantification requires segmentation from multiple image slices and leads to longer review time, increased inter-reader variability and intra-reader variability. AI is well suited to reducing the labor and measurement errors in quantification. Automatic segmentation methods can provide reproducible measurements, while human observers could check the accuracy of component identification and further train the models for improved performance.

An additional challenge in VWI is caused by the fact that VWI interpretation is not yet routine clinical practice. Therefore vessel wall analysis requires intensive training at selected centers. These factors also reduce the opportunity for more wide-ranging use of this technology. Once trained and validated, AI systems may provide the opportunity for more medical centers to bring the benefits of plaque imaging to their patients.

Automatic plaque component identification and quantification requires several processing steps. The essential step for quantification is plaque segmentation where each image pixel is classified into a plaque component label. However, there are other steps that may also be required depending upon the imaging modality and anatomical location. If multi-contrast MRI and/or multiple imaging time points need quantification, then image registration will be required. Complex arterial geometries also require additional efforts to identify and localize the plaque region to be quantified.

Plaque Segmentation Several semiautomated methods for plaque analysis using non-AI methods have been proposed [22–28]. While these methods have shown promise in fast segmentation of plaque components, there is additional improvement in accuracy that may be possible to obtain using newer AI-based methods. For example, the morphology-enhanced probability maps (MEPPS) method [22] was validated using histology from carotid endarterectomy specimens and showed correlations (R^2) of 0.78, 0.83, 0.41, and 0.82 for LRNC, calcification, loose matrix, and fibrous tissue, respectively, for segmented areas. Dong et al. introduced a CNN-based segmentation algorithm that, when compared to MEPPS using expert reviewer's manual

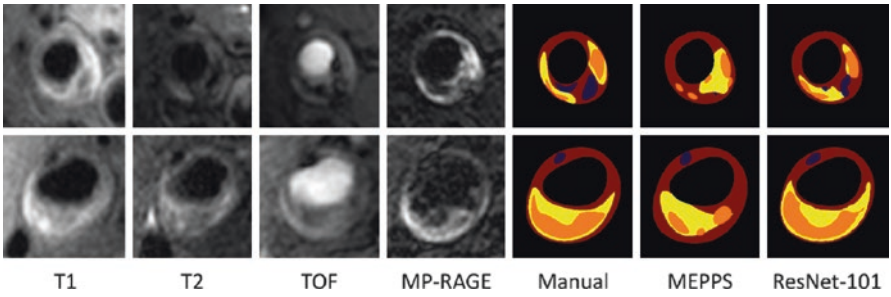

Fig. 15.2 AI-based segmentations using a convolutional neural network (ResNet-101) compared to MEPPS algorithm show better correspondence to the reference standard manual reader's contours. Contours shown are LRNC (yellow), IPH (orange), calcification (dark blue), and fibrous tissue (red). (Printed with permission from Dong et al. [29])

segmentation as the reference standard, showed better performance [29]. Using a residual network with 100 layers (ResNet-101) and a large dataset ($N = 1098$, 80% for training and 20% for testing), the automatic contours are more similar to human reviewers (Fig. 15.2) than the probability-based MEPPS algorithm. This indicates the potential for AI-based solutions to further improve automated plaque segmentation and provide contours similar to human reviewers. However, this was accomplished on pre-registered, well-matched multi-contrast images. In the future, such AI-based segmentation will greatly reduce the burden of plaque analysis and reduce the time to clinical decisions.

Similar AI-based plaque segmentation in other modalities such as ultrasound and computed tomography (CT) have the potential for greater benefits since the soft tissue contrast for discerning different plaque components is lower than for MRI. Using patch-based learning from just 56 subjects, Lekadir et al. trained a CNN using an expert observer's labels. The CNN achieved a Pearson's correlation coefficient of 0.92, 0.87, and 0.93, for the lipid core, fibrous tissue, and calcified tissues, respectively [30], in carotid artery plaques. Using CT images of coronary arteries and a cascade of CNNs, Zreik et al. classified coronary plaques into no plaque, non-calcified, mixed, calcified plaque [31]. While there was no segmentation done in this case, information about plaque type along the length of the artery was obtained since image patches of straightened arteries were used as input to the CNN.

Relatively straight arteries, such as the carotid bifurcation segment, or short peripheral artery segments may be more amenable for direct CNN-based segmentation. More complicated vessel geometries, such as the coronary arteries or intracranial arteries, will require preprocessing with approaches such as the one used by Zreik et al. [31] where locating the artery centerline was the first step using CT angiography.

Locating the Artery The segmentation methods above require the artery to be identified before the AI-based segmentation. In the above referenced works, identification of the artery was done by humans, either by drawing lumen/wall contours or

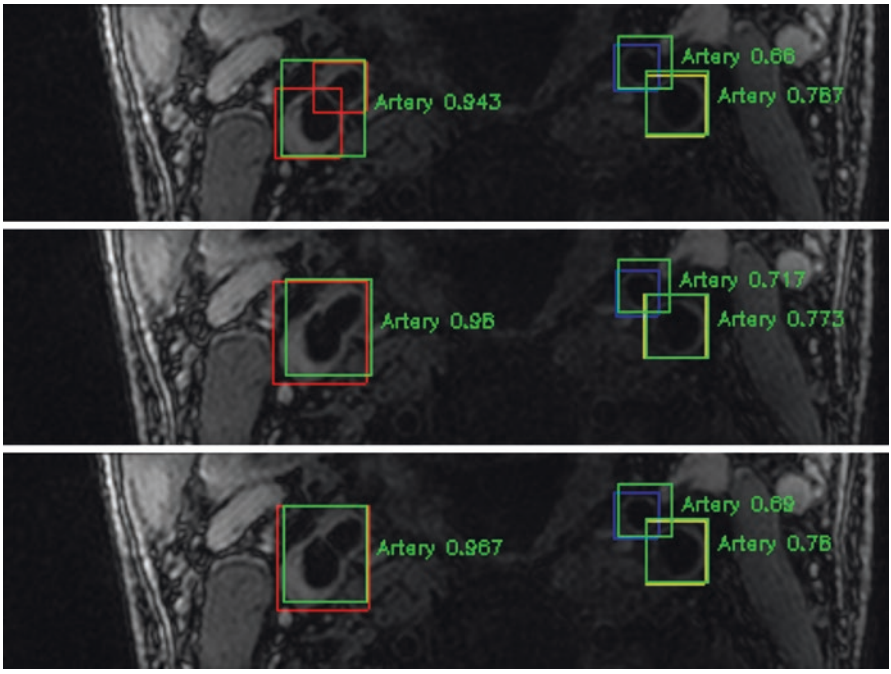

Fig. 15.3 Carotid artery locations are identified on axial reformats of 3D MERGE vessel wall MRI using a CNN approach. Three slices centered on the carotid bifurcation are shown. The artery locations are shown by green bounding boxes. After locating the artery, the state of the vessel wall can also be classified using CNN as done here with the red box indicating artery with wall thickening, yellow box indicating mild wall thickening, and blue box indicating normal wall. The numbers show the confidence in the artery classification (scale from 0.0 to 1.0)

identifying an image ROI to process. In contrast to tasks such as pixel classification or segmentation, identification of the artery in the entire scanned volume is a more difficult task for AI-based algorithms, whereas it is much easier for human observers. However, fully automated end-to-end analysis of scans requires automated methods to locate the artery. Li et al. demonstrated a CNN-based artery location algorithm that locates the carotid artery slice-by-slice directly on 3D MERGE vessel wall MRI [32]. Such an algorithm is capable of identifying the artery location (Fig. 15.3) and can be followed up by a classification or segmentation AI algorithm. This combination of 3D MERGE and vessel location and lesion detection may present unique methods for vessel wall screening.

Locating long and tortuous arteries such as intracranial arteries requires a different approach since it is difficult to obtain an image slice axial to the axis of the artery. Li et al. demonstrated an approach to identifying the artery location by AI-based segmentation of intracranial non-contrast MRA [33]. Figure 15.4 shows results of intracranial arteries identified on TOF MRA indicating that even distal arteries can be detected by the algorithm. Following such segmentation, slices axial to the artery at each point can be calculated automatically. After standard brain

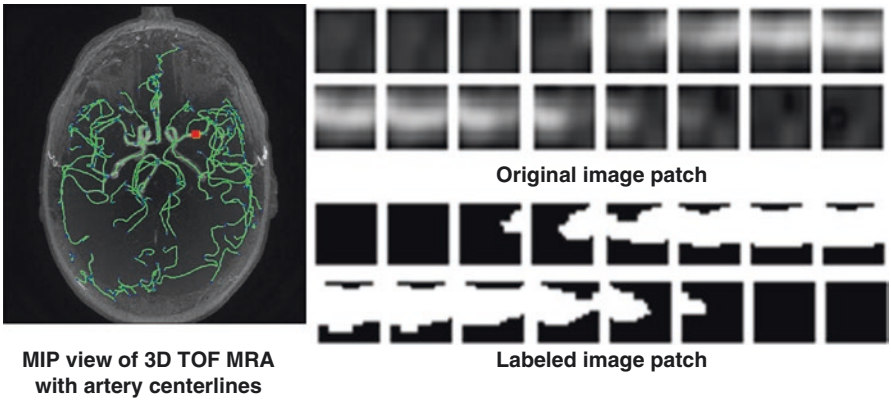

Fig. 15.4 Arterial centerlines shown in green were identified after TOF MRA pixels were segmented using a CNN. The training procedure involved segmentation of image patches (top right) and resulting pixel labels (bottom right) can be used to detect centerlines

registration procedures, the slice locations can be obtained from vessel wall MRI sequences obtained in the scan session.

Quantification of Gadolinium Vessel Wall Enhancement Gadolinium (Gd) contrast can provide improved diagnostic confidence for certain plaque components such as LRNC [34]. Gd enhancement is also indicative of plaque inflammation [35]. Thus quantitative measurement of Gd enhancement may provide additional biomarkers of risk. However, enhancement is difficult to quantify since a reference tissue normalization is required for measuring enhancement. While adjacent muscle may provide suitable reference for extracranial locations, intracranial arteries are challenging due to a lack of suitable reference tissue. An AI-based approach to automatic normalization and Gd enhancement measurement was suggested by Cai et al. [36]. Using a U-Net CNN, enhancement maps (EM) and post-contrast T1-weighted (T1w) images were synthesized from pre-contrast T1w images using the true EM as labels for training (Fig. 15.5).

Inference Based on Vessel Wall Imaging Beyond the process of feature identification, segmentation, and quantification, there is an additional step required to compile these elements into a clinically interpretable form that is predictive of patient outcomes. There is a wealth of informative studies in VWI linking VWI features to clinical outcomes. For example, carotid intraplaque hemorrhage was predictive of recurrent cerebrovascular events in patients with symptomatic high-grade carotid stenosis [18]. Similarly IPH was predictive of fibrous cap rupture (FCR) [20]. Using traditional multivariate analysis, Underhill et al. examined whether plaque components were predictive of IPH or FCR in a cohort of 344 subjects with 60% of subjects as a training set [19]. The carotid atherosclerosis score they developed accurately classified IPH (AUC = 0.91) and FCR (AUC = 0.93). Currently there is no study utilizing AI to link VWI features to clinical outcomes. However, the pre-

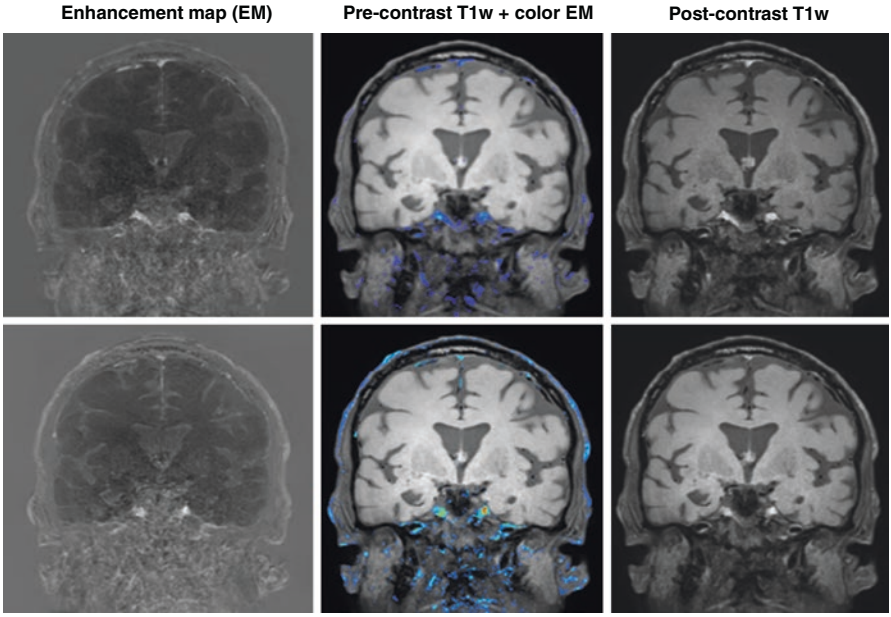

Fig. 15.5 Post-contrast T1w and enhancement maps were synthesized using CNN from pre-contrast T1w. Gadolinium enhancement map is displayed as grayscale in left column and color map in middle column. Top row shows the ground truth, while bottom row shows the synthesized versions

dictive ability of models developed previously, such as the carotid atherosclerosis score, can potentially be improved by using AI. AI algorithms may identify new risk predictors that were not identified by classical methods.

Ultrasound Vessel Wall Measurements

While MRI can provide comprehensive vessel wall measurements, there are other modalities that may be used for noninvasive VWI. Ultrasound is able to provide intima-media thickness (IMT) measurements that are confined to small segments of the artery such as the common carotid artery. IMT measurements have been widely used for population-based studies, and AI analysis can be useful for this application due to the large number of subjects to be analyzed.

Using 353 symptomatic and 420 asymptomatic carotid plaque ultrasound images and 14 bidimensional empirical mode decomposition (BEMD) and entropy features, Molinari et al. achieved accuracy of 91.43%, sensitivity of 97.26%, and specificity of 83.22% for classifying symptomatic and asymptomatic carotid plaques [37]. Machine learning methods have also been used for quantitative measurements for intima-media thickness (IMT) [38]. For example, a support vector machine

trained using 13-year follow-up data from 6459 MESA (the Multi-Ethnic Study of Atherosclerosis) participants outperformed the clinical guidelines-based ACC/AHA Risk Calculator by reducing the prescription of statins (11.4% vs 46.0%) while reducing the proportion of hard cardiovascular outcomes in subjects not prescribed statins (14.4% vs 23.8%), showing the potential for machine learning to improve clinical outcomes [39].

Summary

Vessel wall MRI is entering a new age with the advent of AI. There are exciting opportunities for the use of AI in improving image acquisition methods and analysis methods for VWI. Furthermore, AI may provide new risk predictors and ease the adoption of VWI in the clinical workflow by lowering the barriers for clinical application.

References

1. Mihai G, Chung YC, Merchant A, Simonetti OP, Rajagopalan S. T1-weighted-SPACE dark blood whole body magnetic resonance angiography (DB-WBMRA): initial experience. J Magn Reson Imaging. 2010;31(2):502–9.
2. Qiao Y, Steinman DA, Qin Q, Etesami M, Schär M, Astor BC, Wasserman BA. Intracranial arterial wall imaging using three-dimensional high isotropic resolution black bloodMRI at 3.0 Tesla. J Magn Reson Imaging. 2011;34(1):22–30.
3. J W, Yarnykh VL, Yuan C. Enhanced image quality in black-blood MRI using the improved motion-sensitized driven-equilibrium (iMSDE) sequence. J Magn Reson Imaging. 2010;31(5):1256–63.
4. Li L, Miller KL, Jezzard P. DANTE-prepared pulse trains: a novel approach to motion-sensitized and motion-suppressed quantitative magnetic resonance imaging. Magn Reson Med. 2012;68(5):1423–38.
5. Zhang K, Zuo W, Chen Y, Meng D, Zhang L. Beyond a Gaussian Denoiser: Residual Learning of Deep CNN for Image Denoising. IEEE Trans Image Process. 2017;26(7):3142–55.
6. Kim J, Lee JK, Lee KM. Accurate image super-resolution using very deep convolutional networks. In Proceedings of the IEEE Conference on Computer Vision and Pattern Recognition; 2016, pp. 1646–54.
7. Lim B, Son S, Kim H, Nah S, Lee KM. Enhanced deep residual networks for single image super-resolution. In Proceedings of the IEEE Conference on Computer Vision and Pattern Recognition; 2017, pp. 136–44.
8. Ledig C, Theis L, Huszar F, Caballero J, Cunningham A, Acosta A, Aitken A, Tejani A, Totz J, Wang Z, Shi W. Photo-realistic single image super-resolution using a generative adversarial network. In Proceedings of the IEEE Conference on Computer Vision and Pattern Recognition; 2017, pp. 4681–90.
9. Hennig J, Weigel M, Scheffler K. Calculation of flip angles for echo trains with predefined amplitudes with the extended phasegraph (EPG)-algorithm: principles and applications to hyperecho and TRAPS sequences. Magn Reson Med. 2004;51(1):68–80.
10. Busse RF, Hariharan H, Vu A, Brittain JH. Fast spin echo sequences with very long echo trains: design of variable refocusing flip angleschedules and generation of clinical T2 contrast. Magn Reson Med. 2006;55(5):1030–7.

11. Zhou Z, Chen S, Wu J, Bornert P, Yuan C. Deep convolutional neural network enhanced 3D high resolution turbo spin echo intracranial vessel wall imaging. In Proceedings of the 26th ISMRM Annual Meeting, Paris, France; 2018. p. 1049.
12. Zhu B, Liu J, Koonjoo N, Rosen B, Rosen M. AUTOmated pulse SEQuence generation (AUTOSEQ) using Bayesian reinforcement learning in an MRI physics simulation environment. In Proceedings of the 26th ISMRM Annual Meeting, Paris, France; 2018. p. 0438.
13. Chen Y, Fan Z, Shi F, Tian Z, Christodoulou A, Xie Y, Li D. Efficient super-resolution in intracranial vessel wall magnetic resonance imaging using 3D deep densely connected neural networks. In Proceedings of the 26th ISMRM Annual Meeting, Paris, France; 2018. p. 0657.
14. Yang Y, Sun J, Li H, Xu Z. Deep ADMM-Net for Compressive Sensing MRI. Advances in Neural Information Processing Systems (NIPS); 2016.
15. Hammernik K, Klatzer T, Kobler E, Recht MP, Sodickson DK, Pock T, Knoll F. Learning a variational network for reconstruction of accelerated MRI data. Magn Reson Med. 2018;79(6):3055–71.
16. Mardani M, Gong E, Cheng JY, Vasanawala SS, Zaharchuk G, Xing L, Pauly JM. Deep generative adversarial neural networks for compressive sensing (GANCS) MRI. IEEE Trans Med Imaging. 2019;38(1):167–79.
17. Chen F, Taviani V, Malkiel I, Cheng JY, Tamir JI, Shaikh J, Chang ST, Hardy CJ, Pauly JM, Vasanawala SS. Variable-density single-shot fast spin-echo MRI with deep learning reconstruction by using variational networks. Radiology. 2018;289(2):366–73.
18. Altaf N, MacSweeney ST, Gladman J, Auer DP. Carotid intraplaque hemorrhage predicts recurrent symptoms in patients with high-grade carotid stenosis. Stroke. 2007;38(5):1633–5.
19. Underhill HR, Hatsukami TS, Cai J, Yu W, DeMarco JK, Polissar NL, Ota H, Zhao X, Dong L, Oikawa M, Yuan C. A noninvasive imaging approach to assess plaque severity: the carotid atherosclerosis score. AJNR Am J Neuroradiol. 2010;31(6):1068–75.
20. van Dijk AC, Truijman MT, Hussain B, Zadi T, Saiedie G, de Rotte AA, Liem MI, van der Steen AF, Daemen MJ, Koudstaal PJ, Nederkoorn PJ, Hendrikse J, Kooi ME, van der Lugt A. Intraplaque hemorrhage and the plaque surface in carotid atherosclerosis: the plaque at RISK study (PARISK). AJNR Am J Neuroradiol. 2015;36(11):2127–33.
21. Sun J, Underhill HR, Hippe DS, Xue Y, Yuan C, Hatsukami TS. Sustained acceleration in carotid atherosclerotic plaque progression with intraplaque hemorrhage: a long-term time course study. JACC Cardiovasc Imaging. 2012;5(8):798–804.
22. Liu F, Xu D, Ferguson MS, Chu B, Saam T, Takaya N, Hatsukami TS, Yuan C, Kerwin WS. Automated in vivo segmentation of carotid plaque MRI with Morphology-Enhanced probability maps. Magn Reson Med. 2006;55(3):659–68.
23. Gao S, van 't Klooster R, van Wijk DF, Nederveen AJ, Lelieveldt BP, van der Geest RJ. Repeatability of in vivo quantification of atherosclerotic carotid artery plaque components by supervised multispectral classification. MAGMA. 2015;28(6):535–45.
24. Sun B, Giddens DP, Long R Jr, Taylor WR, Weiss D, Joseph G, Vega D, Oshinski JN. Automatic plaque characterization employing quantitative and multicontrast MRI. Magn Reson Med. 2008;59(1):174–80.
25. Liu W, Balu N, Sun J, Zhao X, Chen H, Yuan C, Zhao H, Xu J, Wang G, Kerwin WS. Segmentation of carotid plaque using multicontrast 3D gradient echo MRI. J Magn Reson Imaging. 2012;35(4):812–9.
26. van 't Klooster R, Naggara O, Marsico R, Reiber JH, Meder JF, van der Geest RJ, Touzé E, Oppenheim C. Automated versus manual in vivo segmentation of carotid plaque MRI. AJNR Am J Neuroradiol. 2012;33(8):1621–7.
27. Smits LP, van Wijk DF, Duivenvoorden R, Xu D, Yuan C, Stroes ES, Nederveen AJ. Manual versus automated carotid artery plaque component segmentation in high and lower quality 3.0 tesla MRI scans. PLoS One. 2016;11(12):e0164267.
28. Liu J, Balu N, Hippe DS, Ferguson MS, Martinez-Malo V, DeMarco JK, Zhu DC, Ota H, Sun J, Xu D, Kerwin WS, Hatsukami TS, Yuan C. Semi-automatic carotid intraplaque hemorrhage detection and quantification on Magnetization-Prepared Rapid Acquisition Gradient-Echo (MP-RAGE) with optimized threshold selection. J Cardiovasc Magn Reson. 2016;18(1):41.

29. Dong Y, Pan Y, Zhao X, Li R, Yuan C, Xu W. Identifying carotid plaque composition in MRI with convolutional neural networks. In Proceedings of the IEEE International Conference on Smart Computing (SMARTCOMP); 2017. https://doi.org/10.1109/SMARTCOMP.2017.7947015.
30. Lekadir K, Galimzianova A, Betriu A, Del Mar Vila M, Igual L, Rubin DL, Fernandez E, Radeva P, Napel S. A convolutional neural network for automatic characterization of plaque composition in carotid ultrasound. IEEE J Biomed Health Inform. 2017;21(1):48–55.
31. Zreik M, van Hamersvelt RW, Wolterink JM, Leiner T, Viergever MA, Isgum I. A recurrent CNN for automatic detection and classification of coronary artery plaque and stenosis in coronary CT angiography. IEEE Trans Med Imaging. 2018; https://doi.org/10.1109/TMI.2018.2883807.
32. Chen L, Zhao H, Balu N, Zhao X, Li R, Xu J, Hatsukami TS, Hwang JN, Yuan C. Automatic segmentation of carotid vessel wall using convolutional neural network. In Proceedings of the 26th ISMRM Annual Meeting, Paris, France; 2018. p. 3494.
33. Chen L, Xie Y, Sun J, Balu N, Mossa-Basha M, Pimentel K, Hatsukami TS, Hwang JN, Yuan C. 3D intracranial artery segmentation using a convolutional autoencoder. In Proceedings of the IEEE International Conference on Bioinformatics and Biomedicine (BIBM); 2017. pp. 714–7.
34. Takaya N, Cai J, Ferguson MS, Yarnykh VL, Chu B, Saam T, Polissar NL, Sherwood J, Cury RC, Anders RJ, Broschat KO, Hinton D, Furie KL, Hatsukami TS, Yuan C. Intra- and interreader reproducibility of magnetic resonance imaging for quantifying the lipid-rich necrotic core is improved with gadolinium contrast enhancement. J Magn Reson Imaging. 2006;24(1):203–10.
35. Kerwin WS, O'Brien KD, Ferguson MS, Polissar N, Hatsukami TS, Yuan C. Inflammation in carotid atherosclerotic plaque: a dynamic contrast-enhanced MR imaging study. Radiology. 2006;241(2):459–68.
36. Cai J, Balu N, Chen L, Zhou Z, Mossa-Basha M, Hatsukami TS, Yuan C. Contrast enhancement pattern study based on U-net. In Proceedings of the ISMRM Workshop on Machine Learning- Part II; 2018.
37. Molinari F, Raghavendra U, Gudigar A, Meiburger KM, Rajendra Acharya U. An efficient data mining framework for the characterization of symptomatic and asymptomatic carotid plaque using bidimensional empirical mode decomposition technique. Med Biol Eng Comput. 2018;56(9):1579–93.
38. Sudha S, Jayanthi KB, Rajasekaran C, Madian N, Sunder T. Convolutional neural network for segmentation and measurement of intima media thickness. J Med Syst. 2018;42(8):154.
39. Kakadiaris IA, Vrigkas M, Yen AA, Kuznetsova T, Budoff M, Naghavi M. Machine learning outperforms ACC/AHA CVD risk calculator in MESA. J Am Heart Assoc. 2018;7(22):e009476.

Part VII
Hemodynamics

Chapter 16
Hemodynamic Aspects of Vessel Wall Imaging: 4D Flow

Pim van Ooij and Michael Markl

Introduction

Cardiovascular MRI has undergone substantial developments over the last decades and offers capabilities for evaluating cardiac anatomy and function including the assessment of vascular anatomy and blood flow dynamic. Phase contrast (PC) MRI can be used to measure and quantify pulsatile blood flow in the human vascular system.

The basic principle has already been introduced by Carr and Purcell in 1954 who reported the observation of coherent motion on the MR signal [1] and by Hahn in 1960 who proposed to use nuclear precession to measure the velocity of sea water by means of phase shifts produced by magnetic field gradients [2]. Two decades later, Grant and Back were among the first to investigate the possibility of measuring flow velocity with MRI [3]. They called the technique "NMR rheotomography" and were visionary by remarking that "rheotomography may prove to be particularly useful for the noninvasive diagnosis of cardiovascular defects." Nearly 40 years later, many groups worldwide are using MRI flow measurements for the noninvasive diagnosis of cardiovascular defects. The first in vivo velocity map images and applications were reported in the early 1980s [4–7]. The initial measurement of a through-plane velocity profile in a two-dimensional (2D) slice of water flowing

P. van Ooij
Department of Radiology & Nuclear Medicine, Amsterdam University Medical Centers, location AMC, Amsterdam, The Netherlands

M. Markl (✉)
Department of Radiology, Northwestern University, Feinberg School of Medicine, Chicago, IL, USA

Department of Biomedical Engineering, McCormick School of Engineering, Northwestern University, Evanston, IL, USA
e-mail: mmarkl@northwestern.edu

C. Yuan et al. (eds.), *Vessel Based Imaging Techniques*,
https://doi.org/10.1007/978-3-030-25249-6_16

through a glass U-tube has evolved, and 2D and time-resolved (ECG-gated "CINE" imaging) PC-MRI has become available on all modern MR systems and is an integral part of clinical protocols assessing blood flow in the heart and large vessels [8–10]. More recently, the combination of CINE PC-MRI with three-dimensional (3D) spatial encoding and three-directional velocity encoding (termed "4D flow MRI") has made possible measurements of 3D blood flow dynamics in a 3D volume and over time (4D = 3D + time) [11–13].

This chapter will review the journey from simple 2D to 4D flow MRI for the advanced quantification and visualization of hemodynamic measures in vessel wall disease. We will describe the fundamental concepts of 4D flow MRI in terms of acquisition, data processing, as well as its applications to the assessment of altered blood flow dynamics in vascular diseases. A special emphasis is on the potential of 4D flow MRI to quantify important characteristics of the vessel wall such as wall shear stress (WSS) or pulse wave velocity (PWV). The chapter will conclude with a discussion of the current role of 4D flow MRI and future directions.

Background

From 2D to 4D Flow Image Acquisition

Flow imaging with MRI is based on the phase contrast (PC) technique, which enables the acquisition of spatially registered information on blood flow velocities simultaneously with morphological data within a single MRI measurement. In current clinical routine, PC-MRI is typically accomplished using methods that resolve two spatial dimensions (2D) in individual slices and encode a single time-resolved component of velocity directed perpendicularly to the 2D slice (through-plane velocity encoding). This approach allows measurements of forward, regurgitant, and shunt flows in congenital and acquired heart disease. In MRI, magnetic field gradient coils can create linearly varying magnetic fields along all three spatial dimensions on top of the main (static) magnetic field B_0. These magnetic field gradients cause spatially varying phase shifts of the source of the MRI signal (^{1}H proton spins in the human body) depending on the location of the source along the gradient. Spins that move along the direction of the gradient, e.g., flowing blood, acquire a different phase shift than the spins in adjacent static tissue [14].

The phase shift of the static media can be nulled by applying a magnetic field gradient with opposite polarity, whereas a phase shift for the moving spins will accumulate. The combination of both gradients is called a bipolar gradient [4] (see Fig. 16.1).

Using appropriate bipolar velocity encoding gradients, flow-dependent phase changes can be measured by playing out two acquisitions with different velocity dependent signal phase but otherwise identical sequence parameters. Subtraction of the two resulting phase images (i.e., calculation of phase difference images) allows

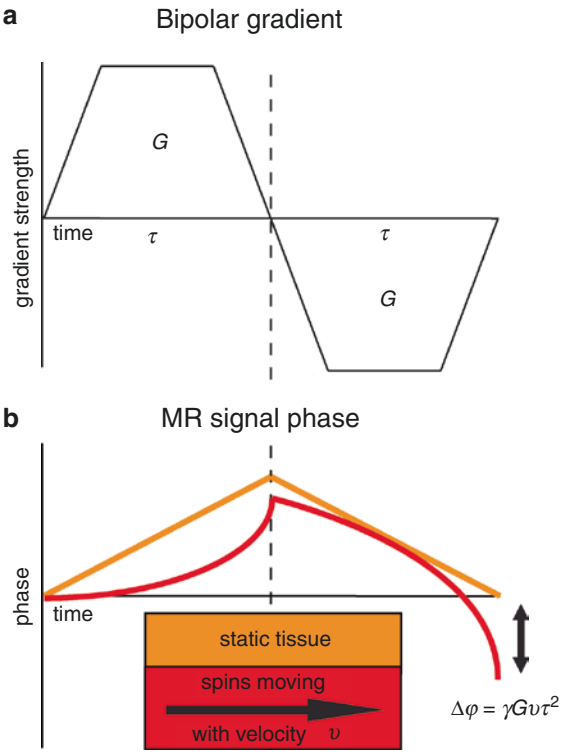

Fig. 16.1 (**a**) A bipolar gradient that causes (**b**) a phase shift for moving spins compared to zero phase for static spins. The phase shift $\Delta\varphi$ is proportional to the gyromagnetic ratio γ, the gradient strength G, the velocity of the moving spins v, and the gradient duration τ. Note that the equation represents a simplified situation where grant ramps are ignored for then coagulation of the calculation of phase shift $\Delta\varphi$

for the removal of the unknown background phase and calculation of velocity images [9].

With a bipolar gradient applied to the main direction of the blood flow, single-direction (e.g., through-plane) blood flow velocity is measured. Bipolar gradients can also be subsequently applied to two or three orthogonal axes to resolved blood flow velocities in two or three dimensions [15, 16].

To measure temporally resolved pulsatile blood flow velocities, a time-resolved (CINE) measurement can be performed [17, 18]. As illustrated in Fig. 16.2, PC-MRI data acquisition is split over multiple heartbeats, and data acquisition is gated to the cardiac cycle using the ECG signal (e.g., the R-wave) or a pulse oximeter reading. A series of time-resolved (CINE) images is collected representing the dynamics of the pulsatile blood flow during the cardiac cycle. Usually, one-directional ("through-plane") velocity encoding along the predominant blood flow direction is used to quantify blood flow in the heart, through cardiac valves, and in arteries and veins throughout the body. Typical 2D CINE PC-MRI images are illustrated in Fig. 16.2.

For over three decades, 2D CINE PC-MRI has been widely used for flow quantification in the aorta [19], the carotid arteries [20] and the intracranial vessels [21]. For routinely used 2D CINE PC-MRI, a slice for a 2D measurement is manually

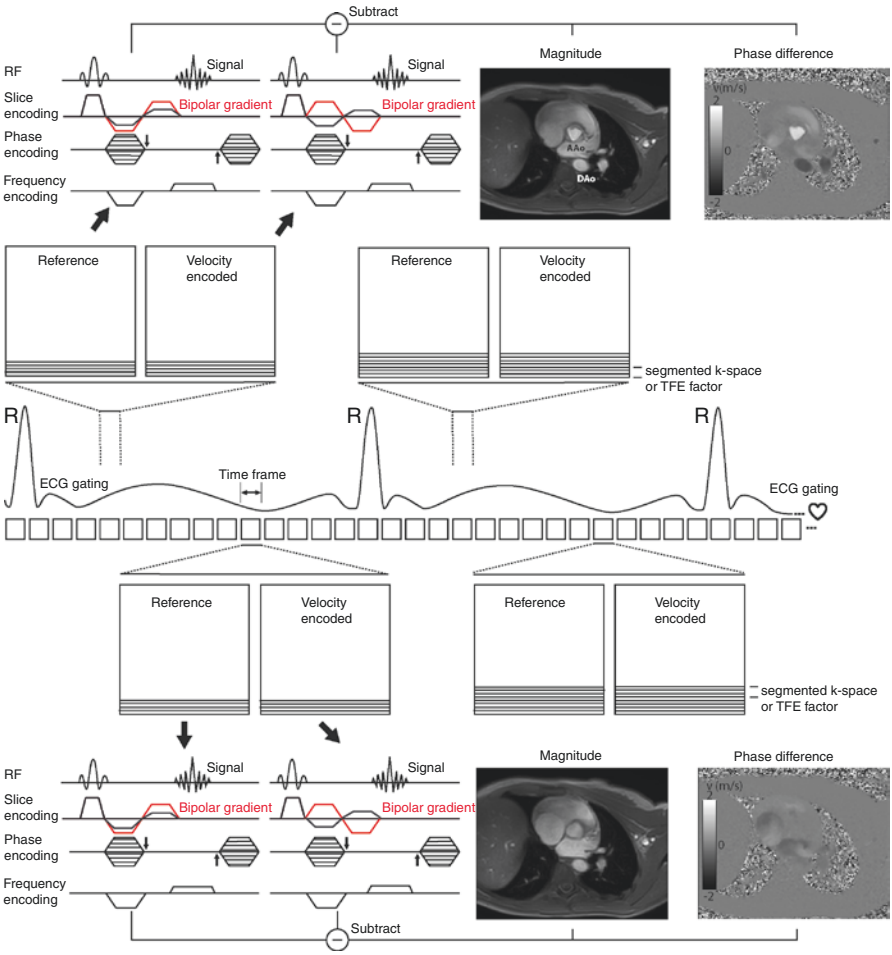

Fig. 16.2 In 2D CINE PC-MRI, ECG triggering over multiple R-R intervals is used to acquire a series of time frames over the cardiac cycle. For each time frame, reference MRI raw data (k-space) lines (without bipolar gradient) and velocity encoded k-space lines (with bipolar gradient) are acquired. The number of k-space lines acquired for each time frame is determined by the segmented k-space or turbo field echo factor. After completion, phase contrast magnitude anatomical images and phase difference containing the velocity information are reconstructed. The figure illustrates 2D PC-MRI acquisition at the site of the aortic valve peak systole (top) and diastole (bottom)

positioned perpendicular to a vessel, and blood flow velocity is encoded in one direction through the 2D slice. However, placement of the acquisition plane remains challenging and can lead to the underestimation of peak velocities if misplaced or not orthogonal to the flow of interest. This is a common occurrence in cases involving complex flow and where changes in flow direction occur throughout the cardiac cycle, such as with valvular stenosis, valvular regurgitation, complex congenital

heart disease, or aneurysms. These challenges can be addressed by three-dimensional (3D) PC-MRI with three-directional velocity encoding which can provide comprehensive information on the in vivo 3D blood flow dynamics with full volumetric coverage of the vascular region of interest. Wigström et al. were the first to implement a high spatial resolution and electrocardiogram (ECG)-gated 3D cine phase contrast pulse sequence, currently known as 4D flow MRI (4D = 3D+ time over the cardiac cycle, flow = three-directional velocity encoding) [22].

4D Flow Acquisition Methods and Techniques

Data Acquisition

In 4D flow MRI, velocity is encoded along all three spatial dimensions throughout the cardiac cycle, thus providing a time-resolved 3D velocity field [8, 23, 24]. As shown in Fig. 16.3a, three-directional velocity measurements can be achieved by interleaved four-point velocity encoding which acquires one reference image and three velocity-encoded images along three orthogonal (x, y, z) directions [25–27]. As for 2D CINE PC-MRI, data acquisition is synchronized with the cardiac cycle, and data collection is distributed over multiple cardiac cycles using "k-space segmentation" techniques (only a fraction of the entire 4D flow data is measured during each cardiac cycle; the data is successively collected over multiple RR intervals). For prospective ECG gating, where the acquisition starts after receiving the R signal of the QRS complex, some dead time toward the next R-wave should be reserved to account for heartbeat variations. The late portion of diastole is therefore not measured [17]. With retrospective gating, continuous acquisition is not synchronized to the heartbeat. Each k-space line is time-stamped and retrospectively interpolated to fixed time frames in the cardiac cycle, thereby enabling acquisition of the diastolic phases. After completion of the 4D flow acquisition, four time-resolved (CINE) 3D data sets are generated ("magnitude" data depicting anatomy and three flow data sets representing velocities "V_x, V_y, and V_z") as illustrated in Fig. 16.3b.

It should be noted that increasing 4D flow spatial resolution by reducing voxel size is possible but is accompanied by a decrease in signal-to-noise ratio (SNR) and thus image quality. Moreover, for volumetric acquisitions such as 4D flow MRI, scan times increase cubically with isotropic voxel size reduction.

An important (user-defined) 4D flow MRI parameter is the velocity encoding sensitivity (VENC), which represents the maximum flow velocity that can be acquired without velocity aliasing. When a velocity in a voxel exceeds VENC, velocity aliasing can occur which is typically visible as a sudden change from high to low velocity within a region of flow (see Fig. 16.4). If aliasing artifacts are present, accurate flow visualization and quantification may be compromised unless anti-aliasing correction can be successfully performed [28]. It is important to note, however, that velocity noise is directly related to the VENC [8]. Therefore, selecting a high VENC may alleviate the issue of velocity aliasing but will also increase the

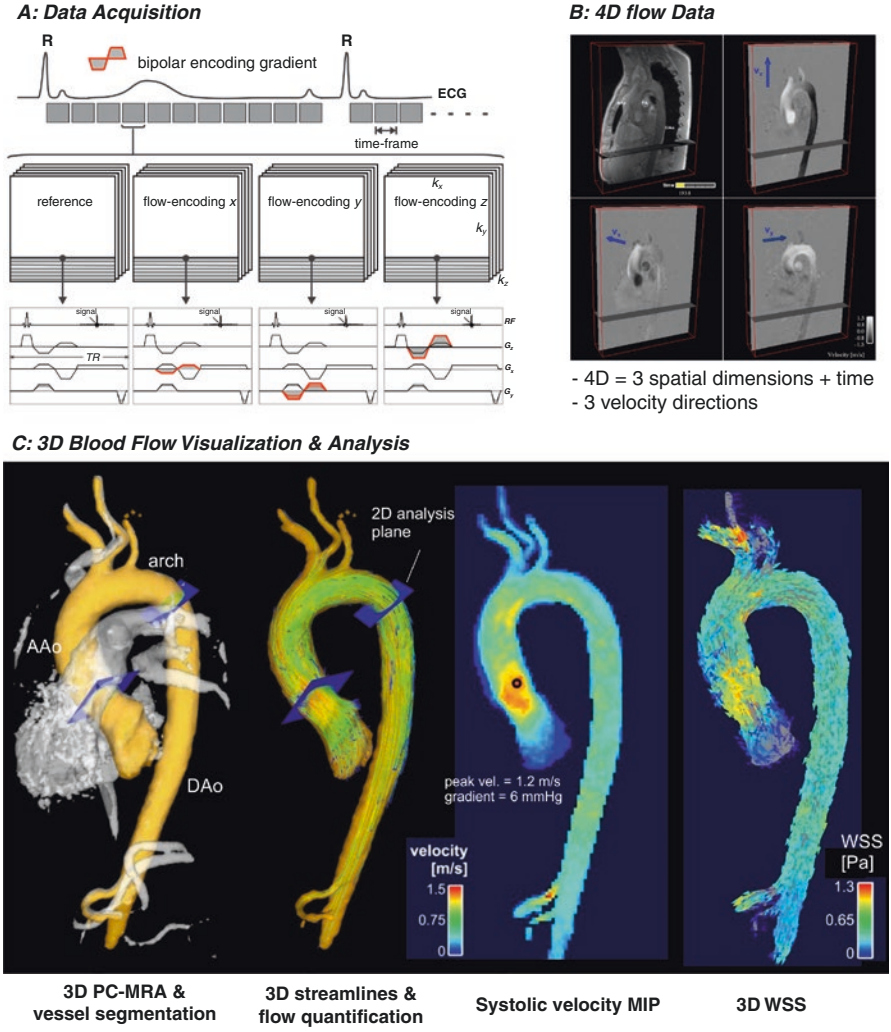

Fig. 16.3 Acquisition of 4D flow MRI data and analysis of hemodynamic metrics in the thoracic aorta of a healthy subject. (**a**) ECG synchronized 4D Flow MRI data acquisition. For each time frame, four 3D raw data sets are collected to measure three-directional blood flow velocities (v_x, v_y, v_z) with a reference scan and three velocity encoded acquisitions. k-space segmentation is used to collect a subset (N_{Seg}) of all required raw data (k-space) lines for each time frame. The selection of N_{Seg} determines the temporal resolution and total scan time. (**b**) 4D flow data comprises information along all three spatial dimensions, three velocity directions, and time in the cardiac cycle. (**c**) A 3D phase contrast angiogram (3D PC-MRA) can be calculated from 4D flow MRI data to aid visualization and provide a basis for the 3D segmentation of the aorta (orange rendering of aorta). Systolic streamlines allow for visual assessment of flow patterns and placement of analysis planes for retrospective flow quantification. Calculation of a systolic velocity maximum intensity projections (MIP) provides an overview over systolic velocity distribution and allows for volumetric quantification of peak systolic velocity (location of peak velocity is indicated by black circle in the ascending aorta). Advanced vessel wall characteristics can be derived such as systolic 3D wall shear stress (WSS) vectors along the aorta. AAo ascending aorta, DAo descending aorta

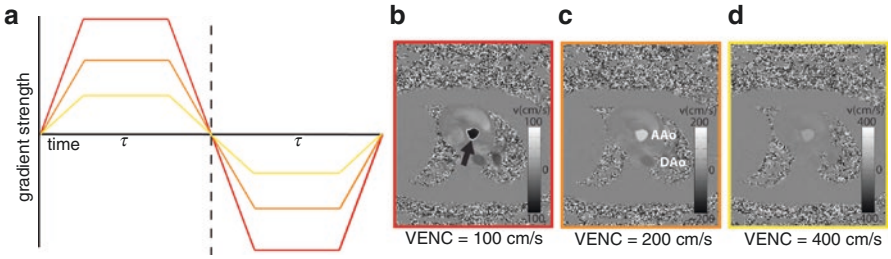

Fig. 16.4 (**a**) Bipolar gradients of higher strength and thus a low-VENC cause (**b**) aliasing (black arrow) in the phase difference images of the aorta, whereas aliasing is avoided when VENC is tailored to the expected maximum velocity in (**c**). (**d**) At a high VENC, the sensitivity to changes in aortic velocities is decreased. AAo ascending aorta, DAo descending aorta

Table 16.1 Typical (ranges of) scan parameters for three different anatomical regions

	k-space segmentation (turbo field echo factor)	(Isotropic) spatial resolution (mm^3)	Temporal resolution (ms)	VENC (cm/s)
Heart/aorta	1–3	2.0–3.0	20–60	150–400
Carotid	2–3	0.8–1.4	40–60	100–150
Intracranial	2–4	0.5–1.2	40–80	70–150

level of velocity noise in flow velocity images. VENC should thus be chosen as close to the peak velocity as possible. This is often accomplished by performing a fast low-resolution 2D PC-MRI "VENC scout" scan prior to 4D flow MRI to estimate the highest velocity in the vessel of interest and adjust VENC accordingly.

In Fig. 16.4, the principle of VENC is shown for through-plane 2D phase difference images of the aorta with severe velocity aliasing when the VENC is selected too low (high bipolar gradient). Unaliased flow velocities are achieved when the VENC is tailored to the expected maximum velocity (lower bipolar gradient).

In Table 16.1 typical ranges of scan parameters are shown for heart/aorta, carotid, and intracranial 4D flow MRI applications.

Data Acquisitions: Imaging Acceleration Techniques

Long scan times on the order of 10–20 minutes have previously relegated 4D flower MRI to the realm of research. However, current implementations are quickly approaching clinically feasible scan times, on the order of 2–8 minutes. Methodological improvements include echo planar imaging (EPI), where multiple Cartesian readouts are acquired after one excitation to obtain high spatial resolution [29]. Additional imaging acceptation is based on parole imaging such as sensitivity encoding (SENSE) [30, 31], generalized autocalibrating partially parallel acquisitions (GRAPPA) [32], k-t acquisition speed-up techniques (k-t BLAST) [33, 34], k-t GRAPPA [35], k-t principal component analysis (k-t PCA) [36, 37], and

CIRCUS [38]. Another promising technique to accelerate 4D flow MRI is compressed sensing where data is acquired in a sparse and random manner followed by nonlinear recovery of data [39, 40]. For example, aortic 4D flow MRI is now possible with a scan time of less than 2 minutes without substantial degradation of image quality [41].

Data Acquisitions: Non-Cartesian Sampling

An alternative technique that is increasingly used to accelerate 4D flow MRI is radial data sampling combined with undersampling (e.g., PC-VIPR – vastly undersampled isotropic projection reconstruction [42]). Radial sampling has two important advantages over Cartesian readouts: (1) sparse sampling results in streak image instead of fold-over artifacts which allows for higher undersampling factors [42] and (2) the center of k-space is continuously sampled and results in insensitivity to subject motion [43]. As an alternative, spiral k-space sampling can cover the entire k-space uniformly and rapidly [44], allowing for rapid 4D flow MRI velocity measurements [45–47]. However, both radial and spiral sampling are sensitive to eddy current effects which require efficient correction strategies, and image reconstruction is more computationally demanding. Alternatively, radial- and spiral-like trajectories can be implemented on a Cartesian grid, called pseudo-radial and pseudo-spiral trajectories [48, 49]. For example, a recently reported combination of pseudo-Cartesian acquisition schemes coupled with compressed sensing for imaging acceleration has shown great potential for fast and robust pediatric 4D flow MRI [50].

Data Acquisitions: Respiratory Control (Gating, Self-Gating)

For cardiothoracic and abdominal applications, methods for respiration control are needed to prevent image deterioration due to respiratory motion. Early efforts in MRI have focused on gating of the respiratory signal using bellows [51] or navigator echoes in a longitudinal beam placed on the diaphragm [52]. Most methods are based on accepting data in the expiration phase when chest motion is minimal and rejecting data acquired in the inspiration phase when the chest is moving. Other strategies minimize respiration-related image degradation by respiratory ordered phase encoding (ROPE): measurements at inspiration are attributed to the center of k-space, whereas the measurements at expiration are attributed to the edges of k-space [53]. Such strategies have been successfully implemented for 4D flow MRI [54] in combination with navigator gating [55]. Other promising approaches employ self-gating techniques, e.g., cross-correlation with reference breathing motion to identify different respiratory phases [56] or extracting respiratory and cardiac motion signals from additional and repeatedly sampled central k-space data [57].

4D Flow Analysis Methods and Techniques

Preprocessing and Phase Offset Error Corrections

4D flow MRI data are affected by systematic velocity encoding errors caused by magnetic field inhomogeneity, concomitant magnetic fields (Maxwell terms) [58], and eddy currents [59, 60]. Correction of these errors typically includes the identification of image regions that contain static tissue in order to estimate the spatial distribution of background phase offsets (using a first- or second-order fit to the static tissue phase difference data) [61]. Background phase errors can subsequently be removed by subtraction of the estimated offset from the entire velocity data [62].

It is common in 4D flow MRI that the VENC setting is lower than the maximum velocity in the measurement and that velocity aliasing occurs. With the assumption that adjacent pixel velocities in the temporal or slice direction should not differ more than VENC [28], aliased velocities can be automatically detected and corrected [63].

Visualization and Quantification of 4D Flow MRI Hemodynamics

For effective visualization of the information encoded in the large 4D flow MRI data sets (see Fig. 16.3b), many methods have been developed and include velocity vector display in three-dimensional space [64, 65] streamlines [66, 67], and path lines/particle traces [67].

Figure 16.3c illustrates 4D flow MRI-based evaluation of fundamental (flow, peak velocity) and advanced hemodynamic metrics (wall shear stress, WSS) based on a single acquisition. Visualization of the vascular geometry can be achieved from a 4D flow acquisition by generating a non-contrast 3D PC-MR angiogram (MRA). A surface rendering of the vascular structure of interest (see Fig. 16.3c, left) allows for regional orientation, analysis, and flow visualization. For qualitative visualization of 4D flow MRI data, 3D streamlines or time-resolved 3D path lines can be used for flow pattern visualization. Streamlines represent the instantaneous blood flow vector field for a single cardiac time-frame. For example, Fig. 16.3c illustrates the use of systolic 3D streamlines to visualize the spatial distribution and orientation of blood flow velocities. Color-coding by velocity magnitude facilitates the visual identification of regions with high systolic flow velocities. For visualization of the temporal evolution of 3D blood flow, time-resolved path lines are the method of choice. Time-resolved path lines are best viewed and displayed dynamically (movie mode) to fully appreciate the dynamic information and changes in blood flow over the cardiac cycle. It is important to differentiate between streamlines and path lines since the former represents the instantaneous tangent to the velocity vector at a given time in the cardiac cycle (e.g., peak systole), while the latter resemble traces of the dynamically time-varying blood flow over the cardiac cycle. 4D flow MRI can also be used to derive volumetric and maximum intensity projections (MIPs) of

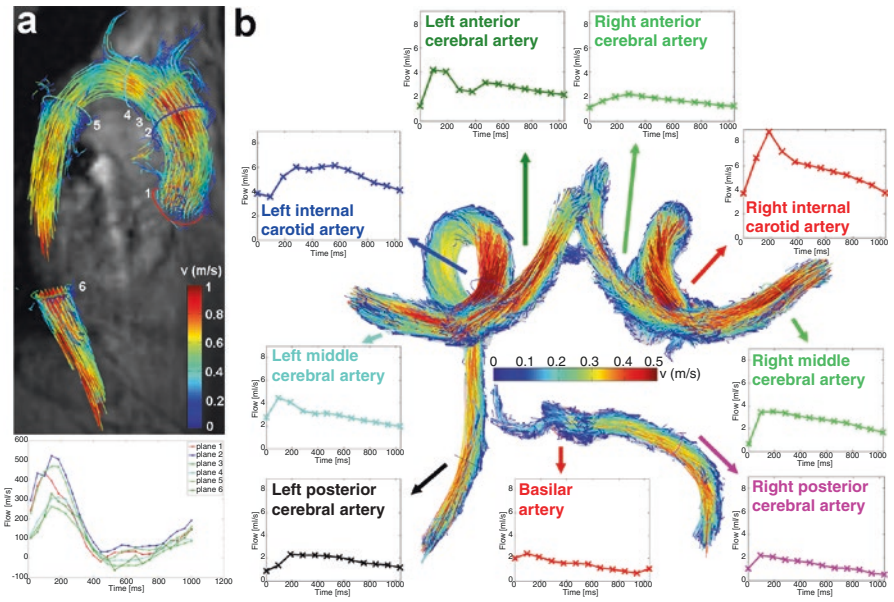

Fig. 16.5 (**a**) 3D flow visualization (path lines and with flow quantification in perpendicular 2D analysis planes at standardized locations in the healthy aorta) [68]. (**b**) 3D segmentation and flow visualization in the circle of Willis of a healthy volunteer. Flow quantification based on perpendicular 2D analysis planes allows for the systematic assessment of blood flow over the cardiac cycle in the entire circle of Willis

peak velocity for easy volumetric identification of peak flow velocities (see Fig. 16.3c).

For quantification of flow in a vessel, 2D analysis planes can be placed at any location along the vessel of interest (Fig. 16.3c) to calculate peak and mean velocities, total flow, net flow, or retrograde flow. Figure 16.5a illustrates aortic 4D flow MRI with subsequent 3D flow visualization (path lines) and flow quantification in six 2D analysis planes distributed along the thoracic aorta. Figure 16.5b depicts an example of comprehensive cerebrovascular 4D flow with 3D blood flow visualization in the large intracranial arteries and quantification of flow-time curves at all major circle of Willis arteries.

Advanced Hemodynamic Vessel Wall Metrics

In addition to 3D blood flow visualization and planar flow quantification, 4D flow MRI offers the opportunity to derive advanced hemodynamic measures such as vorticity [69, 70] and helicity [71, 72], wall shear stress (WSS) [73, 74],

pressure gradients [75, 76], viscous energy loss [77, 78], turbulent kinetic energy [79, 80], or pulse wave velocity (PWV) [81, 82]. This article will focus on the two parameters most relevant for vascular wall characterization: PWV and WSS.

Pulse Wave Velocity

It is well understood that arterial vascular stiffening (i.e., reduction of vessel wall elasticity) can lead to atherosclerosis and the development of vessel wall abnormalities and atherosclerotic plaques. Pulse wave velocity (PWV), the best known surrogate measure for arterial stiffness, is the speed of the pulsatile pressure wave that propagates along arteries in a heartbeat [83–85]. PWV is determined by the elastic modulus of the vessel, the vessel wall thickness, the vessel radius, and the density of blood (Moens-Korteweg equation) [85]. Thus, increased PWV is directly associated increased elastic modulus (i.e., stiffening) and vessel wall thickness. Both processes occur in early atherosclerosis, and PWV is thus considered an important indicator for the onset of this disease. A meta-analysis revealed that increased PWV and thus reduced aortic compliance is a strong predictor of future cardiovascular events and all-cause mortality. Moreover, an increase in aortic PWV by 1 m/s corresponded to an age-, sex-, and risk factor-adjusted risk increase of ca. 15% in total cardiovascular events [86]. Reliable measurement of PWV is thus of high interest, e.g., for monitoring vessel compliance during therapy [87, 88].

Carotid-femoral PWV using tonometry is the current reference standard to measure aortic compliance [89]. This method, however, is prone to errors and does not focus on regional compliance. Time-resolved 2D CINE PC-MRI provides a noninvasive estimate of PWV based on flow waveform measurements in analysis planes and allows focusing on the region of interest in patients, e.g., the thoracic aorta or carotid arteries [90–92]. Transit-time (TT) methods are typically employed to calculate temporal differences of specific flow waveforms features, e.g., timing differences of the foot of the waveform between two locations with known distance, as first described in 1989 for the aortic arch [93]. The accuracy of PWV quantification can be improved by adding velocity encoding directions [81] or using multiple measurement locations [94, 95].

PWV can be retrospectively quantified from 4D flow MRI data based on multiple pulsatile flow waveforms distributed homogenously along the entire course of the vessel. As shown in Fig. 16.6 for 4D flow-based PWV estimation in the thoracic aorta, flow-time curves are automatically extracted for each analysis plane, and a measure of blood travel time (e.g., time-to-foot) is derived. Aortic PWV (in m/s) is determined by a linear fit from data of the entire aorta [82, 96]. However, reliable PWV assessment requires measure of the rapid changes of which can only be achieved with sufficient temporal resolution.

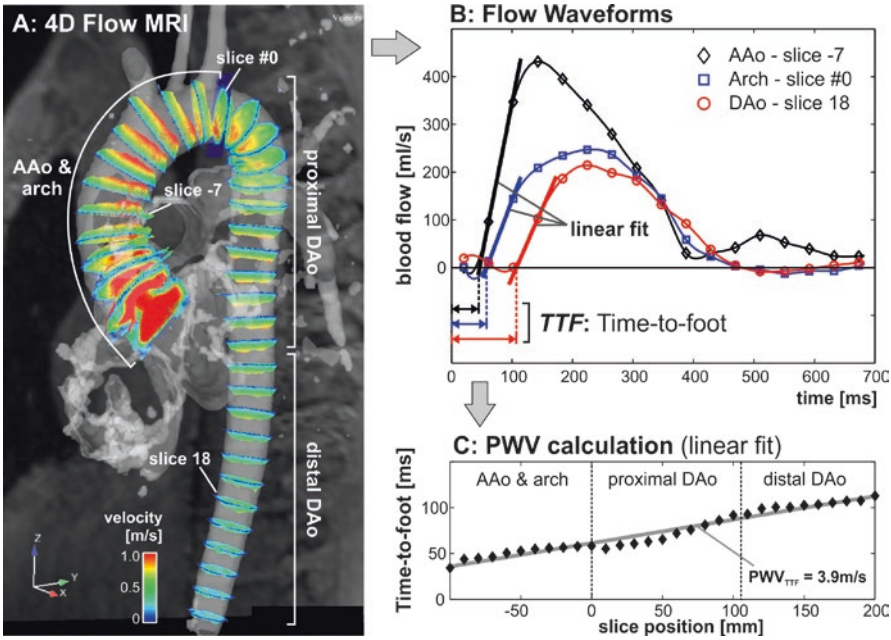

Fig. 16.6 Derivation of aortic pulse wave velocity from 4D flow MRI: (**a**) flow curves are automatically extracted in multiple planes along the aortic centerline. An initial plane #0 is positioned at the proximal asking aorta. Subsequently, all other 2D analysis planes will be positioned downstream in fixed intervals. (**b**) For each analysis plane, flow-time curves are calculated and the time-delay between adjacent planes is derived. (**c**) Aortic PWV (in m/s) is determined by a linear fit from data of the entire aorta. AAo: ascending aorta, DAo: descending aorta

Wall Shear Stress

The three-directional velocity fields can be used to calculate WSS (i.e., the blood shear rate on the endothelial cells that line the vessel wall multiplied by blood viscosity), a known pathophysiological stimulus cited to alter gene expression and endothelial cell function [97]. Altered shear forces at the intimal surface can promote endothelial changes and create areas at risk for vascular remodeling, i.e., when high WSS is sensitized, growth factors and other molecules such as nitric oxide (NO) and matrix metalloproteinases (MMPs) are released to dilate the vessel to restore the normal WSS value [98]. Altered WSS has been associated with the development of vulnerable plaques in the carotid arteries [99], progressive aortic dilation [100, 101], or development of cerebrovascular aneurysms [102–104]. WSS can be estimated from 4D flow MRI data by multiplying the deformation tensor $\dot{\varepsilon}$ that contains the velocity gradients in all directions at the wall, with the viscosity of blood. As schematically illustrated in Fig. 16.7 (top), initial studies have employed 4D flow MRI to quantify regional time-resolved WSS based on 2D analysis planes [105]. The variation of WSS direction over the cardiac cycle can be used to calculate the oscillatory shear index (OSI) [106]. More recently, methods have been

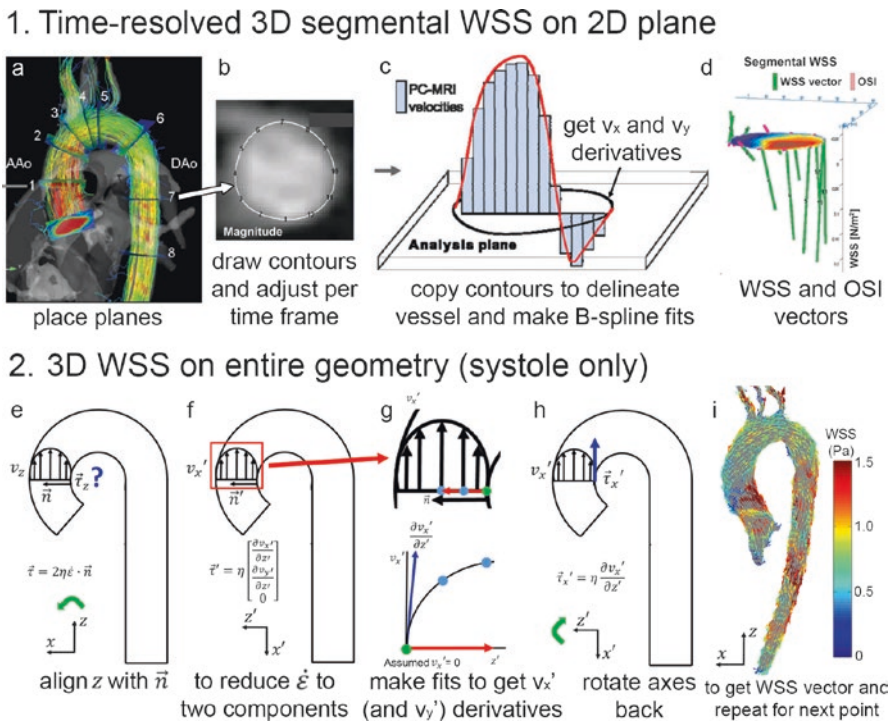

Fig. 16.7 (1) 3D segmental WSS in 2D planes. (**a**) Planes are placed perpendicularly to the aorta measured with 4D flow MRI, (**b**) contours are manually drawn to delineate the vessel wall and to define the segments for WSS calculation, (**c**) B-spline fits through the v_x and v_y velocities are created to derive the gradients at the wall that after multiplication with blood viscosity, (**d**) yield the WSS vectors in the plane. When repeated for all time frames, OSI can be calculated. (2) 3D WSS on the entire aorta surface. (**e**) At each point along the vessel wall, the *z*-axis is aligned with the inward normal vector, and with the assumption that there is no velocity through the wall, the deformation tensor is reduced from nine components to two (**f**). Spline fits along the *x* and *y* velocities along the normal vector yield the v_x and v_y derivatives. After multiplication with viscosity and rotation back to the original axes system, the local WSS vector is obtained

developed to compute volumetric 3D WSS along the 3D surface of the entire aorta, carotid or intracranial vasculature, or aneurysms (Fig. 16.7, bottom) [74, 107–109]. For the aorta, a method for the quantification of turbulent WSS variation was recently developed [110].

Although 3D WSS mapping allows for compact visualization of hemodynamic parameters (see Fig. 16.7, (2)), it does not detect where "abnormal" values are present. In addition, aortic WSS undergoes significant changes during healthy aging which underlines the importance of age-matched control cohorts in clinical studies to identify patients with altered WSS [111]. To address this limitation, a "WSS heatmap concept" was recently developed which offers the opportunity to quantify the extent of altered WSS [112]. The method is based on aortic 4D flow MRI data of a healthy control population to create an aortic "WSS atlas." As shown in Fig. 16.8, the aortic

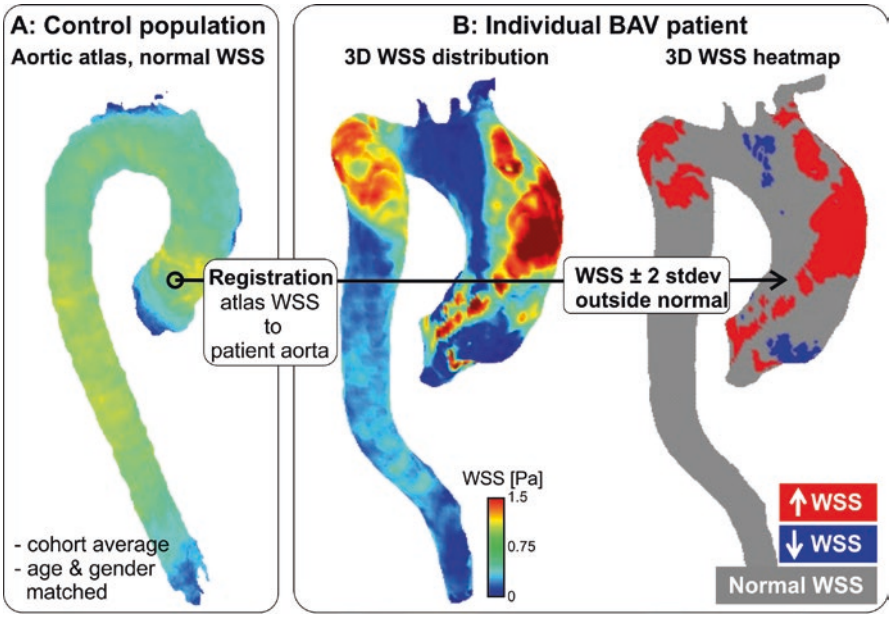

Fig. 16.8 Patient-specific WSS heatmaps. (**a**) A 3D cohort-averaged WSS map of a control cohort ("WSS atlas") is used as reference to provide mean, median, and normal confidence intervals (CI = ± 2 standard deviations, SD) of the normal physiologic aortic WSS distribution. (**b**) After delineating the regions of abnormal WSS for an individual patient, defined as values outside the CI, heatmaps of abnormally elevated or decreased WSS are created

atlas establishes regional confidence intervals for normal physiologic WSS throughout the aorta. Patient-specific WSS is then co-registered to the healthy control atlas to calculate heatmaps which represent regions of abnormally low or high WSS (i.e., outside of the 95% confidence interval provided by the control WSS atlas).

It should be noted that the discrete nature of the 4D flow MRI measured velocity field will result in a systematic underestimation of WSS. This is a common limitation of the technique. While absolute accuracy when assessing WSS in vivo is challenging, the relative pattern of expression (and magnitude) can reliably be inferred, especially if scan parameters and the procedure for WSS estimation are consistent between study populations [113, 114].

4D Flow MRI in Vessel Wall Disease: From Head to Toe

Head

In clinical practice, transcranial Doppler ultrasound is routinely used for cerebrovascular flow measurements. However, the technique is operator-dependent and limited by the acoustic windows of the head. 2D PC-MRI can provide reliable flow

measurements in large intracranial arteries and veins, not limited by location. However, challenges for using 2D PC-MRI for flow measurement include small and tortuous vessels [115], complex vascular anatomy, and need for the manual placement of 2D imaging planes in multiple vessel segments. As an alternative, 4D flow MRI is increasingly used to assess cerebrovascular 3D blood flow [116, 117]. Emerging applications include the hemodynamic evaluation of intracranial aneurysms, arteriovenous malformations (AVM), and intracranial atherosclerotic disease (ICAD). Several groups have reported the successful measurement and evaluation of flow and WSS in intracranial aneurysms in patient feasibility studies [107, 118–121], indicating the potential of flow MRI to assist in the classification of individual aneurysms pre-intervention.

Arteriovenous Malformations (AVMs)

In patients with cerebral AVMs, flow information is potentially valuable for a better understanding of the impact of a focal AVM on the flow redistribution in the brain and/or in treatment planning by attempting to identify the feeding arteries with highest flow (see Fig. 16.9), enabling efficient and targeted embolization treatment. Recent reports include the quantification of flow and WSS in patients using a highly optimized radial 4D flow technique [108, 122]. Additional studies demonstrated the potential of 4D flow MRI for the evaluation of global and regional AVM flow

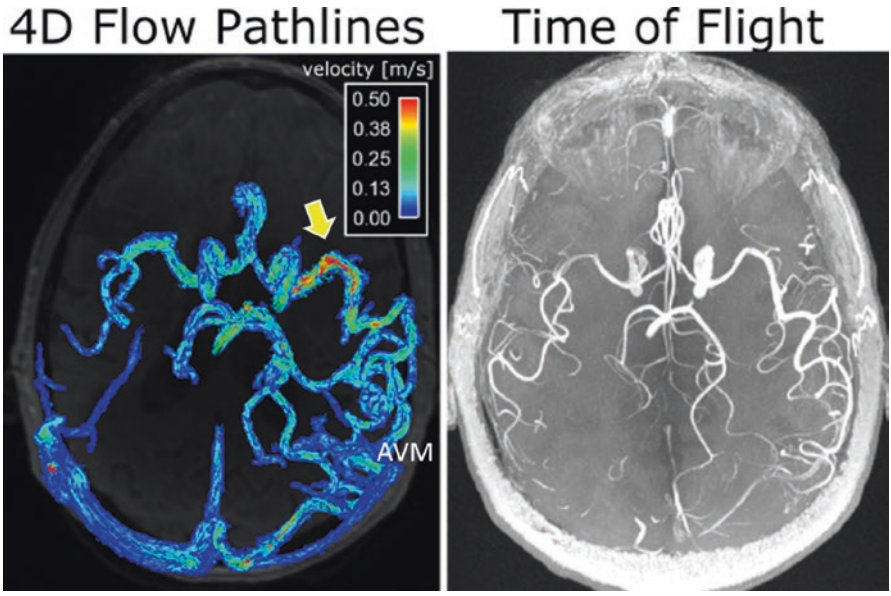

Fig. 16.9 Intracranial 4D flow MRI (left) and time-of-flight (TOF) 3D angiogram (right) in a 62-year-old male patient with a large cerebral AVM (Spetzler-Martin grade = 3). The dense AVM vascular network and high flow velocity in a main AVM feeding artery (arrow) can clearly be appreciated

characteristics [123, 124]. The findings showed that 4D flow MRI can assess treatment-induced changes in cerebrovascular flow distribution and was able to demonstrate significant associations between 4D flow metrics, cerebral perfusion indices, and AVM risk factors such as the Spetzler-Martin grade [124].

Intracranial Atherosclerotic Disease (ICAD)

Intracranial atherosclerotic plaques can alter local and global hemodynamics (particularly proximal or distal to stenosed vessels). Currently, intracranial hemodynamic disturbance in patients with ICAD is primarily assessed using transcranial Doppler ultrasound. Few studies have been performed to characterize the 3D blood flow disturbance and flow redistribution across the major cerebral arteries in patients with ICAD. An early study by Hope et al. reported that TOF MRA overestimated the degree of stenosis and that 4D flow MRI velocity measurements could improve accuracy of diagnosis, when compared to catheter angiography [119]. It should be noted that current flow imaging techniques (2D and 4D) are limited by insufficient spatial resolution for the characterization of blood flow at sites of critical or severe stenosis. Instead, post-stenotic flow is typically used to represent the regional flow in the stenotic artery. Higher magnetic field (7 Tesla) with increased spatial resolution may be required for improved flow assessment in the smaller vessels [125].

Intracranial Aneurysm

A large number of studies investigating flow patterns in intracranial aneurysms were based on computational fluid dynamics (CFD) techniques in conjunction with subject-specific geometries extracted from medical images [126–129]. Findings from these studies revealed a wide variety of complex intra-aneurysmal flow patterns that were strongly dependent on patient-specific vascular geometry. In addition, a number of studies showed that changes in WSS along the wall of intracranial aneurysms may be associated with risk of aneurysm growths or rupture [73, 107, 121]. However, CFD has limitations such as assumptions concerning blood properties, boundary conditions, and vessel properties [129–131]. As an alternative, 4D flow MRI is increasingly used to assess intra-aneurysmal 3D hemodynamics in vivo. Several groups have reported the successful measurement and evaluation of intra-aneurysmal flow and WSS in patient feasibility studies [73, 116, 119, 132–137], indicating the potential of flow MRI to assist in the classification of individual aneurysms pre-intervention.

Neck

Carotid artery stenosis is a leading cause of ischemic stroke, and detailed insights into the causes for the development of atherosclerosis at this site are of interest. Among other risk factors, it is assumed that the development of atherosclerosis in

the naturally bulbic ICA is related to local hemodynamic conditions such as flow deceleration or recirculation associated with reduced and oscillating WSS [138]. Particularly, low absolute WSS and high OSI are hypothesized to determine the composition of atherosclerotic lesions and the development of high-risk plaques [99, 102]. Since blood flow through the carotid bifurcation is complex with non-symmetric flow profiles, the full three-directional velocity information by 4D flow MRI can be useful for a complete in vivo assessment of the segmental distribution of WSS.

4D flow studies analyzing WSS in the normal carotid bifurcation confirmed that potentially atherogenic wall (e.g., low WSS) parameters were predominantly concentrated at the posterior wall of the proximal ICA [139, 140]. Cibis et al. found lower WSS in regions of higher wall thickness in the carotid bifurcation [141, 142]. An example of a cohort-averaged map showing low WSS at locations of high wall thickness is displayed in Fig. 16.10. The wall thickness map is in concordance with the tendency of carotid atherosclerosis to affect the outer walls of arterial bifurcations and to mostly develop in the proximal part of the ICA bulb [143, 144]. Moreover, a significant relationship between the size of regions exposed to altered wall parameters and the individual bifurcation geometry was demonstrated, similar to carotid bifurcation study using CFD [138]. In patients with ICA stenosis, markedly altered filling and helix formation in the ICA bulb were observed, while revascularization partly restored normal filling and helix formation [145]. Furthermore, a direct comparison of mean and absolute flow velocities in the common carotid artery (CCA) between 4D flow MRI and Doppler ultrasound showed good agreement despite general underestimation of peak velocities by MRI [146].

4D flow MRI-derived WSS quantification could thus be a valuable technique to assess the individual risk of flow-mediated atherosclerosis and carotid plaque progression.

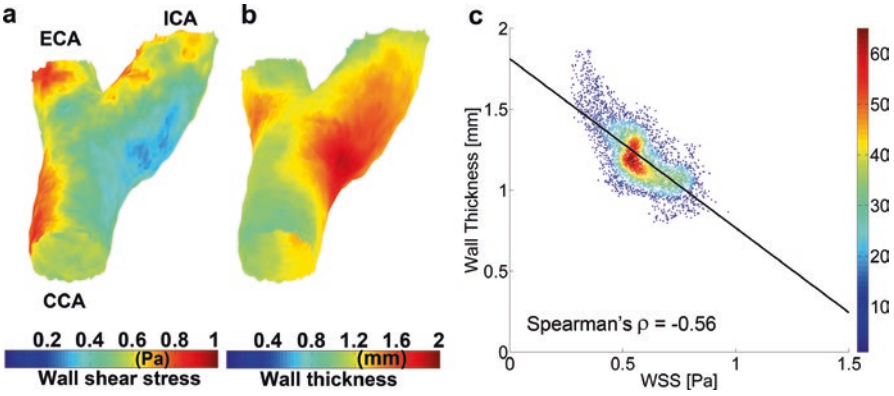

Fig. 16.10 Three-dimensional (**a**) wall shear stress and (**b**) wall thickness carotid bifurcation maps averaged over 20 subjects with plaques. In (**c**) the correlation between WSS and WT is shown with color-coding for the density of the points

The assessment of PWV in the carotid arteries as a measure of vessel stiffness (and thus atherosclerotic burden) is challenging due its small size that necessitates high spatial and temporal resolution [147]. It is thus challenging to derive PWV using 4D flow MRI in the carotid arteries. For the determination of local PWV in the carotid arteries, the temporal resolution of through-plane 2D CINE PC-MRI was recently drastically improved by compressed sensing acceleration [148]. These novel acquisition strategies hold promise for future applications of either 2D or 4D flow MRI-derived PWV.

Thorax

Cardiothoracic 4D flow imaging is typically performed as part of a standard-of-care aortic/pulmonary imaging protocol, which includes additional MRI techniques for the assessment of cardiac function and wall motion (CINE imaging), aortic and pulmonary dimensions and geometry (MR angiography), as well as aortic and pulmonary valve morphology and dynamics (CINE imaging). The combination with 4D flow MRI provides a comprehensive assessment of aortic/pulmonary structure and function. These data have contributed to the understanding of the development of vessel wall abnormalities (atherosclerosis, aortic dilation, aneurysm) as a consequence of thoracic vascular diseases such as aortic valve diseases (stenosis, insufficiency, congenital bicuspid aortic valve (BAV)), aortic coarctation, or Marfan syndrome.

Aortic Valve Disease and Aortopathy

The presence of aortic valve disease significantly alters the hemodynamic environment in the thoracic aorta. Several studies have shown promise of 4D flow MRI-based blood flow visualization for the investigation of valve-related abnormal flow patterns (e.g., aberrant vortex or helix flow) as shown in Fig. 16.11. However, the visual evaluation of changes in aortic flow patterns (e.g., grading of vortex of helix flow) can be limited by lack of standardization, observer bias, and thus reproducibility. A more effective and representative assessment is provided by the calculation of 4D flow-derived measures that quantify the impact of altered flow characteristics on the vessel wall, such as flow displacement and WSS.

Flow displacement is an easy to obtain quantitative marker that represents outflow asymmetry (i.e., deviation for a symmetric flow profile). Studies have shown that flow displacement can detect altered systolic outflow patterns in patients with different types and severity of aortic valve disease [149–153] or in patients with aortic dilation [154]. For example, recent studies showed that different aortic valve fusion phenotypes in patients with BAV resulted in distinctly altered eccentric aortic outflow jet patterns [101, 155]. Differences in aortic dilation type were associated

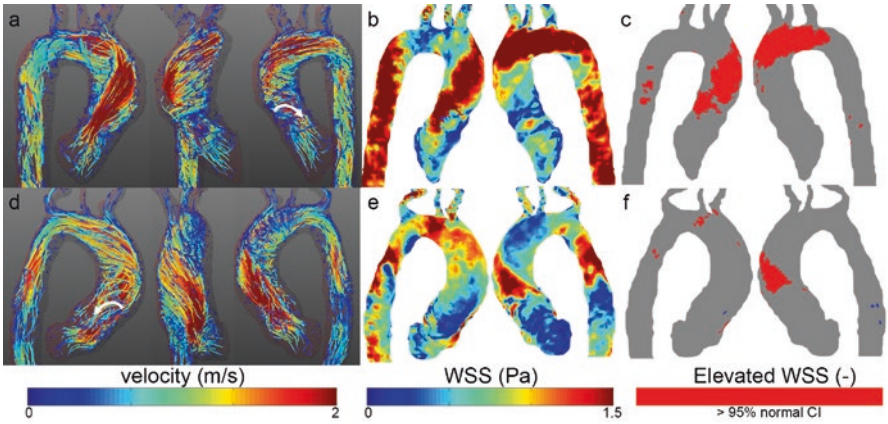

Fig. 16.11 Velocity and WSS in two patients with a stenosed bicuspid aortic valve. (**a**, **d**) Peak systolic velocity path lines showing right-handed helical flow (top) and left-handed helical flow (bottom). Vortex flow can be seen as well (white arrows). (**b**, **e**) Stenotic flow leads to high wall shear stress on the right-anterior aortic wall (top) and left-posterior wall (bottom) which can be concisely visualized by elevated WSS heatmaps (**c**, **f**)

with altered flow displacement in the ascending aorta, suggesting a physiologic mechanism by which valve morphology can influence aortic wall remodeling.

Patient studies have demonstrated the potential of WSS to quantify the impact of deranged flow on the aortic wall. Initial 4D flow studies were based on 2D-based planar quantification of WSS changes in patients with aortic dilation [156], aortic atherosclerosis [157], or aortic valve abnormalities such BAV disease [101, 158–160]. Bieging et al. were the first to create a 3D segmentation of the aorta for the purpose of regional WSS estimation in patients with ascending aortic aneurysms [74]. More recently, Potters et al. used a modified algorithm to estimate 3D WSS on the entire aorta surface [109].

Interestingly, several 4D flow MRI studies have shown that the presence of aortic valve disease has a very different effect on aortic hemodynamics as compared to aortic dilation or aneurysm alone. Aortic dilation with an otherwise normal aortic valve generally leads to slow helix-type flow with significantly reduced WSS in the ascending aorta. In contrast, BAV or aortic valve stenosis will result in significantly elevated flow velocities, high-velocity transvalvular outflow jets, and eccentrically elevated WSS. These findings have been confirmed by a series of studies by Bissel et al., Mahadevia et al., Shan et al., and Rodríguez-Palomares et al. in larger cohorts (65–142 subjects, respectively) [100, 101, 155, 161]. A recent large cohort 4D flow MRI study in patients with aortic valve disease (>500 subjects) confirmed these findings. As shown in Fig. 16.12, aortic 4D flow MRI can be used to show the incidence of elevated WSS for specific groups of patients and healthy controls. Results clearly showed that aortic valve stenosis resulted in a marked increase in regional WSS compared to patients with aortic dilation but normal tricuspid aortic valve

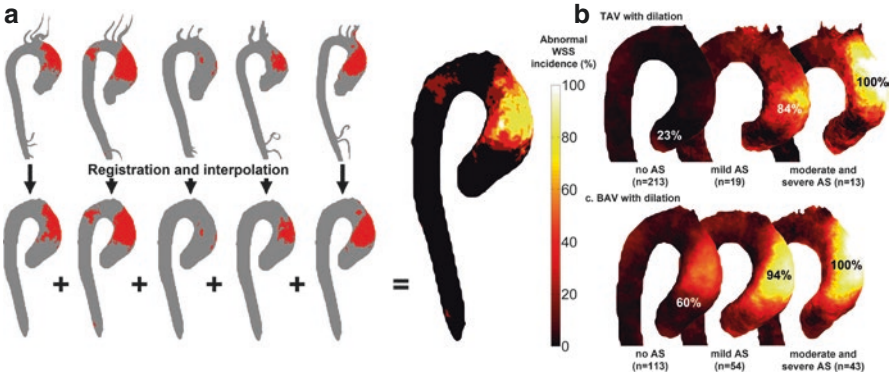

Fig. 16.12 (**a**) Registration and interpolation techniques are used to project regions of elevated WSS onto a shared aortic geometry. Summing elevated WSS regions yields a map of the regional incidence of elevated WSS. Group-specific 3D maps of abnormally elevated WSS for (**b**) tricuspid aortic valve (TAV) with dilation with no aortic valve stenosis (AS), mild AS and moderate and severe AS, and (**c**) BAV patients with right non-valve function morphology (RN-BAV) with no AS, mild AS, and moderate and severe AS

[162]. In addition, the WSS heatmap concept can be employed to highlight regions with abnormally elevated WSS in individual patients (see Fig. 16.12) [163].

A recent study utilized the WSS heatmap concept to assess the correlation between abnormal in vivo 3D WSS and regional aortic tissue remodeling in BAV patients with AS [164]. BAV patients undergoing ascending aortic resection received preoperative 4D flow MRI to regionally map 3D WSS and correlate these findings with histologic examination of surgically resected tissue samples. Paired aortic wall samples (i.e., regions of both elevated and normal WSS within the same patient) were collected and compared for medial elastin degeneration by histology. Regions of increased WSS showed greater medial elastin degradation compared to adjacent areas with normal WSS. Another study confirmed these results and showed that in the presence of aortic stenosis, the correlation between WSS and elastin fiber thickness was stronger than without AS [165]. These data suggest that regional valve-mediated hemodynamics could serve as potential prognostic biomarkers of aortic disease.

Marfan Syndrome

Marfan syndrome is an inherited autosomal dominant connective tissue disease, mostly related to mutations in the fibrillin-1 (FBN1) gene. Many organ systems can be involved, but most life-threatening complications are related to the cardiovascular system and include aortic wall abnormalities leading to dissection and aortic rupture. Although the entire aorta may dilate in Marfan syndrome, the aortic root and the proximal descending aorta are prone for progressive dilation and dissection [166–168]. Few studies have investigated aortic WSS in MFS disease cohorts

[169–171]. Altered WSS was most pronounced in the proximal ascending aorta and the proximal descending aorta, which corresponds to locations where aortic dissection and rupture are most likely to occur. A recent longitudinal study in Marfan patient with baseline and mean follow-up 4D flow MRI (mean duration of 3.5 ± 1.2 years) confirmed these findings [169]. MFS patients had lower segmental WSS in the inner proximal DAo segment which correlated with increased localized aberrant vortex/helix flow patterns and an enlarged diameter. Aortic hemodynamics were stable over multi-year follow-up, but subtle localized flow changes in the descending aorta were already present at young age and tended to be more pronounced in the course of time. This is an important and intriguing finding, as the proximal descending aorta is a known initiation region for type B aortic dissections.

4D flow MRI was also used to calculate PWV as a measure for aortic stiffness in the aorta of BAV patients compared to controls and Marfan patients [172, 173]. Marfan patients had markedly higher aortic PWV and thus stiffer aortas compared to controls and BAV patients. The increased aortic stiffness may lead to further deterioration of aortic and LV function and may thus constitute important parameter for longitudinal monitoring of risk for progressive aortic dilation in these patients.

Aortic Coarctation

Aortic coarctation accounts for 6% of congenital cardiac malformations, is associated with hypertension and peripheral vascular disease, and often requires surgical repair [174]. This disease is characterized by a congenital narrowing of the aorta, usually at the level of the distal arch or proximal descending aorta. To provide insight into the degree of stenosis and impact on distal flow as a result of the coarctation, traditional assessment includes aorta diameter measurements and post-coarctation flow velocity assessment. Using 4D flow MRI to assess this cohort of patients has proven to provide useful characteristics about the impact of coarctation and coarctation repair on flow features throughout the aorta. Recent studies have shown that 4D flow MRI can measure and visualize alterations in 3D aortic hemodynamics in coarctation patients such as elevated helix and vortex flow throughout the entire aorta, including the region of repair [175–178]. Patients with aortic coarctation tend to have flow jet eccentricity following the coarctation resulting in jet impingement and elevated WSS along the descending aorta [179, 180].

Aortic Atherosclerosis

Stiffening of the aorta is frequently observed with increasing age and disease (e.g., hypertension, diabetes) due to an increase in the collagen-elastin ratio. Increased stiffness results in greater hemodynamic loading conditions on the aortic endothelium leading to the development of atherosclerosis [84, 181].

The most commonly measured and best surrogate for arterial stiffness is pulse wave velocity (PWV) [85, 182, 183]. In 2 studies with 37 and 98 subjects, respectively, the reliability of 4D flow-based estimation of global aortic PWV was demonstrated in volunteers and patients with aortic atherosclerotic disease with a good observer dependence and excellent test-retest reliability [82, 184]. Both studies demonstrated significant correlations of aortic stiffness with age. In addition, in patients with atherosclerosis, the PWV was significantly increased compared with controls demonstrating the sensitivity of the technique to detect elevated aortic stiffness. In a recent study, 4D flow MRI-derived PWV parameters correlated significantly with echocardiographic stiffness parameters and intima-media thickness in the descending aorta of stroke patients [185]. Harloff et al. showed an increase in aortic PWV in older subjects that had more aortic plaque [186].

Peripheral Arteries

Peripheral arterial occlusive disease (PAOD) is commonly explored with basic clinical tests such as the ankle-brachial-index, constant load treadmill test, and Doppler ultrasound due to its excellent temporal and spatial resolution. A number of studies have reported the use of 2D PC MRI for the quantitative assessment of PAOD severity [187–190]. Similar to Doppler ultrasound, the waveforms derived in locations superior or inferior to stenoses were being used to characterize the severity of PAOD [191, 192]. In a similar fashion, 4D flow MRI can be applied to the peripheral arteries, but only few studies have been reported to date. Application of this technique in the lower extremities has been limited to a single study which evaluated the iliac and proximal femoral at 3T [193]. Limitations of 4D flow in the extremities include the large anatomical coverage needed for vessel assessment, small vessel size (specially in distal vessels), and thus long scan times to achieve sufficient spatial resolution and SNR. Future research is warranted to extend previously published feasibility results to longitudinal and comparative studies investigating the potential impact of 4D flow MRI in PAOD.

Future Directions and Conclusions

Recent developments related to highly accelerated 4D flow MRI have resulted in increased flexibility for the application of 4D flow MRI with reduced scan times and/or increased spatiotemporal resolutions. These developments have led to more widespread applications of 4D flow MRI, but further improvements in spatial resolution for the reliable quantification of vascular hemodynamics near the vessel wall or in small arteries affected are needed. 4D flow MRI acquisition at higher field strengths, e.g., 7T, and the associated increase in signal-to-noise ratio is promising in this regard. Studies have demonstrated that 7T 4D flow MRI allows for more detailed visualization of 3D velocity fields compared to 3T in the brain [125, 194]

and the aorta [195, 196]. However, 7T scanners are expensive and need tailor-made equipment and specialized operator expertise, which can hamper its clinical application. As an alternative, 4D flow image quality and velocity dynamic range can be improved by dual- or multi-VENC flow encoding. By combining a low-VENC acquisition with phase unwrapping guided by a simultaneous high-VENC acquisition, aliasing-free images can be acquired with high velocity-to-noise ratio [197]. By interleaving the high- and low-VENC acquisitions in combination with imaging acceleration techniques, dual-VENC 4D flow MRI has shown promise for detailed velocity measurements for neurovascular and aortic applications [198, 199]. Alternatively, additional velocity encoding steps further improved velocity-to-noise ratio, and velocity unwrapping can be added to standard acquisitions at the cost of extra scan time [27, 200, 201]. These methods showed improved aortic and neurovascular blood flow velocity visualization [202, 203].

PWV and WSS quantification are promising markers of vessel wall abnormalities but require laborious and time-consuming manual placement of analysis planes or segmentation of the 3D vessel lumen. To make 4D flow MRI data analysis more time-efficient, several groups have developed methods to automate these processing steps. For example, Bustamante et al. used advanced atlas-based methods for time-resolved aortic segmentation and plane placement [204]. The centerline of a 3D aortic segmentation can subsequently be used for automatic plane placement [151]. For 3D segmentation of the intracranial vasculature, highly automated algorithms were developed [205].

In conclusion, 4D flow MRI is a highly versatile technique which can be employed to derive important clinical parameters such as pulse wave velocity and wall shear stress in a large range of vessel wall diseases. Many studies have shown the additional value of 4D flow MRI in a clinical setting, but the methodology is still limitedly used for diagnosis or treatment planning in cardiovascular disease worldwide. Current and future efforts in the field are dedicated to the acceleration of the acquisition and the automated processing of the data, with the ultimate goal of developing 4D flow MRI in a widespread, easy-to-use clinical tool for vessel wall disease assessment.

References

1. Carr HY, Purcell EM. Effects of diffusion on free precession in nuclear magnetic resonance experiments. Phys Rev. 1954;94:630–8.
2. Hahn EL. Detection of sea-water motion by nuclear precession. J Geophys Res. 1960;65:776–7.
3. Grant JP, Back C. NMR rheotomography: feasibility and clinical potential. Med Phys. 1982;9:188–93.
4. Moran PR. A flow velocity zeugmatographic interlace for NMR imaging in humans. Magn Reson Imaging. 1982;1:197–203.
5. Bryant DJ, Payne JA, Firmin DN, Longmore DB. Measurement of flow with NMR imaging using a gradient pulse and phase difference technique. J Comput Assist Tomogr. 1984;8:588–93.

6. van Dijk P. Direct cardiac NMR imaging of heart wall and blood flow velocity. J Comput Assist Tomogr. 1984;8:429–36.
7. Nayler GL, Firmin DN, Longmore DB. Blood flow imaging by cine magnetic resonance. J Comput Assist Tomogr. 1986;10:715–22.
8. Pelc NJ, Herfkens RJ, Shimakawa A, Enzmann DR. Phase contrast cine magnetic resonance imaging. Magn Reson Q. 1991;7:229–54.
9. Chai P, Mohiaddin R. How we perform cardiovascular magnetic resonance flow assessment using phase-contrast velocity mapping. J Cardiovasc Magn Reson. 2005;7:705–16.
10. Nayak KS, Nielsen J-F, Bernstein MA, Markl M, D Gatehouse P, M Botnar R, Saloner D, Lorenz C, Wen H, S Hu B, Epstein FH, N Oshinski J, Raman SV. Cardiovascular magnetic resonance phase contrast imaging. J Cardiovasc Magn Reson. 2015;17:71.
11. Markl M, Kilner PJ, Ebbers T. Comprehensive 4D velocity mapping of the heart and great vessels by cardiovascular magnetic resonance. J Cardiovasc Magn Reson. 2011;13:7.
12. Markl M, Frydrychowicz A, Kozerke S, Hope M, Wieben O. 4D flow MRI. J Magn Reson Imaging. 2012;36:1015–36.
13. Blanken CPS, Farag ES, Boekholdt SM, Leiner T, Kluin J, Nederveen AJ, van Ooij P, Planken RN. Advanced cardiac MRI techniques for evaluation of left-sided valvular heart disease. J Magn Reson Imaging. 2018;48:318–29.
14. O'Donnell M. NMR blood flow imaging using multiecho, phase contrast sequences. Med Phys. 1985;12:59–64.
15. Dumoulin CL, Souza SP, Walker MF, Wagle W. Three-dimensional phase contrast angiography. Magn Reson Med. 1989;9:139–49.
16. Mohiaddin RH, Yang GZ, Kilner PJ. Visualization of flow by vector analysis of multidirectional cine MR velocity mapping. J Comput Assist Tomogr. 1994;18:383–92.
17. Lenz GW, Haacke EM, White RD. Retrospective cardiac gating: a review of technical aspects and future directions. Magn Reson Imaging. 1989;7:445–55.
18. Markl M, Chan FP, Alley MT, Wedding KL, Draney MT, Elkins CJ, Parker DW, Wicker R, Taylor CA, Herfkens RJ, Pelc NJ. Time-resolved three-dimensional phase-contrast MRI. J Magn Reson Imaging. 2003;17:499–506.
19. Bogren HG, Klipstein RH, Firmin DN, Mohiaddin RH, Underwood SR, Rees RS, Longmore DB. Quantitation of antegrade and retrograde blood flow in the human aorta by magnetic resonance velocity mapping. Am Heart J. 1989;117:1214–22.
20. Caro CG, Dumoulin CL, Graham JM, Parker KH, Souza SP. Secondary flow in the human common carotid artery imaged by MR angiography. J Biomech Eng. 1992;114:147–9.
21. Marks MP, Pelc NJ, Ross MR, Enzmann DR. Determination of cerebral blood flow with a phase-contrast cine MR imaging technique: evaluation of normal subjects and patients with arteriovenous malformations. Radiology. 1992;182:467–76.
22. Wigstrom L, Sjoqvist L, Wranne B. Temporally resolved 3D phase-contrast imaging. Magn Reson Med. 1996;36:800–3.
23. Atkinson DJ, Edelman RR. Cineangiography of the heart in a single breath hold with a segmented turboFLASH sequence. Radiology. 1991;178:357–60.
24. Thomsen C, Cortsen M, Söndergaard L, Henriksen O, Ståhlberg F. A segmented K-space velocity mapping protocol for quantification of renal artery blood flow during breath-holding. J Magn Reson Imaging. 1995;5:393–401.
25. Pelc NJ, Bernstein MA, Shimakawa A, Glover GH. Encoding strategies for three-direction phase-contrast MR imaging of flow. J Magn Reson Imaging. 1991;1:405–13.
26. Bernstein MA, Shimakawa A, Pelc NJ. Minimizing TE in moment-nulled or flow-encoded two-and three-dimensional gradient-echo imaging. J Magn Reson Imaging. 1992;2:583–8.
27. Johnson KM, Markl M. Improved SNR in phase contrast velocimetry with five-point balanced flow encoding. Magn Reson Med. 2010;63:349–55.
28. Bock J, Kreher W, Hennig J, Markl M. Optimized pre-processing of time-resolved 2D and 3D phase contrast MRI data. Proc Int Soc Mag Reson Med. 2007;15:3138.
29. Firmin DN, Klipstein RH, Hounsfield GL, Paley MP, Longmore DB. Echo-planar high-resolution flow velocity mapping. Magn Reson Med. 1989;12:316–27.

30. Pruessmann KP, Weiger M, Scheidegger MB, Boesiger P. SENSE: sensitivity encoding for fast MRI. Magn Reson Med. 1999;42:952–62.
31. Thunberg P, Karlsson M, Wigstrom L. Accuracy and reproducibility in phase contrast imaging using SENSE. Magn Reson Med. 2003;50:1061–8.
32. Griswold MA, Jakob PM, Heidemann RM, Nittka M, Jellus V, Wang J, Kiefer B, Haase A. Generalized autocalibrating partially parallel acquisitions (GRAPPA). Magn Reson Med. 2002;47:1202–10.
33. Tsao J, Boesiger P, Pruessmann KP. k-t BLAST and k-t SENSE: dynamic MRI with high frame rate exploiting spatiotemporal correlations. Magn Reson Med. 2003;50:1031–42.
34. van Ooij P, Guedon A, Marquering HA, Schneiders JJ, Majoie CB, van Bavel E, Nederveen AJ. k-t BLAST and SENSE accelerated time-resolved three-dimensional phase contrast MRI in an intracranial aneurysm. MAGMA. 2013;26:261–70.
35. Schnell S, Markl M, Entezari P, Mahadewia RJ, Semaan E, Stankovic Z, Collins J, Carr J, Jung B. k-t GRAPPA accelerated four-dimensional flow MRI in the aorta: effect on scan time, image quality, and quantification of flow and wall shear stress. Magn Reson Med. 2014;72:522–33.
36. Pedersen H, Kozerke S, Ringgaard S, Nehrke K, Kim WY. k-t PCA: temporally constrained k-t BLAST reconstruction using principal component analysis. Magn Reson Med. 2009;62:706–16.
37. Giese D, Wong J, Greil GF, Buehrer M, Schaeffter T, Kozerke S. Towards highly accelerated Cartesian time-resolved 3D flow cardiovascular magnetic resonance in the clinical setting. J Cardiovasc Magn Reson. 2014;16:42.
38. Liu J, Koskas L, Faraji F, Kao E, Wang Y, Haraldsson H, Kefayati S, Zhu C, Ahn S, Laub G, Saloner D. Highly accelerated intracranial 4D flow MRI: evaluation of healthy volunteers and patients with intracranial aneurysms. MAGMA. 2018;31:295–307.
39. Lustig M, Donoho D, Pauly JM. Sparse MRI: the application of compressed sensing for rapid MR imaging. Magn Reson Med. 2007;58:1182–95.
40. Cheng JY, Hanneman K, Zhang T, Alley MT, Lai P, Tamir JI, Uecker M, Pauly JM, Lustig M, Vasanawala SS. Comprehensive motion-compensated highly accelerated 4D flow MRI with ferumoxytol enhancement for pediatric congenital heart disease. J Magn Reson Imaging. 2016;43:1355–68.
41. Bollache E, Barker AJ, Dolan RS, Carr JC, van Ooij P, Ahmadian R, Powell A, Collins JD, Geiger J, Markl M. k-t accelerated aortic 4D flow MRI in under two minutes: feasibility and impact of resolution, k-space sampling patterns, and respiratory navigator gating on hemodynamic measurements. Magn Reson Med. 2018;79:195–207.
42. Gu T, Korosec FR, Block WF, Fain SB, Turk Q, Lum D, Zhou Y, Grist TM, Haughton V, Mistretta CA. PC VIPR: a high-speed 3D phase-contrast method for flow quantification and high-resolution angiography. AJNR Am J Neuroradiol. 2005;26:743–9.
43. Glover GH, Pauly JM. Projection reconstruction techniques for reduction of motion effects in MRI. Magn Reson Med. 1992;28:275–89.
44. Ahn CB, Kim JH, Cho ZH. High-speed spiral-scan echo planar NMR imaging-I. IEEE Trans Med Imaging. 1986;5:2–7.
45. Dyvorne H, Knight-Greenfield A, Jajamovich G, Besa C, Cui Y, Stalder A, Markl M, Taouli B. Abdominal 4D flow MR imaging in a breath hold: combination of spiral sampling and dynamic compressed sensing for highly accelerated acquisition. Radiology. 2015;275:245–54.
46. Bastkowski R, Weiss K, Maintz D, Giese D. Self-gated golden-angle spiral 4D flow MRI. Magn Reson Med. 2018;80:904–13.
47. Petersson S, Sigfridsson A, Dyverfeldt P, Carlhäll CJ, Ebbers T. Retrospectively gated intracardiac 4D flow MRI using spiral trajectories. Magn Reson Med. 2016;75:196–206.
48. Haider CR, Hu HH, Campeau NG, Huston J, Riederer SJ. 3D high temporal and spatial resolution contrast-enhanced MR angiography of the whole brain. Magn Reson Med. 2008;60:749–60.
49. Liu J, Saloner D. Accelerated MRI with CIRcular Cartesian UnderSampling (CIRCUS): a variable density Cartesian sampling strategy for compressed sensing and parallel imaging. Quant Imaging Med Surg. 2014;4:57–67.

50. Cheng JY, Zhang T, Alley MT, Uecker M, Lustig M, Pauly JM, Vasanawala SS. Comprehensive multi-dimensional MRI for the simultaneous assessment of cardiopulmonary anatomy and physiology. Sci Rep. 2017;7:5330.
51. Runge VM, Clanton JA, Partain CL, James AE. Respiratory gating in magnetic resonance imaging at 0.5 Tesla. Radiology. 1984;151:521–3.
52. Wang Y, Rossman PJ, Grimm RC, Riederer SJ, Ehman RL. Navigator-echo-based real-time respiratory gating and triggering for reduction of respiration effects in three-dimensional coronary MR angiography. Radiology. 1996;198:55–60.
53. Bailes DR, Gilderdale DJ, Bydder GM, Collins AG, Firmin DN. Respiratory ordered phase encoding (ROPE): a method for reducing respiratory motion artefacts in MR imaging. J Comput Assist Tomogr. 1985;9:835–8.
54. Markl M, Harloff A, Bley TA, Zaitsev M, Jung B, Weigang E, Langer M, Hennig J, Frydrychowicz A. Time-resolved 3D MR velocity mapping at 3T: improved navigator-gated assessment of vascular anatomy and blood flow. J Magn Reson Imaging. 2007;25:824–31.
55. van Ooij P, Semaan E, Schnell S, Giri S, Stankovic Z, Carr J, Barker AJ, Markl M. Improved respiratory navigator gating for thoracic 4D flow MRI. Magn Reson Imaging. 2015;33:992–9.
56. Uribe S, Beerbaum P, Sorensen TS, Rasmusson A, Razavi R, Schaeffter T. Four-dimensional (4D) flow of the whole heart and great vessels using real-time respiratory self-gating. Magn Reson Med. 2009;62:984–92.
57. Kim WS, Mun CW, Kim DJ, Cho ZH. Extraction of cardiac and respiratory motion cycles by use of projection data and its applications to NMR imaging. Magn Reson Med. 1990;13:25–37.
58. Norris DG, Hutchison JMS. Concomitant magnetic field gradients and their effects on imaging at low magnetic field strengths. Magn Reson Imaging. 1990;8:33–7.
59. Jehenson P, Westphal M, Schuff N. Analytical method for the compensation of eddy-current effects induced by pulsed magnetic field gradients in NMR systems. J Magn Reson. 1990;90:264–78.
60. Bernstein MA, Zhou XJ, Polzin JA, King KF, Ganin A, Pelc NJ, Glover GH. Concomitant gradient terms in phase contrast MR: analysis and correction. Magn Reson Med. 1998;39:300–8.
61. Walker PG, Cranney GB, Scheidegger MB, Waseleski G, Pohost GM, Yoganathan AP. Semiautomated method for noise reduction and background phase error correction in MR phase velocity data. J Magn Reson Imaging. 1993;3:521–30.
62. Giese D, Haeberlin M, Barmet C, Pruessmann KP, Schaeffter T, Kozerke S. Analysis and correction of background velocity offsets in phase-contrast flow measurements using magnetic field monitoring. Magn Reson Med. 2012;67:1294–302.
63. Wigstrom L, Ebbers T, Fyrenius A, Karlsson M, Engvall J, Wranne B, Bolger AF. Particle trace visualization of intracardiac flow using time-resolved 3D phase contrast MRI. Magn Reson Med. 1999;41:793–9.
64. Mohiaddin RH, Yang GZ, Burger P, Firmin DN, Longmore DB. Automatic enhancement, animation, and segmentation of flow in peripheral arteries from MR phase-shift velocity mapping. J Comput Assist Tomogr. 1992;16:176–81.
65. Walker PG, Cranney GB, Grimes RY, Delatore J, Rectenwald J, Pohost GM, Yoganathan AP. Three-dimensional reconstruction of the flow in a human left heart by using magnetic resonance phase velocity encoding. Ann Biomed Eng. 1996;24:139–47.
66. Napel S, Lee DH, Frayne R, Rutt BK. Visualizing three-dimensional flow with simulated streamlines and three-dimensional phase-contrast MR imaging. J Magn Reson Imaging. 1992;2:143–53.
67. Buonocore MH. Visualizing blood flow patterns using streamlines, arrows, and particle paths. Magn Reson Med. 1998;40:210–26.
68. Hiratzka LF, Bakris GL, Beckman JA, Bersin RM, Carr VF, Casey DE Jr, Eagle KA, Hermann LK, Isselbacher EM, Kazerooni EA, Kouchoukos NT, Lytle BW, Milewicz DM, Reich DL, Sen S, Shinn JA, Svensson LG, Williams DM, American College of Cardiology Foundation/American Heart Association Task Force on Practice G, American Association for Thoracic S, American College of R, American Stroke A, Society of Cardiovascular A, Society for

Cardiovascular A, Interventions, Society of Interventional R, Society of Thoracic S, Society for Vascular M. 2010 ACCF/AHA/AATS/ACR/ASA/SCA/SCAI/SIR/STS/SVM guidelines for the diagnosis and management of patients with thoracic aortic disease. A report of the American College of Cardiology Foundation/American Heart Association Task Force on Practice Guidelines, A. J Am Coll Cardiol. 2010;55:e27–e129.
69. Elbaz MSM, Calkoen EE, Westenberg JJM, Lelieveldt BPF, Roest AAW, van der Geest RJ. Vortex flow during early and late left ventricular filling in normal subjects: quantitative characterization using retrospectively-gated 4D flow cardiovascular magnetic resonance and three-dimensional vortex core analysis. J Cardiovasc Magn Reson. 2014;16:78.
70. Hirtler D, Garcia J, Barker AJ, Geiger J. Assessment of intracardiac flow and vorticity in the right heart of patients after repair of tetralogy of Fallot by flow-sensitive 4D MRI. Eur Radiol. 2016;26:3598–607.
71. Lorenz R, Bock J, Barker AJ, von Knobelsdorff-Brenkenhoff F, Wallis W, Korvink JG, Bissell MM, Schulz-Menger J, Markl M. 4D flow magnetic resonance imaging in bicuspid aortic valve disease demonstrates altered distribution of aortic blood flow helicity. Magn Reson Med. 2014;71:1542–53.
72. von Knobelsdorff-Brenkenhoff F, Trauzeddel RF, Barker AJ, Gruettner H, Markl M, Schulz-Menger J. Blood flow characteristics in the ascending aorta after aortic valve replacement--a pilot study using 4D-flow MRI. Int J Cardiol. 2014;170:426–33.
73. Boussel L, Rayz V, Martin A, Acevedo-Bolton G, Lawton MT, Higashida R, Smith WS, Young WL, Saloner D. Phase-contrast magnetic resonance imaging measurements in intracranial aneurysms in vivo of flow patterns, velocity fields, and wall shear stress: comparison with computational fluid dynamics. Magn Reson Med. 2009;61:409–17.
74. Bieging ET, Frydrychowicz A, Wentland A, Landgraf BR, Johnson KM, Wieben O, Francois CJ. In vivo three-dimensional MR wall shear stress estimation in ascending aortic dilatation. J Magn Reson Imaging. 2011;33:589–97.
75. Ebbers T, Wigström L, Bolger AF, Engvall J, Karlsson M. Estimation of relative cardiovascular pressures using time-resolved three-dimensional phase contrast MRI. Magn Reson Med. 2001;45:872–9.
76. Bock J, Frydrychowicz A, Lorenz R, Hirtler D, Barker AJ, Johnson KM, Arnold R, Burkhardt H, Hennig J, Markl M. In vivo noninvasive 4D pressure difference mapping in the human aorta: phantom comparison and application in healthy volunteers and patients. Magn Reson Med. 2011;66:1079–88.
77. Barker AJ, van Ooij P, Bandi K, Garcia J, Albaghdadi M, McCarthy P, Bonow RO, Carr J, Collins J, Malaisrie SC, Markl M. Viscous energy loss in the presence of abnormal aortic flow. Magn Reson Med. 2014;72:620–8.
78. Elbaz MSM, van der Geest RJ, Calkoen EE, de Roos A, Lelieveldt BPF, Roest AAW, Westenberg JJM. Assessment of viscous energy loss and the association with three-dimensional vortex ring formation in left ventricular inflow: in vivo evaluation using four-dimensional flow MRI. Magn Reson Med. 2017;77:794–805.
79. Dyverfeldt P, Hope MD, Tseng EE, Saloner D. Magnetic resonance measurement of turbulent kinetic energy for the estimation of irreversible pressure loss in aortic stenosis. JACC Cardiovasc Imaging. 2013;6:64–71.
80. Zajac J, Eriksson J, Dyverfeldt P, Bolger AF, Ebbers T, Carlhäll C-J. Turbulent kinetic energy in normal and myopathic left ventricles. J Magn Reson Imaging. 2015;41:1021–9.
81. Westenberg JJM, de Roos A, Grotenhuis HB, Steendijk P, Hendriksen D, van den Boogaard PJ, van der Geest RJ, Bax JJ, Jukema JW, Reiber JHC. Improved aortic pulse wave velocity assessment from multislice two-directional in-plane velocity-encoded magnetic resonance imaging. J Magn Reson Imaging. 2010;32:1086–94.
82. Markl M, Wallis W, Brendecke S, Simon J, Frydrychowicz A, Harloff A. Estimation of global aortic pulse wave velocity by flow-sensitive 4D MRI. Magn Reson Med. 2010;63:1575–82.
83. Geddes LA, Voelz MH, Babbs CF, Bourland JD, Tacker WA. Pulse transit time as an indicator of arterial blood pressure. Psychophysiology. 1981;18:71–4.

84. Blacher J, Safar ME. Large-artery stiffness, hypertension and cardiovascular risk in older patients. Nat Clin Pract Cardiovasc Med. 2005;2:450–5.
85. Wentland AL, Grist TM, Wieben O. Review of MRI-based measurements of pulse wave velocity: a biomarker of arterial stiffness. Cardiovasc Diagn Ther. 2014;4:193–206.
86. Vlachopoulos C, Aznaouridis K, Stefanadis C. Prediction of cardiovascular events and all-cause mortality with arterial stiffness: a systematic review and meta-analysis. J Am Coll Cardiol. 2010;55:1318–27.
87. Ait-Oufella H, Collin C, Bozec E, Laloux B, Ong K-T, Dufouil C, Boutouyrie P, Laurent S. Long-term reduction in aortic stiffness: a 5.3-year follow-up in routine clinical practice. J Hypertens. 2010;28:2336–41.
88. Saito T, Saito T, Sugiyama S, Asai K, Yasutake M, Mizuno K. Effects of long-term treatment for obstructive sleep apnea on pulse wave velocity. Hypertens Res. 2010;33:844–9.
89. Reference Values for Arterial Stiffness' Collaboration. Determinants of pulse wave velocity in healthy people and in the presence of cardiovascular risk factors: 'establishing normal and reference values.'. Eur Heart J. 2010;31:2338–50.
90. Mohiaddin RH, Firmin DN, Longmore DB. Age-related changes of human aortic flow wave velocity measured noninvasively by magnetic resonance imaging. J Appl Physiol. 1993;74:492–7.
91. Ibrahim E-SH, Johnson KR, Miller AB, Shaffer JM, White RD. Measuring aortic pulse wave velocity using high-field cardiovascular magnetic resonance: comparison of techniques. J Cardiovasc Magn Reson. 2010;12:26.
92. Hardy CJ, Bolster BD, McVeigh ER, Adams WJ, Zerhouni EA. A one-dimensional velocity technique for NMR measurement of aortic distensibility. Magn Reson Med. 1994;31:513–20.
93. Mohiaddin RH, Longmore DB. MRI studies of atherosclerotic vascular disease: structural evaluation and physiological measurements. Br Med Bull. 1989;45:968–90.
94. Yu H-Y, Peng H-H, Wang J-L, Wen C-Y, Tseng W-YI. Quantification of the pulse wave velocity of the descending aorta using axial velocity profiles from phase-contrast magnetic resonance imaging. Magn Reson Med. 2006;56:876–83.
95. Fielden SW, Fornwalt BK, Jerosch-Herold M, Eisner RL, Stillman AE, Oshinski JN. A new method for the determination of aortic pulse wave velocity using cross-correlation on 2D PCMR velocity data. J Magn Reson Imaging. 2008;27:1382–7.
96. Dyverfeldt P, Ebbers T, Länne T. Pulse wave velocity with 4D flow MRI: systematic differences and age-related regional vascular stiffness. Magn Reson Imaging. 2014;32:1266–71.
97. Malek AM, Jackman R, Rosenberg RD, Izumo S. Endothelial expression of thrombomodulin is reversibly regulated by fluid shear stress. Circ Res. 1994;74:852–60.
98. Lehoux S, Tedgui A. Cellular mechanics and gene expression in blood vessels. J Biomech. 2003;36:631–43.
99. Cheng C, Tempel D, van Haperen R, van der Baan A, Grosveld F, Daemen MJAP, Krams R, de Crom R. Atherosclerotic lesion size and vulnerability are determined by patterns of fluid shear stress. Circulation. 2006;113:2744–53.
100. Bissell MM, Hess AT, Biasiolli L, Glaze SJ, Loudon M, Pitcher A, Davis A, Prendergast B, Markl M, Barker AJ, Neubauer S, Myerson SG. Aortic dilation in bicuspid aortic valve disease: flow pattern is a major contributor and differs with valve fusion type. Circ Cardiovasc Imaging. 2013;6:499–507.
101. Mahadevia R, Barker AJ, Schnell S, Entezari P, Kansal P, Fedak PW, Malaisrie SC, McCarthy P, Collins J, Carr J, Markl M. Bicuspid aortic cusp fusion morphology alters aortic three-dimensional outflow patterns, wall shear stress, and expression of aortopathy. Circulation. 2014;129:673–82.
102. Malek AM, Alper SL, Izumo S. Hemodynamic shear stress and its role in atherosclerosis. JAMA. 1999;282:2035–42.
103. Dolan JM, Kolega J, Meng H. High wall shear stress and spatial gradients in vascular pathology: a review. Ann Biomed Eng. 2013;41:1411–27.
104. Boussel L, Rayz V, McCulloch C, Martin A, Acevedo-Bolton G, Lawton M, Higashida R, Smith WS, Young WL, Saloner D. Aneurysm growth occurs at region of low wall shear

stress: patient-specific correlation of hemodynamics and growth in a longitudinal study. Stroke. 2008;39:2997–3002.
105. Stalder A, Russe M, Frydrychowicz A, Bock J, Hennig J, Markl M. Quantitative 2D and 3D phase contrast MRI: optimized analysis of blood flow and vessel wall parameters. Magn Reson Med. 2008;60:1218–31.
106. Ku DN, Giddens DP, Zarins CK, Glagov S. Pulsatile flow and atherosclerosis in the human carotid bifurcation. Positive correlation between plaque location and low oscillating shear stress. Arteriosclerosis. 1985;5:293–302.
107. Van Ooij P, Potters WV, Guédon A, Schneiders JJ, Marquering HA, Majoie CB, Vanbavel E, Nederveen AJ. Wall shear stress estimated with phase contrast MRI in an in vitro and in vivo intracranial aneurysm. J Magn Reson Imaging. 2013;38:876–84.
108. Chang W, Loecher MW, Wu Y, Niemann DB, Ciske B, Aagaard-Kienitz B, Kecskemeti S, Johnson KM, Wieben O, Mistretta C, Turski P. Hemodynamic changes in patients with arteriovenous malformations assessed using high-resolution 3D radial phase-contrast MR angiography. AJNR Am J Neuroradiol. 2012;33:1565–72.
109. Potters WV, van Ooij P, Marquering HA, VanBavel E, Nederveen AJ. Volumetric arterial wall shear stress calculation based on cine phase contrast MRI. J Magn Reson Imaging. 2015;41:505–16.
110. Ziegler M, Lantz J, Ebbers T, Dyverfeldt P. Assessment of turbulent flow effects on the vessel wall using four-dimensional flow MRI. Magn Reson Med. 2017;77:2310–9.
111. van Ooij P, Garcia J, Potters WV, Malaisrie SC, Collins JD, Carr JC, Markl M, Barker AJ. Age-related changes in aortic 3D blood flow velocities and wall shear stress: implications for the identification of altered hemodynamics in patients with aortic valve disease. J Magn Reson Imaging. 2016;43:1239–49.
112. van Ooij P, Potters WV, Collins J, Carr M, Carr J, Malaisrie SC, Fedak PWM, McCarthy PM, Markl M, Barker AJ. Characterization of abnormal wall shear stress using 4D flow MRI in human bicuspid aortopathy. Ann Biomed Eng. 2015;43:1385–97.
113. Markl M, Wallis W, Harloff A. Reproducibility of flow and wall shear stress analysis using flow-sensitive four-dimensional MRI. J Magn Reson Imaging. 2011;33:988–94.
114. van Ooij P, Powell AL, Potters WV, Carr JC, Markl M, Barker AAJ. Reproducibility and interobserver variability of systolic blood flow velocity and 3D wall shear stress derived from 4D flow MRI in the healthy aorta. J Magn Reson Imaging. 2016;43:236–48.
115. Schubert T, Bieri O, Pansini M, Stippich C, Santini F. Peak velocity measurements in tortuous arteries with phase contrast magnetic resonance imaging: the effect of multidirectional velocity encoding. Investig Radiol. 2014;49:189–94.
116. Wetzel S, Meckel S, Frydrychowicz A, Bonati L, Radue EW, Scheffler K, Hennig J, Markl M. In vivo assessment and visualization of intracranial arterial hemodynamics with flow-sensitized 4D MR imaging at 3T. AJNR Am J Neuroradiol. 2007;28:433–8.
117. Václavů L, Baldew ZAV, Gevers S, Mutsaerts HJMM, Fijnvandraat K, Cnossen MH, Majoie CB, Wood JC, VanBavel E, Biemond BJ, van Ooij P, Nederveen AJ. Intracranial 4D flow magnetic resonance imaging reveals altered haemodynamics in sickle cell disease. Br J Haematol. 2018;180:432–42.
118. Isoda H, Ohkura Y, Kosugi T, Hirano M, Alley MT, Bammer R, Pelc NJ, Namba H, Sakahara H. Comparison of hemodynamics of intracranial aneurysms between MR fluid dynamics using 3D cine phase-contrast MRI and MR-based computational fluid dynamics. Neuroradiology. 2010;52:913–20.
119. Hope TA, Hope MD, Purcell DD, von Morze C, Vigneron DB, Alley MT, Dillon WP. Evaluation of intracranial stenoses and aneurysms with accelerated 4D flow. Magn Reson Imaging. 2010;28:41–6.
120. Chang W, Landgraf B, Johnson KM, Kecskemeti S, Wu Y, Velikina J, Rowley H, Wieben O, Mistretta C, Turski P. Velocity measurements in the middle cerebral arteries of healthy volunteers using 3D radial phase-contrast HYPRFlow: comparison with transcranial doppler sonography and 2D phase-contrast MR imaging. AJNR Am J Neuroradiol. 2011;32:54–9.

121. van Ooij P, Schneiders JJ, Marquering HA, Majoie CB, van Bavel E, Nederveen AJ. 3D cine phase-contrast MRI at 3T in intracranial aneurysms compared with patient-specific computational fluid dynamics. AJNR Am J Neuroradiol. 2013;34:1785–91.
122. Chang W, Wu Y, Johnson K, Loecher M, Wieben O, Edjlali M, Oppenheim C, Roca P, Hald J, Aagaard-Kienitz B, Niemann D, Mistretta C, Turski P. Fast contrast-enhanced 4D MRA and 4D flow MRI using constrained reconstruction (HYPRFlow): potential applications for brain arteriovenous malformations. AJNR Am J Neuroradiol. 2015;36:1049–55.
123. Ansari SA, Schnell S, Carroll T, Vakil P, Hurley MC, Wu C, Carr J, Bendok BR, Batjer H, Markl M. Intracranial 4D flow MRI: toward individualized assessment of arteriovenous malformation hemodynamics and treatment-induced changes. AJNR Am J Neuroradiol. 2013;34:1922–8.
124. Wu C, Ansari SA, Honarmand AR, Vakil P, Hurley MC, Bendok BR, Carr J, Carroll TJ, Markl M. Evaluation of 4D vascular flow and tissue perfusion in cerebral arteriovenous malformations: influence of Spetzler-Martin grade, clinical presentation, and AVM risk factors. AJNR Am J Neuroradiol. 2015;36:1142–9.
125. van Ooij P, Zwanenburg JJM, Visser F, Majoie CB, VanBavel E, Hendrikse J, Nederveen AJ. Quantification and visualization of flow in the circle of Willis: time-resolved three-dimensional phase contrast MRI at 7 T compared with 3 T. Magn Reson Med. 2013;69:868–76.
126. Cebral JR, Castro MA, Burgess JE, Pergolizzi RS, Sheridan MJ, Putman CM. Characterization of cerebral aneurysms for assessing risk of rupture by using patient-specific computational hemodynamics models. AJNR Am J Neuroradiol. 2005;26:2550–9.
127. Hassan T, Ezura M, Timofeev EV, Tominaga T, Saito T, Takahashi A, Takayama K, Yoshimoto T. Computational simulation of therapeutic parent artery occlusion to treat giant vertebrobasilar aneurysm. AJNR Am J Neuroradiol. 2004;25:63–8.
128. Jou LD, Quick CM, Young WL, Lawton MT, Higashida R, Martin A, Saloner D. Computational approach to quantifying hemodynamic forces in giant cerebral aneurysms. AJNR Am J Neuroradiol. 2003;24:1804–10.
129. Steinman DA, Milner JS, Norley CJ, Lownie SP, Holdsworth DW. Image-based computational simulation of flow dynamics in a giant intracranial aneurysm. AJNR Am J Neuroradiol. 2003;24:559–66.
130. Tateshima S, Murayama Y, Villablanca JP, Morino T, Nomura K, Tanishita K, Viñuela F. In vitro measurement of fluid-induced wall shear stress in unruptured cerebral aneurysms harboring blebs. Stroke. 2003;34:187–92.
131. Castro MA, Putman CM, Cebral JR. Computational fluid dynamics modeling of intracranial aneurysms: effects of parent artery segmentation on intra-aneurysmal hemodynamics. AJNR Am J Neuroradiol. 2006;27:1703–9.
132. Isoda H, Ohkura Y, Kosugi T, Hirano M, Takeda H, Hiramatsu H, Yamashita S, Takehara Y, Alley M, Bammer R, Pelc N, Namba H, Sakahara H. In vivo hemodynamic analysis of intracranial aneurysms obtained by magnetic resonance fluid dynamics (MRFD) based on time-resolved three-dimensional phase-contrast MRI. Neuroradiology. 2010;52:921–8.
133. Rayz VL, Boussel L, Ge L, Leach JR, Martin AJ, Lawton MT, McCulloch C, Saloner D. Flow residence time and regions of intraluminal thrombus deposition in intracranial aneurysms. Ann Biomed Eng. 2010;38:3058–69.
134. Meckel S, Stalder AF, Santini F, Radü E-W, Rüfenacht DA, Markl M, Wetzel SG. In vivo visualization and analysis of 3-D hemodynamics in cerebral aneurysms with flow-sensitized 4-D MR imaging at 3 T. Neuroradiology. 2008;50:473–84.
135. Kecskemeti S, Johnson K, Wu Y, Mistretta C, Turski P, Wieben O. High resolution three-dimensional cine phase contrast MRI of small intracranial aneurysms using a stack of stars k-space trajectory. J Magn Reson Imaging. 2011; https://doi.org/10.1002/jmri.23501.
136. Schnell S, Ansari SA, Vakil P, Wasielewski M, Carr ML, Hurley MC, Bendok BR, Batjer H, Carroll TJ, Carr J, Markl M. Three-dimensional hemodynamics in intracranial aneurysms: influence of size and morphology. J Magn Reson Imaging. 2014;39:120–31.
137. Blankena R, Kleinloog R, Verweij BH, Van Ooij P, Ten Haken B, Luijten PR, Rinkel GJE, Zwanenburg JJM. Thinner regions of intracranial aneurysm wall correlate with regions of higher wall shear stress: a 7T MRI study. Am J Neuroradiol. 2016;37:1310–7.

138. Lee SW, Antiga L, Spence JD, Steinman DA. Geometry of the carotid bifurcation predicts its exposure to disturbed flow. Stroke. 2008;39:2341–7.
139. Markl M, Wegent F, Zech T, Bauer S, Strecker C, Schumacher M, Weiller C, Hennig J, Harloff A. In vivo wall shear stress distribution in the carotid artery: effect of bifurcation geometry, internal carotid artery stenosis, and recanalization therapy. Circ Cardiovasc Imaging. 2010;3:647–55.
140. Cibis M, Potters WV, Gijsen FJ, Marquering H, vanBavel E, van der Steen AF, Nederveen AJ, Wentzel JJ. Wall shear stress calculations based on 3D cine phase contrast MRI and computational fluid dynamics: a comparison study in healthy carotid arteries. NMR Biomed. 2014;27:826–34.
141. Cibis M, Potters WV, Selwaness M, Gijsen FJ, Franco OH, Arias Lorza AM, de Bruijne M, Hofman A, van der Lugt A, Nederveen AJ, Wentzel JJ. Relation between wall shear stress and carotid artery wall thickening MRI versus CFD. J Biomech. 2016;49:735–41.
142. van Ooij P, Cibis M, Rowland EM, Vernooij MW, van der Lugt A, Weinberg PD, Wentzel JJ, Nederveen AJ. Spatial correlations between MRI-derived wall shear stress and vessel wall thickness in the carotid bifurcation. Eur Radiol Exp. 2018;2:27.
143. Stokholm R, Oyre S, Ringgaard S, Flaagoy H, Paaske WP, Pedersen EM. Determination of wall shear rate in the human carotid artery by magnetic resonance techniques. Eur J Vasc Endovasc Surg. 2000;20:427–33.
144. Gelfand BD, Epstein FH, Blackman BR. Spatial and spectral heterogeneity of time-varying shear stress profiles in the carotid bifurcation by phase-contrast MRI. J Magn Reson Imaging. 2006;24:1386–92.
145. Harloff A, Berg S, Barker AJ, Schöllhorn J, Schumacher M, Weiller C, Markl M. Wall shear stress distribution at the carotid bifurcation: influence of eversion carotid endarterectomy. Eur Radiol. 2013;23:3361–9.
146. Harloff A, Albrecht F, Spreer J, Stalder A, Bock J, Frydrychowicz A, Schöllhorn J, Hetzel A, Schumacher M, Hennig J, Markl M. 3D blood flow characteristics in the carotid artery bifurcation assessed by flow-sensitive 4D MRI at 3T. Magn Reson Med. 2009;61:65–74.
147. Kroner ES, Lamb HJ, Siebelink HM, Cannegieter SC, van den Boogaard PJ, van der Wall EE, de Roos A, Westenberg JJ. Pulse wave velocity and flow in the carotid artery versus the aortic arch: effects of aging. J Magn Reson Imaging. 2014;40:287–93.
148. Peper ES, Strijkers GJ, Gazzola K, Potters WV, Motaal AG, Luirink IK, Hutten BA, Wiegman A, van Ooij P, van den Born B-JH, Nederveen AJ, Coolen BF. Regional assessment of carotid artery pulse wave velocity using compressed sensing accelerated high temporal resolution 2D CINE phase contrast cardiovascular magnetic resonance. J Cardiovasc Magn Reson. 2018;20:86.
149. Sigovan M, Hope MD, Dyverfeldt P, Saloner D. Comparison of four-dimensional flow parameters for quantification of flow eccentricity in the ascending aorta. J Magn Reson Imaging. 2011;34:1226–30.
150. Burris NS, Sigovan M, Knauer HA, Tseng EE, Saloner D, Hope MD. Systolic flow displacement correlates with future ascending aortic growth in patients with bicuspid aortic valves undergoing magnetic resonance surveillance. Investig Radiol. 2014;49:635–9.
151. Garcia J, Barker AJ, Murphy I, Jarvis K, Schnell S, Collins JD, Carr JC, Malaisrie SC, Markl M. Four-dimensional flow magnetic resonance imaging-based characterization of aortic morphometry and haemodynamics: impact of age, aortic diameter, and valve morphology. Eur Hear J Cardiovasc Imaging. 2015. jev228
152. Hope MD, Sigovan M, Wrenn SJ, Saloner D, Dyverfeldt P. MRI hemodynamic markers of progressive bicuspid aortic valve-related aortic disease. J Magn Reson Imaging. 2014;40:140–5.
153. Raghav V, Barker AJ, Mangiameli D, Mirabella L, Markl M, Yoganathan AP. Valve mediated hemodynamics and their association with distal ascending aortic diameter in bicuspid aortic valve subjects. J Magn Reson Imaging. 2018;47:246–54.
154. Kauhanen SP, Hedman M, Kariniemi E, Jaakkola P, Vanninen R, Saari P, Liimatainen T. Aortic dilatation associates with flow displacement and increased circumferential wall shear stress in patients without aortic stenosis: a prospective clinical study. J Magn Reson Imaging. 2019; https://doi.org/10.1002/jmri.26655.

155. Rodríguez-Palomares JF, Dux-Santoy L, Guala A, Kale R, Maldonado G, Teixidó-Turà G, Galian L, Huguet M, Valente F, Gutiérrez L, González-Alujas T, Johnson KM, Wieben O, García-Dorado D, Evangelista A. Aortic flow patterns and wall shear stress maps by 4D-flow cardiovascular magnetic resonance in the assessment of aortic dilatation in bicuspid aortic valve disease. J Cardiovasc Magn Reson. 2018;20:28.
156. Burk J, Blanke P, Stankovic Z, Barker A, Russe M, Geiger J, Frydrychowicz A, Langer M, Markl M. Evaluation of 3D blood flow patterns and wall shear stress in the normal and dilated thoracic aorta using flow-sensitive 4D CMR. J Cardiovasc Magn Reson. 2012;14:84.
157. Harloff A, Nussbaumer A, Bauer S, Stalder AF, Frydrychowicz A, Weiller C, Hennig J, Markl M. In vivo assessment of wall shear stress in the atherosclerotic aorta using flow-sensitive 4D MRI. Magn Reson Med. 2010;63:1529–36.
158. Hope MD, Hope TA, Crook SE, Ordovas KG, Urbania TH, Alley MT, Higgins CB. 4D flow CMR in assessment of valve-related ascending aortic disease. JACC Cardiovasc Imaging. 2011;4:781–7.
159. Barker AJ, Markl M, Burk J, Lorenz R, Bock J, Bauer S, Schulz-Menger J, von Knobelsdorff-Brenkenhoff F. Bicuspid aortic valve is associated with altered wall shear stress in the ascending aorta. Circ Cardiovasc Imaging. 2012;5:457–66.
160. Meierhofer C, Schneider EP, Lyko C, Hutter A, Martinoff S, Markl M, Hager A, Hess J, Stern H, Fratz S. Wall shear stress and flow patterns in the ascending aorta in patients with bicuspid aortic valves differ significantly from tricuspid aortic valves: a prospective study. Eur Heart J Cardiovasc Imaging. 2012;14:797–804.
161. Shan Y, Li J, Wang Y, Wu B, Barker AJ, Markl M, Wang C, Wang X, Shu X. Aortic shear stress in patients with bicuspid aortic valve with stenosis and insufficiency. J Thorac Cardiovasc Surg. 2017;153:1263–1272.e1.
162. van Ooij P, Markl M, Collins JD, Carr JC, Rigsby C, Bonow RO, Chris Malaisrie S, McCarthy PM, Fedak PWM, Barker AJ. Aortic valve stenosis alters expression of regional aortic wall shear stress: new insights from a 4-dimensional flow magnetic resonance imaging study of 571 subjects. J Am Heart Assoc. 2017;6:1–14.
163. van Ooij P, Markl M, Collins JD, Carr JC, Malaisrie SC, McCarthy PM, Nederveen AJ, Fedak PWM, Barker AJ. Mapping of abnormal aortic hemodynamics in 515 patients with aortopathy. Proc Int Soc Mag Reson. 2017;25:0754.
164. Guzzardi DG, Barker AJ, van Ooij P, Malaisrie SC, Puthumana JJ, Belke DD, Mewhort HEM, Svystonyuk DA, Kang S, Verma S, Collins J, Carr J, Bonow RO, Markl M, Thomas JD, Mccarthy PM, Fedak PWM. Valve-related hemodynamics mediate human bicuspid aortopathy: insights from wall shear stress mapping. J Am Coll Cardiol. 2015;66:892–900.
165. Bollache E, Guzzardi DG, Sattari S, Olsen KE, Di Martino ES, Malaisrie SC, van Ooij P, Collins J, Carr J, McCarthy PM, Markl M, Barker AJ, Fedak PWM. Aortic valve-mediated wall shear stress is heterogeneous and predicts regional aortic elastic fiber thinning in bicuspid aortic valve-associated aortopathy. J Thorac Cardiovasc Surg. 2018;156:2112–2120.e2.
166. Alpendurada F, Mohiaddin R. 1039 prevalence of cardiovascular manifestations in patients with Marfan syndrome: a cardiovascular magnetic resonance study. J Cardiovasc Magn Reson. 2008;10:A164.
167. Engelfriet PM, Boersma E, Tijssen JGP, Bouma BJ, Mulder BJM. Beyond the root: dilatation of the distal aorta in Marfan's syndrome. Heart. 2006;92:1238–43.
168. Mariucci EM, Lovato L, Rosati M, Palena LM, Bonvicini M, Fattori R. Dilation of peripheral vessels in Marfan syndrome: importance of thoracoabdominal MR angiography. Int J Cardiol. 2013;167:2928–31.
169. Geiger J, Hirtler D, Gottfried K, Rahman O, Bollache E, Barker AJ, Markl M, Stiller B. Longitudinal evaluation of aortic hemodynamics in Marfan syndrome: new insights from a 4D flow cardiovascular magnetic resonance multi-year follow-up study. J Cardiovasc Magn Reson. 2017;19:33.
170. van der Palen RLF, Barker AJ, Bollache E, Garcia J, Rose MJ, van Ooij P, Young LT, Roest AAW, Markl M, Robinson JD, Rigsby CK. Altered aortic 3D hemodynamics and geometry in pediatric Marfan syndrome patients. J Cardiovasc Magn Reson. 2017;19:30.

171. Wang H-H, Chiu H-H, Tseng W-YI, Peng H-H. Does altered aortic flow in marfan syndrome relate to aortic root dilatation? J Magn Reson Imaging. 2016;44:500–8.
172. Kröner ESJ, Scholte AJHA, de Koning PJH, van den Boogaard PJ, Kroft LJM, van der Geest RJ, Hilhorst-Hofstee Y, Lamb HJ, Siebelink H-MJ, Mulder BJM, Groenink M, Radonic T, van der Wall EE, de Roos A, Reiber JHC, Westenberg JJM. MRI-assessed regional pulse wave velocity for predicting absence of regional aorta luminal growth in marfan syndrome. Int J Cardiol. 2013;167:2977–82.
173. Guala A, Rodriguez-Palomares J, Dux-Santoy L, Teixido-Tura G, Maldonado G, Galian L, Huguet M, Valente F, Gutiérrez L, González-Alujas T, Johnson KM, Wieben O, Sao Avilés A, Garcia-Dorado D, Evangelista A. Influence of aortic dilation on the regional aortic stiffness of bicuspid aortic valve assessed by 4-dimensional flow cardiac magnetic resonance: comparison with Marfan syndrome and degenerative aortic aneurysm. JACC Cardiovasc Imaging. 2018; https://doi.org/10.1016/j.jcmg.2018.03.017.
174. Abbruzzese PA, Aidala E. Aortic coarctation: an overview. J Cardiovasc Med (Hagerstown). 2007;8:123–8.
175. Hope MD, Meadows AK, Hope TA, Ordovas KG, Saloner D, Reddy GP, Alley MT, Higgins CB. Clinical evaluation of aortic coarctation with 4D flow MR imaging. J Magn Reson Imaging. 2010;31:711–8.
176. Frydrychowicz A, Markl M, Hirtler D, Harloff A, Schlensak C, Geiger J, Stiller B, Arnold R. Aortic hemodynamics in patients with and without repair of aortic coarctation: in vivo analysis by 4D flow-sensitive magnetic resonance imaging. Investig Radiol. 2011;46:317–25.
177. Riesenkampff E, Fernandes JF, Meier S, Goubergrits L, Kropf S, Schubert S, Berger F, Henneumuth A, Kuehne T. Pressure fields by flow-sensitive, 4D, velocity-encoded CMR in patients with aortic coarctation. JACC Cardiovasc Imaging. 2014;7:920–6.
178. Vasanawala SS, Hanneman K, Alley MT, Hsiao A. Congenital heart disease assessment with 4D flow MRI. J Magn Reson Imaging. 2015;42:870–86.
179. Allen BD, Barker AJ, Carr JC, Silverberg RA, Markl M. Time-resolved three-dimensional phase contrast MRI evaluation of bicuspid aortic valve and coarctation of the aorta. Eur Heart J Cardiovasc Imaging. 2013;14:399.
180. Farag ES, van Ooij P, Boekholdt SM, Planken RN, Dukker KC, Bouma BJ, Groenink M, Koolbergen DR, Sojak V, Nederveen AJ, Hazekamp MG, de Mol BA, Kluin J. Abnormal blood flow and wall shear stress are present in corrected aortic coarctation despite successful surgical repair. J Cardiovasc Surg. 2019;60:152–4.
181. Janić M, Lunder M, Sabovič M. Arterial stiffness and cardiovascular therapy. Biomed Res Int. 2014;2014:621437.
182. Tomiyama H, Yamashina A. Non-invasive vascular function tests: their pathophysiological background and clinical application. Circ J. 2010;74:24–33.
183. Sethi S, Rivera O, Oliveros R, Chilton R. Aortic stiffness: pathophysiology, clinical implications, and approach to treatment. Integr Blood Press Control. 2014;7:29–34.
184. Markl M, Wallis W, Strecker C, Gladstone BP, Vach W, Harloff A. Analysis of pulse wave velocity in the thoracic aorta by flow-sensitive four-dimensional MRI: reproducibility and correlation with characteristics in patients with aortic atherosclerosis. J Magn Reson Imaging. 2012;35:1162–8.
185. Wehrum T, Günther F, Kams M, Wendel S, Strecker C, Mirzaee H, Harloff A. Quantification of aortic stiffness in stroke patients using 4D flow MRI in comparison with transesophageal echocardiography. Int J Cardiovasc Imaging. 2018;34:1629–36.
186. Harloff A, Mirzaee H, Lodemann T, Hagenlocher P, Wehrum T, Stuplich J, Hennemuth A, Hennig J, Grundmann S, Vach W. Determination of aortic stiffness using 4D flow cardiovascular magnetic resonance - a population-based study. J Cardiovasc Magn Reson. 2018;20:43.
187. Goyen M, Heuser LJ. Improved peripheral MRA using multi-velocity-encoding phase contrast-enhanced MRA techniques. Acta Radiol. 2000;41:139–41.
188. Steffens JC, Link J, Müller-Hülsbeck S, Freund M, Brinkmann G, Heller M. Cardiac-gated two-dimensional phase-contrast MR angiography of lower extremity occlusive disease. AJR Am J Roentgenol. 1997;169:749–54.

189. Swan JS, Grist TM, Weber DM, Sproat IA, Wojtowycz MM. MR angiography of the pelvis with variable velocity encoding and a phased-array coil. Radiology. 1994;190:363–9.
190. Yucel EK, Dumoulin CL, Waltman AC. MR angiography of lower-extremity arterial disease: preliminary experience. J Magn Reson Imaging. 1992;2:303–9.
191. Krug B, Kugel H, Friedmann G, Bunke J, van Dijk P, Schmidt R, Hirche HJ. MR imaging of poststenotic flow phenomena: experimental studies. J Magn Reson Imaging. 1991;1:585–91.
192. Krug B, Kugel H, Harnischmacher U, Heindel W, Schmidt R, Krings F. MR pulsatility measurements in peripheral arteries: preliminary results. Magn Reson Med. 1995;34:698–705.
193. Frydrychowicz A, Winterer JT, Zaitsev M, Jung B, Hennig J, Langer M, Markl M. Visualization of iliac and proximal femoral artery hemodynamics using time-resolved 3D phase contrast MRI at 3T. J Magn Reson Imaging. 2007;25:1085–92.
194. Kang C-K, Park C-A, Lee DS, Lee Y-B, Park C-W, Kim Y-B, Cho Z-H. Velocity measurement of microvessels using phase-contrast magnetic resonance angiography at 7 Tesla MRI. Magn Reson Med. 2016;75:1640–6.
195. Hess AT, Bissell MM, Ntusi NAB, Lewis AJM, Tunnicliffe EM, Greiser A, Stalder AF, Francis JM, Myerson SG, Neubauer S, Robson MD. Aortic 4D flow: quantification of signal-to-noise ratio as a function of field strength and contrast enhancement for 1.5T, 3T, and 7T. Magn Reson Med. 2014. n/a-n/a.
196. Schmitter S, Schnell S, Uğurbil K, Markl M, Van de Moortele P-F. Towards high-resolution 4D flow MRI in the human aorta using kt-GRAPPA and B1+ shimming at 7T. J Magn Reson Imaging. 2016;44:486–99.
197. Nett EJ, Johnson KM, Frydrychowicz A, Del Rio AM, Schrauben E, Francois CJ, Wieben O. Four-dimensional phase contrast MRI with accelerated dual velocity encoding. J Magn Reson Imaging. 2012; https://doi.org/10.1002/jmri.23588.
198. Schnell S, Ansari SA, Wu C, Garcia J, Murphy IG, Rahman OA, Rahsepar AA, Aristova M, Collins JD, Carr JC, Markl M. Accelerated dual-venc 4D flow MRI for neurovascular applications. J Magn Reson Imaging. 2017;46:102–14.
199. Schnell S, Rose MJ, Wu C, Garcia J, Robinson JD, Markl M, Rigsby CK. Improved assessment of aortic hemodynamics by k-t accelerated dual-venc 4D flow MRI in pediatric patients. J Cardiovasc Magn Reson. 2016;18:O96.
200. Lee AT, Pike GB, Pelc NJ. Three-point phase-contrast velocity measurements with increased velocity-to-noise ratio. Magn Reson Med. 1995;33:122–6.
201. Pipe JG. A simple measure of flow disorder and wall shear stress in phase contrast MRI. Magn Reson Med. 2003;49:543–50.
202. Binter C, Knobloch V, Manka R, Sigfridsson A, Kozerke S. Bayesian multipoint velocity encoding for concurrent flow and turbulence mapping. Magn Reson Med. 2013;69:1337–45.
203. Loecher M, Ennis DB. Velocity reconstruction with nonconvex optimization for low-velocity-encoding phase-contrast MRI. Magn Reson Med. 2018;80:42–52.
204. Bustamante M, Petersson S, Eriksson J, Alehagen U, Dyverfeldt P, Carlhäll C-J, Ebbers T. Atlas-based analysis of 4D flow CMR: automated vessel segmentation and flow quantification. J Cardiovasc Magn Reson. 2015;17:87.
205. Schrauben E, Wåhlin A, Ambarki K, Spaak E, Malm J, Wieben O, Eklund A. Fast 4D flow MRI intracranial segmentation and quantification in tortuous arteries. J Magn Reson Imaging. 2015;42:1458–64.

Chapter 17
Computational Fluid Dynamics for Evaluating Hemodynamics

David Saloner

Overview

Blood flow in vessels plays an important role in the physiological response of the vasculature in health and disease and in preserving the function of the end organs. While many of the descriptors that are important in evaluating the health of a vascular territory are well established, many others remain the domain of active investigation. The ability to establish the relationship between adverse hemodynamics and patient outcome has dramatically improved with the advent of robust high-resolution, noninvasive imaging measures of the local disease in the vessel wall, the prevailing flow conditions, and the status of the end organ. However, establishing causal connections between hemodynamic descriptors and physiological impact requires detailed knowledge of the spatial and temporal distribution of those descriptors. Computational Fluid Dynamics (CFD) methods are well suited to this task. The ever-increasing power of computational platform resources permits simulations of appropriately complex anatomic models in manageable compute times. In this chapter, the assumptions that underlie the CFD modeling approaches that are widely used in describing flow in the human vasculature are discussed. A description will be provided of the computational pipeline. Finally, examples of applications to patient-specific conditions will be presented.

D. Saloner (✉)
Department of Radiology and Biomedical Imaging, University of California San Francisco, San Francisco, CA, USA
e-mail: David.Saloner@ucsf.edu

C. Yuan et al. (eds.), *Vessel Based Imaging Techniques*,
https://doi.org/10.1007/978-3-030-25249-6_17

Assessing the Velocity Field

In the same way that the motion of solid objects in space is described by Newton's equations of motion, fluid flow is described by the Navier-Stokes equations which include pressure terms and the fluid viscosity [1]. These equations can be used to describe fluid flow in a broad range of conditions including external flows (e.g., air flowing around the exterior of a vehicle) or internal flows (such as blood flowing in a blood vessel.) However, it is not possible to provide analytic solutions for the Navier-Stokes equations for any but a few limited geometries and conditions. For this reason, most practical approaches to describing details of hemodynamics rely on numerical simulations, referred to as Computational Fluid Dynamics (CFD). Initial CFD studies were developed in an era of limited computational power and used rudimentary numerical schemes. In the early applications of CFD to the study of vascular physiology, idealized representations of relevant anatomical structures were used [2]. Those began with 2D models which, while informative about important hemodynamic features, failed to capture important effects from secondary flow. The limitations of those models were recognized early on as the dominant role of geometry in governing critical features of hemodynamics became increasingly apparent. Extensions of the idealized models were developed to provide fully three-dimensional representations but were of limited use for patient-specific analyses [3, 4]. An example is presented in Fig. 17.1 of a schematic model of flow in the extracranial carotid arteries. The model is based on representative values of the bifurcation angle between the internal and external carotid arteries and uses typical values

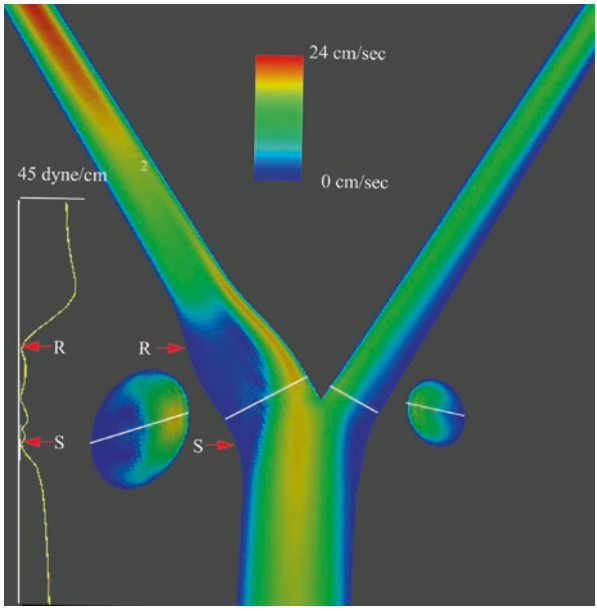

Fig. 17.1 A color-coded CFD-computed velocity field with high velocities encoded in red for a schematic representation of the extracranial carotid bifurcation. Slow recirculating flow in the bulb can be observed (blue region). A plot of the derived wall shear stress along the lateral wall of the internal carotid artery shows an extended area of low wall shear stress in the bulb from the point of flow separation (S) to reattachment (R)

for the diameters of each vessel. General features of the flow in that territory include slow recirculating flow in the bulb of the internal carotid artery and a high velocity region in the medial aspect of the internal carotid artery. Planes transverse to the proximal internal and external carotid arteries are also useful to show those features. Such idealized models became increasingly sophisticated with inclusion of compliant walls, features of wall disease, and modeling of varying blood viscosity properties [5, 6].

More recently, advances in computational methods have been included into commercial solvers with much of that development being spurred by applications to the aerospace, auto, and other industries where flow conditions are significantly more extreme than in the human vasculature. These solvers are now sufficiently sophisticated to readily incorporate realistic geometries and physiological flow conditions and can therefore be applied to patient-specific anatomy and flow.

Imaging Approaches

The interest in utilizing CFD methods in considerations of hemodynamics in vascular disease is manifold. While there are a variety of methods for assessing important features of hemodynamics in vivo, these have relatively coarse spatial and temporal resolution and suffer from technical and physiological challenges. Ultrasound is noninvasive and relatively inexpensive and has excellent temporal resolution for determining the full spectrum of velocities in a fixed insonation volume. It has strong abilities for quantifying peak velocities in flow jets which can be used to infer the degree of stenosis. It is unable to similarly map the velocity field through a three-dimensional volume and, in many cases, is obscured by bowel gas, calcifications, or overlying bone – as is the case for the brain. Furthermore, it is highly operator-dependent and is unsuited to measurement of volume flow. Catheter-injected angiography provides qualitative visualization of flow dynamics which is important for determining important physiological features such as vascular patency and the existence of collateral pathways. However, it is invasive and expensive and is not quantitative. MR imaging, particularly 4D Flow, has a number of desirable features: it is noninvasive and can depict the velocity field in space and time without limitations of overlying anatomy [7, 8]. This offers the possibility of determining derived descriptors such as volume flow and wall shear stress, the frictional force exerted by blood on the vessel wall. However, MR has moderate spatial and temporal resolution. Unlike ultrasound which determines the spectrum of velocities in the insonation volume, MR provides a voxel-averaged velocity measurement. Because of practical imaging constraints such as signal to noise ratios and acquisition times (which are often longer than 10 minutes), studies in a number of vascular territories are acquired with less than three or four voxels across the vascular lumen. The derivation of critical parameters such as the wall shear stress rely on an accurate measurement of the spatial gradient of velocities at the vessel wall, and MR-derived estimates of these measures must therefore be viewed with appropriate caution. A

major attraction of CFD methods is the ability to specify very high resolution in space and time and calculate velocity fields with resolution far beyond anything that is currently achievable with in vivo imaging methods.

Computational Fluid Dynamics (CFD)

In most vascular territories and under a broad range of healthy and pathologic states, a numerical solution of the Navier-Stokes equations can be attained with limited and reasonable assumptions. While methods exist to accommodate each of the following, they are often neglected in conventional CFD calculations of hemodynamics: the vessel wall is assumed to be rigid; blood is assumed to be a Newtonian fluid; and blood flow is considered to be laminar without the presentation of turbulence. With those assumptions, CFD calculations can be conducted if the surface boundary of the vascular structure of interest is specified, if the inlet flow waveform is defined, and if the outlet flow conditions are appropriately conditioned.

Vascular Compliance Returning to the major assumptions, the importance of neglecting vascular compliance is not fully understood given the difficulty in conducting a simulation that includes wall motion – a so-called fluid-structure interaction (FSI) problem [9]. Results of FSI compared to CFD with rigid walls indicate that neglecting compliance in a number of vascular territories (such as the intracranial vessels) has little effect [10]. In other territories such as the aorta, larger differences are reported [11]. It is, however, difficult to assess the extent to which the wall motion is correctly incorporated into the FSI models given their reliance on unreliable in vivo imaging to condition their boundary values. Furthermore, in conditions such as atherosclerosis, aneurysmal disease, or in the elderly population in general, resorting to an FSI simulation is likely unwarranted since vessels lose their compliance under those conditions, and conventional CFD methods are likely to suffice.

Newtonian Viscosity Fluid viscosity describes how the shear stress varies with changes in the shear rate, and if shear stress changes linearly with shear rate, the viscosity is constant. It is then referred to as a Newtonian fluid. Most CFD models assume that blood is a Newtonian fluid. There are in vivo situations where this condition is violated. On one limit, when blood recirculates slowly, red blood cells can aggregate, resulting in an increase in viscosity. Regions of slowly recirculating flow can occur in regions of aneurysmal dilatation. There are a number of analytical formulas that can be incorporated into CFD solvers that attempt to provide more physical models of blood viscosity at low shear rates [12]. There are reports that these effects are relatively small. On the other limit, the viscosity of blood decreases substantially when passing through narrow (<300 micron) vessels when red blood cells move to the center of the vessel leaving only plasma near the wall of the vessel (the Fåhraeus–Lindqvist effect). These vessels are of the scale of arterioles and capillaries and are generally not of current interest for the determination of detailed features in their velocity fields.

Turbulence The caliber and flow rates in healthy vessels are such that flow is laminar with the components of blood moving along well-ordered and predictable trajectories. Flow patterns can still be extremely complex with strong components of vorticity, but flow patterns remain highly predictable. As inertial effects, characterized by the product of velocity and vessel diameter, begin to dominate drag forces, characterized by viscosity, flow transitions from the well-ordered laminar condition to a more chaotic and unpredictable state and manifests as turbulent flow [13, 14]. Conditions that lend themselves to turbulent flow include flow distal to stenoses. Although velocities through the stenosis may increase dramatically, the reduced diameter can ensure that flow remains laminar in the stenosis throat. However, distal to the stenosis, high velocity persists in the flow jet which is now located in a region with a much larger diameter. Flow can then be turbulent with chaotic eddies being shed from the boundaries of the jet, generally accompanied by a dissipation of energy and an audible bruit [14]. Correct numerical simulation of this situation requires a far greater degree of complexity than is required for laminar flow. Models for including turbulence into CFD simulations range from imposition of some simplifying assumptions such as in the most widely used model of turbulence, the k-epsilon model, where it is assumed that the turbulence viscosity is isotropic. Although inclusion of turbulence models into CFD analysis of blood flow in vessels is computationally expensive, commercial codes generally provide a k-epsilon model option [1, 15, 16]. More accurate simulations can be rendered using large eddy simulations [16] or an approach referred to as direct numerical simulation (DNS) [14]. An example of the manifestation of turbulence in a DNS simulation is presented in Fig. 17.2 for flow through an idealized model of an arterial stenosis for flow through a regular cylindrical vessel with a slightly eccentric stenosis representing a 75% reduction in cross-sectional area. This presentation of velocity fluctuations shows a breakdown of the orderly flow in the flow jet into chaotic vortices several diameters distal to the throat of the stenosis. DNS simulations obtain their accuracy by directly computing all flow effects down to the smallest scales needed to accurately describe the relevant flow effects. They are thus extremely computationally intensive, and, while important in regimes such as hypersonic flow over airplane wings, DNS is rarely used in application to physiologic flows. In situations of high flow rates, such as distal to stenoses, flow conditions can be such that flow is no longer truly laminar, and the physics of flow dictates that flow becomes transitional and finally manifests true turbulence. In that case, it is challenging, and sometime

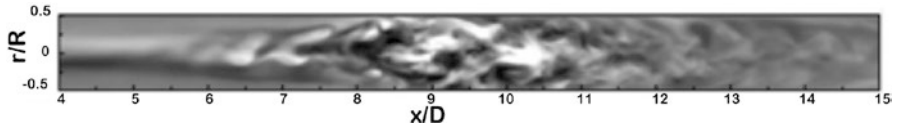

Fig. 17.2 A DNS simulation of flow in the longitudinal plane of a tube with a non-stenosed diameter D, and a 75% eccentric stenosis by area. Streamwise velocity fluctuations are shown (x) along the length of the vessel (x) between 4 and 15 diameters distal to the stenosis. This map shows the transition from regular to complex flow as the flow jet breaks into vortical eddies. (Varghese et al. [14], reproduced with permission)

impossible – even with an extremely high resolution – for code defined for laminar flow to converge to a stable solution, a situation that is manifested by increasingly long computational run times and inconsistent data. To avoid these types of computational failures, commercial CFD solvers are often constructed to include an artificial damping term which ensures that the solution remains stable. In that case, the user needs to realize that although a solution is generated, it is likely inaccurate, and appropriate caution must be used in drawing conclusions from those results.

In general, many physiological conditions of interest can be closely approximated by laminar flow through rigid-walled vessels with Newtonian viscosity. For those cases, conventional CFD simulations can then be applied to generate highly accurate estimates of the velocity field. However, in cases where those conditions are not met, in vivo imaging modalities, in particular 4D Flow MRI methods, provide the intriguing prospect of more accurately determining the velocity field than is possible with CFD as the true physiological behavior is inherently present on a patient-specific basis, and does not require modeling. In the remainder of this chapter, we will restrict ourselves to a discussion of the application of conventional CFD to the analysis of hemodynamics in vivo.

CFD in the Laminar Flow Regime

A CFD analysis provides a numerical solution of the Navier-Stokes equations, the governing equations of fluid motion. The key components required as input to the numerical model are a description of the lumenal surface of the vessels of interest and specification of the inlet and outlet flow boundary conditions.

Lumen Surface Patient-specific modeling requires in vivo images of the vessels of interest [17–19]. The resolution of the images must be sufficient to permit an accurate representation of the associated velocity fields – preferably with greater than five to ten voxels across the vascular lumen. Achieving this is most challenging in regions of pronounced curvature such as at the neck of a saccular aneurysm or in stenotic vessels. For example, an 80% diameter stenosis of the extracranial carotid arteries corresponds to a residual lumenal diameter of little more than 1 mm. For 3D volumetric modalities (MRA or CTA), this provides at most 2–3 voxels across the stenosis. This is even more limiting in territories with stenoses of smaller caliber vessels such as the coronary arteries or the intracranial vessels. However, current imaging modalities provide 3D angiographic images of the vascular lumen with high contrast to noise ratio to the adjacent tissue and with adequate spatial resolution to support high-quality CFD in relatively smooth vessels whose caliber is 3 mm or larger. Segmentation of the lumenal surface from the 3D data set can then be performed and be provided as input into the solver for the geometric boundary condition. Care is needed to avoid misrepresentations of important vascular features as in cases where aneurysmal bulges fold back into close proximity with the parent vessel. Unless the imaging modality has sufficient resolution, the two distinct

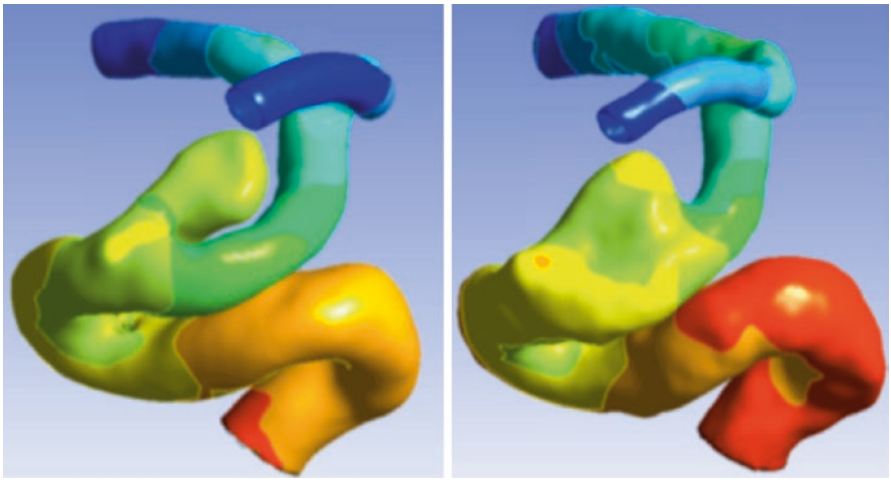

Fig. 17.3 Impact of acquisition resolution. CFD-calculated pressure distribution in a distal internal carotid artery with a cavernous segment aneurysm. Left: pressure map using surface segmentation from a rotational DSA study with 0.2 mm isotropic resolution clearly shows the separation between distal ICA and the aneurysm. Right: pressure map using surface segmentation from a CE-MRA study with 0.7 mm isotropic resolution fails to correctly resolve the inferior aspect of the aneurysm

regions can appear to be merged into one volume. This is illustrated in Fig. 17.3 where a rotational DSA study of an aneurysm of the internal carotid artery clearly identifies the aneurysm as a distinct saccular structure, whereas the lower resolution CE-MRA study merges aneurysm and parent vessel giving the appearance of a fusiform dilatation.

Flow Boundary Conditions In addition to specification of the surface geometry, it is important to provide suitable boundary conditions to define the inlet and outlet flow conditions. The inlet boundary condition is invariably provided by specifying the time-varying volume flow into the vessel of interest – optimally as measured in vivo at the corresponding location for the specific patient. If those are not available, idealized waveforms using representative volume flow values from the literature are often used. In order to have a realistic spatial distribution of velocities across the lumen, the inlet vessel can be extended proximal to the patient-specific domain a sufficient length to ensure that flow is fully developed. More complex models of inlet flow conditions have been formulated to account for cardiac dynamics [20]. Specification of the outlet boundary conditions depends on whether flow is monophasic or triphasic indicating the presence of a reflected wave as in the infrarenal aorta. For monophasic flow, it is sufficient to describe the outlet boundary condition by specifying zero pressure at the outlet. For locations where there is retrograde flow, more complicated modeling of the outlet conditions is required. The presence of retrograde flow indicates the presence of a compliant reservoir in the peripheral vessels or the distal vascular bed that is the source of the pressure that

drives the retrograde flow. Among the approaches used to model the outline boundary conditions has been the use of an electrical circuit analog of the downstream vasculature that consists of a resistance (R1) connected in series with a parallel combination of a second resistance,(R2), and a capacitance, (C) [21–24]. Care is required to appropriately model the values of the resistances and capacitance to ensure that the appropriate triphasic outlet waveform is reproduced [25]. Evaluations have been performed to investigate the sensitivity of computed flow fields to different models of the outlet flow conditions [26]. Models have also been developed that compare flow conditions under different physiology, such as different exercise regimens [24].

CFD Computational Framework

The computation of the velocity field for a patient-specific representation begins with a segmentation of the vascular surface from in vivo imaging. The marching cubes algorithm can be used to render the segmented surface of the lumen as a polygonal (triangular) mesh [27]. In CFD the Navier-Stokes equations are solved at a number of discrete points within a defined computational domain, and it is therefore necessary to create a mesh whereby the fluid volume is discretized into cells [28]. A variety of different techniques have been formulated to perform these simulations with both finite difference and finite volume methods having enjoyed wide use [29]. In both cases, the computational domain is resolved into a network of nodes and elements. The finite element method utilizes approximations of derivatives using the Taylor expansion and requires a structured mesh that is uniform and highly regular. It is therefore inflexible and difficult to implement for realistically complex geometries and the finite volume, which is more flexible is more commonly used. The finite volume method converts the governing equations into algebraic equations that can be numerically solved over discrete control volumes throughout the computational domain. Average values for each cell are calculated by computing fluxes through the cell faces. Conservation of physical properties is ensured as the computational algorithms enforce that flux into the cell element equals the flux out of the cell. With this approach it is no longer necessary to solve on a uniform structured mesh. Semiautomated tools for generating unstructured meshes now exist that can create the computational nodes needed with a specified mesh density [30]. The use of increasingly finer meshes ensures not only better resolution of the structure of the flow fields but inherently more accurate [31]. However, computational times can become prohibitively lengthy if the mesh density is excessive. On the other hand, if the mesh density is insufficient, computational errors can result. In order to have high confidence in the CFD results, it is important to incrementally refine the mesh density to ensure that the calculated velocity fields converge to an acceptable residual error [32]. Careful construction of the mesh can serve to provide a compromise between high accuracy and speed of computation by prescribing variable mesh density. High-density mesh elements can be prescribed

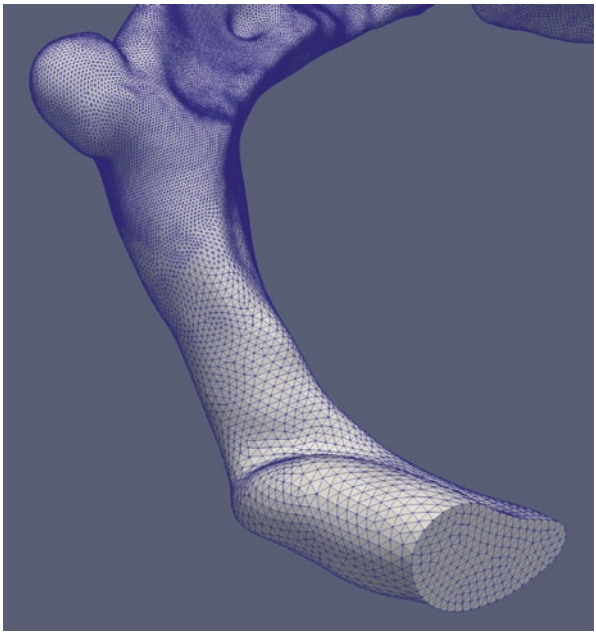

Fig. 17.4 Mesh generated through the volume defined by the surface segmented from an MRA study of the transverse and sigmoid sinus of a subject with venous diverticulum. A spatially varying mesh is defined with high mesh density proximal to and through the diverticulum and with low mesh density in the more uniform segment of anatomy

where these are most needed, such as at locations of high surface curvature or irregularity or close to the vessel wall where gradients of velocity must be determined to provide rigorous estimates of wall shear stress [33]. On the other hand, velocities in the center of low-curvature segments of a vessel are expected to vary smoothly, and low mesh densities can be used there. An example showing a spatially adaptive mesh designed to provide increased accuracy in regions requiring higher sensitivity is shown in Fig. 17.4.

Application to Vascular Disease

The great promise of methods that provide quantitative hemodynamic measures lies in the potential of those methods to serve as biomarkers for the increased likelihood of disease progression [34]. If, indeed, hemodynamic forces are drivers of disease evolution over time, it is reasonable to assume that a careful analysis of hemodynamic descriptors could serve to identify, on a patient-specific basis, individuals who are likely to show rapid disease progression and others where the condition is expected to remain stable over time. Extensive work is being actively pursued to establish the relationship between hemodynamic descriptors and disease progression. Those studies can be quite challenging in cases where the disease condition does not have high prevalence, where the disease evolution is slow and potentially occurring over decades, and where rigorous clinical outcomes – such as aneurysm rupture – need to be established. This analysis is further complicated by

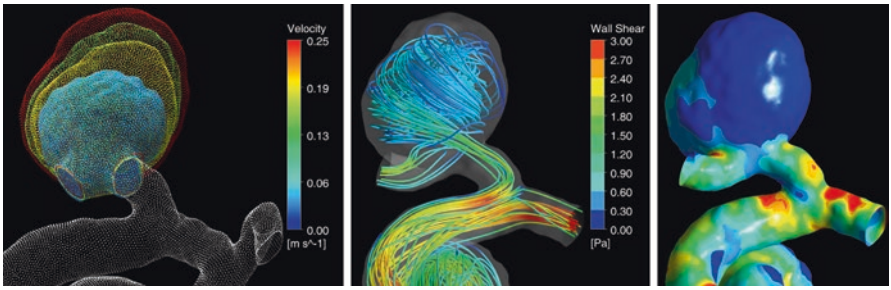

Fig. 17.5 CFD in a growing aneurysm of the anterior communicating artery. Left: four serial MRA studies show interval growth from baseline (blue) to 18-month follow-up scan (red). Center: flow streamlines generated from CFD-computed velocity field shows strong recirculating flow in the aneurysm. Right: wall shear stress map from CFD-computed velocity field shows low wall shear stress (deep blue) colocalizing with region of observed growth

the wide variety of secondary descriptors that can be, and have been, postulated to be the critical markers. These descriptors include intravascular pressure; zones of jet impingement; wall shear stress (which can be further investigated in terms of peak wss, mean wss, or OSI – the oscillating shear index which characterizes the variation of wss through the cardiac cycle); presentation and number of vortices; and the extent of the deposition of turbulent kinetic energy – to name a few [18, 35–39]. Insights into the roles of the different descriptors do not necessarily need to be based solely on clinical outcomes (such as stroke or myocardial infarction) but can be gleaned from longitudinal imaging studies where evolution of vascular geometry can be detected [19]. Figure 17.5 presents results from a study where a patient with an untreated aneurysm of the anterior communicating artery was followed with noninvasive CE-MRA at 6-month intervals for a total of four imaging sessions. The sequential studies are spatially colocalized and visualized with a transparent mesh showing a near doubling on volume of the aneurysm over an 18-month period. Also shown are the CFD-computed flow streamlines (presented for the final imaging timepoint) and the derived wall shear stress map. In this case, the region of pronounced growth is seen to colocalize with the region of low wall shear stress.

As noted above, an alternative to CFD is to directly measure the velocity field using 4D MR Flow. While that approach circumvents the need to develop the entire computational pipeline, it faces the inaccuracies of the acquisition, specifically the limited spatial and temporal resolution. These differences can be noted when comparing visual representation of streamlines from CFD with those from 4D Flow for the same geometry. Streamlines are a common method of displaying qualitative visualizations of the prevailing flow and are created at fixed points of time in the cardiac cycle by tracing out the path followed through the domain as dictated by the velocity field. To the extent that there is limited resolution of inconsistencies in the predicted velocity field, streamlines will follow irregular paths and will have variable filling of the flow domain. Figure 17.6 shows streamlines generated from a CFD simulation based on a CE-MRA acquired from a patient

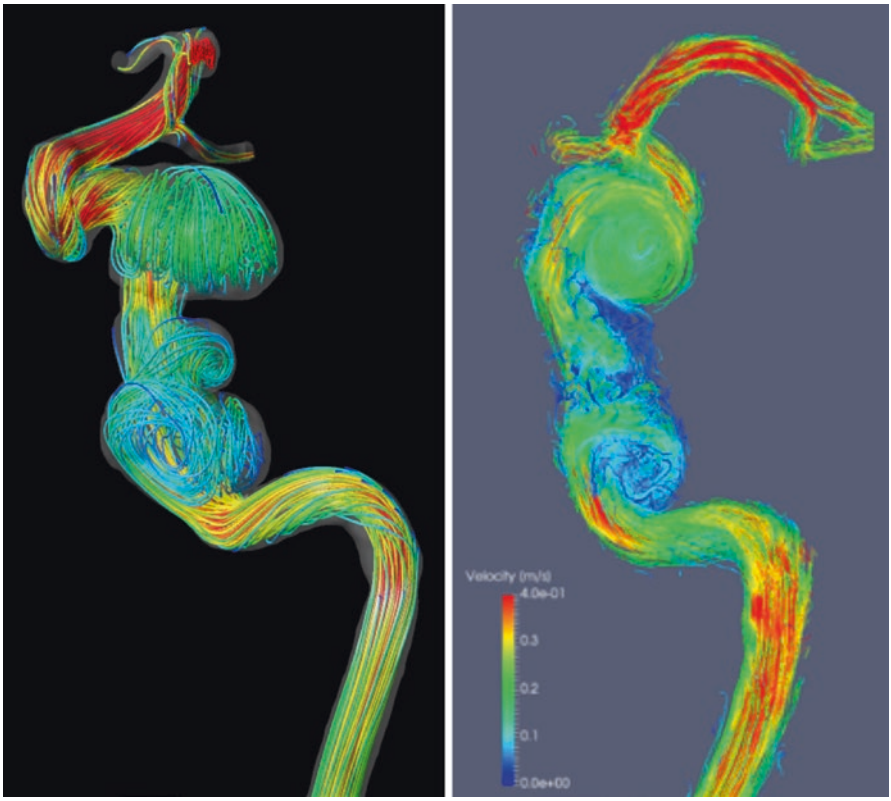

Fig. 17.6 Study of a patient with three aneurysms of the internal carotid artery comparing streamlines from CFD simulations with those from 4D Flow demonstrating that CFD is noise-free. Left: streamlines generated from the CFD-calculated velocity map based on the boundary conditions from the in vivo CE-MRA and the flow waveform measured with 2D PC-MRI in the proximal ICA. Right: streamlines generated from a 4D Flow PC-MRI study

with three aneurysms of the internal carotid artery and from a 4D Flow study on the same patient. The CFD-based streamlines are smooth and uniform, whereas the 4D Flow-based streamlines are noisy.

There is a great deal of interest in using CFD to investigate the effects of planned interventions [40]. To the extent that the intervention makes significant changes to flow conditions, this is clearly a situation where pre-treatment imaging plays little role. On the other hand, CFD can be used to estimate what the probable results of surgical interventions might be [41, 42]. The validity of such predictions, however, depends importantly on the boundary conditions that will exist following surgery. In certain cases, reasonable assumptions can be made based on considerations of normal physiology, as for example in a planned bypass procedure where it is expected that the intervention will restore normal flow to the distal organ. Other considerations include using vessel caliber of the targeted bypass implantation site as a predictor of what the likely flow into that vessel will be. In other

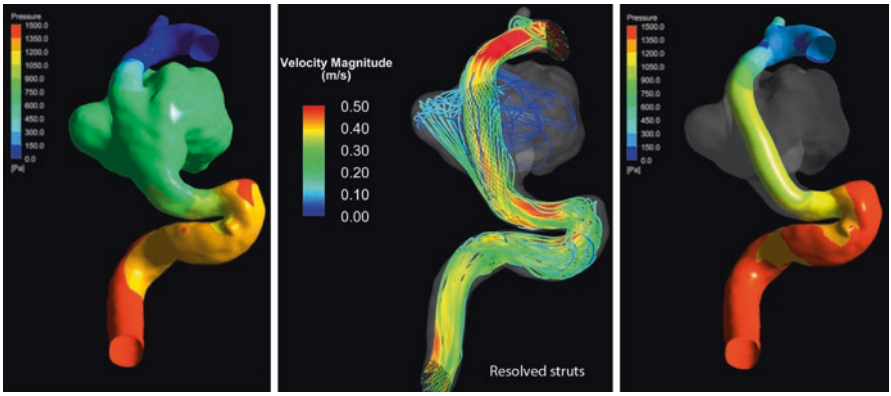

Fig. 17.7 CFD calculation of a simulation that models deployment of a flow diverter stent in a distal ICA aneurysm. Left: CFD-calculated pressure map in the untreated aneurysm. Center: streamlines calculated with modeling of the deployed flow diverter. Right: CFD-calculated pressure map for the simulated treatment

scenarios, predictive simulations are better able to incorporate the actual geometric and functional morphology that will result from intervention. Examples are simulations that have been performed to evaluate the impact of deploying different numbers of coils to treat an aneurysm [43], or others that estimate the likelihood that a flow-diverting stent deployed through a fusiform aneurysm will reduce flow into the aneurysm sac thereby promoting thrombotic occlusion of the sac [44–47]. In that case, the flow boundary conditions following treatment can be clearly defined, and the geometry of elements of the deployed stent – which is well known – can be included in the simulation. Figure 17.7 shows modeling of planned treatment in a fusiform aneurysm. Not only is CFD able to predict the pressure distribution in the presenting anatomy prior to intervention, but careful inclusion of the detailed geometry of the deployed flow-diverting stent permits prediction of the flow streamlines and pressure map in the vasculature following stent deployment. This example shows a strong reduction of flow into the aneurysmal sac through the pipeline walls.

An additional strength of CFD is to explore flow conditions across a range of conditions that are not amenable to variation in vivo [48, 49]. Vortical flow has been postulated as a contributor to audible sound in patients with pulsatile tinnitus. In vivo assessment of flow is able to establish the presence of a strong component of vorticity inflow in the bulb of the jugular vein. However, the extent to which the relationship between the geometric structure of the bulb and the total volume flow through the vein plays a role in determining the presence of flow vorticity is unknown. CFD can be performed for the given geometry but with incremental reduction of the inlet flow conditions from what presents in vivo until a flow rate where the vorticity is no longer detected. This is illustrated in

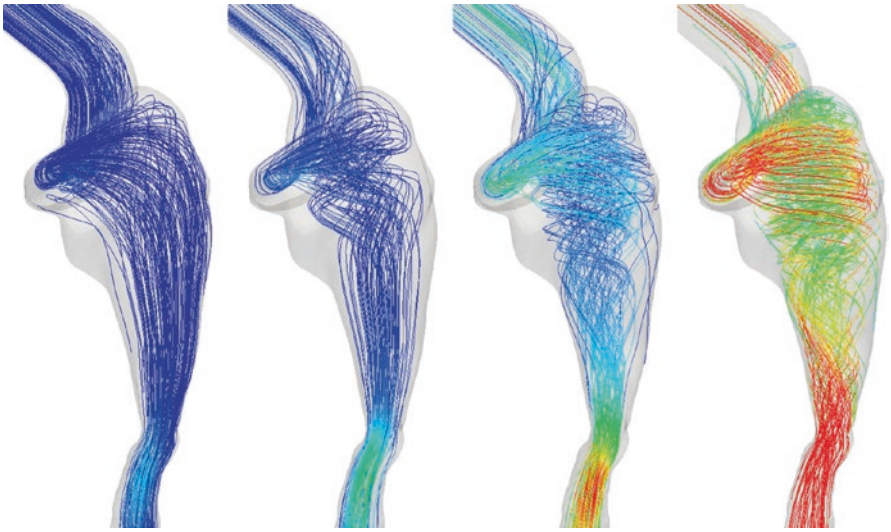

Fig. 17.8 Flow streamlines generated from CFD for flow through a patient-specific model of the jugular vein. This demonstrates the ability to explore flow conditions in simulation that do not present in vivo. Streamlines are displayed with incremental adjustment of the inlet flow from a slow flow rate on the left to the flow rate measured in vivo, on the right. A strong rotational component of flow is visualized in the jugular vein at all conditions apart from the slowest (and highly non-physiologic) flow rate on the left

Fig. 17.8. Flow streamlines were calculated for the geometry and inlet waveform, as detected from CE-MRA and 2D phase-contrast MRI, respectively, in the jugular vein of a patient with pulsatile tinnitus. In addition, the volume flow was reduced in simulation until the vortical flow disappeared showing, in this case, that the vorticity was largely dominated by the flow geometry and was only absent at very low flow rates.

The high fidelity of CFD data permits the use of advanced algorithms for extracting features of flow that are not immediately available from the calculated velocity field [50]. An additional metric that is of interest in vascular disease is the potential for flow conditions to result in intraluminal thrombus deposition [44]. A convenient metric for that is the particle residence time. Particle residence time bears some similarities to the passage of contrast material injected intra-arterially during dynamic catheter angiography runs, particularly in the late phase as the contrast washes out. It is possible to utilize the data generated by the CFD-calculated velocity field to create a visualization of what the expected wash out of material in the modeled geometry will be, and hence, in effect, display the particle residence time. Figure 17.9 is a series of estimated contrast distributions in a fusiform aneurysm of the vertebral-basilar system following complete opacification of the territory. Serial time windows show the contrast as it is transported out of the vessel.

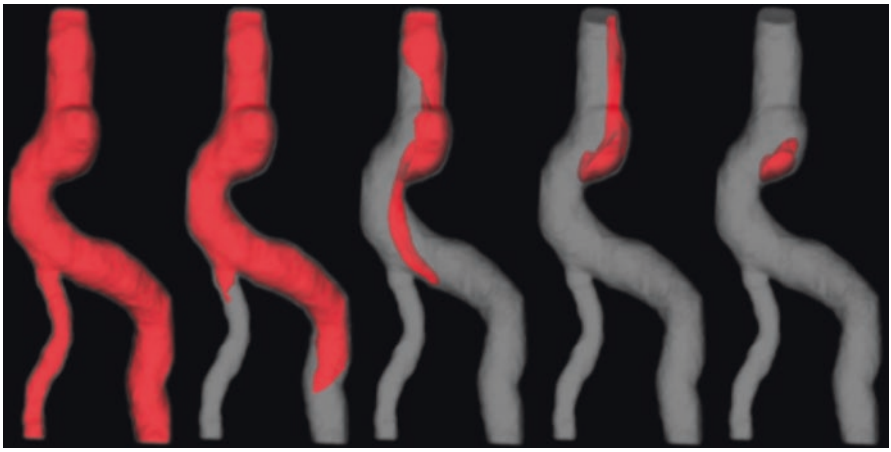

Fig. 17.9 Contrast passage through an aneurysmal segment distal to the vertebral-basilar junction. A virtual injection of contrast material is shown in red within the lumenal geometry (gray). These images estimate from the CFD-computed velocity field, the washout of contrast from full opacification (left) to late in the injection run (right) showing extended dwell time of contrast in the aneurysmal dilation

Conclusion

Computational Fluid Dynamics is a powerful methodology for providing highly accurate estimates of the hemodynamics on a patient-specific basis. This approach will remain the gold standard for defining velocity fields until in vivo imaging modalities attain greater resolution than they currently provide. CFD can be used to generate biomarkers that can be used to assess the risk posed by vascular dysfunction on a patient-specific basis. Commercial codes are available that are suitable for application to in vivo physiology. Current CFD models make important assumptions, and care should be taken when relying on CFD-generated data to evaluate the extent to which the actual in vivo conditions are consistent with the underlying assumptions. Finally, CFD presents the potential to model the hemodynamic outcomes of planned vascular revisions, providing the treating surgeon with quantitative data on which to base their treatment.

References

1. Ferziger J, Peric M. Computational methods for fluid dynamics. Berlin: Springer-Verlag; 1996.
2. Jou L, Berger S. Numerical simulation of the flow in the carotid bifurcation. Theor Comput Fluid Dyn. 1998;10:239–48.
3. Perktold K, Resch M, Florian H. Pulsatile non-Newtonian flow characteristics in a three-dimensional human carotid bifurcation model. J Biomech Eng. 1991;113(4):464–75.

4. Perktold K, Resch M, Peter RO. Three-dimensional numerical analysis of pulsatile flow and wall shear stress in the carotid artery bifurcation. J Biomech. 1991;24(6):409–20.
5. Perktold K, Thurner E, Kenner T. Flow and stress characteristics in rigid walled and compliant carotid artery bifurcation models. Med Biol Eng Comput. 1994;32(1):19–26.
6. Stroud JS, Berger SA, Saloner D. Numerical analysis of flow through a severely stenotic carotid artery bifurcation. J Biomech Eng. 2002;124(1):9–20.
7. Dyverfeldt P, Bissell M, Barker AJ, Bolger AF, Carlhall CJ, Ebbers T, et al. 4D flow cardiovascular magnetic resonance consensus statement. J Cardiovasc Magn Reson. 2015;17:72.
8. Garcia J, van der Palen RLF, Bollache E, Jarvis K, Rose MJ, Barker AJ, et al. Distribution of blood flow velocity in the normal aorta: effect of age and gender. J Magn Reson Imaging. 2018;47(2):487–98.
9. Cebral JR, Yim PJ, Lohner R, Soto O, Choyke PL. Blood flow modeling in carotid arteries with computational fluid dynamics and MR imaging. Acad Radiol. 2002;9(11):1286–99.
10. Dempere-Marco L, Oubel E, Castro M, Putman C, Frangi A, Cebral J. CFD analysis incorporating the influence of wall motion: application to intracranial aneurysms. Med Image Comput Comput Assist Interv. 2006;9(Pt 2):438–45.
11. Lantz J, Renner J, Karlsson M. Wall shear stress in a subject specific human aorta — influence of fluid-structure interaction. J Appl Mech. 2011;3:759–78.
12. Gijsen FJ, van de Vosse FN, Janssen JD. The influence of the non-Newtonian properties of blood on the flow in large arteries: steady flow in a carotid bifurcation model. J Biomech. 1999;32(6):601–8.
13. Chien KY. Predictions of channel and boundary-layer flows with a low-Reynolds-number turbulence model. AIAA J. 1982;20(1):33–8.
14. Varghese SS, Frankel SH, Fischer PF. Direct numerical simulation of stenotic flows. Part I steady flow. J Fluid Mech. 2007;582:253–80.
15. Ferziger J. Large eddy numerical simulations of turbulent flows. AIAA J. 1977;15(9):1261–7.
16. Ghosal S, Lund T, Moin P, Selvoll K. A dynamic localization model for large-eddy simulation of turbulent flows. J Fluid Mech. 1995;286:229.
17. Long Q, Xu XY, Bourne M, Griffith TM. Numerical study of blood flow in an anatomically realistic aorto-iliac bifurcation generated from MRI data. Magn Reson Med. 2000;43(4):565–76.
18. Cebral JR, Duan X, Chung BJ, Putman C, Aziz K, Robertson AM. Wall mechanical properties and hemodynamics of unruptured intracranial aneurysms. AJNR Am J Neuroradiol. 2015;36(9):1695–703.
19. Boussel L, Rayz V, McCulloch C, Martin A, Acevedo-Bolton G, Lawton M, et al. Aneurysm growth occurs at region of low wall shear stress: patient-specific correlation of hemodynamics and growth in a longitudinal study. Stroke. 2008;39(11):2997–3002.
20. Kim HJ, Vignon-Clementel IE, Figueroa CA, LaDisa JF, Jansen KE, Feinstein JA, et al. On coupling a lumped parameter heart model and a three-dimensional finite element aorta model. Ann Biomed Eng. 2009;37(11):2153–69.
21. Kung EO, Les AS, Medina F, Wicker R, McConnell MV, Taylor CA. In vitro validation of finite-element model of AAA hemodynamics incorporating realistic outlet boundary conditions. J Biomech Eng. 2011;133:1003–11.
22. Kung EO, Taylor CA. Development of a physical windkessel module to re-create in-vivo vascular flow impedance for in-vitro experiments. Cardiovasc Eng Technol. 2011;2(1):2–14.
23. Taylor CA, Figueroa CA. Patient-specific modeling of cardiovascular mechanics. Annu Rev Biomed Eng. 2009;11:109–34.
24. Les AS, Shadden SC, Figueroa CA, Park JM, Tedesco MM, Herfkens RJ, et al. Quantification of hemodynamics in abdominal aortic aneurysms during rest and exercise using magnetic resonance imaging and computational fluid dynamics. Ann Biomed Eng. 2010;38(4):1288–313.
25. Romarowski RM, Lefieux A, Morganti S, Veneziani A, Auricchio F. Patient-specific CFD modelling in the thoracic aorta with PC-MRI-based boundary conditions: a least-square three-element Windkessel approach. Int J Numer Method Biomed Eng. 2018;34(11):e3134.

26. Pirola S, Cheng Z, Jarral OA, O'Regan DP, Pepper JR, Athanasiou T, et al. On the choice of outlet boundary conditions for patient-specific analysis of aortic flow using computational fluid dynamics. J Biomech. 2017;60:15–21.
27. Lorensen W, Cline HE. Marching cubes: a high resolution 3D surface construction algorithm. ACM SIGGRAPH Comput Graph. 1987;21:163.
28. Cebral JR, Lohner R, Choyke PL, Yim PJ. Merging of intersecting triangulations for finite element modeling. J Biomech. 2001;34(6):815–9.
29. Jeong W, Seong J. Comparison of effects on technical variances of computational fluid dynamics (CFD) software based on finite element and finite volume methods. Int J Mech Sci. 2014;78:19–26.
30. Berg P, Janiga G, Thévenin D. Detailed comparison of numerical flow predictions in cerebral aneurysms using different CFD software 2012.
31. Zhou Y, Lee C, Wang J. The computational fluid dynamics analyses on hemodynamic characteristics in stenosed arterial models. J Healthc Eng. 2018;2018:4312415.
32. Khan MO, Valen-Sendstad K, Steinman DA. Narrowing the expertise gap for predicting intracranial aneurysm hemodynamics: impact of solver numerics versus mesh and time-step resolution. AJNR Am J Neuroradiol. 2015;36(7):1310–6.
33. Valen-Sendstad K, Piccinelli M, Steinman DA. High-resolution computational fluid dynamics detects flow instabilities in the carotid siphon: implications for aneurysm initiation and rupture? J Biomech. 2014;47(12):3210–6.
34. Liang L, Steinman DA, Brina O, Chnafa C, Cancelliere NM, Pereira VM. Towards the clinical utility of CFD for assessment of intracranial aneurysm rupture - a systematic review and novel parameter-ranking tool. J Neurointerv Surg. 2019;11(2):153–8.
35. Botnar R, Rappitsch G, Scheidegger MB, Liepsch D, Perktold K, Boesiger P. Hemodynamics in the carotid artery bifurcation: a comparison between numerical simulations and in vitro MRI measurements. J Biomech. 2000;33(2):137–44.
36. Burleson A, Strother C, Turitto V. Computer modeling of intracranial saccular and lateral aneurysms for the study of their hemodynamics. Neurosurgery. 1995;37(4):774–84.
37. Burleson AC, Turitto VT. Identification of quantifiable hemodynamic factors in the assessment of cerebral aneurysm behavior. On behalf of the Subcommittee on Biorheology of the Scientific and Standardization Committee of the ISTH. Thromb Haemost. 1996;76(1):118–23.
38. Cebral JR, Mut F, Weir J, Putman CM. Association of hemodynamic characteristics and cerebral aneurysm rupture. AJNR Am J Neuroradiol. 2011;32(2):264–70.
39. Jou LD, Mawad ME. Timing and size of flow impingement in a giant intracranial aneurysm at the internal carotid artery. Med Biol Eng Comput. 2011;49(8):891–9.
40. Cebral JR, Mut F, Raschi M, Scrivano E, Ceratto R, Lylyk P, et al. Aneurysm rupture following treatment with flow-diverting stents: computational hemodynamics analysis of treatment. AJNR Am J Neuroradiol. 2011;32(1):27–33.
41. Acevedo-Bolton G, Jou LD, Dispensa BP, Lawton MT, Higashida RT, Martin AJ, et al. Estimating the hemodynamic impact of interventional treatments of aneurysms: numerical simulation with experimental validation: technical case report. Neurosurgery. 2006;59(2):E429–30; author reply E-30.
42. Aneis M, Stancampiana AP, Wakhloo AJ, Lieber BB. Modeling of flow in a straight stented and non-stented side wall aneurysm model. J Biomech Eng. 1997;119:206–12.
43. Groden C, Laudan J, Gatchell S, Zeumer H. Three-dimensional pulsatile flow simulation before and after endovascular embolization of a terminal cerebral aneurysm. J Cereb Blood Flow Metab. 2001;21:1464–71.
44. Bluestein D, Niu L, Schoephoerster RT, Dewanjee MK. Steady flow in an aneurysm model: correlation between fluid dynamics and blood platelet deposition. J Biomech Eng. 1996;118:280–6.
45. Hirabayashi M, Ohta M, Rufenacht DA, Chopard B. Lattice Boltzmann analysis of the flow reduction mechanism in stented cerebral aneurysms for the endovascular treatment. Lect Notes Comput Sci. 2003;2657:1044–53.

46. Hirabayashi M, Ohta M, Rufenacht DA, Chopard B. Characterization of flow reduction properties in an aneurysm due to a stent. Phys Rev E Stat Nonlinear Soft Matter Phys. 2003;68(2):1918.
47. Hodis S, Ding YH, Dai D, Lingineni R, Mut F, Cebral J, et al. Relationship between aneurysm occlusion and flow diverting device oversizing in a rabbit model. J Neurointerv Surg. 2016;8(1):94–8.
48. Taylor CA, Draney J, Ku DN, Parker D, Steele BN, Wang K, et al. Predictive medicine: computational techniques in therapeutic decision-making. Comput Aided Surg. 1999;4:231–47.
49. Jou LD, Quick CM, Young WL, Lawton MT, Higashida R, Martin A, et al. Computational approach to quantifying hemodynamic forces in giant cerebral aneurysms. AJNR Am J Neuroradiol. 2003;24(9):1804–10.
50. Cebral JR, Mut F, Chung BJ, Spelle L, Moret J, van Nijnatten F, et al. Understanding angiography-based aneurysm flow fields through comparison with computational fluid dynamics. AJNR Am J Neuroradiol. 2017;38(6):1180–6.

Index

C. Yuan et al. (eds.), *Vessel Based Imaging Techniques*,
https://doi.org/10.1007/978-3-030-25249-6